

Refinery Integration of By-Products from Coal-Derived Jet Fuels

FINAL REPORT

September 18, 2003 – March 31, 2008

Caroline E. Burgess Clifford, André Boehman, Chunshan Song,
Bruce Miller, Gareth Mitchell

Date Issued: July 25, 2008

Grant DE-FC26-03NT41828

The Pennsylvania State University
The Energy Institute
C211 Coal Utilization Laboratory
University Park, PA 16802

DISCLAIMER

This report was prepared as an account of work sponsored by an agency of the United States Government. Neither the United States Government nor any agency thereof, nor any of their employees, makes any warranty, express or implied, or assumes any legal liability or responsibility for the accuracy, completeness, or usefulness of any information, apparatus, product, or process disclosed, or represents that its use would not infringe privately owned rights. Reference herein to any specific commercial product, process, or service by trade name, trademark, manufacturer, or otherwise does not necessarily constitute or imply its endorsement, recommendation, or favoring by the United States Government or any agency thereof. The views and opinions of authors expressed herein do not necessarily state or reflect those of the United States Government or any agency thereof.

Abstract

The final report summarizes the accomplishments toward project goals during length of the project. The goal of this project was to integrate coal into a refinery in order to produce coal-based jet fuel, with the major goal to examine the products other than jet fuel. These products are in the gasoline, diesel and fuel oil range and result from coal-based jet fuel production from an Air Force funded program.

The main goal of Task 1 was the production of coal-based jet fuel and other products that would need to be utilized in other fuels or for non-fuel sources, using known refining technology. The gasoline, diesel fuel, and fuel oil were tested in other aspects of the project. Light cycle oil (LCO) and refined chemical oil (RCO) were blended, hydrotreated to removed sulfur, and hydrogenated, then fractionated in the original production of jet fuel. Two main approaches, taken during the project period, varied where the fractionation took place, in order to preserve the life of catalysts used, which includes 1) fractionation of the hydrotreated blend to remove sulfur and nitrogen, followed by a hydrogenation step of the lighter fraction, and 2) fractionation of the LCO and RCO before any hydrotreatment. Another aspect was to hydrotreat decant oil for testing of the delayed coker. The yield and quality of jet fuel and the quality of all fuels were better when hydrotreating the whole blend to remove sulfur and nitrogen and fractionating gasoline and jet fuel for further hydrogenation. When fractionating the RCO and LCO before any hydrotreatment, the yield of jet fuel and diesel fuel decreased, and the yield of the fuel oil increased and was a low quality.

Task 2 involved assessment of the impact of refinery integration of JP-900 production on gasoline and diesel fuel. Fuel properties, ignition characteristics and engine combustion of model fuels and fuel samples from pilot-scale production runs were characterized. The model fuels used to represent the coal-based fuel streams were blended into full-boiling range fuels to simulate the mixing of fuel streams within the refinery to create potential “finished” fuels. The representative compounds of the coal-based gasoline were cyclohexane and methyl cyclohexane, and for the coal-base diesel fuel they were fluorine and phenanthrene. Both the octane number (ON) of the coal-based gasoline and the cetane number (CN) of the coal-based diesel were low, relative to commercial fuels (~60 ON for coal-based gasoline and ~ 20 CN for coal-based diesel fuel). Therefore, the allowable range of blending levels was studied where the blend would

achieve acceptable performance. However, in both cases of the coal-based fuels, their ignition characteristics may make them ideal fuels for advanced combustion strategies where lower ON and CN are desirable. The ignition characteristics and reaction pathways were examined for these fuels in a modified octane rating engine used as a form of rapid compression machine and in an ignition quality tester (IQT). Methyl cyclohexane was observed to have similar ignition temperature as *n*-heptane and to exhibit two-stage ignition under a narrow range of test conditions. The impact of the coal-derived diesel fuel on ignition limits its use to a 5 vol.% blend in the commercial diesel fuel. Studies of the combustion characteristics at this blend level showed modest impact on emissions, with a slight increase in NO_x emissions and an increase in particle number density. Overall, these coal-based streams can be blended into conventional fuel streams at between as much as 20% for the coal-based gasoline and at as much as 5% for the coal-based diesel fuel while maintaining acceptable performance.

Task 3 was designed to develop new approaches for producing ultra clean fuels and value-added chemicals from refinery streams involving coal as a part of the feedstock. It consisted of the following three parts: 1) desulfurization and denitrogenation which involves both new adsorption approach for selective removal of nitrogen and sulfur and new catalysts for more effective hydrotreating and the combination of adsorption denitrogenation with hydrodesulfurization; 2) saturation of two-ring aromatics that included new design of sulfur-resistant noble-metal catalysts for hydrogenation of naphthalene and tetralin in middle distillate fuels, and 3) value-added chemicals from naphthalene and biphenyl, which aimed at developing value-added organic chemicals from refinery streams such as 2,6-dimethylnaphthalene and 4,4'-dimethylbiphenyl as precursors to advanced polymer materials. Major advances were achieved in this project in designing the catalysts and sorbent materials, and in developing fundamental understanding.

The objective of Task 4 was to evaluate the effect of introducing coal into an existing petroleum refinery on the fuel oil product, specifically trace element emissions. Activities performed to accomplish this objective included analyzing two petroleum-based commercial heavy fuel oils (*i.e.*, No. 6 fuel oils) as baseline fuels and three co-processed fuel oils, characterizing the atomization performance of a No. 6 fuel oil, measuring the combustion performance and emissions of the five fuels, specifically major, minor, and trace elements when fired in a watertube boiler designed for natural gas/fuel oil, and determining the boiler

performance when firing the five fuels. Two different co-processed fuel oils were tested: one that had been partially hydrotreated, and the other a product of fractionation before hydrotreating. The partially hydrotreated fuel oil performed similarly or better than fuel oil No. 6, but the fuel oil from RCO fractionation performed very poorly relative to No. 6 fuel oil. The testing illustrated that the introduction of coal-derived liquids can introduce trace metals of environmental concern into liquid hydrocarbon products produced during co-processing with petroleum derived liquids. This is evident by the presence of trace elements in the emissions produced during combustion of the co-processed “fuel oil” fraction as compared to emissions produced during combustion of No. 6 fuel oil. The amount of Hg and As emitted ($\text{lb}/10^{12} \text{ Btu}$) was found to be 10 times greater than two of the No. 6 fuel oils. A majority of the Hg emitted by the co-processed fuels was concentrated in the particulate phase, whereas, the Hg in the fuel oil occurred in the gas phase as oxidized Hg. Pb emissions were also increased over a 100 times during combustion of the co-processed fuel.

Task 5 focused on examining refining methods that would utilize coal and produce thermally stable jet fuel, included delayed coking and solvent extraction. Delayed coking was done on blends of decant oil and coal, with the goal to produce a premium carbon product and liquid fuels. Coking was done on bench scale and large laboratory scale cokers. Two coals were examined for co-coking, using Pittsburgh seam coal and Marfork coal product. Reactions in the large, laboratory scaled coker were reproducible in yields of products and in quality of products. While the co-coke produced from both coals was of sponge coke quality, minerals left in the coke made it unacceptable for use as anode or graphite grade filler. Liquids generated by the process contained ~5-10% jet fuel, but the liquids mainly boiled in the fuel oil range, indicating further processing will need to be done to make greater quantities and quality of jet fuel. The liquids were fractionated to make a pitch material. The pitch material generated had similarities to other pitches, but more work was needed to produce a pitch similar to the viscosity and molecular weight of commercial pitches. Hydrotreatment of the decant oil prior to delayed coking improved the liquid quality and the coke quality slightly. Coal extraction using LCO provided extraction yields of ~50-70%. Based on solubility parameters, LCO and decant oil are good solvents for extraction of medium rank coals.

Table of Contents

Disclaimer.....	ii
Abstract	iii
Introduction	x
Executive Summary.....	x
Experimental.....	xiii
Results and Discussion	xiii
Conclusions	xiii
Technical Discussion.....	1
Background.....	1
Objectives.....	3
Task 1. Pilot-Scale Fuel Production at PARC	5
1.1 Introduction	5
1.2 Experimental	6
1.2.1 LCO, RCO, and Decant Oil Procurement	6
1.2.2 Catalyst Preparation	7
1.2.2.1 Hydrotreatment of RCO:LCO 1:1 Ratio	7
1.2.2.1.1 Hydrotreatment to Remove Sulfur and Nitrogen	7
1.2.2.1.2 Hydrotreatment to Hydrogenate Two-Ring Aromatics.....	7
1.2.2.2 Hydrotreatment of Decant Oil.....	9
1.3 Results and Discussion.....	11
1.3.1 Processing of RCO and LCO Blends for Jet Fuel and By-Product Gasoline, Diesel, and Fuel Oil.....	11
1.3.1.1 First Run: Hydrotreatment, Distillation, and Hydrogenation	11
1.3.1.1.1 Hydrotreating to Remove Sulfur and Nitrogen	11
1.3.1.1.2 Distillation to separate heavy fractions	12
1.3.1.1.3 Hydrogenation of Jet Fuel/Gasoline and Distillation of Products.....	12
1.3.1.2 Second Run: Distillation of RCO and LCO, Hydrotreatment	12
1.3.1.2.1 Distillation of RCO and LCO	12
1.3.1.2.2 Hydrotreatment of Light Fraction	13
1.3.1.2.3 Hydrogenation of Light Fraction	13
1.3.1.2.4. Comparison of Two Jet Fuel Production Runs	13
1.3.2 Hydrotreatment of Decant Oil.....	14
Task 2. Evaluation of Coal-Based Gasoline and Diesel Products in IC Engines and Related Studies	17
2.1 Impact on Gasoline Quality and Performance.....	17
2.1.1 Preparation of Laboratory and Instrumentation.....	17
2.1.2 Impact on Chemical and Physical Properties	21
2.1.3 Impact on SI Engine Emissions and Performance.....	25
2.2 Impact on Diesel Fuel Quality and Performance.....	34
2.2.1 Acquisition, Installation, and Instrumentation of Ignition Test Equipment	34
2.2.2 Development of Analytical Methods and Test Procedures	34
2.2.3 Evaluation of Capabilities and Needs for Supplemental Measurements and Analyses	34

2.2.4 Impact on Chemical and Physical Properties	35
2.2.5 Impact on CI Engine Emissions and Performance	41
2.3 Conclusions	70
Task 3. Desulfurization, Denitrogenation, Saturation of Aromatics, Chemicals from Coal	71
3.1 Desulfurization and Denitrogenation	71
3.1.1 Experimental	72
3.1.1.1 Adsorptive desulfurization and denitrogenation	72
3.1.1.2 Adsorptive desulfurization and denitrogenation of LCO	74
3.1.1.3 Unsupported Mo sulfide catalysts with promoters	75
3.1.2 Results and Discussion	75
3.1.2.1 Adsorption on Zeolite-based Adsorbent	75
3.1.2.2 Adsorption on Nickel-based Adsorbent	79
3.1.2.3 Adsorption on Activated Alumina	80
3.1.2.4 Adsorption on activated carbon	82
3.1.2.5 Adsorption of light cycle oil (LCO) on activated carbon	83
3.1.2.6 Hydrotreating of LCO treated by adsorption	86
3.1.2.7 Hydrodesulfurization of 4,6-DMDBT	87
3.1.2.8 Development of unsupported Mo sulfide catalysts for HDS	93
3.1.2.8.1 Comparison of unsupported Mo sulfide catalysts with commercial catalysts	93
3.1.2.8.2 The promoter effects on HDS over unsupported Mo sulfide catalysts	97
3.1.2.8.3 Comparison between unsupported Mo sulfide catalysts	97
3.1.3 Summary	100
3.1.3.1 Adsorptive desulfurization and denitrogenation	100
3.1.3.2 Adsorptive desulfurization and denitrogenation of LCO	101
3.1.3.3 Hydrodesulfurization of 4,6-DMDBT	101
3.1.3.4 Development of unsupported Mo sulfide catalysts for HDS	102
3.2 Saturation of Two-Ring Aromatics	102
3.2.1 Experimental	103
3.2.1.1 Preparation and Screening of Zeolite-supported Pd and Pt Catalysts	103
3.2.1.2 Catalytic Preparation for Detailed Catalytic Study	107
3.2.1.3 Catalytic evaluation in hydrogenation experiments	109
3.2.1.4 Catalyst characterization	110
3.2.2 Results and Discussion	111
3.2.2.1 Effect of Support Acidity	111
3.2.2.2 Effect of Preparation Method	112
3.2.2.3 Effect of Palladium Precursor	114
3.2.2.4 Effect of Support Type	115
3.2.2.5 Poisoning effect of different sulfur compounds	120
3.2.2.6 Hydrogenation of tetralin over Pd on various types of Elite	124
3.2.2.6.1 Effect of elite type	124
3.2.2.6.2 Effect of silica coating	125
3.2.2.6.3 Effect of hybrid catalysts	129
3.2.2.7 Catalyst Characterization	132
3.2.2.7.1 SEM image of catalysts prepared	132
3.2.2.7.2 Temperature programmed reduction of catalysts	135
3.2.2.7.3 Temperature programmed desorption of catalysts	138
3.2.3 Summary	138
3.3 Value-Added Chemicals from Naphthalene	140
3.3.1 Experimental	140
3.3.1.1 Modification of ZSM 5 using iron	140
3.3.1.2 Catalyst preparation	140
3.3.1.3 Synthesis of magnesium containing AlPO-11 by dry gel conversion	141
3.3.2 Results and Discussion	145
3.3.2.1 Methylation of 2-MN with methanol	145

3.3.2.2 Methylation of 4-MBP with methanol	151
3.3.2.3 Synthesis and Evaluation of MAPO-11 for 2 MN- with methanol	155
3.3.2.4 Additional Synthesis and Characterization of Fe-ZSM-5 for 2-MN	160
methlyation	160
3.3.3 Summary	164
Task 4. Evaluation of Coal-Based Fuel Oil Products	165
4.1 Introduction	165
4.2 No. 6 Fuel Oil and Co-Processed Fuel Oil Analyses	167
4.2.1 Trace Elemental Analysis	170
4.2.2.1 Mercury in Fuel Oil	171
4.2.2 Trace Element Analyses Results and Discussion	174
4.2.2.1 Commercial Laboratories	174
4.2.2.2 Microwave Digestion Technique	175
4.2.2.3 EPA 3052	176
4.2.2.4 Evaluation of LECO Mercury Analyzer for Liquid Hydrocarbons	177
4.2.3 Summary of Fuel Oil Element Analysis	178
4.3 Fuel Atomization	179
4.4 Watertube Boiler Combustion Tests	184
4.4.1 Description of Research Boiler, Ancillary Equipment, and Testing Procedures	184
4.4.2 Combustion Testing	187
4.4.2.1 Year 1	187
4.4.2.2 Year 2	188
4.4.2.3 Year 3	190
4.4.3 Trace Element Emissions Testing of No. 6 Fuel Oils and Co-Processed Fuel Oils	195
4.4.3.1 Sampling Procedure and Analytical Methodology	197
4.4.3.2 Results and Discussion	198
4.5 Conclusions	222
4.6 Miscellaneous Activities	223
4.6.1 In-Furnace Camera	223
4.6.2 Upgrading Data Acquisition System	224
4.7 Acknowledgments	224
Task 5. Pitch and Coke Material	225
5.1 Sample Procurement and Preparation	225
5.1.1 Experimental	227
5.1.2 Results and Discussion	229
5.1.3 Conclusions	229
5.2 Co-Coking of Coal and Heavy Petroleum Stream	231
5.2.1 Co-Coking Runs Using the Pittsburgh EI-186) and Marfork (EI-187) Coal Products	231
5.2.1.1 Experimental	232
5.2.1.2 Results and Discussion	236
5.2.2 A Statistical Consideration of the Chemistry of Co-coking Liquids	238
5.2.2.1 Results and Discussion	240
5.2.2.2 Conclusions	247
5.3 Analysis of Co-coking Coke	248
5.3.1 Petrographic Methods Applied to Delayed Coke	248
5.3.2 Co-coking with 30% Coal Additions	263
5.3.2.1 Results and Discussion	264
5.3.3.2 Conclusions	268
5.4 Manufacture and Testing of Carbon Artifacts	268
5.4.1 Evaluation of Co-coke as Carbon Filler for Anodes	269
5.4.1.1 Quality of Calcined Co-coke	270
5.4.1.2 Quality of Test Anodes Using Co-coke	272
5.4.1.2.1 Experimental	273
5.4.2.2.2 Results and Discussion	276

5.4.2.2.3 Conclusions.....	277
5.4.2 Evaluation of Co-coke as a Feedstock for Graphite	281
5.4.2.1 Calcination	281
5.4.2.2 Graphitization.....	284
5.4.2.2.1 Results and Discussion	287
5.4.2.2.2 Conclusions.....	293
5.5 Analysis of Co-Coking Binder Pitch	295
5.5.1 Experimental	295
5.5.2 Results and Discussion.....	303
5.5.3 Conclusions and Future Work.....	345
5.6 Deeply Hydrotreated Decant Oil Reactions: Characterization of petroleum cokes generated from tubing bomb by X-Ray Diffraction and CTE	347
5.6.1 Feedstock Characterization	347
5.6.1.1 Experimental	347
5.6.1.2 Results and Discussion.....	365
5.6.1.2.1 Characterization of Decant Oil and Hydrotreated Derivatives	348
5.6.1.2.2 Characterization of Coal	363
5.6.2 Evaluation of Co-cokes Generated from Hydrotreated Decant Oil and Coal.....	364
5.6.3 Evaluation of Liquids from Co-coking.....	374
5.6.3.1 Experimental.....	374
5.6.3.2 Results and Discussion.....	375
5.6.3.3 Conclusions.....	383
5.7 Production of Coal Tar from Coal Extracts.....	385
5.7.1 Experimental	386
5.7.2 Results and Discussion.....	393
5.8 Solubility Prediction of Coals in Some Petroleum Streams	402
5.8.1 Experimental	403
5.8.2 Results and Discussion.....	405
5.8.3 Conclusions.....	410
References	411
Appendices	431
Appendix 4-A.....	432
Appendix 4-B.....	435
Appendix 4-C.....	460
Appendix 5-A.....	462

Refinery Integration of By-Products from Coal-Derived Jet Fuels

Introduction

This program investigated the fate of each major product from a refinery complex, except jet fuel, resulting from the refinery integration of coal-derived jet fuel production via a combined RCO/LCO strategy by studying the physical and chemical nature of all products that are perturbed by introduction of coal components into the refinery.

The impact of the proposed research provided the scientific and fundamental engineering basis to integrate the production of coal-based jet fuel into existing refinery operations in a time frame consistent with availability and economic forecasts related to petroleum-derived as opposed to coal-based feedstocks. The results of these studies lead to the integration of all non-jet-fuel streams into current refinery operations in concert with desired production of coal-based jet fuel engine testing toward the end of the first decade of the new century. For successful utilization of coal-based jet fuels all non-jet-fuel components must fit existing and future product stream specifications.

Executive Summary

Penn State has been working for more than a decade on the development of an advanced, thermally stable, coal-based jet fuel, JP-900. Two process routes to JP-900 have been identified, one involving the hydrotreating of blends of refined chemical oil (RCO, a by-product of the coal tar industry) with light cycle oil (LCO), and the other involving the addition of coal to delayed cokers. However, no refinery is operated for the primary purpose of making jet fuel. The conversion of the jet fuel section of a refinery to production of coal-based JP-900 would necessarily impact the quantity and quality of the other refinery products, such as gasoline, diesel fuel, fuel oil, and coke. The overall objective of this project was to examine the characteristics and quality of the streams *other than the jet fuel*, and to determine the effect those materials would have on other unit operations in the refinery.

The final report documents the activities of project, which was funded for only three out of the four years of the proposed activities, so the overall goals of the project were not in a final state. Our collateral work on jet fuel, funded by the Air Force Office of Scientific Research, is focused exclusively on that product. Thus as we branched out into the study of the other refinery streams, under the present contract, much of the effort of the project was devoted to the evaluation of product streams to streamline operations.

The overall project involves pilot-scale production of materials at Intertek PARC Technical Services (Harmarville, PA). The coal-based gasoline and diesel fuel was evaluated in

appropriate internal combustion engines. Desulfurization, denitrogenation, and saturation of aromatics were tested. There was also a component to examine the production of high-value aromatic compounds. The coal-based fuel oils were tested in a research boiler. The pitch and coke co-coking from runs using different coals were evaluated. These interrelated activities are designed to evaluate the full range of products from coal-based thermally stable jet fuel production and to lead toward process integration in existing refineries.

The main goal of Task 1 was the production of coal-based jet fuel and other products that would need to be utilized in other fuels or for non-fuel sources, using known refining technology. The gasoline, diesel fuel, and fuel oil were tested in other aspects of the project. Light cycle oil (LCO) and refined chemical oil (RCO) were blended, hydrotreated to remove sulfur, and hydrogenated, then fractionated in the original production of jet fuel. Two main approaches, taken during the project period, varied where the fractionation took place, in order to preserve the life of catalysts used, which includes 1) fractionation of the hydrotreated blend to remove sulfur and nitrogen, followed by a hydrogenation step of the lighter fraction, and 2) fractionation of the LCO and RCO before any hydrotreatment. Another aspect was to hydrotreat decant oil for testing of the delayed coker. The yield and quality of jet fuel and the quality of all fuels were better when hydrotreating the whole blend to remove sulfur and nitrogen and fractionating gasoline and jet fuel for further hydrogenation. When fractionating the RCO and LCO before any hydrotreatment, the yield of jet fuel and diesel fuel decreased, and the yield of the fuel oil increased and was a low quality.

Task 2 involved assessment of the impact of refinery integration of JP-900 production on gasoline and diesel fuel. Fuel properties, ignition characteristics and engine combustion of model fuels and fuel samples from pilot-scale production runs were characterized. The model fuels used to represent the coal-based fuel streams were blended into full-boiling range fuels to simulate the mixing of fuel streams within the refinery to create potential “finished” fuels. The representative compounds of the coal-based gasoline were cyclohexane and methyl cyclohexane, and for the coal-based diesel fuel they were fluorine and phenanthrene. Both the octane number (ON) of the coal-based gasoline and the cetane number (CN) of the coal-based diesel were low, relative to commercial fuels (~60 ON for coal-based gasoline and ~ 20 CN for coal-based diesel fuel). Therefore, the allowable range of blending levels was studied where the blend would achieve acceptable performance. However, in both cases of the coal-based fuels, their ignition characteristics may make them ideal fuels for advanced combustion strategies where lower ON and CN are desirable. The ignition characteristics and reaction pathways were examined for these fuels in a modified octane rating engine used as a form of rapid compression machine and in an ignition quality tester (IQT). Methyl cyclohexane was observed to have similar ignition temperature as *n*-heptane and to exhibit two-stage ignition under a narrow range of test conditions. The impact of the coal-derived diesel fuel on ignition limits its use to a 5 vol.% blend in the commercial diesel fuel. Studies of the combustion characteristics at this blend level showed modest impact on emissions, with a slight increase in NO_x emissions and an increase in particle number density. Overall, these coal-based streams can be blended into conventional fuel streams at between as much as 20% for the coal-based gasoline and at as much as 5% for the coal-based diesel fuel while maintaining acceptable performance.

Task 3 was designed to develop new approaches for producing ultra clean fuels and value-added chemicals from refinery streams involving coal as a part of the feedstock. It consisted of the following three parts: 1) desulfurization and denitrogenation which involves both new adsorption approach for selective removal of nitrogen and sulfur and new catalysts for

more effective hydrotreating and the combination of adsorption denitrogenation with hydrodesulfurization; 2) saturation of two-ring aromatics that included new design of sulfur-resistant noble-metal catalysts for hydrogenation of naphthalene and tetralin in middle distillate fuels, and 3) value-added chemicals from naphthalene and biphenyl, which aimed at developing value-added organic chemicals from refinery streams such as 2,6-dimethylnaphthalene and 4,4'-dimethylbiphenyl as precursors to advanced polymer materials. Major advances were achieved in this project in designing the catalysts and sorbent materials, and in developing fundamental understanding.

The objective of Task 4 was to evaluate the effect of introducing coal into an existing petroleum refinery on the fuel oil product, specifically trace element emissions. Activities performed to accomplish this objective included analyzing two petroleum-based commercial heavy fuel oils (*i.e.*, No. 6 fuel oils) as baseline fuels and three co-processed fuel oils, characterizing the atomization performance of a No. 6 fuel oil, measuring the combustion performance and emissions of the five fuels, specifically major, minor, and trace elements when fired in a watertube boiler designed for natural gas/fuel oil, and determining the boiler performance when firing the five fuels. With the exception of the RCO bottoms fuel (X1333), which was exceptionally viscous, the co-processed fuel oils handled and combusted similarly to the commercial No. 6 fuel oils. Sulfur dioxide and nitrogen oxide emissions were significantly less for the co-processed fuels oils due to their low sulfur and nitrogen concentrations. Boiler efficiencies from all liquid fuel tests were comparable. While the data presented only represent a limited number of samples and there was significant variation between the co-processed fuel oils (possibly due to differences in processing), it can be said that the incorporation of coal derived liquids in the refinery stream can introduce elements of environmental concern. The level of their emissions upon utilization varies drastically but warrant further investigation to ensure that they pose no greater environmental threat than petroleum-derived liquids.

One of the main highlights of Task 5 was the evaluation of products in a laboratory scaled coker to determine the quality of co-coke and liquids produced. Two coals (Pittsburgh and Marfork) processed to a low mineral content were co-coked with decant oil. Evaluation of the coke indicated that while the coke produced is of very good quality for utilization as filler for anode production, the metals content of the carbon is still high in iron and silica. The liquids produced mainly boil in the fuel oil range, however, additional processing would increase the lighter fraction yield. Marfork coal produced the best quantity and quality liquids from co-coking. Co-cokes were also evaluated as graphite filler; co-coke from Powellton/Eagle coal produced materials closet to graphitic characteristics. Hydrotreatment reduced levels of heteroatoms and increased coke quality under atmospheric conditions. When co-coking with hydrotreated decant oil in the lab scale coker, increased hydrotreatment improved the quality of the liquids produced. Introduction of coal into the co-coking process increased the aromatic content of the liquids. Methods to improve the quality of pitch produced from the liquids from co-coking have been helpful (soaking and oxidation), although pitch produced from co-coking and these methods are not quite the same as current pitches derived from coal or petroleum. Coal extraction using refinery solvents is being evaluated as a method to produce a material similar to the blend of RCO and LCO. The most recent research indicates that filtering the product hot and engineering a multi-stage unit will increase the extraction yield to ~70% and reduce the LCO/RCO ratio. Solubility parameter data indicated that LCO and decant oils are good solvents for Marfork, Blind Canyon, Illinois #6 and Pittsburgh coals, but research is still needed to determine how this parameter may affect the delayed coking and extraction processes.

Experimental

The respective experimental details for each of the tasks of this project are described within the individual Tasks 1-5 detailed later in this report.

Results and Discussion

The results of each task of this project are documented and discussed within the appropriate Task 1-5 detailed later in this report.

Conclusions

Each of the individual tasks of this project progressed as proposed or to a greater extent than originally proposed, up to what was proposed through Year 3 of the project. Year 4 was not funded, therefore, the goals originally proposed may not have been completed. Each task individually contributes to the ultimate goal of refinery integration. This report describes 1) the fuels that were generated at a pilot scale; 2) research for utilization of coal-based gasoline and diesel fuel in internal combustion engines; 3) progress on design of catalysts for desulfurization/denitrogenation of aromatic compounds, saturation of aromatics, and for production of value-added chemicals; 4) research for utilization of coal-based fuel oil in pilot-scale boilers; and 5) research into methods of production of coal-based fuels using coal and petroleum solvents in delayed cokers and a heated solvent extraction process.

The main goal of Task 1 was the production of coal-based jet fuel and other products that would need to be utilized in other fuels or for non-fuel sources, using known refining technology. The gasoline, diesel fuel, and fuel oil were tested in other aspects of the project. Light cycle oil (LCO) and refined chemical oil (RCO) were blended, hydrotreated to removed sulfur, and hydrogenated, then fractionated in the original production of jet fuel. Two main approaches taken during the project period varied where the fractionation took place, in order to

preserve the life of catalysts used, which includes 1) a fractionation step of the hydrotreated blend to remove sulfur and nitrogen, followed by a hydrogenation step of the lighter fraction, and 2) fractionation of the LCO and RCO before any hydrotreatment. Another aspect was to hydrotreat decant oil for testing of the delayed coker. The yield and quality of jet fuel and the quality of all fuels were better when hydrotreating the whole blend to remove sulfur and nitrogen and fractionating gasoline and jet fuel for further hydrogenation. When fractionating the RCO and LCO before any hydrotreatment, the yield of jet fuel and diesel fuel decreased, and the yield of the fuel oil increased and was a low quality. The hydrotreated decant oils were tested as solvents in co-coking, described in Task 5 of the report.

Task 2 involved assessment of the impact of refinery integration of JP-900 production on gasoline and diesel fuel. Fuel properties, ignition characteristics and engine combustion of model fuels and fuel samples from pilot-scale production runs were characterized. The model fuels used to represent the coal-based fuel streams were blended into full-boiling range fuels to simulate the mixing of fuel streams within the refinery to create potential “finished” fuels. The representative compounds of the coal-based gasoline were cyclohexane and methyl cyclohexane, and for the coal-base diesel fuel they were fluorine and phenanthrene.

Both the octane number (ON) of the coal-based gasoline and the cetane number (CN) of the coal-based diesel were low, relative to commercial fuels (~60 ON for coal-based gasoline and ~20 CN for coal-based diesel fuel). Therefore, the allowable range of blending levels was studied where the blend would achieve acceptable performance. However, in both cases of the coal-based fuels, their ignition characteristics may make them ideal fuels for advanced combustion strategies where lower ON and CN are desirable. Methyl cyclohexane was observed to have similar ignition temperature as *n*-heptane and to exhibit two-stage ignition under a narrow range of test conditions. The impact of the coal-derived diesel fuel on ignition limits its use to a 5 vol.% blend in the commercial diesel fuel. Studies of the combustion characteristics at this blend level showed modest impact on emissions, with a slight increase in NO_x emissions and an increase in particle number density. Overall, these coal-based streams can be blended into conventional fuel streams at between as much as 20% for the coal-based gasoline and at as much as 5% of coal-based diesel while maintaining acceptable performance.

Major progress has been made in the DOE Refinery Integration project in developing new catalytic and adsorption approaches for desulfurization and denitrogenation of refinery

streams, in developing novel concept and sulfur-resistant noble-metal catalysts for saturation of two-ring aromatics in middle distillate fuels, and in producing value-added chemicals and materials from two-ring aromatics including naphthalene and biphenyl. The results and major findings from this research provided new insight into the key factors affecting: 1) the materials formulation including the adsorption capacity and selectivity for selective nitrogen and sulfur removal and for the catalysts for hydrotreating, 2) a new design for sulfur-resistant noble metal catalysts and low-temperature catalytic activity towards aromatic ring saturation, and 3) the shape-selective catalysts for shape-selective methylation of naphthalene and biphenyl. The work and the knowledge generated in this project paved the road for the future development.

The objective of Task 4 was to evaluate the effect of introducing coal into an existing petroleum refinery on the fuel oil product, specifically trace element emissions. Activities performed to accomplish this objective included analyzing two petroleum-based commercial heavy fuel oils (*i.e.*, No. 6 fuel oils) as baseline fuels and three co-processed fuel oils, characterizing the atomization performance of a No. 6 fuel oil, measuring the combustion performance and emissions of the five fuels, specifically major, minor, and trace elements when fired in a watertube boiler designed for natural gas/fuel oil, and determining the boiler performance when firing the five fuels.

With the exception of the RCO bottoms fuel (X1333), which was exceptionally viscous, the co-processed fuel oils handled and combusted similarly to the commercial No. 6 fuel oils. Sulfur dioxide and nitrogen oxide emissions were significantly less for the co-processed fuels oils due to their low sulfur and nitrogen concentrations. Similarly, NO_x emissions correlated with fuel-bound nitrogen content. Boiler efficiencies from all liquid fuel tests were comparable.

Emissions produced during combustion of No. 6 fuel oil as compared to calculated emissions using emission factors AP-42. The data showed that the correlation of measured emission data to the calculated emission is a function of the element itself. Testing of fuel oil for emissions illustrated that the introduction of coal-derived liquids can introduce trace metals of environmental concern into liquid hydrocarbon products produced during co-processing with petroleum derived liquids. This is evident by the presence of trace elements in the emissions produced during combustion of the co-processed “fuel oil” fraction as compared to emissions produced during combustion of No. 6 fuel oil. The amount of Hg and As emitted (lb/10¹² Btu) was found to be 10 times greater than two of the No. 6 fuel oils. While the data presented only

represent a limited number of samples and there was significant variation between the co-processed fuel oils (possibly due to differences in processing), it can be said that the incorporation of coal derived liquids in the refinery stream can introduce elements of environmental concern. The level of their emissions upon utilization varies drastically but warrant further investigation to ensure that they pose no greater environmental threat than petroleum-derived liquids.

Two processes were examined to produce coal liquids from coal within a refinery: delayed coking of coal and decant oil and coal extraction using light cycle oil. Refineries deploy delayed coking to process heavy hydrocarbons from other processes, and typically produce additional liquids for sale and carbons of varying qualities. During the course of this project, two coals were prepared into clean coal products suitable for co-coking and for the production of anode-quality carbon for the aluminum industry. Run-of-mine and flotation samples of the Pittsburgh seam and a coking coal product from the Marfork Cleaning Plant (a blend of coals) were collected, a process of wet sieving and gravity-liquid flotation were used to prepare ultra-clean coal products, each exceeding the capabilities of current cleaning plant technology. Generally, our processing scheme reduced the ash yield to <1.0% and increased the concentration of vitrinite >90% without a decrease in the thermoplastic properties. Sufficient sample was prepared to generate ~19 kg of delayed co-coke for laboratory testing and coke quality assessment. Operating conditions for the two co-coking series (Pittsburgh and Marfork coals) were remarkably similar, with both coals producing similar coke yields and Marfork producing a 7.0% increase in liquids was obtained. Reproducibility of co-coking of coal with a decant oil in four separate experiments, in terms of yields of green coke, liquid, and gas, was shown to be very good.

The quality of the products from co-coking, both liquids and coke, were examined. For the liquids, time-dependent samples (as the reaction progressed), showed a slight decrease in aliphatic hydrogen/carbon but an increase in total aromatic hydrogen/carbon as determined ^1H and ^{13}C NMR analyses. Liquids taken in certain time intervals were shown to have reproducible characteristics. When comparing the chemical character (using GC/MS and NMR) of the gasoline, jet fuel, and diesel fractions, the lighter liquids were more aliphatic and the heavier liquids were more aromatic. The jet fuel fraction contained a significant quantity of two-ring aromatics, that upon hydrogenation, would produce an excellent thermally stable jet fuel.

However, the main liquid product was material that boiled in the fuel oil range, therefore, this fraction may need to undergo catalytic cracking and hydrotreatment to produce additional jet fuel.

Co-coke quality varied depending on the conditions used. It appeared that the main influence of increasing the coal concentration to 30 wt% during co-coking was a decrease of the overall liquids yield and thereby increasing the coke yield. Also, it was found that the yield of liquids (gasoline, jet fuel and diesel) was increased at the expense of the fuel oil fraction. The quality of the coke produced was much diminished, as shot coke was generated from all three coals at the higher concentration. The co-cokes were evaluated depending on different applications. The most important conclusion regarding the preparation of a premium petroleum coke product for co-coking deeply cleaned coal with decant oil, was that if not for the high silicon and iron content, co-coke appeared to be superior in every way to other straight-run petroleum cokes. While the mineral cleaning technique used perhaps represented the best that can be done currently, the carbon generated was insufficient to meet all of the current specification for premium anode grade calcined carbon. The co-cokes were also characterized and evaluated as fillers for graphite production. In terms of the values of four parameters, d_{002} , L_c , L_a and degree of graphitization, the graphitizability of the four coal samples in order are: Powellton/Eagle > Marfork > Canterbury > Pittsburgh (EI186).

Bulk characterization of pitch by means of nuclear magnetic resonance (NMR) was performed on six pitch samples, four pitches obtained from industrial sources (SCTP-2, PP-1, GP-115, WVU-5), and two generated in-house from co-coking liquids (HTCCP and OXCCP). By combining results obtained from the NMR techniques, i.e. aromaticity, degree of condensation, and types of hydrogen and carbon atoms, with the elemental analysis and number average molecular mass from MALDI, average structural information of pitch was determined. The two pitches made from co-coking liquids, HTCCP and OXCCP, were similar in their structures. They contained three peri-condensed fused rings on average for every molecule, but would need further processing to be more similar to standard coal-derived and petroleum-derived pitch. ^1H *in-situ* high temperature NMR and the solid echo pulse program were used to study the change in mobility of model compounds, pitch and their mixtures with petroleum coke. In the pitch/coke mixtures, pitch that contained a higher hexane soluble fraction seemed to enhance the mobility between pitch and coke.

Hydrotreated decant oils (HTDOs) were coked alone and as blends with coal. The carbon and liquid products were characterized and evaluated to determine the effect of HTDOs. Mild hydrotreatment enhanced the co-coke quality. However, the greater the hydrotreating, the lighter the liquids generated. The data support hydrotreatment of the decant oil as a means of providing a potentially thermal stable jet fuel via increasing the saturated cyclics and decalins contents of jet fuel fraction. Further hydrotreatment/hydrogenation of the overhead liquid could increase the quantities of thermally stable jet fuel.

Coal extraction using refinery solvents was evaluated as a method to produce a material similar to the blend of RCO and LCO. Early work indicated that a 10/1 ratio of LCO to coal can extract ~50% of coal, but the final ratio of LCO to RCO is only 9/1. The most recent research indicates that filtering the product hot and engineering a multi-stage unit will increase the extraction yield to ~70% and reduce the LCO/RCO ratio. The solubility parameter of several solvents were calculated and compared to coals that were swelled using a range of solvents. According to our results, we expect to achieve better coal conversions from Marfork, Blind Canyon, Illinois # 6 and possibly with Pittsburgh coal when processed with LCO and decant oil in our coal extraction plant. Kittanning coal should interact better with solvent of a higher solubility parameter.

Technical Discussion

Background

Penn State has been involved in a multi-phase fifteen-year program to develop an advanced thermally stable jet fuel for the Air Force [1-1 -1-4]. This fuel would resist breaking down at high temperatures (900°F), so it could be used for cooling sensitive parts on high-performance aircraft, as well as providing the propulsion. It is provisionally called JP-900.

At its inception, the JP-900 program presumed that this new fuel would be made entirely or substantially from coal. There are three reasons for this.

Scientific validity. Penn State's researchers have shown clearly that the kinds of chemicals in the fuel that make it stable at 900°F (hydroaromatics and naphthenes) can be derived in abundant amounts from coal. This has been demonstrated in numerous peer-reviewed publications [1-5 – 1-10].

Long-term security. Unlike petroleum, coal is a secure, domestic energy resource, for which centuries' worth of reserves remain in the U.S.

Stable procurement. Both petroleum and natural gas are vulnerable to significant price spikes. In contrast, coal companies are willing to write twenty-year delivery contracts at a guaranteed stable price. In turn, this would help stabilize the price of military fuel for decades to come.

To ultimately produce an advanced thermally stable coal-based jet fuel a practical and economically viable process, compatible with current refinery practice, is necessary. The evaluation of this scenario is the subject of this proposal. No refinery is operated for the specific purpose of making jet fuel. Furthermore, refineries are highly integrated, in that many of the individual operations are dependent on, or use streams from, other operations. Therefore, in order to insure that the production of coal-based JP-900 in the

jet fuel section of a refinery is acceptable to refinery operators, it is crucial to have data showing the effect of the by-products from coal-based JP-900 production (i.e., the <180°C and the >270°C fractions) on the quantity and quality of the other refinery products: gasoline, diesel, fuel oil, pitch, and coke.

Options for integrating coal, or a coal liquid product that is currently available commercially (a by-product coal tar distillate from the metallurgical coke industry) into existing refineries are illustrated in **Figure 1-1**. With respect to the first two options, coal can either be added to the coker directly or be co-processed with the resid. Of these, addition of the coal to coker has been selected – in consultation with our refinery partner – as the better option to produce sufficient quantities of coal-based fuel for thermal stability and combustion testing. Each of these approaches has a unique set of technical challenges in terms of specifying the proper feedstocks (for both petroleum- and coal-based components), process conditions (temperature and pressure) and processing approaches.

Previous work at Penn State has resulted in significant progress in identifying the remaining critical barriers to realization of coal-based fuels [1-11 – 1-20].

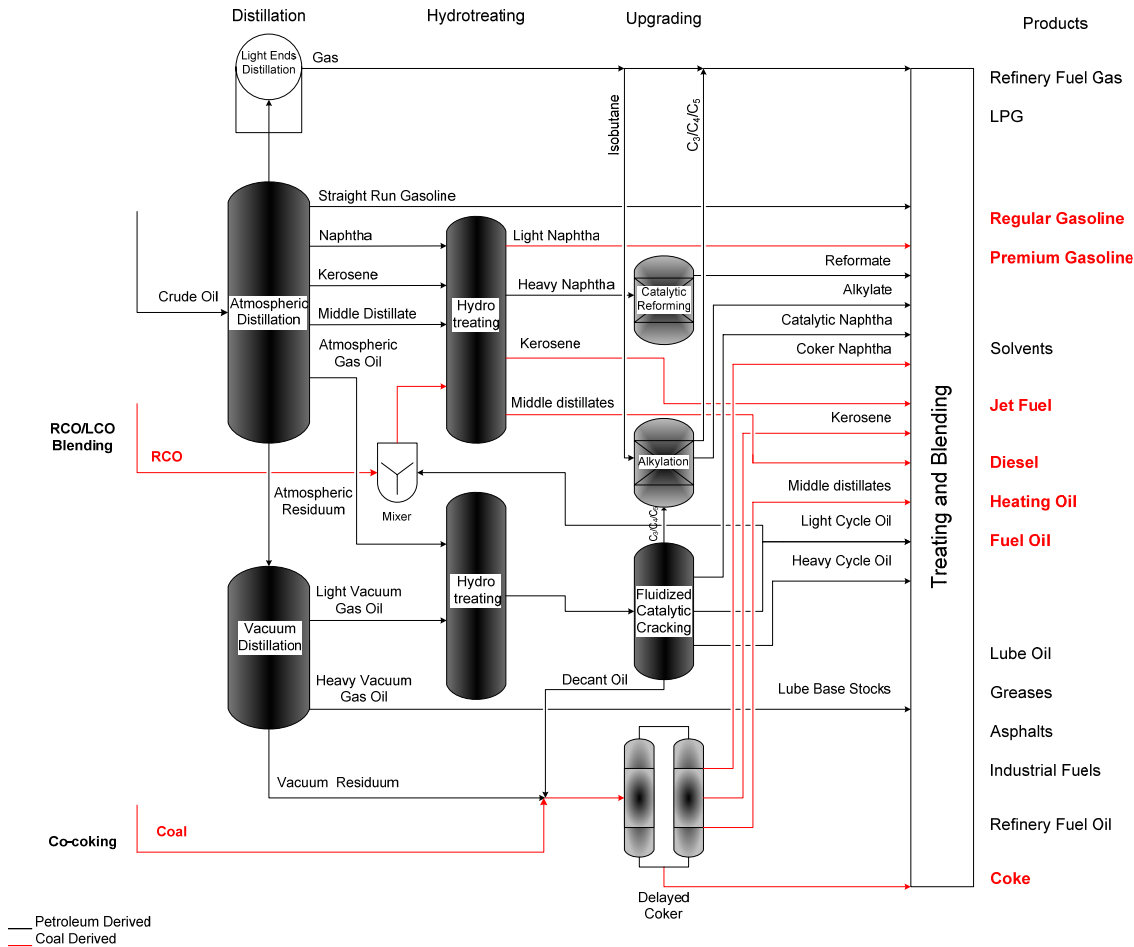


Figure 1-1. Possible Integration of Coal into Existing Refineries.

Objectives

A number of potential JP-900-type jet fuels have been produced by Pennsylvania Applied Research Corporation (PARC) from the hydrotreatment of a coal-derived refined chemical oil (RCO) and its mixture with a petroleum-derived light cycle oil (LCO).

The overall objective of this project is to examine the characteristics and quality of the streams other than the jet fuel, and what effect those materials would have on the other unit operations in the refinery, the quality and value of the other products. Broadly, these additional by-products are the liquids lighter and heavier than jet fuel itself, i.e., the <180°C and the >270°C fractions produced after hydrotreating the RCO/LCO blend and fractionating to recover the jet fuel and other refinery streams.

Prior to the beginning of this project, virtually all work was focused on the jet fuel. However, as we have noted above, no refinery is run for the specific purpose of making jet fuel. Therefore, to make these processes acceptable for adoption in refineries, it is vital to assess their impact on the other major operations and products in a refinery. The acquisition of that knowledge is the basis of this project.

These studies will impact all of the major product streams in a conventional petroleum-based refinery. Therefore, replacing petroleum feedstock with domestic coal, gasoline, diesel, fuel oil and pitch components will favorably impact reducing dependence on, and security of supply of, foreign petroleum resources.

The objectives of the project are to:

- Investigate and develop an understanding of the most promising refinery integration of all process streams resulting from the production of coal-based jet fuel.
- Demonstrate the quality of each of the process streams in terms of refinery requirements to maintain a stable, profitable refinery operation.
- Demonstrate the performance of key process streams in practical testing used for application of these streams.

This fundamental research was proposed as a four-year program. In this document we report activities and accomplishments for the first half of the second contract year. The approach chosen draws on previous work that has now successfully produced a coal-based JP-900 fuel at pilot-plant scale for initial investigations in the fuel stabilization and combustion studies [1-21 – 1-23]. In that work, it has been shown that hydrotreated blends of light cycle oil and refined chemical oil (a coal-derived liquid) resulted in the most thermally stable product to date.

This program is investigating the fate of each major product from a refinery complex, except jet fuel, resulting from the refinery integration of coal-derived jet fuel production via a combined RCO/LCO strategy by studying the physical and chemical nature of all products that are perturbed by introduction of coal components into the refinery.

The impact of the proposed research is to provide the scientific and fundamental engineering basis to integrate the production of coal-based jet fuel into existing refinery operations in a time frame consistent with availability and economic forecasts related to petroleum-derived as opposed to coal-based feedstocks. The results of these studies lead to the integration of all non-jet-fuel streams into current refinery operations in concert with desired production of coal-based jet fuel engine testing toward the end of the first decade of the new century. For successful utilization of coal-based jet fuels all non-jet-fuel components must fit existing and future product stream specifications.

Coal tar fractions have been successfully demonstrated to be suitable feedstocks for the production of jet fuels for high-speed aircraft [1-22, 1-23]. The jet fuel, as prepared and evaluated in our Air Force project, is a 180-270°C product, cut from a mixture of RCO/LCO total liquid product. Of this product the <180°C cut represents ~4% of the total product and the >270°C fraction represents just over 40% of the total liquid product [1-24]. These streams must either be blended as is, chemically converted and then blended, converted to chemicals, or used as feed to the coker.

Task 1. Pilot-Scale Fuel Production at Intertek PARC

C. Burgess Clifford (PSU), Leslie R. Rudnick (formerly of PSU), J. Banes (Intertek PARC), G. Wilson (Intertek PARC), and R. Absil (Intertek PARC)

1.1 INTRODUCTION

The main goal of this task was the production of coal-based jet fuel and other products that would need to be utilized in other fuels or for non-fuel sources, using known refining technology. The gasoline, diesel fuel, and fuel oil were tested in other aspects of the project. Light cycle oil (LCO) and refined chemical oil (RCO) were blended, hydrotreated to removed sulfur, and hydrogenated, then fractionated in the original production of jet fuel. Two main approaches taken during the project period varied where the fractionation took place, in order to preserve the life of catalysts used. All three approaches are shown in **Figure 1-2**: 1) fractionation at the end of the hydrotreatment, 2) a fractionation step of the hydrotreated blend to remove sulfur and nitrogen, followed by a hydrogenation step of the lighter fraction, and 2) fractionation of the LCO and RCO before any hydrotreatment. Another aspect was to hydrotreat decant oil for testing of the delayed coker. Descriptions of both aspects are included in the Task 1 report.

1.2 EXPERIMENTAL

1.2.1. LCO, RCO, and Decant Oil Procurement

Light cycle oil (LCO) was procured from United Refining Company in Warren, PA. Refined chemical oil (RCO) was procured from Koppers, Inc., Harmarville, PA. These materials were blended to provide a feedstock RCO/LCO blend that was upgraded by deep hydrotreatment and fractionated in subsequent tasks. Simulated distillation GC (D2887) of LCO and RCO samples is shown in **Table 1-1**. Decant oil was provided by United Refining, Warren Pennsylvania and contained a high level of sulfur (2.99 wt%)

and is a heavy oil with a high gravity (1.1203 gm/ml, API -5.2). The ultimate and proximate analyses of the decant oil (EI-107) is shown in **Table 1-2**.

1.2.2 Catalyst Preparation

Catalysts used and prepared for the various processes are as follows:

1.2.2.1. Hydrotreatment of RCO:LCO 1:1 ratio

1.2.2.1.1. Hydrotreatment to remove sulfur and nitrogen

Intertek PARC used two different catalysts to hydrotreat samples. In research done previous to this project, a SYNCAT Criterion Ni-Mo catalyst was used to remove sulfur and nitrogen through hydrotreatment, similar to what is described in the following section for hydrotreatment of decant oil. [1-1, 1-2, 1-3, 1-24] In the second hydrotreatment, Intertek PARC used a Grace Ni-Mo AT-505 catalyst. The reactor unit and the amount of catalyst loaded are detailed in the Refinery Integration report semi-annual report submitted in April 2007. [1-25]

The catalyst was sulfided before feed was put into the unit. Sulfiding feed consisted of hydrotreated diesel with 1.5 wt% sulfur as dimethyldisulfide. Details of the sulfiding procedure were detailed in previous reports. [1-25, 1-26] Once a temperature of 450°F was reached, and H₂S breakthrough took place, the temperature was raised to 550°F, held for one hour, and then reduced to 300°F and the unit was then ready for run feed.

1.2.2.1.2. Hydrotreatment to hydrogenate two-ring aromatics

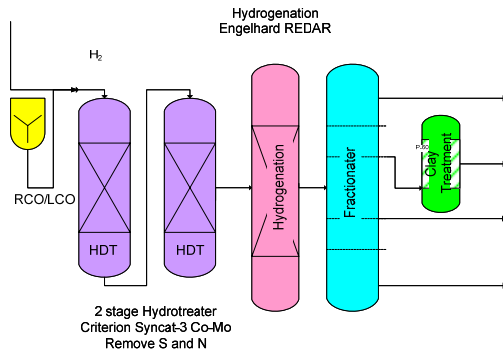
PARC's adiabatic unit P67 was charged with fresh and USED Engelhard REDAR precious metals hydrogenation catalyst. Details have been discussed in previous reports. [1-25, 1-26]

The catalyst was reduced prior to introducing run feed. Hydrogen was introduced at a flow rate of about 47 scf/hr at 600 psig. The unit was held at 392°F for about 2 hrs and then the heats turned down and the unit was cooled to 300°F. Additional details were discussed in previous reports. [1-25, 1-26]

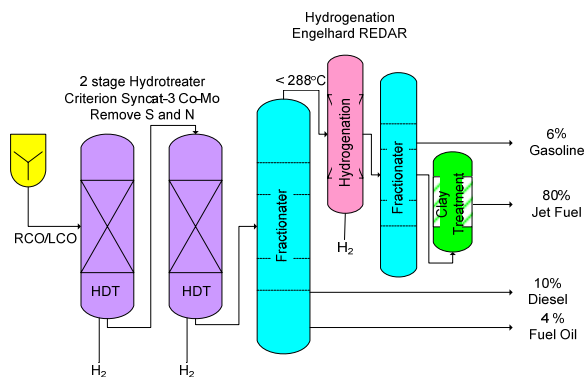
1.2.2.2. Hydrotreatment of decant oil

Decant oil (Heavy FCC Cycle Oil) was hydrotreated at several different levels of severity to produce feeds for Penn State's co-coking component of the Refinery Integration Study. PARC's adiabatic hydrotreatment pilot unit was used for the hydrotreating. The catalyst used was Criterion NiMo Syncat-37. Seven hydrotreated products were produced with a range of sulfur removal from 37.9 to 99.0 wt%. Details of the catalyst loadings are discussed in previous semi-annual reports. [1-25, 1-26] Briefly, a sulfiding procedure was provided by the catalyst vendor and was modified to fit PARC's unit. The SYNCAT-37 catalyst was received pre-impregnated with a sulfur compound. A commercial diesel containing 0.25wt% sulfur as dimethyl disulfide in addition to the naturally occurring sulfur in the base diesel (about 300 ppm) was used as the catalyst activation feedstock. The sulfur in the feedstock would ensure that the catalyst had an adequate supply of sulfur during the sulfiding procedure. Catalyst bed temperatures were brought up to 530°F (Reactor 1) and 545°F (Reactor 2) prior to switching to run feed.

(a)



(b)



(c)

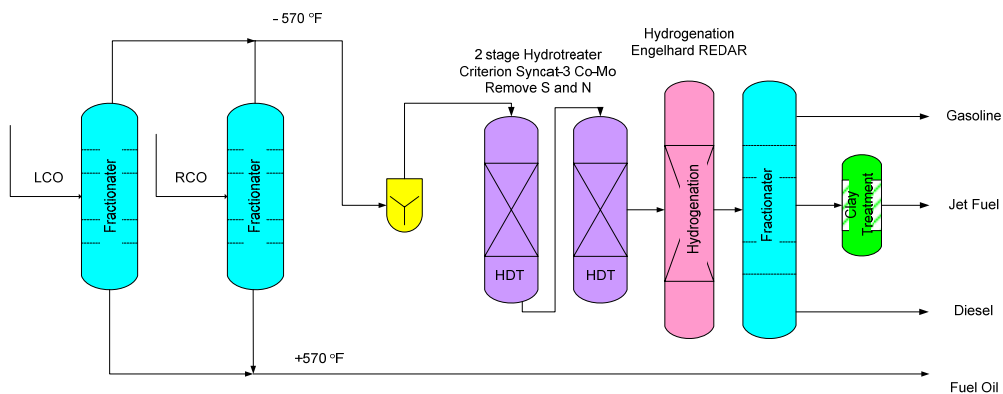


Figure 1-2: (a) Schematic of Fuel Hydrotreating and Hydrogenation, first runs, (b) Schematic of Fuel Hydrotreating and Hydrogenation, second runs, (c) Modification of Schematic of Fuel Hydrotreating and Hydrogenation currently being run at Intertek PARC, Harmaville, PA.

Table 1-1: United Refining LCO, DO, and Koppers RCO Simulated Distillation GC

SAMPLE	LCO	RCO	1:1 RCO:LCO	DO
	PR 1244	PR 1238	PR 1251	
Instrument	5880	5880	5880	5880
IBP	350	335	341	453
5%	451	390	396	632
10%	485	429	431	665
20%	516	433	436	712
30%	533	435	440	741
40%	553	437	486	756
50%	570	438	534	775
60%	593	451	551	794
70%	618	500	577	819
80%	651	545	625	845
90%	684	598	667	887
95%	705	650	704	919
FBP	771	894	813	966

Table 1-2: United Refining Decant Oil

Ultimate Analyses	Percentage, dry weight
Carbon	89.59
Hydrogen	7.32
Nitrogen	0.22
Sulfur	2.99
Ash content	0.0
Conradson carbon residue	n.d.
Asphaltene content	0.21

1.3 RESULTS AND DISCUSSION

1.3.1. Processing of RCO and LCO Blends for Jet Fuel and By-Product Gasoline, Diesel, and Fuel Oil

Prior to the Refinery Integration project, Intertek PARC produced large quantities of jet fuel using blends of 1:1 RCO and LCO by hydrotreating the whole liquid (mainly to remove sulfur and nitrogen while partially hydrogenating the liquids) and then fractionating the liquid into four fractions, as depicted in **Figure 1-2 (a)**. [1-1, 1-2, 1-3, 1-24] During the course of the research, there were two issues that caused some problems that needed resolving during the Refinery Integration project. One of the issues was the jet fuel made needed to be hydrogenated further, to produce saturated cycloalkanes (i.e., decalins) rather than hydroaromatics (i.e., tetralin) to reduce the smoke point of the fuel. It was also noticed that the catalyst deactivation was occurring at a higher rate than what a refinery would experience. Therefore, it was decided to examine removal of the heavier components by distillation prior to hydrotreatment. For the first run (see **Figure 1-2 (b)**), the RCO/LCO blend was hydrotreated, the products distilled to remove the heavy ends, then the jet fuel/gasoline hydrogenated and distilled. The second run (see **Figure 1-2 (c)**) was to distill RCO and LCO before any treatment to remove the diesel and fuel oil fractions, then the hydrotreatment and hydrogenation done on the jet fuel/gasoline fraction followed by distillation at the end. The following summarizes the methods used and the yield and quality of the fuels.

1.3.1.1. First Run: Hydrotreatment, Distillation, and Hydrogenation

1.3.1.1.1. Hydrotreating to Remove Sulfur and Nitrogen

Hydrotreating was done for several hundred gallons of a 1:1 RCO/LCO blend, in a differently funding program. It was done similarly to the hydrotreatment of decant oil, using a SYNCAT Criterion Ni/Mo catalyst. Details can be found elsewhere. [1-1, 1-2, 1-3, 1-24, 1-25, 1-26]

1.3.1.1.2. Distillation to separate heavy fractions

The feed was from a previous jet fuel program [1-1, 1-2, 1-3, 1-24], of a RCO:LCO blend, that had been hydrotreated to remove nitrogen and sulfur to various extents (samples labeled X-1099, X-1100, and X-1101). These three samples were blended and distilled to remove the heavy fraction (diesel and fuel oil, the material); the distillation cut off point was at 550°F. Details can be found in a previous report.[ref, 2005 report] The 550°F+ fraction was further distilled with a cut point of ~650°F to produce a diesel fraction and fuel oil fraction. The second feed, the 550°F- fraction, fraction were hydrogenated as discussed in the following section.

1.3.1.1.3. Hydrogenation of Jet Fuel/Gasoline and Distillation of Products

The hydrogenation catalyst that was used was Engelhard REDAR, which was reduced with hydrogen at ~115 psig and temperature of 392°F. After reducing the catalyst, the 550°F- fraction was hydrogenated at 280-462°F, monitoring the products to maximize the cycloalkanes and minimize the aromatics and hydroaromatics until the products had 1-2 ppm sulfur, <1 ppm nitrogen, a specific gravity of 0.8633, and a tetralin level of <1%. The sample was then distilled to separate the gasoline and jet fuel fractions at a cut point of ~320°F. The jet fuel fraction was then passed through an Englehard F-24 clay catalyst to remove any material that may form carbon in situ. **Table 1-3** shows the yields and characterization of the products. Details are discussed in previous reports. [1-1, 1-2, 1-3, 1-24, 1-25, 1-26]

1.3.1.2. Second Run: Distillation of RCO and LCO, Hydrotreatment of Light Fraction

1.3.1.2.1. Distillation of RCO and LCO

For this run, both RCO and LCO were distilled prior to hydrotreating. The RCO was distilled at Intertek PARC in Harmaville, PA. The RCO was distilled at a separation temperature of 570°F. The simulated distillation GC of the light ends, the 570°F-

fraction, is shown in **Table 1-4**. The heavy ends, the 570°F+ fraction, was sent as the fuel oil fraction and labeled as RCO bottoms of X-1333 for Task 4. Details are discussed in previous reports. [1-24, 1-25, 1-26]

LCO was distilled at United Refining to have a 95 wt% value of 594°F (PR 1850) versus a value of for the full range LCO (PF 1639) of 684°F. **Table 1-4** contains the simulated distillation of the light fraction of RCO, LCO full range, and the light fraction of LCO.

1.3.1.2.2. Hydrotreatment of Light Fraction

The light fractions of LCO and RCO (550°F-) were then blended in a 1:1 ratio and hydrotreated. The Grace Ni-Mo catalyst was sulfided as described previously, and the blended material was hydrotreated at 550°F and a hydrogen pressure of 600 psig. Details are discussed in previous semi-annual reports. Details are discussed in previous reports. [1-25, 1-26]

1.3.1.2.3. Hydrogenation of Light Fraction

The product from the hydrotreating was then fed for hydrogenation, using the Engelhard REDAR catalyst. The conditions were a flow rate of 0.5 cc/cc-hr (LHSV), 700°F, and hydrogen pressure of 1200 psig. The product made had a smoke point of 23.0, tetralin content of 0.6 wt%, aromatic content 4.8%, decalin content of 14.3 wt %. The yield for the overall process of jet fuel, gasoline, and fuel oil (570°F+) was 6.8 wt%, 55.8 wt%, and 37.4%. The properties of the jet fuels, gasolines, and heavy fractions are shown in **Table 1-3**. Details are discussed in previous reports. [1-25, 1-26]

1.3.1.2.4. Comparison of Two Jet Fuel Production Runs

One of the major observations between Run No. 13 and No. 14 is the yield of jet fuel is lower for Run No. 14, and the yield of decalins in jet fuel is also lower for Run No. 14 (see **Table 1-3**). For Run No. 14, the RCO and LCO were distilled prior to any hydrotreatment in order to reduce the compounds that might deactivate catalysts sooner than what a refinery might experience. However, the distillation also reduced the yield and types of compounds that are expected for the jet fuel fraction. Another issue with the

distillation is the quality of the RCO bottoms that was tested as a fuel oil. This will be discussed in detail within the Task 4 section, but the quality of the RCO bottoms of X-1333 was very heavy and difficult work with.

1.3.2. Hydrotreatment of Decant Oil

The feed rate was set at 5500gm/hr. (about 1 LHSV) and the inlet hydrogen rate at 75 scf/hr. (2,400 scf/bbl). Feed was processed at nominally seven different conditions representing seven levels of severity. To achieve the different levels of severity, the reactor temperature and feed rate were varied in the first four runs. Since there was some difficulty reducing the sulfur and nitrogen, it was therefore decided to increase the reactor pressure to 1200 psig to achieve a target of about 95% desulfurization. The last three runs achieved desulfurization levels of 88 and 99%. **Table 1-5** summarizes the conditions that were used to produce the samples. Details of the conditions have been discussed in previous semi-annual reports. [1-25, 1-26] Characterization of the products was done at PSU and will be discussed in detail in Task 5, as these materials were used to produce coke.

Table 1-3: Properties of Fuels Generated for Initial Products for Testing

	Jet Fuel	Gasoline	Diesel	Fuel Oil	Jet Fuel	Gasoline	570F+
PSU Sample Code	EI-171			EI-176	X-1390		
Run at Intertek PARC	13	13	13	13	14	14	14
Product Weight, lbs	2428	181.7	287.5	158.2			
Yield, wt%	79.5	5.9	9.4	5.2	55.8	5.9	37.4
SIMDIS GC wt%							
IBP, °F	296	108	499	597	271		452
5, °F	343	187	529	622	322		519
10 °F	359	189	539	631	339		589
50, °F	401	269	577	682	386		625
95, °F	520	357	626	880	508		963
FBP, °F	574	366	653	956	611		1082
Specific gravity, g/cc	0.8713	0.7976	0.9652	1.004	0.8508		
Sulfur, ppm	0.71	15.3	182.7	336.3	1.07		
Nitrogen, ppm	0.70	5.3	13.4	381.3	0.30		
Composition, wt%							
Cyclohexane	0.50	6.24			0.04		
Xylenes	0.07	1.04			0.23		
Indan	0.24	0.25			0.65		
Indene	0.48	0.11			0.40		
t-Decalin	29.33	4.16			22.35		
c-Decalin	5.97	0.11			3.94		
Tetralin	0.41	-			0.93		
Naphthalene	1.21	-			1.03		
2-Methylnaphthalene	0.36	-			0.15		
1- Methylnaphthalene	1.05	-			0.23		
Ethylnaphthalenes	0.59	-			0.23		
Dimethylnaphthalenes	0.83	-			0.50		
Trimethylnaphthalenes	0.79	-			0.07		
T, P, & H Methylnaph	0.64	-			0.34		

Table 1-4: Simulated distillation of LCO, light fraction of LCO after distillation, and light fraction of RCO after distillation.

SAMPLE	LCO PF 1639	LCO, 570°F- PR 1850	RCO, 570°F- X-1333
Instrument	5880	5880	5880
IBP	233	284	354
5%	405	445	508
10%	447	448	509
20%	489	479	510
30%	516	489	518
40%	536	492	520
50%	561	514	538
60%	587	525	539
70%	618	539	540
80%	640	554	543
90%	665	577	550
95%	684	594	563
FBP	739	645	608

Table 1-5: Summary of reaction conditions and sulfur/nitrogen levels and specific gravity of hydrogenated decant oil.

PARC No.	Run	EI No.	Run Conditions		% HDS	%HDN	SG (g/mL)
			H ₂ Pressure (psig)	Avg Temp (°F)			
P67-69-1		133	600	568	37.7	0	1.08
P67-69-2		133	600	606	50.6	7.7	1.07
P67-69-3		134	600	624	65.5	23.1	1.06
P67-69-4		135	600	675	81.9	27.4	1.06
P67-69-5		136	600	650	88.1	47.8	1.05
P67-69-6		137	1200	750	98.8	86.2	1.03
P67-69-7		138	1200	734	99.0	88.2	1.02

Task 2. Evaluation of Coal-based Gasoline and Diesel Products in IC Engines and Related Studies

By introducing coal-derived streams into the refinery, several perturbations to the quality and quantity of refinery streams may result and directly impact vehicular fuels production. The coal contribution to the refinery streams will affect the quality, composition and performance of the resulting vehicular fuels. The fraction of the hydrotreated streams that boils below 180°C will be directed to the gasoline pool. Having components from coal is expected to boost octane number and aromatic content, and therefore, boost value. The >270°C cut of the hydrotreated stream would be low in sulfur due to the severe hydrotreatment. The effect on flash point will need to be determined if this stream is sent to the fuel oil pool and/or diesel pool. If this stream is combined with diesel fuel, it will add cycloparaffins, which will increase energy density and boost value. However, the impact on cetane number and sooting tendency is unclear. The following task structure permits assessment of the impact of refinery integration of JP-900 production on gasoline and diesel fuel.

2.1. Impact on Gasoline Quality and Performance

Under this subtask, our efforts consisted of preparation and refinement of facilities for the SI engine testing activity and ignition studies of relevant compounds to understand the impact of the coal-derived compounds on knocking and flame propagation.

2.1.1 Preparation of Laboratory and Instrumentation

Combustion and emission properties of the coal-based gasoline in SI engine applications were studied in a single-cylinder Waukesha CFR octane rating engine and were to be studied in the single-cylinder Ricardo Hydra research engine. Under this section, we acquired and installed the Ricardo Hydra single-cylinder research engine for use under Section 2.1.2 and developed instrumentation for combustion analysis. Additionally, we modified the fuel delivery system on a CFR Octane Rating engine for ignition quality and reaction pathway tests. Based upon evolving needs for fundamental

combustion data on “unconventional” fuels (recently expressed in the report from the “Basic Research Needs Workshop on 21st Century Transportation Fuels”), we chose to emphasize the work on the CFR Octane Rating engine which could directly address this need expressed by the scientific community.

GC-MS results have shown that the major components in the coal-based gasoline samples are cycloalkanes, whose octane ratings are lower than that of the commercial-grade gasoline and therefore may cause knocking in SI engine combustion. Flame propagation across the combustion chamber and the auto-oxidation chemistry of the unburned mixture (end gas) has been identified as the two determining factors in engine knock [2-1]. The auto-oxidation chemistry of the end gas is being studied in a Waukesha CFR octane rating with modified intake system and running at the motoring mode. To date, our examination of the decomposition chemistry of methyl cyclohexane (a model for coal-derived gasoline) has resulted in an ACS preprint [2-2] and a manuscript submission to the 32nd International Symposium on Combustion to be held in August, 2008. In addition, we have secured industrial research funding for continuing studies of the ignition chemistry of conventional and unconventional fuels as a consequence of this research capability of line of inquiry.

Two devices designed for studying the flame propagation in SI engine were obtained and installed in the Ricardo Hydra engine. Signal conditioning and data acquisition systems for these probes were designed and developed for monitoring flame propagation..

A head gasket equipped with 6 ion probes (**Figure 2-1**) has been designed and fabricated for the Hydra engine which enables detecting the flame arrival along the plane of head gasket. The related signal conditioning board has been build and data acquisition boards have been purchased. Another in-cylinder flame detector, optical sensor equipped spark plug, has also been obtained (**Figures 2-2 and 2-3**) which allows the flame detection on the top of the combustion chamber.

The two devices designed for studying the flame propagation in SI engine have been obtained. Description for the ion-probe head gasket was included in the previous annual report. The recently received fiber-optic spark plugs (**Figures 2-2 and 2-3**) utilize eight optical probes installed on the plug rim (**Figure 2-2**) to “see” the flame propagation

during engine combustion. Two such spark plugs were obtained and will be installed in the Ricardo Hydra engine and CFR octane rating engine. The signal conditioning and data acquisition system are being built.

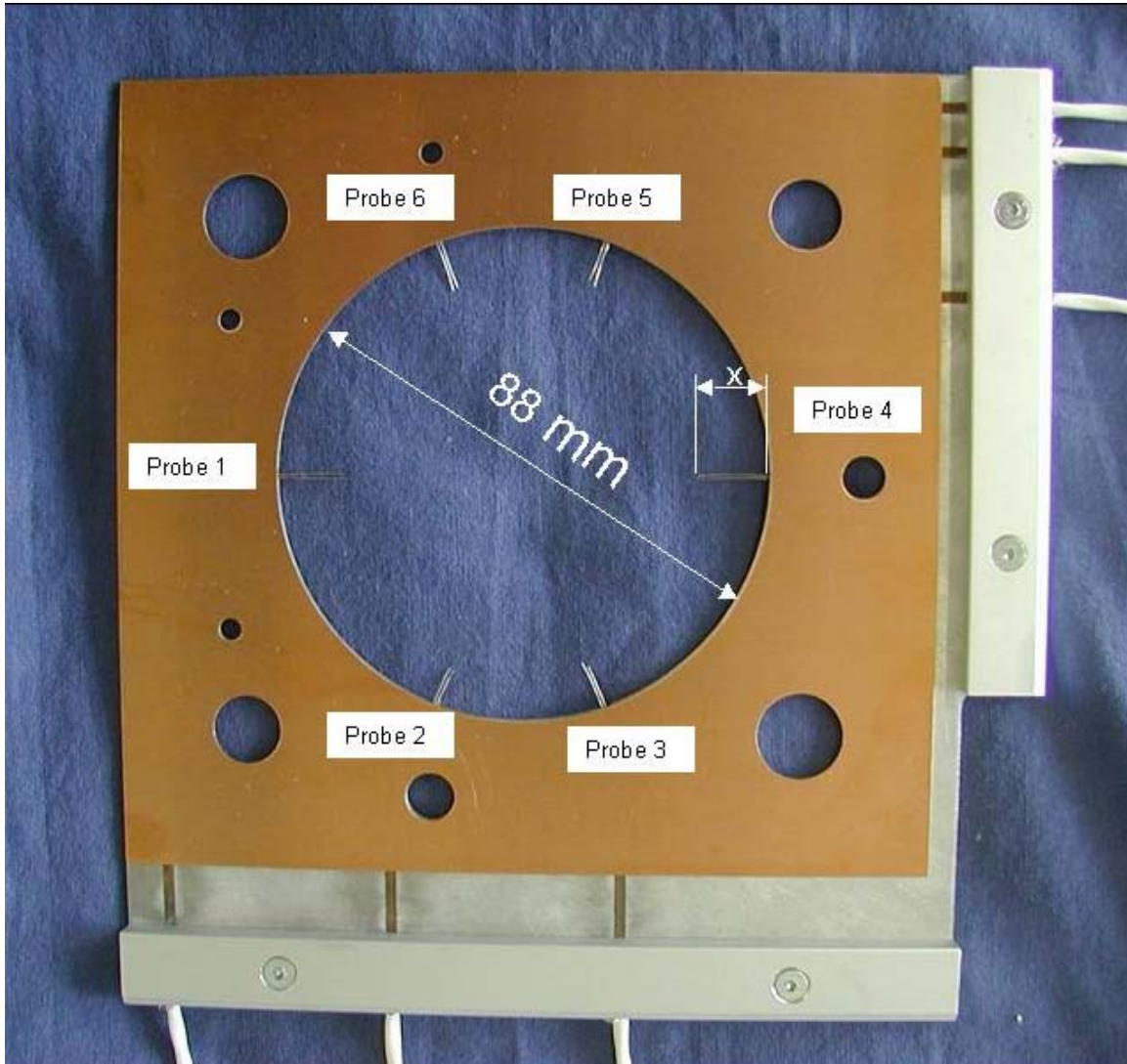


Figure 2-1: Ion probe equipped head gasket for the Hydra engine



Figure 2-2: Optic-fiber Spark Plug for the CFR Octane Rating Engine



Figure 2-3: Close-up of the Electrodes and Eight Optical Openings

Low temperature heat release during the oxidation of model compound methylcyclohexane was observed with modified operation conditions. Two-stage ignition of methylcyclohexane was also detected. This is in contrast to previous tests where no heat release was detected prior to the sudden autoignition (knocking). Comparison of the operation condition is listed in **Table 2-1**. The decreased engine speed gives more time for the low temperature oxidation to occur. Lowered intake temperature shifts the reaction from the intermediate region that has the negative temperature dependence (heat release is inhibited) to the low temperature region where heat release can be easily detected.

Table 2-1: CFR Engine Operation Conditions for Previous and Current Autoignition Study

	Previous	Current
Engine speed (RPM)	900	600
Intake Temperature (K)	533	393

Finally, the method has been upgraded for condensing products from the low temperature oxidation. A dry-ice/acetone bath replaced the previous ice/water bath. A gas bubbler containing a known volume of dichloromethane is immersed in the bath. Gas flow rate into the bubbler is regulated and measured, which enables the quantification of the condensed species. The obtained dichloromethane solution is then directly analyzed by GC-MS without water extraction. Non-condensed gases after the cold trap are collected in Tedlar bags and analyzed by GC-FID/TCD. With these improvements, a much more complete picture of methylcyclohexane low temperature oxidation was obtained.

2.1.2 Impact on Chemical and Physical Properties

Under this section, we performed detailed chemical analyses and physical analyses of fuel samples. From several runs at PARC, fuel fractions were provided representing the gasoline and diesel fuel cuts. The primary fuel characterization for the gasoline cut was through ignition studies which are presented under Section 2.1.3. Octane rating measurements of the coal-derived gasoline, blends of the coal-derived gasoline in a reference gasoline (“UTG 96,” 96 RON fuel provided by ConocoPhillips in

support of this project) and blends of model compounds in the reference gasoline have been completed. The research octane number was measured on the CFR octane rating engine according to the ASTM D2699 standard.

Chemical composition of a coal-based gasoline (CBG) from latest JP-900 production, EI-174, is analyzed by GC-MS (Shimadzu QP-5000). The chromatogram is shown in **Figure 2-4** together with identified major components and their research octane number. With the high severity hydrotreatment, almost all aromatic compounds are converted to cycloparaffins with cyclohexane and its short-chain derivatives being the dominant components. The conversion from aromatic nature to cycloparaffin nature is expected to significantly affect octane rating of this fuel, as suggested by the octane number of the major compounds.

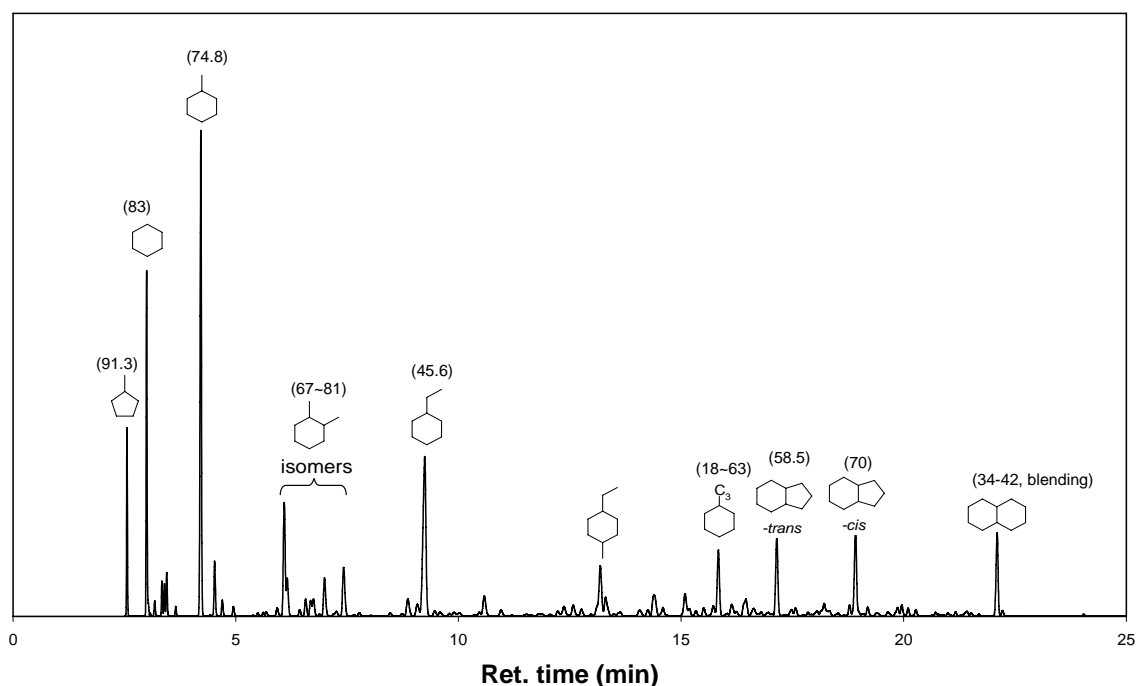


Figure 2-4 Chemical composition of CBG EI-174 analyzed by GC-MS. Number in parenthesis is the research octane number of the identified compound.

Octane number measurements of coal-based gasoline (CBG) and its blends with other components are measured on the Waukesha CFR octane rating engine. The engine was calibrated according to the ASTM D2699 standard, as shown in **Table 2-2**. In most

cases calibration is within the rating tolerance, and the largest deviation (RON=85 vs. 84.1) is less than 1 RON unit, showing the engine is in good shape.

Table 2-2 Calibration results of CFR octane rating engine by using toluene standardization fuels

Octane No.	Measurement	Rating tolerance
65.2	65.4	±0.4
85.0	84.1	±0.3
89.3	89.3	±0.3
93.4	93.0	±0.3
96.9	96.8	±0.2
99.6	99.3	±0.3

Research octane number (RON) of the coal-based gasoline, EI-174, the latest from JP-900 production, was measured as 61.0. EI-174 was blended with a commercial gasoline provided by Conoco-Phillips which has the RON of 96. Research octane number at various blending levels were tested and plotted in **Figure 2-5**. The measured RON is seen very close to that is predicted by the linear relationship based on volumetric percentage v_i , $RON_{mix} = \sum RON_i \times v_i$.

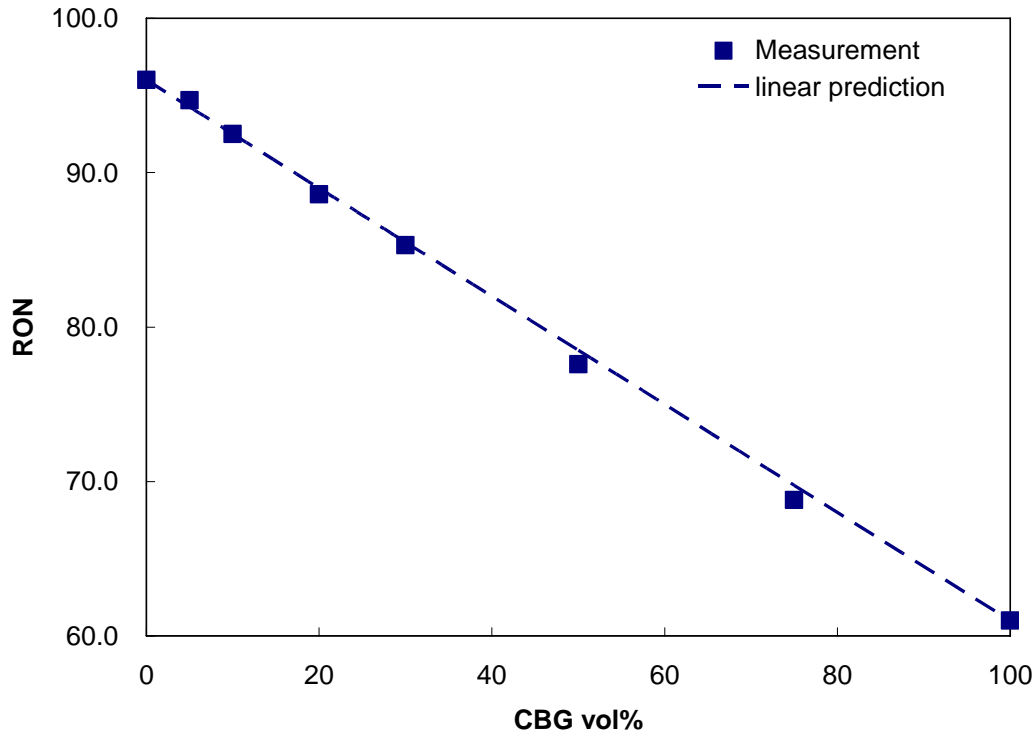


Figure 2-5. RON vs. CBG blending level in RON 96 gasoline. Dots: experiment measurements. Line: $RON_{mix} = \sum RON_i \times v_i$.

Research octane number (RON) and motor octane number (MON) of CBG EI-174 was measured as 61.0 and 60.3, respectively. The small octane sensitivity (RON-MON) is largely due to the paraffinic nature of this fuel, especially the dominant presence of short-chain cyclohexanes which have similar RON and MON [2-3].

EI-174 was blended with a commercial-grade gasoline sample, UTG96, provided by Conoco-Phillips with RON=96. Blending octane properties were tested at various blending ratios and plotted in **Figure 2-6**. The blending RON and MON are very close to that is predicted by the linear relationship, $ON_{mix} = \sum ON_i \times v_i$, based on volumetric percentage v_i . The low octane rating of neat CBG indicates that it needs to blend with high octane components, such as toluene, to make a viable gasoline of required antiknock property. However, CBG could possibly be a good fuel for HCCI combustion which requires autoignition property lying in between gasoline and diesel fuel.

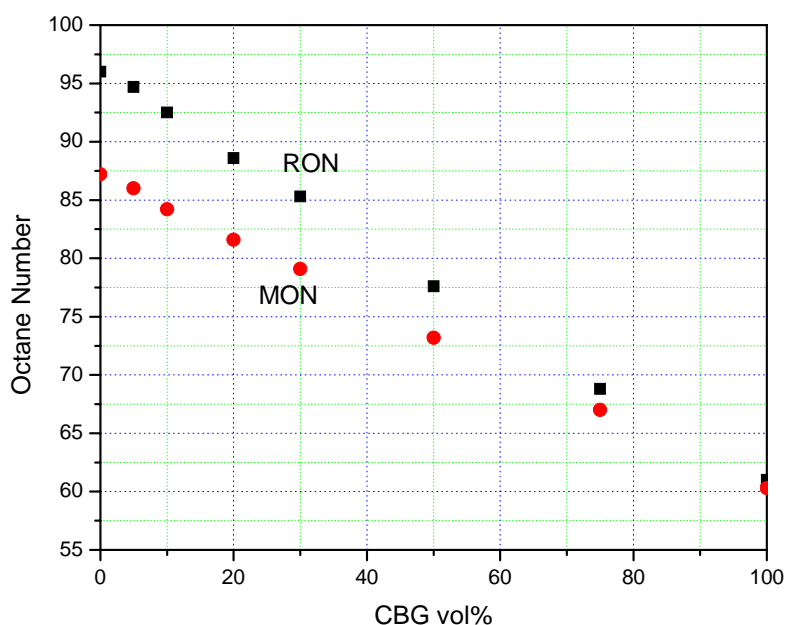


Figure 2-6 Octane rating of mixtures of coal-based gasoline (EI-174) and a commercial gasoline (UTG-96).

2.1.3 Impact on SI Engine Emissions and Performance

The low temperature oxidation of methylcyclohexane has been successfully achieved in the CFR engine with the recent modifications on engine operation conditions.

Heat release from the low temperature oxidation is shown in **Figure 2-7**. This low temperature heat release does not lead to main combustion because reaction is quenched during the expansion stroke. Note the maximum temperature during this cycle is only 886 K, well below the normal combustion temperature ($>1800\text{K}$). The start of cool flame ignition, which is defined as the point where heat release rate turns from negative to positive, occurs at 1.8 crank angles after TDC with the temperature of 831 K and pressure of 1314 kPa. The ignition temperature of methylcyclohexane is comparable with the 1st-stage ignition of n-heptane ($\sim 780\text{ K}$, in the last report) under similar conditions. However, the cool flame combustion of methylcyclohexane occurs at a much later timing than that of n-heptane which is well before TDC. This is consistent with the longer ignition delay of methylcyclohexane observed in rapid compression machine studies [2-4]. The later-than-TDC ignition timing also implies that two-stage ignition, which is

commonly observed for n-heptane and other straight-chain alkanes, occurs only under a narrow range of conditions for methylcyclohexane. Later tests at high compression ratios confirmed this speculation.

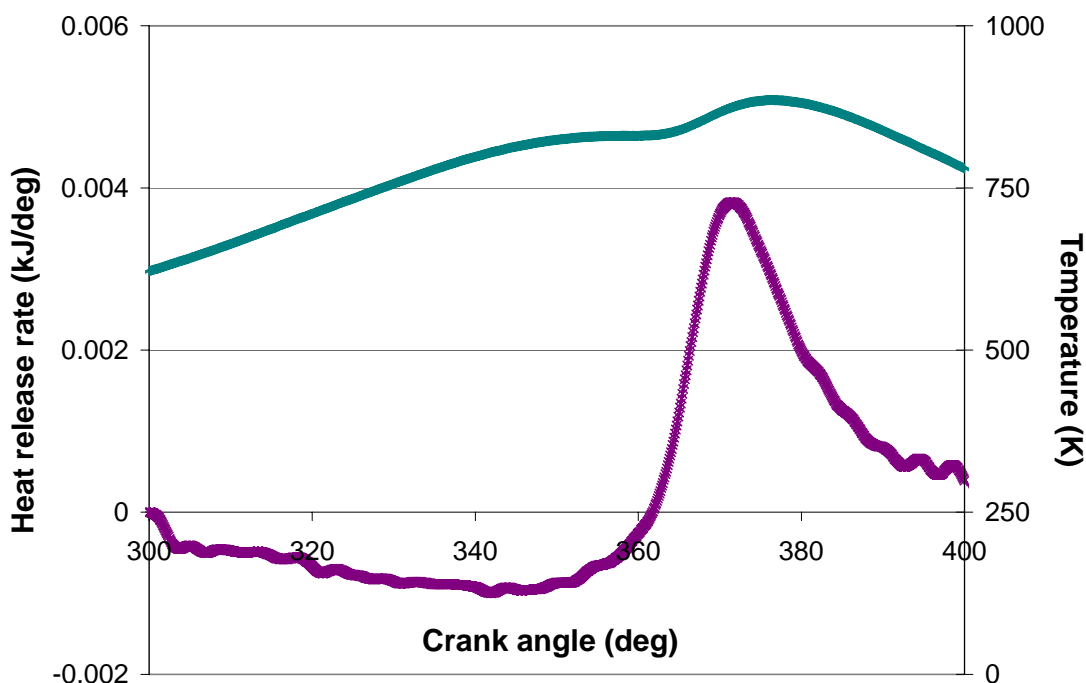


Figure 2-7 Heat release and cylinder temperature of methylcyclohexane during cool flame combustion. Condition: intake 120°C, 600 rpm, compression ratio 7.47, equivalence ratio 0.13 (nitrogen 50 SCFH).

To further investigate methylcyclohexane oxidation in an SI engine, especially the formation of aromatic compounds, a series of tests were conducted. While the other conditions are kept constant, the engine compression ratio was increased so that the transition from low temperature heat release to the major combustion can be studied.

The oxidation products were collected and analyzed by the methods described above. GC results of non-condensable species after the cold trap have been studied. **Figure 2-8** shows the concentration variation of O₂, CO, and CO₂ with compression ratio detected by TCD. **Figure 2-9** shows the concentration variations of methane, ethane/ethylene, propylene, and unreacted methylcyclohexane with compression ratio by

FID. Note that except methylcyclohexane, all species in **Figures 2-8 and 2-9** are only present in the gas phase. Most methylcyclohexane is absorbed by the cold dichloromethane liquid and appears on GC-MS spectra. It is seen that as compression ratio increases, fuel consumption increases as indicated by the steady decrease of O₂ and fuel concentrations. Significant amount of CO, methane, ethane and ethylene are formed as compression ratio increases. They are relatively stable comparing to other intermediates and can be consumed if the combustion is complete. The build-up of CO concentration retards CO₂ formation, therefore the CO₂ concentration stays at low concentration (<0.5%) during the course of the test. A considerable amount of propylene is also formed whose concentration increases at early stage (lower compression ratio) and decreases at late stage. This means that propylene is a relatively reactive intermediate and is converted to other species at higher temperature.

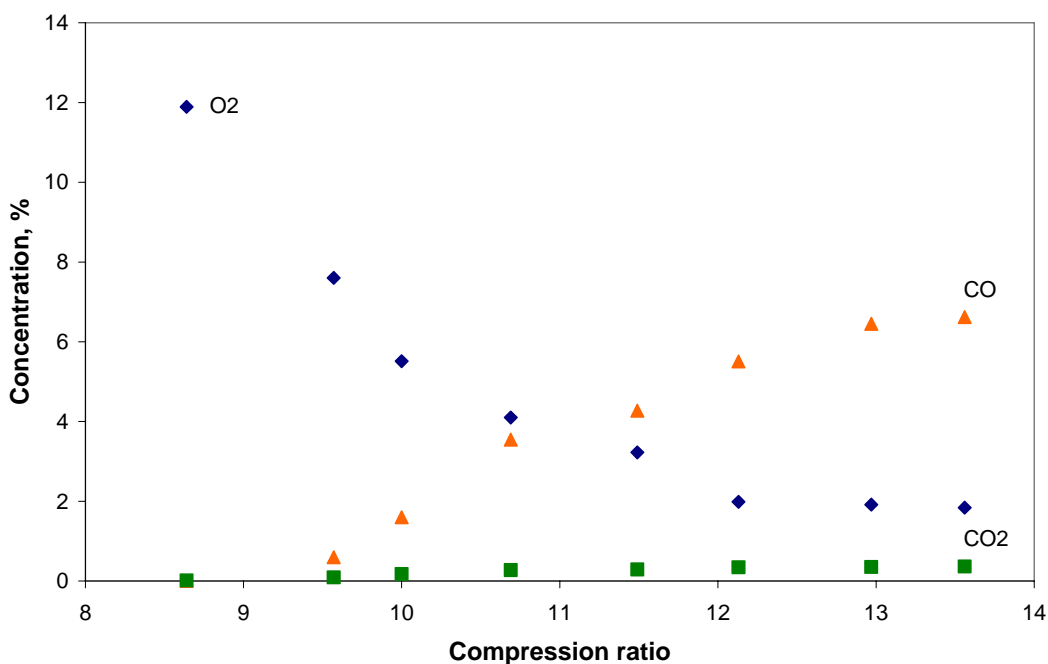


Figure 2-8 Concentrations of O₂, CO, and CO₂ vs. compression ratio by TCD. Condition: intake 120°C, 600 rpm, equivalence ratio 1.2 (nitrogen 125 SCFH).

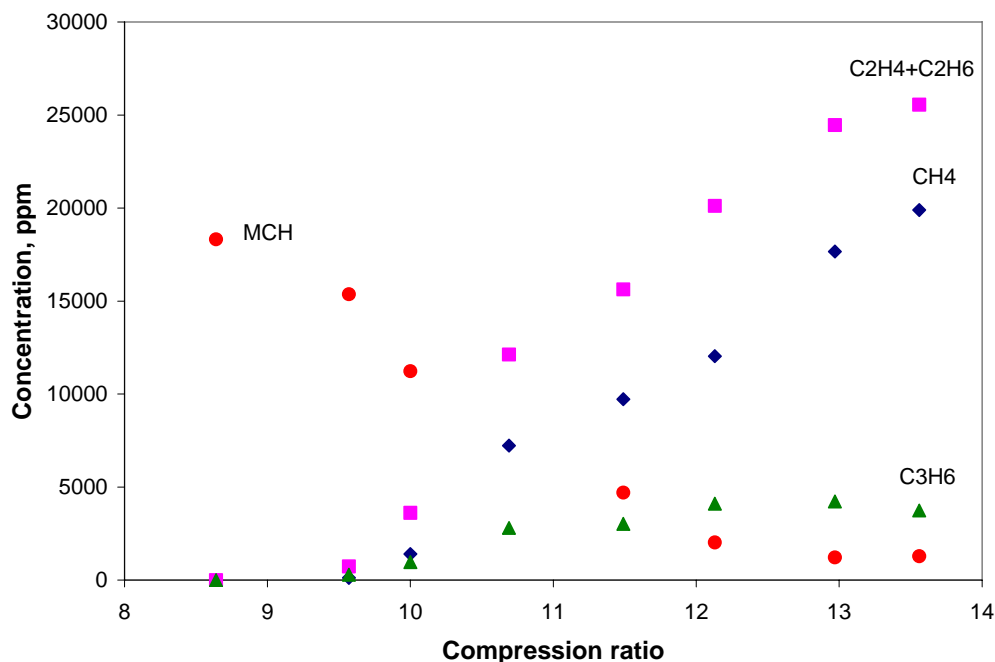


Figure 2-9 Concentration of CH₄, C₂H₄/C₂H₆, C₃H₆, and methylcyclohexane vs. compression ratio by FID. Conditions are same as in Figure 2-5.

GC-MS results of the condensable species continued to be analyzed. Our preliminary results suggested that the intermediate species are formed via two pathways: dehydrogenation and partial oxidation. Methylcyclohexenes are the major products at low compression ratio while benzene and toluene are the major products at high compression ratio, indicating that the dehydrogenation is the dominant reaction path. Benzene formation is directly from such dehydrogenation reactions. On the other hand, partial oxidation products, such as cycloketones and cycloepoxides, are observed at low compression ratio but disappeared at high compression ratio, which suggests these early formed intermediates are consumed at high temperature.

Note that our initial results only reported the oxygen-containing species in the condensed phase because the gas-collecting method was not able to effectively condense the unreacted fuel and related dehydrogenation products. We developed a new method of exhaust sample collection that enables us to study the complete product compositions (in both liquid and gas) of many hydrocarbons from the current system.

The final suite of experiments on MCH oxidation is summarized below. As in the previous measurements, the engine runs at 600 rpm with intake charge heated at 120°C.

Intake air is diluted by 125 SCFH nitrogen ($\sim 1:1$ to air) and the equivalence ratio (Φ) is about 4.5. A portion of the exhaust gas is bubbled through dichloromethane solvent that is cooled in a dry ice/acetone bath (~ 200 K). Collected DCM solutions are analyzed by a Shimadzu QP-5000 GC-MS. Uncondensed gases are collected in Tedlar bags and analyzed by a Shimadzu GC-17A.

Time-resolved cylinder pressure is measured for calculating cylinder temperature and heat release during MCH oxidation. **Figure 2-10** shows the maximum cylinder temperature as a function of compression ratio, and heat release rate as a function of crank angle at these compression ratios. Beginning with a compression ratio of 9, low temperature heat release (LTHR) is observed but the amount of energy released and the resultant increase of maximum temperature are modest. As compression ratio increases, a larger heat release peak appears to lag the LTHR peak, indicating a quasi two stage ignition process. With further compression ratio increase, the LTHR is suppressed and heat release occurs by a single stage ignition process. The maximum cylinder temperature increases to above 1500 K. The results shown in **Figure 2-10** are consistent with the results from rapid compression machine tests that showed two-stage ignition of cyclohexane at low temperatures and single-stage ignition at higher temperatures [2-5]. The coefficient of variation (COV), an indication of engine cycle-to-cycle repeatability, shows that at low compression ratios the engine runs at a highly unsteady condition with the COV greater than 100%. The COV decreases as compression ratio increases, and at CR=13.5 it decreases to $\sim 4\%$, suggesting that the engine combustion becomes characteristic of HCCI combustion.

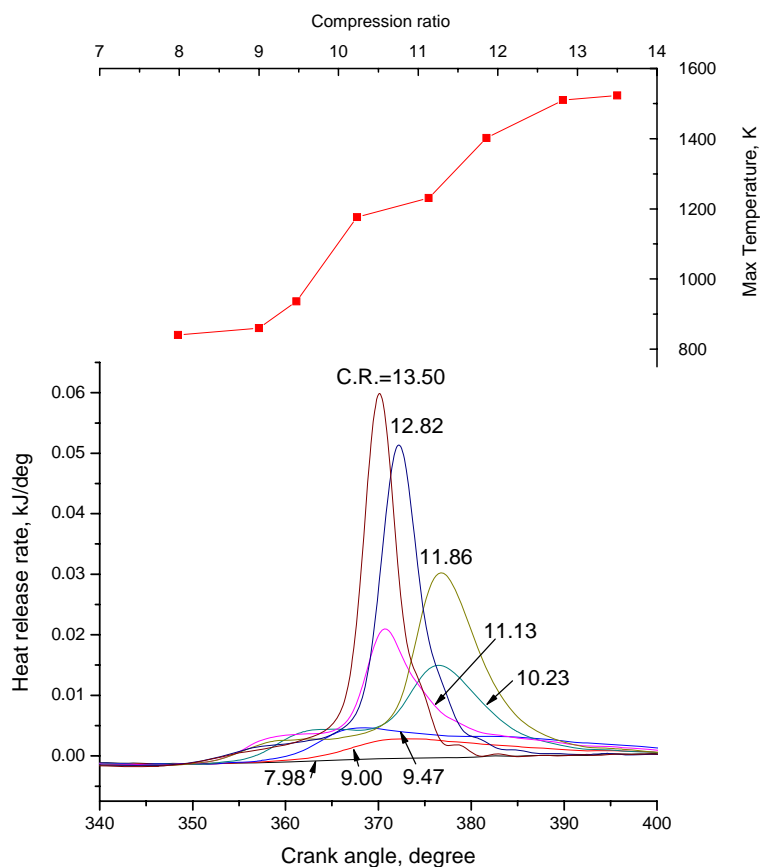


Figure 2-10 **Calculated maximum cylinder temperature and heat release rate of MCH oxidation as a function of compression ratio.**

Gaseous species Figure 2-11 shows the concentration of gaseous species (uncondensed at the cold trap) as a function of compression ratio. Species concentrations are determined by standard gas mixtures. It can be seen that the concentrations of the reactants, MCH and O_2 , decrease consistently with compression ratio increase, and simultaneously the concentrations of CO, methane, and ethylene steadily increase. Propylene concentration increases at a much slower rate and the maximum occurs at a compression ratio of 12.8, a further increase of compression ratio results in more propylene being consumed than produced. CO_2 concentration increases modestly to $\sim 0.3\%$ and remains nearly constant as compression ratio increases. High CO, CH_4 , and C_2H_4 concentrations and low CO_2 concentrations at the highest compression ratio shows that the oxidation is far from complete. This is probably due to the high equivalence ratio (~ 4.5) and low cylinder temperature (~ 1520 K at CR=13.5).

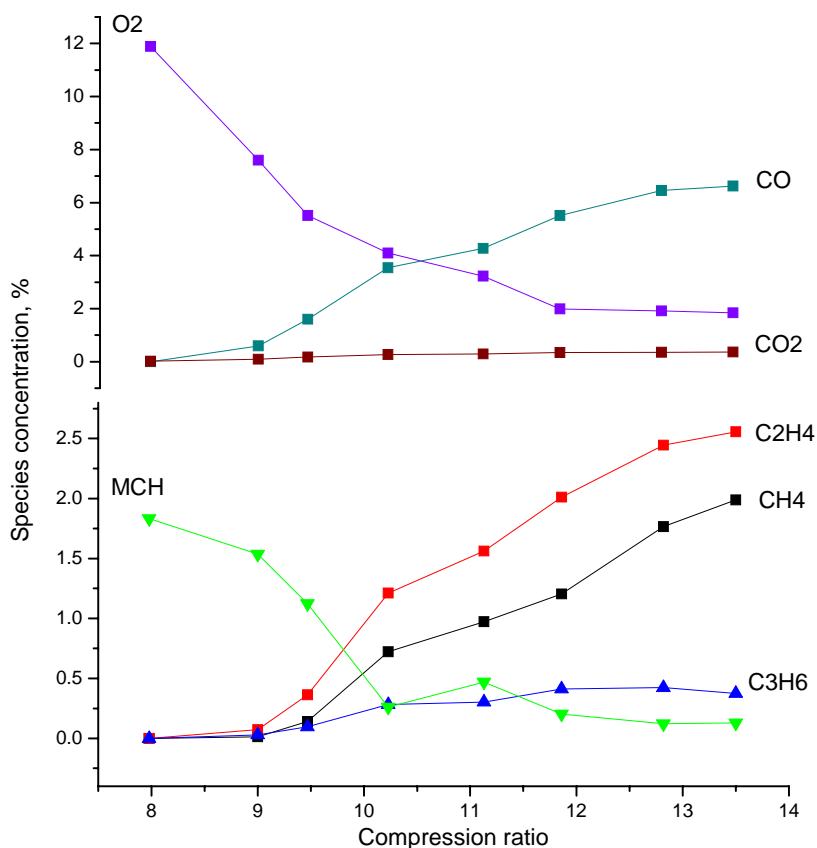


Figure 2-11 Concentrations of gaseous exhaust species as a function of compression ratio.

Condensed species Dichloromethane solution with condensed reaction intermediates were analyzed by GC-MS. Species identification and quantification are done by external standards with various concentrations. The principal result is that the reaction intermediates are dominated by species produced by dehydrogenation of the cyclohexane-ring. **Figure 2-12** shows the concentration variations of the major intermediates with compression ratio. At the lowest compression ratio the major species are (a) mixture of 3-, 4-methylcyclohexene, (b) 1-methylcyclohexene, (c) cyclohexene, and (d) methylcyclohexane. As compression ratio is increased, the concentrations of these four species gradually decrease, while benzene and toluene concentrations increase and become more important. At the highest compression ratio, reaction intermediates are composed mostly of benzene, toluene and other aromatics including styrene, indene, and naphthalene etc. Products from peroxidation path, such as methylcyclohexene epoxides,

cyclohexanone, 3-methylcyclohexanone, benzaldehyde, phenol, etc. are detected at very low concentrations compared to the products from the dehydrogenation path. This is likely due to the fuel rich condition of this study. Products from ring-opening reactions are barely detected at all test conditions. These observations confirm the results from rapid compression machine [2-5] and static reactor [2-6] that the cyclohexane ring remains intact during the early stage of oxidation.

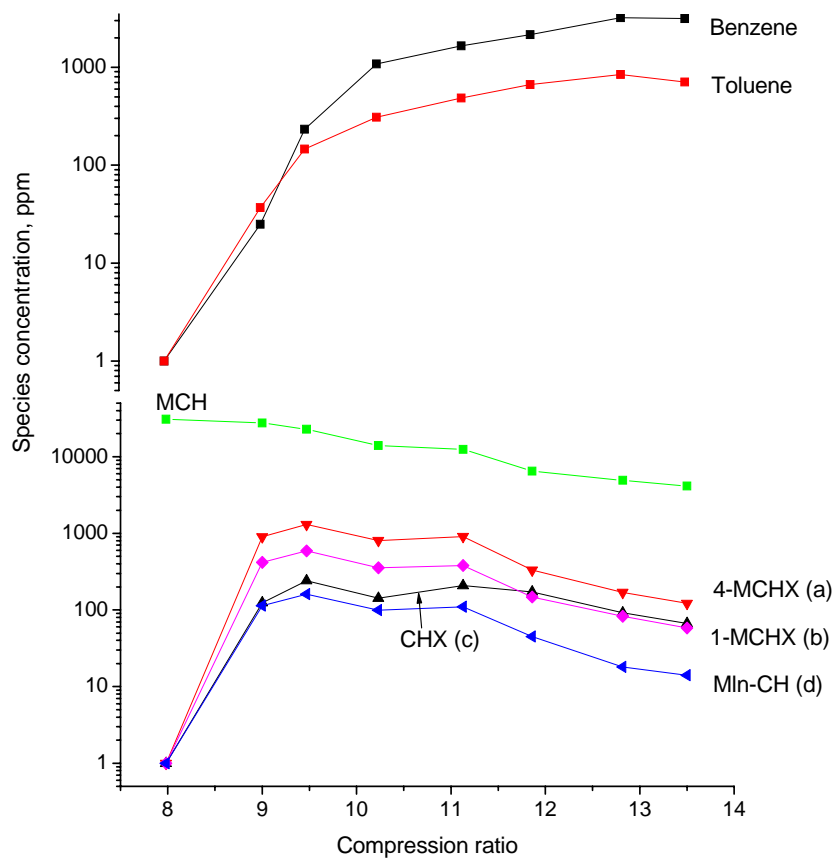


Figure 2-12 Concentrations of condensed exhaust species as a function of compression ratio.

The compounds (a) to (d) appear, increase, decrease in the similar manner with compression ratio, suggesting that they are competing reactions with similar temperature/pressure dependence. Distribution of their concentrations at low compression ratio provides insight for the early reaction paths of MCH oxidation.

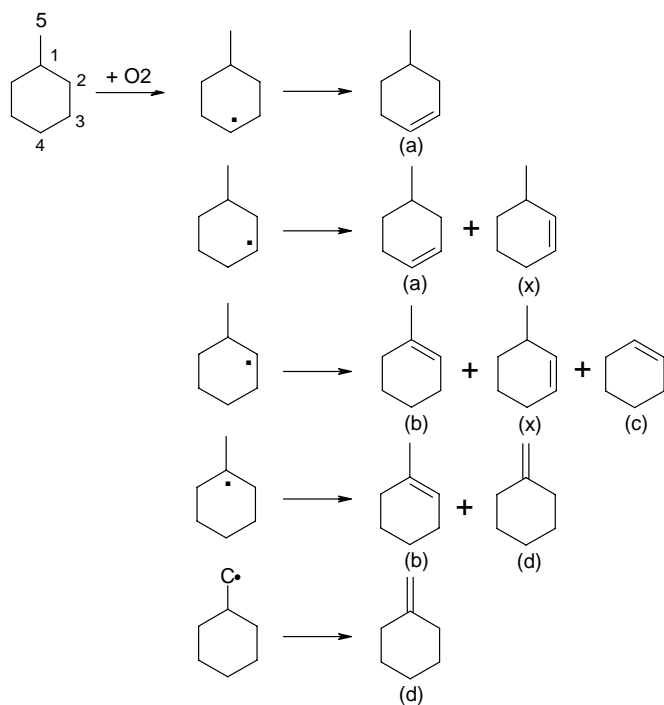


Figure 2-13 Reaction paths for early MCH oxidation.

Figure 2-13 shows the initial steps during MCH low temperature oxidation. Starting from a MCH molecule, five radicals can be possibly formed depending on where the first H-abstraction reaction occurs. The production of 1-, 3-, and 4-methylcyclohexenes are similar but 3- and 4-methylcyclohexenes co-elute from the GC column, Restek Rtx-5. In a later effort with another column, Restek VMS, these isomers are separated and found in similar amount. Concentration of methylenecyclohexane (d) is about one order of magnitude lower than that of (a), suggesting that the early H-abstraction is highly unlikely to occur on the methyl group. This can be explained by the difficulty to form a primary radical. On the other hand, once it is formed the unstable primary radical would react rapidly to form methylenecyclohexane (d), while the contribution from the stable tertiary radical for (d) should be small. Cyclohexene (c) is at a similar level to (d), suggesting that the 2-methylcyclohexyl radical is more likely to lose one more hydrogen at position 1 (by colliding with another O_2 or MCH) and form (b), instead of β -scission to remove the methyl group and form (c). At high compression ratio, the β -scission path seems favored as more cyclohexene than 1-methylcyclohexene is formed.

2.2 Impact on Diesel Fuel Quality and Performance

Under this subtask, our focus shifted from facility development activities to fuel and combustion characterization. The facilities work has been refinement and enhancement of two existing engine test stands, one housing a Navistar V-8 7.3L turbodiesel engine and the other housing a DDC 4-cylinder 2.5L turbodiesel engine.

2.2.1 Acquisition, Installation and Instrumentation of Ignition Test Equipment

This work has been completed, with some updated information on configuration and procedures given in Section 2.1.1. The equipment was applied to ignition studies of diesel and other fuels and has resulted in a publication in *Combustion & Flame* [2-7].

2.2.2. Development of Analytical Methods and Test Procedures

The modification of the CFR Octane Rating engine to serve as a rapid compression machine for ignition studies represents a unique adaptation of a standard instrument and will provide a means of comparing experimental data with kinetic models of the ignition process.

In addition, through other DOE and industrial sponsored research, we have developed extensive capabilities and methodologies for characterization of diesel soot, with the intention of determining how fuel and how combustion conditions can alter the morphology of soot aggregates, primary particle nanostructure and the surface chemistry of diesel soot. Some of these observations have been reported in journals and conferences recently [2-8, 2-9, 2-10].

2.2.3. Evaluation of Capabilities and Needs for Supplemental Measurements and Analyses

The analytical methods developed for the characterization of the fuel cuts from the PARC runs can now serve as the basis for subsequent fuel and SOF chemical analyses. We have developed procedures for use of an existing FTIR spectrometer to

speciate the products of our ignition tests, which has already highlighted significant differences in the intermediate species present as we pass through first and second stage ignition for different fuels. We have also developed a plan for upgrading an existing gas chromatograph for hydrocarbon speciation from engine exhausts. We intend to perform the upgrade of the GC (from packed to capillary columns) and use a method that is the same as in the Shimadzu GC-MS. This will allow the GC results to be interpreted through the species identification capabilities of the GC-MS.

Given the impact observed in Year 2 of the coal derived diesel fuel (CDD) on particulate emissions, in Year 3 we acquired a scanning mobility particle sizer (SMPS) to enable observation of the impact of fuel composition on the particle size distribution of diesel soot and particulates. The instrument became operational near the end of Year 3.

2.2.4. Impact on Chemical and Physical Properties

We have completed tests on the impact of coal-derived compounds on the DCN of base diesel fuels. This work resulted in the preparation of an ACS preprint [2-10].

Two major components of coal-derived diesel fuel (cut #3) were identified by GC-MS. Fluorene and phenanthrene were found to be present in sample # EI 175 in concentrations of 3 wt% and 1.5 wt%, respectively. These compounds were used as representatives for similar compounds, such as hydrophenanthrenes, that form a large portion of the coal-derived diesel.

Physical property analyses were performed on solutions of various concentrations of fluorene, or phenanthrene, in an ultra low-sulfur diesel fuel (BP15). BP15 is petroleum-derived and primarily comprises of long chain aliphatic compounds (C8 to C13). Both fluorene and phenanthrene are already present in BP15 at concentrations of <1 wt%. Solubility issues arose at concentrations greater than 5 wt% for fluorene, in all likelihood due to the aliphatic nature of BP15.

Evaluation of combustion characteristics of doped BP15 will be performed. To remove the influence of ignition delay ethyl hexyl nitrate (EHN) was added to 5% phenanthrene doped BP15 at 250, 500, and 750 ppm. The ignition delay of these mixtures was determined using the IQT and results are presented in **Table 2-3**.

Table 2-3 Fuel Properties of Ultra Low Sulfur Diesel Fuel Doped with Three-Ringed Aromatics

Fuel	BP15	BP15/5%Phenathrene/EHN			
Additive (ppm)	-	0	250	500	750
DCN	47.2	46.7	50.8	50.2	49.9

The derived cetane number (DCN) for each of the fuel blends was measured in accordance with ASTM D6890-03a. A correlation has been developed to convert the measured ignition delay into a DCN, which is correlated with the CN measured by ASTM D613 (CFR Cetane Rating engine). The ignition delay (defined as the elapsed time from injection to where the chamber pressure reaches $P_{\text{initial}} + 50$ psi) under specified conditions is measured using the Ignition Quality Tester (IQT) (**Figure 2-14**). The system is fully automated and an experiment consists of 15 pre-injections (to equilibrate system temperatures) followed by 32 injections. The reported DCNs are the averages of these 32 injections of pre-filtered fuels. A sample of data from a single injection is presented as a screen shot in **Figure 2-15**.

Very little affect on DCN was observed with the addition of varying concentrations of EHN. This result is confusing and work is continuing to determine what might be neutralizing the affect of the EHN. Similar trends, or lack thereof, in fuel properties related to phenanthrene-doped BP15 have been presented in previous reports. Methods used in sample preparation are being examined.

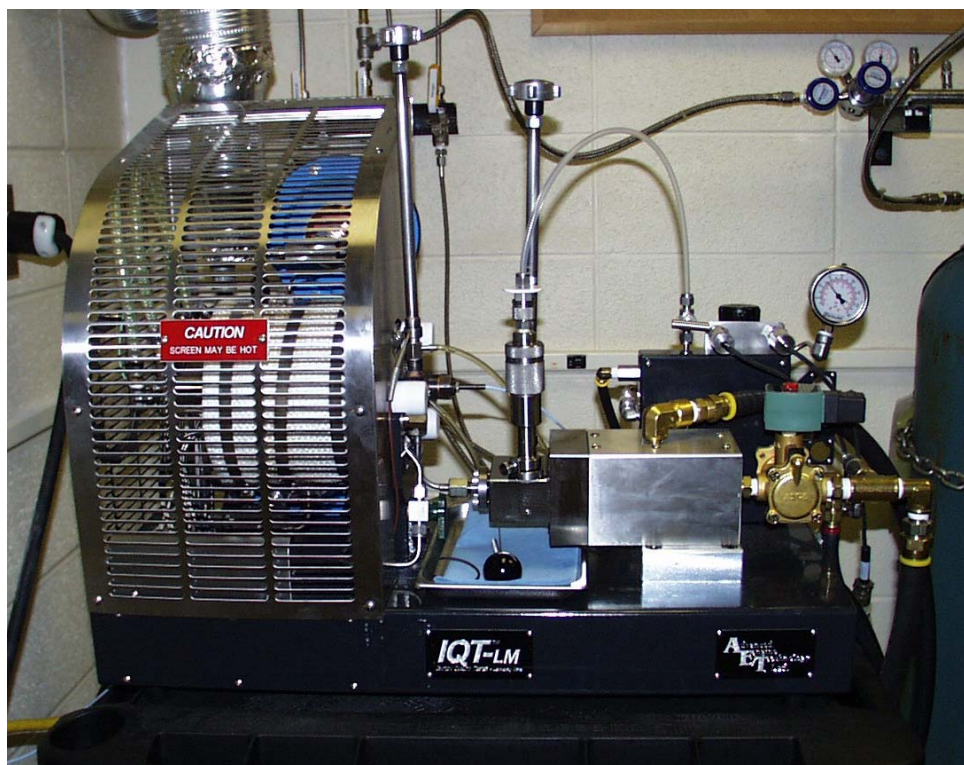


Figure 2-14 Photograph of the Ignition Quality Tester (IQT) at the Penn State Energy Institute

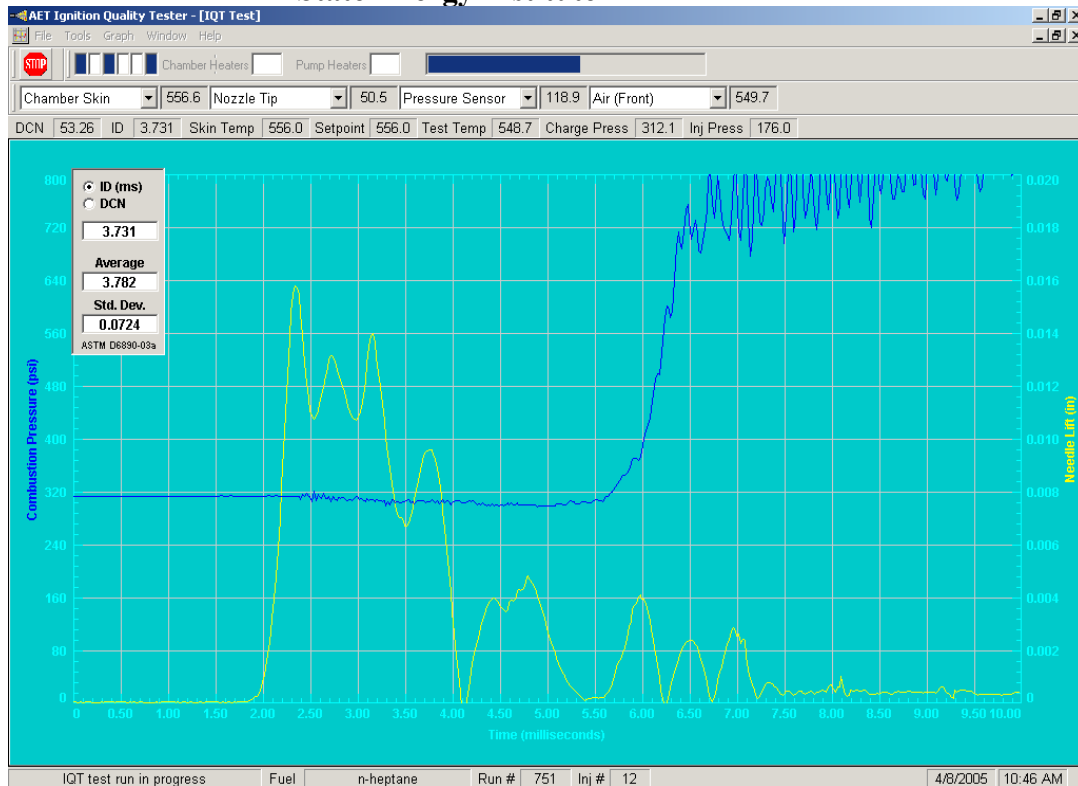


Figure 2-15 Sample data readout from the IQT. Needle lift is displayed in yellow and combustion pressure in blue.

A recent effort has focused on the impact of coal-derived compounds on the smoke point (and thereby the sooting tendency) of diesel fuel. To that end, tests were performed using Ultra Low Sulfur Diesel (BP15) and a mixture of 20 vol% biodiesel in BP15 (B20) as basestocks into which fluorene was added. The biodiesel used was SoyGold.

Smoke Point (SP) - Smoke Point data were recorded using a Smoke Point Lamp. Each sample preparation and measurement followed the ASTM D-1322 Standard Test Method for Smoke Point of Kerosene and Aviation Turbine fuel. A fuel sample was burned in the smoke point lamp, and the maximum flame height (millimeters) obtainable without smoking was measured.

Ramsbottom Carbon Residues (RCR %) - Each sample preparation and measurement followed the ASTM D-524, Standard Test Method for Ramsbottom Carbon Residue of Petroleum Products. The carbon residue of a fuel is the tendency to form carbon deposits under high temperature conditions. A 4 g sample of a filtered bulk was placed in a tared glass-coking bulb and heated at 550°C for 20 minutes. The heating expels all volatile material, leaving only the carbon residue. After cooling, the bulb was re-weighed to determine the amount of residue, which is reported as a percent RCR. The carbon residue is a measurement of the tendency of a hydrocarbon to form coke, expressed in weight percent. Equation (1) was used to obtain the weight percent carbon residues (RCR %).

$$RCR\% \approx \frac{(residuebulb - emptybulb)}{(samplebulb - emptybulb)} * 100 \quad (1)$$

In the smoke point analysis the effects of adding fluorene to BP15 and B20 were observed, **Figure 2-16**. Generally flame height decreased with the addition of fluorene, therefore sooting tendency increased [2-12]. An unexpected result was recorded for the affect of 1 wt % fluorene addition to BP15. Previous work has established that increasing aromatic composition in the fuel will produce a key shift to soot precursors [2-13].

However, a slight suppression of sooting tendency is suggested by the small increase in the SP.

SP of B20 samples were higher than their respective BP15 counterparts. This result may be due to the presence of oxygen in the fuel molecule, or simple dilution of the affect from aromatics already present in BP15 (6.9 wt% PAH).

RCR % reached a minimum at 1 wt % fluorene in both BP15 and B20. This decrease in the coke formation may be due to Hydrogen Abstraction. Hydrogen Abstraction occurs when the concentration of radicals is below critical limits i.e. low enough to increase the frequency for the radicals to react with other non-radical molecules instead of recombination (condensation) reactions with itself. **Figure 2-17**, shows how fluorene may perform this function.

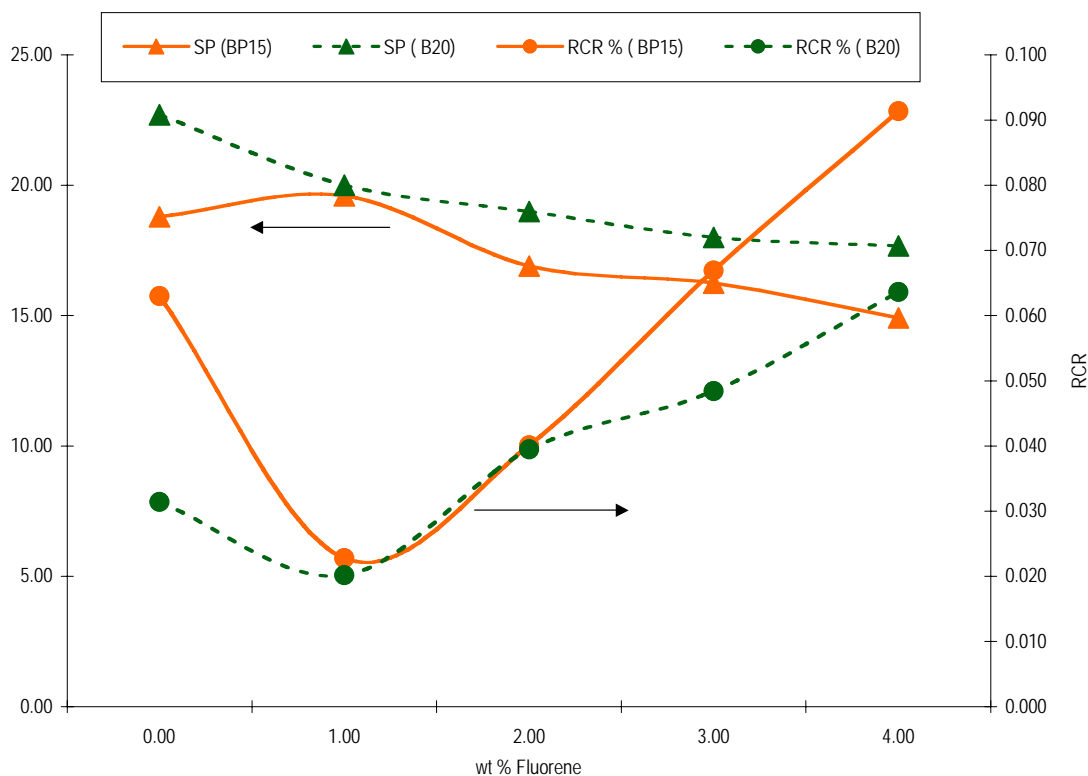


Figure 2-17 Effect of fluorene addition on the Smoke Point (SP) and Ramsbottom Carbon Residue (RCR) of both Ultra Low Sulfur Diesel (BP15) and a biodiesel blend (B20)

Previous research revealed that fluorene provides five hydrogens, the first to be released being those in sp^3 configurations (Carbon-9) [2-14]. The sp^3 hybridized carbons require lower amounts of energy to transform a chemical bond to radicals, whilst the associated aromatic rings can delocalize, and thus stabilize, the radical. Once fluorene concentrations increase, so does the concentration of fluorene radicals and the benefits of hydrogen radical production are lost due to fluorene radical recombination.

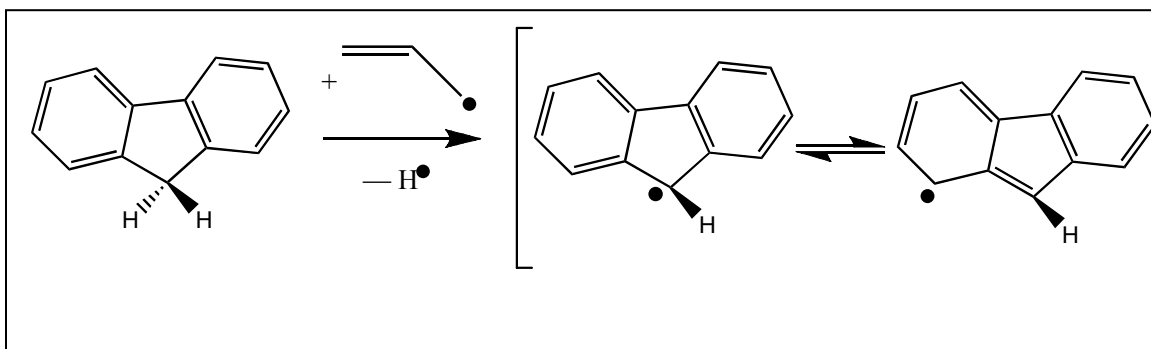


Figure 2-17 Hydrogen abstraction mechanism for fluorene

Similar RCR%s were recorded for 1 and 2 wt% fluorene with BP15 and B20, respectively. Initially, the addition of 20 vol% biodiesel to BP15 (B20) improved the RCR% (0.063 to 0.031). Once fluorene was added this degree of improvement was not attained again. Improvement in coking tendency due to fluorene addition was not as pronounced for B20 as for BP15, hinting at the presence of two competing processes.

In summary, fluorene addition to diesel and B20 fuels increases sooting tendency. Some suppression of sooting tendency was apparent when 1 wt% fluorene was added to diesel fuel. Coking tendency of both diesel and B20 was suppressed by the addition of low concentrations of fluorene. At higher concentrations fluorene increased the coking tendency of both diesel and B20 (>2.9 and >1.6 wt% fluorene, respectively). A larger affect on the coking tendency of diesel, compared to B20, suggests competing mechanisms for coking suppression between biodiesel and fluorene.

2.2.5 Impact on CI Engine Emissions and Performance

The engine testing was performed on a DDC/VM 2.5L common-rail diesel engine. Engine specifications are listed in **Table 2-4**. A 5% volume of coal-derived diesel fuel (EI-175) blended with BP15 (CDD5) was selected for the engine testing with BP15 performed as the baseline fuel. AVL mode 2 and mode 3 represent the low load and medium load conditions with low engine speeds. These two modes were chosen as the engine testing conditions at this stage. Detailed engine testing conditions can be seen in **Table 2-5**.

Table 2-4 Engine specification

Engine	DDC 2.5L TD DI-4V automotive diesel engine
Displacement	2.5L
Bore	92mm
Stroke	94mm
Compression Ratio	17.5
Connecting rod length	159mm
Rated Power	103KW@4000 RPM
Peak Torque	340Nm@1800 RPM
Injection system	Electronically controlled common-rail(Bosch)
Valve train	4 valves/cylinder

Table 2-5 Engine testing conditions

Mode	Speed (rpm)	Load (ft.lb)	BMEP (MPa)	Pilot SOI (Deg BTDC)	Main SOI (Deg BTDC)
AVL2	1330	46.5	0.32	22	-4
AVL3	1630	153.8	1.05	34	3

As shown in **Figure 2-18** and **Figure 2-19**, there were no observably significant differences found in the bulk overall combustion characteristics between coal-derived diesel blend and BP15 under both AVL mode2 and mode 4 conditions. As the engine condition was changed from AVL mode2 to mode 3, both pilot injection and main injection were advanced. As a result, reduction of premixed heat release due to main injection was observed. As to the heat release due to pilot injection, when the pilot

injection timing was advanced from AVL mode 2 to mode 3, a small amount of low temperature heat release prior to the main premixed heat release was found. Also, there was a significantly increase in the diffusion combustion fraction as the engine load was increased with the change of injection timings.

From the needle lift characteristics shown in **Figures 2-20** and **2-21**, there was no injection timing difference observed between coal-derived diesel blend and BP15 under both of the engine conditions despite that there was a bulk modulus difference between these two fuels. In conventional pump-line-nozzle diesel engines, there was a fuel pressure propagation speed difference due to the different fuel bulk modulus. However, in the common-rail diesel engines, bulk modulus effect can be eliminated due to different fuel injection system features.

Also, as shown from **Figures 2-22** to **2-25**, almost the same pressure traces and bulk cylinder temperature profiles were observed between coal-derived diesel blend and baseline BP15. Although, 5% coal-derived diesel fuel blend and baseline BP15 shared almost same injection and overall combustion characteristics, there were emissions results differences found between these two fuels. Error bars in the testing results represent the 95% confidence interval for random error and 1% full-scale system calibration error.

NO_x emissions were found higher for the coal-derived diesel blend consistently through the increased engine load conditions (**Figures 2-26**). A 0.9% NO_x increase at mode 2 conditions and 3.8% NO_x increase at mode 3 for 5% coal derived diesel blend were observed. Since there was no injection timing and overall combustion characteristics difference, adiabatic flame temperature difference between these two fuels were expected to be the reason causing the increased NO_x emissions for coal derived diesel blend. It is known that the addition of aromatic content will increase the adiabatic flame temperature and NO_x emission is very sensitive to the flame temperature and produced in the local high flame temperature regions. Coal-derived diesel fuel has a significantly higher aromatic content than normal diesel fuel, therefore the addition of coal derived diesel fuel in the baseline fuel will increase the adiabatic flame temperature and NO_x emissions. Under this condition, although there was no difference in the bulk

cylinder gas temperature profile, there were locally higher flame temperature regions formed for the coal derived diesel fuel blend.

As engine load was increased, significant decreases in the total unburned hydrocarbon and carbon monoxide emissions were observed (**Figures 2-27** and **2-28**). The decrease is mainly due to the significant increase in the combustion temperature when the engine load was increased. This increase facilitates more complete oxidation for hydrocarbon and carbon monoxide. Also, under low load condition, coal-derived diesel fuel was observed to produce more carbon monoxide emissions. This can be explained by the lower air-fuel ratio for the coal-derived diesel fuel blend as shown in **Figures 2-30**. Also, the addition of coal-derived diesel fuel increases the quantity of ring structures in the fuel, which will tend to increase the unburned hydrocarbon emissions.

Finally, a slightly higher brake specific fuel consumption for coal-derived diesel blend was observed throughout the engine testing conditions as shown in **Figures 2-29**.

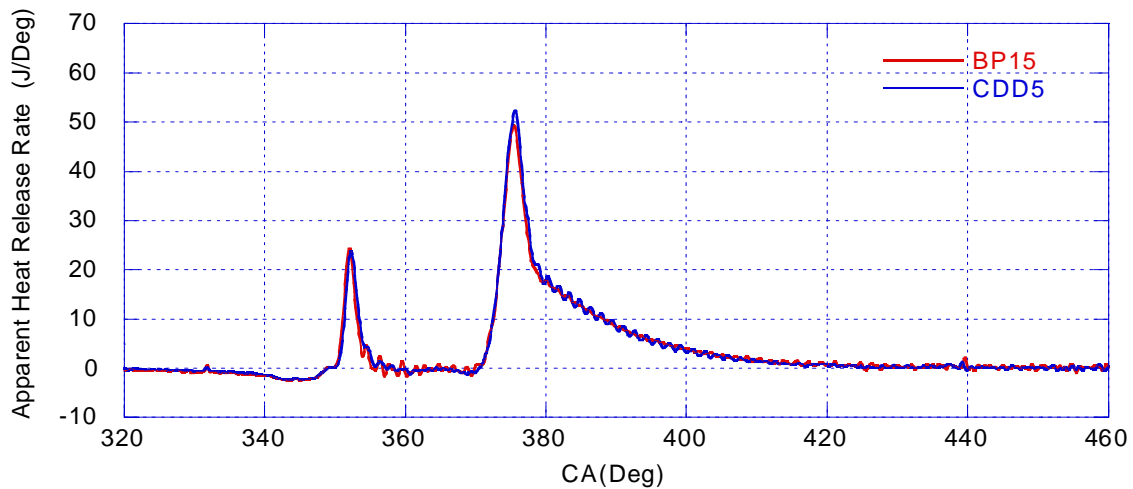


Figure 2-18 Apparent heat release rate at AVL mode 2

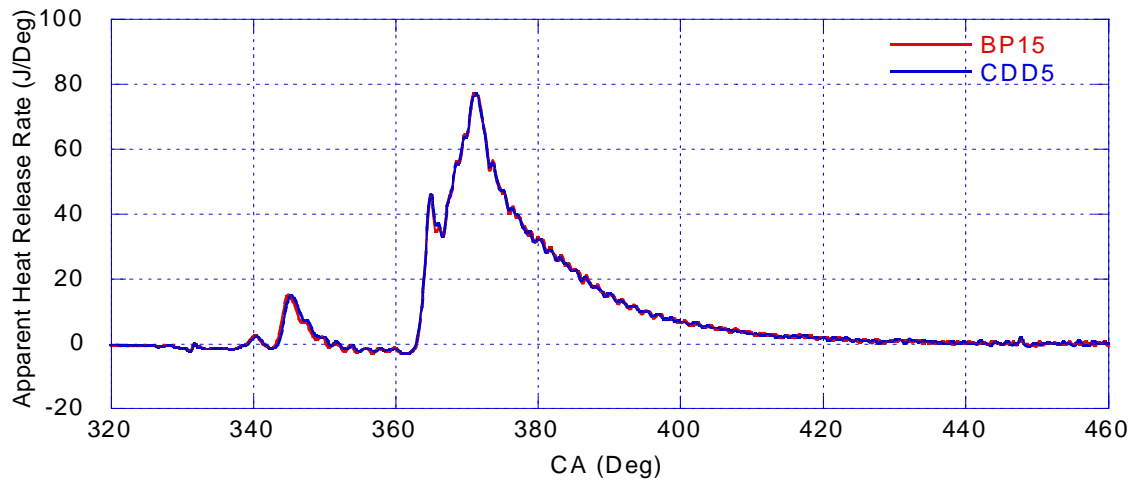


Figure 2-19 Apparent heat release rate at AVL mode 3

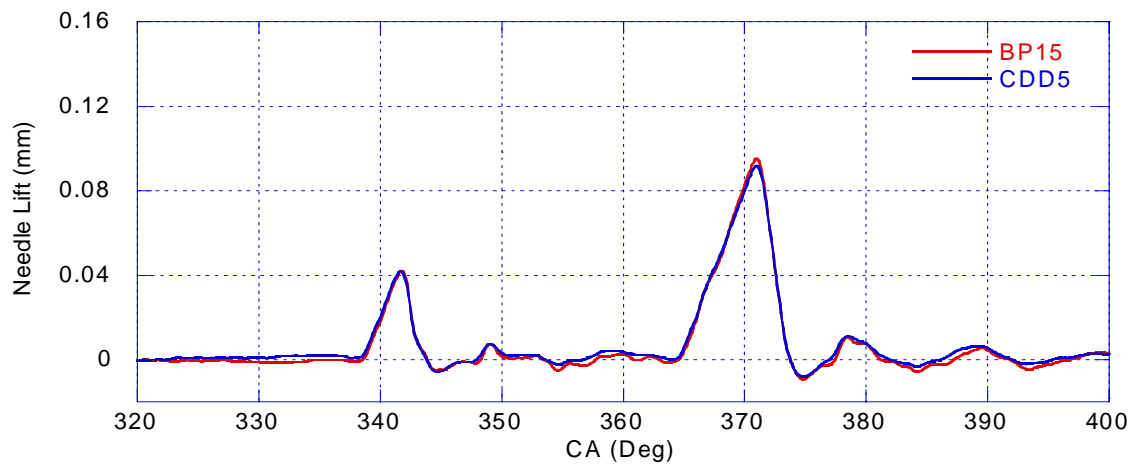


Figure 2-20 Needle lift signal at AVL mode 2

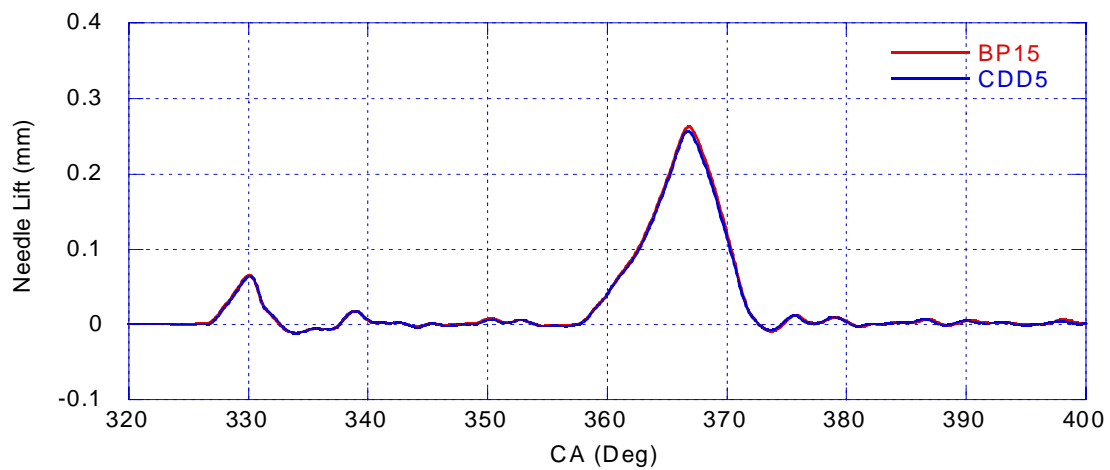


Figure 2-21 Needle lift signal at AVL mode 3

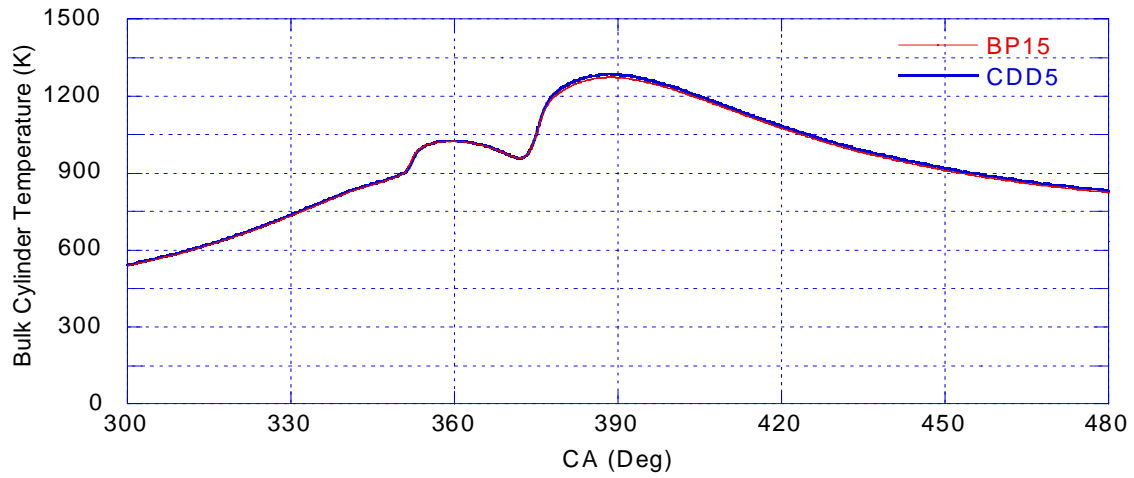


Figure 2-22 Bulk cylinder gas temperature at AVL mode 2

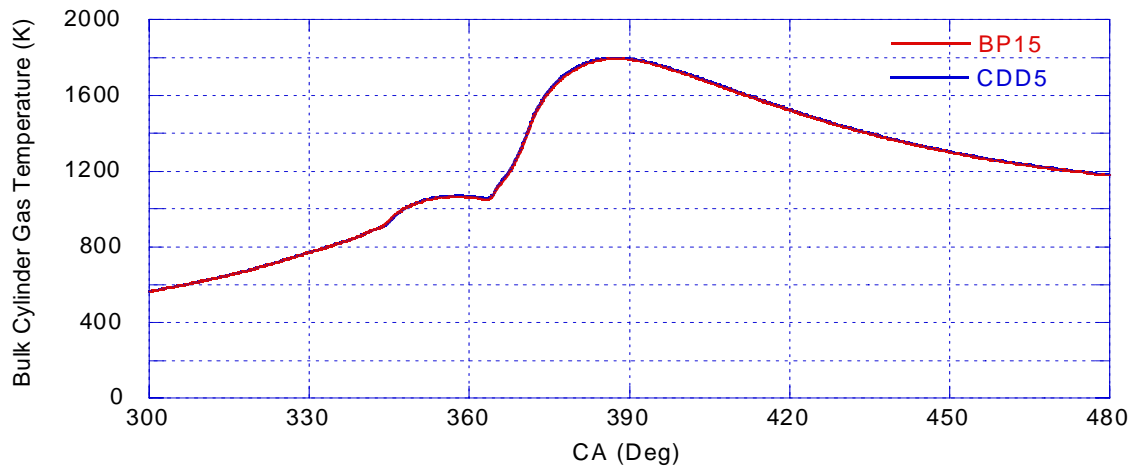


Figure 2-23 Bulk cylinder gas temperature at AVL mode 3

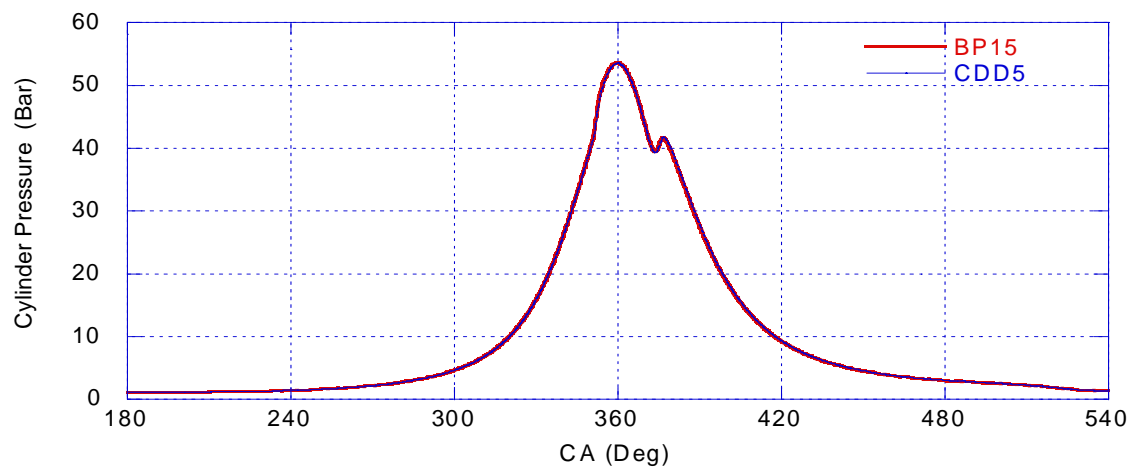


Figure 2-24 Cylinder pressure trace at AVL mode 2

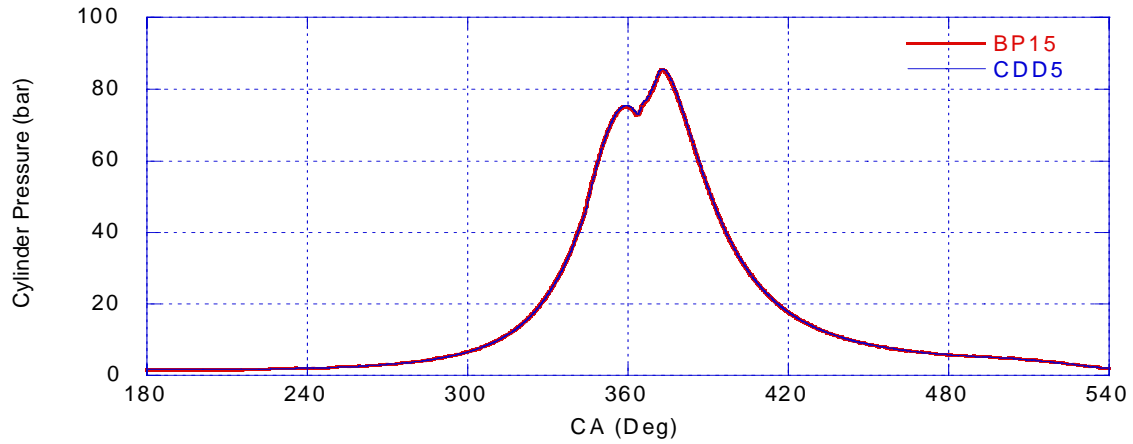


Figure 2-25 Cylinder pressure trace at AVL mode 3

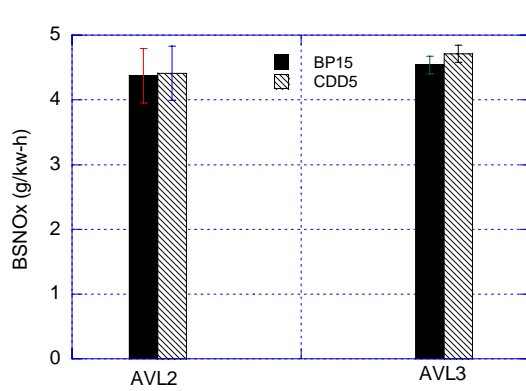


Figure 2-26 Brake specific NO_x emissions

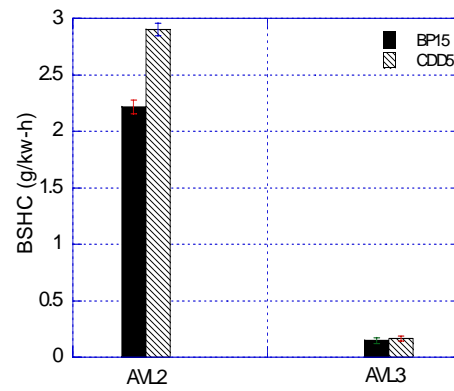


Fig. 2-27 Brake specific unburned hydrocarbon emissions

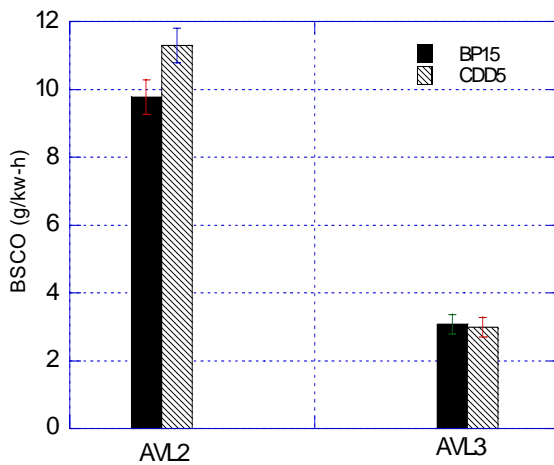


Figure 2-28 Brake specific CO emissions

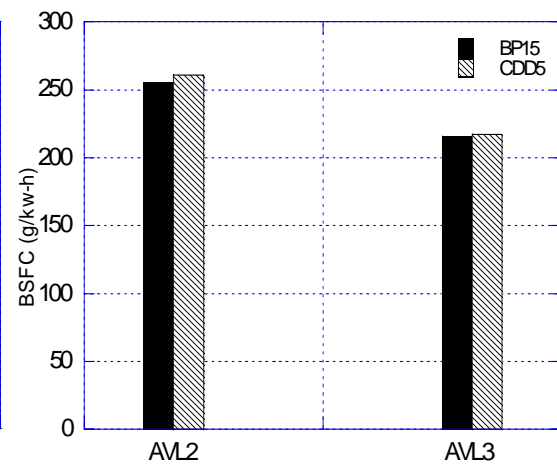


Figure 2-29 Brake specific fuel consumption

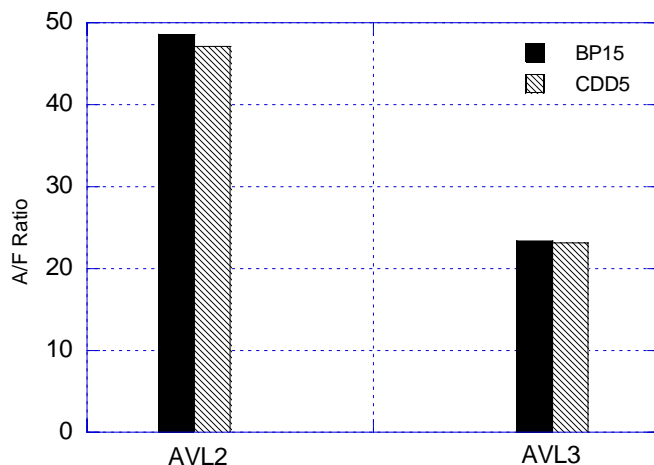


Figure 2-30 Air to fuel ratio

Engine Performance and Emissions Studies Including PM Size Distribution

For these tests, coal-derived diesel (CDD) was blended into ultra low sulfur diesel (ULSD) at 5 vol%. Engine studies were then performed on the ULSD and the 5 vol% blend (5CDD). These engine studies were performed on a DDC 2.5 L common rail diesel engine, run at 3600 rpm at 25% and 75% load (51 and 153 ft-lb torque, respectively). A pilot injection was used. Both pilot and main injection timings were kept constant for all fuels at each test mode. Exhaust gas recirculation (EGR) was kept at 0%.

Gaseous emissions were measured using analyzers integrated into an AVL CEB II emissions bench. Exhaust gases were kept at a constant temperature of 190°C with a heated sample line. NO_x emissions were measured without exhaust cooling using an EcoPhysics chemiluminescence analyzer. A portion of the sample gas was chilled to strip the water before being analyzed with Rosemount CO (IR), CO₂ (IR), and O₂ (paramagnetic) detectors. All gaseous emissions were sampled continuously throughout the testing and measurements were automatically logged by the data acquisition system every 15 seconds via serial communication.

Particulate Matter (PM) emission masses were measured using a Sierra BG-2 dilution bench and a Tapered Element Oscillating Microbalance (TEOM). For the BG-2 measurement, 150 mm filters were pre-extracted with dichloromethane (DCM) then kept in a humidity chamber for 48 hours before weighing. PM emissions were collected at a

sample flow rate of 10 SLPM for 5 minutes. After one disposable filter, five sample filters were collected and stored in a humidity chamber for 48 hours before reweighing.

For the TEOM measurement, PM emissions were collected at a sample flow rate of 10 SLPM using the BG-2 to dilute the sample. The sample was taken for three minutes before recording started to allow PM to collect on both the BG-2 and TEOM filters to reduce pressure fluctuations due to initial PM collection. Mass collection was recorded to achieve a plot of mass vs. time. The mass acquired after 5 minutes was then calculated for direct comparison with BG-2 data.

PM was also measured to determine its particle size distribution. A diluted exhaust stream was sampled by the Scanning Mobility Particle Sizer (SMPS) at 1.4 SLPM through a Thermodenuder (TD). Total particles were sized with the TD at 40°C. Non-volatile particles were sized with the TD at 350°C. Results are presented as concentration of size fraction and non-volatile particles as a percentage of the total particles on a particle number basis.

Plots can be explained following the extensive review by Kittelson [2-15]. Two distinct particle size regions exist in the particle size analysis of diesel PM (**Figure 2-31**): the nuclei region and the accumulation region. The nuclei region (<50 nm) consists of a large number of small particles and contributes to the majority of the number of particles. The accumulation region (at a maximum around 150-200 nm) contributes to the majority of the mass of the particles even though these particles are much lower in number.

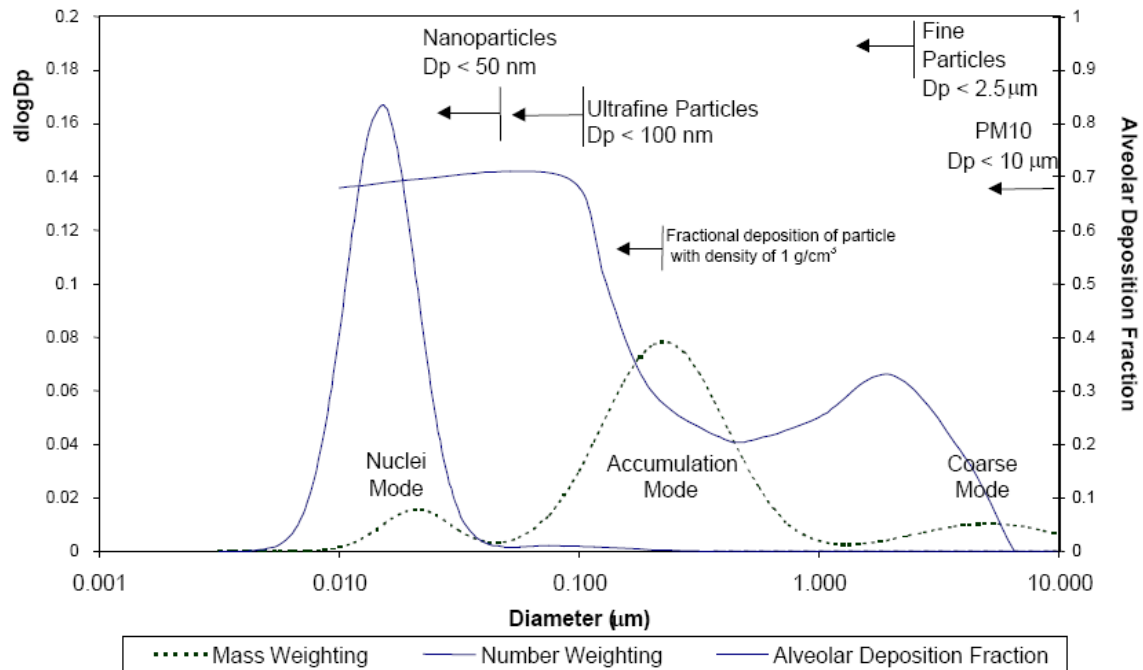


Figure 2-31 Typical engine exhaust size distribution. Both mass and number weightings are shown [2-25].

Table 2-6 presents the physical properties of the two fuels studied. Setting the same injection timings for both fuels led to almost identical pressure and heat release signals (Figures 2-32 and 2-33). This was expected due to the similar DCN and calorific values of the two fuels.

Table 2-6: Fuel Properties

	ULSD (BP-15)	5CDD (EI-175/BP-15)
Additive (vol%)	-	5
DCN	47.2	44.9
Flash Point (°C)	66.4	69.0
Viscosity (cSt)	2.553	2.484

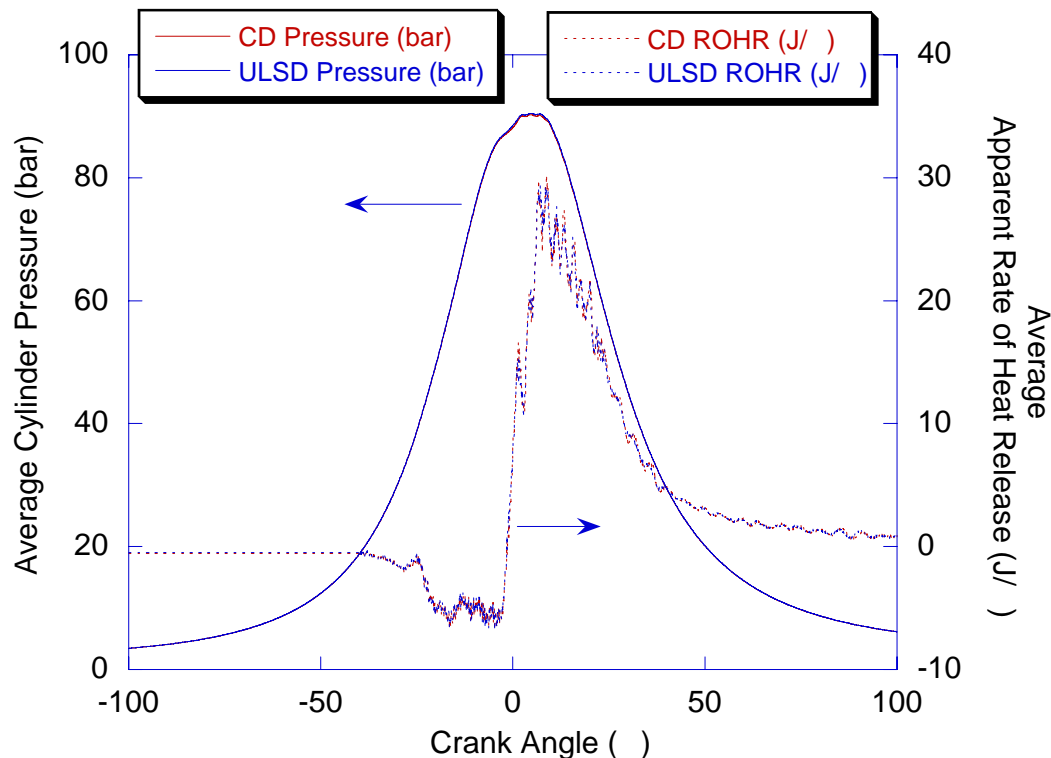


Figure 2-32 Pressure and Heat Release curves for ULSD and 5CDD at 3600 rpm and low load.

Gaseous emissions of unburned hydrocarbons, carbon monoxide, and carbon dioxide were the same for the two fuels at either performance mode. NO_x emissions are illustrated in **Figure 2-34**, and were slightly higher, under both conditions, when using the 5CDD fuel. As heat release magnitude and timing were the same for the 2 fuels, another possible source of NO_x could be fuel-borne nitrogen.

PM mass emissions are presented in **Figure 2-35** for both BG-2 and TEOM measurements. Although absolute values are not the same both PM measurement techniques trend the same. Sampling for the TEOM was maintained at 50°C , whereas sampling for the BG-2 was kept below 52°C . Therefore at low load the sampling temperature is lower than 50°C and at high load the sampling temperature increased closer to its maximum. At lower temperatures more exhaust condensed on the filter increasing the PM yield, hence at high load, when temperatures increased, the PM yield for the two techniques was closer.

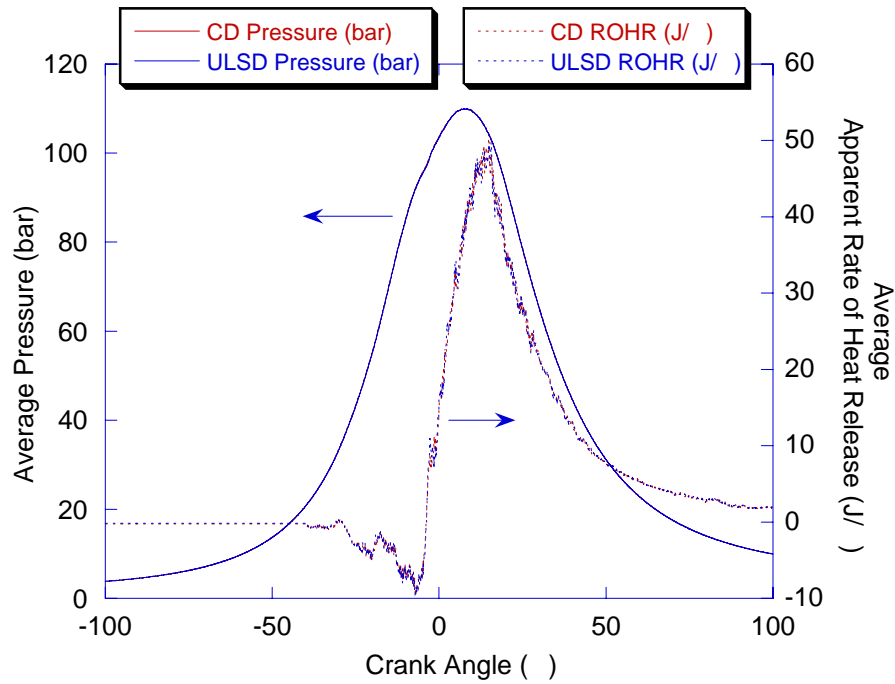


Figure 2-33 Pressure and Heat Release curves for ULSD and 5CDD at 3600 rpm and high load.

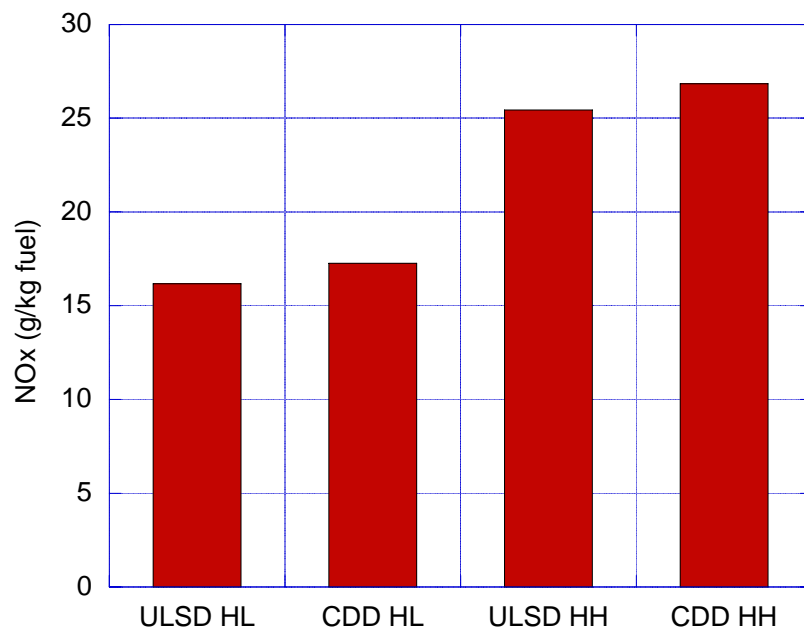


Figure 2-34 NO_x emissions for ULSD and 5CDD at 3600 rpm and low and high load.

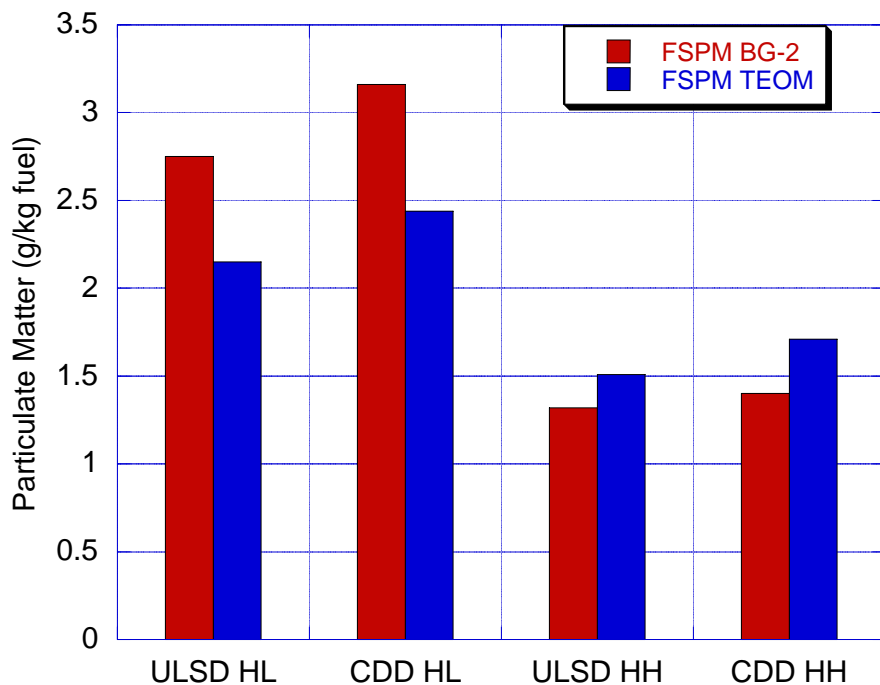


Figure 2-35 PM emissions for ULSD and 5CDD at 3600 rpm and low and high load.

PM emissions increased when using 5CDD for both engine modes and both measurement techniques. Slightly higher aromatic content in 5CDD would be expected to contribute to the production of more soot. **Figures 2-36 and 2-37** illustrate particle size distributions of PM from an SMPS. Total number of particles increased under both engine conditions when using 5CDD. 5CDD also produced larger particles than ULSD at low load, whereas at high load particle sizes appear consistent.

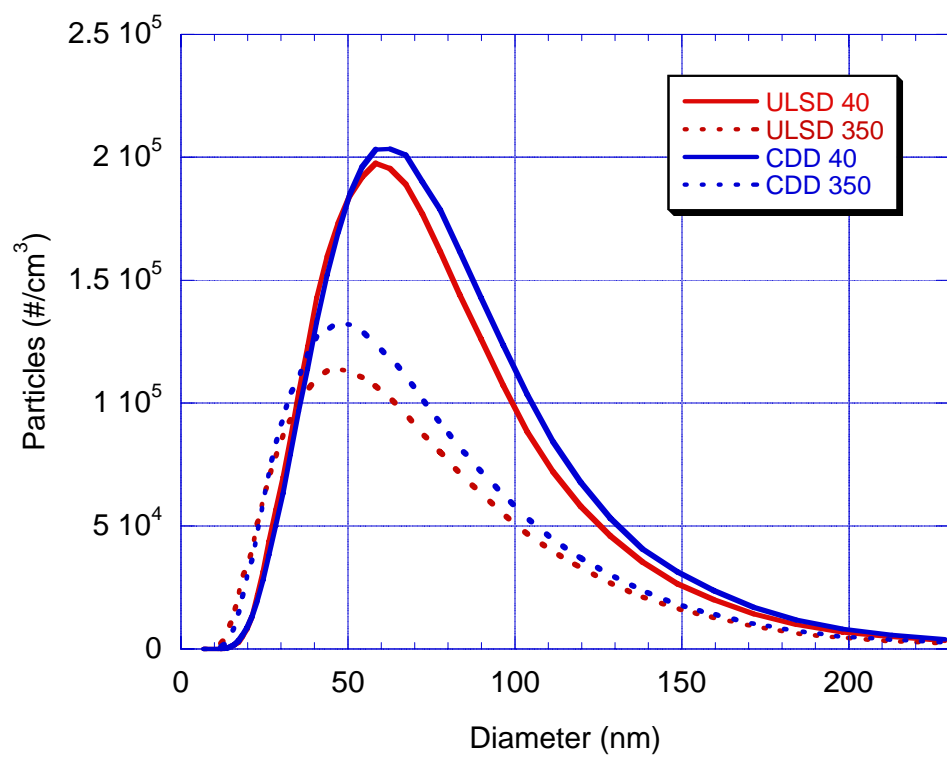


Figure 2-36 SMPS of PM emissions from ULSD and 5CDD at 3600 rpm and low load.

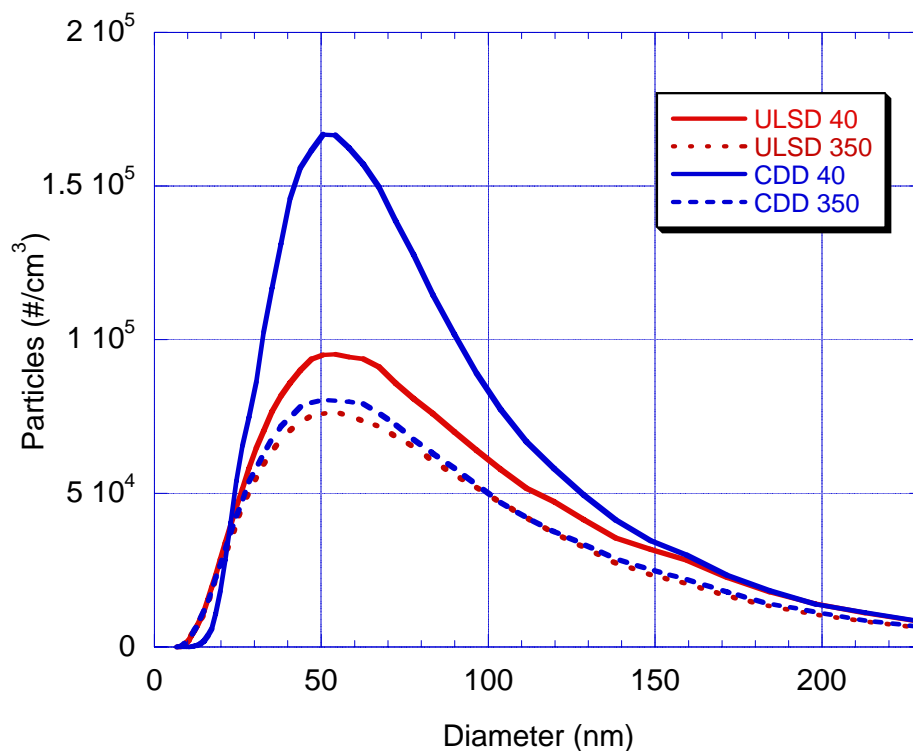


Figure 2-37 SMPS of PM emissions from ULSD and 5CDD at 3600 rpm and high load.

At the high load condition 5CDD produced a much greater number of particles of 50-100 nm. However, when the temperature of the TD was increased this difference was no longer observed, suggesting that the 5CDD fuel may be producing an aerosol of volatile droplets at high load.

Overall, 5CDD fuel performed well in a common-rail diesel engine compared to ULSD. However, even at only 5 vol% increases in both NO_x and PM emissions were observed in the presence of CDD.

Impacts of Addition of Phenanthrene on Engine Performance and NO_x Emissions

Since phenanthrene has been identified in the coal-based diesel fuel and similar compounds form a large portion of the coal based diesel fuel, it is of interest to investigate the impacts of addition of phenanthrene on engine performance and

emissions. To that end, 1 wt.% and 5 wt.% phenanthrene were doped into neat biodiesel fuel for engine tests. The engine was operated at 1350 rpm, high load conditions.

All of the three test fuels had very similar needle lift and heat release rate profiles, as shown in **Figures 2-38 and 2-39**. **Figure 2-40** shows that the brake specific fuel consumption decreased as more phenanthrene was added into the baseline biodiesel fuel. Since phenanthrene has significantly higher sooting tendency than biodiesel, more soot will be expected to form in the diffusion flame region when phenanthrene is added. Higher soot formation in the flame zone can cause increases in soot radiative heat transfer from the diffusion flame, which can lead to decreases of actual flame temperatures. Due to the high sensitivity of thermal NO formation on flame temperature, NO_x emissions were anticipated to decrease as the actual flame temperature decreases. Therefore, the addition of phenanthrene is expected to result in the decrease of NO_x emissions. However, on the other hand, the addition of phenanthrene into biodiesel will also increase the adiabatic flame temperature of the blend. Hence, two competing effects co-exist in the NO formation when phenanthrene is added. **Figure 2-41** shows the NO_x emissions for the three test fuels under different load conditions. As can be seen, 1% addition of phenanthrene causes an increase in NO_x emissions at 13.2 bar gIMEP condition. But, at lower load conditions, it generally showed no obvious effect on NO_x emissions. When 5% phenanthrene is added, an evident decrease in NO_x emissions throughout the load conditions was observed, which indicated the soot radiation effects had become more dominant at this concentration of phenanthrene. Exhaust temperatures shown in **Figure 2-42** were also found decreased for 5% phenanthrene blend, which was also an indication of lower combustion temperatures for the biodiesel containing 5% phenanthrene. Further investigation will be performed to confirm the results from this study.

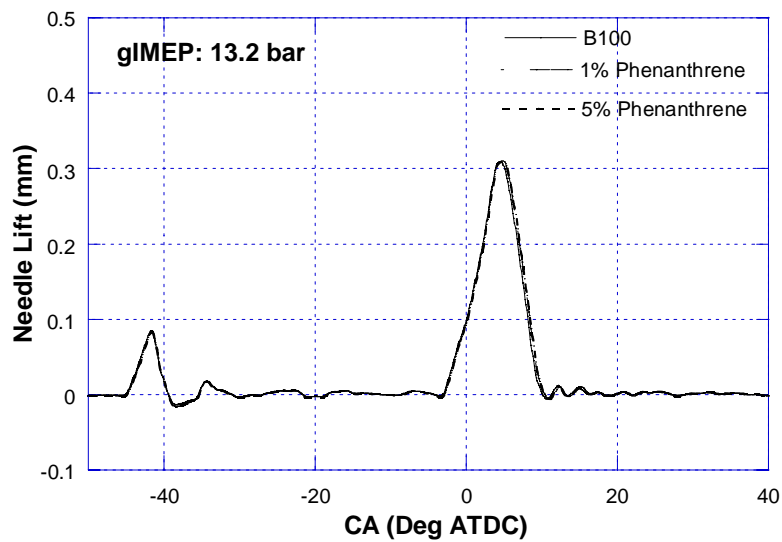


Figure 2-38: Needle Lift Profile at 13.2 bar gIMEP Condition

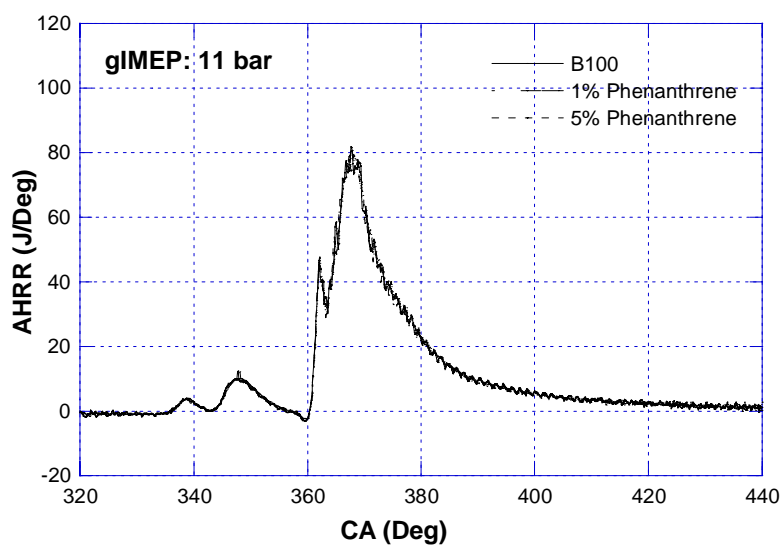


Figure 2-39: Apparent Heat Release Rate at 11 bar gIMEP Condition

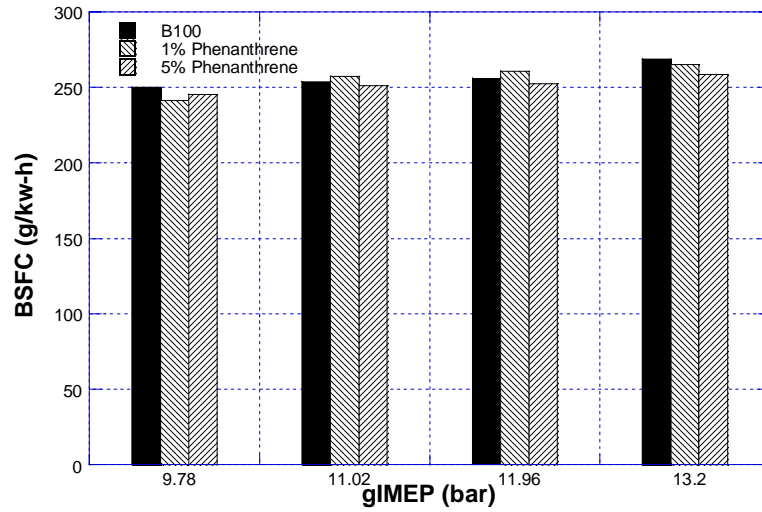


Figure 2-40: Brake Specific Fuel Consumption

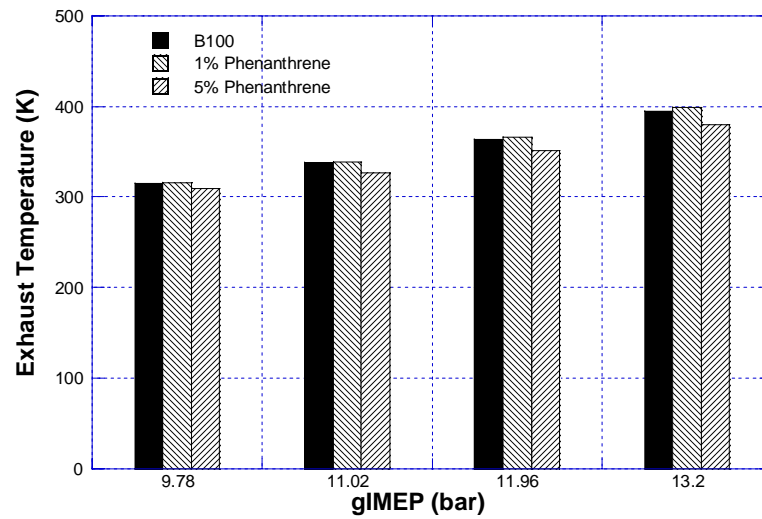


Figure 2-41: Brake Specific NO_x Emissions

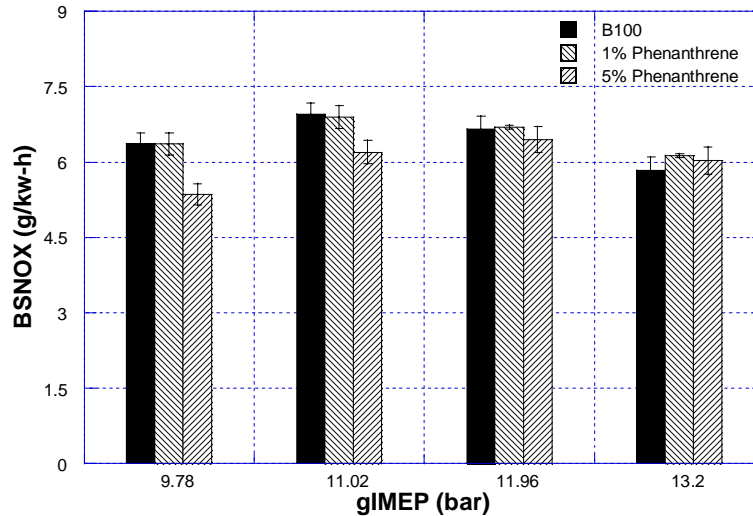


Figure 2-42: Exhaust Temperature

Impact of Fuel Composition on Combustion and the Properties of Diesel Soot

Previously in the Year 2 Annual Report [2-16] we presented a comparison between BP15, 10%CDD, and 20%CDD. Emission data was obtained for BP15 and 20%CDD fuels. The oxidation behavior of the soot from engine combustion of BP15 and 10%CDD was determined by using the thermogravimetric and Differential Scanning Calorimetry (TGA-DSC). The engine used in this experiment is a single cylinder DI diesel engine operated at 75% load and 3600 rpm. This section of the report provides a comparison between BP15, 10%CDD, and 20%CDD.

Single-Cylinder DI diesel Engine - A highly instrumented, single-cylinder direct injection (DI) diesel engine with a maximum power output of 7 hp. Cylinder pressure and fuel-line pressures will be measured using Kistler piezoelectric pressure transducer models 6052B1 and 601B1, respectively. A Hall-effect proximity sensor will be used to measure needle-lift in the injector. An AVL 364 shaft encoder installed on the engine crankshaft, along with a Keithley DAS 1800 data acquisition board enabled 0.1 CA degree resolutions of these signals. NO_x emissions will be measured using an Eco-Physics NO_x analyzer integral in an AVL GEM 110 emissions bench.

Fuels - The test fuels considered in this work are: an ultra low sulfur diesel with 15ppm sulfur content (BP15) and BP15 blended with 10% and 20% CDD.

Soot Oxidation Reactivity - In this study, The BP15 and 10% CDD soots were collected from the raw exhaust of a single-cylinder DI diesel engine. The soot oxidation behavior was conducted on the Thermogravimetric Analysis (TGA) and Differential Scanning Calorimetry (DSC). TGA-DSC provides data on soot mass reduction as a function of temperature and the oxidation temperature and time.

Emissions - The preliminary investigations on the effects of the coal-derived diesel on engine emissions were conducted on the single-cylinder DI engine. The engine was operated at 75% load and 3600rpm.

Table 2-7 shows emission data for BP15 and 20%CDD. The injection of 20%CDD (-7.6 CA BTDC) is advanced relative to the BP15 fuel (-6.98 CA BTDC). As a result, the 20%CDD produces higher NO_x than the BP15 fuel.

Figure 2-43 shows pressure data for BP15 and 20%CDD. BP15 has a relatively higher peak temperature. As seen in the heat release profile in **Figure 2-44**, the start of combustion is retarded for the 20%CDD relative to the BP15 fuel, due to the low cetane number of the 20%CDD fuel.

Table 2-7. Emission data for BP15 and 20%CDD

	BP15	20%CDD
NO _x (ppm)	569	616
CO ₂ (%)	7.9	8.3
CO (ppm)	831	1060
UHC (ppm)	286	404

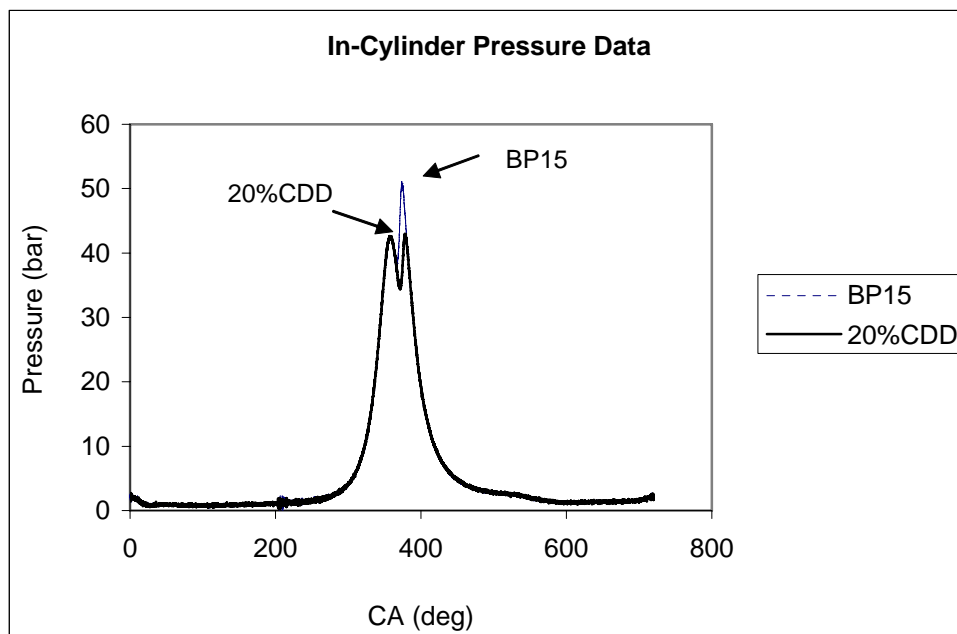


Figure 2-43 In-cylinder pressure data for BP15 and 20%CDD fuels.

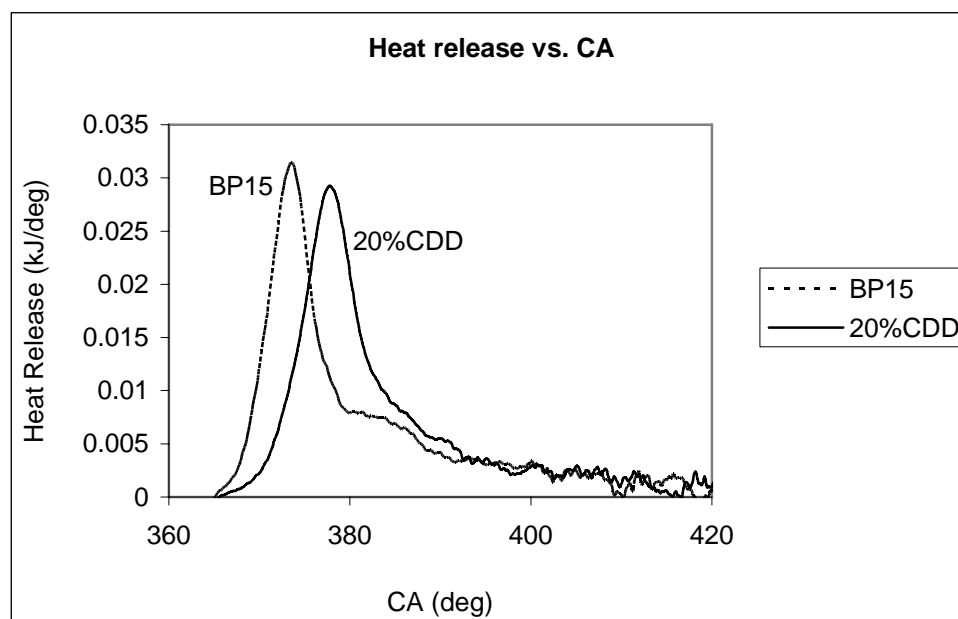


Figure 2-44 Heat release profile for BP15 and 20%CDD fuels.

Soot Characterization - For temperature programmed oxidation (TPO) experiments, TGA-DSC tests were performed on a Q-600 thermogravimetric analyzer. Soot particles were collected from the raw exhaust of the single-cylinder DI diesel

engine. The soot was collected on Teflon filters and then removed and heated at 500°C for 1 hour under nitrogen gas to remove the soluble organic fraction. Soot samples were then placed in TGA-DSC furnace and heated in air in the temperature range 20-700 °C using heating rate of 10 °C/min. **Figure 2-45** shows the mass reduction and heat release profiles as a function of temperature for BP15 and 10%CDD. It is obvious that the oxidation characteristics of the soot from both fuels are identical. This would indicate that the soot formation mechanisms and the physical/chemical properties of both soots are similar. **Table 2-8** shows some important thermal parameters of both soots.

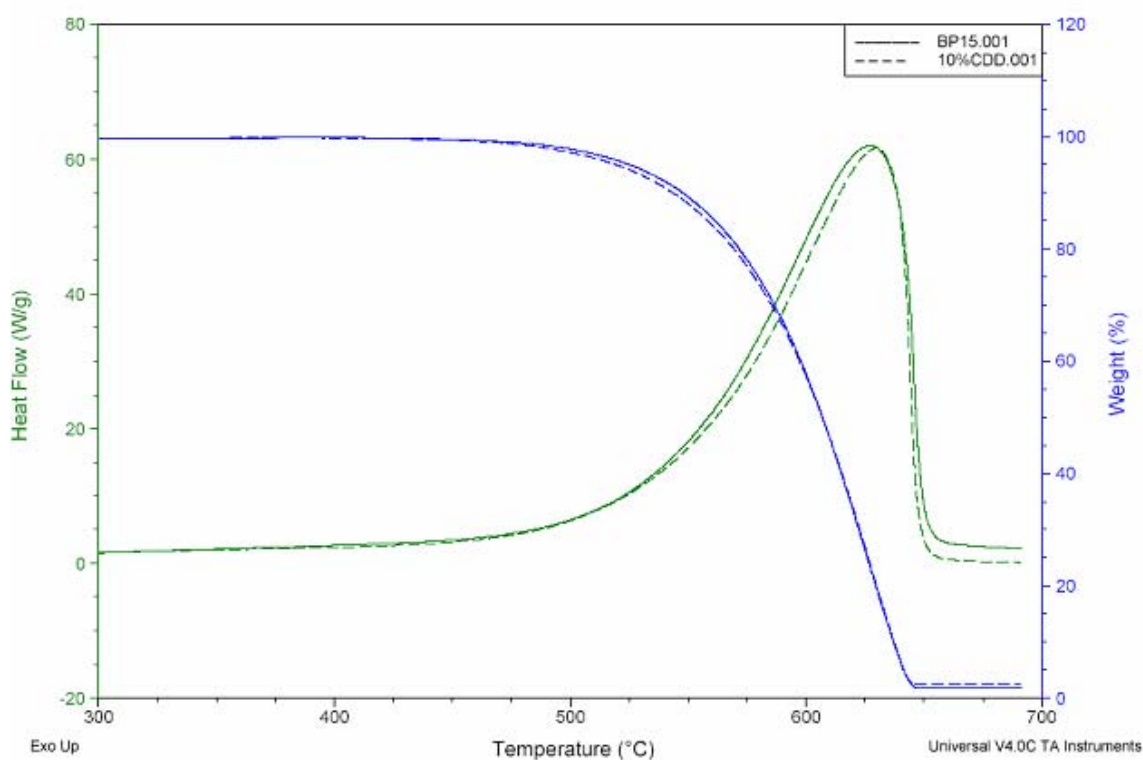


Figure 2-45 TGA-DSC profiles for different soot samples.

Table 2-8. Thermal properties of diesel soot.

	BP15	10%CDD
*Onset temp. (°C)	525	519
Maximum peak temp. (°C)	627.65	630.43
Heat of reaction (kJ/g)	24.4	23.5

*T_{onset}: temperature at 5 wt.% weight loss

Soot Structure - To gain better understanding about structural properties of diesel soot, the HRTEM imaging was obtained. The experiment was conducted on a field emission JEOL 2010F instruments located in the Materials Research Institute (MRI) of Penn State. For the HRTEM imaging, thermophoretic sampling unit was used to capture soot particles from the raw exhaust. Soot particles were captured on a 3 mm diameter copper grid coated with a lacey carbon film. **Figure 2-46** shows the nanostructure of the 20% CDD soot. It exhibits the classical soot nanostructure: long fringes arranged concentrically at the edges and randomly oriented fringes in the center.

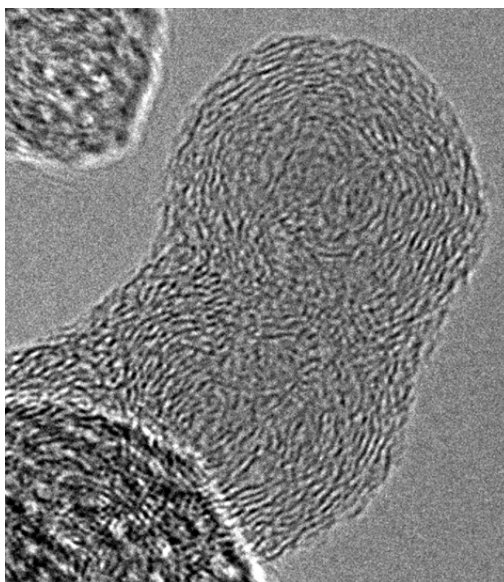


Figure 2-46 Soot Nanostructure of 20% CDD soot.

Future Work - The impacts of engine operating conditions such as EGR, injection timing and injection strategies on soot oxidative reactivities will be evaluated. Bulk soot samples will be collected from the raw exhaust of the DDC engine. Further experiments will be conducted on the TGA-DSC to obtain the oxidation kinetics of diesel soot.

X-Ray Diffraction (XRD) will be used to obtain the interlayer spacing (d002) and the layer dimension (La). Raman Spectroscopy (RS) will be used to obtain the intensities of the amorphous and graphitic peaks and the intensity ratio will be interpreted as a measure of the in-plane crystallite dimensions. The density, pore size distribution, and active surface areas of different soots will also be determined. The CHN analyzer will be used to obtain information about the elemental composition of the soot. FTIR will provide data about the functional groups.

Impact of EGR on Combustion and the Properties of Diesel Soot

In the Year 2 Annual Report [2-16] for future work, we proposed to examine the impacts of engine operating conditions such as EGR, injection timing and injection strategies on soot oxidative reactivity. Bulk soot samples were to be collected from the raw exhaust of the DDC engine. Experiments were to be conducted on the TGA-DSC to obtain the oxidation kinetics of diesel soot and various characterization techniques were to be applied to these soot samples, for comparison with the fuel effects.

Recent findings in our laboratory have shown that fuel formulation can affect the oxidative reactivity of the soot (see for instance the Year 2 Annual Report [2-16]). The inclusion of biodiesel in the fuel lowers the ignition temperature of soot and consequently lowers the temperature required for regeneration of the diesel particulate filter (DPF) and this was attributed to the high surface oxygen content of biodiesel soot. In addition, the oxidation rate of biodiesel was found to be two times faster than that of diesel soot [2-8].

Here, we present a potential method to improve the regenerability of the DPF by enhancing the oxidative reactivity of diesel soot. We show that EGR can be utilized to generate more reactive soot. Carbon dioxide CO₂ was used to simulate particle free and cold EGR, which is proposed as a possible pathway to generate soot that is more prone to oxidize in DPF.

Soot Origin and Sampling. A highly instrumented single cylinder direct injection diesel engine was used to produce the soot samples. The engine was running under fixed load (75%) and speed (3600 rpm). Diesel particulate matter samples were collected from the raw exhaust of the engine on Teflon filters. The diesel particulate matter was subsequently removed from the filters and thermally treated under UHP nitrogen at 500°C to remove volatile compounds. Thus, the soot considered in this work is the volatile-free fraction of the diesel particulate. Simulated EGR (SEGR) was introduced to the engine intake system from high pressure cylinders of CO₂ at different concentrations: 0, 3, 6, and 9 vol.%. The fuel considered was an ultra low sulfur diesel with 15 ppm sulfur content (BP15).

Soot Oxidative Reactivity. A Thermogravimetric Analyzer (TGA) was used to investigate the difference in reactivity between the soot samples. Two experiments were considered to elucidate the soot reactivity: (1) the isothermal in which the soot was heated in air (100cc/min) at 475°C and, (2) the nonisothermal in which the soot was heated in air (100cc/min) from 30°C to 600°C at a heating rate of 2.5°C/min. The kinetic parameters of soot oxidation were derived from the nonisothermal profiles [2-17].

Raman Spectroscopy. A visible Renishaw spectroscopy was used to determine the degree of graphitization of the soot samples. The excitation laser was an Ar ion laser ($\lambda_0 = 514$ nm, source power 10mW). The laser was focused on the sample through a microscope with 100X objective lens. Two soot samples, designated as S0 and S9 were considered, where 0 and 9 correspond to the CO₂ concentrations under which the soot was formed. The integrated intensity ratio IG/ID was used to investigate the degree of graphitization of the soot samples and Tuinstra and Koenig (TK) expression was used to determine the crystallite width (La) [2-17].

X-Ray Diffraction (XRD). The XRD investigation was done using a Philips MPD instrument. The XRD spectra of S0 and S9 were recorded and the interlayer spacing (d002) was calculated according to Bragg's equation [Chen and Dobbins, 2000], the stacking height (Lc) and the crystallite width (La) were calculated according Scherrer's equation [2-18].

Soot Nanostructure Imaging. To investigate the nanostructure of the diesel soot, the high resolution transmission electron microscopy (HRTEM) images were

recorded using a Joel 2010F instrument operated at 200kV and equipped with a field emission gun. A small amount of the sample was suspended and sonicated in ethanol. A drop of the solution was then transferred to a copper grid coated with a lacy carbon film for analysis.

Soot Reactivity. **Figure 2-47a** shows the isothermal TGA profiles for S0 and S9. The impact of CO₂ is obvious. Increasing the CO₂ enhances the oxidation behavior of the soot. **Figure 2-47a** also shows that by increasing the CO₂ concentration in the engine intake, further increase in the reactivity is observed. The oxidation rate of S9 was found to be two times faster than that of S0. The results here suggest that low temperature combustion via high EGR level is advantageous.

Figure 2-47b shows the nonisothermal and differential TGA (DTG) profiles of S0 and S9. Compared to S0, S9 exhibits a lower ignition temperature by about 50°C. The oxidation time was cut nearly by 50%. The activation energies were estimated to be 145 kJ/mol and 105 kJ/mol for S0 and S9, respectively. The reported activation energies were independent of gas flow rate and sample mass and therefore free from heat and mass transfer limitations. From the DTG, it can be seen that the reaction rate of S9 increases with temperature as expected, is higher than the reaction rate of S0 and reaches a maximum at lower temperature than S0.

XRD. From the XRD patterns (not shown), the key structural parameters can be determined. The d₀₀₂ results obtained from Bragg's equation [2-18] were calculated as 0.345 nm and 0.354 for S0 and S9, respectively. Using Scherrer's equation [2-18], L_c values were found to be 1.19 nm and 1.15 nm for S0 and S9, respectively. The crystallite width (L_a) was determined as 2.24 nm and 1.65 nm for S0 and S9, respectively. From these data it can be seen that the difference in reactivities between S0 and S9 is not explained by the d₀₀₂ or L_c. The crystallite width, on the other hand, is shorter for S9. It is well-known that soot with short fringes is more prone to oxidation because of the increase in the ratio between edge carbon and basal plane carbon [2-19]. Accordingly, it is expected that the number of active sites in S9 is higher than those in S0. This speculation can be proved by performing oxygen chemisorption analysis on both samples.

Raman Spectroscopy. Figure 2-48 shows the Raman spectra obtained for S0 and S9. Two distinct peaks are shown: the G peak (1580 cm^{-1}), which is referred to the graphitic band, and the D peak (1350 cm^{-1}), which can be assigned to the disordered band. The integrated intensity ratio I_G/I_D can be used as a reactivity index. The I_G/I_D for S0 and S9 was found to be 0.443 and 0.375, respectively. These values indicate that S0 has more graphitic structure than S9 in agreement with the TGA data. According to the Tuinstra and Koenig (TK) expression [2-17], the crystallite width (L_a) is found to be 1.95 nm and 1.65 for S0 and S9, respectively. Despite the fact that the TK expression holds well only for L_a between 2.5 and 250 nm [2-20], the values of L_a from the Raman spectra agrees with those from XRD.

Soot Nanostructure. The HRTEM investigations were conducted in order to obtain information about soot structure at the atomic level. The HRTEM images of S0 and S9 are shown in Figure 2-49. Both soots have a classic core/shell structure. S0 soot is characterized by a small disordered core which was estimated to be about 2-3 nm. The outermost part is built of straight fringes arranged concentrically and parallel to the particle perimeter. On the other hand, S9 soot has a larger disordered core of about 9-10 nm. The core is characterized by randomly oriented short fringes. The outermost regions of the primary particles are characterized by wavy-long graphene layers. The coexistence of the wavy layers and short fringes in S9 are partly responsible for the observed higher reactivity.

The results presented here show that changing the combustion conditions via CO_2 alters the soot properties. EGR can be utilized to enhance the oxidative reactivity of diesel soot. We employed CO_2 to simulate cold and particle free EGR; a condition that can be achieved in real world engines by recirculation of the EGR from downstream of the DPF (particle free EGR) and to increase the cooling of the EGR (cold EGR).

It is well-known that CO_2 suppresses the soot formation through its dilution, thermal, and chemical effects [2-21, 2-22]. It can be speculated that adding CO_2 results in different pyrolysis chemistry. The nature of the pyrolysis species and the way they contribute to soot formation and growth are altered. Due to its higher heat capacity (the thermal effect of CO_2), incorporating CO_2 into the combustion process results in lowering the flame temperature. Therefore, one can expect that the degree of

carbonization/graphitization of the soot is lowered and less mature soot is produced. The chemical effect of CO_2 , on the other hand, is believed to also influence the soot reactivity. The dissociation of CO_2 leads to an increase in O atoms and the reaction of CO_2 with H atoms results in increasing the OH and decreasing the H concentration [2-21]. Hence, the oxidation rates increase as a result of high O and OH concentrations and the formation of large PAH is suppressed due to the lack of H atoms, the key component for soot formation via the HACA mechanism [2-23]. Accordingly, small particle size, and hence higher surface area, and short fringe length are formed; the characteristics of more oxidatively reactive soot. However, further work is necessary to determine the mechanism by which CO_2 influences the soot reactivity.

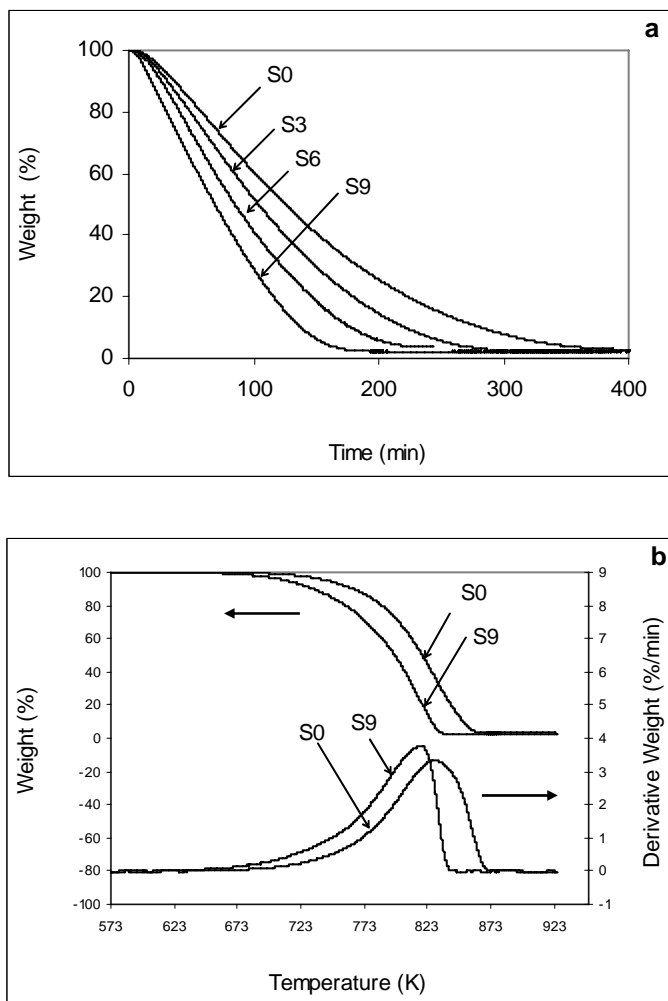


Figure 2-47 (a) Isothermal profiles at 475°C under air ; 0, 3, 6, and 9 correspond to the concentrations of CO_2 injected to engine intake (b) Weight loss profiles of S0 and S9.

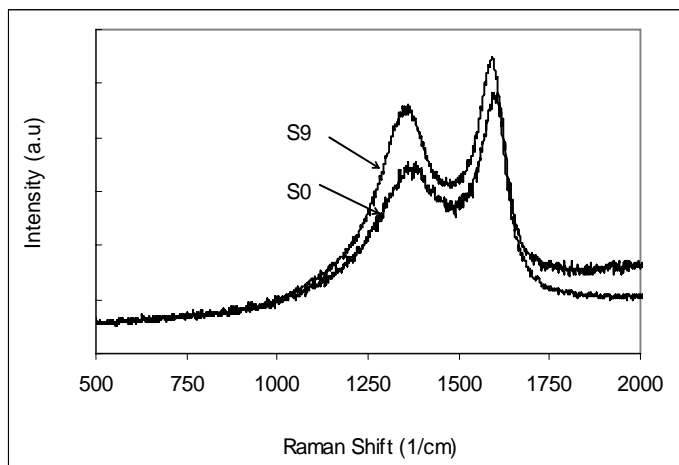
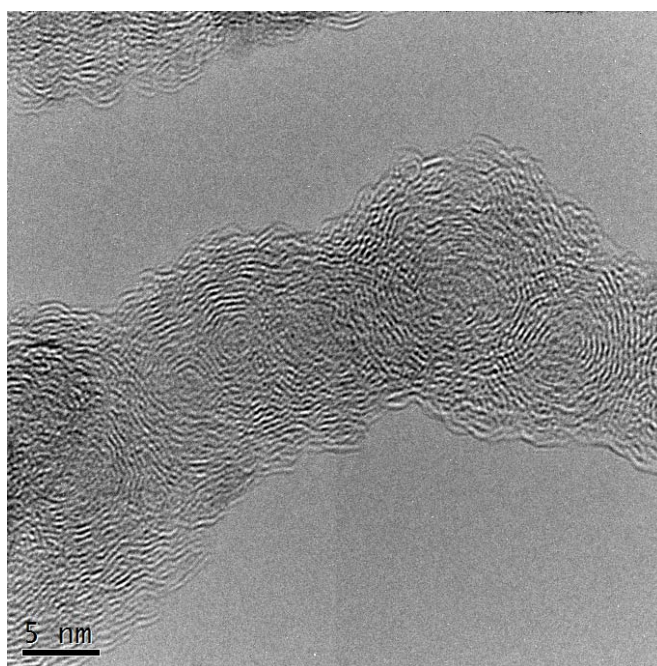
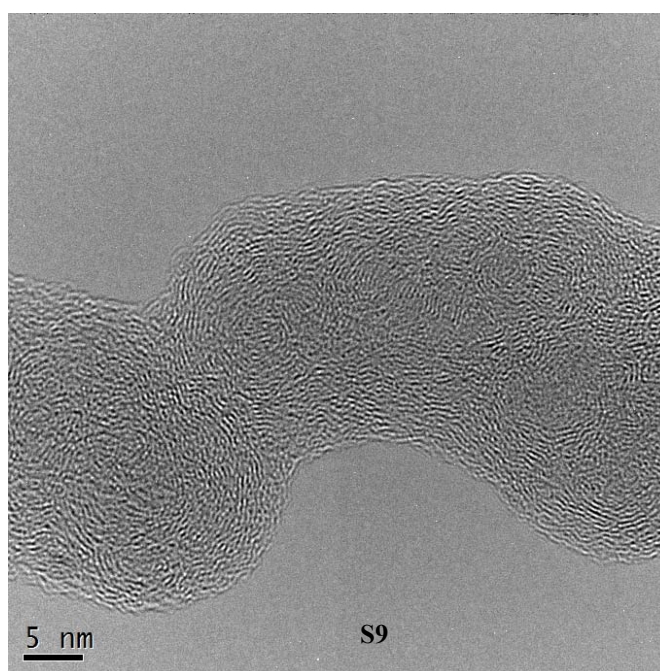


Figure 2-48. Raman spectra of S0 and S9 ($\lambda_0 = 514$ nm)



(a)



(b)

Figure 2-49. HRTEM images of (a) S0 and (b) S9.

2.3 Conclusions

The task involved assessment of the impact of refinery integration of JP-900 production on gasoline and diesel fuel. Fuel properties, ignition characteristics and engine combustion of model fuels and fuel samples from pilot-scale production runs were characterized. The model fuels used to represent the coal-based fuel streams were blended into full-boiling range fuels to simulate the mixing of fuel streams within the refinery to create potential “finished” fuels. The representative compounds of the coal-based gasoline were cyclohexane and methyl cyclohexane, and for the coal-base diesel fuel they were fluorine and phenanthrene.

Both the octane number (ON) of the coal-based gasoline and the cetane number (CN) of the coal-based diesel were low, relative to commercial fuels (~60 ON for coal-based gasoline and ~ 20 CN for coal-based diesel fuel). Therefore, the allowable range of blending levels was studied where the blend would achieve acceptable performance. However, in both cases of the coal-based fuels, their ignition characteristics may make them ideal fuels for advanced combustion strategies where lower ON and CN are desirable. The ignition characteristics and reaction pathways were examined for these fuels in a modified octane rating engine used as a form of rapid compression machine and in an ignition quality tester (IQT). Methyl cyclohexane was observed to have similar ignition temperature as *n*-heptane and to exhibit two-stage ignition under a narrow range of test conditions. The impact of the coal-derived diesel fuel on ignition limits its use to a 5 vol.% blend in the commercial diesel fuel. Studies of the combustion characteristics at this blend level showed modest impact on emissions, with a slight increase in NO_x emissions and an increase in particle number density. Overall, these coal-based streams can be blended into conventional fuel streams at between as much as 20% for the coal-based gasoline and at as much as 5% for the coal-based diesel fuel while maintaining acceptable performance.

Task 3. Desulfurization, Denitrogenation, Saturation of Aromatics, Chemicals from Coal

Chunshan Song, Jae Hyung Kim, Xiaochun Xu, Hyun Jae Kim, Brian Senger, Vasudha Dhar, Boonyawan Yoosuk, Shamal Kumar Saha, and Xiaoliang Ma

3.1 Desulfurization and Denitrogenation

Ultra-deep hydro desulfurization (HDS) of diesel fuel has become an important research area because of increasingly stringent environmental regulations on sulfur content in fuel [3-1]. The diesel containing high sulfur compounds leads to higher level of SO_x in the exhaust, which results in acid rain and poisons catalysts in catalytic exhaust gas treatment devices for reducing NO_x and CO [3-2]. Consequently, the sulfur level in diesel fuel has been reduced from the pre-2006 level of 500 ppmw to 15 ppmw by Sept 2006 in the US. Further regulations for lower sulfur contents of transportation fuels are expected in the near future. Therefore, many studies on deep hydrodesulfurization of model and real diesel fuels are being conducted with various methods and different catalysts by many research groups [3-1, 3-3~3-8].

Hydrodesulfurization is currently a major process in petroleum refineries to reduce the sulfur in the liquid hydrocarbon fuels. However, it was found by many researchers that the nitrogen compounds coexisting in middle-distillate oil inhibit the deep hydrodesulfurization and the removal of such nitrogen compounds from the middle-distillate oil can improve significantly the deep hydrodesulfurization performance [3-3, 3-4, 3-9]. Recently, a new process, called PSU-SARS, is being explored in our laboratory. The idea in this process is to remove sulfur in the fuels by selective adsorption. The major advantages of this process are that the process can run at ambient temperature and pressure without using hydrogen gas and the spent adsorbents can be regenerated either by solvent washing or by oxidation using air. The idea in PSU-SARS process can be also applied to pre-denitrogenation of the middle-distillate oil to improve the deep hydrodesulfurization performance.

In the adsorption part of this study, we are focusing on the adsorptive denitrogenation of basic or very reactive nitrogen compounds such as quinoline or indole,

which strongly influences hydrodesulfurization. It is expected that these nitrogen compounds may be removed easily by adsorption as compared with sulfur compounds because they are much more reactive than sulfur compounds in hydrotreating process. Therefore, the performance of HDS may be improved, even though basic or reactive nitrogen compounds are removed from middle-distillate oil. We have also explored novel dispersed (unsupported) sulfide catalysts for deep desulfurization of more refractory sulfur compounds in middle distillate fuels.

3.1.1. Experimental

3.1.1.1. Adsorptive desulfurization and denitrogenation

In order to investigate adsorption properties of aromatic, sulfur and nitrogen compounds over different adsorbents, adsorptive denitrogenation/desulfurization was performed in a flow system and collected samples by adsorption were analyzed by Antek total S/N analyzer and GC-FID. On adsorptive denitrogenation in flow system, a model fuel containing 152 ppmw of N as quinoline and 151 ppmw of N as indole in the mixture solvent of decane and hexadecane was used in this study. The total nitrogen concentration in the fuel was 303 ppmw. Total sulfur concentration was 686 ppmw of S as same amount of DBT and 4,6-DMDBT. **Table 3-1** shows the composition of model fuel for adsorptive denitrogenation in flow system.

According to the results of adsorptive denitrogenation in the batch system in our previous report, zeolite supported Cu and CuCe adsorbents were selected and Ag/Y-zeolite was also chosen because it has been reported that Ag adsorbs aromatic compounds through π -complexation, which is one of the important adsorption factors. These zeolite-based adsorbents were pretreated with He flow at 350°C for 1 h for the reduction of metal before adsorptive denitrogenation/desulfurization.

Also, activated alumina and activated carbon which are used widely for adsorption processes in industries were tested. The activated alumina was purchased from Aldrich Chemical Co. and has a surface area of 173 m²/g and a pore size of 59.4 Å. In general, activated alumina is used for removing nitrogen compounds and polar compounds in real fuels and is expected to show good adsorption properties of nitrogen compounds in the model fuel. The activated carbon was provided from Westvaco and has

a surface area of 1843 m²/g and a pore size of 28.6 Å. Both adsorbents were pretreated with nitrogen flow at 200 °C for 1 h in order to remove water adsorbed in their surface, which might significantly influence the adsorption properties. Also, A-5 (Ni/Si-Al) adsorbents, which were developed in our lab, was tested and compared with other adsorbents. **Table 3-2** shows the surface area, pore volume and pore diameter of zeolite-based adsorbents, nickel-based adsorbent, activated alumina and activated carbon measured by N₂ adsorption (ASAP2010, Micromeritics).

Table 3-1 Concentration of each compound in model fuel.

Chemicals	Concentration		Molar concentration (mmol/kg)
	(wt %)	ppmw S or N	
Sulfur compounds			
DBT(99+%)	0.20	343.3	10.7
4,6-DMDBT(97%)	0.23	343.4	10.7
Total		686.7	
Nitrogen compounds			
Quinoline	0.14	152.0	10.8
Indole	0.13	151.0	10.8
Total		303.0	
Aromatics			
Naphthalene	0.14		10.7
1-Methylnaphthalene	0.15		10.7
tert-Butylbenzene	9.92		
Total	10.21		
Paraffins			
n-Decane	44.01		
n-Hexadecane (99+%)	44.02		
n-Tetradecane (99+%)	0.06	(Internal standard)	
Total	100.00		

Table 3-2 Properties of zeolite-based adsorbents, activated alumina and activated carbon.

	Surface Area m ² /g	Pore Volume cm ³ /g	Pore diameter (Å)
Cu/Y-zeolite	584	0.0	~7.4
CuCe/Y-zeolite	383	0.1	~7.4
Ag/Y-zeolite	273	0.1	~7.4
A-5 (Ni/SiO ₂ -Al ₂ O ₃)	157	-	-
Activated carbon	1843	1.2	28.6
Activated alumina	173	0.3	59.4

These adsorbents were pretreated with H₂ flow at 200°C for 1 h and cooled down to room temperature. The adsorptive denitrogenation of the model fuel on all adsorbents was performed in a flow system at room temperature with LHSV of 4.8 h⁻¹. Analysis of fuel samples was conducted using an Antek 9000 series nitrogen and sulfur analyzer for more accurate quantitative analysis, along with a SRI GC equipped with a capillary column (XTI-5, Restek) and a flame ionized detector (FID) for identification of each compound.

The adsorption of light cycle oil (LCO, EI-163 from United Refinery) was also performed at the same conditions as the adsorption of model fuels. The LCO used in this project contains 1.5wt% S and 464 ppmw N with a lot of aromatic compounds. The sulfur concentration was much higher than that (687 ppmw S) in the model fuel, while the nitrogen concentration was similar to that (303 ppmw N) in the latter.

3.1.1.2 Adsorptive desulfurization and denitrogenation of LCO

The adsorptive denitrogenation/desulfurization of light cycle oil (LCO, EI-163 from United Refinery) was performed on the activated carbon which had shown the best adsorption properties on sulfur and nitrogen compounds in a model fuel as reported in the previous report. The activated carbon was provided from MeadWestvaco and has surface area of 1843 m²/g and pore size of 28.6 Å. It was pretreated in nitrogen flow at 200 °C for 1 h in order to remove water and other contaminants adsorbed in their surface which might significantly influence the adsorption properties. Then the adsorbent was cooled down to room temperature and the adsorption experiment was performed in a flow system with LHSV of 4.8 h⁻¹. Analysis of fuel samples was conducted using and Antek

9000 series nitrogen and sulfur analyzer for more accurate quantitative analysis along with a HP GC equipped with a capillary column (XTI-5, Restek) and a pulsed flame photometric detector (PFPD) for identification of only sulfur compounds.

3.1.1.3 Unsupported Mo sulfide catalysts with promoters

The unsupported Mo sulfide catalysts with/without Co promoter were synthesized by the hydrothermal method developed in our laboratory. The catalysts were compared with commercial catalysts and unsupported Mo and NMo sulfides which were reported in the previous report. Aqueous ammonium tetrathiomolybdate (ATTM) and a promoter precursor $\text{Co}(\text{NO}_3)_2 \cdot 6\text{H}_2\text{O}$ were mixed with organic solvent (decalin) and decomposed and reacted under 400 psi of hydrogen pressure and 350 °C in 25 ml of microautoclave. All catalysts were evaluated with simultaneous HDS of DBT and 4,6-DMDBT, which was carried out in a horizontal micro-reactor. The HDS reaction conditions were 400 psi of H_2 pressure and 350°C of reaction temperature. The liquid products were collected and analyzed by Shimadzu GC/MS (GC12A/QP-500) for identification and HP GC-FID (HP5890) with XTI-5 capillary column (Restek) for quantification. For the kinetics study, HDS reaction was conducted under 300 psi of H_2 pressure and 300°C in order to obtain reliable kinetics data. In general, HDS of individual sulfur compounds follow pseudo-first-order kinetics. To calculate individual rate constant for each reaction pathway, the kinetic equation was combined with the ratio of initial selectivity of primary products for each reaction pathway which provides more reliable kinetic data because the initial selectivity is calculated at the initial rate [3-9]. The unsupported Mo sulfide catalysts were characterized by XRD (Scintag Powder Diffractometer with $\text{Cu } K_\alpha$ emission, 30 mA 35 KV), N_2 adsorption (Micromeritics ASAP 2000) and TEM (JEOL JEM-2010F electron microscope operated at 200 kV).

3.1.2. Results and discussion

3.1.2.1. Adsorption on Zeolite-based Adsorbent

The breakthrough curves of the six adsorbates, naphthalene (Nap), 1-methylnaphthalene (1-MNap), 4,6-dimethyldibenzothiophene (4,6-DMDBT), dibenzothiophene (DBT), quinoline, and indole, over Cu, CuCe and Ag/Y-zeolite

adsorbents at 25°C and 4.8 h⁻¹ LHSV are shown in **Figures 3-1~3-3**. For the Cu/Y-zeolite adsorbent, the aromatic and sulfur compounds had almost same breakthrough and their breakthrough amount was 1.0 gram of the treated fuel per gram of adsorbent (g-F/g-A). The breakthrough of nitrogen compounds was later than other compounds and the breakthrough amount of treated fuel was 2.2 g-F/g-A for indole and 3.4 g-F/g-A for quinoline. For the CuCe/Y-zeolite adsorbent, the breakthrough of aromatic and sulfur compounds was very similar and their breakthrough amount of treated fuel was 3.4 g-F/g-A. Therefore, the addition of Ce on Cu/Y-zeolite increased the capacity of aromatic and sulfur compounds. As the breakthrough of nitrogen compounds, the Ce addition did not affect the breakthrough amount of quinoline while the breakthrough amount of indole increased little. According to the breakthrough order, the adsorptive selectivity for the six adsorbates over Cu and CuCe/Y-zeolite can be represented by the order of Nap \approx 1-MNap \approx 4,6-DMDBT \approx DBT < indole \leq quinoline. The breakthrough and saturate capacities for each adsorbate were calculated and listed in **Table 3-3**. In order to facilitate the quantitative discussion of the adsorptive selectivity, a relative selectivity factor was used in the present study, which was defined as:

$$\alpha_{i-n} = \text{Cap}_i / \text{Cap}_n \quad (1)$$

where, Cap_i is the adsorptive capacity of compound *i* corresponding to the breakthrough point and Cap_n is the adsorptive capacity of the reference compound, Nap, corresponding to its breakthrough point. It should mention that as using the kinetics breakthrough capacities instead of the equilibrium capacity in equation 1, the defined selectivity factor is not for the equilibrium selectivity. The calculated relative selectivity factor on the basis of the breakthrough curves are tabulated as shown in **Table 3-4**. α_{i-n} value for Cu/Y-zeolite is 1.0, 1.0, 1.0, 1.0, 2.2 and 3.5, and the value for CuCe/Y-zeolite is 1.0, 1.0, 1.0, 0.9, 1.2 and 1.3, respectively, for Nap, 1-MNap, 4,6-DMDBT, DBT, quinoline and indole.

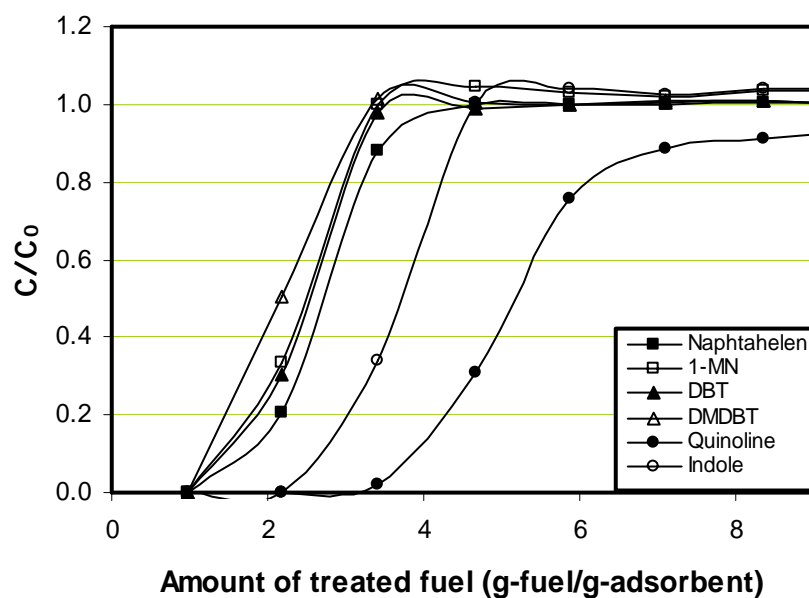


Figure 3-1 Breakthrough of aromatic, sulfur and nitrogen compounds over Cu/Y-zeolite.

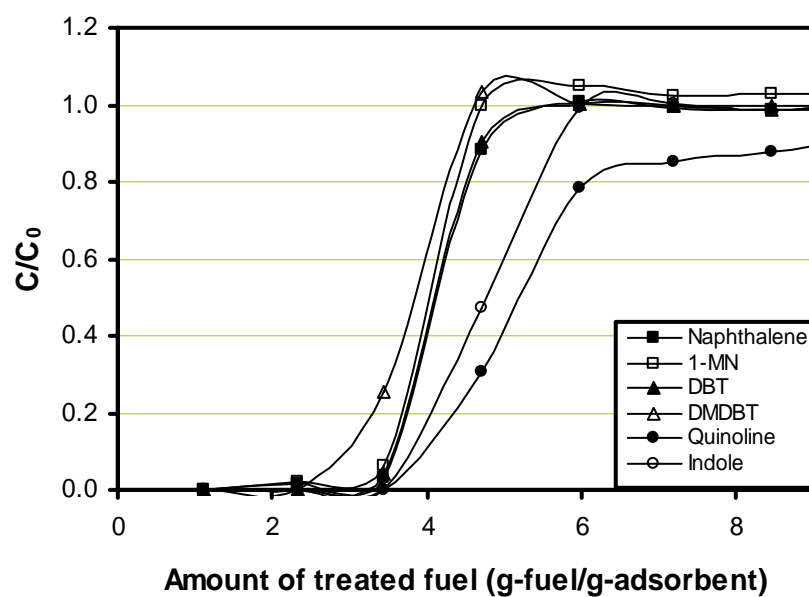


Figure 3-2 Breakthrough of aromatic, sulfur and nitrogen compounds over CuCe/Y-zeolite.

Table 3-3 The breakthrough and saturate capacity of each compound in model fuel for different adsorbents.

Adsorptive capacity (mmol/g)		Nap	1-MNap	DBT	DMDBT	Indole	Quinoline
Cu/Y-zeolite	Breakthrough	0.011	0.011	0.011	0.011	0.024	0.037
	Saturate	0.022	0.018	0.020	0.017	0.032	0.057
CuCe/Y-zeolite	Breakthrough	0.036	0.036	0.036	0.034	0.044	0.047
	Saturate	0.038	0.035	0.038	0.033	0.044	0.055
Ag/Y-zeolite	Breakthrough	0.007	0.007	0.007	0.007	0.037	0.052
	Saturate	0.014	0.010	0.011	0.008	0.044	0.067
Ni/SiO ₂ -Al ₂ O ₃	Breakthrough	0.017	0.017	0.052	0.039	0.167	0.125
	Saturate	0.022	0.021	0.070	0.043	0.186	0.151
Activated alumina	Breakthrough	0.015	0.015	0.024	0.033	0.195	0.251
	Saturate	0.019	0.020	0.040	0.038	0.227	0.289
Activated carbon	Breakthrough	0.066	0.089	0.202	0.295	0.705	0.536
	Saturate	0.091	0.105	0.252	0.336	0.732	0.579

Table 3-4 Selectivity of each compound in model fuel for different adsorbents.

Selectivity ¹	Nap	1-MNap	DBT	DMDBT	Indole	Quinoline
Cu/Y-zeolite	1.0	1.0	1.0	1.0	2.2	3.5
CuCe/Y-zeolite	1.0	1.0	1.0	0.9	1.2	1.3
Ag/Y-zeolite	1.0	1.0	1.0	1.0	5.0	7.0
Ni/SiO ₂ -Al ₂ O ₃	1.0	1.0	3.1	2.0	10.1	7.6
Activated alumina	1.0	1.0	2.2	2.2	12.8	16.5
Activated carbon	1.0	1.3	3.0	4.5	10.6	8.1

¹Selectivity is the capacity ratio of each compound to naphthalene

On the Ag/Y-zeolite adsorbent, the breakthrough of aromatic and sulfur compounds was similar and their breakthrough amount of treated fuel was 0.7 g-F/g-A. The breakthrough of quinoline was later than that of indole. The breakthrough amount of nitrogen compounds was 3.5 g-F/g-A for indole and 4.1 g-F/g-A for quinoline. According to the breakthrough order, the adsorptive selectivity for the six adsorbates over Ag/Y-zeolite can be represented by the order of Nap \approx 1-MNap \approx 4,6-DMDBT \approx DBT < indole

< quinoline. The relative selectivity factor on the basis of the breakthrough curves, α_{i-n} value, on Ag/Y-zeolite is 1.0, 1.0, 1.0, 1.0, 5.0 and 7.0, respectively, for Nap, 1-MNap, 4,6-DMDBT, DBT, quinoline and indole.

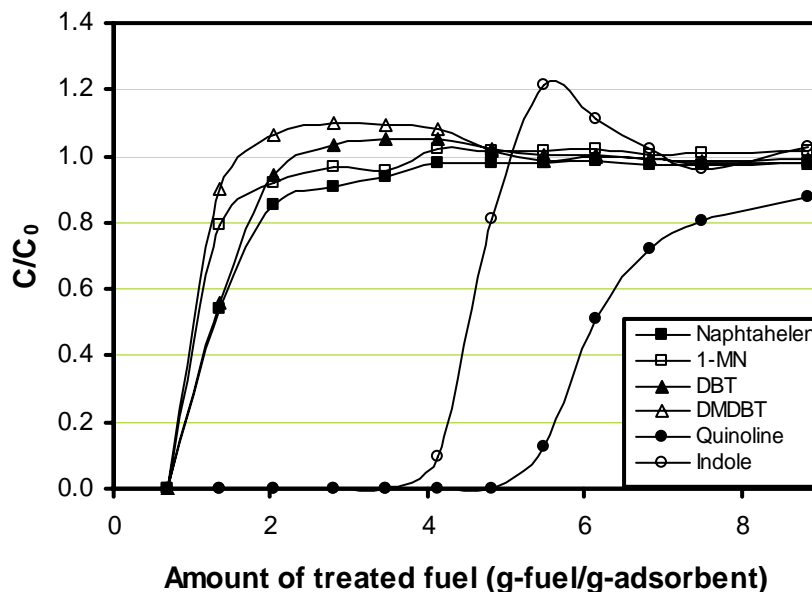


Figure 3-3 Breakthrough of aromatic, sulfur and nitrogen compounds over Ag/Y-zeolite.

3.1.2.2. Adsorption on Nickel-based Adsorbent

The breakthrough curves of the six adsorbates, Nap, 1-MNap, 4,6-DMDBT, DBT, quinoline and indole, over A-5 (Ni/SiO₂-Al₂O₃) at 25 °C and 4.8 h⁻¹ LHSV are shown in **Figure 3-4**. The first two breakthrough compounds were Nap and 1-MNap, with almost the same breakthrough amount of the treated fuel, 1.6 g-F/g-A. After breakthrough, the C/C₀ value (a ratio of the outlet concentration to the initial concentration in the model fuel) for the two aromatics increased sharply to over 1.0. The third breakthrough compound was 4,6-DMDBT with the breakthrough amount of the treated fuel of 3.2 g-F/g-A. Interestingly, DBT broke through at an amount of the treated fuel of 4.9 g-F/g-A, the breakthrough amount of the treated fuel was about 1.6 times higher than that for 4,6-DMDBT. The amount of the treated fuel corresponding to the saturated point was 4.9 and 8.7 g-F/g-A, respectively, for 4,6-DMDBT and DBT. After saturate point, the C/C₀ value for 4,6-DMDBT rose sharply until C/C₀ = 1.4, while the C/C₀ value for DBT increased

gradually to 1.16. This phenomenon was not shown in the breakthrough of aromatic and sulfur compounds on zeolite-based adsorbents. Quinoline and indole broke through at the treated-fuel amount of 11.6 and 15.5 g-F/g-A, respectively. According to the breakthrough order, the adsorptive selectivity for the six adsorbates over A-5 can be represented by the order of Nap \approx 1-MNap < 4,6-DMDBT < DBT < quinoline < indole. The relative selectivity factor on the basis of the breakthrough curves, α_{i-n} value is 1.0, 1.0, 2.0, 3.1, 6.2, and 10.1, respectively, for Nap, 1-MNap, 4,6-DMDBT, DBT, quinoline and indole as shown in **Table 3-4**. Based on the selectivity of DBT and DMDBT, the nickel-based adsorbent is good for selective removal of the sulfur compounds without the steric hindrance from hydrocarbon stream, such as gasoline, kerosene and jet fuel. The adsorbent seems to have the direct interaction between the heteroatom in the adsorbate and the surface nickel play an important role.

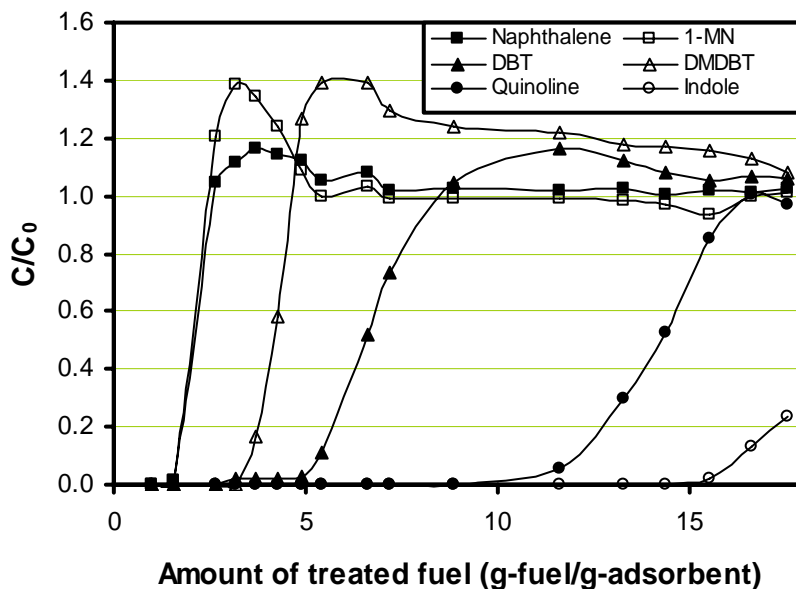


Figure 3-4 Breakthrough of aromatic, sulfur and nitrogen compounds over A-5.

3.1.2.3. Adsorption on Activated Alumina

The breakthrough curves of the six adsorbates over the activated alumina at 25°C and 4.8 h⁻¹ LHSV are shown in **Figure 3-5**. Both Nap and 1-MNap broke through at the treated-fuel amount of 1.4 g-F/g-A. After the breakthrough point, the C/C₀ value for the two aromatics rose sharply to about 1.4 and then returned to 1.0 when the column was

saturated by DBT and 4,6-DMDBT. 4,6-DMDBT and DBT broke through with almost the same breakthrough treated-fuel amount (3.1 g-F/g-A). After the breakthrough, the C/C_0 values increased synchronously to around 1.15, and then, stayed at this value until indole broke through. The C/C_0 values for the two sulfur compounds decreased gradually to 1.0 when the adsorbent was saturated by indole. Indole broke through at an amount of the treated fuel of 18.9 g-F/g-A. After the breakthrough, the C/C_0 value of indole increased to 1.17, and then, returned to 1.0 when the adsorbent was saturated by quinoline. The last breakthrough compounds was quinoline with the breakthrough treated-fuel amount of 23.2 g-F/g-A, and the amount of treated fuel corresponding to saturate point was 31.1 g-F/g-A. The breakthrough and saturate capacities for each adsorbate were calculated and listed in **Table 3-3**. The adsorptive selectivity for the six adsorbates over the activated alumina increased in the order of naphthalene \approx 1-methylnaphthalene < 4,6-DMDBT \approx DBT \ll indole < quinoline. The relative selectivity factor (α_{i-n}) was 1.0, 1.0, 2.2, 2.2, 12.8, and 16.5 for Nap, 1-MNap, 4,6-DMDBT, DBT, indole and quinoline.

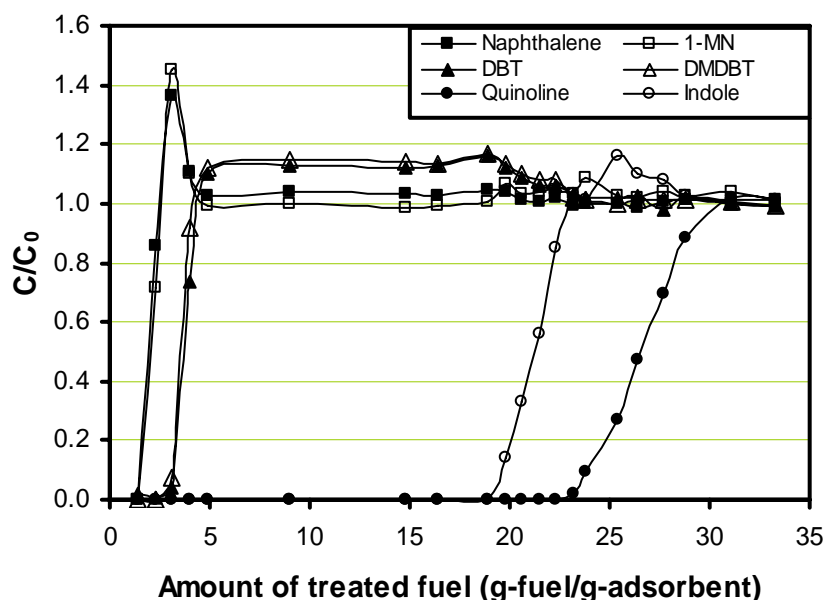


Figure 3-5 Breakthrough of aromatic, sulfur and nitrogen compounds over activated alumina.

The activated alumina was activated to be acidic and that kind of alumina is used widely to remove polar compounds and nitrogen compounds which have unpaired electrons on nitrogen atom. Therefore, the adsorption selectivity on the activated alumina depends on the polarity and the acidic-basic interaction. The activated alumina is very good for selective separation of nitrogen compounds, especially for basic nitrogen compounds, but not very successful for separating the sulfur compounds from hydrocarbons.

3.1.2.4. Adsorption on Activated Carbon

The breakthrough curves over the activated carbon at 25°C and 4.8 h⁻¹ LHSV are shown in **Figure 3-6**. Nap broke through at a treated-fuel amount of 6.2 g-F/g-A. After the breakthrough, the C/C₀ value for Nap rose sharply to over 1.4, and then, returned to 1.0 gradually at the treated-fuel amount of 30 g-F/g-A. 1-MNap broke through at a treated-fuel amount of 8.4 g-F/g-A, and then, the C/C₀ value increased sharply to over 1.3. The breakthrough amount of the treated fuel for DBT was 19 g-F/g-A. After that the C/C₀ values for DBT increased sharply to around 1.4, and then, stayed at this value until the column was saturated by 4,6-DMDBT. 4,6-DMDBT broke through with a treated-fuel amount of 27.6 g-F/g-A, and then, increased sharply to over 1.2. The C/C₀ value for the two sulfur compounds decreased gradually to 1.0 when the column was saturated by indole. The breakthrough amount of the treated fuel for quinoline and indole was 49.3 and 66.1 g-F/g-A, respectively, and the saturated amount of the treated fuel was 60.3 and 86.7 g-F/g-A, respectively. The corresponding breakthrough and saturate capacities for each adsorbate are listed in **Table 3-3**. The adsorptive selectivity for the six adsorbates over the activated carbon increased in the order of Nap < 1-MNap < 4,6-DMDBT < DBT < quinoline < indole. The relative selectivity factor (α_{i-n}) was 1.0, 1.3, 3.0, 4.5, 8.1, and 10.6 for Nap, 1-MNap, DBT, 4,6-DMDBT, quinoline and indole, as shown in **Table 3-4**.

The activated carbon shows higher adsorptive capacity and selectivity for sulfur and nitrogen compounds, especially for the sulfur compounds with methyl groups, such as 4,6-DMDBT as compared with other adsorbents. In this study, the activated carbon was the best adsorbent for removing sulfur compounds as well as nitrogen compounds.

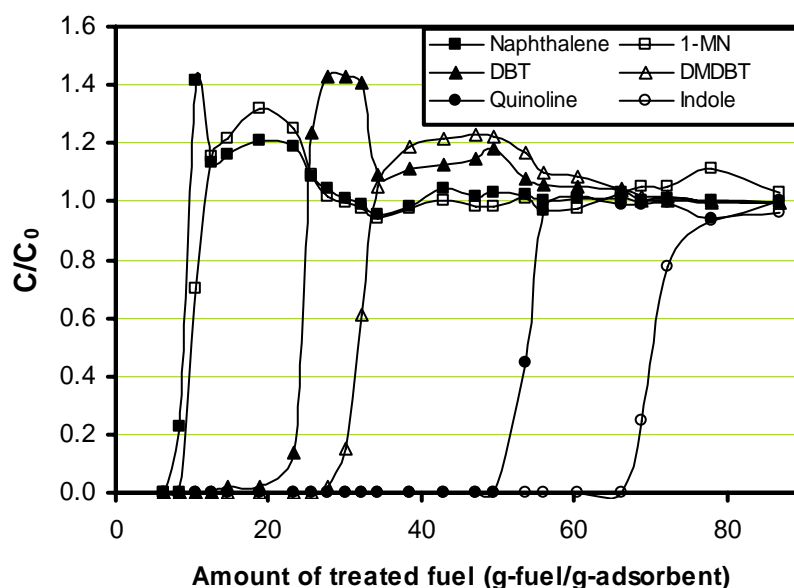


Figure 3-6 Breakthrough of aromatic, sulfur and nitrogen compounds over activated carbon.

3.1.2.5. Adsorption of light cycle oil (LCO) on activated carbon

The adsorptive denitrogenation and desulfurization of light cycle oil (LCO) was performed at 25°C and 4.8 h⁻¹ LHSV on the activated carbon which showed excellent adsorption properties of the model fuel and very high adsorption capacity of sulfur and nitrogen compounds. LCO used in this study contains 1.5 wt% S and 464 ppmw N. **Figure 3-7** shows the breakthrough of sulfur and nitrogen. The breakthrough amount of the treated fuel for sulfur was less than 1.3 g-F/g-A, and the C/C_0 values for sulfur increased sharply to around 1.0 after the breakthrough. Nitrogen concentration broke through with a treated-fuel amount of 4.9 g-F/g-A. Then, the C/C_0 value increased sharply to 0.8 and then slowly to 1.0 until the breakthrough amount up to 45 g-F/g-A.

To investigate fuel compositions, LCO was analyzed by GC-PFPD which detects only sulfur compounds and the results of GC-PFPD are shown in **Figure 3-8**. The LCO contains a wide range of sulfur compounds from two-ring sulfur compounds, benzothiophene (BT), to three-ring sulfur compounds with alky groups, dibenzothiophene (DBT). Major compounds are C₂-BT (specifically 2,3-DMBT) and C₁-

DBT (specifically 4-MDBT). As well, 4,6-DMDBT, one of the most refractory sulfur compounds, is contained although its amount is relatively lower than the major compounds. To investigate the adsorption mechanism, the LCO treated by adsorptive desulfurization and denitrogenation was analyzed. **Figure 3-9** shows the GC-PFPD charts of the LCO treated by adsorption. After treated at 1.3 g-F/g-A (grams of treated LCO per grams of adsorbent), the LCO contains 2878 ppm S (analyzed by Antek S/N analyzer) only and small amounts of 2,3-DMBT and C₃-BT were detected on GC-PFPD chart while nitrogen compounds were not detected in this sample on the basis of Antek nitrogen analysis. In the GC-PFPD analysis, the sample fuels were diluted with solvent and therefore, the peaks of sulfur compounds might look less. After treated at 3.1 g-F/g-A, sulfur concentration almost reached to the initial concentration of LCO and it was 1.47 wt% S and most of sulfur compounds contained in untreated LCO were detected. Further treated LCO samples contain almost same amount of sulfur and show same GC-PFPD chart as shown in **Figure 3-9** while nitrogen concentration was still lower than 50 ppm N after treated at 6.7 g-F/g-A.

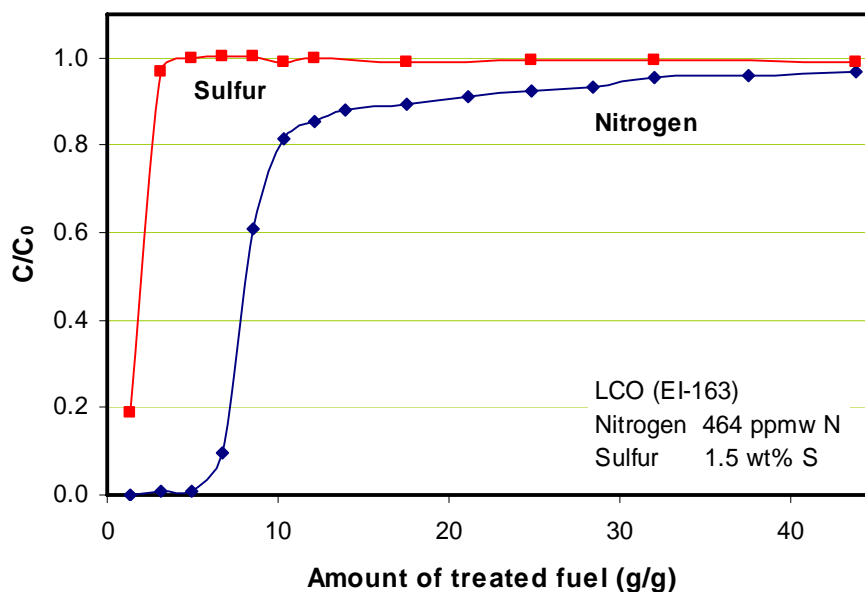


Figure 3-7. The breakthrough of sulfur and nitrogen in LCO over activated carbon.

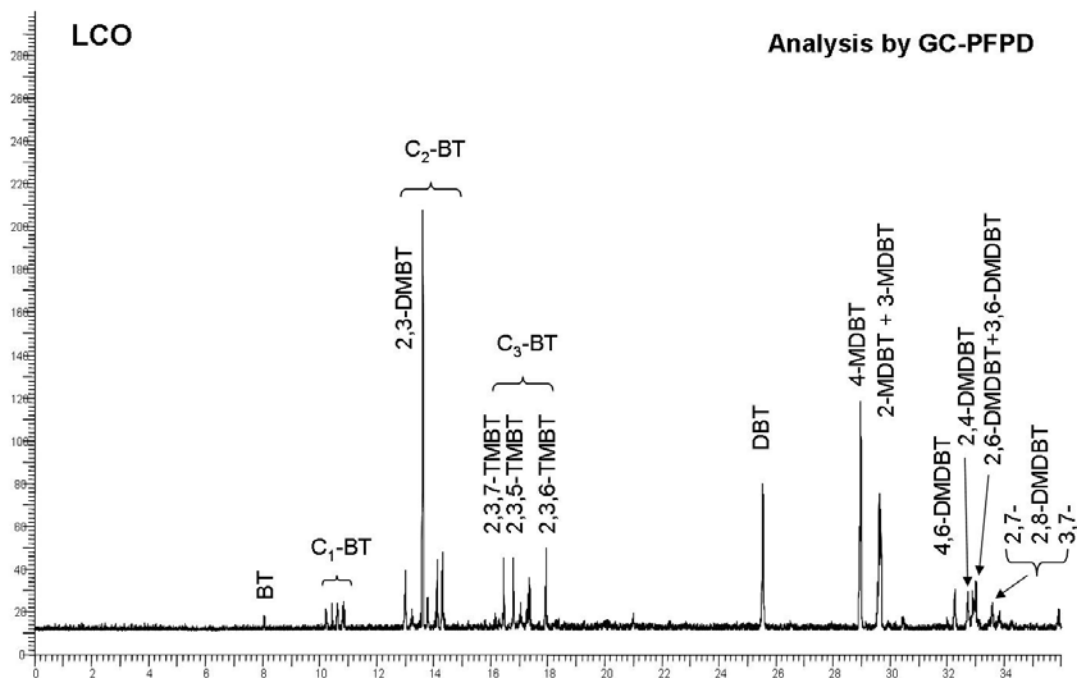


Figure 3-8. GC-PFPD analysis of light cycle oil (LCO).

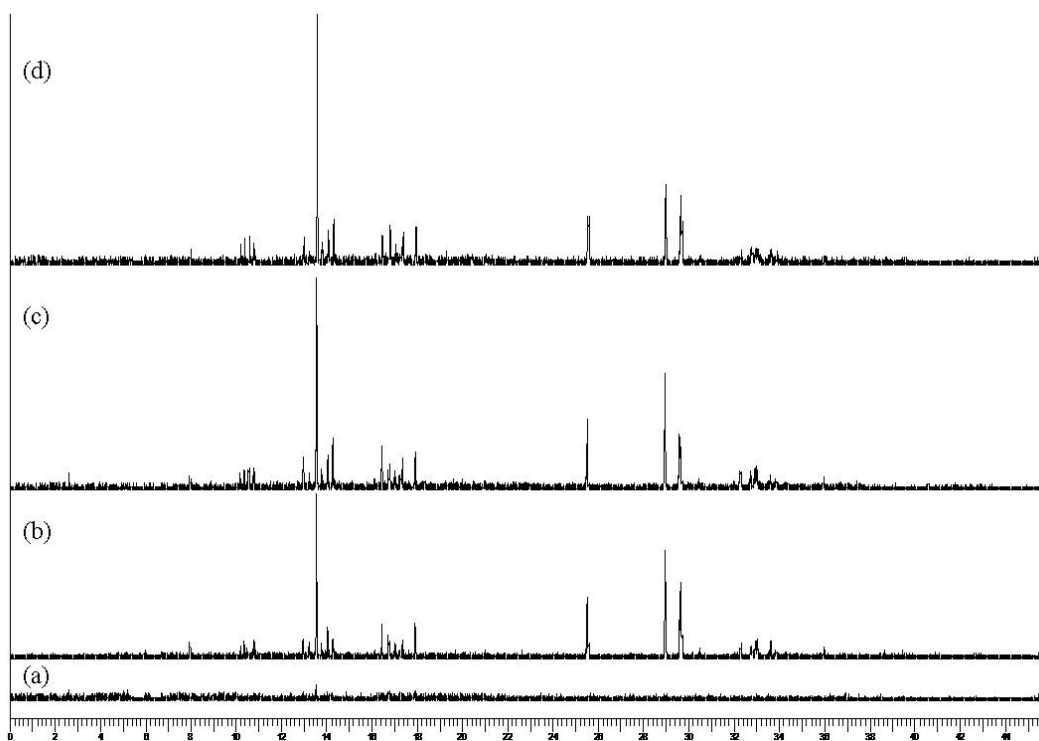


Figure 3-9. GC-PFPD analysis of LCO treated by adsorption on activated carbon after the amount treated of (a) 1.3 g-F/g-A, (b) 3.1 g-F/g-A, (c) 4.9 g-F/g-A and (d) 6.7 g-F/g-A.

Table 3-5. The breakthrough and saturate capacity of sulfur and nitrogen in LCO on activated carbon by Antek total S/N analyzer.

Capacity (mmol/g-A)	Sulfur	Nitrogen
Breakthrough	< 0.497	0.162
Saturate	0.869	0.357

3.1.2.6. Hydrotreating of LCO treated by adsorption

For hydrotreating of LCO treated by adsorption (adsorption data in **Table 3-5**), the samples treated by 6.7 g-F/g-A were collected and it contains 1.3 wt% S and 14 ppm N. HDS of LCOs untreated and treated by adsorption was performed at 300°C and 300 psi of H₂ pressure for 30 min. First, the products were analyzed by GC-PFPD as shown in **Figure 3-10**. Based on the GC-PFPD analysis, the hydrotreating removed all range of sulfur compounds and specifically sulfur compounds in BT range were removed more significantly than those in DBT range as compared between (a) and (b) in **Figure 3-10**. On the other hand, adsorption treatment removed more sulfur compounds in DBT range than those in BT range as compared between (a) and (c) in **Figure 3-10**. It is because the activated carbon has excellent adsorption properties of heavy and alkylated DBTs as reported in the previous year. **Figure 3-10** (d) shows sulfur compounds in LCO treated by adsorption followed by hydrotreating. All range of sulfur compounds were removed significantly although C₂-BT and C₂-DBT remain still. Therefore, it is certain that hydrodesulfurization (HDS) of LCO is improved significantly after following adsorption treatment. However, quantitative analysis of LCO treated by hydrotreating and adsorption was not conducted with GC-PFPD due to its poor reliability. Therefore, reliable quantitative analysis is required further in future research.

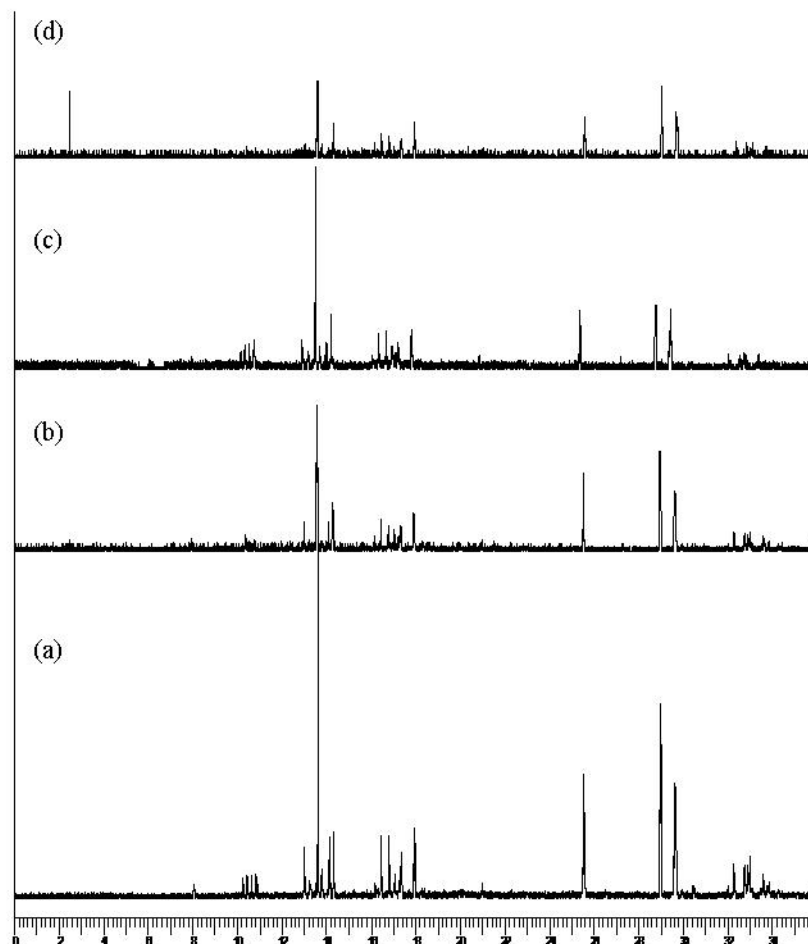


Figure 3-10. The improvement of HDS of LCO after treatment by adsorption. (a) LCO, (b) hydrotreated, (c) treated by adsorption and (d) treated by adsorption followed by hydrotreating.

3.1.2.7. Hydrodesulfurization of 4,6-DMDBT

To develop deep HDS catalysts, several NiMo, CoMo and Ni phosphide catalysts were prepared. The prepared NiMo/MCM-41 catalyst contains 27 wt% MoO₃ and 6 wt% NiO, which are higher metal amounts as compared with commercial CoMo and NiMo catalysts, which contain 14 wt% MoO₃ and 3 wt% NiO or CoO. The MCM 41 support which was prepared with SiO₂/Al₂O₃ ratio of 50 in our laboratory has around 1000 m²/g and higher pore volume 1.33 ml/g, which is much higher than those of Al₂O₃. So, the high concentrations of Ni and Mo metals were able to be loaded on the MCM-41 support. In the first year, we tried to prepare NiMo and CoMo catalysts supported on MCM-41,

but their results were not enough to be attractive. At that time, the catalysts were prepared with incipient wetness impregnation, which might be affected by the acidity of MCM-41 support. Therefore, wet impregnation with enough water was employed this year to prepared NiMo and CoMo catalysts on MCM-41 support and other supports (CeO_2 and Al_2O_3). **Tables 3-6 ~ 3-8** and **Figures 3-11 ~ 3-13** show the conversion of 4,6-DMDBT and the selectivity of products over the catalysts prepared in this study after HDS of 4,6-DMDBT under the reaction conditions with 300°C, 325°C or 350°C and 300 psi of H_2 pressure for 30 min.

High metal loaded NiMo and CoMo/MCM-41 catalyst show high activity of 4,6-DMDBT at 300 and 325°C. Specifically, NiMo/MCM-41 has higher HDS activity than other catalysts and even higher than commercial NiMo catalyst (Cr424) which contains 14wt% MoO_3 and 3wt% NiO on alumina before sulfidation. The conversion of 4,6-DMDBT over the NiMo/MCM-41 was 28% and 36% at 300 and 325°C, respectively and it is much higher than that over the commercial catalyst, which was 18% and 33%, respectively. CoMo/MCM-41 catalysts also showed high activity at those temperatures and the conversion was 19% and 32%, respectively. Therefore, wet co-impregnation improved the HDS activity of NiMo and CoMo/MCM-41 catalysts as compared with the same catalysts prepared by incipient wetness impregnation in first year. It may be because the acidity of MCM-41 support was affected by water solution and preparation method. In the case of incipient wetness impregnation, small amount of solution of Mo and/or Ni (or Co) was dripped onto solid support and penetrated immediately inside the pore. The metals in small amount water may have strong interaction with high acidic support. In the case of wet impregnation, however, the metals are dissolved in enough water and the metals' mobility may be high on even acidic support. Then their dispersion will be increased.

In the HDS of 4,6-DMDBT at high temperature, e.g., 350°C, the conversion of 4,6-DMDBT over NiMo and CoMo/ MCM-41 catalysts increased to 42% and 39%, respectively. But they were lower than the commercial catalyst over which the conversion was 47%. NiMo and CoMo/MCM-41 prepared with NTA (hereafter NiMo-NTA and CoMo-NTA) and supported on CeO_2 showed pretty good HDS activity although the conversions over them were not higher than the commercial catalyst. The

conversion was 14% and 11% over NiMo-NTA and CoMo-NTA and 15% and 12% over NiMo and CoMo/CeO₂, respectively at 300°C. The conversion increased with increasing temperature. Interestingly, NiMo-NTA catalyst has very high HDS/DDS ratio of around 15, which was simply calculated with the sum of hydrogenated products (HDMDBT, MCHT and DMBCH) and direct desulfurized product (DMBP).

In the product distribution, only NiMo/MCM-41 had isomerized DMDBT (dimethyldibenzothiophene) at 300°C, which was produced after one or two methyl-groups moved to the other position on benzene ring, from 4- and 6- position, but could not be identified by GC-FID and GC/MS. At higher temperatures, the isomerized products increased and were detected on all NiMo and CoMo catalysts while the HYD/DDS ratio decreased significantly. 4,6-DMDBT has two methyl groups at 4- and 6-positions, which may hinder the direct adsorption of sulfur atom in DBT to catalytic active site. When one or two methyl groups move to another position, the DMDBT has less steric hindrance by a methyl group and may be converted easily to DMBP through DDS pathway. This results in lower HYD/DDS ratio while the selectivity of DMBP increased.

Supported Ni phosphide catalysts were also tested at the same conditions as the NiMo and CoMo catalysts were. They had lower activity than the latter catalysts and did not produce isomerized DMDBT at all temperature ranges tested in this study, but showed different activity and selectivity dependent on supports. Ni₂P/MCM-41 had higher activity than the other phosphide catalysts and Ni₂P/Al₂O₃ had a very high HYD/DDS ratio, while CeO₂ supported Ni phosphide had a lower the ratio.

Based on the results, high metal loaded NiMo/MCM-41 catalyst had higher activity in 4,6-DMDBT HDS at 300 and 325°C than other catalysts tested in this project. At 350°C, however, the commercial NiMo catalyst had higher activity. Therefore, MCM-41 supported sulfide catalysts which had higher activity than others might be promising deep HDS catalysts after they are investigated further and improved.

Table 3-6. Conversion and selectivity of products over the catalysts prepared after HDS of 4,6-DMDBT at 300°C and 300 psi of H₂ pressure.

Catalyst	Conv. (%)	Selectivity (%)					HYD/DDS ¹
		HDMDBT	DMBP	MCHT	DMBCH	Isomer	
NiMoS/Al ₂ O ₃ (Cr424)	17.8	39.8	9.6	44.5	6.2	0.0	9.43
6%NiO 27%MoO ₃ /MCM-41	28.2	66.3	11.3	9.6	5.8	7.0	7.20
6%CoO 27%MoO ₃ /MCM-41	19.2	58.4	15.0	15.5	11.0	0.0	5.65
6%NiO 27%MoO ₃ -NTA /MCM-41	14.3	67.6	6.2	20.0	6.2	0.0	15.02
6%CoO 27%MoO ₃ -NTA/MCM-41	10.6	47.9	34.3	11.1	6.6	0.0	1.91
3%NiO 14%MoO ₃ /CeO ₂ (Rhoda)	15.4	59.6	20.0	16.1	4.4	0.0	4.00
3%CoO 14%MoO ₃ /CeO ₂ (Rhoda)	11.5	57.2	32.1	5.1	5.6	0.0	2.11
Ni ₂ P/MCM-41	8.1	50.9	17.8	27.3	3.9	0.0	4.61
Ni ₂ P/CeO ₂	5.1	36.7	48.7	8.3	6.3	0.0	1.05
Ni ₂ P/Al ₂ O ₃	7.1	62.0	9.7	23.2	5.1	0.0	9.31

¹HYD/DDS = [HDMDBT+MCHT+DMBCH]/[DMBP]

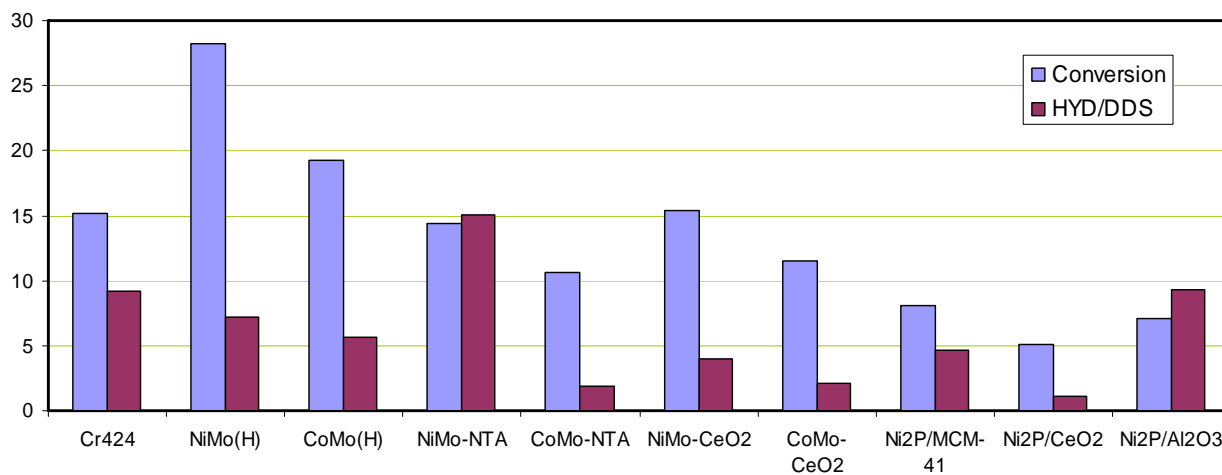


Figure 3-11. Conversion and selectivity of products over the catalysts prepared after HDS of 4,6-DMDBT at 300°C and 300 psi of H₂ pressure.

Table 3-7. Conversion and selectivity of products over the catalysts prepared after HDS of 4,6-DMDBT at 325°C and 300 psi of H₂ pressure.

Catalyst	Conv. (%)	Selectivity (%)					HYD/DDS ¹
		HDMDBT	DMBP	MCHT	DMBCH	Isomer	
NiMoS/Al ₂ O ₃ (Cr424)	32.8	26.2	17.6	43.0	7.0	6.2	4.34
6%NiO 27%MoO ₃ /MCM-41	36.4	40.2	30.4	7.9	3.8	17.7	1.71
6%CoO 27%MoO ₃ /MCM-41	32.3	35.9	24.5	7.7	6.6	25.2	2.05
6%NiO 27%MoO ₃ -NTA /MCM-41	24.9	39.2	17.1	39.5	4.2	0.0	4.84
6%CoO 27%MoO ₃ -NTA/MCM-41	13.6	34.9	26.9	35.2	3.0	0.0	2.71
3%NiO 14%MoO ₃ /CeO ₂ (Rhoida)	19.3	54.0	5.5	28.9	8.0	3.6	16.56
3%CoO14%MoO ₃ /CeO ₂ (Rhoida)	18.0	59.5	9.9	17.3	5.2	8.1	8.28
Ni ₂ P/MCM-41	11.3	42.5	23.2	21.3	1.5	11.5	2.82
Ni ₂ P/CeO ₂	5.2	41.3	43.5	10.0	5.2	0.0	1.30
Ni ₂ P/Al ₂ O ₃	6.3	64.1	12.4	19.2	4.4	0.0	7.09

¹HYD/DDS = [HDMDBT+MCHT+DMBCH]/[DMBP]

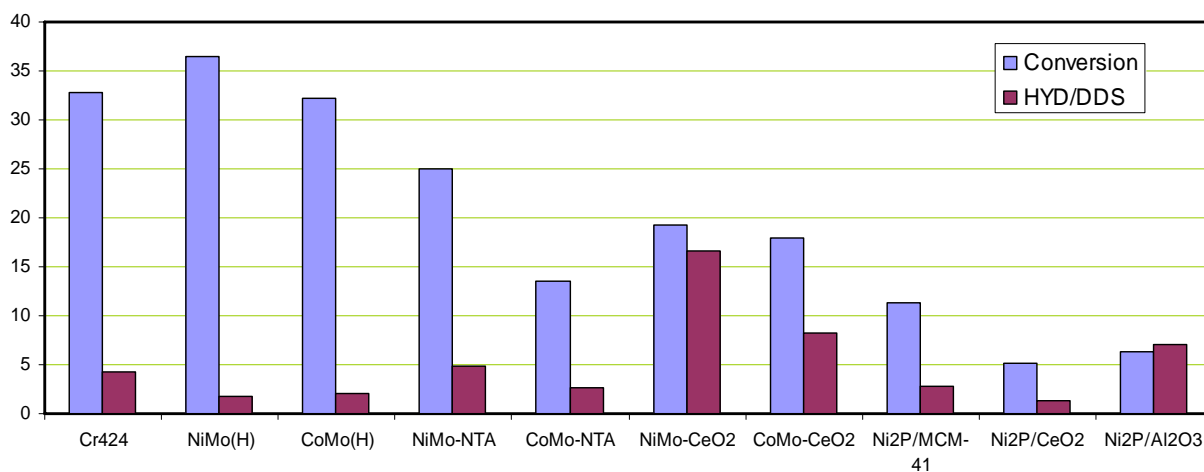


Figure 3-12. Conversion and selectivity of products over the catalysts prepared after HDS of 4,6-DMDBT at 325°C and 300 psi of H₂ pressure.

Table 3-8. Conversion and selectivity of products over the catalysts prepared after HDS of 4,6-DMDBT at 350°C and 300 psi H₂ pressure.

Catalyst	Conv. (%)	Selectivity (%)					HYD/DDS ¹
		HDMDBT	DMBP	MCHT	DMBCH	Isomer	
NiMoS/Al ₂ O ₃ (Cr424)	46.7	9.9	35.7	42.8	6.5	5.1	1.66
6%NiO 27%MoO ₃ /MCM-41	42.3	20.6	50.9	4.5	4.7	19.3	0.59
6%CoO 27%MoO ₃ /MCM-41	38.9	22.5	40.6	5.8	6.1	25.0	0.85
6%NiO 27%MoO ₃ -NTA /MCM-41	29.9	22.8	28.2	39.1	2.9	7.0	2.30
6%CoO 27%MoO ₃ -NTA/MCM-41	19.0	20.1	37.8	35.6	2.6	3.9	1.54
3%NiO 14%MoO ₃ /CeO ₂ (Rhoida)	25.2	42.5	13.9	32.9	6.2	4.5	5.88
3%CoO 14%MoO ₃ /CeO ₂ (Rhoida)	22.6	41.7	21.3	22.2	4.3	10.6	3.21
Ni ₂ P/MCM-41	12.5	39.2	39.9	19.1	1.9	0.0	1.51
Ni ₂ P/CeO ₂	4.7	48.4	38.6	7.7	5.3	0.0	1.59
Ni ₂ P/Al ₂ O ₃	7.0	61.2	14.5	19.6	4.7	0.0	5.92

¹HYD/DDS = [HDMDBT+MCHT+DMBCH]/[DMBP]

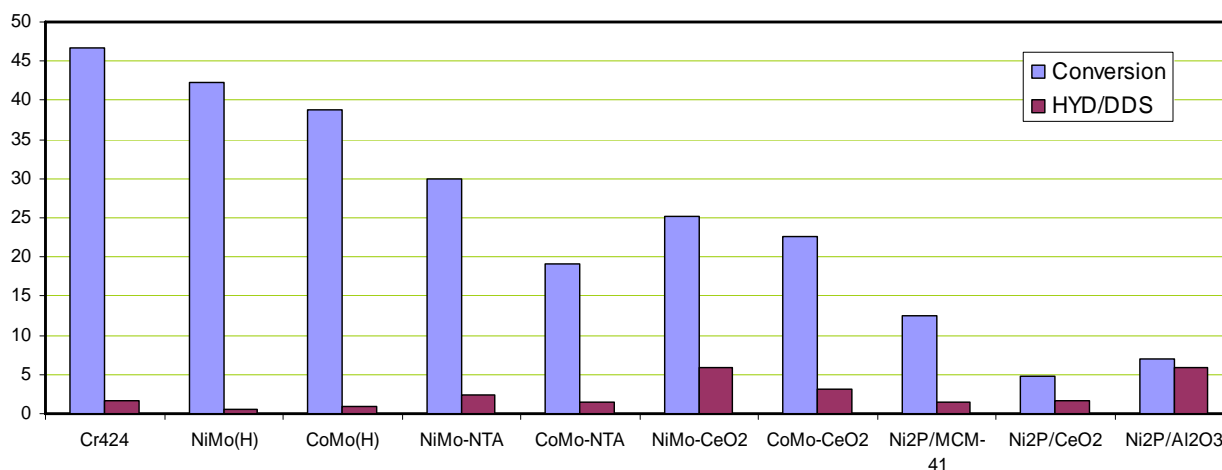


Figure 3-13. Conversion and selectivity of products over the catalysts prepared after HDS of 4,6-DMDBT at 350°C and 300 psi of H₂ pressure.

3.1.2.3. Development of unsupported Mo sulfide catalysts for HDS

3.1.2.3.1. Comparison of unsupported Mo sulfide catalysts with commercial catalysts

The study of the simultaneous DBT and 4,6-DMDBT HDS was performed and the catalytic activity of unsupported Mo sulfide catalysts with Ni and Co were compared with commercial HDS catalysts. Figure 3-14 shows the comparison of DBT and 4,6-DMDBT conversion on the unsupported NiMo and CoMo sulfide catalysts with sulfided commercial catalysts. The conversion of DBT and 4,6-DMDBT on the unsupported Mo sulfides are significantly higher than those of the commercial catalysts (Cr424 and Cr344). On the conversion of 4,6-DMDBT, specifically, the unsupported NiMo sulfide showed two times higher activity than commercial NiMo catalyst (Cr424), while the unsupported CoMo sulfide was three times higher in activity than commercial CoMo catalyst (Cr344). The results indicate that the unsupported NiMo and CoMo sulfide catalysts are certainly superior to the commercial HDS catalysts on the HDS activity of the refractory sulfur compounds because 4,6-DMDBT is one of the most refractory sulfur compounds to be desulfurized. This improvement of HDS performance is not only due to the higher surface area and metal loading on the unsupported catalysts, but also their higher HDS activity than commercial catalysts. Based on the kinetic evaluation as shown in Figure 3-15, the high HDS activity of unsupported Mo sulfide catalysts came from their high activity for a hydrogenation (HYD) pathway. The unsupported NiMo and CoMo sulfides have higher HYD activity than commercial catalysts on HDS of both sulfur compounds. Particularly, the unsupported CoMo sulfide has interestingly high HYD activity on 4,6-DMDBT HDS and even higher than the unsupported NiMo sulfide.

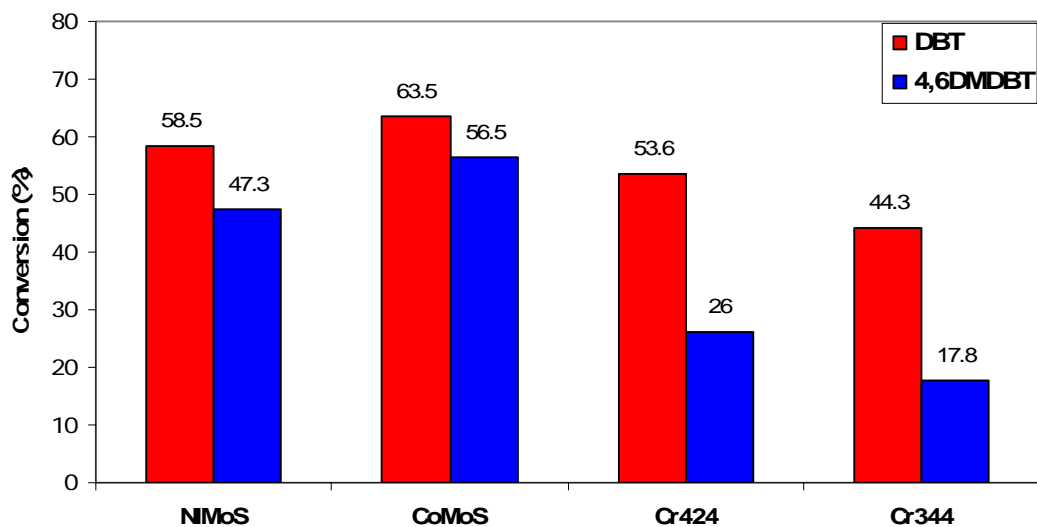


Figure 3-14. Conversion of DBT and 4,6-DMDBT on simultaneous HDS over the unsupported NiMo and CoMo sulfide catalysts and sulfided commercial NiMo/Al₂O₃ (Cr424) and CoMo/Al₂O₃ (Cr344).

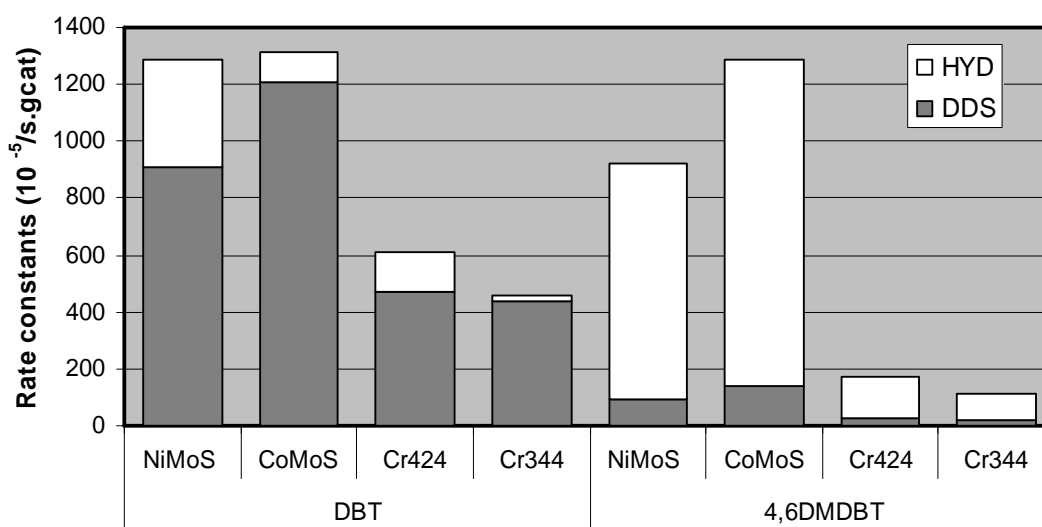


Figure 3-15. Rate constants for simultaneous HDS of DBT and 4,6-DMDBT over the unsupported sulfide catalysts and sulfided commercial catalysts.

3.1.2.3.2. The promoter effects on HDS over unsupported Mo sulfide catalysts

Table 3-9 shows the reactivity and product distribution of DBT and of 4,6-DMDBT on unsupported Mo sulfide catalyst and compared to those obtained with NiMo and CoMo sulfide catalysts. Surprisingly, the conversion of 4,6-DMDBT was higher than that of DBT over the unsupported Mo sulfide. This is mainly due to high activity for HYD pathway, which was the prominent pathway for HDD of both compounds on the sulfide catalyst. However, if concentrating on HDS activity (desulfurized products), DBT is about twice as reactive as 4,6-DMDBT. The promoted Mo sulfide catalysts were much more active than the Mo sulfide catalysts for the HDS of both DBT and 4,6-DMDBT. However, the promoting effect was essentially due to the enhancement of the rate of the DDS pathway on both promoted sulfides. The promoters may decrease the strength of the bond between molybdenum and the sulfur atoms resulting from the decomposition of the organic molecules. In the same way it can be supposed that the promoter decreases the metal–sulfur bond in the sulfide itself and increases the electronic density on the sulfur atoms [3-10]. Unlike other HDS catalysts, the unsupported Mo sulfides have quite high activity on 4,6-DMDBT HDS as compared with DBT HDS (approximately 0.8 times compare with 2-6 times as reported in the literature).

The effect of the Me/(Me+Mo) atomic ratio (Me=Co or Ni) on the HDS activity of both NiMo and CoMo catalyst is shown in **Figure 3-16**. The effect of Ni promoter was reported in previous year and compared with that of Co promoter in this study. For both series of catalysts, the HDS activity increased with increasing amount of Co or Ni, but it reached a maximum at the 0.5 of Me/(Me+Mo) ratio and then decreased at higher ratio. Higher addition of promoters may help to generate more active phase on the catalysts because of better incorporation with the crystallites of Mo sulfide in small cluster. In this study, therefore, it is certainly observed the significant synergetic effect of Ni and Co promoters on the unsupported Mo sulfide catalysts for simultaneous HDS of DBT and 4,6-DMDBT, as shown in **Figure 3-16**.

Table 3-9. Product distribution for the simultaneous HDS of DBT and 4,6-DMDBT over unsupported Mo, NiMo and CoMo sulfide catalysts.

Catalysts	Mo	NiMo ^c	CoMo ^c
DBT Conversion (%)	28.0	58.5	63.5
Selectivity(%)			
THDBT	42.9	6.2	4.0
BP	30.0	41.1	78.1
CHB	20.6	42.6	12.9
BCH	6.5	10.1	5.0
THDBT/CHB	2.1	0.1	0.3
HYD/DDS ^a	2.4	1.4	0.3
4,6-DMDBT Conversion (%)	32.2	47.3	56.5
Selectivity (%)			
THDMDBT	87.0	37.8	33.4
3,3'DMBP	7.7	33.2	43.1
MCHT	4.0	27.0	20.1
DMBCH	1.2	2.0	3.4
THDMDBT/MCHT	21.5	1.4	1.7
HYD/DDS ^b	12.2	2.0	1.3

^a HYD/DDS = Selectivity (THDBT+CHB+BCH)/Selectivity (BP)

^b HYD/DDS = Selectivity (THDMDBT+MCHT+DMBCH)/Selectivity (3,3'DMBP)

^c Me/(Me+Mo) = 0.43

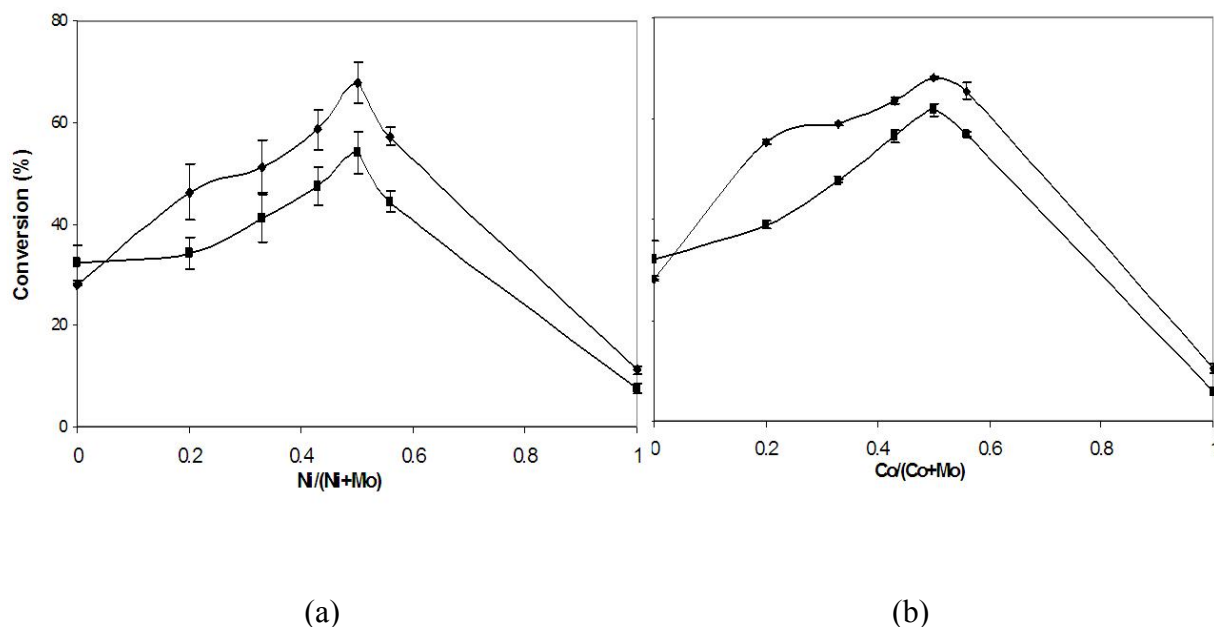


Figure 3-16. The effect of Me/(Me+Mo) atomic ratio (Me=Ni or Co) on HDS of DBT and 4,6-DMDBT over unsupported (a) NiMo and (b) CoMo sulfide catalysts (♦ DBT conversion, ■ 4,6-DMDBT conversion).

3.1.2.3.3. Comparison between unsupported Mo sulfide catalysts

Table 3-10 shows the physical properties of unsupported Mo sulfides synthesized by hydrothermal method. The unsupported Mo sulfide has 283 m²/g of surface area and 0.68 cm³/g of pore volume. These values are considerably higher than those of other Mo sulfide catalysts in the literature, where generally, Mo sulfide has less than 50 m²/g of surface area. After the addition of promoters, a decrease was observed for the surface area and pore volume. In the pore size distribution (**Figure 3-17**), the unsupported Mo sulfides show bimodal pore systems and the volume of larger pore size is higher than that of smaller pore size on unsupported Mo sulfide without promoters. However, the volume of larger pore size to smaller pore size was decreased when the promoters were added. These results indicate that the promoter influences the morphology the unsupported Mo sulfides.

Table 3-10. Surface area, pore volume and average pore size of fresh catalysts prepared from ATTM.

Sulfide Catalysts	Surface Area (m ² /g)	Pore volume (cm ³ /g)
Mo	283	0.68
NiMo	199	0.28
CoMo	168	0.19

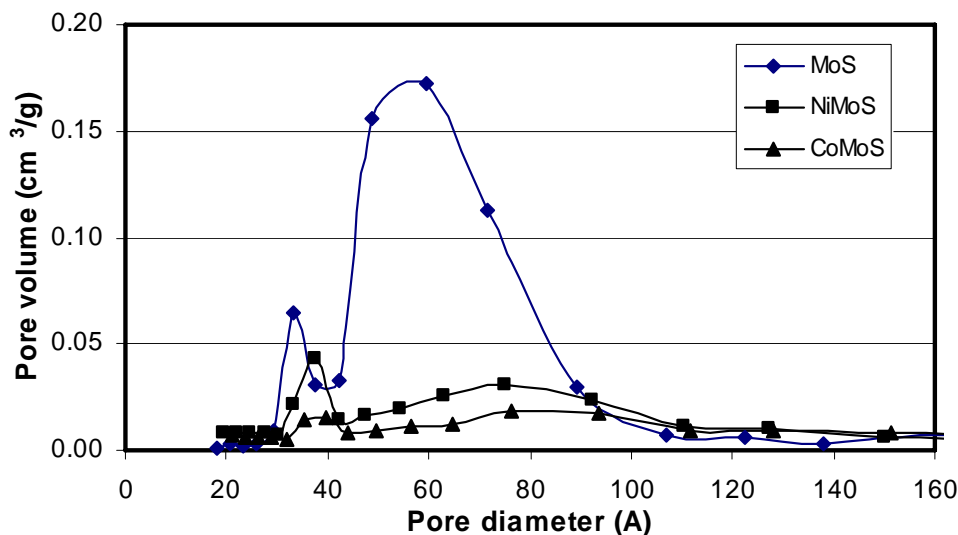


Figure 3-17 Pore distribution of unsupported Mo sulfides with promoters (Ni and Co).

For further characterization of unsupported Mo sulfides, XRD and TEM analysis were conducted. From XRD patterns (**Figure 3-18**) in the comparison to commercial available MoS_2 , all unsupported Mo sulfides showed broad X-ray reflections characteristic of a poorly crystallized MoS_2 structures, and in particular, it became more broad when the promoters were present. The intensity of most MoS_2 peaks decreased significantly and specifically with promoters; in particular, the (002) peak at $2\theta = 14.4^\circ$ became very low for the unsupported CoMo sulfide. In other words, a much smaller size of (002) phase of MoS_2 is generated when adding Co or Ni, specifically on the (002) phase. It results in few stacked layers and fracture of MoS_2 crystals, which are also observed in HRTEM analysis as shown in **Figure 3-19**. On the sulfides with promoters, the diffractions of Ni and Co sulfides were detected due to high loading amount of these metals and they are crystallized Ni_3S_4 and Co_9S_8 . These metal (Ni and Co) sulfide particles might help hydrogen adsorb and dissociate. The H species are mobile enough in the conditions of catalysis to attack the MoS_2 particles and create coordinative unsaturation at the edges [3-11].

Figure 3-19 shows the HRTEM images of the unsupported Mo sulfides with/without Ni promoter. Unsupported Mo sulfide showed well organized long and multi-layered stacking of MoS_2 . With addition of Ni promoter, however, it is clearly

observed the increase of curvature of MoS₂ slabs and the decrease of slab length. Therefore, the HRTEM results coincide with the results of XRD analysis. In the absence of promoters, MoS₂ form large crystallized particles during the hydrothermal synthesis methods. However, the growth of crystallized particles is suppressed when the promoters are incorporated with them.

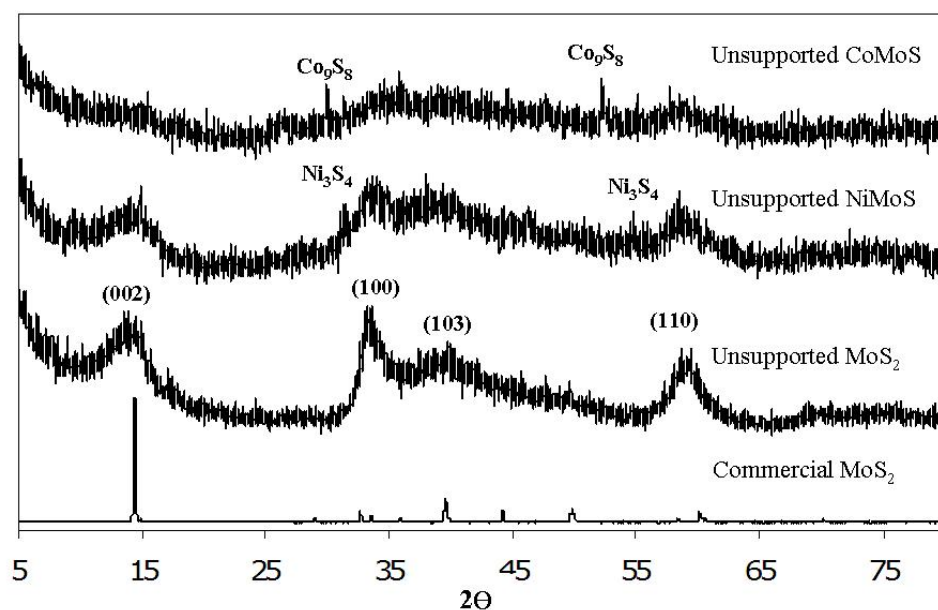


Figure 3-18. XRD patterns of unsupported Mo based sulfide catalysts.

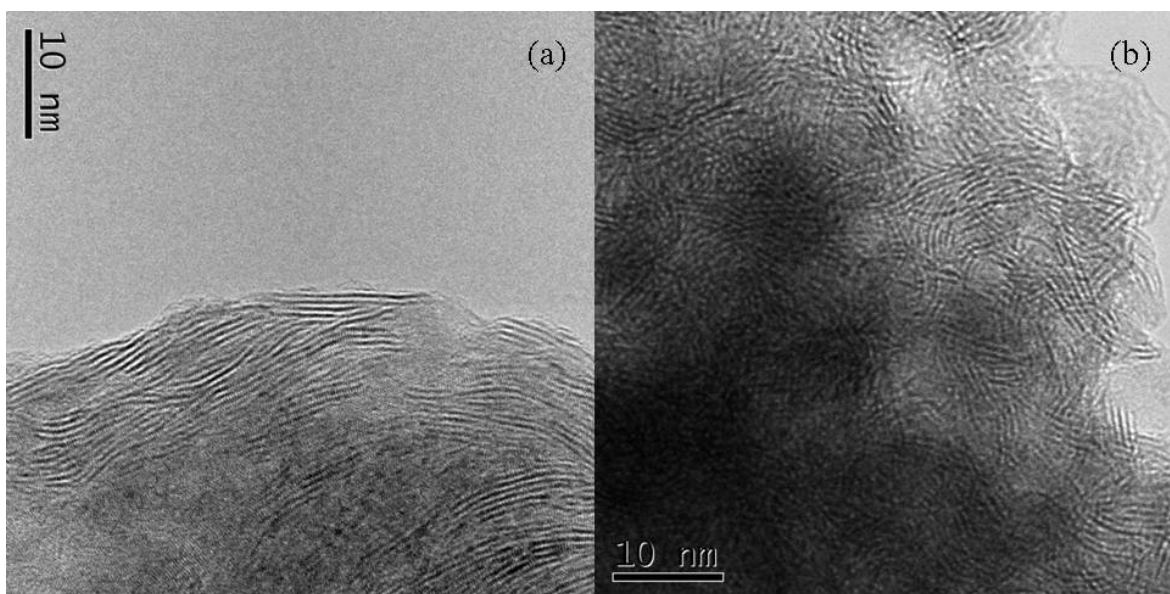


Figure 3-19. HRTEM images of unsupported (a) Mo and (b) NiMo sulfide catalysts.

3.1.3. Summary

3.1.3.1. Adsorptive desulfurization and denitrogenation

- 1) Liquid-phase adsorption of a model fuel containing aromatics, sulfur and nitrogen compounds over different adsorbents were carried out in a fix-bed adsorption system. Different breakthrough curves and selectivity provided an insight into the fundamental understanding of the adsorption mechanism over various adsorbents. Each adsorbent showed very different adsorption properties and capacities (breakthrough and saturate) of aromatic, sulfur and nitrogen compounds.
- 2) For the zeolite-based adsorbents, the breakthrough of sulfur compounds was not separated from that of aromatic compounds, but it was clearly separated from the breakthrough of nitrogen compounds of which capacity was higher than those of aromatic and sulfur compounds. The selectivity of indole and quinoline were 5.0 and 7.0, respectively. For the nickel-based adsorbent, the breakthrough capacities of adsorbates were higher than the zeolite-based adsorbent, especially the capacities of sulfur compounds were higher than those of aromatic compounds, but not than those of nitrogen compounds. The selectivity of DBT and DMDBT were 3.1 and 2.0, respectively. It also indicates that the nickel-based adsorbent could be good for selective removal of the sulfur compounds without the steric hindrance from hydrocarbon stream, such as gasoline, kerosene and jet fuel.
- 3) The adsorption selectivity on the activated alumina depends on the polarity and the acidic-basic interaction. The activated alumina is very good for selective separation of nitrogen compounds, especially for basic nitrogen compounds, but not very successful for separating the sulfur compounds from hydrocarbons.
- 4) The activated carbon shows higher adsorptive capacity and selectivity for sulfur and nitrogen compounds compared to other adsorbents used in this study. In the adsorption of sulfur compounds, the activated carbon was good for the sulfur compounds with methyl groups, such as 4,6-DMDBT.
- 5) In the adsorption of LCO on the activated carbon, the capacity of sulfur was pretty similar to that in the adsorption of model fuel while that of nitrogen was much lower than that in that of model fuel. It may be because LCO contains non-basic nitrogen

compounds and carbazole-type nitrogen compounds, which has very low reactivity and adsorptivity on catalytic active sites. Therefore, the earlier breakthrough for nitrogen compounds resulted from the non-basic nitrogen compounds to 0.8 of C/C_0 ratio and then basic nitrogen compounds adsorb further on the activated carbon to saturation of nitrogen compounds.

3.1.3.2. Adsorptive desulfurization and denitrogenation of LCO

- 1) GC-PFPD analysis showed that the LCO contains wide range of sulfur compounds from BT (benzothiophene) and alkyl-BTs to alkyl-DBTs (dibenzothiophenes) in molecular size. Major compounds are C_2 -BT, specifically 2,3-DMBT and 4-MDBT.
- 2) Based on the analysis of LCO treated by adsorption and hydrotreating by GC-PFPC, the adsorptive desulfurization on activated carbon preferentially removes sulfur compounds in DBT range due to the adsorbent's excellent adsorption properties for heavy and alkylated sulfur compounds. Hydrotreating favors to remove relatively light sulfur compounds in BT ranges because these sulfur compounds are generally more reactive than heavy sulfur compounds in DBT range, particularly 4,6-DMDBT. Therefore, adsorptive desulfurization and denitrogenation followed by hydrotreating improved considerably the removal of sulfur compounds in LCO.

3.1.3.3. Hydrodesulfurization of 4,6-DMDBT

- 1) Supported NiMo and CoMo catalysts were prepared with wet co-impregnation, which provided more activity to NiMo and CoMo/MCM-41 catalysts as compared with catalysts prepared with incipient wetness impregnation. It may be because the acidity of MCM-41 support was affected by water solution and preparation method. High metal loaded NiMo/MCM-41 catalyst has higher activity at 300 and 325°C than other catalysts tested in this project and even higher than a commercial NiMo catalyst (Cr424), but which had higher activity at 350°C than NiMo/MCM-41.
- 2) Isomerized product of DMDBT was detected on NiMo/MCM-41 at 300°C and most of catalysts at 325 and 350°C except Ni phosphide catalysts. The catalysts which had isomerized product had low HYD/DDS ratio and high DMBP selectivity. 4,6-DMDBT has steric hindrance of two methyl groups at 4- and 6- positions which hinders the

direct adsorption of sulfur atoms on catalytic active sites. If one or two of them move to other positions of DBT, their steric hindrance will disappear or be reduced and sulfur atoms may directly adsorb on active sites. This results in higher production of DMBP and lower HYD/DDS ratio.

3.1.3.4. Development of unsupported Mo sulfide catalysts for HDS

- 1) The unsupported Mo sulfide catalysts with Ni and Co promoters synthesized by hydrothermal method have much higher activity of simultaneous DBT and 4,6-DMDBT HDS than sulfided commercial HDS catalysts (Cr424 and Cr344). Based on the kinetic results, the unsupported NiMo and CoMo sulfides have much higher activity for DDS pathway as well as for HYD pathway than the commercial catalysts.
- 2) The unsupported Mo sulfide has higher 4,6-DMDBT conversion than DBT conversion at the conditions employed in this study, unlike other conventional HDS catalysts. However, the desulfurized activity of the catalyst was higher on DBT and 4,6-DMDBT and it is because the HDS activity mostly comes from high HDY activity. The addition of promoters (Ni and Co) on the Mo sulfide improved significantly DDS activity and, as well, HDY activity.
- 3) For the effects of promoters, large amounts of Ni and Co were added on the unsupported Mo sulfides as compared with conventional supported NiMo and CoMo catalysts. Therefore, some of promoters were not coordinated with Mo sulfides and their sulfide phases were observed by XRD analysis. These may result in the decrease of surface area and pore volume. However, the addition of promoters generates the increase of curvature of MoS₂ slabs and the decrease of slab length on the basis of XRD and HRTEM analysis because Ni and Co may be placed inside or on the edge of MoS₂ structure and prevent the growth (or aggregation) of crystallite size. These results provide more active phase for simultaneous HDS of DBT and 4,6-DMDBT.

3.2. Saturation of Two-Ring Aromatics

As a part of the DOE refinery integration project, this section discusses the saturation of aromatics for high-quality diesel and distillate fuels. High aromatics content in distillate fuels is undesirable since it lowers the fuel quality and contributes to the

formation of environmentally harmful emissions. In general, lower aromatics content leads to increase thermal stability, improve combustion characteristics and less soot formation. The conventional method of dearomatization is by aromatics saturation (hydrogenation) and, typically, sulfided CoMo/Al₂O₃ or NiMo/Al₂O₃ catalysts are employed. However, these catalysts are most active at higher temperatures where equilibrium limitations may prevent complete hydrogenation. Noble-metal catalysts are active at lower temperatures, where equilibrium limitations can be overcome. However, sulfur-tolerance is a major obstacle to their commercial application.

To meet the fuel performance and compositional specifications for diesel fuel, it is necessary for both RCO and LCO to be hydrogenated. This work focused on the development of increasingly sulfur-tolerant, noble-metal catalysts for the low-temperature hydrotreating and dearomatization (LTHDA) of distillate fuels for the production of ultra-clean and low-aromatic diesel fuels. In this report, the screening of zeolite-supported catalysts, the influence of zeolite support type, silica coating of catalysts and hybrid catalysts were examined. It is expected that the contact of sulfur molecules with noble metal particles on zeolite surface can be eliminated by silica coating on catalyst surface, meanwhile, the noble metal particles inside the zeolite pores may be still accessible to hydrogen molecules. Therefore, we can observe the performance of metal particles inside the zeolite pore excluding the catalytic activity on catalyst surface. A hybrid catalyst is prepared in order to verify the catalyst design concept proposed by Song [3-12,3-13] and compared the activity and resistance to sulfur poisoning with other uniform catalyst.

3.2.1 Experimental

3.2.1.1 Preparation and Screening of Zeolite-supported Pd and Pt Catalysts

Zeolite supports were obtained from Zeolyst International (formerly PQ Corporation). All zeolite supports were first calcined in air flow (~60 mL/min) for 4 hours at 450 °C, with a heating rate of approximately 1.5 °C/min, before catalyst preparation. Thus, any supports received in the NH₄⁺ form were converted to the H⁺ form. Properties of catalyst supports used in this work are summarized in **Table 3-11**.

All catalysts were prepared by the incipient wetness impregnation (IWI) technique. The pore volume of a given support was determined by measuring the volume of water added dropwise to a known weight of the support until the support changed appearance from dry to slightly liquid. The appropriate amount of metal precursor, calculated for the desired metal loading, was dissolved in a total volume of water (and HCl) equal to the pore volume for the support being impregnated. All catalysts in this work were prepared with a metal loading of 2 wt%. The precursor metal salt solution was then added dropwise to the support. After a few drops were added, the mixture was stirred thoroughly, then a few more drops were added and the mixture was stirred again. Impregnation continued in this manner until all of the metal solution was loaded on the support. After the impregnation was complete, the catalysts were dried at 110 °C for at least 2 hours. After drying, the catalysts were calcined in air flow (~60 mL/min) at 450 °C for 4 hours, with a heating rate of approximately 1.5 °C/min. The calcined catalysts were then pelletized, crushed and sieved to a particle size of 18-35 U.S.A. Standard Testing Sieve Mesh (0.5 – 1.0 mm).

Table 3-11 Properties of catalyst supports, as-received.

Support Type	Support Code	SiO₂/Al₂O₃ Ratio	Surface Area (m²/g)	Cation Form
Mordenite	CBV21A	20	500	NH ₄ ⁺
Mordenite	CBV30A	38	512	NH ₄ ⁺
Mordenite	CBV90A	90	500	H ⁺
Y Zeolite	CBV720	30	780	H ⁺
Y Zeolite	CBV780	80	780	H ⁺
ZSM-5	CBV5524G	50	425	NH ₄ ⁺
ZSM-5	CBV8014	80	425	NH ₄ ⁺

The metal precursors used in this study were: PdCl₂ (Pressure Chemical), Pd(NO₃)₂·xH₂O (Aldrich, 99.9%) and PtCl₄ (Pressure Chemical). For Pd(NO₃)₂·xH₂O, it was determined from the manufacturer that the degree of hydration is approximately 2. In order to dissolve PdCl₂ in water, it is necessary to add HCl to form soluble PdCl₄²⁻ species. For the first series of catalysts, large amounts of HCl were used – approximately 90% of the pore volume was added as 37 wt% HCl. It was hypothesized that so much

HCl might cause dealumination of the zeolite framework. Also for the first series of catalysts, the supports were not dried prior to impregnation. For all catalysts prepared after the initial series, supports were dried at 110 °C overnight prior to impregnation and HCl was only added in sufficient quantities to dissolve PdCl₂ (< 0.4 mL). It should be noted that for Pt precursors and for Pd(NO₃)₂·xH₂O, it was not necessary to add HCl.

A list of catalysts prepared for this work is given in **Table 3-12**. The first series of catalysts, prepared without drying of the support and with large quantities of HCl added, are given no special designation (e.g. Pd/CBV30A). Catalysts prepared with overnight drying of the support prior to impregnation and added HCl sufficient only to dissolve PdCl₂ are denoted with an asterik (e.g. Pd/CBV30A*). Catalysts prepared from Pd(NO₃)₂·xH₂O are denoted with a carrot (e.g. Pd/CBV30A^). It should be noted that catalysts prepared from Pd(NO₃)₂·xH₂O also used supports that were also dried overnight prior to impregnation. Bimetallic catalysts were prepared by co-impregnation of both metal precursors.

Table 3-12 Catalysts prepared for this work.

Catalyst	Metal Loading (wt%)	Precursor Metal	Support (SiO ₂ /Al ₂ O ₃ Ratio)	Notes
Pd/CBV21A	2.0	PdCl ₂	Mordenite (20)	
Pd/CBV30A	2.0	PdCl ₂	Mordenite (38)	
Pd/CBV90A	2.0	PdCl ₂	Mordenite (90)	
Pd/CBV720	2.0	PdCl ₂	Y Zeolite (30)	
Pd/CBV780	2.0	PdCl ₂	Y Zeolite (80)	
Pd/CBV5524G	2.0	PdCl ₂	HZSM-5 (50)	
Pd/CBV8014	2.0	PdCl ₂	HZSM-5 (80)	
Pd/Al ₂ O ₃ *	2.0	PdCl ₂	Alumina	
Pd/CBV30A*	2.0	PdCl ₂	Mordenite (38)	
Pd/CBV720*	2.0	PdCl ₂	Y Zeolite (30)	
Pd/CBV5524G*	2.0	PdCl ₂	HZSM-5 (50)	
Pd/MCM-41(50)*	2.0	PdCl ₂	MCM-41 (50)	
Pt/CBV720*	2.0	PtCl ₄	Y Zeolite (30)	
Pd-Pt/CBV720*	2.0	PdCl ₂ , PtCl ₄	Y Zeolite (30)	Pd:Pt = 4:1 mol
Pd/CBV30A^	2.0	Pd(NO ₃) ₂ ·xH ₂ O	Mordenite (38)	
Pd/CBV720^	2.0	Pd(NO ₃) ₂ ·xH ₂ O	Y Zeolite (30)	

BET surface area data was obtained using a Quantachrome Autosorb 1 apparatus. Metal dispersion data was obtained using a Micrometrics 2910 Autochem analyzer. For

CO pulse chemisorption, the catalyst was reduced in 5% hydrogen flow in argon (20 mL/min), at atmospheric pressure, under the same temperature ramp as for an experiment (2 °C/min to 225 °C). The sample was outgassed in argon for 10 min, then the temperature was brought down to 50 °C for chemisorption analysis. The sample was dosed with discrete volumes of 10% CO in argon and the uptake was recorded. The doses were repeated until no more CO uptake was detected. The volume of CO adsorbed was used to calculate the percent metal dispersion, assuming a metal:CO stoichiometric ratio of 1:1. For hydrogen chemisorption, the catalyst was reduced in 5% hydrogen flow in argon (20 mL/min), at atmospheric pressure, with a heating rate of 5 °C/min, from ambient to 250 °C. The sample was then degassed in argon for 120 min, then the temperature was brought down to 50 °C for chemisorption analysis. The sample was dosed with discrete volumes of 25% hydrogen in argon and the uptake was recorded. The doses were repeated until no more hydrogen uptake was recorded. The volume of hydrogen adsorbed was used to calculate the percent metal dispersion, assuming a metal:H₂ ratio of 2:1. The accuracy of metal dispersion data is given by the manufacturer to be +/- 5%.

The Micrometrics 2910 Autochem Analyzer was also used for the temperature programmed reduction of the catalyst samples. The sample was reduced in 5% hydrogen in argon as the temperature was increased from ambient to 500 °C at 5 °C/min. Hydrogen uptake is monitored and reveals the temperature at which the catalyst is reduced.

The elemental surface concentrations, metal oxidation states and binding energies of selected catalysts were determined using XPS. A Kratos Analytical Axis Ultra instrument was used. XPS quantification was performed by applying the appropriate instrumental transmission function and elemental relative sensitivity factors (RSFs) for the Kratos instrument to the integrated peak areas. The RSFs are determined taking into consideration the X-ray cross section and relative inelastic mean free paths of the photoelectrons. The approximate sampling depth was 50 Å under these conditions.

Feedstock composition for hydrogenation experiments was approximately 20 wt% tetralin (Aldrich, 99%), 75 wt% hexadecane (Aldrich, 99+%), and 5 wt% nonane (Aldrich, 99+%), with ppm quantities of sulfur, added as benzothiophene (BT) (Fluka,

99%), dibenzothiophene (DBT) (Aldrich, 98%), 4,6-dimethyldibenzothiophene (4,6-DMDBT) (Aldrich, 97%) or tetrahydrothiophene (THT) (Aldrich, 99%).

The reaction was carried out in a down flow reactor system as described in previous report. For each experiment, 0.5g of catalyst particles (18-35 mesh) were used. 3.0g of α -Al₂O₃ particles, also 18-35 mesh, were mixed with the catalyst particles to act as a diluent. Prior to each experiment, catalysts were reduced *in situ*, under a hydrogen flow of 100 mL/min. The pressure was maintained at 100 psi. The temperature was increased from room temperature to 225 °C at a rate of 2 °C/min. The temperature was maintained at 225 °C for two hours prior to the introduction of liquid feed. After the reduction step was complete, the pressure was increased to 600 psi and the hydrogen flow was reduced to 80 mL/min. Liquid feed was then introduced at a rate of 0.08 mL/min. This corresponds to a gas-to-liquid ratio (G/L) of approximately 1000 and a weight hourly space velocity (WHSV) of approximately 8 hr⁻¹. After starting the HPLC pump to introduce liquid feedstock, the system was allowed to equilibrate for 1.5 hr. Therefore, 90 min after the start of feedstock was designated as time-on-stream (TOS) equal to zero. Liquid samples were then collected at 30 min intervals until the experiment was terminated. For the majority of experiments, sulfur-free feedstock was fed until TOS = 2 hr, at which point sulfur-containing feedstock was introduced. Exceptions to this practice were experiments using only sulfur-free feed, and a series of experiments using only sulfur-containing feedstock. The liquid products were analyzed using a Shimadzu GC-17a gas chromatograph coupled with a Shimadzu QP-5000 quadrupole mass spectrometer. The capillary column (30m x 0.25mm, Restek XTI-5) was coated with a 0.25 μ m stationary phase of 5% phenyl-95% methyl polysiloxane.

For selected experiments, the gaseous effluent was analyzed for the presence of hydrogen sulfide (H₂S) using Sensidyne GASTEC detector tubes. The tubes contain lead acetate (Pb(CH₃COO)₂), which reacts with H₂S to form lead sulfide (PbS), changing color from white to reddish-brown. The liquid products from certain other experiments were also analyzed for sulfur content using an ANTEK 9000 Series Sulfur Analyzer with a lower detection limit of 0.5 wppm sulfur.

3.2.1.2 Catalyst Preparation for Detailed Catalytic Study

Zeolite supports were obtained from Zeolyst International (formerly PQ Corporation). All zeolite supports were first calcined in air flow (~60 mL/min) for 4 hours at 450 °C, with a heating rate of approximately 1.5°C/min, before catalyst preparation. Thus, any supports received in the NH_4^+ form were converted to the H^+ form. Properties of catalyst supports used in this work were summarized in **Table 3-13**. As A zeolite was sodium form, it needs pretreatment for ion exchange before calcination. A zeolite was dispersed in 1 M ammonium chloride solution. The zeolite and supernatant solution were then agitated by continuous shaking at room temperature for 3 h to come to equilibrium and then separated by vacuum filtration. The zeolite was rinsed with de-ionized water to remove excess ammonium solution. This procedure was repeated 3 times for zeolite to change to ammonium form thoroughly. The ammonium ion exchanged zeolite was dried in an oven at 50°C and calcined as the same way described above.

All catalysts were prepared by incipient wetness impregnation (IWI) technique. The pore volume of a given support was determined by measuring the volume of water added dropwise to a known weight of the support until the support changed appearance from dry to slightly liquid. The appropriate amount of metal precursor, calculated for the desired metal loading, was dissolved in a total volume of water (and HCl) equivalent to the pore volume for the support being impregnated.

Table 3-13. Properties of zeolite supports as-received.

Support Type	Support Code	$\text{SiO}_2/\text{Al}_2\text{O}_3$ Ratio	Surface Area (m^2/g)	Pore size (Å)	Cation Form
Mordenite	CBV30A	38	512	7.0×6.5 (L) 5.7×2.6 (M) 4.8×3.4 (S)	NH_4^+
Y Zeolite	CBV720	30	780	11.2×11.2 (L) 7.4×7.4 (S)	H^+
A Zeolite	Advera 401	1.0	425	4.1×4.1	Na^+

All catalysts in this work were prepared with a metal loading of 2 wt%. The solution of precursor metal salt was then added dropwise to the support. After a few drops were added, the mixture was stirred thoroughly, then a few more drops were added and the mixture was stirred again. Impregnation continued in this manner until all of the

metal solution was loaded on the support. After the impregnation was complete, the catalysts were dried at 110°C for at least 2 h and then calcined in air flow (~60 ml/min) at 450°C for 4 h at a ramping rate of approximately 1.5°C/min. The calcined catalysts were then palletized, crushed and sieved to a particle size of 18-35 U.S.A. Standard Testing Sieve Mesh (0.5–1.0 mm). The metal precursors used in this study were PdCl₂ (Sigma Aldrich). In order to dissolve PdCl₂ in water, it was necessary to add HCl to form soluble PdCl₄²⁻ species. For all catalysts prepared, HCl was added in sufficient quantities to dissolve PdCl₂ (2.35 g of 37% HCl solution for 0.167 g of PdCl₂).

Pd/HA and Pd/CBV30A catalysts were modified with TEOS by sol-gel process to form the silica wall on the catalyst surface. 1.5 g of catalyst prepared was mixed with 20ml of tetraethyl orthosilicate (TEOS, Aldrich, 98%) in a conical flask at room temperature with continual agitation for 12 h. The sample was settled using centrifuge and the supernatant TEOS was decanted and then evaporated off in an oven at 80°C overnight. The sample was then mixed with 2.5 ml of acetone in order to hydrolyze the remaining organo-silicate bonds and fix the coating and the acetone was then evaporated to dryness [3-14]. The Pd/HA-Pd/Y720 and Pd/HA-SiO₂-Pd/Y720 hybrid catalysts were prepared by physically mixing and co-grinding Pd/HA and Pd/Y720 or Silica coated Pd/HA and Pd/Y720, respectively, at the ratio of 1:1 by weight, and pressure molding of mixture to granules (18-35 mesh).

Table 3-14. The list of catalysts prepared in this study.

Catalyst	Metal Loading (wt%)	Precursor Metal	Support (SiO ₂ /Al ₂ O ₃ Ratio)	Notes
Pd/CBV720	2.0	PdCl ₂	Y Zeolite (30)	
Pd/CBV30A	2.0	PdCl ₂	Mordenite (38)	
Pd/HA	2.0	PdCl ₂	A Zeolite (1.0)	
Pd/CBV30A-SiO ₂	2.0	PdCl ₂	Mordenite (38)	Coated with TEOS
Pd/HA-SiO ₂	2.0	PdCl ₂	A Zeolite (1.0)	
Pd/HA-Pd/CBV720	2.0	PdCl ₂	A and Y zeolite	Mixed at the ratio of 1:1
Pd/HA-SiO ₂ -Pd/CBV720	2.0	PdCl ₂	A and Y zeolite	

3.2.1.3 Catalytic evaluation in hydrogenation experiments

Feed composition for hydrogenation experiments was approximately 20 wt% tetralin (Aldrich, 99%), 75 wt% hexadecane (Aldrich, 99+%), and 5 wt% nonane (Aldrich, 99+%), with 100ppm of sulfur added as benzothiophene (BT) (Aldrich, 99%).

The reaction was carried in a down flow reactor system. For each experiment, 0.5 g of catalyst particles (screened between 18-35 meshes) were used. 3.0 g of α -Al₂O₃ particles as a diluent were mixed with the catalyst particles. The volume of catalytic bed in all experiments was around 9.65 ml. Before each experiment, catalysts were reduced *in situ* under a hydrogen flow of 100 ml/min and the pressure was maintained under 100 psi. The temperature was increased from room temperature to 225°C at a rate of 2°C/min. The temperature was maintained at 225°C for two hours prior to the introduction of liquid feed. After the reduction step was complete, the pressure was increased to 600 psi and the hydrogen flow was reduced to 80 ml/min. Liquid feed was then introduced at a rate of 0.08 ml/min. This corresponds to a gas-to-liquid ratio (G/L) of approximately 1000 and a weight hourly space velocity (WHSV) of approximately 8 h⁻¹. After starting the HPLC pump to introduce liquid feedstock, the system was allowed to equilibrate for 1.5 h. Therefore, 90 min after the start of feedstock was designated as time-on-stream (TOS) equal to zero. Liquid samples were then collected at 30 min intervals until the experiment was terminated. The liquid products were analyzed using a Shimadzu GC-17a gas chromatograph coupled with a Shimadzu QP-5000 quadrupole mass spectrometer. The capillary column (30m x 0.25mm, Restek XTI-5) was coated with a 0.25µm stationary phase of 5% phenyl-95% methyl polysiloxane.

3.2.1.4 Catalyst characterization

In order to examine the characteristics of catalysts prepared, several different analysis techniques were employed. Surface morphology was explored by scanning electron microscopy (Hitachi S-3500N). Micromeritics AutoChem 2910 was applied for temperature programmed reduction (TPR) and Temperature Programmed desorption (TPD). TPR is used to reveal the temperature at which the reduction occurs and TPD analysis of hydrogen can determine the type and strength of active metal sites available on the surface of a catalyst from measurement of the amount of gas desorbed at various temperatures.

3.2.2 Results and discussion

3.2.2.1 Effect of support acidity

The results of hydrogenation experiments on a series of mordenite catalysts with different acidities (as indicated by their $\text{SiO}_2/\text{Al}_2\text{O}_3$ ratios), are shown in **Figures 3-20 and 3-21**. No clear differences were observed in the conversion or decalin ratio. It might be expected that the more acidic support would exhibit greater sulfur tolerance, due to the imparting of electron deficiency on the Pd metal by the acid sites [3-10], however this was not observed. The effect of support acidity therefore, remains to be determined.

Because no discernable differences were observed in catalysts with different support acidities, it was hypothesized that the method of catalyst preparation was potentially flawed. Since large amounts of HCl were used in order to dissolve the PdCl_2 metal precursor, it is possible that dealumination of the zeolite support was occurring. This would render the differences in support acidity negligible.

It was also determined that, just as a matter of good preparation technique, the catalyst supports should be thoroughly dried before impregnation, so the support surface would be free of any water and the true pore volume of the support could be exploited. The effects of this new method of catalyst preparation are examined in the next section.

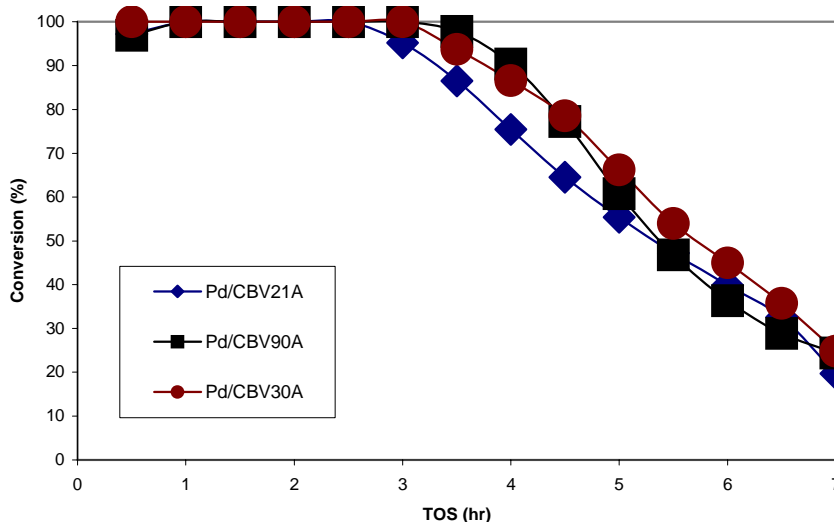


Figure 3-20 Conversion vs. TOS for the hydrogenation of tetralin at 225 °C and 600 psig hydrogen pressure in the presence of 100 ppm sulfur as BT.

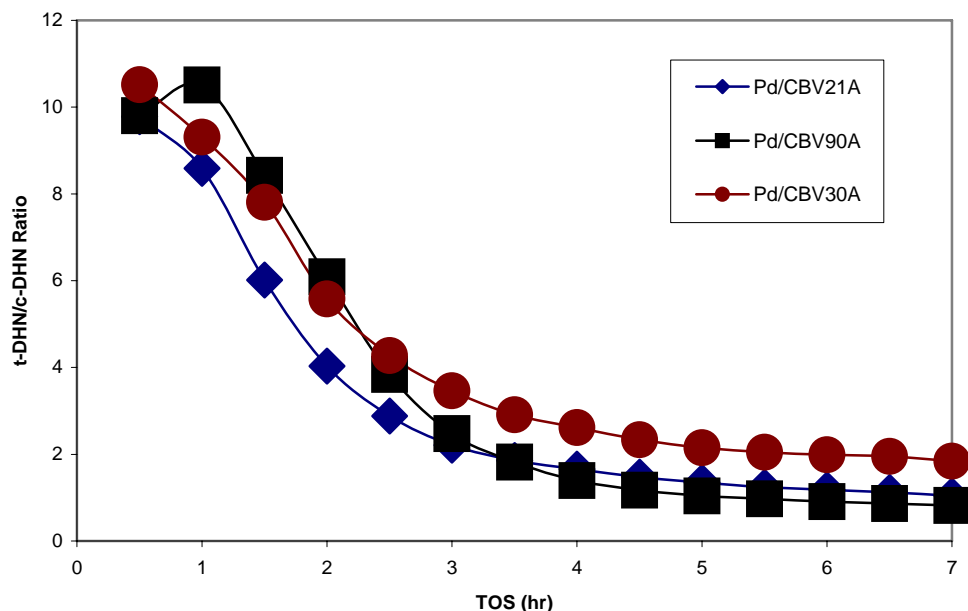


Figure 3-21 t-DHN/c-DHN ratios for the hydrogenation of tetralin at 225 °C and 600 psig hydrogen pressure in the presence of 100 ppm sulfur as BT.

3.2.2.2 Effect of Preparation Method

As previously mentioned, the new method of catalyst preparation used about one-tenth the amount of HCl, just enough to dissolve PdCl₂, and the supports were carefully dried overnight prior to impregnation. The characterization properties of catalysts prepared by the old and new methods are presented in **Table 3-15**. Little difference can be seen in BET surface area or dispersion between the two sets of catalysts. Hydrogenation experiments with CBV720 catalysts prepared by the old and new methods, shown in **Figure 3-22**, also show little improvement. The conversion of tetralin and *trans*-/*cis*-decalin ratio was slightly higher for the catalyst prepared by the new method. XPS analysis of the spent Pd/CBV720 and Pd/CBV720* samples revealed that the Pd 3d_{5/2} binding energies were 336.4 and 336.3 eV, respectively. This is an indication that little difference can be discerned in the Pd-support interaction in both catalyst samples.

Table 3-15 Characterization of selected catalysts prepared by the old and new methods.

Catalyst	BET Surface Area (m ² /g)	Dispersion (CO)	Dispersion (H ₂)
Pd/Al ₂ O ₃	156	32%	54%
Pd/CBV720	610	34%	39%
Pd/CBV30A	317	35%	41%
Pd/CBV5524G	355	27%	31%
Pd/MCM-41(50)	705	29%	36%
Pd/Al ₂ O ₃ *	165	24%	47%
Pd/CBV720*	590	31%	42%
Pd/CBV30A*	392	35%	47%
Pd/CBV5524G*	328	34%	33%
Pd/MCM-41(50)*	1044	29%	43%

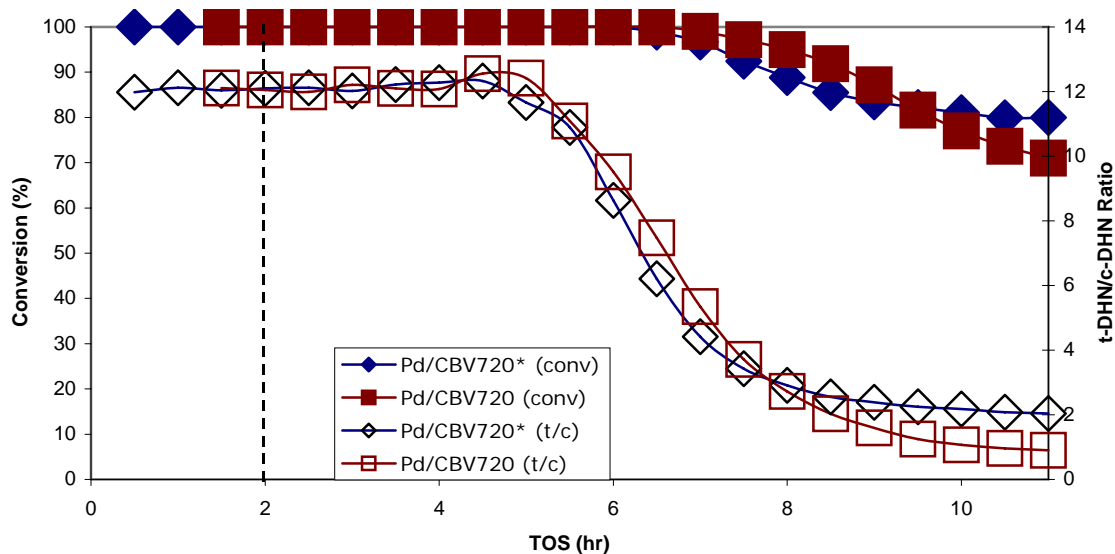


Figure 3-22 Conversion and t-DHN/c-DHN ratio for the hydrogenation of tetralin at 225 °C and 600 psig hydrogen pressure in the presence of 100 sulfur as BT.

Though the improvement in catalytic properties and hydrogenation activity is only marginal at best, it is nevertheless recommended that the new method of catalyst preparation, with about one-tenth the amount of HCl and careful drying of the support, should be preferred as a matter of good catalyst preparation technique.

3.2.2.3 Effect of Palladium Precursor

Two Pd catalysts, Pd/CBV720[^] and Pd/CBV30A[^], were prepared from Pd(NO₃)₂·xH₂O (x ~ 2) to examine the effect of metal precursor on catalytic characteristics and performance. It was hypothesized that, since the Pd(NO₃)₂·xH₂O does not require any HCl to be dissolved in water, catalysts prepared using it as a precursor might exhibit beneficial characteristics compared with those prepared from PdCl₂, which requires addition of HCl. However, this was not observed to be the case. As is seen in **Figure 3-23** and **Figure 3-24**, the catalysts prepared from nitrate precursors significantly underperformed their chloride counterparts.

The properties of the catalysts from nitrate precursors and those of their chloride counterparts, are shown in **Table 3-16**. The most glaring difference between the catalysts prepared from nitrate precursors is their poor dispersion. It is unclear why catalysts prepared from Pd(NO₃)₂·xH₂O would be so poorly dispersed. It should be mentioned that, upon obtaining such poor results with the first set of catalysts prepared from Pd(NO₃)₂·xH₂O, both Pd/CBV720[^] and Pd/CBV30A[^] were prepared and characterized a second time and both catalysts had similarly poor dispersions, as measured by CO pulse chemisorption (7% and 8%, respectively).

Table 3-16 Properties of catalysts from nitrate and chloride precursors.

Catalyst	BET Surface Area (m ² /g)	Dispersion (CO)	Dispersion (H ₂)
Pd/CBV720*	590	31%	42%
Pd/CBV720 [^]	747	8%	7%
Pd/CBV30A*	392	35%	47%
Pd/CBV30A [^]	412	8%	10%

XPS analysis of the spent Pd/CBV720* and Pd/CBV720[^] catalyst samples revealed Pd 3d_{5/2} binding energies of 336.4 and 335.7 eV, respectively. The higher binding energy of the Pd/CBV720* catalyst sample indicates a stronger metal-support interaction, representative of smaller and more electron-deficient metal particles [3-11]. This is consistent with the hydrogen pulse chemisorption data, from which the average

metal particle diameters were calculated to be 2.6 nm for Pd/CBV720* and 15.3 nm for Pd/CBV720^.

It can be concluded that catalysts prepared from PdCl₂, under the conditions for catalyst preparation used in this study, are superior to catalysts prepared from Pd(NO₃)₂·xH₂O, both in terms of catalyst characteristics and sulfur tolerance during the hydrogenation of tetralin in the presence of sulfur, under the reaction conditions used in this study.

3.2.2.4 Effect of Support Type

The effect of support type was re-examined with catalysts prepared by the new method. The results are presented in **Figure 3-25** and **Figure 3-26**. Not surprisingly, the catalytic performance is very similar to the catalysts prepared by the old method. The Y-zeolite-supported (CBV720*) catalyst exhibited the greatest sulfur tolerance of the catalysts tested. As before, there is no clear trend between catalytic performance and BET surface area or metal dispersion. It is again obvious, therefore, that support structure has a significant impact on the sulfur tolerance of Pd catalysts.

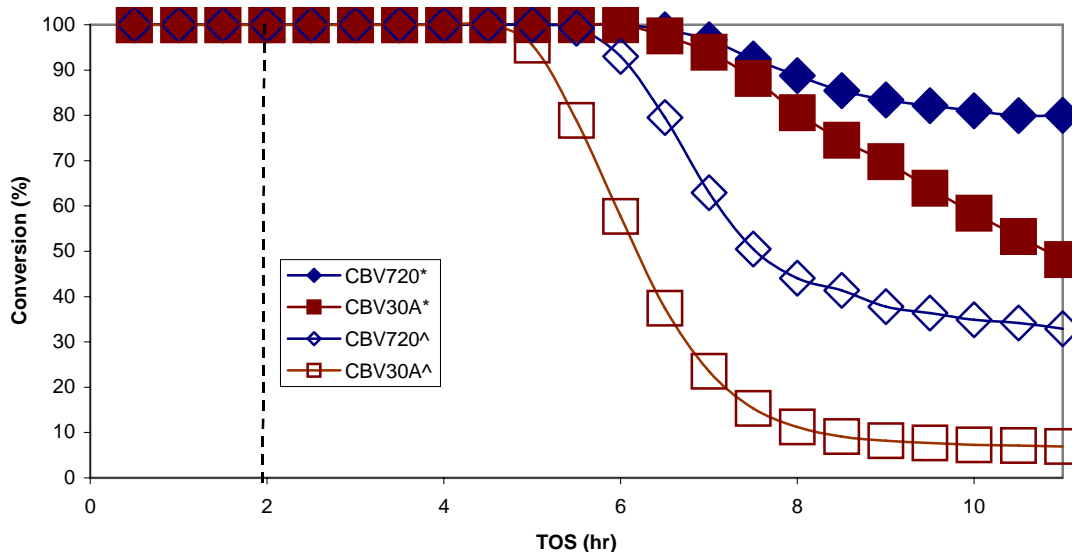


Figure 3-23 Conversion vs. TOS for the hydrogenation of tetralin at 225 °C and 600 psig hydrogen pressure in the presence of 100 ppm sulfur as BT.

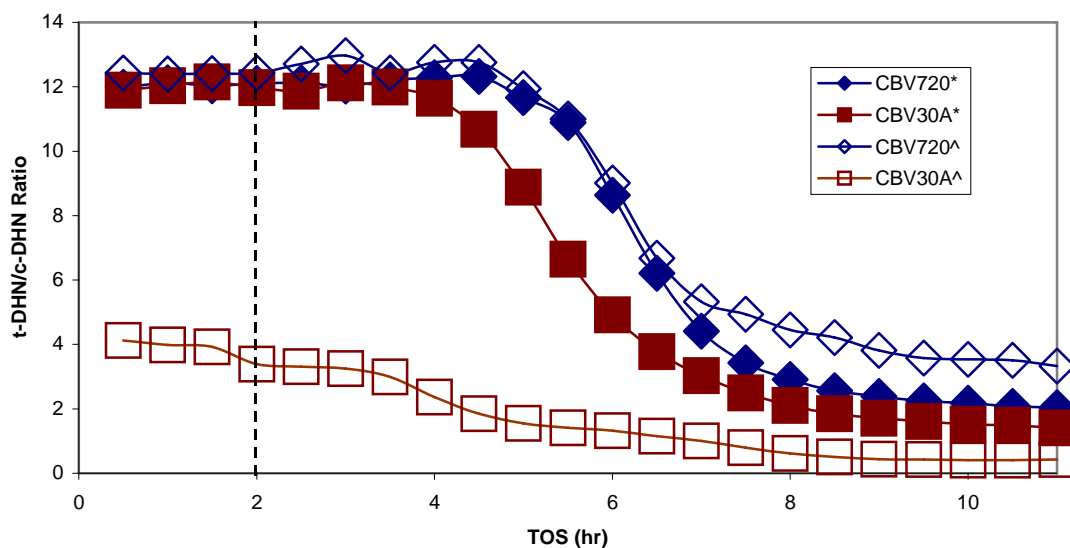


Figure 3-24 t-DHN/c-DHN ratio for the hydrogenation of tetralin at 225 °C and 600 psig hydrogen pressure in the presence of 100 ppm sulfur as BT.

Considering that the average particle diameters, shown in **Table 3-17**, are larger than the zeolite pore openings, it is likely that the majority of metal particles do not reside in the zeolite pore structure, but rather on the zeolite exterior surface. It is therefore difficult to speculate why one support would intrinsically perform better than another.

Table 3-17 Properties of selected catalysts.

Catalyst	Dispersion (H ₂)	Active Particle Diameter (nm)	Zeolite Pore Size (Å)
Pd/Al ₂ O ₃ *	47%	2.3	-
Pd/CBV720*	42%	2.6	7.4
Pd/CBV30A*	47%	2.4	6.7 x 7.0
Pd/CBV5524G*	33%	3.5	5.3 x 5.6
Pd/MCM-41(50)*	43%	2.6	15 – 100

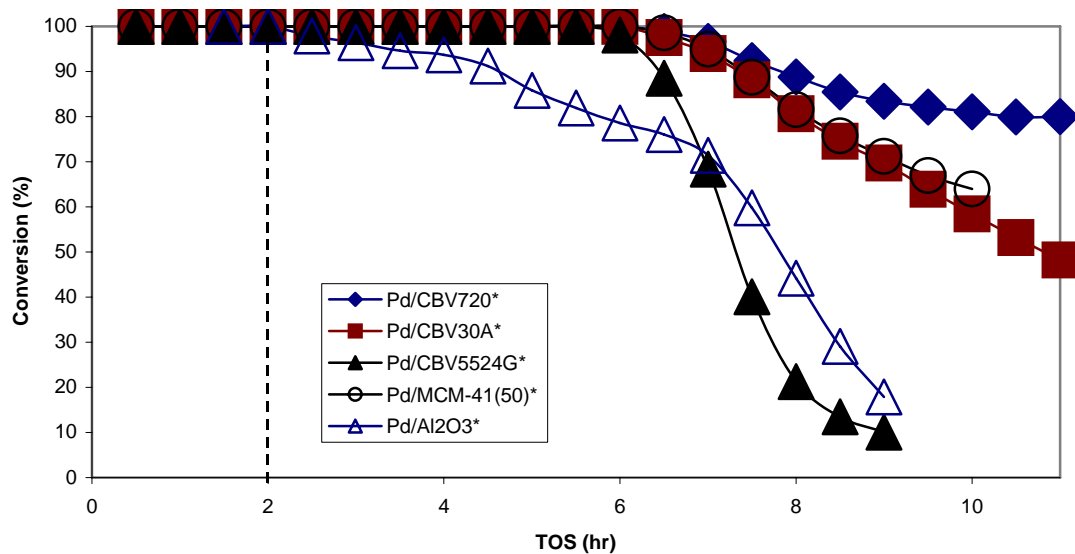


Figure 3-25 Conversion vs. TOS for the hydrogenation of tetralin at 225 °C and 600 psig hydrogen pressure in the presence of 100 ppm sulfur as BT.

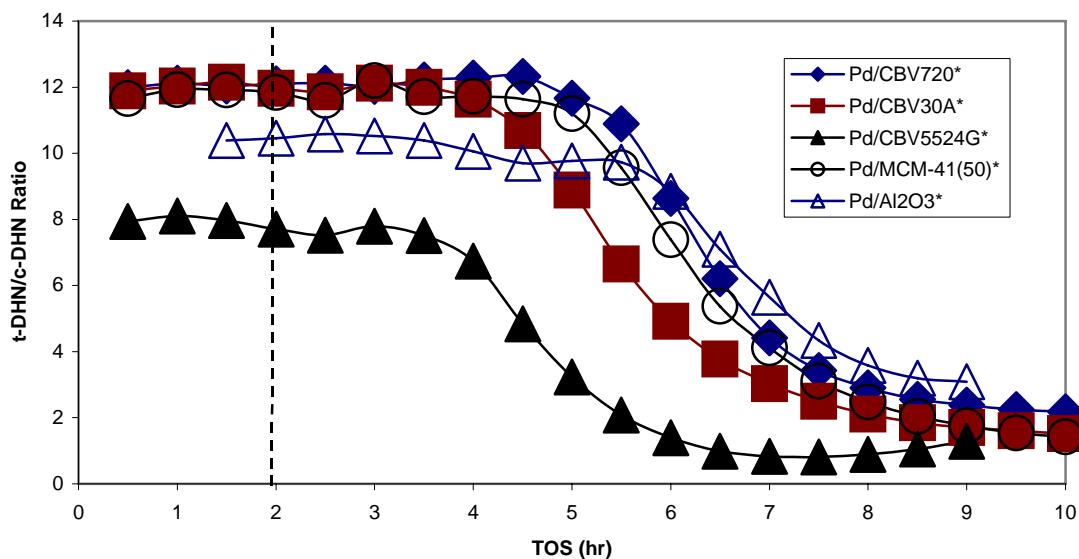


Figure 3-26 t-DHN/c-DHN ratio for the hydrogenation of tetralin at 225 °C and 600 psig hydrogen pressure in the presence of 100 ppm sulfur as BT.

3.2.2.5 Bimetallic Pd-Pt Catalyst

The addition of Pt to Pd catalysts has been reported to increase the hydrogenation activity and improve resistance to poisoning by sulfur. Specifically [3-12, 3-13], it has been shown that optimum content of Pd and Pt is found at a mole ratio of 4 Pd to 1 Pt. Therefore, a Pd-Pt(4:1)/CBV720* catalyst was synthesized and compared to Pd/CBV720* and Pt/CBV720*. The results are presented in **Figure 3-27** and **Figure 3-28**.

The Pd-Pt/CBV720* catalyst maintained 100% tetralin conversion even after both Pd/CBV720* and Pt/CBV720* catalysts began to show deactivation due to sulfur poisoning. Additionally, the *trans*-/*cis*-decalin ratio was maintained at a higher level. This indicates that the bimetallic combination did, in fact, provide an enhancement in sulfur tolerance, as compared with the monometallic catalysts. The characterization of the Pd, Pt and Pd-Pt catalysts is presented in **Table 3-18**.

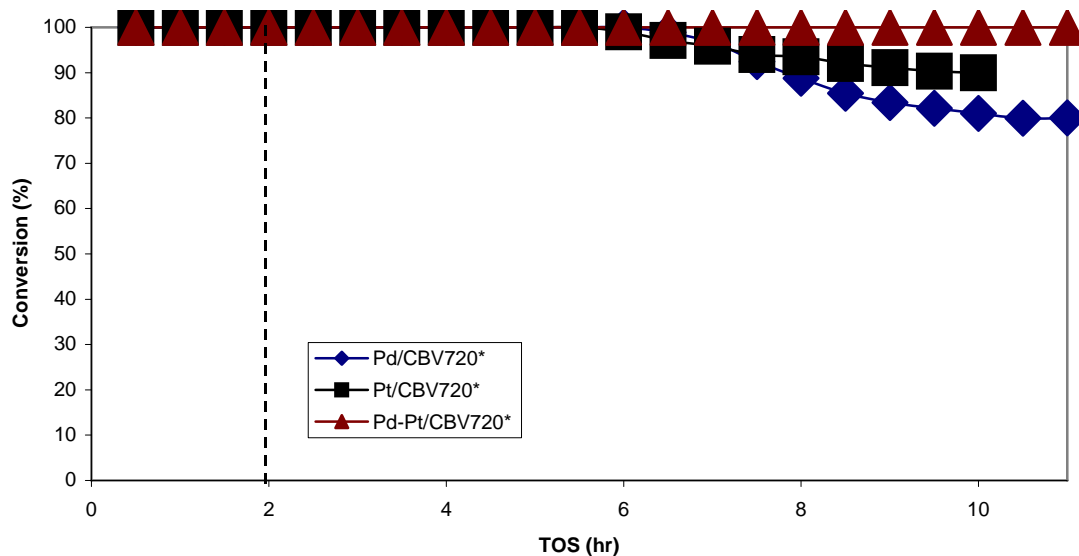


Figure 3-27 Conversion vs. TOS for the hydrogenation of tetralin at 225 °C and 600 psig hydrogen pressures in the presence of 100 ppm sulfur as BT.

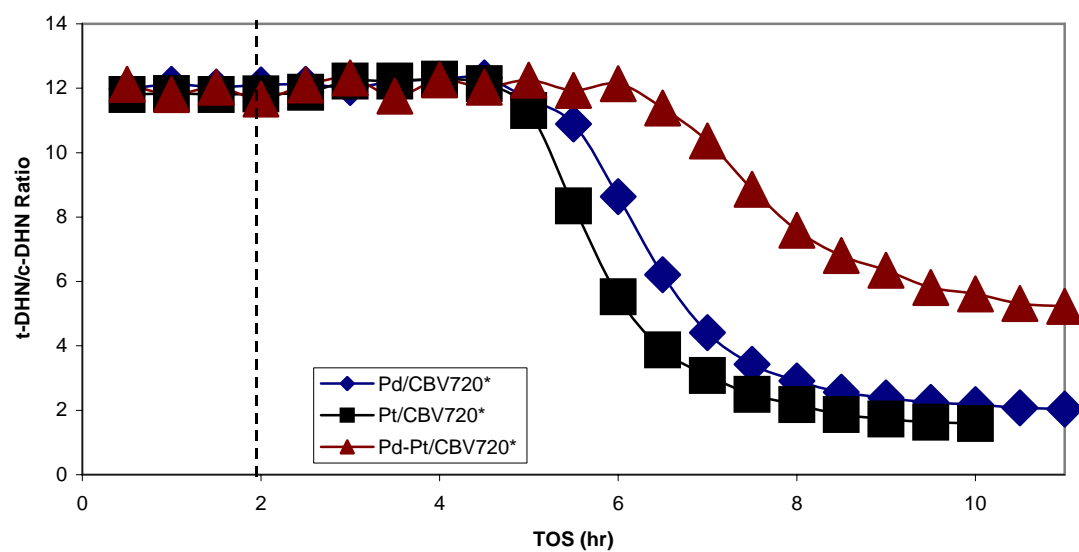


Figure 3-28 t-DHN/c-DHN ratio for the hydrogenation of tetralin at 225 °C and 600 psig hydrogen pressure in the presence of 100 ppm sulfur as BT.

Table 3-18 Characterization of Pd, Pt and Pd-Pt catalysts supported on CBV720*.

Catalyst	BET Surface Area (m ² /g)	Dispersion (CO)	Dispersion (H ₂)
Pd/CBV720*	590	31%	42%
Pt/CBV720*	618	60%	63%
Pd-Pt/CBV720*	623	42%	52%

The dispersion of the Pt/CBV720* catalyst is exceptionally high, which may explain why it performed slightly better than Pd/CBV720*. However, dispersion alone cannot be responsible for increased sulfur tolerance, as the bimetallic Pd-Pt catalyst outperformed the Pt catalyst, despite having a lower dispersion. It is noted [3-12] that Pd and Pt form an alloy at structure at Pd:Pt = 4:1. The high sulfur tolerance of Pd-Pt (4:1)/USY(680) catalyst was attributed to “structural and electronic effects rather than to the degree of metal dispersion” [3-12]. Furthermore, EXAFS analysis of a Pd-Pt (4:1)/SiO₂-Al₂O₃ catalyst revealed a chemical bond between Pd and Pt, and the high hydrogenation activity of the catalyst was attributed to this direct interaction [3-13].

Binding energies from XPS analysis of spent catalyst samples are shown in **Table 3-19**. The increase in the binding energy for both the Pd 3d_{5/2} and Pt 4f_{7/2} in the bimetallic catalyst indicates a greater metal-support interaction compared with the individual monometallic catalysts.

Table 3-19 Binding energies from XPS analysis for Pd, Pt and Pd-Pt catalysts.

Spent Catalyst Sample	Pd 3d _{5/2} Binding Energy (eV)	Pt 4f _{7/2} Binding Energy (eV)
Pd/CBV720*	336.4	-
Pt/CBV720*	-	72.2
Pd-Pt/CBV720*	336.7	72.3

3.2.2.5 Poisoning effect of different sulfur compounds.

The hydrogenation of tetralin was tested on Pd/CBV30A* catalyst with 100 ppm sulfur feedstock using DBT, 4,6-DMDBT and THT, in addition to BT, in order to examine the effect of the type of sulfur species on sulfur poisoning of hydrogenation catalysts. The conversion results of the hydrogenation experiments are presented in **Figure 3-29**. The results with BT, DBT and

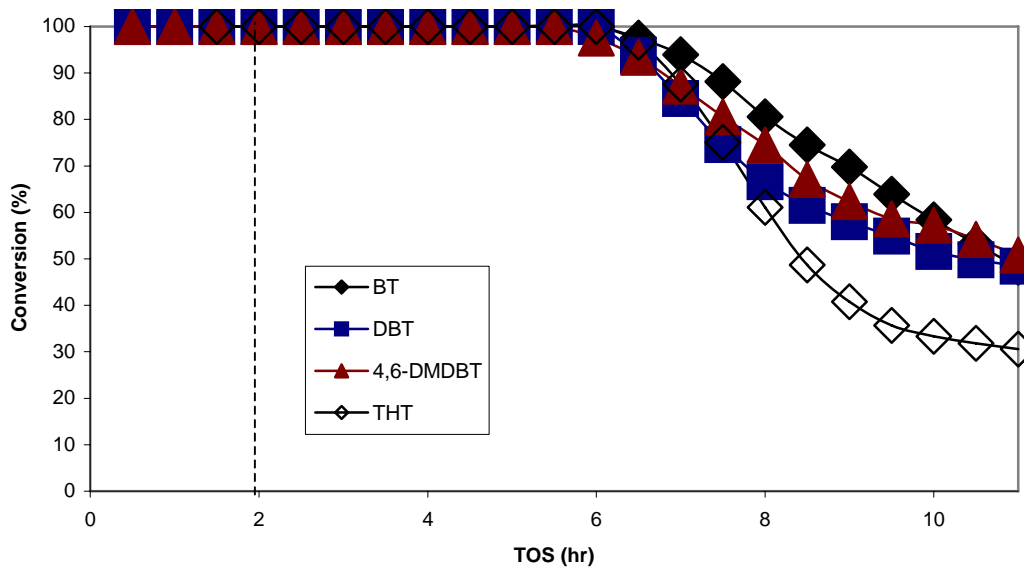


Figure 3-29 Conversion vs. TOS for the hydrogenation of tetralin over Pd/CBV30A* catalyst at 225 °C and 600 psig hydrogen pressure in the presence of 100 ppm sulfur as different sulfur compounds.

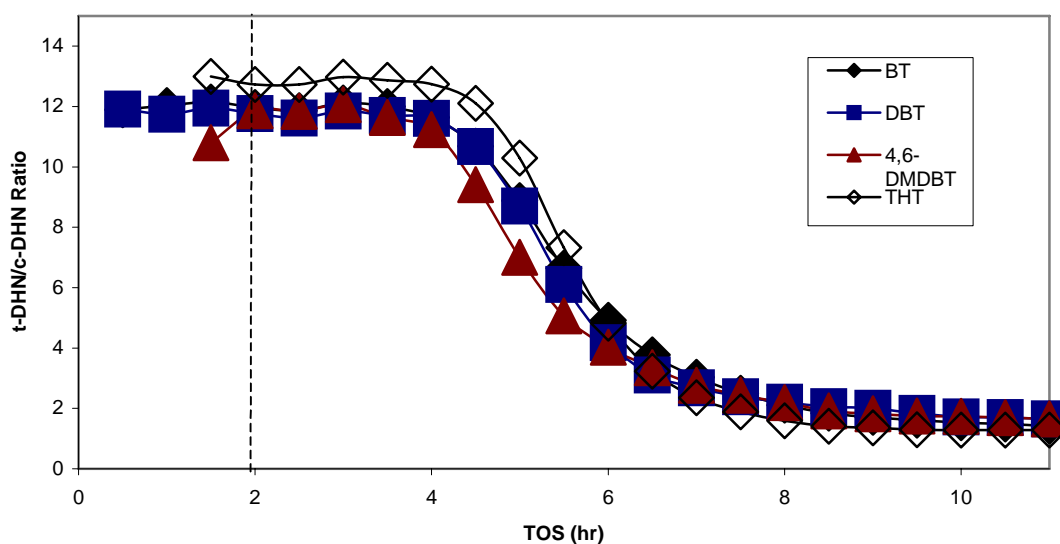


Figure 3-30 t-DHN/c-DHN ratio vs. TOS for the hydrogenation of tetralin over Pd/CBV30A* catalyst at 225 °C and 600 psig hydrogen pressure in the presence of 100 ppm sulfur as different sulfur compounds.

4,6-DMDBT are remarkably similar. The Pd/CBV30A* catalyst exhibited almost identical deactivation with these three sulfur compounds. The deactivation was somewhat accelerated and final tetralin conversion was somewhat lower when THT was the sulfur compound in the feed. One possible explanation of this behavior may be the electron density on the sulfur atom of the particular sulfur compound, shown in **Table 3-20 [3-14]**. The electron densities on the sulfur atoms in BT, DBT and 4,6-DMDBT are very similar, however for THT, the electron density is much greater. The higher electron density may result in a stronger interaction with the Pd particles, resulting in a greater poisoning effect.

The *trans*-/*cis*-decalin ratios are shown in **Figure 3-30**. The *trans*-/*cis*-decalin ratio appears to be unaffected by the species of sulfur present in the feedstock.

Table 3-20 Electron density on the sulfur atom for selected sulfur compounds [3-14]

Sulfur Compound	Electron Density on Sulfur Atom
Benzothiophene (BT)	5.739
Dibenzothiophene (DBT)	5.758
4,6-dimethyldibenzothiophene (4,6-DMDBT)	5.760
Tetrahydrothiophene (THT)	6.042

In order to attempt to determine the fate of sulfur compounds during the hydrogenation experiments, several analyses were performed. There are three possible scenarios for the sulfur species in the feedstock; 1) The sulfur compounds have a weak interaction with the catalyst and pass through the reactor without undergoing reaction, 2) The sulfur compounds adsorb on the catalyst and remain there unreacted, or 3) The sulfur compounds are adsorbed on the catalyst and undergo reaction.

In experiments with each sulfur compound, the gaseous effluent of the reactor was analyzed for the presence of hydrogen sulfide. In all cases, H₂S was detected, and the concentration of H₂S present in the product gasses increased with TOS. Therefore, at least some of the sulfur species present in the feedstock are undergoing hydrodesulfurization reactions to form H₂S.

The outlet sulfur concentrations of the liquid products from the hydrogenation of tetralin over Pd/CBV30A* were analyzed. These results are shown in **Figure 3-31**.

Even after 11 hours TOS, the sulfur concentration of the products is below 10 ppm (except in the case of 4,6-DMDBT). Since the inlet sulfur concentration is 100 ppm, the majority of the sulfur is either converted to H₂S or retained on the catalyst. It is interesting that the outlet sulfur concentration plot resembles breakthrough curves for sulfur compounds on adsorbents for sulfur removal of liquid fuels, e.g. [3-15, 3-16, 3-17]. Indeed, 4,6-DMDBT is

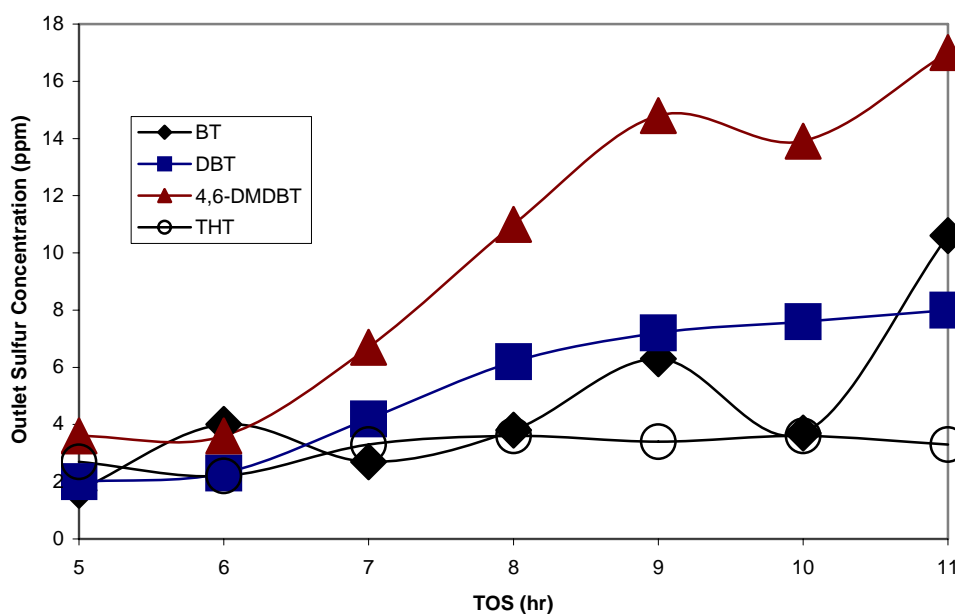


Figure 3-31 Outlet sulfur concentration vs TOS for the hydrogenation of tetralin over Pd/CBV30A* catalyst at 225 °C and 600 psig hydrogen pressure in the presence of 100 ppm sulfur as various sulfur compounds.

most difficult to remove from liquid fuels due to the steric hinderance of the methyl groups in the 4 and 6 positions, which shield the sulfur atom. It is not surprising, therefore, that as the reaction proceeds and perhaps the surface coverage of sulfur is very high, that the order of final outlet sulfur concentration proceeds in the order of steric hinderance to sulfur adsorbtion: 4,6-DMDBT > DBT ~ BT > THT. Since most of the THT is retained, this might also explain the fact that tetralin conversion is inhibited to a larger extent when THT is the sulfur compound in the feed.

The XPS analysis of spent catalyst samples from several experiments was unable to detect any sulfur and provide any information regarding the presence of sulfur on the spent catalyst or the nature of any sulfur on the catalyst. It is possible that the sulfur on the catalyst was removed by the flushing of the reactor with hexadecane after the experiments, or more likely, by the hexane wash prior to XPS analysis. Alternatively, it is also possible that the sulfur is present in a concentration too low to be detected by XPS.

Previously [3-18], it has been shown that Pd catalysts which have experienced deactivation due to sulfur will completely regain tetralin hydrogenation activity after the feedstock is switched to one which contains no sulfur. The reversibility of Pd hydrogenation catalysts was also demonstrated by [3-19] with *in-situ* removal of H₂S using ZnO in batch reactions. It is therefore likely that any sulfur species adsorbed on the catalyst is undergoing hydrodesulfurization reactions to form H₂S, rather than remaining on the Pd particle as a metal-sulfide.

3.2.2.6 Hydrogenation of tetralin over Pd on various types of zeolite

Based on the above screening study, more detailed experimental investigation was conducted on zeolite-supported Pd catalyst.

3.2.2.6.1 Effect of zeolite type

The results for conversion of tetralin over 2 wt% Pd on various types of zeolite (mordenite, Y and A zeolite) were compared and the trans- and cis- decalin composition were also shown in **Figure 3-32**. Y zeolite supported catalyst exhibited the greatest sulfur tolerance among the catalysts tested. As shown in **Figure 3-32(a)**, Pd/CBV30A and Pd/HA catalysts deactivated drastically and showed less than 30% tetralin conversion after 7 h. In case of Pd/HA, the catalytic activity disappeared at 5 h. On the other hand, the conversion of tetralin was maintained around 80% with the Pd/CBV720 catalyst after 7 h. As deactivation due to sulfur proceeds, the selectivity toward trans-decalin decreases and all trans- and cis- decalin compositions are converged on around 62% and 38%, respectively. It is expected that mordenite is more acidic (SiO₂/Al₂O₃:38) and would exhibit greater sulfur tolerance due to the imparting of electron deficiency on the Pd metal by the acid sites. However, Y zeolite shows higher tetralin conversion which can be

explained with the type of pore structure and large BET surface area from the data of previous report.

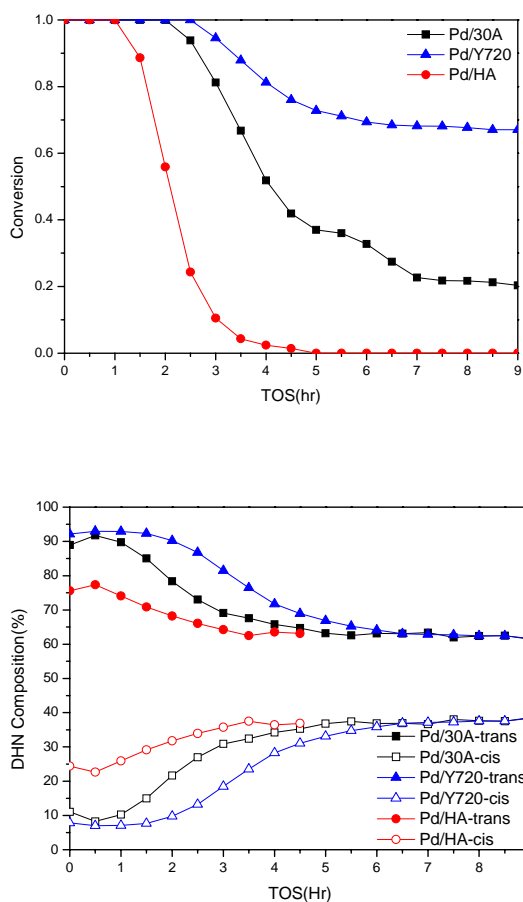


Figure 3-32. Conversion vs. TOS for the hydrogenation of (a) tetralin and (b) t-DHN, c-DHN selectivity for the hydrogenation of tetralin at 225 °C and 600 psig hydrogen pressure in the presence of 100 ppm sulfur as BT.

3.2.2.6.2 Effect of silica coating

Two Pd catalysts, Pd/CBV30A-SiO₂ and Pd/HA-SiO₂, were prepared by sol-gel method to examine the effects of internal pore on catalytic characteristics and performance. It was hypothesized that since the molecule size of TEOS (tetraethyl orthosilicate) is too large to enter the small pore of the zeolite, a silica wall might be formed not inside of zeolite pore but on its surface, allowing catalysts to perform inside pore opening but preventing outer surface reaction of zeolite.

The effect of silica coating was examined with two types of catalysts, Pd/CBV30A-SiO₂ and Pd/HA-SiO₂ and presented in **Figure 3-33** and **Figure 3-34**, respectively. For comparison, each result was plotted together with non silica coated catalysts. As seen in **Figure 3-33**, Pd/CBV30A-SiO₂ did not maintain tetralin conversion but drastically decreased. It can be explained that TEOS might coat outside of the large pore opening and reduce the pore size, but which was unclear assumption and needed to be examined by means of further characterization technique. This problem was dealt with temperature programmed reduction profile in next chapter.

From **Figure 3-34**, the results of tetralin conversion with Pd/HA and its coated catalysts were remarkably similar. As hypothesized, silica coating was successfully formed and the pore opening of zeolite remained allowing hydrogen molecules to enter but barring bulky organic sulfur compound like benzothiophene. However, inorganic sulfur, H₂S deactivated the novel metal inside pore and reduced tetralin conversion. There is a distinctive trend of trans-decalin selectivity over two silica coated catalysts. After the tetralin conversion drastically decreased, 100% of trans-decalin selectivity was shown. Since it was reported that SiO₂ wall does not have catalytic activity, it is an indication that coated wall might influence the surface structure of pore opening, but there is no supporting results. Therefore, the effect of silica coating remains to be determined.

Figure 3-35 shows the comparison between Pd/HA-SiO₂ and Pd/CBV30A-SiO₂. It is difficult to speculate why coated catalysts showed similar trend of conversion and decalin selectivity. When the catalytic activity decreases, the productivity of trans-decalin suddenly increased to 100%, and cis-decalin disappeared.

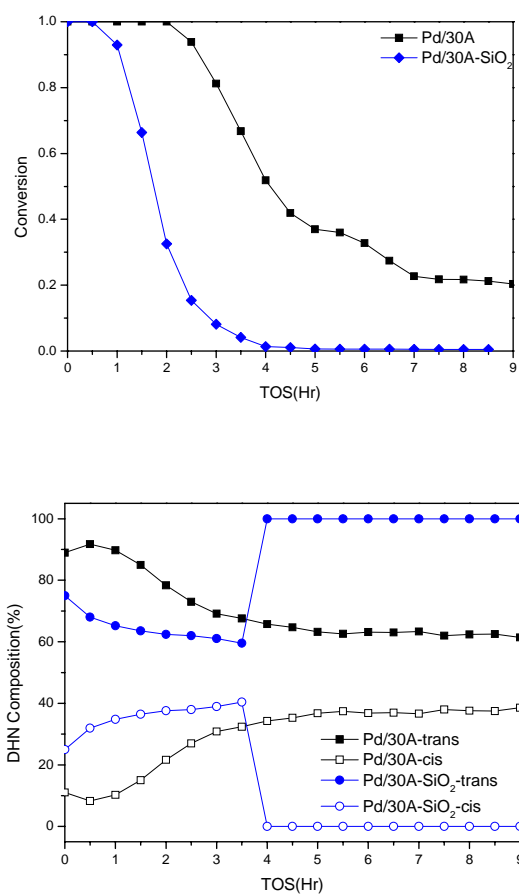


Figure 3-33. (a) Conversion vs. TOS for the hydrogenation of tetralin and (b) t-DHN, c-DHN selectivity for the hydrogenation of tetralin over Pd/CBV30A and Pd/CBV30A-SiO₂ at 225 °C and 600 psig hydrogen pressure in the presence of 100 ppm sulfur as BT.

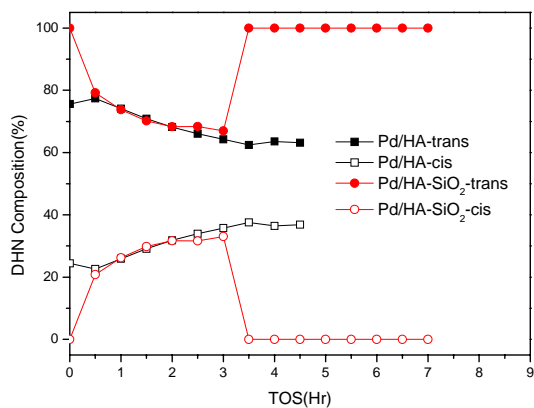
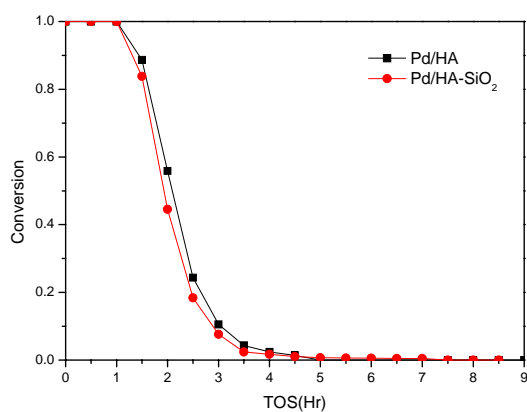


Figure 3-34. (a) Conversion vs. TOS for the hydrogenation of tetralin and (b) t-DHN, c-DHN selectivity for the hydrogenation of tetralin over Pd/HA and Pd/HA-SiO₂ at 225°C and 600 psig hydrogen pressure in the presence of 100 ppm S as BT.

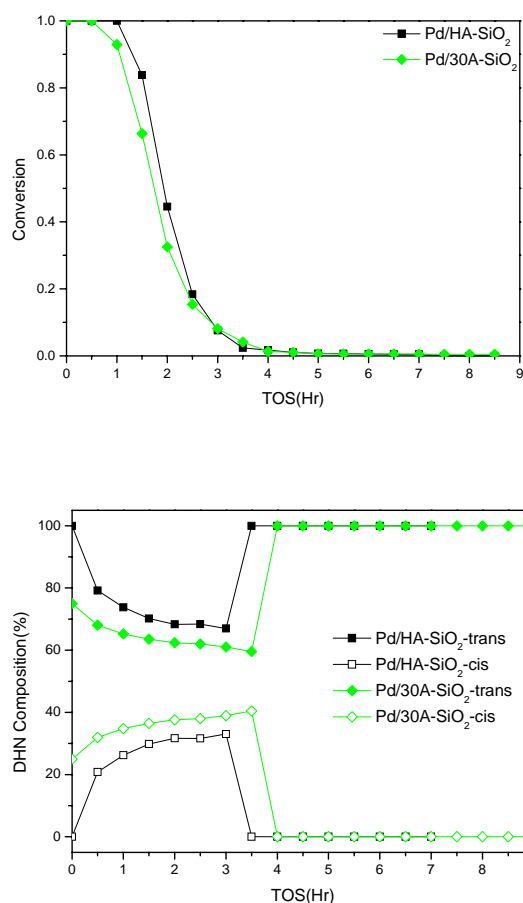


Figure 3-35. (a) Conversion vs. TOS for the hydrogenation of tetralin and (b) t-DHN, c-DHN selectivity for the hydrogenation of tetralin over Pd/CBV30A-SiO₂ and Pd/HA-SiO₂ at 225°C and 600 psig hydrogen pressure in the presence of 100 ppm sulfur as BT.

3.2.2.6.3 Effect of hybrid catalysts

Hybrid catalysts were prepared in order to verify the catalyst design concept proposed by Song [3-12,3-13]. The Pd/CBV720 catalyst has a uniform pore size distribution and is used as a reference to compare the catalytic activity. **Figure 3-36** and **Figure 3-37** show the reaction conversion and selectivity of decalin over Pd/HA, Pd/CBV720, Pd/HA-Pd/CBV720 hybrid catalyst and Pd/CBV720, silica coated Pd/HA catalyst, Pd/HA-SiO₂-Pd/CBV720 hybrid catalyst, respectively. Even though it was reported that Pd/HA-Pd/Y zeolite is more sulfur resistant, Pd/CBV720 has higher conversion than other catalysts in this research. However, these results are not evidence

to prove the design concept. As the mixing ratio is fixed to 1:1, the amount of Pd/CBV720 might not be sufficient to show significant results for the concept of hybrid catalyst. The effect of hybrid catalysts needs to be further examined by increasing the ratio of Pd/CBV catalyst.

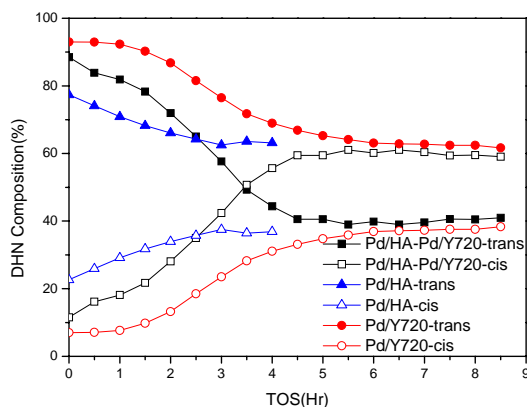
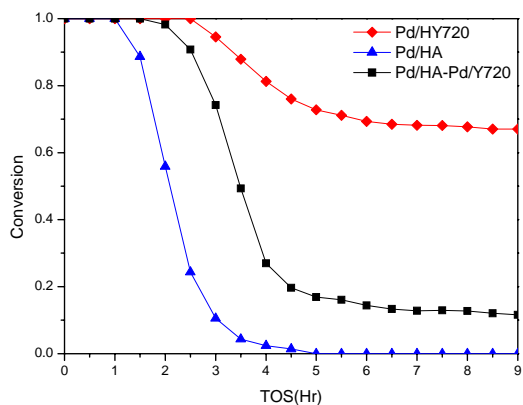


Figure 3-36. (a) Conversion vs. TOS for the hydrogenation of tetralin and (b) t-DHN, c-DHN selectivity for the hydrogenation of tetralin over Pd/CBV30A-SiO₂ and Pd/HA-SiO₂ at 225 °C and 600 psig hydrogen pressure in the presence of 100 ppm sulfur as BT.

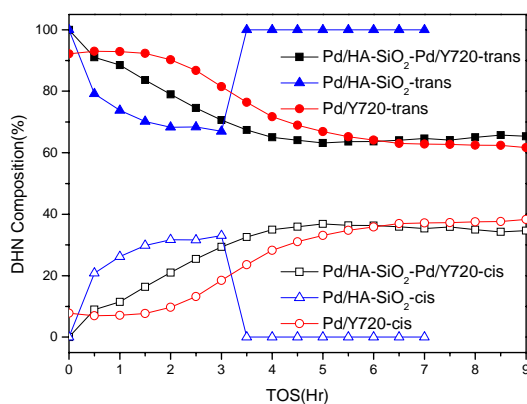
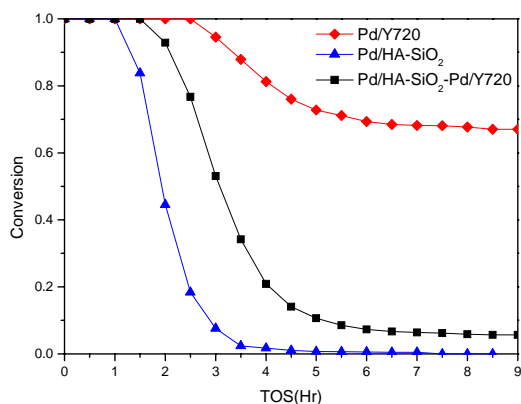


Figure 3-37. (a) Conversion vs. TOS for the hydrogenation of tetralin and (b) t-DHN, c-DHN selectivity for the hydrogenation of tetralin over Pd/CBV30A-SiO₂ and Pd/HA-SiO₂ at 225 °C and 600 psig hydrogen pressure in the presence of 100 ppm sulfur as BT.

Figure 3-38 shows the comparison between Pd/HA-SiO₂-Pd/CBV720 and Pd/HA-Pd/CBV720. Compared to other catalysts including Pd/HA-SiO₂-Pd/CBV720 hybrid catalyst which has high trans-decalin selectivity, Pd/HA-Pd/CBV720 hybrid catalyst shows high cis-decalin selectivity. As mentioned before, it should be also further studied for finding the optimal ratio of hybrid catalysts.

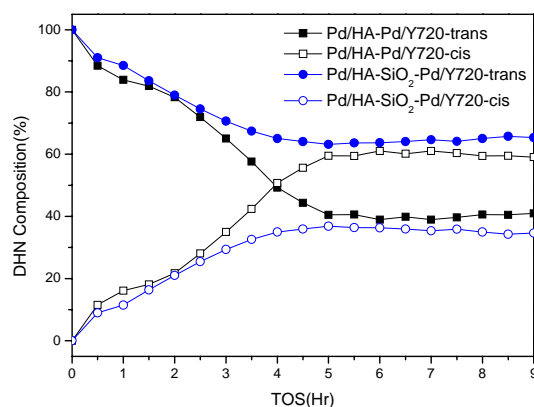
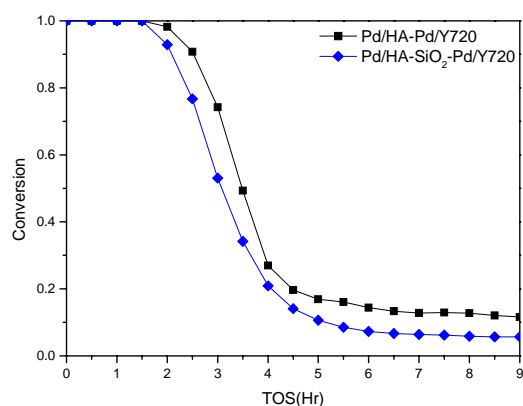


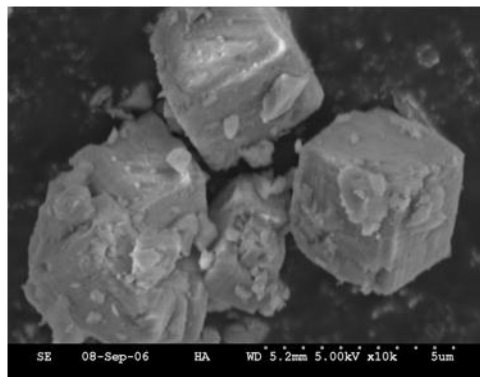
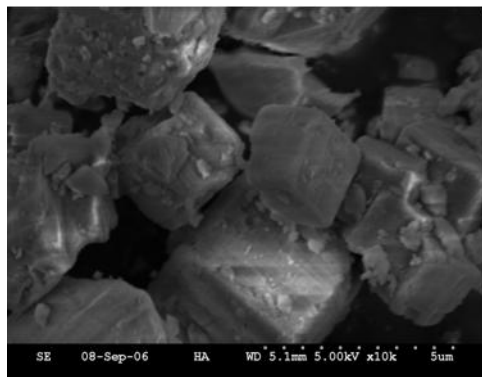
Figure 3-38. (a) Conversion vs. TOS for the hydrogenation of tetralin and (b) t-DHN, c-DHN selectivity for the hydrogenation of tetralin over Pd/CBV30A-SiO₂ and Pd/HA-SiO₂ at 225 °C and 600 psig hydrogen pressure in the presence of 100 ppm sulfur as BT.

3.2.2.7 Catalyst Characterization

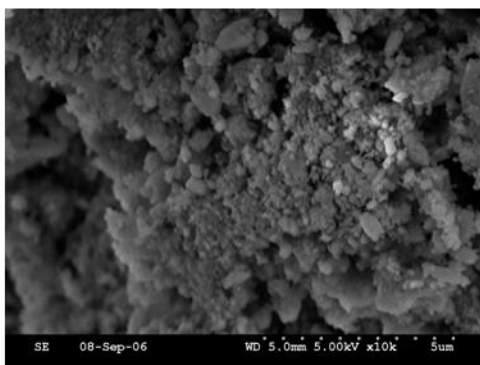
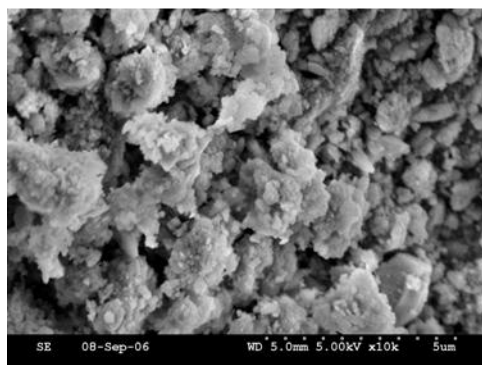
3.2.2.7.1 SEM image of catalysts prepared

Figure 3-39, Figure 3-40, and Figure 3-41 show SEM images of catalysts prepared, zeolite examined before Pd impregnation, Pd impregnated zeolite and silica coated zeolite, respectively. As shown in these figures, it is supposed that no significant morphological change was occurred during catalyst preparation and coating procedure. The shapes of HA zeolite particle and its derivatives looked like regular hexahedron with edge length between 30-35 μm . Y zeolite CBV720 was composed of small even particles, which sizes were 3-7 μm . The crystallites of Mordenite CBV30A and its derivatives were

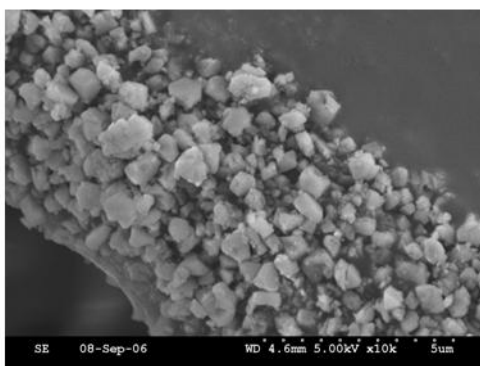
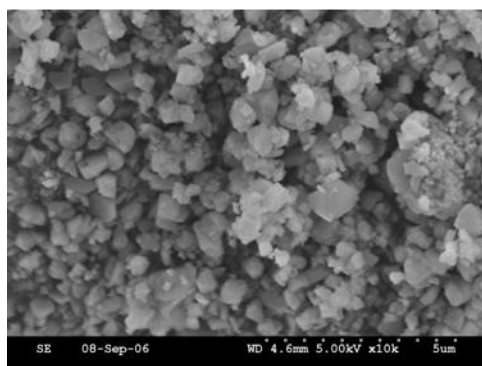
uneven and small particles with various sizes (1-8 μ m) aggregated and formed large particles. These small sized particles of Mordenite and Y zeolite which increase contact area might cause high catalytic activity. Compared to these zeolites, HA zeolite might have mass transfer (diffusion) limitation caused from its large particle size.



(a)HA (zeolite A)

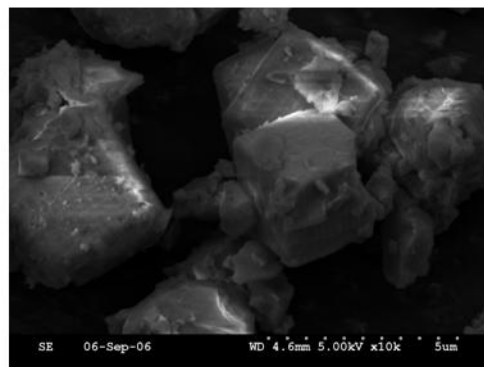
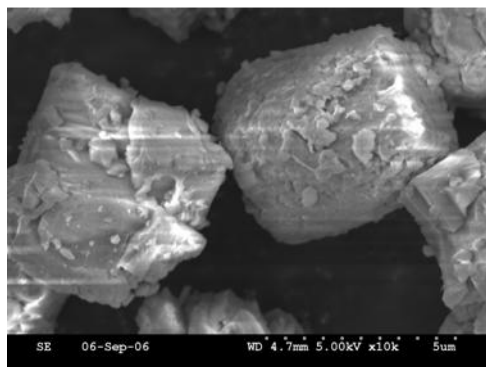


(b) CBV30A (Mordenite)

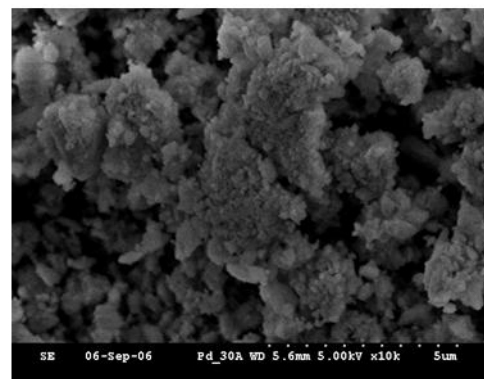
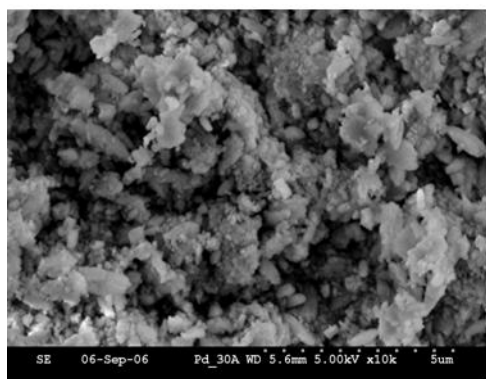


(c) CBV720 (zeolite Y)

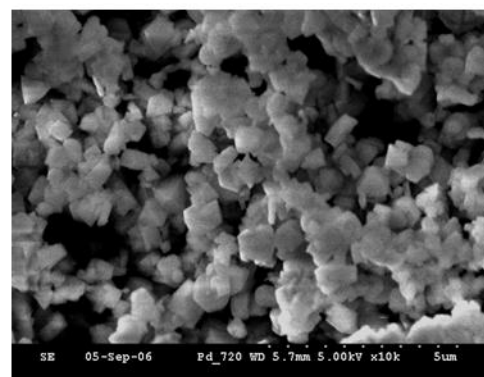
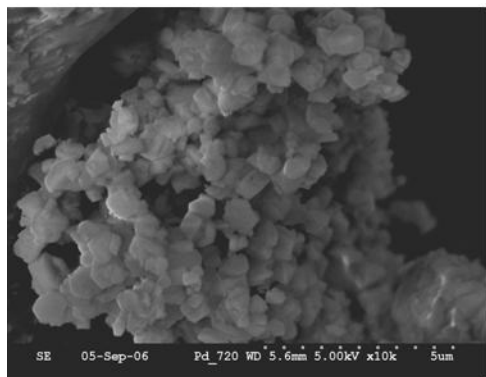
Figure 3-39. SEM image of zeolite used in this research.



(a) 2wt of Pd on HA (Pd/HA catalyst)

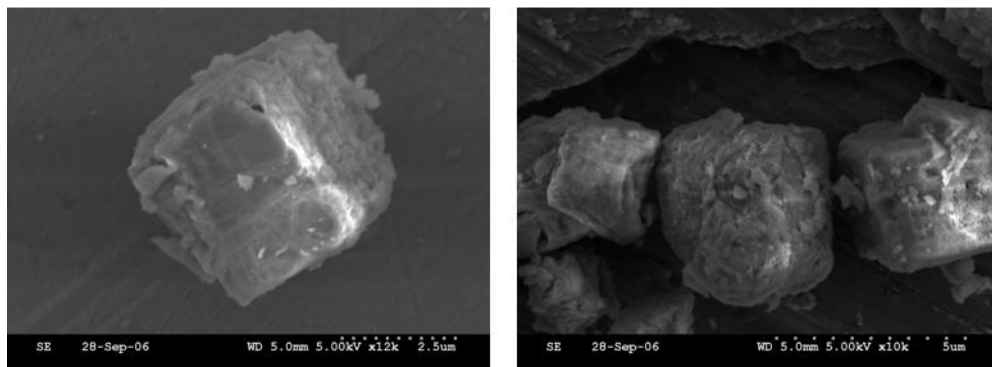


(b) 2wt% Pd on CBV30A (Pd/30A catalyst)

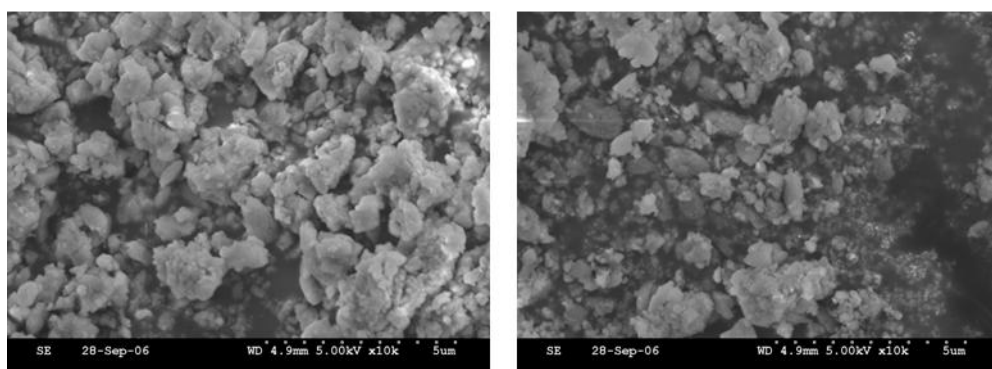


(c) 2wt% Pd on CBV720 (Pd/Y720 catalyst)

Figure 3-40. SEM image of catalysts prepared in this research.



(a)Pd/HA-SiO₂



(b)Pd/CBV30A-SiO₂

Figure 3- 41. SEM image of catalysts coated with TEOS in this research.

3.2.2.7.2 Temperature programmed reduction of catalysts

Figure 3-42 shows the temperature programmed reduction profiles of catalysts prepared in this study. The positive sharp peak of Pd/30A and Pd/HA at the low temperature (70°C) is caused by H₂ evolution from Pd hydride decomposition. TPR result of Pd/Y720 only shows one single negative peak. The negative broad peaks are contributed by H₂ consumption due to the reduction of Pd²⁺ ions to Pd⁰ atoms. **Figure 3-42** also shows that the negative peak of silica coated Pd/30A is shifted to right, which means it is hard to fully reduce to the Pd⁰ form at the reduction temperature in the flow reactor.

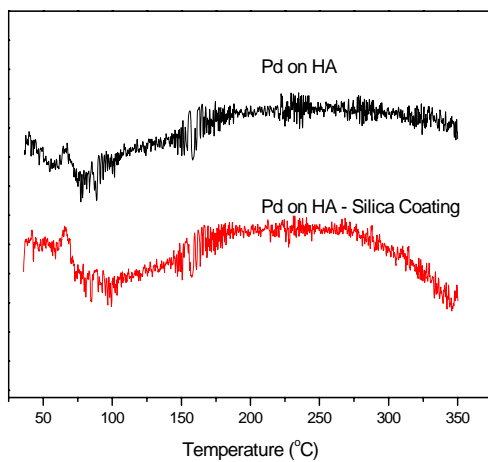
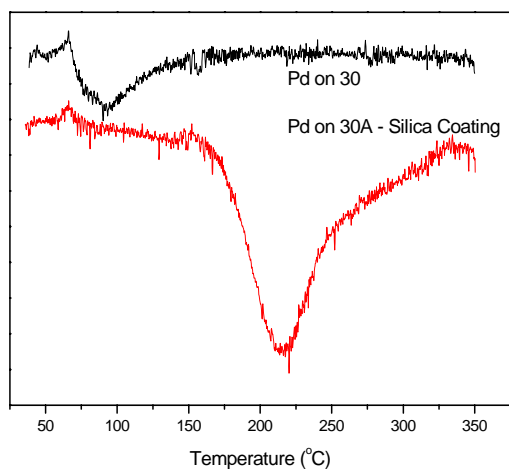
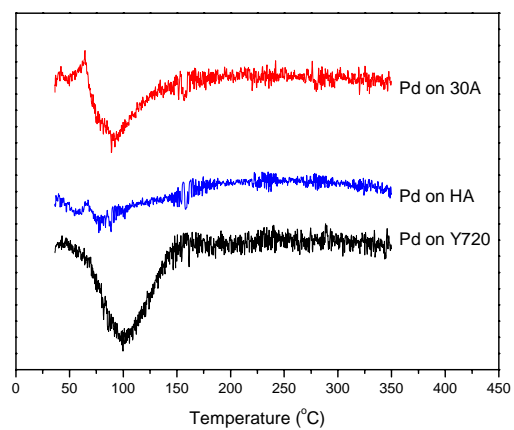


Figure 3-42. Temperature programmed reduction profile of catalysts prepared.

3.2.2.7.3 Temperature programmed desorption of catalysts

Figure 3-43 exhibits the result for TPD of hydrogen over various zeolite supported palladium catalysts. They are almost the same in terms of peak trend except that the desorption peak in Pd/CBV30A appears at higher temperature than the others. This implies that the hydrogen adsorbed in Pd/CBV30A is more difficult to desorb than other catalysts.

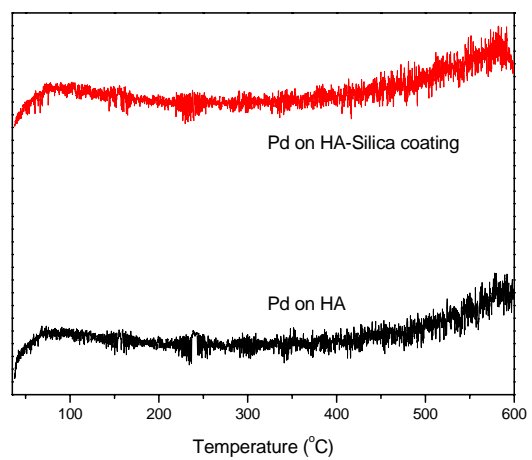
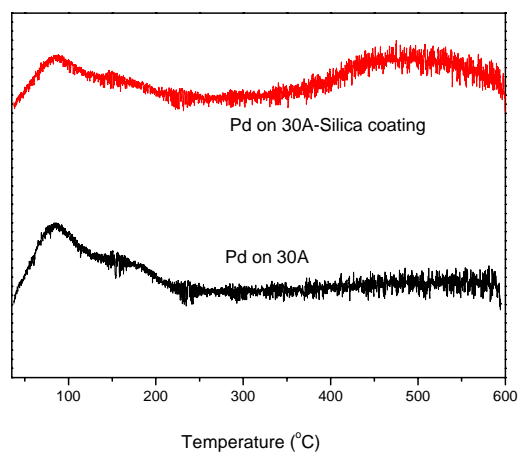
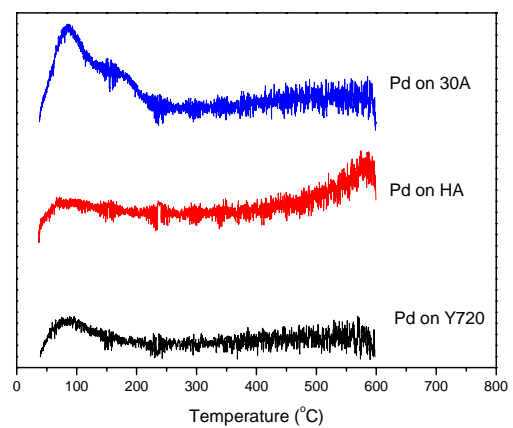


Figure 3-43. Temperature programmed desorption profile of catalysts prepared.

3.2.3 Summary

Based on experiments on various catalysts for the hydrogenation of tetralin at 225°C and 600 psig of hydrogen pressure, in the presence of sulfur, and also on the characterization of the catalysts prepared for this study, the following conclusions can be stated:

- 1) Y-zeolite supported catalysts exhibit higher sulfur tolerance than any of the other supports tested under the reaction conditions and methods of catalyst preparation employed in this study.
- 2) The effect of support acidity remains to be determined. A series of mordenite catalysts with different $\text{SiO}_2/\text{Al}_2\text{O}_3$ ratios (20, 38 and 90) were tested and no discernable differences were observed in activity for tetralin hydrogenation.
- 3) Catalysts prepared from the metal precursor $\text{Pd}(\text{NO}_3)_2 \cdot x\text{H}_2\text{O}$ have very poor metal dispersion and significantly underperform catalysts synthesized from PdCl_2 in the hydrogenation of tetralin.
- 4) The addition of Pt to Pd, in the mole ratio of 4 Pd:1 Pt, exhibits greater sulfur tolerance than Pd or Pt catalysts alone.
- 5) The *trans*-/ *cis*-decalin ratio was unaffected by the type of sulfur compound present in the feedstock, among BT, DBT, 4,6-DMDBT and THT.
- 6) The conversion of tetralin was largely unaffected by the type of sulfur compound among BT, DBT and 4,6-DMDBT, however THT has a greater poisoning effect than the others. This may be due to the high electron density of the sulfur atom in THT, which could potentially produce a greater sulfur-palladium interaction.
- 7) The Silica wall by TEOS was well coated onto the catalyst surface and didn't affect the catalytic conversion of Pd on HA catalyst. However, the coated Pd on CBV30A catalyst needs higher reduction temperature.
- 8) The selectivity of *trans*- and *cis*-Decalin on all catalysts prepared converged into 62% and 38%, respectively. However, Pd/HA-Pd/CBV720 hybrid catalyst showed high *cis*-decalin selectivity. On the other hand, 100% of *trans*-decalin selectivity was observed after catalysts deactivated at the test of silica coated catalysts, which remains to be further examined.

- 9) There was no discernable morphological change observed during the preparation of catalyst. The size of HA zeolite particle and the catalysts prepared from it is around 5 times bigger than Y zeolite CBV720 and Mordenite CBV30A, which might cause mass transfer (diffusion) limitation and low catalytic conversion.
- 10) The hybrid catalyst should be further studied by changing the ratio of catalysts.

3.3. Value-Added Chemicals from Naphthalene and Biphenyl

The shape-selective alkylation of naphthalene is carried out to develop 2,6-dialkylnaphthalene which is one of monomers for highly value-added chemicals for making advanced polymer materials such as liquid crystalline polymers (LCPs). LCPs have outstanding mechanical properties at high temperature, excellent chemical resistance and good weatherability. However, the key challenge lies in the selection of materials for shape-selective catalysis for the formation of 2,6-dialkylnaphthalene (2,6 DMN). This year, we developed new catalytic materials such as AlPOs and their modified acidic versions with different metals, ZSM-5 and Fe-ZSM-5. The new materials were developed by a classical hydrothermal synthesis and new and convenient dry-gel conversion method. The ZSM 5 was modified with iron using the impregnation method. The developed materials will be evaluated for alkylation of 2-methylnaphthalene and biphenyl.

3.3.1. Experimental

3.3.1.1. Modification of ZSM 5 using iron

Iron-modified ZSM-5 catalysts were prepared by modifying the HZSM-5 with iron (III) fluoride ($\text{FeF}_3 \cdot 3\text{H}_2\text{O}$) and ammonium hydrogen fluoride (NH_4HF_2) at a temperature of 92°C . The ZSM 5 was first converted to the HZSM 5 form from the ammoniated form by calcining in a muffle furnace at a temperature of 550°C for 6 hs. The temperature ramp is $1.52^\circ\text{C}/\text{min}$. The ZSM-5 (Zeolyst International) with $\text{SiO}_2/\text{Al}_2\text{O}_3$ ratio of 50 (CBV5524G) was used. Four samples were prepared by this method and used for catalytic testing of the methylation of 2-methylnaphthalene (2-MN). These catalysts were characterized by the temperature programmed desorption (NH_3 –

TPD). The carbon content in the spent catalyst samples was also analyzed using the Leco Carbon Analyzer.

3.3.1.2 Catalyst preparation

HZSM-5 (Supplied by Zeolyst International) with $\text{SiO}_2/\text{Al}_2\text{O}_3$ ratio of 50 (CBV5524G), 80 (CBV8014) and 280 (CBV28014) were used as catalyst. For methylation of 2-MN, iron-modified ZSM-5 was tested as catalyst. Iron-modified ZSM-5 catalysts were prepared by modifying the HZSM-5 with iron fluoride ($\text{FeF}_3 \cdot 3\text{H}_2\text{O}$) and ammonium hydrogen fluoride (NH_4HF_2) at elevated temperature. In this modification procedure, about 15 g of HZSM 5 (50) was mixed in 150 g of deionized water and was placed in a stirrer for an hour in an oil bath at 92°C . Slurry of $\text{FeF}_3 \cdot 3\text{H}_2\text{O}$ and NH_4HF_3 was made in 100 g of deionised water. This salt slurry was added to the ZSM 5 –water slurry mixture drop by drop in one hour. The solution was then stirred at total reflux for 24 h at 92°C . The resultant solution was then washed, filtered by a vacuum filter and then dried in an oven at 110°C for 12 h. This mixture was powdered and then calcined in a muffle furnace for 6 h at a temperature of 550°C at a temperature ramp of $1.52^\circ\text{C}/\text{min}$. The calcined catalysts were then palletized, crushed and sieved to a particle size of 18-35 U.S.A. Standard Testing Sieve Mesh (0.5–1.0 mm). **Table 3-21** shows the concentration of $\text{FeF}_3 \cdot 3\text{H}_2\text{O}$ and NH_4HF_3 in each sample.

For methylation of 4-MBP, the catalysts were prepared by modifying the HZSM-5 with 15% NH_4F . In a typical process, 5 g HZSM-5 was mixed with 50 ml 15% NH_4F solution with stirring overnight at room temperature. Then, the mixture was dried at 100°C and calcined at 450°C for 5 h.

Table 3-21. The notation of Fe/ZSM-5 catalysts and concentration of $\text{FeF}_3 \cdot 3\text{H}_2\text{O}$ and NH_4HF_2 .

S.No	Name of the Catalyst	Amount of $\text{FeF}_3 \cdot 3\text{H}_2\text{O}(\text{g})$	Amount of $\text{NH}_4\text{HF}_2(\text{g})$
1	Fe ZSM 5 1	0.129	0.102
2	Fe ZSM 5 2	0.258	0.204
3	Fe ZSM 5 3	0.555	0.417
4	Fe ZSM 5 4	0.813	0.615

3.3.1.3 Synthesis of magnesium containing AlPO-11 by dry-gel conversion method

Aluminophosphate molecular sieves are a new class of microporous crystalline materials. In 1982, Wilson et al. first reported the synthesis of microporous aluminophosphate (AlPOs) molecular sieves by using a hydrothermal synthesis method [3-15]. Microporous materials such as zeolites and aluminophosphate molecular sieves ($\text{AlPO}_4\text{-n}$) are widely used in catalysis and separations, and are being developed for applications in membranes, sensors, optics etc. [3-16]. AlPO-11 is one of the microporous aluminophosphate material developed by Flanigen et al. in 1982 [3-17]. It has a three dimensional structure with orthorhombic symmetry [3-18]. These materials are characterized by a 1-dimensional channel system parallel to c-axis with elliptical 10-membered ring with pore dimension of 0.39 x 0.63 nm [3-19]. The magnesium substituted MAPO-11, which has the acidic version of AEL structure might exhibit shape-selective catalysis of methylation of naphthalene.

Recently, new crystallization methods such as microwave technique [3-20] and dry-gel conversion technique [3-21,3-22] have been developed in zeolite synthesis in order to reduce the crystallization time and consumption of structure directing agent, respectively. The different aluminosilicate [3-22,3-23], boron-substituted aluminosilicate [3-24], titanium-substituted aluminosilicate [3-25,3-26] and aluminophosphate such as $\text{AlPO}_4\text{-5}$, $\text{AlPO}_4\text{-11}$, SAPO-5 [3-27], MAPO-36 [3-28] MAPO-5 [3-29,3-30] and series of alkaline earth metal-substituted MAPO-5 (M: Mg, Ca, Sr and Ba) [3-31] molecular sieves have been synthesized by DGC method. The method has the following advantages over the hydrothermal crystallization method: allows nearly complete conversion, reduces the consumption of structure-directing agents, and involves minimization of waste disposal and reduction of reactor volume [3-21]. The uniform crystals with smaller particle size and also improvement of catalytic activity can be obtained by this method [3-32,3-33]. Moreover, there are some examples in which dry-gel conditions are useful or convenient technique to form particular phase and properties [3-22,3-23,3-28,3-33].

In this study, we first report the synthesis of MAPO-11 by DGC method. The crystallization behavior and properties of MAPO-11 was investigated in different synthesis methods. Catalytic performance was studied for alkylation of naphthalene and biphenyl.

Synthesis

The syntheses of Mg-containing AEL were carried out by HTS and DGC methods. DGC method is divided into two interrelated techniques: steam assisted conversion (SAC) and vapor-phase transport (VPT). Here, we verified HTS, SAC and VPT methods for the synthesis of MAPO-11. A typical gel composition was as follows: $1.0\text{Al}_2\text{O}_3\text{-}0.10\text{MgO-}1.0\text{P}_2\text{O}_5\text{-}1.0\text{DPN-}40\text{H}_2\text{O}$.

In a typical procedure of HTS, aluminum isopropoxide (8.33 g, 20.0 mmol) was mixed in water (7.72 g). To this suspension, 85% phosphoric acid (4.62 g, 20.0 mmol) diluted in water (3.00 g) was added dropwise over a period of 0.5 h with constant magnetic stirring. To the resulting mixture, a solution of magnesium acetate (0.43 g, 2.0 mmol, with 3.0 g water) was added dropwise over a period of 0.5 h and the stirring was further continued for 0.5 h. Finally n-dipropylamine (n-DPN) (2.023 g, 20.0 mmol) was added dropwise to the mixture and stirred for another 1 h. The homogeneous hydrogel was charged into a 125-ml Teflon-lined autoclave and statically heated at 175 °C for 24 h.

In the SAC method, hydrogel was prepared in the same manner as that of HTS method. The hydrogel was dried at 80 °C in a heating mantle to remove water. When the gel became thick and viscous, it was homogenized manually using a Teflon-rod until it dried. The drying period varied ~ 1.0 h with the gel composition. A white solid formed material was then ground to a fine powder, and finally transferred in a small Teflon cup (25 mm x 25 mm i.d.). This cup was placed in a 125-ml Teflon-lined autoclave with the support of a Teflon holder. A small amount (0.3 g per 1.0 g of dry gel) of water was placed at the bottom of the autoclave in such a manner that the external bulk water never came into the direct contact with the dry-gel. The crystallization was carried out in steam in an oven with autogenous pressure.

In VPT method, the initial gel was prepared and dried without the addition of SDA, and the SDA was finally mixed with the external bulk water and taken as the source of water-organic vapor in the bottom of the autoclave.

After the crystallization, in all cases, the products were washed with distilled water, separated by filtration, and dried at 100°C overnight. The as-synthesized samples

were calcined in a muffle furnace in a flow of air with a rate of 80 ml/min as follows: the temperature was raised from room temperature to 550°C over 8 h, and kept at this temperature for another 6 h, and finally cooled to room temperature in ambient condition.

3.3.1.4. Catalyst characterization and evaluation

X-ray powder diffraction (XRD) was done on a Scintag 3100 diffractometer using nickel-filtered Cu K α radiation. Samples were mixed with ca. 10 wt% 325 mesh silicon internal standard for 2 θ correction. Jada Program was used to calculate the lattice constants.

Imaging of the samples was obtained through high resolution transmission electron microscopy (HR-TEM). For this purpose, a Philips 420 electron microscope was used and operated at 120 kV. Samples were positioned on a carbon microgrid, supported on copper, by placing a few droplets of a suspension of ground sample in ethanol. The grid was dried at ambient conditions.

Composition of the catalysts was analyzed by a Leeman Labs PS3000UV ICP (inductively coupled plasma emission spectrophotometer). The relative acidity of these catalysts was characterized using NH₃-TPD.

Catalytic testing was carried out in a down-flow fixed bed reactor system. In a typical run, 0.3 g of catalyst (10-18 mesh) loaded in reactor tube (Pyrex, I.D.: ½ inch) was placed in the furnace center. The catalyst was activated at 450°C for 1 h under the inert N₂ gas flow (20 ml/min). Then the temperature was cooled down to the reaction temperature. Reactant dissolved in mesitylene solvent (2-MN:methanol:mesitylene=1:5:5 mol ratio) was fed into a reactor through a HPLC pump at the flow rate of 1.98 ml/min together with 20 ml/min of carrier N₂ gas flow. The reaction product was collected at 1 h interval. Both the reactants and products were analyzed by HP 5890 gas chromatography (GC) with a β -Dex 120 capillary column (60m, 0.25 mm I.D. column with 0.25 micrometer coating film thickness).

Approximately 0.05 g of the spent catalyst was used in determining the extent of the carbon deposition on the sample during the reaction. Temperature-programmed oxidation (TPO) consists of exposing the sample containing carbonaceous deposits to a flowing O₂ gas /O₂-inert gas mixture stream in a furnace while increasing the temperature

of the furnace from a minimum of 100°C to a maximum of 900°C. A constant heating rate of 30°C/min was used in the TPO experiments with a holding period of 3 min at 900°C. A constant O₂ flow rate of 750 ml/min was used in all the analyses. Carbon in the sample, placed in a quartz boat, is oxidized by reacting with O₂. A downstream CuO catalyst bed ensures that any CO produced during the reaction is converted to CO₂. A calibrated IR cell measures the amount of total CO₂ produced by the oxidation of the deposit as a function of furnace temperature. Thus, a profile of CO₂ evolution (also designated as a TPO profile) normalized by the geometric area of the sample substrate gives the amount of carbon in the deposit (in µg/cm²) as well as information on the *oxidation reactivity* of the carbonaceous deposit.

3.3.2. Results and discussion

3.3.2.1 Methylation of 2-MN with methanol

Characterization of Fe-MFI catalysts

HZSM-5 and iron modified HZSM-5 catalysts, which were tested in the previous year, were characterized by XRD and their unit cell dimensions were calculated. The results are listed in **Table 3-22**. These results revealed that the a axis expanded after the HZSM-5 zeolite was modified with iron. The a axis is the zigzag channel of the HZSM-5, which will have significant effect on the shape selective properties of the catalysts. However, the degree of a axis expansion is different for different modification methods. With the same Fe loading, the wet chemistry iron modification method (M-Fe-06) resulted the biggest expansion on a axis. The a axis did not change for Fe-MFI catalyst prepared by physical mixing method. The more the Fe loadings, the bigger the a axis expansion. Interestingly, the a axis dimension also increased when the SiO₂/Al₂O₃ ratio of HZSM-5 increases, which indicate that Fe may substitute the Al position in the ZSM-5.

Element analysis results of the HZSM-5 and iron modified HZSM-5 are listed in **Table 3-23**. After the wet chemistry iron modification, Al₂O₃ content decreased and Fe₂O₃ content increased (M-Fe-06), while the Al₂O₃ content did not change for ion-exchange (M-Fe-16) or physical mixture method (M-Fe-11). These results indicated that iron was isomorphous substituted the Al position in the framework of HZSM-5 after wet

chemistry iron modification. Therefore, the a axis expansion after the wet chemistry iron modification can also be ascribed to the iron isomorphous substitution of the Al position in the framework of HZSM-5. For Fe-MFI catalyst prepared by physical mixing method, since iron did not enter the framework of HZSM-5, the a axis did not expand after modification.

Two samples, i.e., Fe isomorphous substituted HZSM-5 (M-Fe-06) and Fe ion-exchanged HZSM-5 (M-Fe-16), which have similar Fe contents, were selected for high-resolution transmission electron micrographs measurement. The photographs are shown in **Figure 3-44**. Although the two samples have the similar Fe content, their TEM micrographs are essentially different. For Fe isomorphous substituted HZSM-5, no significant presence of large Fe-containing clusters was observed in most area, although there is Fe-containing cluster in some small area. On the contrary, Fe ion-exchanged HZSM-5 shows big Fe-containing particles on the external surface of the HZSM-5 crystals. These observations indicate that ion dispersion was better in M-Fe-06 than in M-Fe-16. The better iron dispersion of M-Fe-06 than M-Fe-16 may also be one the reasons for the better catalytic performance (in terms of activity, selectivity and stability) of M-Fe-06 than that of M-Fe-16.

The HZSM-5 and Fe-MFI catalysts were further characterized by DMNs selective adsorption experiment. The results are listed in **Table 3-24**. The HZSM-5 only adsorbs 2,7-, 2,3-, and 1,4-DMNs. For the HZSM-5 modified with iron, the Fe-MFI can adsorb all the DMN isomers, which may attribute to the expansion of axis of HZSM-5. The change of the adsorption properties of HZSM-5 after modification may correlate with the change of catalytic properties of HZSM-5 after modification for the selective methylation of 2-MN to 2,6-DMN. However, detailed characterization of the catalysts should be carried out before make a conclusion.

Table 3-22 Lattice constants determined from XRD for HZSM-5 or iron modified HZSM-5

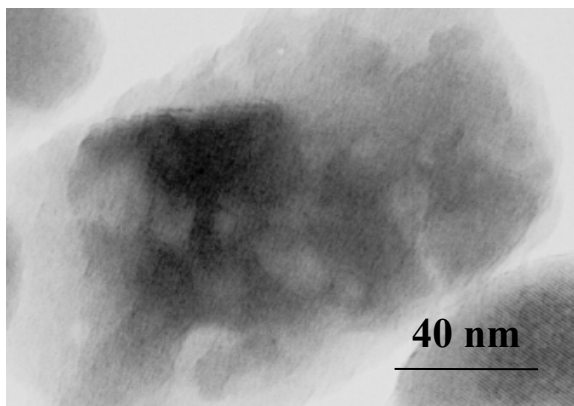
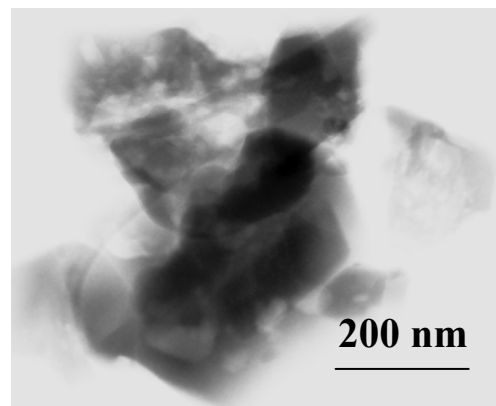
Sample Name	Description	a	b	c
CBV5524G	HZSM-5 SiO ₂ /Al ₂ O ₃ =50	20.0065	19.9362	13.3781
M-Fe-05	Fe/Al=0.16	19.9992	19.9367	13.3631
M-Fe-06	Fe/Al=0.5	20.0587	19.9368	13.3888
M-Fe-07	Fe/Al=1.35	20.0818	19.9521	13.3775
M-Fe-08	Fe/Al=1.75	20.0973	19.938	13.3798
M-Fe-09	Fe/Al=7.0	20.1162	19.9331	13.38
M-Fe-10	Fe/Al=25	20.0711	19.9113	13.3673
M-Fe-11	Fe/Al=0.5, Physical Mix	19.9996	19.965	13.3699
M-Fe-12	Fe/Al=0.5, Fe(NO ₃) ₃	20.0777	19.9587	13.3906
M-Fe-13	Fe/Al=0.5, FeCl ₃	20.0499	19.9816	13.3828
M-Fe-14	Fe/Al=0.5, NH ₄ F	20.085	20.0806	13.393
M-Fe-15	Fe/Al=0.5, FeF ₃ only	20.0421	19.9455	13.3678
M-Fe-16	Ion-exchange	20.0395	19.9491	13.3867
CBV8014	HZSM-5 SiO ₂ /Al ₂ O ₃ =80	20.034	20.0577	13.3769
CBV28014	HZSM-5 SiO ₂ /Al ₂ O ₃ =280	20.0701	20.0284	13.3554
M-Fe-02	CBV28014, Fe/Al=0.5	20.0708	19.9608	13.3683
M-Fe-03	CBV8014, Fe/Al=0.5	20.0609	19.9444	13.3618
M-Fe-04	CBV8014, Fe/Al=5	20.0733	20.0158	13.3502
M-D-Al-01	CBV5524G, NH ₄ HF ₂ only	20.0411	19.9638	13.3734

Table 3-23 Element analysis of HZSM-5 and iron modified HZSM-5.

Sample Name	Al ₂ O ₃ (%)	Fe ₂ O ₃ (%)	Na ₂ O (%)	SiO ₂ (%)	LOI (900C)	SiO ₂ /Al ₂ O ₃ (Mol)	Fe ₂ O ₃ /Al ₂ O ₃ (Mol)
CBV5524G	3.06	0.06	<.05	92	4.23	51.11	0.01
M-D-Al-01	2.44	0.08	<.05	92	4.10	64.10	0.02
M-Fe-05	2.56	0.59	<.05	92	3.80	61.09	0.15
M-Fe-06	2.23	1.01	<.05	91	4.11	69.37	0.29
M-Fe-07	1.81	2.31	<.05	93	2.56	87.35	0.82
M-Fe-08	1.73	3.35	<.05	92	3.35	90.40	1.24
M-Fe-09	1.22	9.41	<.05	86	2.31	119.84	4.93
M-Fe-10	0.90	20.8	<.05	74	1.89	139.78	14.76
M-Fe-11	2.99	1.35	<.05	88	6.21	50.03	0.29
M-Fe-14	2.25	1.21	<.05	91	5.05	68.76	0.34
M-Fe-15	2.41	1.15	<.05	90	4.92	63.49	0.30
M-Fe-16	2.76	1.15	<.05	87	5.52	53.59	0.27

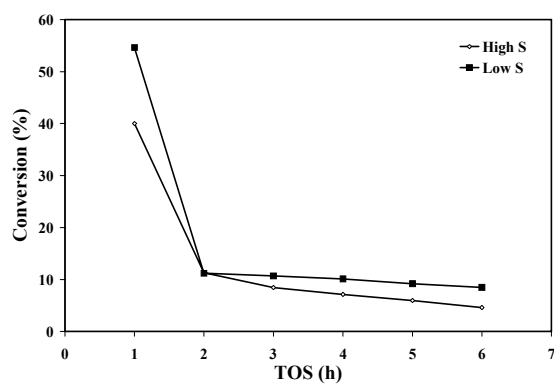
Table 3-24 Selective adsorption of DMNs by HZSM-5 and Fe-MFI catalysts.

Adsorption Capacity (mg/g)	2,6-DMN	2,7-DMN	1,7-DMN	1,3-DMN	1,6-DMN	(2,3+1,4)-DMN	1,5-DMN	1,2-DMN	1,8-DMN
Feed DMN (wt%)	0.968	0.956	1.148	1.12	1.859	2.016	0.318	0.096	0.019
HZSM-5	0	1.87	0	0	0	2.32	0	0	0
M-Fe-06	4.78	9.89	4.64	5.11	9.4	18.97	1.46	0.43	0.05

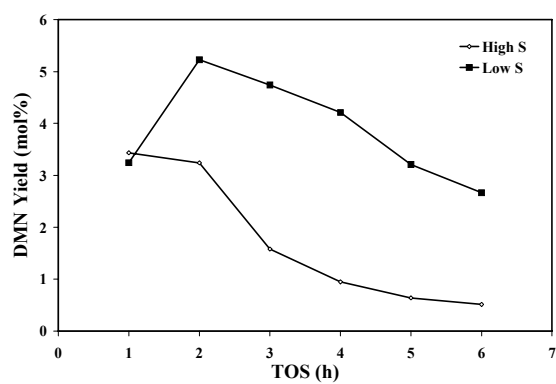
**(a)****(b)****Figure 3-44 TEM micrographs of (a) M-Fe-06, and (b) M-Fe-16**

Effect of sulfur compounds on the methylation of 2-MN

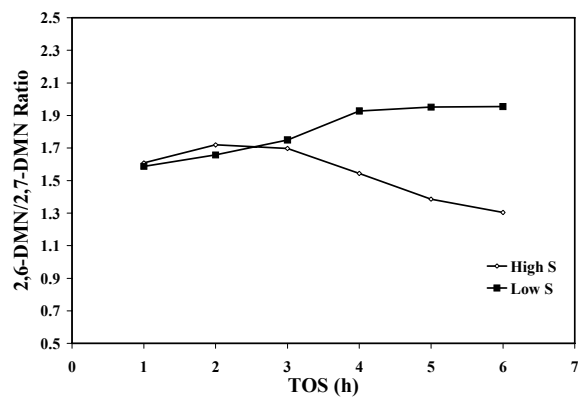
During this period, the feedstock of 2-MN was changed. With this change, it was found that the catalytic properties for the same catalyst were significantly different with a different 2-MN feedstock. Therefore, the sulfur and nitrogen concentration of 2-MN were analyzed. While the nitrogen compounds concentration were the same, the sulfur compound concentration was significantly different for 2-MN from different company. The 2-MN from Aldrich, which was used in previous year, has a sulfur concentration about 5000 ppm, and 2-MN from Acros Organics has a sulfur concentration of 29 ppm. The significant difference on the reaction results between the two 2-MN feedstocks may be ascribed to the different sulfur concentrations. **Figure 3-45** compares the reaction results of Fe-ZSM-5 catalyst for 2-MN with different sulfur concentrations. The conversion of 2-MN with low sulfur content is higher than that with high sulfur content. Also, the deactivation of the catalyst was slow when low sulfur 2-MN was used. The DMN yield, the 2,6-DMN/2,7-DMN ratio, and the 2,6-DMN/DMNs ratio were also improved when low sulfur content 2-MN was used as feedstock. While the catalyst was poisoned by the sulfur compound and the 2,6-DMN/2,7-DMN ratio and 2,6-DMN/DMNs ratio decreased with reaction time for 2-MN with high sulfur concentration, the 2,6-DMN/2,7-DMN ratio and 2,6-DMN/DMNs ratio increased with reaction time for 2-MN with low sulfur compound. The improvement on the catalytic performance for HZSM-5 (CBV8014, $\text{SiO}_2/\text{Al}_2\text{O}_3=80$) was more significant than Fe-MFI catalyst. **Figure 3-46** compares the reaction results of HZSM-5 catalyst for 2-MN with different sulfur concentrations. When the sulfur concentration is low, the DMN yield was 10.6 mol%, which is twice that for Fe-MFI catalyst. However, even with the low sulfur content, 2-MN (29 ppm sulfur), the sulfur still poisoned the catalyst. Fortunately, a PSU-SARS process, which can removed the sulfur compound to 0.1 ppm, has been developed in our lab. In the future, we will combine the PSU-SARS process and methylation of 2-MN reaction together. The sulfur compound in 2-MN will removed through PSU-SARS process before 2-MN methylation reaction. With such low sulfur content, the catalyst is expected to be stable over long period reaction time.



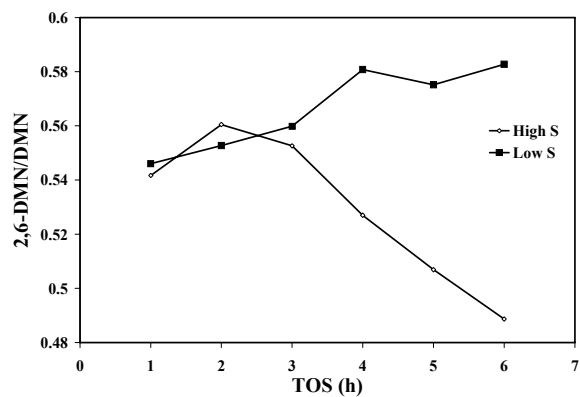
(a)



(b)



(c)



(d)

Figure 3-45 Comparison of the methylation of 2-MN with methanol over Fe-MFI (M-Fe-06) catalyst for 2-MN with different sulfur contents. Reaction conditions: temperature: 300 °C; Feed (2-MN:methanol: mesitylene=1:5:5 mol ratio): 1.98 ml/hr; Catalyst: 0.3 gram; Gas flow: 20 ml/min.

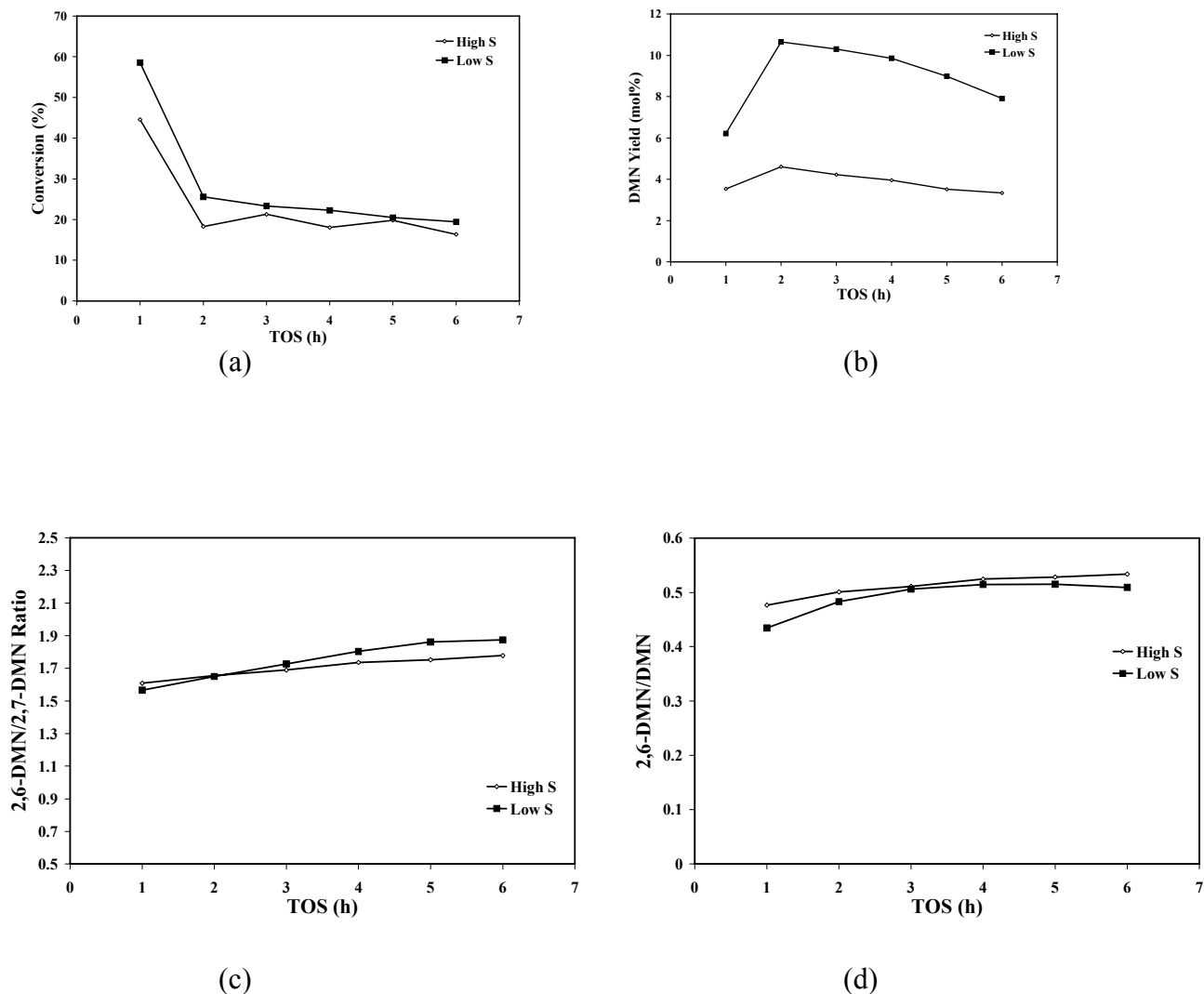


Figure 3-46 Comparison of the methylation of 2-MN with methanol over HZSM-5 (CBV8014) catalyst for 2-MN with different sulfur contents. Reaction conditions: temperature: 300 °C; Feed (2-MN:methanol: mesitylene=1:5:5 mol ratio): 1.98 ml/hr; Catalyst: 0.3 gram; Gas flow: 20 ml/min.

3.3.2.2 Methylation of 4-MBP with methanol

Effect of reaction temperature

Effect of reaction temperature on the methylation of 4-MBP with methanol over NH_4F modified HZSM-5 (CBV8014) was investigated and the results are shown in **Figure 3-47**. The conversion of 4-MBP increased with temperature first, then leveled when the temperature was above 380 °C. The yield of dimethylbiphenyls (DMBPs), 4,4'-DMBP/DMBPs ratio and 4,4'-DMBP/3,4'-DMBP ratio showed a maximum at

temperature between 360-380 °C. Therefore, 380 °C was selected as the reaction temperature for the methylation of 4-MBP in this study.

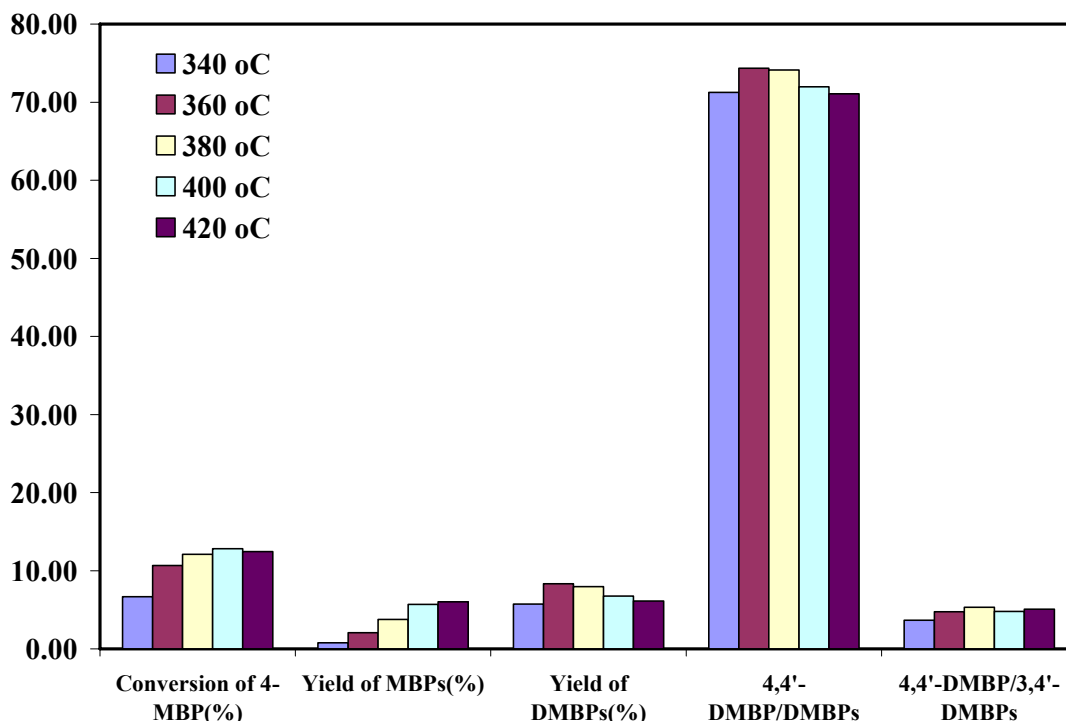


Figure 3-47 Effect of reaction temperature on the methylation of 2-MBP with methanol over NH_4F modified HZSM-5 (CBV8014). Reaction conditions: Feed (2-MBP:methanol: mesitylene=1:5:5 mol ratio): 1.98 ml/hr; Catalyst: 0.3 gram; Gas flow: 20 ml/min.

Effect of NH_4F modification

Methylation of 4-MBP with methanol over HZSM-5 (CBV8014) with and without NH_4F modification was carried out and the results are shown in **Figure 3-48**. After NH_4F modification, the activity of the catalyst decreased and the conversion of 4-MBP sharply decreased from 60.3% to 12.08%. The decrease in the 4-MBP conversion was mainly caused by the inhibition of 4-MBP isomerization. The yield of DMBPs only slightly decreased from 8.89% to 7.96%. The percentage of desired product 4,4'-DMBP in the DMBPs significantly increased after HZSM-5 modified with NH_4F . Also, the formation of main competitor 3,4'-DMBP was inhibited. The 4,4'-DMBP/3,4'-DMBP ratio increased from 0.29 for HZSM-5 to 5.32 for NH_4F modified HZSM-5. The high 4,4'-DMBP/3,4'-DMBP ratio will significantly reduce the separation cost.

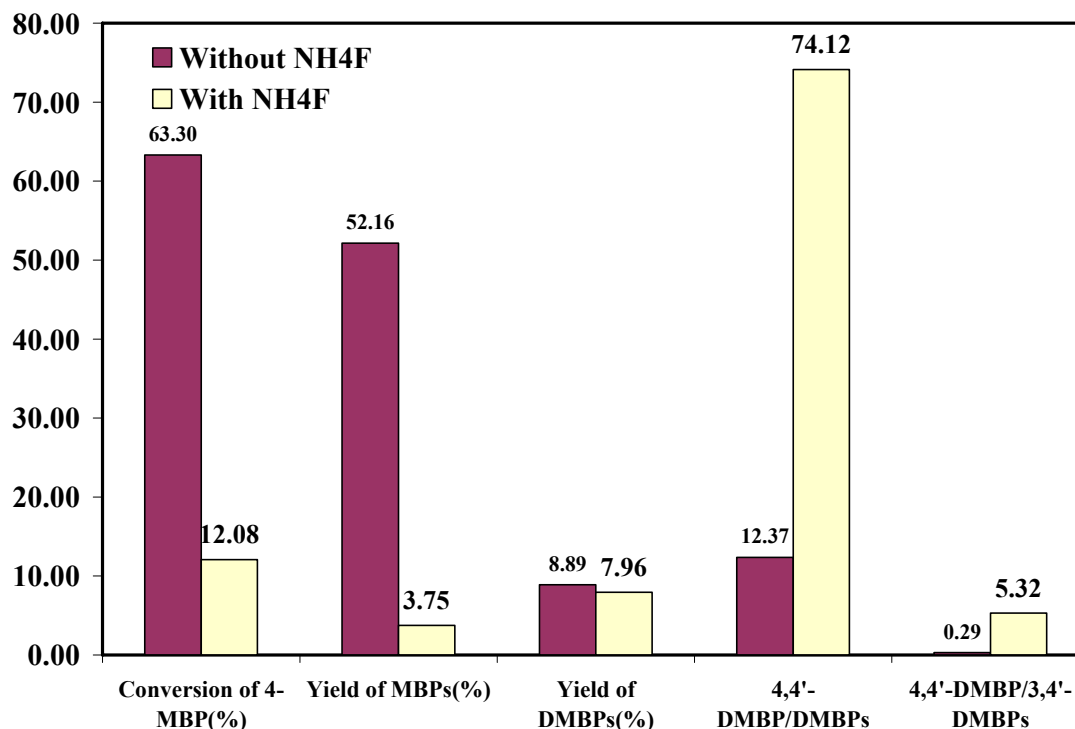


Figure 3-48 Comparison of the methylation of 4-MBP with methanol over HZSM-5 (CBV8014) catalysts with and without NH₄F modification. Reaction conditions: Temperature: 380 °C; Feed (4-MBP:methanol:mesitylene=1:5:5 mol ratio): 1.98 ml/hr; Catalyst: 0.3 gram; Gas flow: 20 ml/min.

Effect of SiO₂/Al₂O₃ ratio of HZSM-5

HZSM-5 with different SiO₂/Al₂O₃ ratio were modified by NH₄F and their catalytic performance on the methylation of 4-MBP with methanol are shown in **Figure 3-49**. The catalytic performance of HZSM-5 with SiO₂/Al₂O₃ ratio of 50 and 80 was not significantly different. However, for HZSM-5 with SiO₂/Al₂O₃ ratio of 280, the catalytic performance was different from that for HZSM-5 with SiO₂/Al₂O₃ ratio of 50 or 80. While the conversion of 4-MBP and yield of DMBPs decreased, the 4,4'-DMBP/DMBPs and 4,4'-DMBP/3,4'-DMBP ratios all increased.

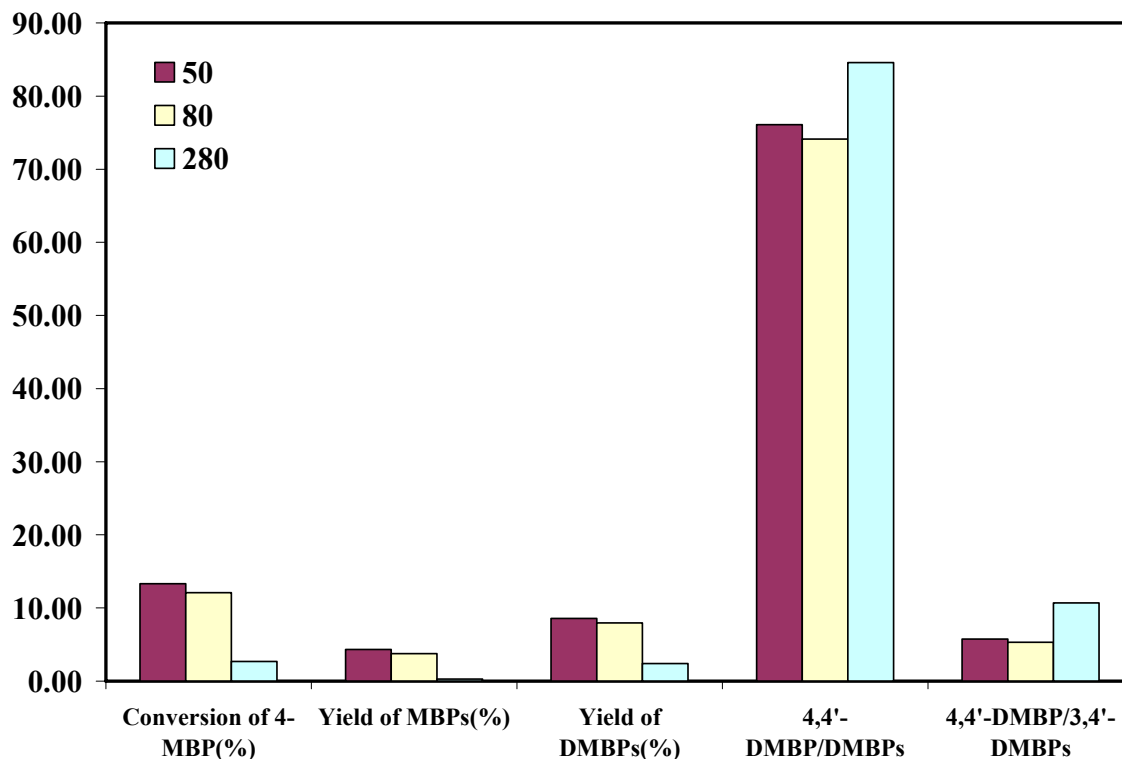


Figure 3-49 Effect of $\text{SiO}_2/\text{Al}_2\text{O}_3$ ratio of NH_4F modified HZSM-5 on the methylation of 4-MBP with methanol. Reaction conditions: temperature: 380 °C; Feed (2-MBP:methanol: mesitylene=1:5:5 mol ratio): 1.98 ml/hr; Catalyst: 0.3 gram; Gas flow: 20 ml/min.

Effect of Iron modification of HZSM-5

Iron modified HZSM-5 (CBV5524G) has shown superior catalytic performance on the selective methylation of 2-MN with methanol to 2,6-DMN. Therefore, M-Fe-06 was tested for the methylation of 4-MBP with methanol and the results are shown in **Figure 3-50**. After iron modification, the conversion of 4-MBP decreased, and the yield of DMBPs, the 4,4'-DMBP/DMBPs and 4,4'-DMBP/3,4'-DMBP ratio all increased. However, although the yield of DMBPs for M-Fe-06 is higher than that for NH_4F modified HZSM-5, 4,4'-DMBP/DMBPs and 4,4'-DMBP/3,4'-DMBP ratios are all much lower than those for NH_4F modified HZSM-5.

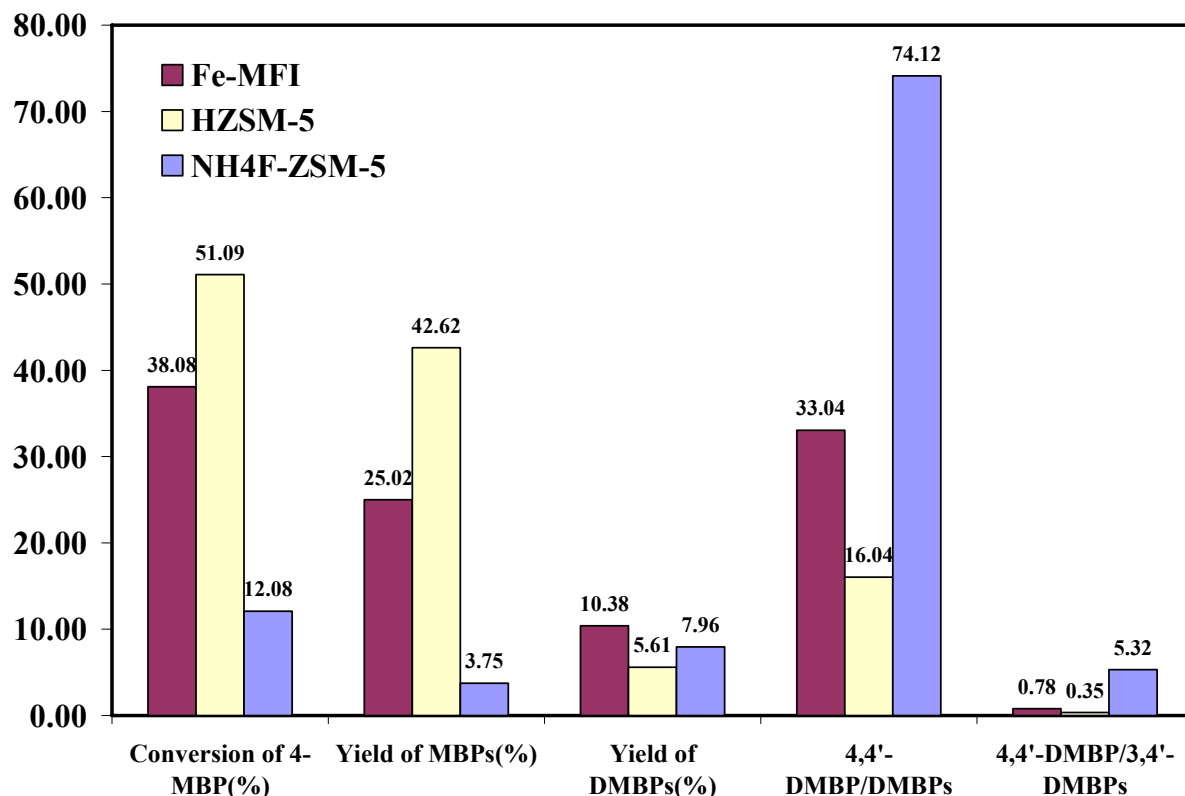


Figure 3-50 Methylation of 4-MBP with methanol over HZSM-5 (CBV5524G) and iron modified HZSM-5 (M-Fe-06) catalysts. Reaction conditions: temperature: 380 °C; Feed (2-MBP:methanol: mesitylene=1:5:5 mol ratio): 1.98 ml/hr; Catalyst: 0.3 gram; Gas flow: 20 ml/min.

3.3.2.3 Synthesis and evaluation of MAPO-11 for 2-MN with methanol

The synthesis conditions and the products obtained by HTS, VPT and SAC methods with different gel compositions are listed in **Table 3-25**. **Figure 3-51, 3-52 and 3-53** show XRD patterns of as-synthesized molecular sieves obtained by HTS, VPT and SAC methods, respectively. The crystallization was carried out at 175°C for 24 h for all samples.

From XRD results, it has been observed that pure AEL phase was only obtained by SAC method under the present conditions. In HTS method, product was contaminated with trace amount of impurities at highest concentration. This means, beyond the ratio of $\text{Mg}/\text{Al}_2=0.05$, magnesium may not enter into the framework of $\text{AlPO}_4\text{-11}$. However, in VPT method, product was contaminated in the lower Mg/Al_2 ratio (0.0~0.05), even

synthesis was done by identical conditions. At further increase of Mg/Al₂ ratio from 0.05 to 1.0, the pure AEL phase was formed. This result indicating that pH of the synthesis media might be affected for formation of pure AEL phase. In VPT method, amine solution was diluted with magnesium acetate salt at higher concentration, which may helpful for formation of pure AEL phase. The maximum concentration of magnesium can be loaded by SAC method. The high quality Mg-containing AEL can be synthesized by SAC method. Based on these results, SAC method has been chosen for further study for optimization of synthesis parameters.

Table 3-25. Synthesis of AlPO₄-11 (AEL) and Mg-containing AFL.

Entry No.	Method ^a	Gel composition					Temp. (° C)	Time (h)	Product
		Al ₂ O ₃	P ₂ O ₅	MgO	DPA	H ₂ O			
1	HTS	1	1	-	1.0	40	175	24	AEL
2	HTS	1	1	0.025	1.0	40	175	24	AEL
3	HTS	1	1	0.05	1.0	40	175	24	AEL
4	HTS	1	1	0.10	1.0	40	175	24	AEL+ trace imp.
5	SAC	1	1	-	1.0	40	175	24	AEL
6	SAC	1	1	0.025	1.0	40	175	24	AEL
7	SAC	1	1	0.05	1.0	40	175	24	AEL
8	SAC	1	1	0.10	1.0	40	175	24	AEL
9	VPT	1	1	-	1.0	40	175	24	AEL+ trace imp.
10	VPT	1	1	0.025	1.0	40	175	24	AEL+ trace imp.
11	VPT	1	1	0.05	1.0	40	175	24	AEL+ trace imp.
12	VPT	1	1	0.10	1.0	40	175	24	AEL
13	VPT	1	1	0.05	0.5	40	175	24	AEL+imp.
14	VPT	1	1	0.05	1.5	40	175	24	AEL+imp.
15	SAC	1	1	0.05	0.5	40	175	24	AEL
16	SAC	1	1	0.05	1.5	40	175	24	AEL
17	SAC	1	1	0.05	1.0	40	175	6	AEL+amorphous
18	SAC	1	1	0.05	1.0	40	175	12	AEL
19	SAC	1	1	0.05	1.0	40	175	48	AEL

^aHTS= hydrothermal synthesis, SAC=steam-assisted conversion, VPT= vapor-phase transport;

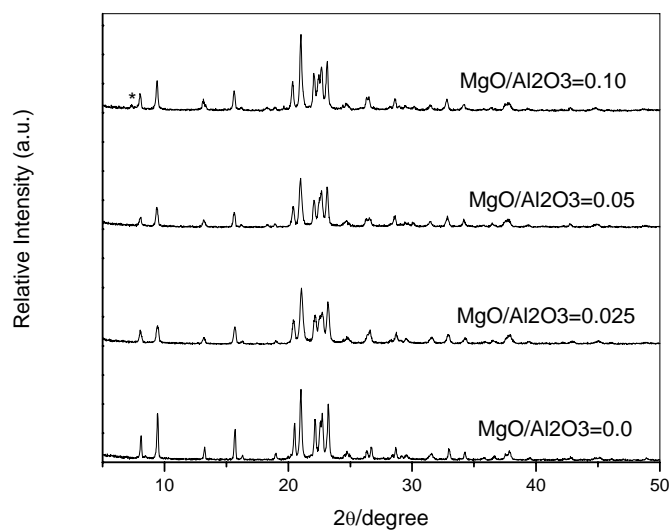


Figure 3-51. XRD pattern of MAPO-11 obtained by HTS (Table 3-25; Entry 1-4); *-impurities.

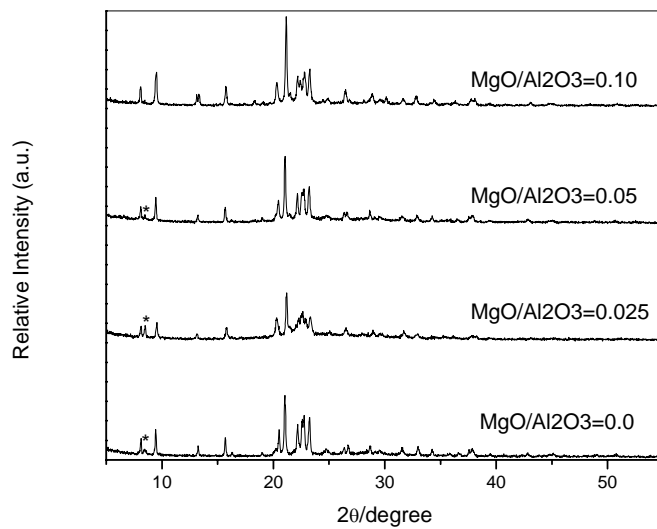


Figure 3-52. XRD pattern of MAPO-11 obtained by VPT (Table 3-25; Entry 9-13); *-impurities.

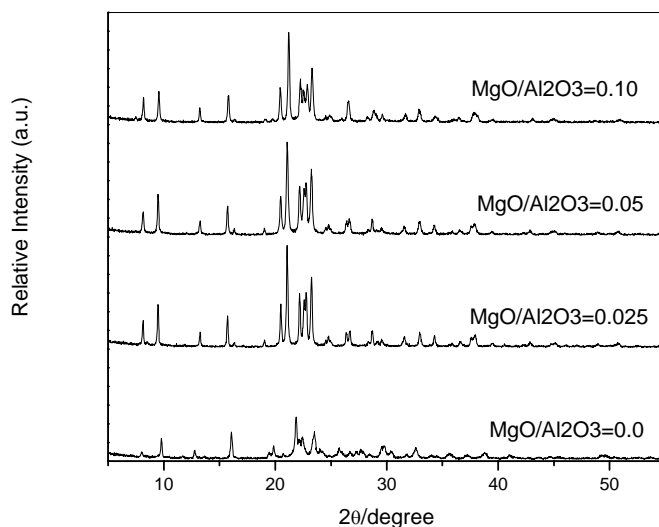


Figure 3-53. XRD pattern of MAPO-11 obtained by SAC (Table 3-25; Entry 5-8).

Effect of SDA amount on the synthesis of MAPO-11 by SAC method ($\text{Mg}/\text{Al}_2=0.05$) has been studied. Pure MAPO-11 was crystallized in all the ratio of SDA/ Al_2 from 0.5~2.0. The phase and crystallinity of the sample does not affect with the variation of structure-directing agent by SAC method. One possibility is most of the SDA was evaporated along with water during drying the gel. As a result, with increasing the SDA concentration, phase and crystallinity does not affect. These results indicating that minimum amount of SDA are sufficient for phase formation of AEL by SAC method.

Effect of crystallization time was varied from 6~48 h. It has been observed that within 6 h AEL phase appeared and further increase of time 6 to 12 h enhanced the crystallinity and complete AEL phase was observed. The highest intensity was observed during 12-24 h. Prolong crystallization time 48 h, did not change the phase and crystallinity. It should be noted that the yield of MAPO-11 by SAC is higher than that of HTS method. The range of yield is 77.0~87.0% obtained by SAC method whereas 63.0%

obtained by HTS method.

Figure 3-54 shows the NH_3 -TPD patterns of MAPO-11 with the variation of Mg/Al_2 ratio. AlPO_4 -11 showed an ammonia desorption peak only at around 200°C (so called *l*-peak), which is due to strongly physisorbed ammonia mainly on the external surface. However, Mg-containing samples show both *l*-peak and higher temperature desorption peak 300 – 500°C (so called *h*-peak). The higher temperature desorption peak due to acidity of MAPO-11 by isomorphous substitution of Al^{3+} with Mg^{2+} . The acid amount corresponded to *h*-peak proportionally increased with increase the Mg/Al_2 ratio. However, at highest $\text{Mg}/\text{Al}_2=0.1$ did not give a proportional increase of the acid amount. This difference suggested that some of the Mg did not act as acid sites and they are on the external surface. This result correlated with the XRD pattern at highest ratio.

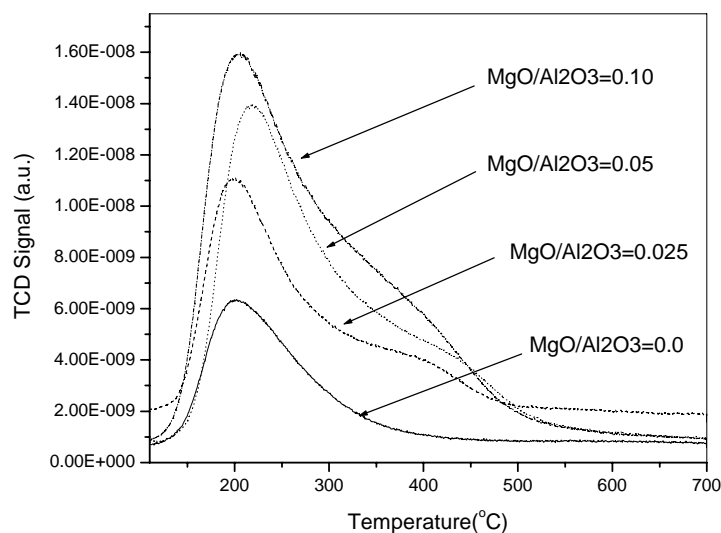


Figure 3-54 NH_3 -TPD profiles of AlPO_4 -11 and MAPO-11 with different Mg/Al_2 ratio obtained by HTS method (Table 3-25; Entry-1-4).

Figure 3-55 shows the catalytic performance of MAPO-11 for methylation of naphthalene in different Mg/Al_2 ratios. It has been observed that highest catalytic activity was shown at $\text{Mg}/\text{Al}_2=0.05$ at 250°C . This result indicated that catalytic activity did not directly relate with acid concentration.

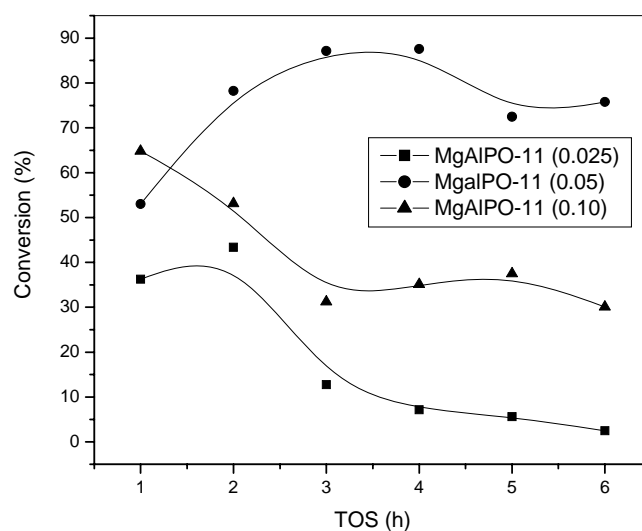


Figure 3-55. Catalytic activity of 2-MN with methanol over MAPO-11 (Condition: Temperature=250°C; WHSV=6.0 h⁻¹).

3.3.2.4. Additional Synthesis and Characterization of Fe-ZSM-5 for 2-MN methylation

Figure 3-56 shows the NH₃-TPD patterns of FeZSM 5 with the variation of Fe/Al ratio. The profile shows two peaks. The peaks around the 200 to 250°C correspond to the weak acid sites which are due to strongly physisorbed ammonia mainly on the external surface. Those at a higher temperature around 450°C correspond to the strong acid sites. The higher temperature desorption peak might be due to acidity of Fe ZSM 5 by isomorphous substitution of Al³⁺ with Fe³⁺. Acid amount corresponding to the strong acid sites in the sample FeZSM 5 2 is the highest and decreases for the other three samples. **Figures 3-56 and 3-57** show TPD profiles of fresh synthesized FeZSM 5 samples and spent ZSM 5 samples.

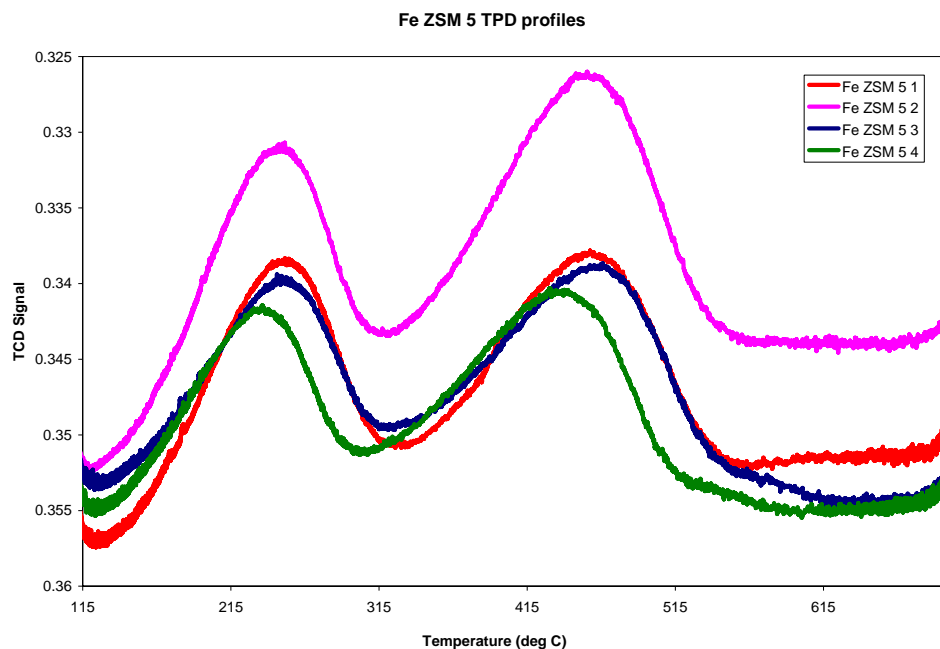


Figure 3-56. Comparison of NH_3 – TPD profiles of Fe ZSM 5 1, Fe ZSM 5 2 , Fe ZSM 5 3 and Fe ZSM 5 4 fresh catalysts.

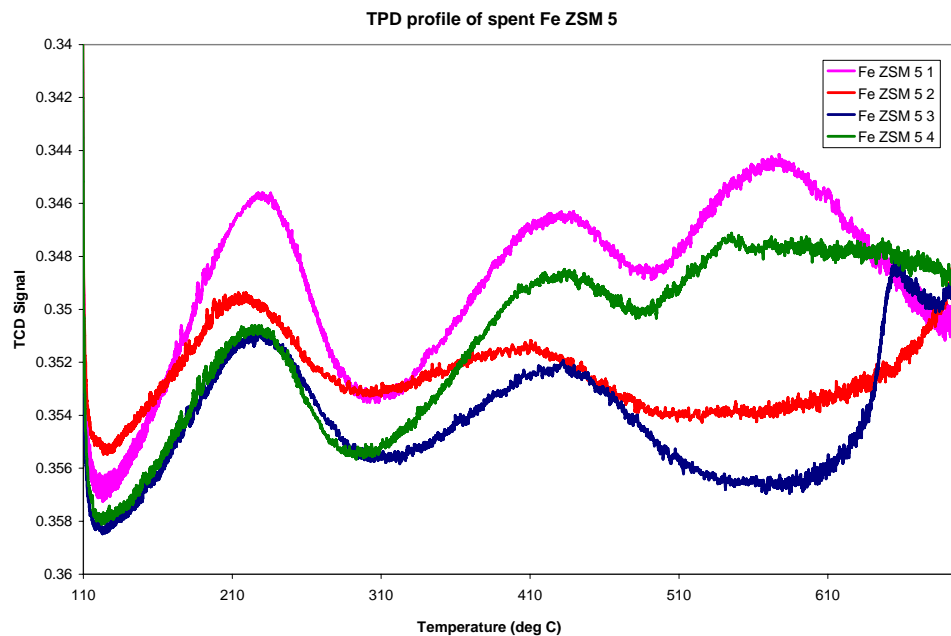


Figure 3-57. Fe ZSM 5 1, Fe ZSM 5 2, Fe ZSM 5 3, Fe ZSM 5 4 Spent catalysts after reaction at 300° C.

In **Figure 3-57**, we can see that in addition to the weak acid and strong acid peaks, we can see a third peak at about 550°C. This peak may be a Lewis acid peak formed due to the dehydroxylation of the catalyst at higher temperatures.

Figure 3-58 shows the catalytic testing of the four samples, where the catalytic conversion of the four catalysts are compared. From **Figure 3-58**, we can observe that the highest conversion over all was obtained for the Fe ZSM 5 2 (Fe/Al = $\frac{1}{4}$).

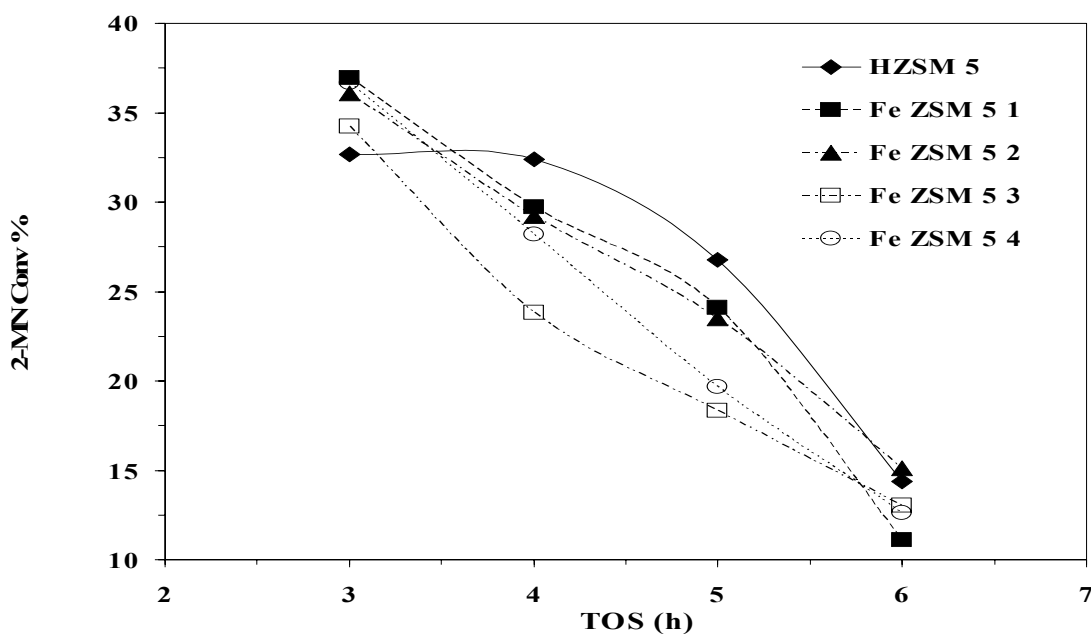


Figure 3-58. Comparison of the Conversion of 2-MN over Fe ZSM 5 catalysts. Reaction conditions: temperature: 300 °C; Feed (2-MN:methanol: mesitylene=1:5:5 mol ratio): 1.98 ml/hr; Catalyst: 0.3 gram; Gas flow: 20 ml/min.

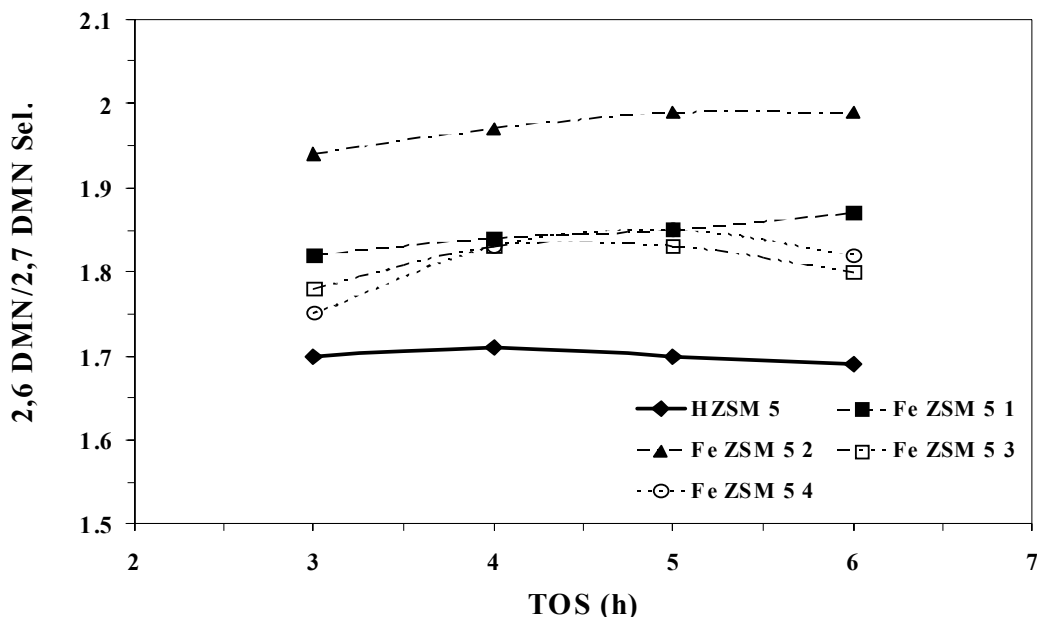


Figure 3-59. Comparison of the selectivity of 2,6DMN/2,7 DMN ZSM 5 catalysts. Reaction conditions: temperature: 300 °C; Feed (2-MN:methanol: mesitylene=1:5:5 mol ratio); 1.98 ml/hr; Catalyst: 0.3 gram; Gas flow: 20 ml/min.

From **Figure 3-59**, we can observe that the 2,6/2,7 selectivity was the highest in the Fe ZSM 5 1 (Fe/Al = 1/8) followed by Fe ZSM 5 2 (Fe/Al = 1/4) and then by the Fe ZSM 5 3(Fe/Al = 1/2) and Fe ZSM 5 4 (Fe/ Al = 3/4).

Figure 5-60 shows the TPO profiles of the catalyst samples. TPO profiles may give multiple CO₂ evolution peaks in the range of 100°– 900°. The peaks around 200°C to 300°C are due to the liquid absorption on the sample. It is considered that CO₂ evolution at relatively low temperatures (typically below 500°C) represents high oxidation reactivity. High oxidation reactivity can, in turn, be related to relatively high H content of the deposits and/or a low degree of structural order present in the carbonaceous solids. In contrast, the CO₂ peaks evolving at higher temperatures (typically above 500°C) suggest the presence of a higher degree of structural order in the carbonaceous

solids based on their lower oxidation reactivity. In this case, most of the peaks are near about in the range of 500°C. So the carbonaceous deposits might be some of the LHPC's.

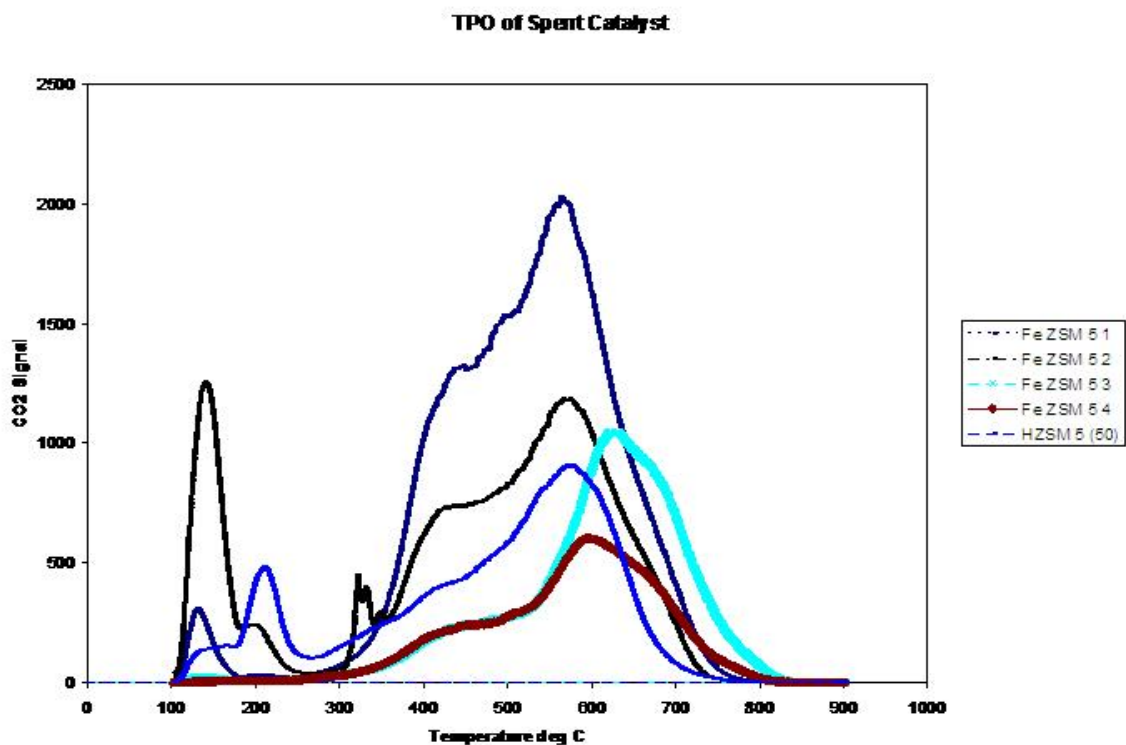


Figure 3- 60. TPO profiles of Spent Fe ZSM 5.

3.3.3. Summary

1. After wet chemistry iron modification, iron isomorphously substitutes the Al in HZSM-5. XRD characterization shows that the a axis of MFI zeolite expand after iron modification. As a results, the iron modified HZSM-5 catalyst can adsorb all the DMN isomers. Before modification, HZSM-5 only adsorb 2,7-DMN and 2,3-DMN or 1,5-DMN.
2. Sulfur compounds can significantly poison effect methylation of 2-MN with methanol over HZSM-5 types zeolite catalyst. When a high sulfur content 2-MN

is used as reactant, 2-MN conversion, DMN yield and 2,6-DMN/2,7-DMN ratio all decreases.

3. The methylation of 4-MBP with methanol over HZSM-5 zeolite prefers to be at 360-380 °C. NH_4F modification significantly improves the catalytic performance of HZSM-5. High DMBPs yield, 4,4'-DMBP/DMBPs ration and 4,4'-DMBP/3,4'-DMBP selectivity are obtained. The best $\text{SiO}_2/\text{Al}_2\text{O}_3$ ratio of HZSM-5 for methylation of 4-MBP is 50 or 80. When the $\text{SiO}_2/\text{Al}_2\text{O}_3$ ratio is too high, the conversion of 4-MBP and yield of DMBPs decreased, although the 4,4'-DMBP/DMBPs and 4,4'-DMBP/3,4'-DMBP ratio all increased. Iron modification dose not show superior catalytic performance for methylation of 4-MBP as that for methylation of 2-MN.
4. MAPO-11 was successfully synthesized by a dry-gel conversion method. SAC method was the best for synthesis of pure MAPO-11 among the studied. The pure MAPO-11 can be synthesized within 12 h by SAC method. NH_3 -TPD results clearly indicated Mg was incorporated into the neutral framework of AIPO-11.
5. MAPO-11 is highly active for methylation of naphthalene at moderate temperature.
6. Fe ZSM 5 2 catalyst turns out to be the best in terms of catalytic activity amongst the four samples. Most of the reaction takes place in the strong acid sites. Due to the porous nature of the solid, there is more absorption of the liquid in the catalyst. The formation of coke decreases from Fe ZSM 5 1 to Fe ZSM 5 4.

Task 4. Evaluation of Coal-Based Fuel Products

(Prepared by Bruce G. Miller, Sharon Falcone Miller, and Ronald T. Wincek)

4.1 Introduction

The objective of Task 4 was to evaluate the effect of introducing coal into an existing petroleum refinery on the fuel oil product, specifically trace element emissions. Activities performed to accomplish this objective included analyzing two petroleum-based commercial heavy fuel oils (*i.e.*, No. 6 fuel oils) as baseline fuels and three co-processed fuel oils, characterizing the atomization performance of a No. 6 fuel oil, measuring the combustion performance and emissions of the five fuels, specifically major, minor, and trace elements when fired in a watertube boiler designed for natural gas/fuel oil, and determining the boiler performance when firing the five fuels. The No. 6 fuel oils used to generate the baseline data were obtained from east coast suppliers and the co-processed fuel oils were produced by PARC. Additional activities included upgrading the data acquisition system on the research boiler to evaluate boiler performance through mass and energy balances (*i.e.*, boiler efficiencies). Details of the various activities are contained in the following sections.

Task 4 was performed over a three-year period. During Year 1, a co-processed fuel oil was not available; therefore, activities focused on establishing the analytical and testing protocols using a baseline No. 6 fuel oil in preparation for co-processed fuel oil testing to be performed in the subsequent years. Three combustion/emissions tests were performed in Year 1 using the baseline No. 6 fuel oil. In Year 2, a co-processed fuel oil and a No. 6 fuel oil were tested while two processed fuel oils and two No. 6 fuel oil tests were performed in Year 3. Two different No. 6 fuel oils were used during the test program, one during Years 1 and 2, and a second fuel oil during Year 3. **Table 4-1** summarizes the tests performed and details of the results are provided in the following sections. Total metals emissions, mercury speciation, and boiler performance were measured during all the tests. In addition, metal partitioning between the gas and solid phases was determined and a comparison of measured emissions with predicted emissions using EPA AP-42 emissions factors was made during the Year 1 No. 6 fuel oil testing.

Table 4-1 Summary of Combustion Tests Performed during Task 4

Program Year	Date of Combustion Testing	Fuel Tested (Identification Number/Name)
Year 1	06/16/04	Baseline No. 6 Fuel Oil ^a
	07/07/04	Baseline No. 6 Fuel Oil ^a
	07/07/04	Baseline No. 6 Fuel Oil ^a
Year 2	05/24/05	Co-Processed Fuel Oil (EI-176)
	05/24/05	Baseline No. 6 Fuel Oil ^a
Year 3	08/02/06	Co-Processed Fuel Oil (RCO/LCO Blend; X610)
	08/07/06	Baseline No. 6 Fuel Oil ^b
	08/07/06	Baseline No. 6 Fuel Oil ^b
	08/14/06	RCO Bottoms (X1333)

^a No. 6 fuel oil, shipment No. 1

^b No. 6 fuel oil, shipment No. 2

4.2 No. 6 Fuel Oil and Co-Processed Fuel Oil Analyses

The fuels tested in Task 4 included two samples of No. 6 fuel oil, used as baseline fuels, and three co-processed fuel oils. The three fuels processed by PARC were labeled as EI-176, X610, and X1333. EI-176 was prepared by hydrotreating and hydrogenating a 1:1 blend of refined chemical oil (RCO) and light cycle oil (LCO). Sample X610 was prepared by hydrotreating followed by fractionating a 1:1 blend of RCO and LCO. Sample X1333 was derived from the bottoms fractionated out of the RCO. Details on their preparation were presented earlier.

Each fuel tested in the boiler underwent a series of analyses. The analyses that were performed and the corresponding ASTM test procedures used are:

- | | |
|--|--|
| • Relative Density, 60/60°F (g/ml) | ASTM D 1298-97e2 |
| • Relative Density, 60/60°F, API (°API) | ASTM D 1298-97 e2 |
| • Viscosity, 100°F (ssu) | ASTM D 445-03 |
| • Viscosity, 130°F (ssu) | ASTM D 445-03 |
| • Viscosity, 210°F (ssu) | ASTM D 445-03 |
| • Total Sulfur (wt/wt) | ASTM D 4239-04a |
| • Water (vol/vol) | ASTM D 1796-97 (2002) |
| • Sediment (vol/vol) | ASTM D 1796-97 (2002) |
| • Ash (wt/wt) | ASTM D 482-03 |
| • Higher Heating Value (Btu/lb; Btu/gal) | ASTM D 240-02 |
| • Total Carbon, Hydrogen, and Nitrogen (wt/wt) | ASTM D 5373-02 |
| • Major, minor, and trace element composition | Various techniques discussed
in Section 4.2.2 |

The analyses were performed to: 1) determine how the co-processed samples compared to standardized fuel oil specifications [4-1]; 2) determine the quantity of trace elements in the test fuels; and 3) classify the co-processed fuels per established specifications [4-1].

No. 6 fuel oil (Bunker C oil) was the fuel oil used for baseline comparison. No. 6 fuel oil is mainly specified by viscosity; however, the full analysis was performed to fully characterize the fuel oil, ensure that its analysis and properties are typical for its grade, and to compare its characteristics to the requirements for the various grades (*e.g.*, Nos. 4, 5, and 6) of fuel oils. The analyses of the No. 6 fuel oil and the co-processed fuel oils are provided in **Table 4-2**.

The co-processed fuel oil (EI-176) exhibited properties that were characteristic of different grades of fuel oils. For example, the density, both relative and API, and the heating values were similar to No. 6 fuel oil [4-1]. Viscosity was noticeably less for the co-processed fuel oil when compared to the No. 6 fuel oil. Viscosity at 100°F was similar to that of No. 5 fuel oil while the viscosity at 130°F was similar to that of No. 4 fuel oil. The two properties that exhibited the greatest deviation from a No. 6 fuel oil sample were ash and sulfur content. The sulfur content of the co-processed fuel oil was 0.02%, which is less than that typically reported in No. 1 fuel oil (*i.e.*, kerosene) and No. 2 fuel oil (home heating fuel). The ash content of <0.2% is typical of fuel oil grades Nos. 1, 2, and 4.

The characteristics of co-processed fuel oil Sample X610 differ from the co-processed fuel oil Sample EI-176. For example, the API gravity is lower than that measured for the Sample EI-176. It is also lower than the API gravity typically reported for No. 6 fuel oil (12°API gravity) [4-1]. A small difference of approximately 700 Btu per gallon was noted in the heating values of the co-processed fuel oils. However, these heating values are typical of those reported for No. 6 fuel oils (*i.e.*, 150,000 Btu/gal) [4-1]. Viscosity for the X610 co-processed fuel oil was not only less than the EI-176 co-processed fuel oil, but significantly lower than viscosities measured for each of the baseline No. 6 fuel oils tested. Two additional properties that exhibited significant deviation from a No. 6 fuel oil sample were ash and sulfur content. The sulfur content of the co-processed fuel oil was 0.06%, which is less than that typically reported

Table 4-2 Analyses of No. 6 Fuel Oils and Co-Processed Fuel Oils

Characteristic	Method	No. 6 Fuel Oil (2004-2005)	Co-Processed Fuel Oil (2005) EI-176	Co-Processed Fuel Oil (2006) X610	No. 6 Fuel Oil (2006)	RCO Bottoms (2006) X1333
Year Tested						
Sample No:						
Specific Gravity, 60/60°F	ASTM D 1298-97 e2	0.975	0.972	1.015	0.970	1.093 ^b
API Gravity, 60/60°F,	ASTM D 1298-97 e2	13.6	14.1	7.9	14.4	ND ^a
Viscosity @ 100°F, ssu	ASTM D 445-03	3,195	165	23	ND	ND
Viscosity @ 130°F, ssu	ASTM D 445-03	990	46	16	ND	ND
Viscosity @ 210°F, ssu	ASTM D 445-03	138	ND	8	ND	22
Total Sulfur, wt. %	ASTM D 4239-04a	0.93	0.02	0.06	1.8	0.54
Water, vol. %	ASTM D 1796-97 (2002)	0	0	0	0	ND
Sediment, vol. %	ASTM D 1796-97 (2002)	0	0	0	0	ND
Ash, wt. %	ASTM D 482-03	0.06	<0.02	0.02	0.2	0.03
Higher Heating Value, Btu/lb	ASTM D 240-02	18,714	18,376	17,890	18,437	16,823
Higher Heating Value, Btu/gal	ASTM D 240-02	152,272	149,046	151,540	149,249	153,452
Total Carbon, wt. %	ASTM D 5373-02	87.12	90.17	89.1	86.4	90.3
Total Hydrogen, wt. %	ASTM D 5373-02	11.44	9.55	7.65	11.3	5.10
Total Nitrogen, wt. %	ASTM D 5373-02	0.22	0.2	0.12	0.3	0.35

^a Analysis not determined

^b Analysis performed using a graduated cylinder

in Nos. 1 and 2 fuel oils. The ash content of 0.02% is typical of fuel oil grades Nos. 1, 2, and 4.

The properties measured for the RCO bottoms also differ from those typically reported for No. 6 fuel oil. The specific gravity measured for this fuel oil exceeded that of each baseline No.6 fuel oil. This measurement was made using a graduated cylinder and not a hydrometer as specified in ASTM Method D 1298-97 e2. The graduated cylinder was used because of the semi-solid nature of this fuel oil at 60°F. The semisolid behavior not only contributes to a greater specific gravity, but also prevented a viscosity measurement at temperatures below 200°F, the temperature at which the solid fraction melted. The viscosity measured at 210°F, however, was significantly lower than that measured for the No. 6 fuel oil used as a baseline in 2004-2005. The sulfur content of the RCO bottoms, while noticeably greater than that measured in either co-processed fuel oil, still falls midway between typical sulfur values of No. 4 (*i.e.*, 0.48 wt.% sulfur) and No. 5 fuel oil (*i.e.*, 0.70 wt.% sulfur). The lack of hydrotreating and dilution by the LCO yields higher sulfur in this type of fuel oil.

4.2.1 Trace Elemental Analysis

It is necessary to quantify the emissions of inorganic hazardous air pollutants (IHAPs) during combustion of commercial fuel oil and heavy fuel oil produced during co-processing. This is especially important with the recent promulgation of national emission standards for hazardous air pollutants (NESHAP) for industrial, commercial, and institutional boilers and process heaters [4-2]. Small (< 10 million Btu/h firing rate) and large (> 10 million Btu/h firing rate) units are affected.

It became apparent early in the project that it was necessary to develop an analytical protocol when determining the inorganic chemical analysis of oils since there is limited information available and there are few commercial laboratories that can satisfactorily analyze fuel oils for major, minor and trace elements, which are not traditionally present in fuel oils (this is discussed in more detail in Section 4.2.2). Oils generally contain inorganic elements at the trace level. The most prominent elements are heavy metals such as vanadium and nickel. However, the introduction of coal as a feedstock in co-processing with petroleum will likely increase the amounts of other

elements as well as trace elements (some classified as IHAPs) in the product. These metals could ultimately be present in stack emissions. Mercury is of particular interest, and is discussed separately, because of recent legislation targeting mercury emissions from coal-fired powerplants.

4.2.1.1 Mercury in Fuel Oil

The distribution of mercury species in oil varies depending upon the sample source and history. These classes of compounds are not routinely analyzed when characterizing liquid hydrocarbons. What is important is that these mercury species have detrimental effects on people, equipment and catalysts. Mercury is detrimental to petroleum processing systems. In chemical manufacturing and refining, mercury poisons catalysts and can become a component of wastewater, which can impact regulatory compliance. Maintenance workers in the petroleum industry can be at risk due to the inhalation of mercury vapor and absorption of organic mercury compounds via the skin. Crude oil and unprocessed gas condensates can contain significant amounts of mercuric sulfide. Organic mercury compounds are also found in raw produced liquids. Ionic mercury compounds are present in liquids but it is not known if they occur naturally or are produced as a byproduct due to post-collection conversion of other mercury species [4-3]. In addition, the partitioning of mercury into different products is a function of how it is processed.

The U.S. EPA announced in December 2000 that emissions of hazardous air pollutants (HAPS), including mercury, from oil- and coal-fired power plants is necessary and appropriate. However, there were significant discrepancies in the precision and reproducibility of mercury analysis of liquid hydrocarbons.

Prior to 1995, emissions of mercury from oil-fired utility boilers were estimated based on emission factors. The emission factors were based on analytical data that was not entirely reliable. The following emission factors were used in the Mercury Study Report to Congress [4-4]:

Residual Oil (No. 6): $2.9\text{kg}/10^{15} \text{ J}$

Distillate Oil (No. 2): $3.0\text{kg}/10^{15} \text{ J}$

However, the emission factors used in the Locating and Estimating Air Emissions Document [4-5] are as follows:

Residual Oil (no. 6): $2.7\text{kg}/10^{15}\text{ J}$

Distillate Oil (No. 2): $30.02\text{kg}/10^{15}\text{ J}$

It is evident that the estimates of air releases based on these emission factors would be inconsistent. Air releases from utility, non-utility, and residential combustion of oil vary as follows:

Utility: 0.2 tons/y

Non-utility: 5.0 – 7.7 tons/y

Residential: 2.8 – 3.2 tons/y

Studies conducted on the content of mercury in fuel oils since 1995 include:

- Bloom [4-6] measured mercury concentrations in 32 samples of utility fuel oil and measured an average concentration of 0.67 ppb and 1.32 ppb in lighter distillates (gasoline, diesel);
- Liang, Hovat, and Danilchik [4-7] measured 0.59 ppb mercury in one heating oil sample; and
- Rising, Sorurbakhsh and Wu [4-8] measured fuel oil from 13 sites and found mercury below detection limits ($<0.2\text{ppb}$). They also measured levels of other metals and found arsenic, cadmium, and selenium to be below detection limits. The detection limits for As, Cd and Se are 0.9, 0.1 and 6 ppb, respectively. The average concentration of chromium, lead, manganese and nickel was 242, 16, 5, 5, and 29 ppb, respectively.

According to Wilhelm [4-9], actual measurements of mercury discharged from utilities are 25 times less than non-utility discharges that were calculated based on mercury concentration measured in oil prior to 1995. Wilhelm [4-9] attributed this discrepancy to the fact that mercury levels in crude oil measured during the 1970's and 1980's were biased high due to analytical methods used at that time. The mean concentration of mercury in crude oil that was calculated in 2001 (based on studies published between 1995 and 2001) was estimated to be less than 5 ppb. Recent data for average mercury content in crude oil ($< 5\text{ ppb}$) and fuel oil (approximately 1 ppb) are in general agreement with one another.

The U.S. EPA, American Petroleum Institute (API) and National Petrochemical and Refiners Association (NPRA) recognize that discrepancies in the mean concentration and range of concentrations of total mercury measured in oils compromise the

development of reliable mercury emission factors. Consequently, several projects are underway to address the problem of analyzing total mercury in liquid hydrocarbons with statistical accuracy [4-9, 4-10]. These newly developed methods of sampling and analyzing mercury in liquid hydrocarbons are reportedly capable of measuring mercury concentrations with good accuracy and precision.

At the end of the 1990's, 6.6 tons mercury/y were being emitted by stationary oil combustion and 48 tons/y were being emitted by stationary coal combustion. The greater emission rate of coal-fired plants is attributed to the higher levels of mercury in coals. The mercury content of coals can average from 0.07 to 0.12 ppm depending upon the rank (lignite to bituminous coal). Most coals contain approximately 0.1 ppm mercury (ten times as much mercury as in oil) whereas crude oil averages about 10 ppb. On March 15, 2005, EPA issued a federal rule cap to reduce mercury emissions from coal-fired power plants permanently [4-11]. The rule is a market-based cap-and-trade program (Section 111 of the Clean Air Act Amendments) and is similar to the program in place for SO₂. The rule is administered in two phases. The first phase places a cap of 38 tons of mercury beginning in 2020. The second phase sets a final cap of 15 tons by 2018. This translates into reductions of 21% and 69%, respectively. With the implementation of the Clean Air Interstate Rule (CAIR) [4-12] to reduce emissions of SO₂ and NO_x in the eastern 28 states, it is expected that the initial phase of the Clean Air Mercury Rule (CAMR) will partially meet the mercury emissions reductions required via co-benefit expected from the additional wet scrubbers and selective catalytic reduction (SCR) systems that will be installed.

The mercury emitted from oil combustion represents about 10% of the U.S. yearly emission rate of atmospheric mercury from coal and oil combustion combined. However, this could change with the integration of coal into the processing/production of liquid hydrocarbon fuels. The emissions from fuel oils derived from petroleum and coal will exhibit mercury concentrations that reflect the concentration of mercury in the parent crude oil as well as any mercury or other trace elements that are extracted from the coal during processing. Therefore it is essential that there be an accurate way to measure the levels of trace elements in these fuels to determine if they pose any environmental threat thereby compromising the fuel.

4.2.2 Trace Element Analyses Results and Discussion

Efforts were made to evaluate how to best measure mercury in liquid hydrocarbons so that material balances could be conducted on the emissions measured during the combustion testing. The following discussion relates our efforts to address the problem of trace element/mercury analysis in liquid hydrocarbons.

4.2.2.1 Commercial Laboratories

Traditionally, solid fuels are easily digested and analyzed via inductively coupled plasma atomic adsorption spectroscopy (ICP), cold vapor atomic adsorption spectroscopy (CVAAS) and graphite furnace atomic adsorption spectroscopy (GFAAS). Liquid fuels are not so easily analyzed due to their combustive nature in analytical techniques, which use flame spectroscopy. In addition, many of the elements traditionally analyzed in coal are not routinely analyzed in oil as they are either not present or present in minute quantities. It was initially decided that the fuels would be analyzed by a commercial lab that routinely handles combustible liquids. The advantage of this is that any industry would have access to such a lab and that the analysis procedure would meet industry standards. The No. 6 fuel oil was sent to Staveley Services/CTC Analytical Services, Portland, Oregon for analysis. Duplicate fuel oil samples were analyzed in addition to NIST Standard Reference Material (SRM) 2722 (Mercury in Crude Oil-Heavy Sweet). Analysis of the No. 6 fuel oil is given in **Table 4-3** and is labeled as Commercial Lab. Analyses were conducted according to ASTM Method D5184 (Standard Test Methods for Determination of Aluminum and Silicon in Fuel Oils by Ashing, Fusion, Inductively Coupled Plasma Atomic Emission Spectrometry, and Atomic Absorption Spectrometry (ICP AAS)) [4-13].

There was concern as to the accuracy of the fuel oil analysis since there were discrepancies in the concentrations reported for the two samples, *i.e.*, As, Hg, Cr, and Pb. In addition, the Hg concentration reported for the NIST SRM was 1,240 ppb; however, the certified value for the SRM is 129.2 ppb. It is not surprising that the Hg data was incorrect given that the commercial lab used ICP AAS to analyze for Hg. Traditionally, mercury is best analyzed by CVAA. ICP MS has also been used for mercury analysis.

The poor agreement of As concentration can also be attributed to the fact that As is best analyzed by GFAAS. It was apparent that other techniques were necessary for use in the project.

Table 4-3 Chemical Analysis of the Petroleum-Derived and Co-Processed Fuel Oils

Element	Concentration (ppm)			
	Petroleum-Derived Fuel Oil (Commercial Lab)	Petroleum-Derived Fuel Oil (Commercial Lab)	Petroleum-Derived Fuel Oil (Microwave Digestion Tech.)	Co-processed Fuel Oil (Microwave Digestion Tech.)
Al	34.0	31.6	11.89	< 0.346
As	3.63	<0.01	< 0.425	< 0.346
Ba	0.38	0.73	36.09	20.09
Be	NA ^a	NA	< 0.425	< 0.346
Cd	0.27	0.2	< 0.425	< 0.346
Co	NA	NA	2.12	1.39
Cr	0.12	0.03	0.425	< 0.346
Cu	0.16	0.96	< 0.425	< 0.346
Hg	0.59	0.13	ND ^b	ND
Mn	0.15	0.39	6.37	1.73
Mo	0.07	0.01	3.40	2.42
Ni	40.5	44.6	1.27	< 0.346
Pb	0.12	0.6	0.42	0.346
Sb	NA	NA	2.12	0.346
Se	1.40	2.18	1.27	0.693
Sr	NA	NA	1.27	0.693
V	116	129	10.19	2.42
Zn	1.46	2.08	2.12	< 0.346

^a NA Not available

^b ND None detected

4.2.2.2 Microwave Digestion Technique

It was decided that a better sample preparation technique and analysis was needed to analyze metals in the fuel oils. The University of North Dakota Energy and Environment Research Center recommended a microwave digestion technique that might be appropriate for liquid hydrocarbons. The petroleum-derived and co-processed fuel oils were “digested” using the microwave procedure outlined in Appendix A and then analyzed by ICP for multi-metals and CVAAS for mercury. Chemical analysis of the fuels by this technique is given in **Table 4-3**.

The results of the petroleum-derived fuel oil analysis using the microwave digestion were not in agreement with the commercial lab results. In fact, the duplicate results from the commercial lab were in greater agreement than with the microwave-

digested sample. The analysis of the co-processed fuel was not satisfactory either since many of the metals were present at or below detection limits of the ICP at Penn State. No mercury was detected in either of the oil samples. A comparison of the microwave-digested fuel oil analyses on a lb/10¹² Btu basis with emissions measured for the respective fuels shows that there is a significant discrepancy between the total mass input of each element as compared to the emissions measured during the testing (which are discussed later). There is greater confidence in the emissions data, based on our experience (over 50 emission tests using the sampling train) than on the ability of the laboratories to duplicate the fuel analysis data.

4.2.2.3 EPA 3052

Analysis of trace metals in liquid hydrocarbons is very difficult and cannot be done in the same manner as solid hydrocarbons. Solid hydrocarbons samples are generally heated forming an ash, which is subsequently heated with lithium borate to form a glass phase, which stabilizes the elements. The glass phase is then digested in an acid solution, which is then aspirated into a flame. The volatilization of the material via a flame or plasma ionizes the element. The emission spectrum of an element's ionization energy is then measured which reflects the concentration of the species in the sample. This technique is not suited to analyze volatile trace elements such as mercury or arsenic as they are lost to the atmosphere. In this case, solid hydrocarbon can be digested directly (whole fuel) and not ashed. The solution can then be analyzed by different spectroscopic techniques. The fuel analysis in **Table 4-4** was conducted using EPA 3052 (Microwave Assisted Acid Digestion of Siliceous and Organically Based Matrices) in which the liquid hydrocarbons are digested and the solution is then analyzed using inductively coupled plasma spectroscopy (ICP). Mercury must be analyzed by cold-vapor atomic adsorption spectroscopy. The analysis presented is not complete as many of the elements were reported as below detection limits of the ICP. In addition, mercury analysis was not completed.

Table 4-4 Fuels Analysis

	#6 Fuel Oil	Co-Processed Fuel Oil X610	RCO Bottoms X1333
Element	ppm		
Al	17.9	<2.85	<2.60
As	*	**	1.52
Ba	1.15	**	***
Be	*	**	***
Cd	*	**	***
Co	0.913	**	***
Cr	0.396	0.451	1.46
Cu	*	**	0.265
Hg	na	na	na
Mn	*	**	***
Mo	0.303	**	***
Ni	50.0	0.405	0.629
Pb	*	**	***
Sb	0.442	**	***
Se	*	**	***
Sr	*	**	***
V	182	0.307	0.362
Zn	0.869	0.479	1.67

*Less than 0.287 ppm

** Less than 0.285 ppm

*** Less than 0.260

na Not available

4.2.2.4 Evaluation of LECO Mercury Analyzer for Liquid Hydrocarbons

A different approach for mercury analysis was attempted in which a model AMA254 mercury analyzer, purchased from the LECO Corporation, was used to determine the mercury concentration in the fuel samples. The primary reason for purchasing this instrument was to provide the Energy Institute with the capabilities of measuring the mercury content of test samples without relying on commercial labs. While the use of a commercial lab would present certain advantages, this instrument could provide an accurate and repeatable method for analyzing samples on short-term basis. Unlike ASTM Method D5184, the LECO AMA254 mercury analyzer is designed to determine total mercury content in various solids and certain liquids without sample pretreatment or sample pre-concentration. The instrument is designed with a front-end combustion tube that is ideal for the decomposition of high carbon samples such as coal or petroleum coke. During this first stage of analysis, the samples are heated inside the

front half of a combustion tube to approximately 750°C within a stream of pure oxygen. Following thermal decomposition, the gaseous products are carried through catalytic compounds pre-packed within the second half of the combustion tube. These compounds serve to remove all interfering impurities (*i.e.*, ash, moisture, and halogens). The cleaned gases are then transported to the amalgamator, a small glass tube containing gold-plated ceramics, which collects the mercury vapor. The amalgamator is then heated to approximately 900°C, releasing the mercury vapor into the path of a standard Atomic Absorption Spectrometer. The Spectrometer uses an element-specific mercury lamp that emits light at a wavelength of 253.7 nm and a silicon UV diode detector for mercury quantification [4-14]. Using this approach, the AMA254 has received ASTM Method Approval D-6722.

The instrument's performance was initially evaluated using NIST Standard Reference Material (SRM) 2685b (Sulfur and Mercury in Coal), SRM1633b (Constituent Elements in Coal Fly Ash), and additional standards produced in-house by diluting a 1000 parts per million (ppm) Inductively Coupled Plasma (ICP) certified standards of mercuric chloride. Following calibration, repeated analyses of these standards showed the instrument's performance was within the specified precision of 2.5 parts per billion (ppb) mercury. Several attempts were made to measure the mercury content in this instrument of the baseline fuel oil burned during the first year of this project. However, incomplete combustion of the heavy oil within the combustion tube produced carbon, which subsequently adsorbed the mercury prior to the amalgamator. Leco, the instrument's manufacturer was not able resolve this problem and the instrument cannot be used for heavy oil liquid samples.

4.2.3 Summary of Fuel Oil Trace Element Analysis

The trace element concentrations in the various fuel samples were not measured with confidence in the project. Although the analyses of the trace elements in the fuel oils and co-processed fuels were not ideal, it did not compromise the results of the emissions data. As discussed in Section 4.4.3, trace element emissions were determined and comparisons of the emissions between baseline No. 6 fuel oil and the co-processed fuels were made. The inability to measure the trace elements in the fuel did limit our ability,

however, to perform a material balance with confidence to ultimately determine the fate of trace metals during the refinery process.

4.3 Fuel Atomization

It was the intent that the No. 6 fuel oil and all co-processed fuel oils undergo atomization tests at the conditions (*i.e.*, temperature and atomization pressures) they were to be tested in the watertube boiler. Atomization is important to determine turndown performance and auxiliary power costs. Differences in atomization characteristics affect the rate of mixing of the fuel droplets with the combustion air and can influence flame structure and stability [4-15]. Atomization tests were to be performed using the commercial, No. 6 fuel oil and the test fuel oils to assist in explaining any combustion performance differences that may be observed. The atomization tests were to be performed in Penn State's atomization facility using a commercial fuel oil atomizer to determine the spray characteristics prior to the combustion tests [4-16]. Only the No. 6 fuel oil underwent atomization tests. As the project proceeded, it became apparent that insufficient quantities of co-processed fuel oils would be available to perform both atomization tests and combustions tests. Quantities varied from less than 1 barrel (≈ 40 gallons) to 2 barrels (≈ 100 gallons). The combustion/emissions testing was more important and took precedent over the atomization tests.

Measurements of the atomization performance for the baseline No. 6 fuel oil were performed using a commercial fuel oil gun. It is expected that the quality of atomization will influence the combustion performance and emissions because the droplet size affects the subsequent rate of oil volatilization and combustion downstream of the atomizing nozzle. To quantify the atomization performance, a type-T oil gun manufactured by Faber Burner Company in Lock Haven, Pennsylvania was selected. The oil gun was used to evaluate the atomization quality for the baseline fuel oil and the subsequent combustion testing. A diagram of the Faber oil gun is provided in **Figure 4-1**.

A type SLC internal-mix atomizer was connected to the outlet end of the oil gun, which was drilled out to an angle of 30° . This spray angle was chosen to prevent impingement of the oil droplets on the refractory-lined burner throat (quarl) during the subsequent combustion testing. It is also important that the spray angle be chosen such

that the fuel droplets are entrained in the swirling combustion air stream. This ensures that they are brought in contact with oxygen in the preheated air as well as with the hot recirculated products of combustion. The combination of oil gun and atomizer used in this study was designed to atomize lighter fuel oils (No. 2, 4, and 5) in addition to the heavier No. 6 fuel oil.

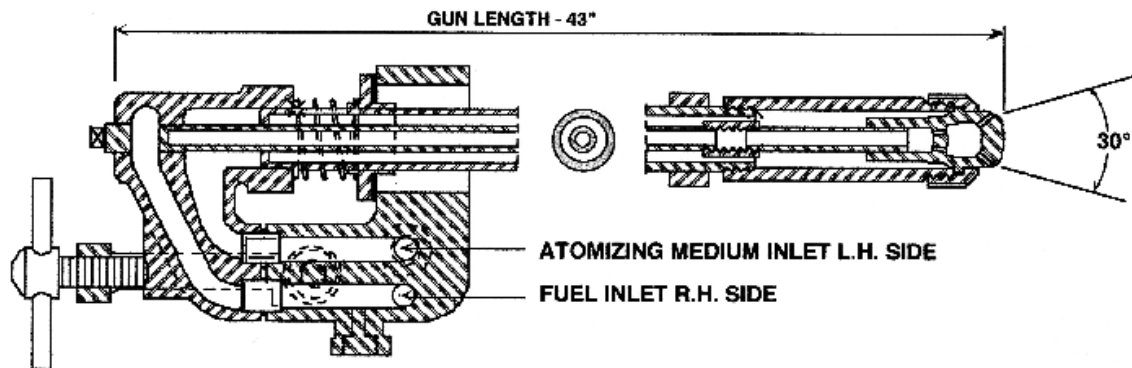


Figure 4-1 Schematic diagram of the Faber oil gun

An atomization test facility (ATF) was used to measure the atomization characteristics of the baseline No. 6 fuel oil. A sketch of the ATF is given in **Figure 4-2**.

Central to the system is a spray chamber connected to an induced draft fan. Prior to entering the chamber, the spray is intersected by the laser beam from a Malvern 2600C Laser Diffraction Particle and Droplet Sizer. The analyzer includes a micro-computer which calculates the droplet size distribution and stores the data to disk. After being analyzed, the spray enters the chamber where most of the large droplets settle to the floor and are collected. The remaining fine droplets are then removed in the demister. A constant sweep of air provided by the induced draft fan ensures that few droplets pass through the laser beam volume more than once. The exhaust air containing very fine droplets is vented to the atmosphere.

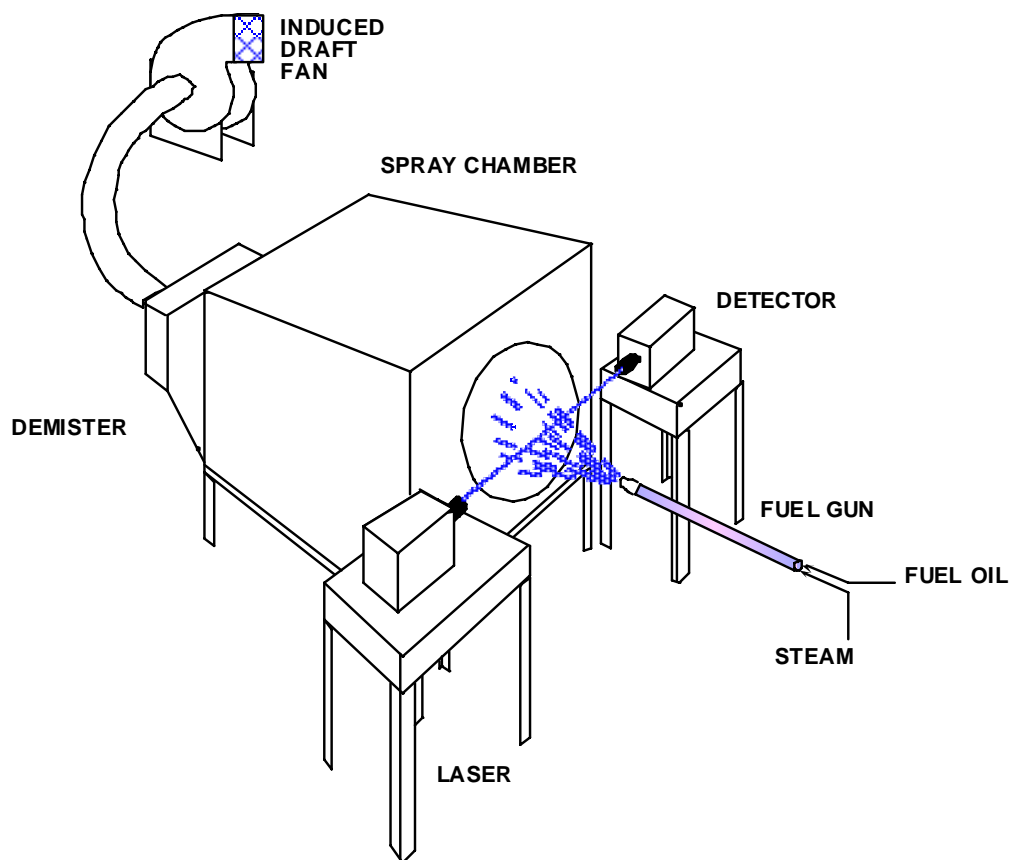


Figure 4-2 Sketch of the atomization test facility

As shown in **Table 4-2**, the viscosity of No. 6 fuel oil is very high (*i.e.*, 3,195 ssu), even at an elevated temperature of 100°F. To achieve acceptable atomization, No. 6 fuel oil must be heated thereby lowering the viscosity prior to introduction into the fuel gun. A temperature of 205 to 220°F, which is typical of industry, was maintained for both the atomization measurements and the combustion testing. Electrical drum heaters were used to heat the fuel prior to testing. Once the desired fuel temperature had been achieved, the fuel oil was delivered to the oil gun by a Moyno progressive cavity pump. The flow rates of both oil and steam were monitored by Micro Motion Mass Flow Meters. A complete schematic diagram of the flow system is shown in **Figure 4-3**.

Spray quality is commonly expressed in terms of the Sauter Mean Diameter (SMD). The SMD is the diameter of the droplets whose ratio of volume to surface area is the same as that of the entire spray and can be defined as:

$$SMD = \frac{\sum n_i d_i^3}{\sum n_i d_i^2} \quad (4-1)$$

where n_i is the number of droplets in size d_i . This definition is derived from the realization that for a given quantity (volume) of fuel oil, the total surface area available for heating, evaporation, and other processes, to a large degree, controls the overall rate of combustion.

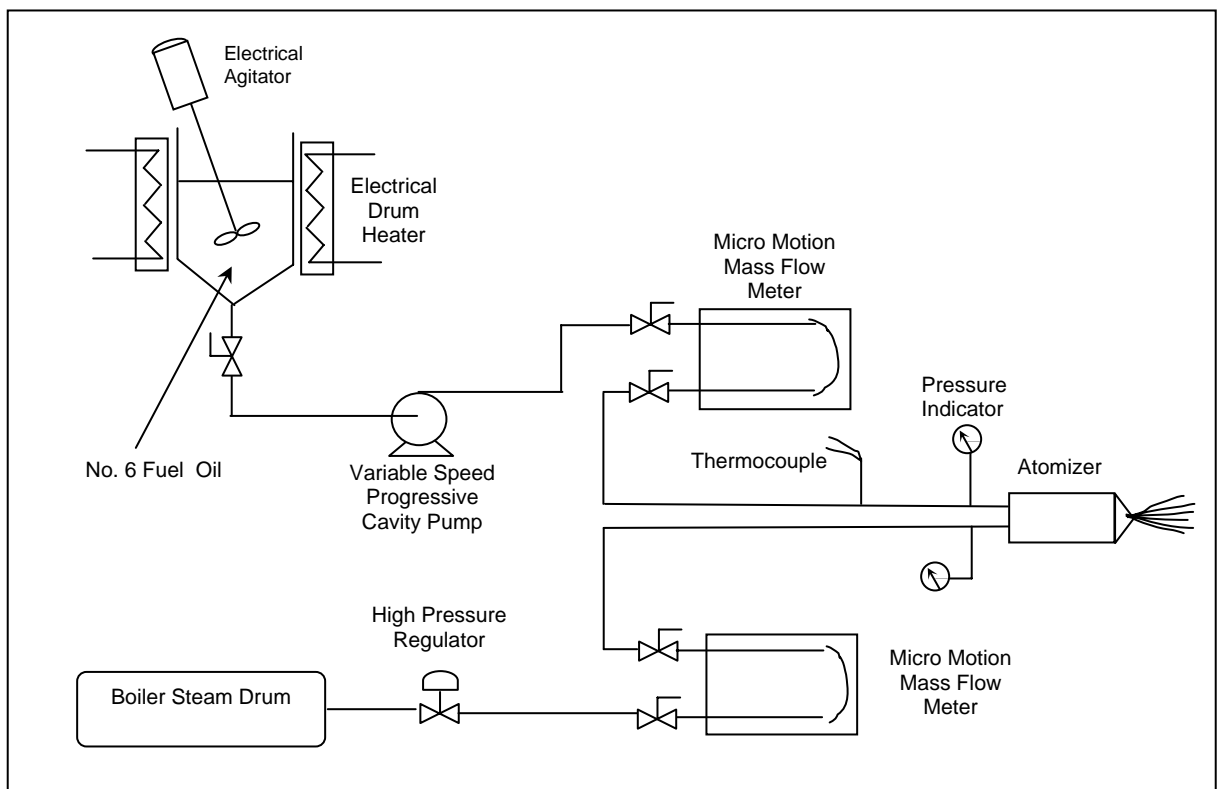


Figure 4-3 Flow diagram of the atomization test facility

For a given fuel/nozzle combination, optimization of the operating parameters consists of determining the minimum flow rate and pressure of the atomizing media (an indication of the amount of energy used in the atomization process) required to achieve the target spray quality. The fuel pressure required to force a liquid through the discharge orifice increases with flow rate and also with the amount of resistance offered to the fuel by the atomizing medium (This applies to internal-mix nozzles; fuel and atomizing media

interact external to the nozzle in external-mix designs.). The fuel is important since it may influence discharge characteristics of the fuel pump. As a corollary to the above, although the atomizing media flow rate is a function strictly of pressure when no fuel is flowing in the nozzle, it becomes dependent also on the fuel flow rate due to the interaction of the two fluids in an internal-mix nozzle [4-16].

Steam is commonly used as the atomizing media for applications burning No. 6 fuel oil because it can be readily supplied from the boiler's steam drum. Compressed air may be substituted during startup until sufficient steam pressure is available. Therefore, steam was used to atomize the baseline fuel oil in this evaluation.

The manufacturer of the fuel oil gun, *i.e.*, Faber, recommended that an atomizing pressure equal to 15 pounds per square inch (psi) greater than the oil delivery pressure be used to achieve sufficient atomization quality. Operating at a flow rate of 79.8 pounds of oil per hour (lb/h), equivalent to a firing rate of 1.5 million Btu per hour during the combustion testing, an atomization pressure of 60 psi was required. Using these conditions, the resulting droplet size distribution was measured and the results are provided in **Table 4-5**. The SMD ($D_{(4,3)}$) for the Faber oil gun was 114 μm . Inquiries to Faber and a literature search found no other studies contrasting the atomization quality of No. 6 fuel oil using the same oil gun design.

Table 4-5 Droplet Size Distribution for No. 6 Fuel Oil Spray using the Faber Oil Gun

Upper	in	Lower	Under	Upper	in	Lower	Under	Upper	in	Lower	Under	Span
				346	2.2	299	97.8	58.9	3.6	50.8	37.6	2.98
				299	10.9	258	87.0	50.8	3.6	43.8	34.0	$D[4,3]$
				258	8.7	222	78.2	43.8	3.6	37.8	30.4	114.46 μm
				222	3.1	192	75.2	37.8	3.6	32.6	26.8	
1128	0.0	973	100	192	3.3	165	71.9	32.6	3.9	28.1	22.9	$D[3,2]$
973	0.0	840	100	165	3.9	143	67.9	28.1	4.5	24.3	18.5	45.58 μm
840	0.0	724	100	143	5.0	123	62.9	24.3	5.4	20.9	13.1	
724	0.0	625	100	123	5.4	106	57.6	20.9	5.1	18.1	8.0	$D[v,0.9]$
625	0.0	539	100	106	4.7	91.7	52.8	18.1	3.9	15.6	4.2	266.98 μm
539	0.0	465	100	91.7	4.2	79.1	48.6	15.6	2.2	13.4	1.9	
465	0.0	401	100	79.1	3.8	68.2	44.8	13.4	0.9	11.6	1.0	$D[v,0.1]$
401	0.0	346	100	68.2	3.6	58.9	41.2	11.6	1.0	3.00	0.0	19.19 μm
Source = Data:refinin				Beam length = 2.2 mm				Model indp [2, 0]				$D[v,0.5]$
Record No. = 9				Log. Diff. = 3.585				Volume Conc. = 0.2808%				83.16 μm
Focal length = 600 mm				Obscuration = 0.3341				Sp.S.A 0.1316 m ² /cc.				Shape OFF
Presentation = lds				Volume distribution								

The steam-oil mass ratio for these conditions was 0.9. This ratio is probably excessive and unacceptable from an industrial point of view. However, this is typical of small, laboratory-scale processes. The efficiency of utilization of the atomizing medium generally increases with scale-up to larger units.

Factors that affect a fuel oil's quality of atomization include not only the flow rate and pressure of the oil and atomizing steam, but also the oil's viscosity. Because there was insufficient fuel for co-processed fuel oil atomization tests, the viscosities of the co-processed fuel oils, reported in **Table 4-2** as a function of temperature, were compared to the viscosities of the commercial fuel oils to select temperatures to which the co-processed fuels were preheated during testing that would yield approximately the same viscosity as the No. 6 fuel oils and thus comparable atomization performance. The No. 6 fuel oils were tested at preheated temperatures of approximately 200°F while the co-processed fuels oils were preheated to temperatures of approximately 110°F, 135°F, and 200°F, depending on their viscosities.

4.4 Watertube Boiler Combustion Tests

The combustion performance attributes that boiler operators are most interested in are flame length, consumption of atomizing medium, turndown ratio, NO_x emissions, and particulate emissions [17]. The introduction of coal into the process streams of a petroleum refinery may result in changes to the fuel oil's composition. These changes may appear as differences in the API gravity, viscosity, or elevated levels of mercury and other metals. To evaluate whether these changes may affect the combustion performance and emissions of the co-processed fuel oils, combustion testing was performed. This testing was conducted in Penn State's watertube research boiler. A description of the boiler and ancillary equipment is provided in Section 4.4.1.

4.4.1 Description of the Research Boiler, Ancillary Equipment, and Testing Procedures

Penn State's research boiler and ancillary equipment are shown in **Figure 4-4**. The 1,000 lb saturated steam (@ 150 psig)/h boiler is an A-Frame watertube boiler, designed and built by Cleaver Brooks. The combustion chamber is a 3x3x7 ft (63ft³)

chamber with a maximum heat release rate of 42,000 Btu/ft³-h. It contains 288 ft² of heating surface and the maximum firing rate is two million Btu/h (60 Hp).

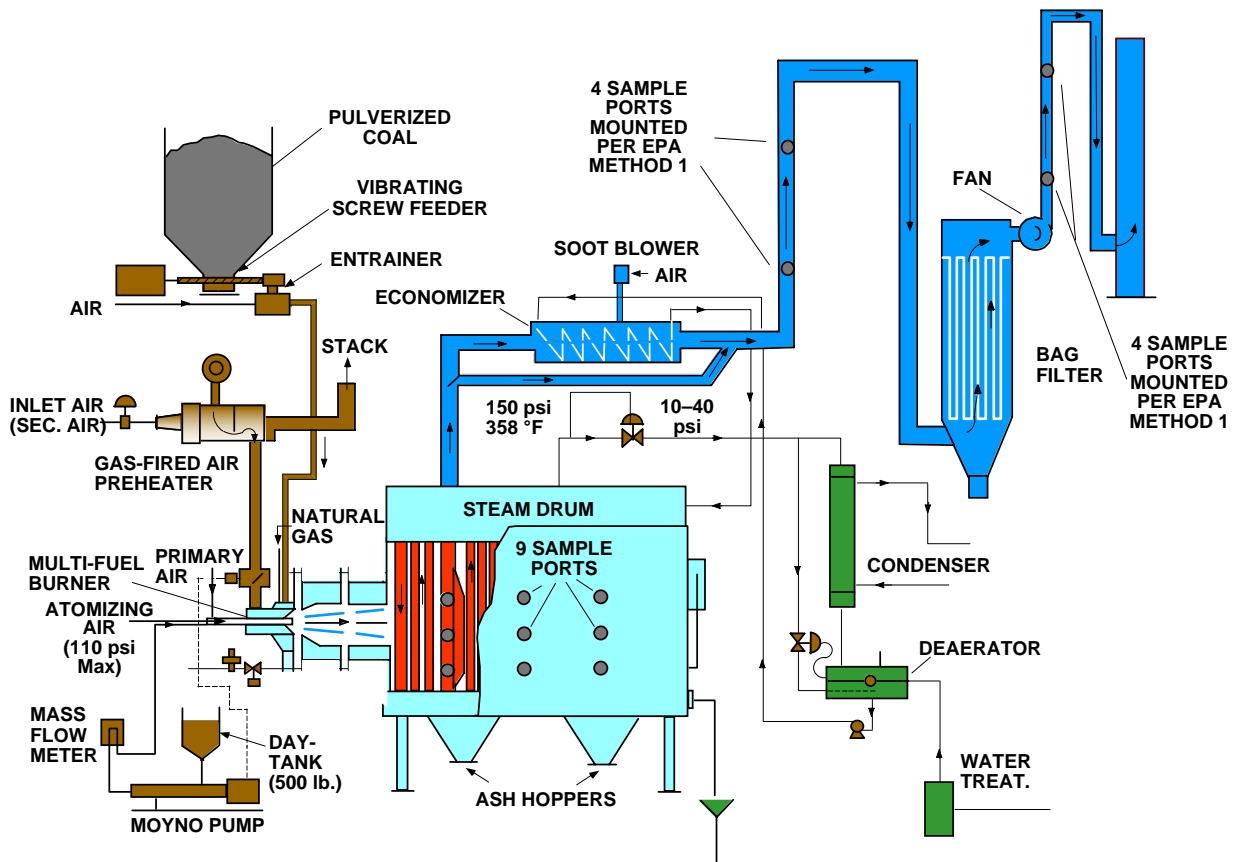


Figure 4-4 Schematic diagram of the research boiler system

The boiler is equipped with eighteen side ports for gaseous and particulate sampling. Fourteen of the ports have diameters of 3 inches and four have diameters of 4 inches. The combustion gases split into two convective sections, one on each side of the radiant combustion chamber. There are access doors into each of the convective sections. There are also two ash hoppers under each convective section and a doorway giving access into the radiant combustion chamber.

During testing, the steam pressure is maintained constant at 150 psig by a back-pressure regulator. The steam flow rate is measured at the outlet of the steam drum by a

steam flow meter before passing through a condenser. The condensed steam then flows into a feedwater tank before returning to the boiler.

To promote and enhance combustion, a ceramic burner throat extends the combustion chamber by two feet. This ceramic section, termed a quarl, is preheated using a natural gas flame prior to introducing the fuel oil. The quarl aids in the support of the fuel's ignition by storing some of the radiant heat energy released by the flame.

Fuels were preheated and transported to the fuel oil gun via the same system used in the atomization testing (See **Figure 4-4**). The fuel oil feed rates were monitored using a Micro Motion Mass Flow Meter, while the temperature was recorded by a thermocouple located at the inlet to the oil gun.

A gas-fired combustion air preheater supplied over 300,000 Btu/h to preheat up to 1,200 lb/h of air to 350°F. The preheated combustion air (primary air) was passed through a conventional swirl ring several inches before the gas distribution ring, both of which are 8 inches in diameter. A small portion of unheated primary air was fed through an annulus gap surrounding the nozzle. Preheated secondary air was introduced into the quarl tangentially through two headers that were balanced for uniform flow. The percentages of air introduced as cooling, primary, and secondary used in this study were approximately 2, 75, and 23, respectively.

The flue gas composition (O_2 , CO_2 , CO , NO_x , and SO_2) was monitored using a continuous emission monitoring system. After leaving the boiler, the combustion products passed through an economizer and a baghouse for the removal of particulate matter. Additional sampling ports have been added to the inlet and outlet ducting of the baghouse per EPA Method 1. All instrumentation readings were recorded by a microcomputer data acquisition system.

The thermal efficiency of the watertube boiler was determined for each test in accordance with the input-output method as described in the ASME Power Test Codes for Steam Generating Units – Section 4.1 [4-18]. The efficiency for this method is expressed by the following equation:

$$\text{Boiler Efficiency (\%)} = \frac{\text{Output}}{\text{Input}} = \frac{\text{Heat adsorbed by working fluids}}{\text{Heat in fuel} + \text{heat credits}} \times 100 \quad (4-2)$$

4.4.2 Combustion Testing

Nine combustion tests were performed firing No. 6 fuel oil and the co-processed fuel oils. A summary of the average boiler operating conditions and combustion/emissions data is provided in **Table 4-6**. The results from the testing are provided by project year in this section with the trace element emissions data provided in Section 4.4.3.

4.4.2.1 Year 1

Three combustion tests were performed firing the No. 6 baseline fuel oil at approximately 1.5 million Btu/h (~80 lbs oil/h) in the research boiler. The research boiler was fired on natural gas for a period of 4 hours to preheat the quarl. After the quarl temperature had reached approximately 1,200°F, the boiler was switched to firing the baseline fuel oil. Similar to the atomization measurements, the fuel oil was heated to between 205 and 220°F prior to being delivered to the fuel oil gun, and an atomization steam pressure of 60 psig was used.

Although the small-scale nozzle yielded a high steam-oil mass ratio, increased atomization steam pressures may provide for improved atomization quality (*e.g.*, finer droplet size). As observed with previous No. 6 fuel oil testing at Penn State's Demonstration Boiler (*i.e.*, firing rate of 20 million Btu/h), the reduction in droplet size produced a shorter flame [4-16]. Also observed was that the NO_x production generally increases with decreasing flame length. This is a direct result of rapid mixing of all the fuel with the combustion air close to the burner. The small droplets evaporate and burn more rapidly. As the droplets become larger, the flame becomes longer and mixing is delayed, thereby producing a potential for substoichiometric firing in the core of the flame structure. The flame length for the baseline fuel oil was approximately 36 inches. Thus, there was no risk of flame impingement on the back wall of the boiler.

Table 4-6 Summary of Average Boiler Operating Conditions

Fuel Type	Baseline Fuel Oil	Baseline Fuel Oil	Baseline Fuel Oil	Baseline Fuel Oil	Co-processed Fuel Oil	Co-processed Fuel Oil	Baseline Fuel Oil	Baseline Fuel Oil	RCO Bottoms
Test Date	06/16/04	07/07/04	07/07/04	05/24/05	05/24/05	08/02/06	08/07/06	08/07/06	08/14/06
Test Duration (h)	6.0	7.0	5.5	1.75	1.25	2.5	3.5	2.0	2.0
Flows									
Fuel Feed Rate (lb/h)	79.8	79.8	79.8	79.5	82.8	83.7	81.4	81.0	67.2
Firing Rate (MMBtu/h)	1.49	1.49	1.49	1.45	1.52	1.50	1.49	1.49	1.13
Total Combustion Air (lb/h)	1,502	1,581	1,543	1,248	1,290	1,364	1,314	1,308	932
Cooling Air (lb/h)	24	24	24	24	24	25	25	25	25
Primary Air (lb/h)	1,135	1,183	1,176	1,022	1,055	1,176	1,128	1,118	742
Secondary Air (lb/h)	343	374	343	202	211	163	161	165	165
Steam Production (lb/h)	1,080	1,070	1,099	1,063	1,098	1,152	1,153	1,164	794
Atomizing Steam (lb/h)	71	75	74	75	74	70	72	71	80
Temperatures (°F)									
Primary Air	356	349	352	346	348	340	345	344	347
Secondary Air	618	582	599	661	668	692	689	691	551
Quarl Top	1,208	1,361	1,306	1,299	1,347	1,246	1,255	1,254	1,169
Fuel Oil	208	211	206	199	134	111	199	213	198
Flue Gas Composition (dry)									
O ₂ (%)	3.8	4.0	3.9	3.9	3.9	4.1	4.0	4.0	5.1
CO @ 3% O ₂ (ppm)	148	138	123	87	45	175	45	51	84
CO ₂ @ 3% O ₂ (%)	14.8	13.4	13.9	13.7	13.8	14.4	13.7	13.8	15.3
SO ₂ @ 3% O ₂ (ppm)	553	302	306	545	42	13.5	929	933	338
NO _x @ 3% O ₂ (ppm)	539	582	NA	308	87	198	356	364	575
Boiler Efficiency (%)	72.3	71.8	73.3	71.0	71.6	70.4	70.3	71.2	62.3

Average NO_x emissions of 560 ppm (corrected to 3% O₂) were measured for the series of tests performed. It should be noted that while the burner installed on the research boiler was designed for firing natural gas and fuel oil, it has not been optimized for low NO_x production.

An average oxygen level of 3.9% in the flue gas was used for the baseline fuel oil combustion tests. This amount of excess oxygen was established by slowly increasing the flow rate of combustion air until an acceptable level of CO was observed within the flue gas. The low concentrations of CO (123 to 148 ppm, corrected to 3% O₂) are not only evidence of good combustion efficiency, but also a general indicator of reduced particulate (soot) formation.

Boiler efficiency was comparable for the three tests. The boiler efficiencies were 72.3%, 71.8%, and 73.3%, respectively, for the three No. 6 fuel oil tests.

4.4.2.2 Year 2

A combustion performance test burning the baseline No. 6 fuel oil and co-processed fuel oil EI-176 was performed on the research boiler during Year 2. The operating conditions (*i.e.*, atomizing steam pressure, firing rate, *etc.*) were similar to those used for the baseline No. 6 fuel oil testing performed during Year 1. A summary of the average operating conditions and combustion data for the tests is provided in **Table 4-6**.

At the beginning of each test, the quarl was heated to a temperature of approximately 1,200°F burning natural gas. The boiler was then switched to firing the baseline No. 6 fuel oil. Burning the baseline No. 6 fuel oil prior to the co-processed fuel oil on 05/24/05 allowed the system to stabilize after the transition from burning natural gas before introducing the co-processed fuel oil. This step was important given the limited quantity of the co-processed fuel oil available. It also provided an additional set of comparison data burning the baseline fuel oil.

Similar excess oxygen levels were maintained in the flue gas for all tests performed. The reduction in the carbon monoxide levels observed burning the co-processed fuel oil relative to the tests burning the baseline No. 6 fuel oil would typically indicate an improvement in the oil's combustion efficiency. However, there is insufficient information to draw this conclusion. The most noticeable change in the emissions is the large reduction in both the sulfur dioxide (SO₂) and oxides of nitrogen (NO_x) when burning the co-processed fuel oil. These changes are apparent in **Figure 4-5** where the emissions, corrected to 3% oxygen, are plotted as a function of time for testing performed on 05/24/05. The decrease in the sulfur dioxide levels can be

attributed to the smaller amount of sulfur contained in the co-processed fuel oil relative to the baseline fuel oil. As reported in **Table 4-2**, the weight percent sulfur in the No. 6 and co-processed fuel oils is 0.93 and 0.02 wt.%, respectively.

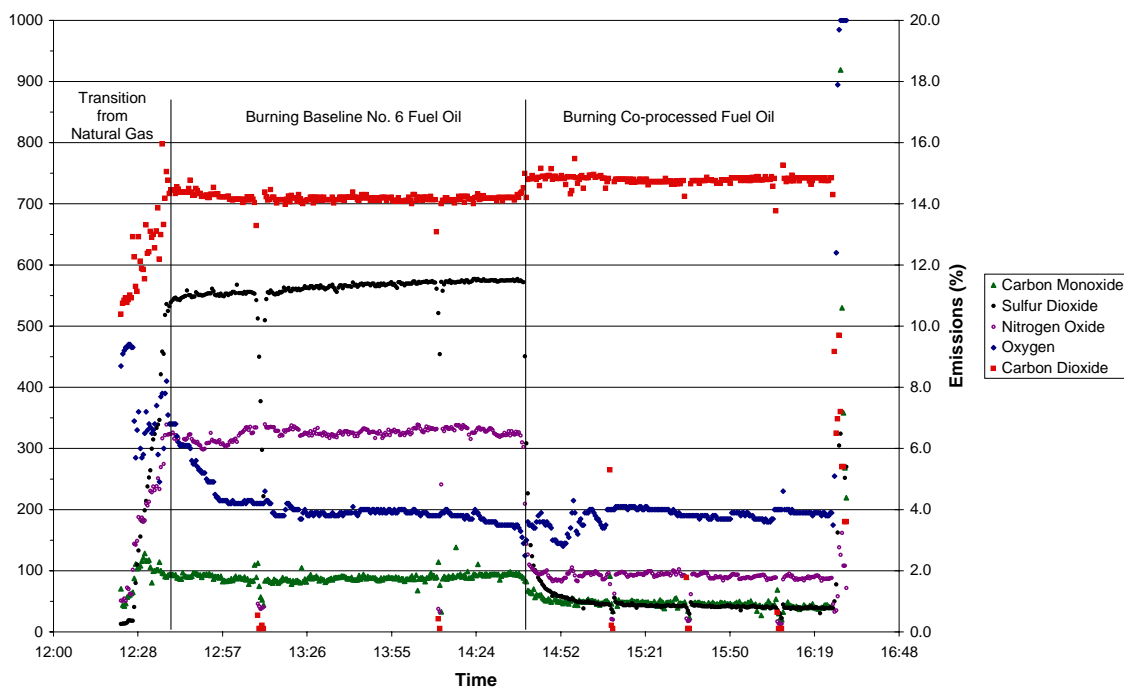


Figure 4-5 Emissions (on a 3% O₂ basis) as a function of time for testing on 05/24/05

It is unlikely that the reduction in the NO_x emissions noted during combustion of the co-processed fuel oil is fuel related (*i.e.*, fuel NO_x) because the co-processed fuel oil nitrogen content is similar to the nitrogen content in the No. 6 fuel oil. The decrease in NO_x emissions when firing the co-processed fuel oil must reflect a decrease in thermal NO_x, which may have resulted from preheating the co-processed fuel oil to a lower temperature.

The boiler efficiency for the four baseline No. 6 fuel oil tests (performed in Years 1 and 2) varied between 71.0 and 73.3%, while the efficiency determined when burning the co-processed fuel oil on 5/24/05 was 71.6%. Since the efficiency for the co-processed fuel oil lies within the spread of efficiencies determined for the baseline fuel oil, there appears to be no differences in boiler performance between the two fuel oils.

4.4.2.3 Year 3

Two combustion performance tests burning the baseline No. 6 fuel oil and one test burning each of the RCO/LCO derived fuel oils were performed on the research boiler during Year 3. With the exception of the RCO bottoms testing, the operating conditions (*i.e.*, atomizing steam pressure, firing rate, *etc.*) for these tests were similar to those used for the baseline and co-processed fuel oil testing performed in Years 1 and 2. A mechanical problem with the fuel oil pump during the RCO bottoms testing resulted in a lower firing rate and higher excess air levels. A summary of the average operating conditions and combustion data for the tests is provided in **Table 4-6**.

At the beginning of each test, the quarl was heated to a temperature of approximately 1,200°F burning natural gas. The boiler was then switched to firing the desired fuel oil. While burning fuel oil, the system was allowed to stabilize after the transition from natural gas. After steady-state operation was achieved, sampling of the boiler's emissions and the logging of the operating conditions were started.

With the exception of the co-processed fuel oil, each fuel oil was heated prior to being delivered to the oil gun. Heating the fuel oils decreases their viscosity, thus improving their atomization quality. Viscosity, measured as function of temperature, was used in determining the required preheat temperature for each fuel. The baseline No. 6 fuel oils were heated to a temperature of 200 – 210°F. This resulted in a viscosity of approximately 138 standard saybolt units (ssu). Targeting a similar viscosity in each of the RCO/LCO-derived fuel oils, no heating of the co-processed fuel oil was required because of its low viscosity at ambient temperature. The temperature required for the RCO bottoms was not determined from viscosity data, but by the temperature at which the semisolid sample melted into a liquid. This temperature was approximately 200°F. **Figure 4-6** shows an open drum of the RCO bottoms prior to heating.



Figure 4-6 Drum of RCO Bottoms prior to heating (Note the screwdriver in the ‘liquid’ fuel)

Similar excess oxygen levels (approximately 4.0%) were maintained in the flue gas for all tests with the exception of the RCO bottoms testing. The percent oxygen for this test steadily rose throughout the test period. This increase resulted from a gradual drop in the fuel oil’s flow rate. After the test was completed, it was noted that the fuel oil had reacted with the rubber lining inside the progressive cavity oil pump resulting in decreased pumping efficiency.

The emissions measured by the CEMs for each test were corrected to a basis of 3% oxygen and are plotted in **Figures 4-7 through 4-10**. The most noticeable difference between the emissions produced from burning the RCO/LCO-derived fuel oils and the baseline No. 6 fuel oils is the large reduction in both the sulfur dioxide (SO_2) and oxides of nitrogen (NO_x). The reduction in the sulfur dioxide levels observed burning the RCO/LCO-derived fuel oils is attributed to the lower sulfur content of these fuel oils compared to the baseline No. 6 fuel oil. As reported in **Table 4-2**, the weight percent of sulfur in the No. 6, co-processed, and RCO bottoms fuel oils is 1.8, 0.06 and 0.54 wt.%, respectively.

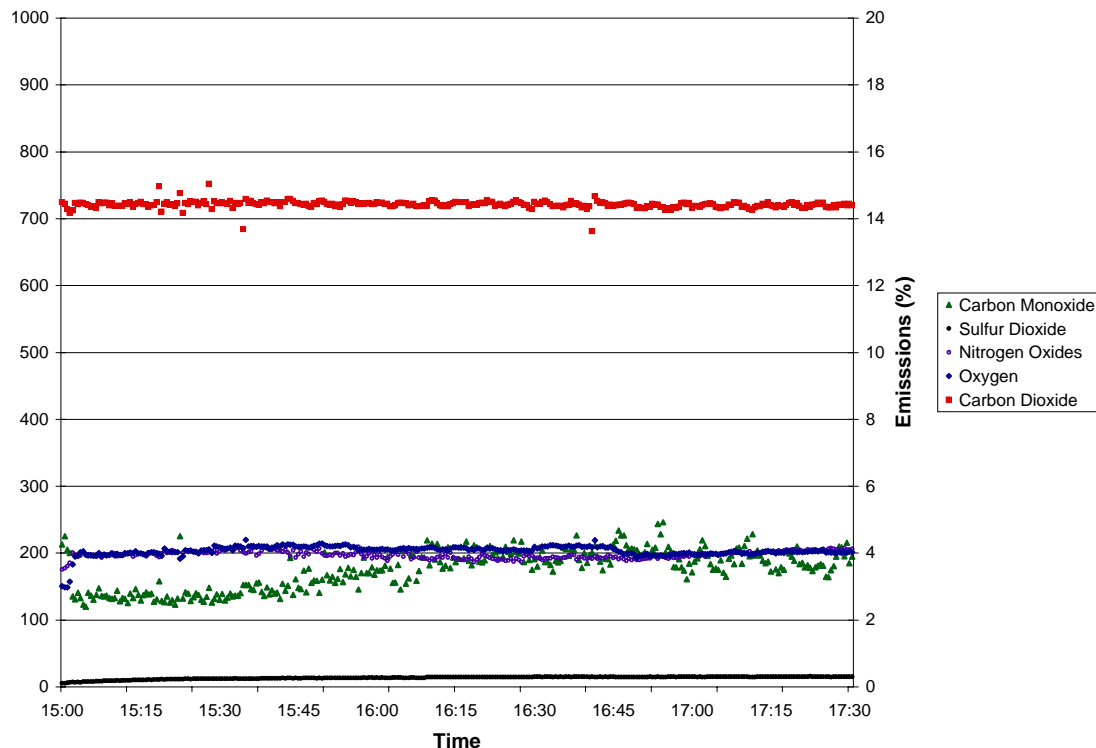


Figure 4-7 Emissions (on a 3% O₂ basis) as a function of time for RCO/LCO co-processed fuel oil testing on 08/02/06

Although numerous researchers have shown fuel NO_x to be an important mechanism in NO_x formation from fuel oil with a strong correlation between the percent nitrogen in the fuel oil versus NO_x formation, there appears to be no such correlation in the various fuel oils tested [4-19]. This may suggest that the differences can be attributed to a more dominant mechanism of thermal NO_x formation within the oil flames. The decrease in NO_x emissions when firing the co-processed fuel oil must reflect a decrease in thermal NO_x, which may have resulted from preheating the co-processed fuel oil to a lower temperature. Although the RCO bottoms fuel oil contains the greatest amount of fuel-bound nitrogen, its believed that the higher NO_x emissions from this fuel oil can be attributed to a greater availability of oxygen resulting from higher excess air levels.

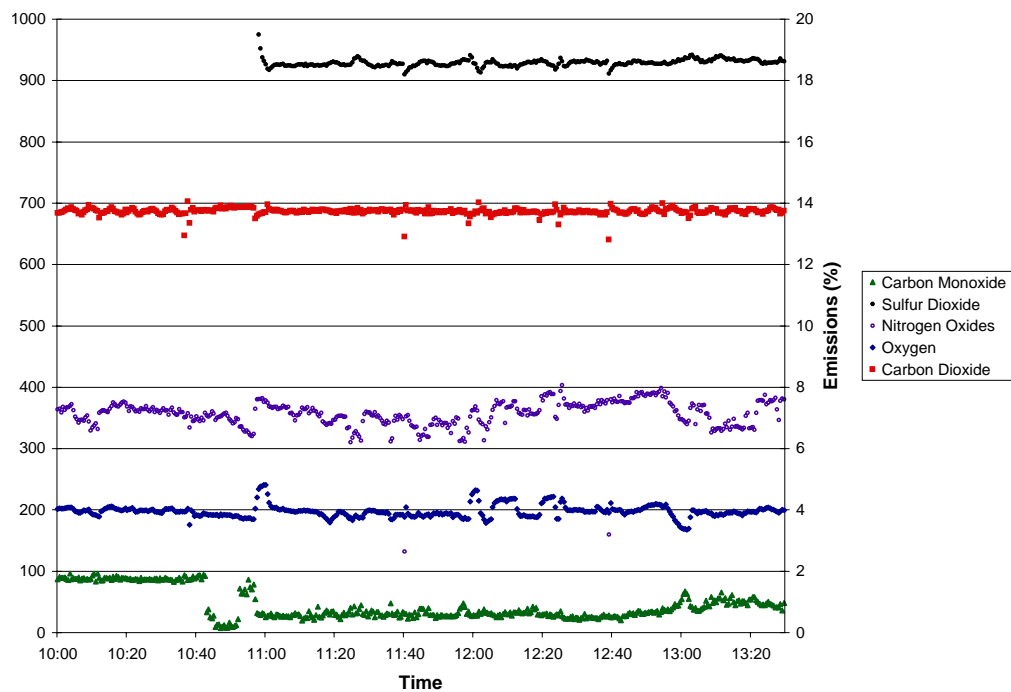


Figure 4-8 Emissions (on a 3% O₂ basis) as a function of time for No. 6 fuel oil testing on 08/07/06

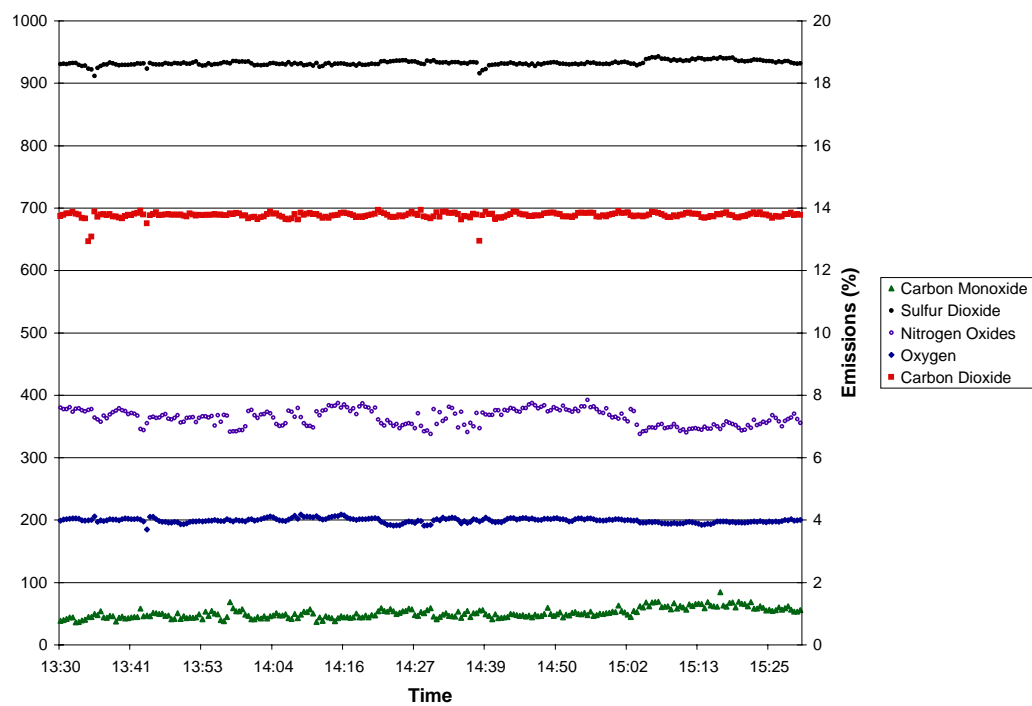


Figure 4-9 Emissions (on a 3% O₂ basis) as a function of time for No. 6 fuel oil testing on 08/07/06

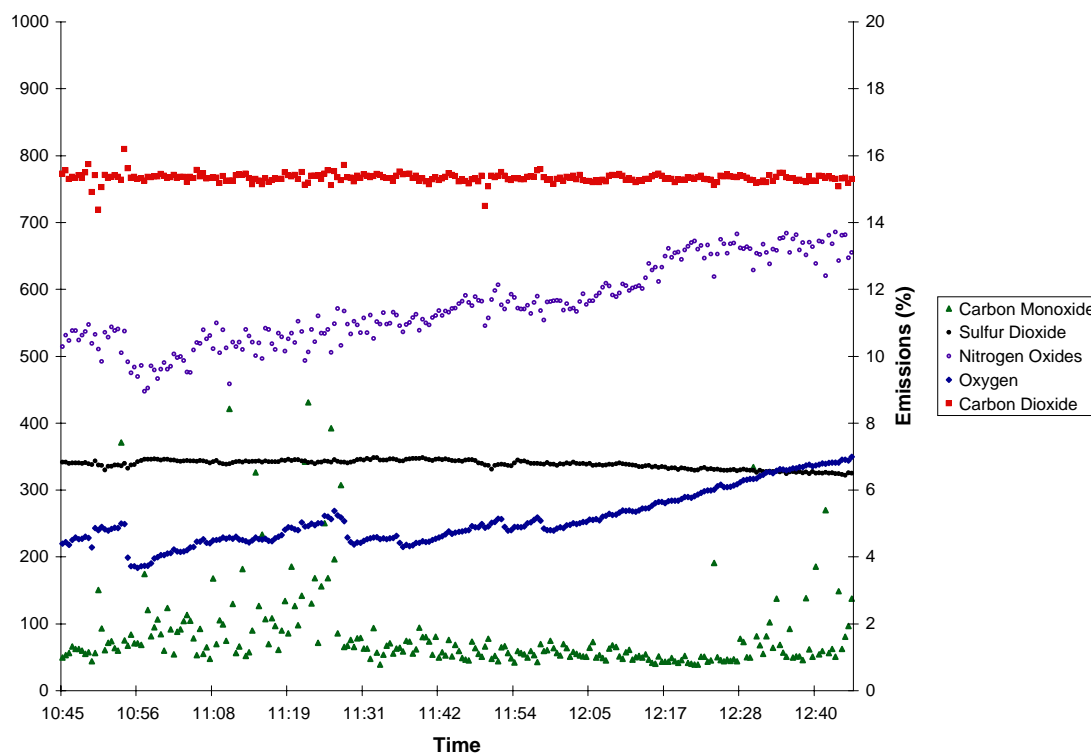


Figure 4-10 Emissions (on a 3% O₂ basis) as a function of time for RCO bottoms (X1333) testing on 08/14/06

The efficiency for the six tests performed burning the baseline No. 6 fuel oil varied between 70.3 and 73.3%, while the efficiency determined when burning the co-processed fuel oil on 05/24/05 and 08/02/06 was 71.6% and 70.4%, respectively. The efficiency determined for the RCO bottoms testing was lower because of the reduced firing rate (1.13 MM Btu/h). Since the efficiency for the co-processed fuel oils lie within the spread of efficiencies determined for the baseline fuel oil, there appears to be no differences in boiler performance between the fuel oils. The detailed thermal efficiency calculations are provided in Appendix B.

4.4.3 Trace Element Emissions Testing of No. 6 Fuel Oils and Co-Processed Fuel Oils

Trace element emissions are a function of combustion conditions, concentration and mode of occurrence of metals in the oil, and type of particulate control device (PCD), as they affect collection efficiency and particle size distribution. The behavior of various elements during coal combustion has been extensively studied. Categories regarding the partitioning of

elements between gas and solid phases have been devised based on the work of several researchers and reported by Clarke and Sloss [20], which are illustrated in **Figure 4-11**.

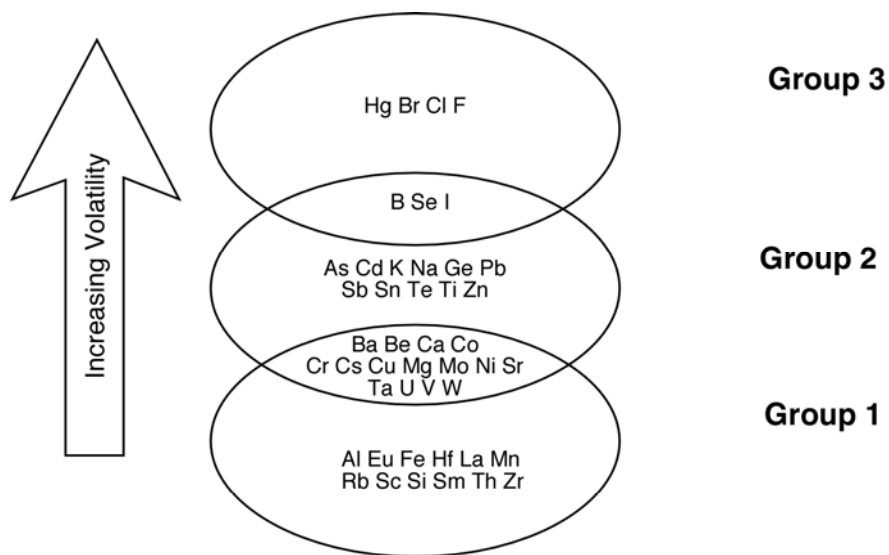


Figure 4-11 Classification of trace elements by their behavior during combustion and gasification. Modified from Clarke and Sloss [4-20]

Group 1: Elements are concentrated in the bottom ash or equally partitioned between bottom ash and fly ash, which is usually trapped by PCDs.

Group 2: Elements concentrated more in the fly ash than the bottom ash. They are also enriched on fine-grained particles, which may escape the PCD.

Group 3: Elements that readily volatilize and are concentrated in the gas phase and depleted in the solid phase.

Some elements demonstrated partitioning behavior that is intermediate between groups. This is a reflection of the volatility of the element and its behavior in varying combustion systems. Although this classification was developed for solid fuels, they are applicable to oil-fired systems.

Operating variables that affect the behavior of inorganic elements (primarily Group 2 elements) during combustion include flame temperature and local O_2 concentration. These variables are especially affected when using low NO_x firing strategies. Lower combustion temperature may reduce the volatilization of Group 2 metals, thereby reducing their

concentration in the fine particulates. Lower O₂ levels decrease the oxidation of volatile metals to less volatile oxides. Group 2 metals would remain in the vapor phase thereby increasing their concentration in the finer particulate. Group 1 and 3 elements would be unaffected. The partitioning behavior of the elements classified as intermediates may shift with changes in temperature and O₂ concentration.

According to a report titled “Compilation of Air Pollution Emission Factors” (AP-42) published by the U.S. EPA, Office of Air Quality planning and Standards (<http://www.epa.gov/ttn/chief/ap42/ch01/>) [4-21], metal behavior based on data obtained from oil-fired boilers were classified as follows (see **Table 4-7**):

Table 4-7 Metal Partitioning in Oil-Fired Combustors

Class	Description	Elements
1	Equal distribution between fly ash and soot	Al, Co, Cr, Fe, Mn, Se, Ti
2	Enriched in fly ash relative to soot	As, Cd, Pb, Sb
3	Intermediate to Class 1 and 2; multiple behavior	Cr, Ni
4	Emitted in gas phase	Hg

4.4.3.1 Sampling Procedure and Analytical Methodology

The metal emissions sampling and recovery procedure during combustion testing of the co-processed fuel oil was performed using the PSU Method, which is a combination of the procedures outlined in the EPA Method 29 and Ontario Hydro Mercury Speciation Methods. EPA Method 29, Determination of Metals Emissions from Stationary Sources, was used to measure trace elements in the gas and particulate phases of the flue gases generated during coal combustion [4-22]. The Ontario Hydro Method is used to determine the speciation of mercury, *i.e.*, elemental and oxidized [4-23]. Modification of the Ontario Hydro train included omission of one KCl impinger and one H₂SO₄/KMnO₄ impinger and the addition of a HNO₃/H₂O₂ impinger. The PSU Method is shown schematically in **Figure 4-12**. The configuration was based on discussions with University of North Dakota Energy and Environmental Research Center and testing conducted at Penn State. The recovery protocol for the filter, filter rinse, HNO₃/H₂O₂ and H₂SO₄/KMNO₄ samples are the same for Method 29 and the Ontario Hydro Mercury Speciation

Method. The recovery and sample preservation of the KCl solution followed the Ontario Hydro Mercury Speciation Method.

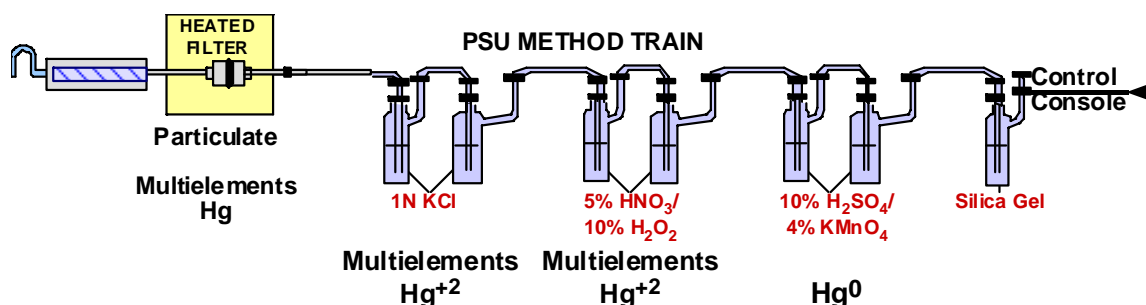


Figure 4-12 PSU Method sample train

The sampling position of the train downstream of the combustor, prior to the baghouse, was in accordance with EPA Method 1 (Sample and Velocity Traverses for Stationary Sources) as shown in **Figure 4-4**. The traverse sampling locations within the duct were modified from EPA Method 1 to include a horizontal traverse consisting of 4 equidistant points. Total volume of gas sampled was 61.7 actual cubic feet (Method 29 specifies 60 actual cubic feet) over a period of 93 minutes.

The sample preparation, *i.e.*, digestion, and analytical techniques for the multielements and mercury for the current PSU Method are shown in **Figure 4-13**. One solid (filter) and three liquid samples (combined KCl impingers, combined HNO₃/H₂O₃ impingers and combined H₂SO₄/KMnO₄ impingers) are generated during each test and analyzed as indicated in **Figure 4-13**. A detailed discussion of sample preparation and analysis for the PSU Method and EPA digestion methods is presented elsewhere [4-24, 4-25, 4-26].

4.4.3.2 Results and Discussion

The results of the trace elements emissions testing are presented by project year. This was done primarily to organize the results in an easily presentable manner.

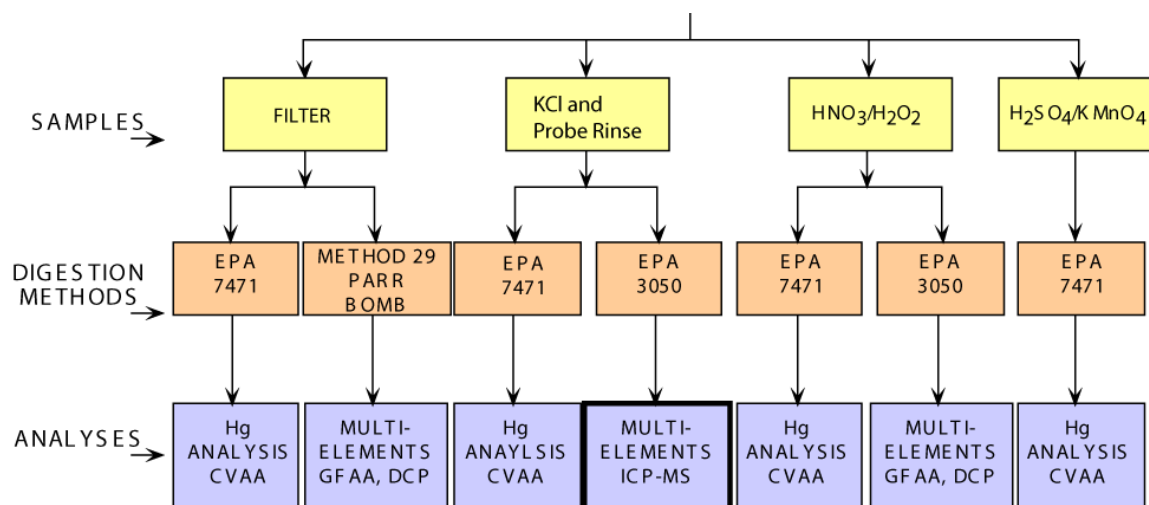


Figure 4-13 Sample preparation and analytical techniques for PSU Method sample train

Year 1 Testing

As previously discussed, in Year 1, no co-processed fuel oil was available from Intertek PARC. Consequently, testing was performed with commercial No. 6 fuel oil to generate baseline emissions data and develop fuel analysis protocols.

Three sampling tests were performed (RI-PSU-1A, RI-PSU-2A, and RI-PSU-2B). RI-PSU-1A is the label for the test with fuel oil No. 6 on 6/16/04, and RI-PSU-2A and RI-PSU-2B are the labels for tests with fuel oil No. 6 on 7/07/04, done on the same day. The emission data sheets are given in Appendix C for each test. The sheets contain operational information as well as the analysis for the fuel oil and each portion of the train. The total emissions for each of the tests are given in **Table 4-8** and are reported in lbs/10¹² Btu. In addition to the measured emissions, calculated emissions based on the emission factors published by the US EPA [4-27] are provided.

The United States EPA has published a document, “Compilation of Air Pollutant Emission Factors”, referred to as AP-42, since 1972. Supplements to AP-42 have been routinely published to add new emissions source categories and to update existing emission factors. This document is also provided on EPA’s website on their CHIEF [Clearinghouse for Inventories and Emissions Factors; www.epa.gov/ttn/chief/ap42] bulletin board. The emission factors used are given in **Table 4-9** and are taken from Report on Revisions to 5th Edition AP-12, Section 1.3 [4-27].

Table 4-8. Total Emissions Measured during Combustion Tests and Calculated Emissions Based on AP-42 Emission Factors

Element	Emissions (lb/10 ¹² Btu)			
	RI-PSU-1A	RI-PSU-2A	RI-PSU-2B	*AP-42 Emission Factor Calculation
Al	2809.33	918.70	1239.14	na
As	20.13	24.22	14.17	8.67
Ba	37.07	16.67	23.67	16.88
Be	0.42	0.16	0.23	0.183
Cd	0.41	0.14	0.19	2.61
Co	39.78	38.61	43.04	39.53
Cr	9.18	3.87	4.73	5.55
Cu	10.84	15.75	17.38	11.59
Hg	0.80	0.29	0.26	0.753
Mn	237.16	62.42	10541.12	19.7
Mo	3.27	4.47	2.88	5.17
Ni	892.00	991.93	1024.00	554.93
Pb	12.72	9.27	4.87	9.92
Sb	13.32	14.78	15.85	34.48
Se	7.78	1.94	3.27	4.49
Sr	43.61	13.23	23.37	--
V	2345.70	2311.23	2531.41	208.8
Zn	106.19	77.57	77.78	191.1

* Based on Revised Emission Factors [4-27].

Na – not available

Table 4-9 Emission Factors for Metals from Oil-fired Combustors

Element	Emission Factor (lb/1000 gallons)	Emission Factor Rating
As	1.32e-03	C
Ba	2.57e-03	D
Be	2.78e-05	C
Cd	3.98e-04	C
Cr	8.45e-04	C
Co	6.02e-03	D
Cu	1.76e-03	C
Pb	1.51e-03	C
Mn	3.00e-03	C
Hg	1.13e-04	C
Mo	7.87e-04	D
Ni	8.45e-02	C
Sb	5.25e-03	E
Se	6.83e-04	C
V	3.18e-02	D
Zn	2.91e-02	D

Emission factors may be appropriate to use in a number of situations such as source-specific emission estimates for area-wide inventories. These inventories have many purposes including ambient dispersion modeling and analysis, control strategy development, in screening sources for compliance investigations, and in some permitting applications. Emission factors in AP-42 are neither EPA-recommended emission limits (*e.g.*, Best Available Control Technology (BACT), or Lowest Achievable Emission Rate (LEAR)) nor standards (*e.g.*, NSPS or NESHAP).

Emission factors and emissions inventories have long been fundamental tools for air quality management. Emission estimates are important for developing emission control strategies, determining applicability of permitting and control programs, ascertaining the effects of sources and appropriate mitigation strategies. Users include Federal, state, and local agencies, consultants, and industry. Data from source-specific emission tests or continuous emission monitors are usually preferred for estimating a source's emissions because those data provide the best representation of the tested source's emissions. However, test data from individual sources are not always available and they may not reflect the variability of actual emissions over time. Consequently, emission factors are often the best or only method available for estimating emissions.

The calculated emissions for the fuel oil testing were derived by the following equation:

$$(EF_{\text{element}})(1/\text{HHV}_{\text{fuel oil}})(1/10^{12} \text{ Btu}) = \text{Calculated Emissions} \quad (4-3)$$

where the units are as follows:

$$(\text{lb}/1,000 \text{ gallons})(1 \text{ gallon fuel}/152,272 \text{ Btu})(10^{12} \text{ Btu}/10^{12} \text{ Btu}) = \text{lb}/10^{12} \text{ Btu}.$$

Note that each average emission factor is given an “emission factor rating” (**Table 4-9**). The reliability of the AP-42 emission factors are rated from A (excellent) through E (poor), which is a general indication of the robustness of that factor. This rating is assigned based on the estimated reliability of the tests used to develop the factor. In general, factors based on many observations, or on more widely accepted test procedures, are assigned higher rankings with A being the best. All of the trace metal emission factors received a rating of C or less and are described as follows:

C-Rating (average): developed only from A- and B-rated test data from a reasonable number of facilities. It is not clear if the facilities tested represent a random sample of the industry. The source category is specific enough so that variability within the source category population may be minimized.

D-Rating (below average): developed only from A- and B-rated test data from a small number of facilities and there is reason to suspect that these facilities do not represent a random sample of the industry. There is also evidence of variability within the source category population. This provides an order-of-magnitude calculation.

E-Rating (poor): emission factor developed from C- and D-rated test data and there is reason to suspect that these facilities do not represent a random sample of the industry. There is also evidence of variability within the source category population.

Graphic comparisons of the measured to the AP-42 calculated emissions are given in **Figures 4-14 and 4-15**. There was a significant amount of variability in the emissions measured and there are only three data points for each element, therefore, comparison of the AP-42 calculated emissions is based on whether the AP-42 value is within the range of the three measured values. Special consideration was taken in the case of elements having a D rating. If the calculated value was within an order of magnitude of the measured value, then it was considered to meet the AP-42 standard.

Calculated emissions that were within the range of measured emission are as follows: Be, Hg, Mo, Se, Cr, Pb, Cu, Ba, and Co. Calculated emissions that were not within the range of

measured emission are as follows: Cd, Sb, Zn, Mn, Ni, and V. Emission factors are not available for Al and Sr. Nine of the 15 elemental emissions for which AP-42 emission factors exist were within the range of the three measured. Given the highly variable nature of the measured data it would be misleading to make any significant conclusions as to the usefulness of AP-42 emission factors in predicting emissions. In order to draw any further conclusions would necessitate conducting several more replicate test runs and doing a statistical analysis of the data. This comparison was made to highlight the need for stack testing to generate reliable metal emissions data.

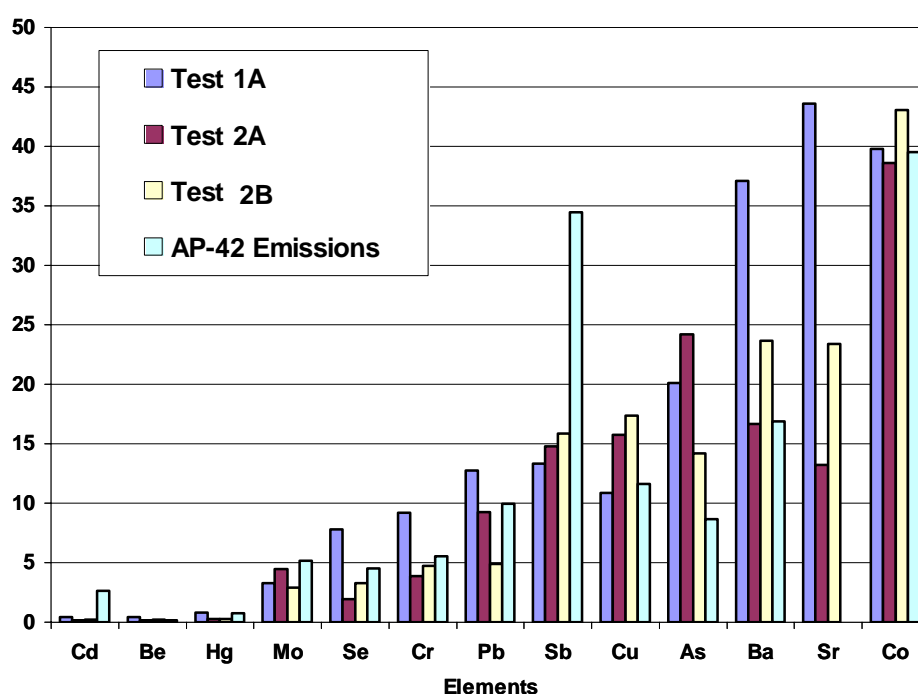


Figure 4-14 Measured and calculated emissions for selected elements

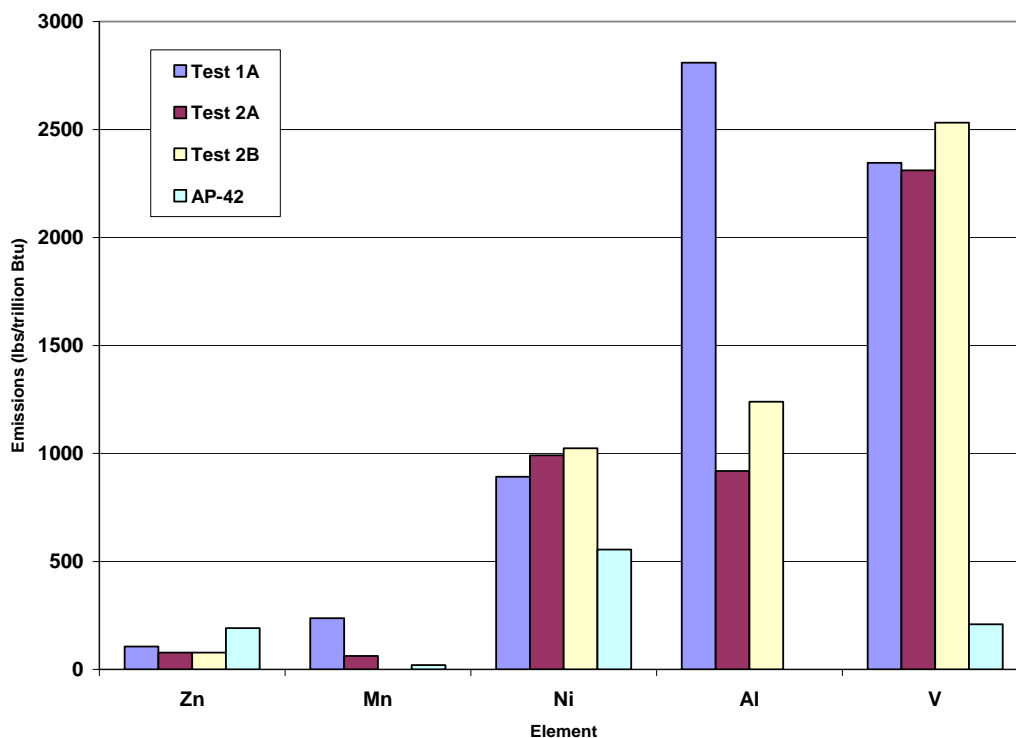


Figure 4-15 Measured and calculated emissions for selected elements

In addition to the total emissions it is important to note the partitioning of the elements as discussed in the previous section. The average percent of each element in the solid and gas phase is given in **Table 4-10** and shown in **Figure 4-16**. The partitioning of the elements (% solid verses % gas phase) for each test is shown in **Figures 4-17 through 4-19**.

There is variability between the three tests; however, the average partitioning of the elements seems to follow the general pattern of behavior discussed earlier. The majority of the elements were concentrated in the solid phase, *i.e.*, particulate matter captured on the train filter. The elements that are of the greatest environmental concern are also those elements that have a significant occurrence in the gas phase, *i.e.*, Hg, As and Se.

Table 4-10 Average Weight % of Each Element in Solid and Gas Phase in Flue Gas Measured During Combustion Tests

Element	Avg Weight %	
	Solid	Gas
Al	93.3	6.7
As	33.0	67.0
Ba	91.6	8.4
Be	100.0	0.0
Cd	95.6	4.4
Co	100.0	0.0
Cr	80.5	19.5
Cu	43.7	56.3
Hg	24.5	75.5
Mn	9.9	90.1
Mo	84.0	16.0
Ni	98.2	1.8
Pb	99.3	0.7
Sb	100.0	0.0
Se	60.8	39.2
Sr	93.3	6.7
V	99.7	0.3
Zn	73.5	26.5

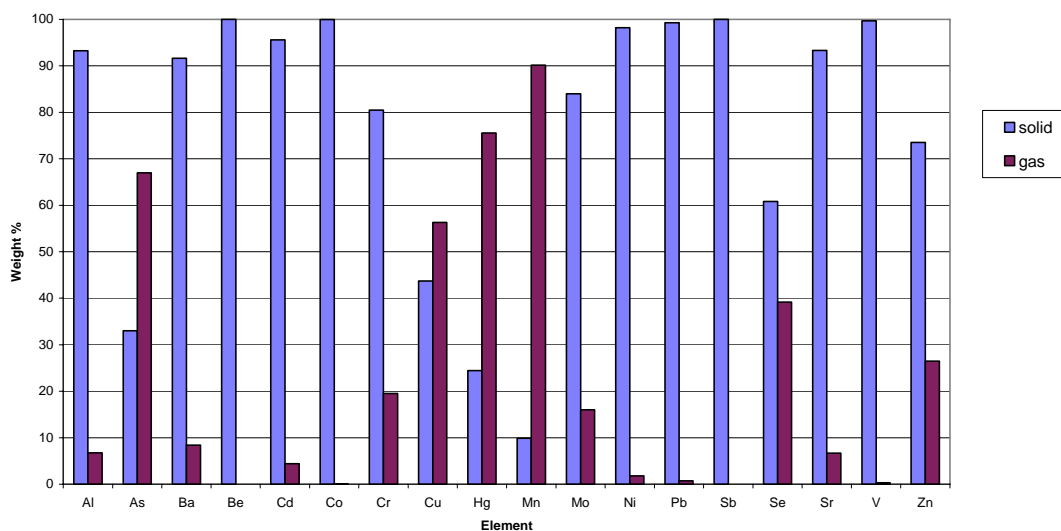


Figure 4-16 Average partitioning of elements between solid and gas phase by weight percent for tests 1A, 2A and 2B

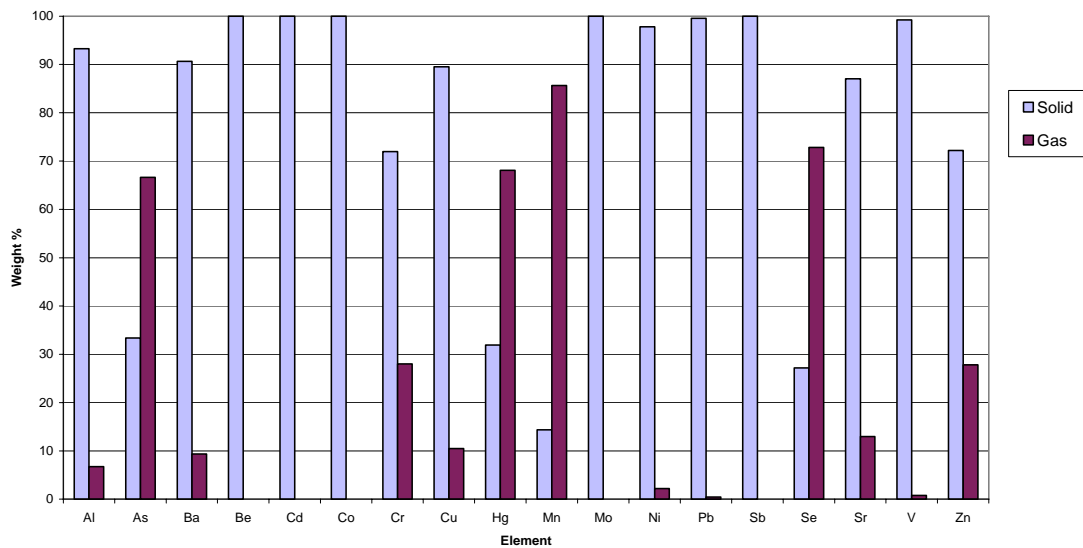


Figure 4-17 Partitioning of elements between solid and gas phase by weight % for test RI-PSU-1A.

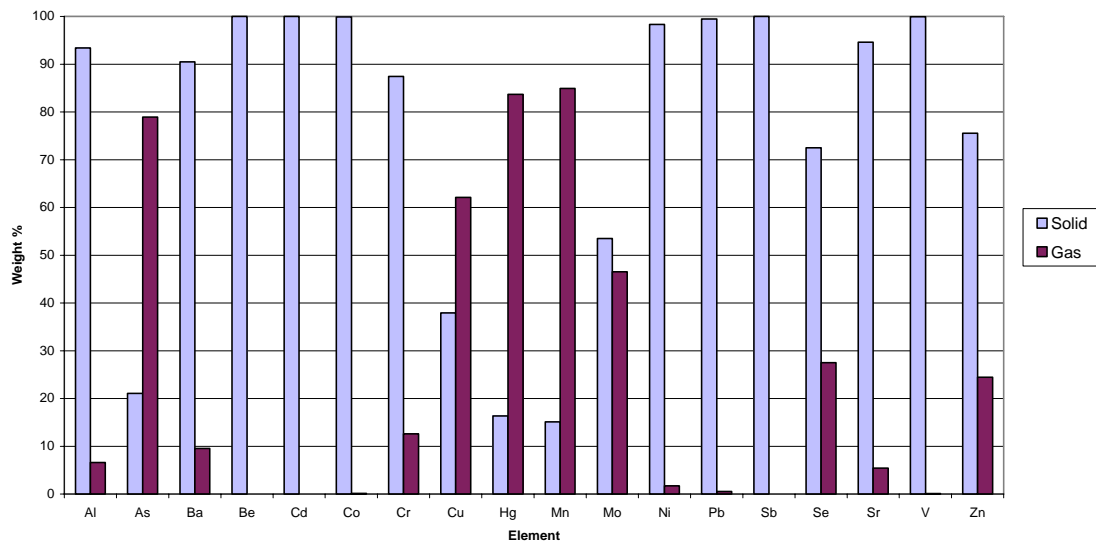


Figure 4-18 Partitioning of elements between solid and gas phase by weight % for test RI-PSU-2A

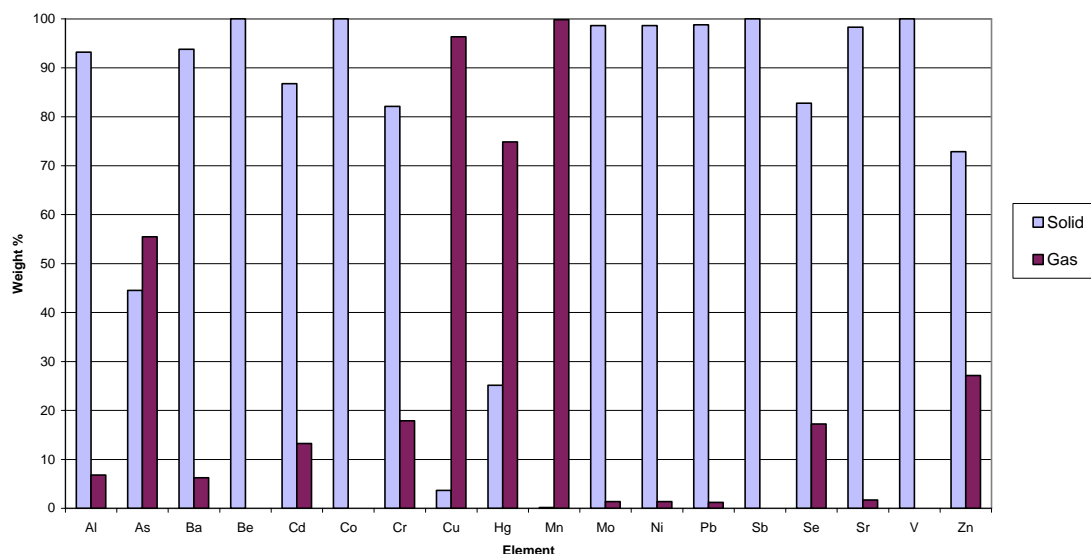


Figure 4-19 Partitioning of elements between solid and gas phase by weight % for test RI-PSU-2B

The Group 3 element Hg occurred primarily in the gas phase (75.5%). Selenium (Group 2-3 transition element) and As (Group 2 element) both have a significant portion in the gas phase (39.2 and 67%, respectively). The Group 1 and 2 elements are concentrated in the particulate matter. The Group 2 elements occurred predominantly in the solid phase as follows: 73.5% (Zn), 95.6% (Cd), 99.3% (Pb), to 100% (Sb). The exception is As. Arsenic has been shown to occur in the gas phase during coal combustion to a greater extent than other Group 2 elements. The concentration of Group 1 and Group 1-2 transition elements (Al, Ba, Be, Co, Mo, Ni, Sr, and V) in the solid phase ranged from 80.5% (Cr) to 100% (Be and Co). Copper and manganese are an exception in that they are concentrated in the gas phase (56.3 and 90.1%, respectively).

It is necessary to study elements that are not typically associated with fuel oils as fuels that are produced during co-processing of coal and petroleum-derived fuels. It is important to understand the effect of incorporating inorganic elements into an oil on gas and particulate emissions.

Year 2 Testing

The metals that are routinely associated with coal are not necessarily present or present in low-levels in petroleum-derived fuel oil. For example, at the end of the 1990's, 6.6 tons mercury/yr was being emitted by stationary oil combustion and 48 tons/yr was being emitted by stationary coal combustion [4-4]. The greater emission rate of coal-fired plants is attributed to the higher levels of mercury in coals. The mercury content of coals can average from 0.07 to 0.12 ppm depending upon the rank (lignite to bituminous coal). Most coals contain approximately 0.1 ppm mercury (ten times as much mercury as in oil) whereas crude oil averages about 10 ppb.

As previously discussed, on March 15, 2005, EPA issued the first ever Federal rule to permanently cap and reduce mercury emissions from coal-fired power plants. When fully implemented in 2018, mercury emissions will be reduced from 48 tons/yr to 15 tons/yr, a reduction of 69%. A question that co-processing coal by-products and oil refinery products raises is – Will oil-fired power plants be subjected to the same regulations as coal-fired plants if coal is a feedstock in producing fuel oil? About 10 billion gallons of residual fuel oil are consumed annually in the United States [4-28]. Of this total, approximately 6, 3, and 1 billion gallons are consumed in the utility, industrial, and commercial sectors, respectively [4-28].

The mercury emitted from oil combustion represents about 10% of the U.S. yearly emission rate of atmospheric mercury from coal and oil combustion combined. However, this could change with the integration of coal into the processing/production of liquid hydrocarbon fuels. The emissions of mercury from fuel oils derived from petroleum and coal will exhibit mercury concentrations that reflect the concentration of mercury in the parent crude oil as well as any mercury or other trace elements that are extracted from the coal during processing. Therefore it is essential that there be an accurate way to measure the levels of trace elements in these fuels to determine if they pose any environmental threat thereby compromising the fuel.

To address this concern, testing began in Year 2 to compare the emissions produced during the combustion of petroleum-derived fuel oil with those from the combustion of co-processed fuel oil. Emissions results for three combustion tests using a No. 6 fuel oil and one combustion test using a co-processed fuel oil are given in **Table 4-11** and **Figures 4-20 and 4-21**. Detailed results are given in Appendix C. In general, the concentration of metals (*i.e.*, As, Ba, Be, Cd, Cr, Cu, Hg, Mo, Sb, Sr, Al, Pb, Zn) in the emissions measured for the co-processed fuel

oil is greater than that measured during combustion of the petroleum-derived fuel oil. Only Ni and V are consistently present in higher levels in the petroleum-derived fuel oil than in the co-processed fuel oil. Co and Se are present in similar levels given the variability of the measurement of those elements in the petroleum-derived fuel oil.

The metals present at higher concentrations in the co-processed fuel oil emissions are metals that are typically found in coal. It might be assumed that the processing of the coal to form the liquid hydrocarbon (*i.e.*, RCO) results in the incorporation of the metals into the liquid phase. Ni and V are traditionally not present in coal in significant amounts but are present in crude oil. This may account for the higher concentration of Ni and V in the petroleum-derived fuel oil emissions.

The manner in which the mercury occurs in the flue gas, *i.e.*, gas phase or associated with the particulate matter, is given on a percentage basis in **Figure 4-22**. In general, oxidized mercury is more problematic since it is water-soluble and tends to react with surface water to form methylated mercury.

Year 3 Testing

In Year 3, trace metal emissions sampling was performed during combustion testing of the baseline No. 6 fuel oil (duplicate sample trains conducted on 08/07/06), sample X610 (conducted on 08/02/06), and the X1333 sample (conducted on 08/14/06) using the PSU Method. It was not possible to conduct two sequential sample trains during testing of the co-processed fuels as there was not enough of either fuel to burn in order to sample the total volume of flue gas as prescribed by the EPA Method 29.

Table 4-11 Combustion test emissions for No. 6 fuel oil and co-processed fuel oil (lb/10¹² Btu)

Element	Emissions (lb/10 ¹² Btu)			
	Petroleum-Derived Fuel Oil (1A)	Petroleum-Derived Fuel Oil (2A)	Petroleum-Derived Fuel Oil (2B)	Co-processed Fuel Oil (3A)
Al	2809.33	918.70	1239.14	36419.10
As	20.13	24.22	14.17	224.08
Ba	37.07	16.67	23.67	187.35
Be	0.42	0.16	0.23	12.09
Cd	0.41	0.14	0.19	1.21
Co	39.78	38.61	43.04	48.35
Cr	9.18	3.87	4.73	69.32
Cu	10.84	15.75	17.38	62.89
Hg	0.80	0.29	0.26	2.09
Mn	237.16	62.42	10541.12	8629.09
Mo	3.27	4.47	2.88	122.89
Ni	892.00	991.93	1024.00	117.26
Pb	12.72	9.27	4.87	1580.45
Sb	13.32	14.78	15.85	27.41
Se	7.78	1.94	3.27	6.85
Sr	43.61	13.23	23.37	122.89
V	2345.70	2311.23	2531.41	227.64
Zn	106.19	77.57	77.78	617.79

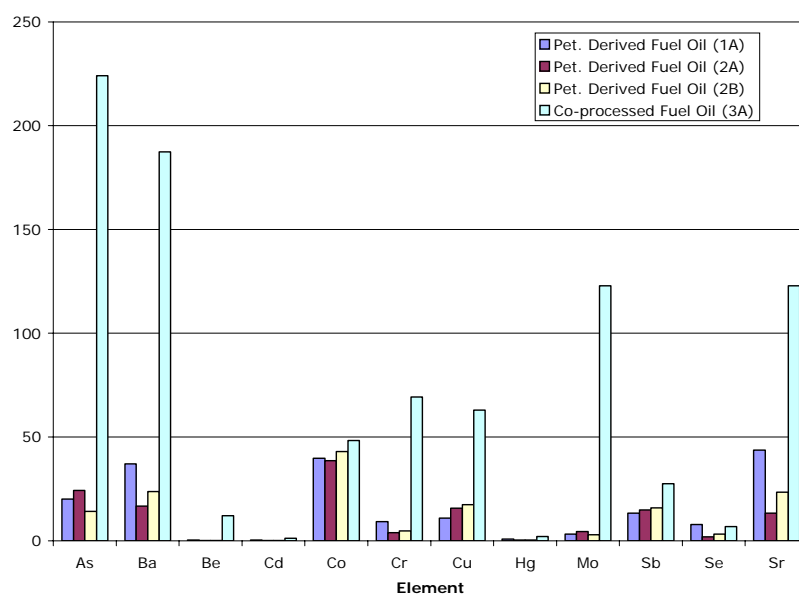


Figure 4-20 Elemental emissions for petroleum-derived and co-processed fuel oils (Part 1)

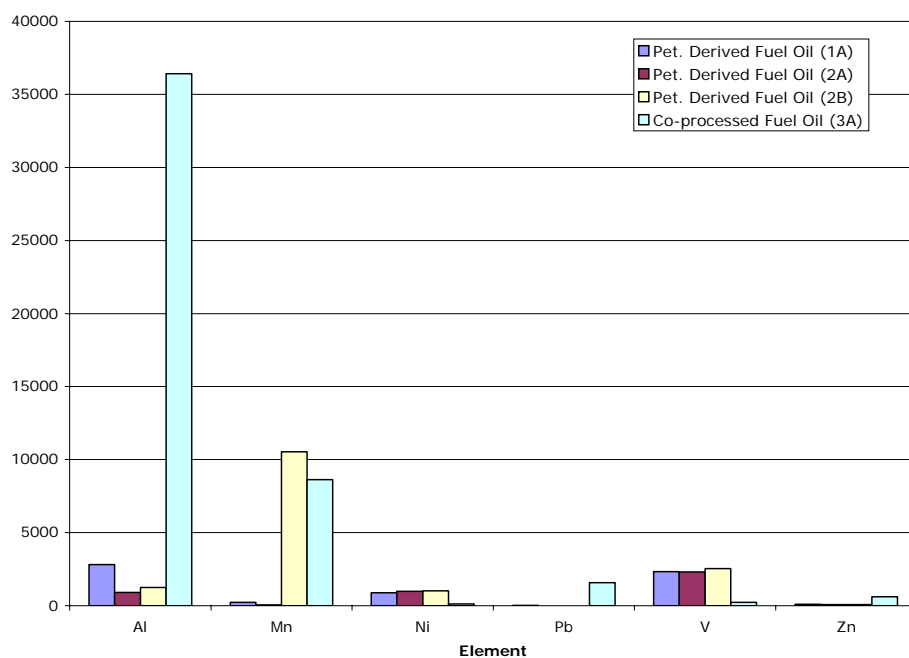


Figure 4-21 Elemental emissions for petroleum-derived and co-processed fuel oil (Part 2)

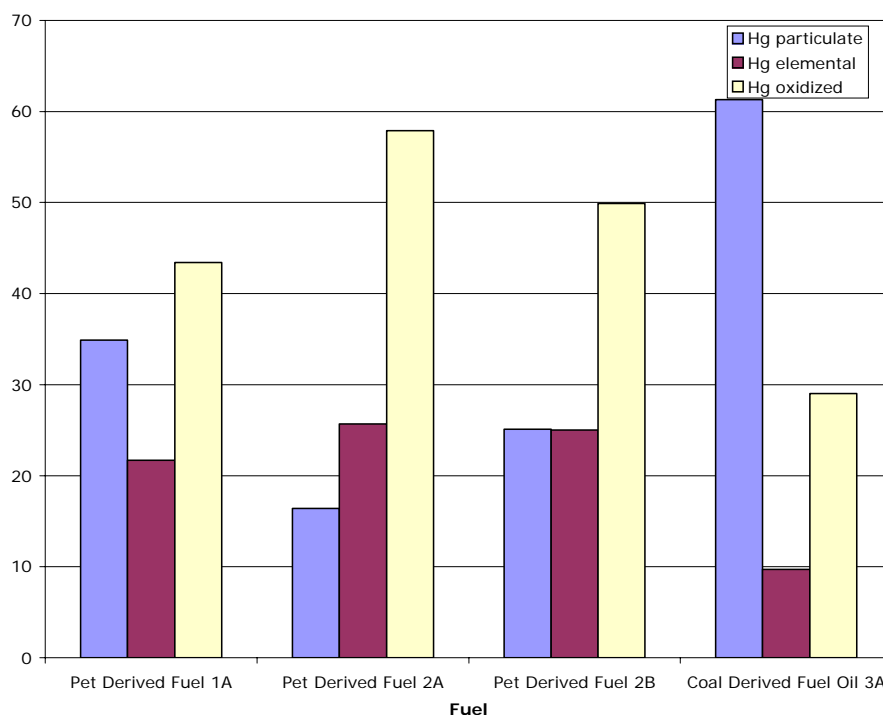


Figure 4-22 Mercury speciation measured in emissions for petroleum-derived fuel oil and co-processed fuel oil.

The elements analyzed for and the emissions measured for the fuels fired during the previous reporting period are given in **Table 4-12**. All elements measured except for Hg are referred to as “Multielements” in Figure 1. Elements of major environmental concern are As, Cd, Hg, Mo, Pb, and Se and are indicated in “red” type. Elements of moderate concern are Cr, Cu, Ni, V, and Zn and are indicated in “green” type. Elements of minor concern are Ba, Co, Mn Sb and Sr and are indicted in “blue” type. A series of graphs showing the relative amounts of emissions of trace metals is given in **Figures 4-23 through 4-33**. The graphs are grouped in order of greatest to least environmental concern.

Table 4-12 Elemental emissions measured at research boiler outlet for test fuels

Date	8/7/2006	8/7/2006	8/2/2006	8/14/2006
Fuel	#6 Fuel Oil	#6 Fuel Oil	Co-Processed Fuel Oil X610	RCO Bottoms X1333
	Emissions (lbs per trillion Btu)			
Al	467.1	788.3	1,678.7	2,541.4
As	6.2	21.2	14.4	14.7
Ba	66.5	65.9	24.5	69.4
Be	0.1	0.1	0.2	1.2
Cd	0.1	0.1	0.2	0.3
Co	25.2	23.5	2.4	9.8
Cr	1.9	2.1	6.5	65.6
Cu	3.4	4.8	11.1	31.4
Hg	0.3	0.3	0.2	0.3
Mn	14,585.4	13,201.5	3,423.7	9,676.9
Mo	4.9	4.4	5.7	6.7
Ni	1,228.3	1,065.0	60.2	164.9
Pb	9.7	7.4	8.9	16.7
Sb	1.8	1.8	1.6	3.3
Se	0.9	0.7	0.6	4.5
Sr	7.6	6.7	14.3	22.8
V	3,811.1	3,732.0	110.1	209.5
Zn	161.6	171.7	172.7	789.2

Elements of Greatest Environmental Concern (Figures 4-23 through 4-27)

The reason for analyzing for trace metals in the emissions from the co-processed fuels is to determine if coal-derived liquids introduce elements, normally associated with coal, of environmental concern into a liquid hydrocarbon fuel that are not commonly found in petroleum-derived fuels.

Co-processed fuel X1333 had the highest level of emissions for four (Pb, Cd, Mo, and Se) of the six elements of greatest environmental concern. Interestingly the No 6 fuel oil had the highest levels of As and Hg emissions which represent the top two elements of greatest environmental health concern due to their neurological effects on humans (**Figures 4-23 and 4-24**) The X610 and X1333 fuels had 38 and 15% less in Hg emissions. It should be noted that the level of As measured in the duplicate sample trains run during the fuel oil test had the least agreement than any other element. The No. 6 fuel oil averaged 13.7 lbs per trillion Btu which is very close to the 14.4 and 14.6 lb/10¹² Btu for the X610 and X1333, respectively. Therefore it is difficult to tell if there is significant difference in As emission between the fuels due to questionable reproducibility of the No. 6 fuel oil test.

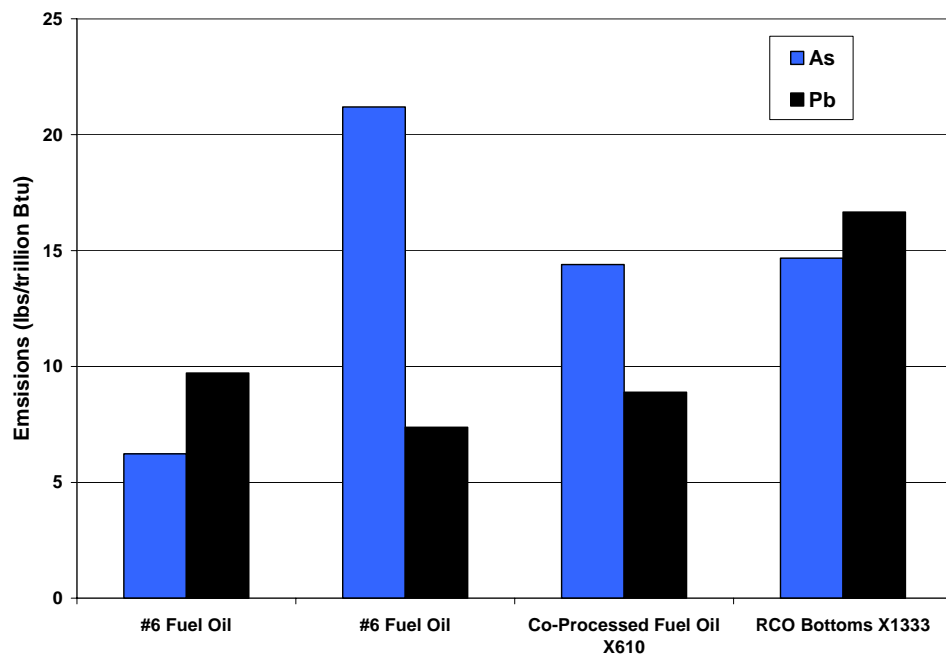


Figure 4-23 Arsenic and lead emissions for test fuels

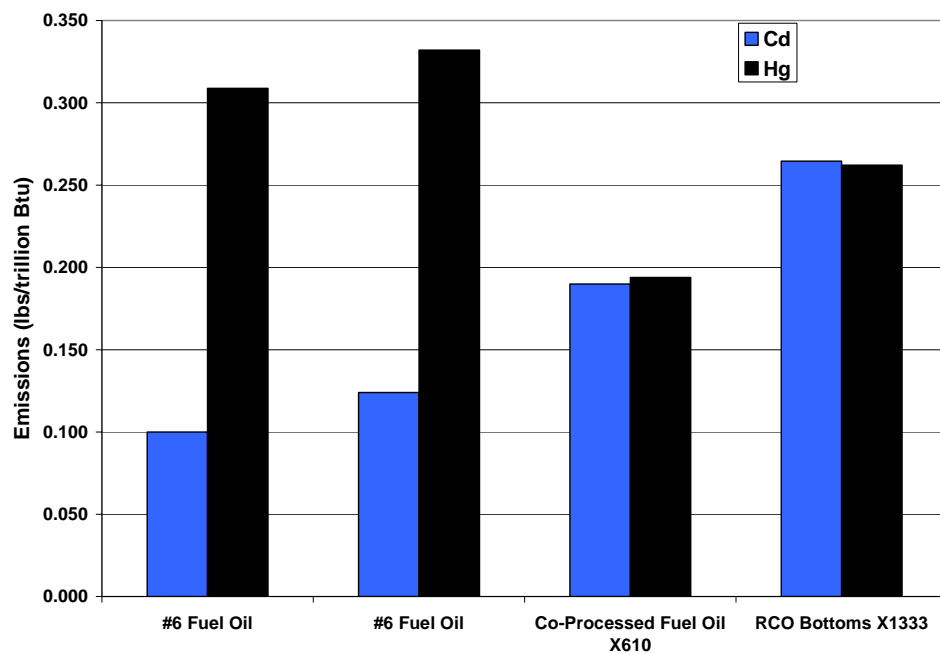


Figure 4-24 Cadmium and mercury emissions for test fuels

The selenium emission level for X1333 was significantly greater (4.5 lbs/10¹² Btu) than that for the X610 fuel (0.56 lbs/10¹² Btu) and the No. 6 fuel oil ((0.70-0.89 lbs/10¹² Btu) as shown in **Figure 4-25**).

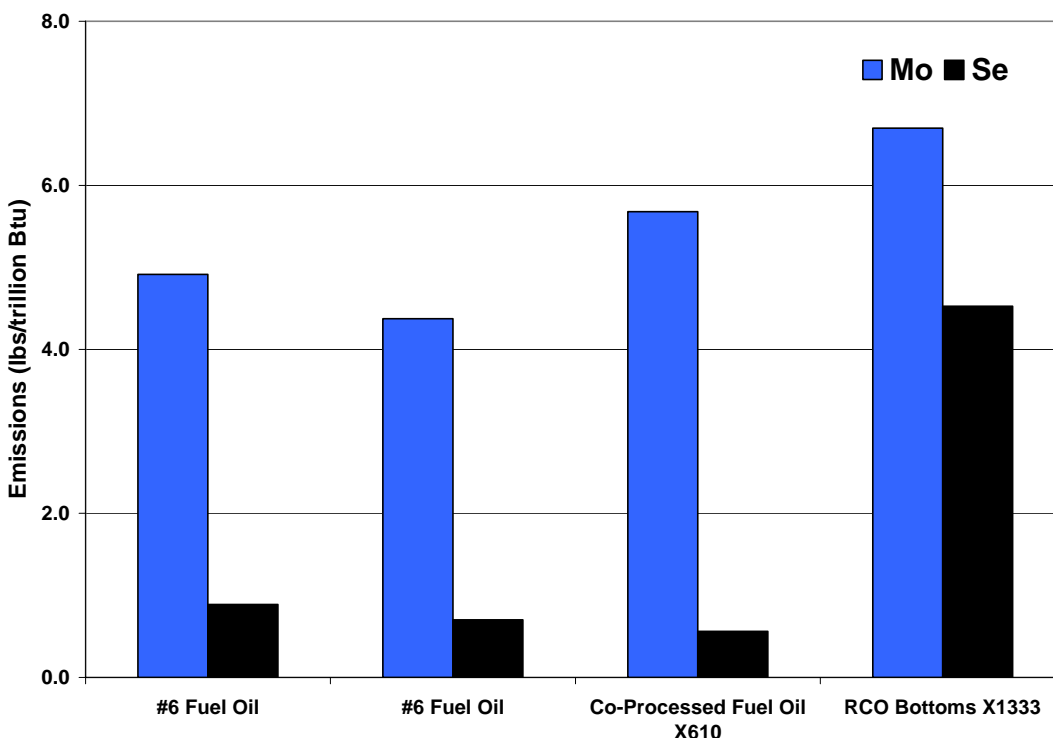


Figure 4-25 Molybdenum and selenium emissions for test fuels

Mercury speciation was also determined using the PSU Method sample train. Oxidized mercury (Hg⁺₂), elemental mercury (Hg⁰) and mercury in the particulate was determined. The data is given in **Table 4-13** and **Figures 4-26 and 4-27**. If the amount of a particular mercury species is present below detection limits then it is treated as a “non-detect” and no values are reported. The oxidized form of Hg is soluble in water and is the most reactive in the atmosphere forming methyl mercury as it reacts with surface and atmospheric water. This reactivity also makes oxidized mercury easier to recover (via control technologies) from the flue gas prior to being emitted into the atmosphere. Current control technologies are focused on oxidizing the elemental Hg so that it may be removed as well.

Table 4-13 Distribution of mercury species in emissions from fuels

Species	Hg^{+2}		Hg^0		Hg Particulate	
	Weight %	lbs/ 10^{12} Btu	Weight %	lbs/ 10^{12} Btu	Weight %	lbs/ 10^{12} Btu
No. 6 Fuel Oil	72.6	0.224	22.2	0.069	5.13	0.016
No. 6 Fuel Oil	74.1	0.246	20.4	0.067	5.49	0.018
X610			35.3	0.069	64.7	0.125
X1333	59.7	0.156			40.3	0.106

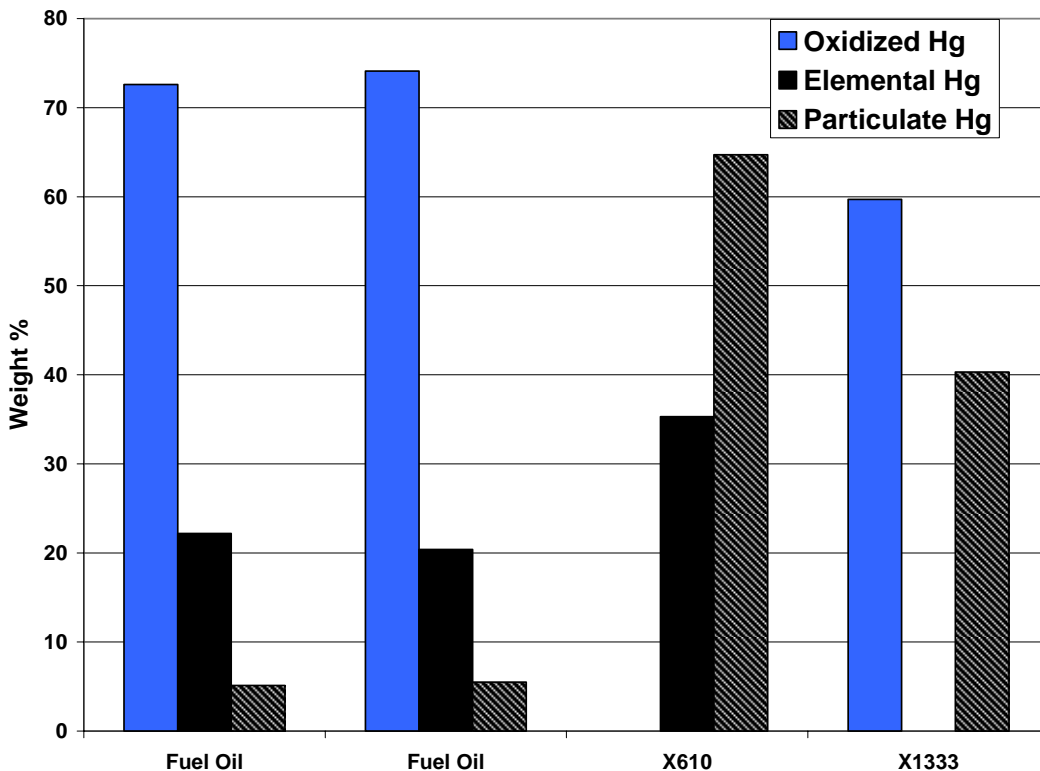


Figure 4-26 Weight percent of total mercury, by species, measured in emission for each fuel

The mercury in the No. 6 fuel oil emissions is present mostly as Hg^{+2} (> 70%) followed by Hg^0 (approximately 20%) with the remainder (5%) as mercury associated with particulate. Note that there is good agreement between the mercury analysis of the duplicate fuel oil trains. The mercury in the flue gas stream had very different modes of occurrence for the co-processed fuels. The X610 fuel has most of the mercury as particulate (65%) and the rest as Hg^0 (35%) and essentially no Hg^{+2} . The X1333 fuel had significant Hg^{+2} (60%) and 40% particulate Hg.

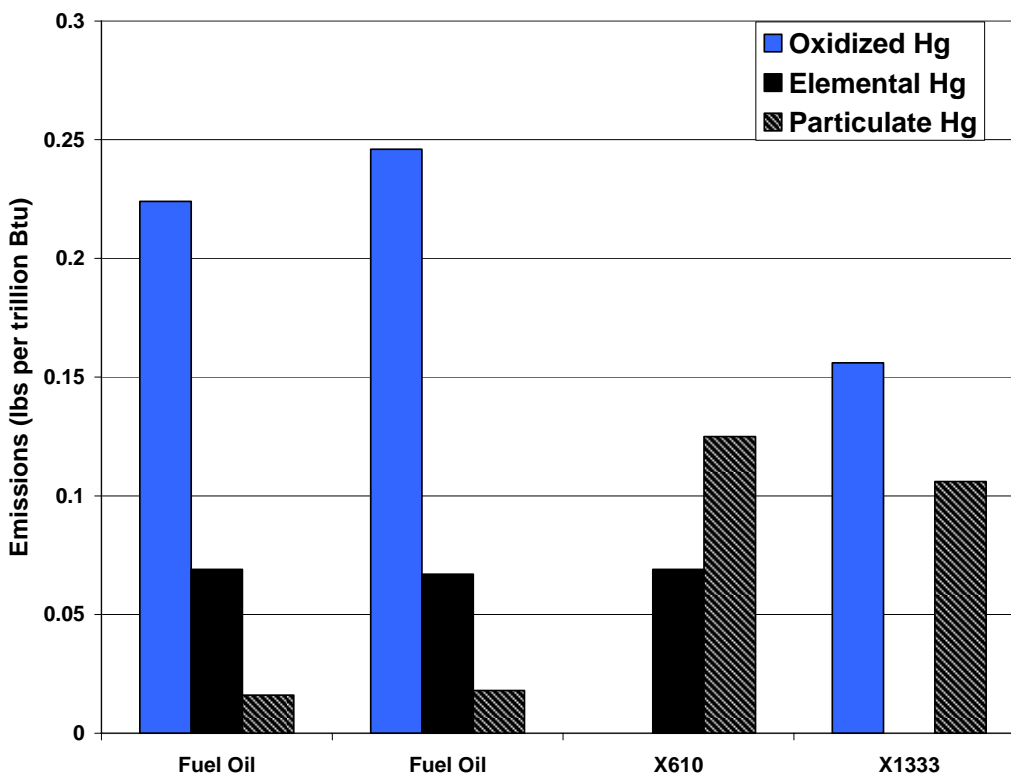


Figure 4-27 Mercury emissions, by species, measured for each fuel

A high percentage of mercury in the particulate during coal combustion is generally associated with low burnout efficiencies resulting in a char with high carbon content. This results in the gas phase mercury reacting with the carbonaceous portion of the char. However, these fuels have low ash content and it is difficult to speculate what the reasons are for the mercury speciation seen in the different flue gases.

Elements of Moderate Environmental Concern (Figures 4-28 through 4-30)

Again the X1333 fuel had the highest concentration in three (Cr, Cu and Z) of the five elements of moderate environmental concern. The No 6 fuel oil had the highest emission levels of Ni and V.

Chromium emissions for the X1333 fuel were approximately 10 times higher than measured for the X610 fuel. Copper emission in the X1333 fuel was 3 times higher than in the X610 and 9 times higher than in the fuel oil (**Figure 4-28**). Zinc emission for the X1333 was

approximately 5 times higher than the X610 and fuel oil (**Figure 4-29**). The X610 and fuel oil Zn emissions were essentially the same.

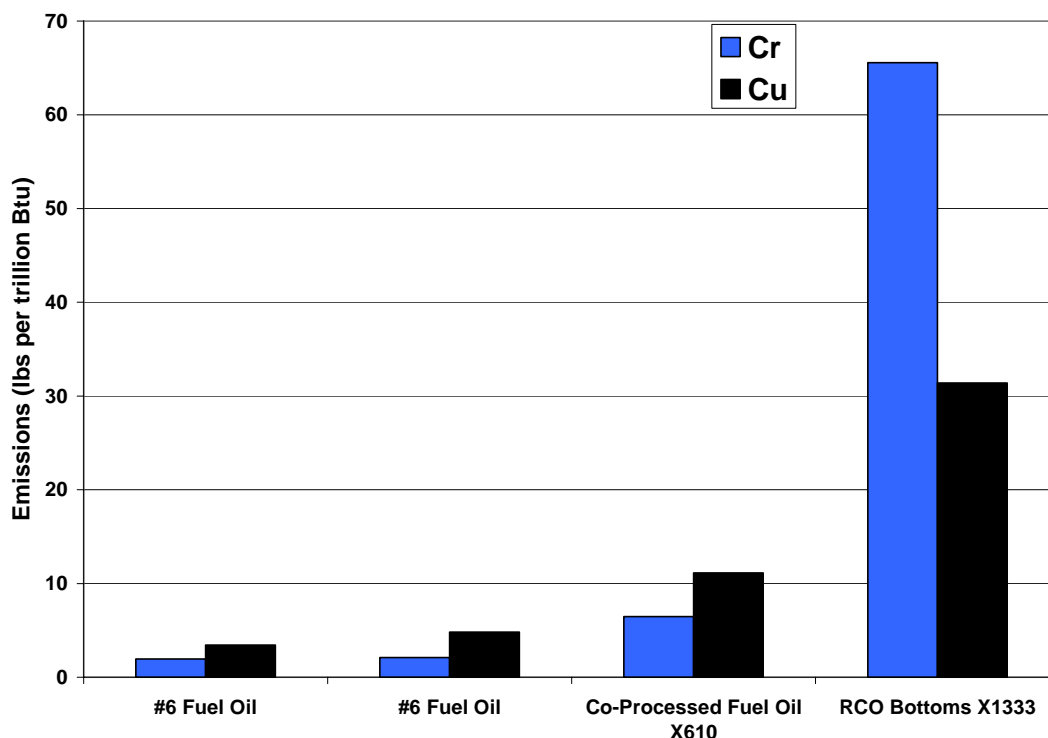


Figure 4-28 Chromium and copper emissions for test fuels

Nickel emissions were a factor of 7 to 19 times greater in the fuel oil than for the X1333 and X610 fuels, respectively (**Figure 4-29**). Vanadium emissions were a factor of 18 to 34 times greater in the fuel oil than for the X1333 and X610 fuels (**Figure 4-30**). This is consistent with the higher levels of Ni and V associated with petroleum-derived fuels as compared to coal. The addition of the coal-derived liquid in the X610 and X1333 acts as a diluent reducing the amounts of these elements. Since the percent of coal-derived liquids in the X610 and X1333 is not known it is difficult to confirm the dilution effect.

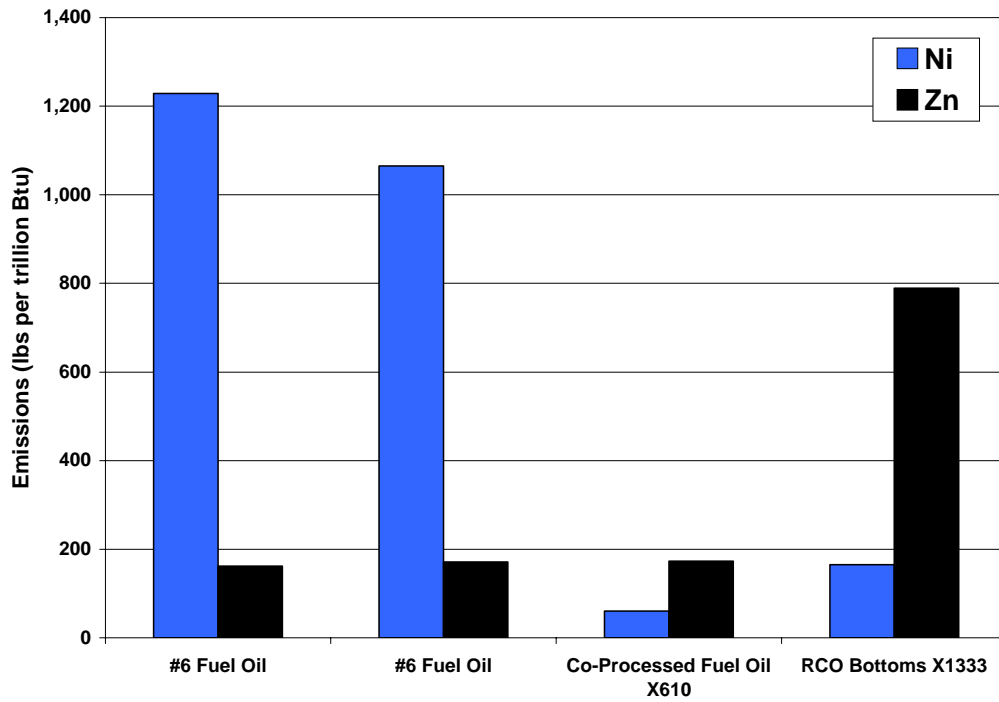


Figure 4-29 Nickel and zinc emissions for test fuels

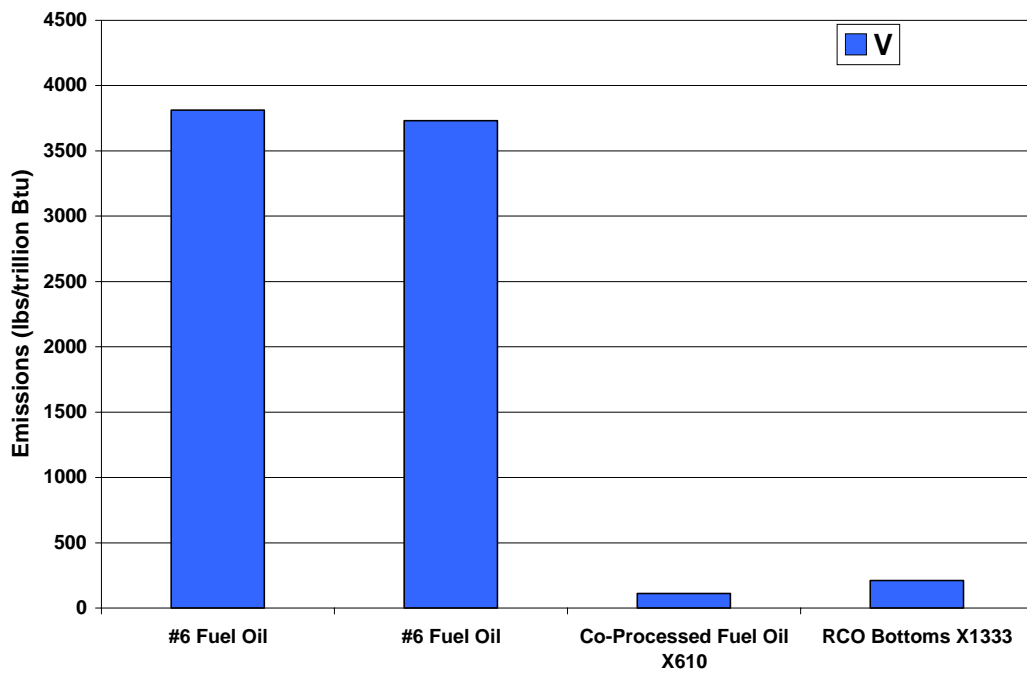


Figure 4-30 Vanadium emissions for test fuels

Elements of Minor Concern (Figures 4-31 through 4-33)

Again fuel X1333 had the highest emission levels of Sr (**Figure 4-31**) and Sb (**Figure 4-33**). The X611 fuel had the lowest emission levels of Co and Ba (**Figure 4-31**) and Mn (**Figure 4-32**). Antimony levels were essentially the same for the fuel oil and the X611 fuel (**Figure 4-33**). Barium emissions for the fuel oil and the X1333 fuel were similar.

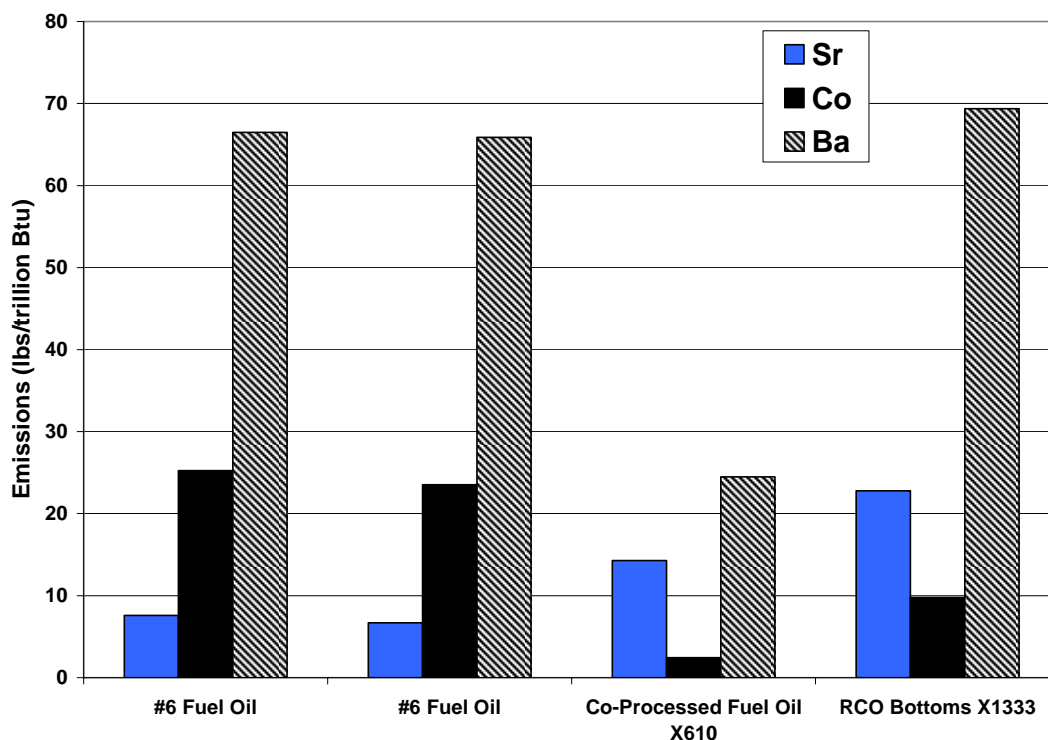


Figure 4-31 Strontium, cobalt and barium emissions for test fuels

Overall the X610 fuel had lower emissions of those elements that are of major or moderate environmental concern than the X1333 fuel. The X1333 fuel had the highest emission levels of more elements than any of the other fuels. Fuel oil had the highest levels of emissions for Ni, V, Hg, Co, and Mn. The average As levels in the fuel oil were essentially the same as the two co-processed fuels.

No comment can be made as to why the two co-processed fuels differ so much in their emission character as no information was provided regarding the feedstocks and processes used to produce the X6101 and X1333 fuels.

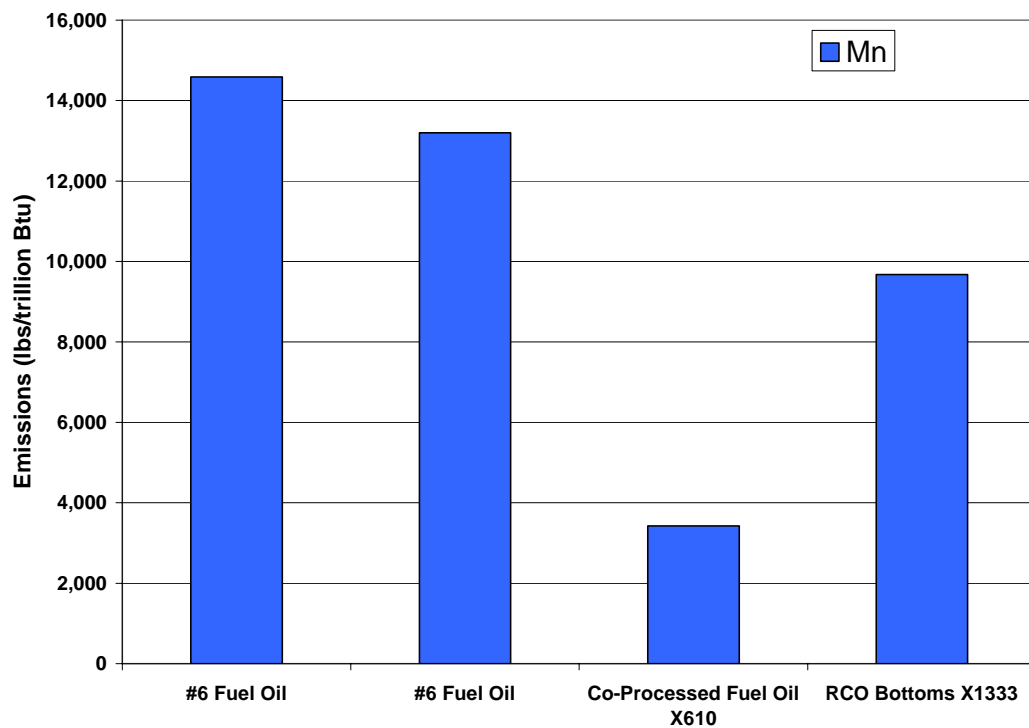


Figure 4-32 Manganese emissions for test fuels

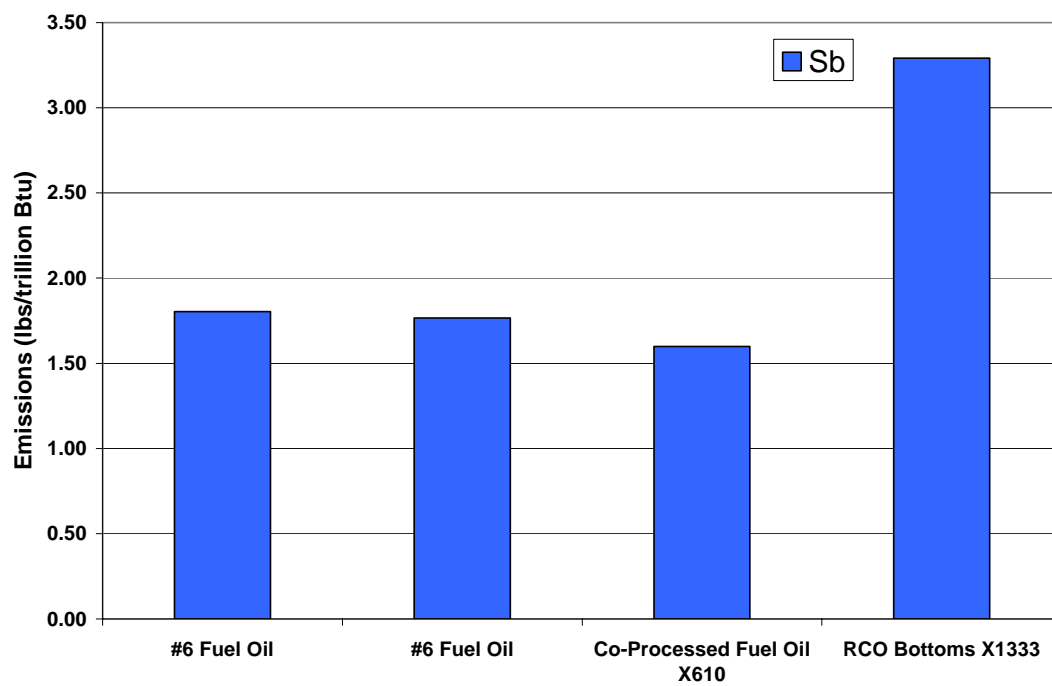


Figure 4-33 Antimony emissions for test fuels

4.5 Conclusions

The objective of Task 4 was to evaluate the effect of introducing coal into an existing petroleum refinery on the fuel oil product, specifically trace element emissions. Activities performed to accomplish this objective included analyzing two petroleum-based commercial heavy fuel oils (*i.e.*, No. 6 fuel oils) as baseline fuels and three co-processed fuel oils, characterizing the atomization performance of a No. 6 fuel oil, measuring the combustion performance and emissions of the five fuels, specifically major, minor, and trace elements when fired in a watertube boiler designed for natural gas/fuel oil, and determining the boiler performance when firing the five fuels. The No. 6 fuel oils used to generate the baseline data were obtained from east coast suppliers and the co-processed fuel oils were produced by Intertek PARC.

With the exception of the RCO bottoms fuel (X1333), which was exceptionally viscous, the co-processed fuel oils handled and combusted similarly to the commercial No. 6 fuel oils. Sulfur dioxide emissions were significantly less for the co-processed fuels oils due to their low sulfur concentrations. Similarly, NO_x emissions correlated with fuel-bound nitrogen content. Lower NO_x emissions were observed from the co-processed fuel oils that contained less fuel nitrogen than the commercial No 6 fuel oils while higher NO_x emissions were observed when firing the RCO bottoms, which had the highest concentration of fuel nitrogen. Boiler efficiencies from all liquid fuel tests were comparable.

Emissions produced during combustion of No. 6 fuel oil as compared to calculated emissions using emission factors AP-42. The data showed that the correlation of measured emission data to the calculated emission is a function of the element itself. Calculated emissions that were within the range of measured emissions include: Be, Hg, Mo, Se, Cr, Pb, Cu, Ba and Co. Calculated emissions that were not within the range of measured emission include: Cd, Sb, Zn, Mn, Ni, and B.

The partitioning of the elements follows the general pattern of behavior discussed in Section 4.4.3. The majority of the elements occur in the solid phase, while, the elements of greatest environments of concern occur in the gas phase (Hg, As, and Se).

The testing illustrated that the introduction of coal-derived liquids can introduce trace metals of environmental concern into liquid hydrocarbon products produced during co-

processing with petroleum derived liquids. This is evident by the presence of trace elements in the emissions produced during combustion of the co-processed “fuel oil” fraction as compared to emissions produced during combustion of No. 6 fuel oil. The amount of Hg and As emitted (lb/10¹² Btu) was found to be 10 times greater than two of the No. 6 fuel oils. A majority of the Hg emitted by the co-processed fuels was concentrated in the particulate phase, whereas, the Hg in the fuel oil occurred in the gas phase as oxidized Hg. Pb emissions were also increased over a 100 times during combustion of the co-processed fuel

While the data presented only represent a limited number of samples and there was significant variation between the co-processed fuel oils (possibly due to differences in processing), it can be said that the incorporation of coal derived liquids in the refinery stream can introduce elements of environmental concern. The level of their emissions upon utilization varies drastically but warrant further investigation to ensure that they pose no greater environmental threat than petroleum-derived liquids.

4.6 Miscellaneous Activities

4.6.1 In-Furnace Camera

A high-temperature in-furnace camera was procured during the project to visually record anticipated changes in the flame structure and stability when firing co-processed fuel oils. The camera system, which consists of a portable camera with straight ahead and right-angle views, compressed air cooling system, remote control module, digital video recorder, monitor, and portable cart, is shown in **Figure 4-34**. The camera was used for the initial tests; however, its use was discontinued because the camera could not detect visual changes in flame shape and stability during initial tests and, in the case of several co-processed fuels, limited quantities were available for testing resulting in all efforts being focused on the trace elements emissions testing to ensure the tests were successful.



Figure 4-34 High-temperature in-furnace camera system

4.6.2 Upgrading Data Acquisition System

The data acquisition system (DAS) for the research boiler was upgraded during the project in order to provide more accurate readings for some parameters, which in turn are used to calculate boiler efficiencies. Some parameters were manually obtained from pressure gauges and flow meters and then used to determine mass and energy balances. By upgrading the DAS on the research boiler, nearly all parameters are continuously monitored by the DAS, which results in more accurate averaging of test variables. Pressure transmitters were installed to measure high and low steam pressure, liquid fuel pressure at the fuel gun, atomizing media pressure, secondary air static and differential (*i.e.*, across an orifice plate) pressures, and primary air static pressure. In addition, a relative humidity sensor and boiler surface temperature probe were installed.

4.7 Acknowledgments

The following staff and undergraduate students are acknowledged for their assistance in analyzing samples, preparing and recovering sampling trains, performing the combustion/emissions testing, and reducing data: Mr. Bradley Maben, Ms. Karen Ross, Ms. Paula Smith, and Mr. Ronald S. Wasco.

Task 5. Pitch and Coke Material (G. Mitchell, C. Clifford, Ö. Gül, M. Escallón, P. Aksoy, Y. Suriyapraphadilok, R. Wasco, J. Griffith)

Integration of coal into existing petroleum refining operations carries a great potential to produce value-added carbon streams, including various pitch and coke products. Co-carbonization of coal and heavy petroleum streams, accomplished in the delayed coking unit, to provide both aromatic carbon units necessary for thermally stable jet fuels and valuable coke and pitch products represented a fundamental objective of this investigation. Originally, the work was divided into six subtasks that included, procurement and preparation of coals (5.1), co-coking of coal and heavy petroleum streams (5.2), analysis of co-coking solid products (5.3) and manufacturing and testing of carbon artifacts (5.4), in addition to analysis of co-coking binder pitch (5.5) and the examination of deeply hydrogenated decant oil reaction (5.6). However, during the course of our research some areas needed to be expanded to answer fundamental questions or they needed to be contracted as being less significant approaches. One of the subjects of immediate importance, production of coal tar from coal extracts (5.7), was included to address the need to identify a potential new and stable source of coal-derived liquids, and a fundamental study on the coal interaction with the solvents for co-coking and extraction. The following is a comprehensive summary of the research that was performed during this Refinery Integration project.

5.1 Sample Procurement and Preparation

The basic philosophy regarding coal selection for co-coking involved the need to find or to generate a coal stream (i) having a suitable fine particle size, (ii) be of low ash yield, and (iii) have a high concentration of those components that provide largely aromatic volatile matter and that become thermoplastic, i.e., vitrinite. Froth flotation streams [5-1-5-3] were identified as a source of fine coal particles. The tendency of the froth flotation fraction to concentrate vitrinite was also a key element. Vitrinite from high volatile bituminous coals generally yields a high volatile content [5-4] and typically develops high thermoplasticity [5-5, 5-6] and would make an excellent co-coking feed since it devolatilizes in the temperature range of the delayed coker (450°-500°C).

Because we are looking for coals that will maximize the production of two-ring aromatic molecules during devolatilization between 450-500°C and that will form a thermoplastic mass

capable of homogenous interaction with the carbon materials being derived from the petroleum residua, high volatile A bituminous metallurgical coking coal products were identified as the most likely raw material for co-coking. In fact, high volatile metallurgical coals were attractive because tertiary cleaning technology was employed in their production which generally included froth flotation. One positive aspect of flotation was that it recovers the friable fine coal particles that are composed mostly of vitrinite, the coal maceral that possess thermoplasticity, becomes the matrix of metallurgical coke and contributes most of the aromatic compounds to the volatile matter given off during pyrolysis. Two negative aspects to the use of this product stream were: 1) the coal usually contains 80% water (but can be compressed or centrifuged to 20% moisture), and 2) dispersed, liberated clay particles that report to this size fraction make a dry product of 6-9% ash yield. Removal of the mineral matter and moisture would be extremely important to the quality of the coke product. Consequently, our research under this task was not only to locate suitable coal product streams, but to investigate means of beneficiation.

Over the duration of this project many potential coal products were evaluated as candidates for co-coking. Our initial selection, a Pittsburgh seam froth flotation cell effluent was obtained from Mine No. 84/Eighty Four Mining, Washington, Co., PA owned and operated by COSOL Energy Inc. This coal was being mined for the steam market and represented one of four mines in the vicinity that were in total producing 8 million tons of coal per year. This particular mine product was used to develop procedures for reducing the ash yield below 1.0%, which was a target that we believed would generate carbon suitable for the aluminum anode market. During a period of about 16 months, three different samples were collected from the Mine No. 84 cleaning plant to generated sufficient cleaned coal (20 kg) for 12 consecutive delayed coker runs. The composite coke from these runs would be evaluated by Alcoa Inc. for potential use as an anode carbon aggregate.

Another coal product which had become an early standard for co-coking research was collected from A.T. Massey's Marfork Cleaning Plant in Raleigh Co., WV. Earlier research had targeted the Powellton coal as a highly thermoplastic coking coal product, but over the years other coal seams and mine products were included in the cleaning plant feed. By July 2006 when we collected a sample for this project, the coal feed included four seams from five different mines including Powellton, Eagle, #2 Gas and Lower Cedar Grove seams. Furthermore, although there was a fairly well defined technique for processing an ultra clean coal product for

co-coking, this particular coal was more troublesome, i.e., screen blinding and damage. Processing and scheduling the coker required seven months before co-coking could begin.

Finally, our original intent was to collect and process a third coal for this project from the Kingwood Coal Co. This high volatile A bituminous Lower Kittanning seam coal which is slightly higher in rank than the Marfork, has the highest thermoplasticity of any coal in North America, is sold as a metallurgical coal product, and is cleaned by tertiary technology. Unfortunately, funding for a fourth year of research was eliminated and the coal could not be obtained, processed and coked with remaining funds. Never-the-less it would be a very good coal to test.

5.1.1 Experimental

In general, the Pittsburgh seam coal and the Marfork product samples were handled in much the same way. In both cases a 90 kg run-of-mine coal sample was collected from the belt leading to clean coal storage at about the same time as the froth flotation effluent was being collected in the cleaning plant. These samples were stage crushed to pass a 6.3 mm (-1/4 inch) sieve, homogenized and split into 4.5 kg aliquots under argon and sealed in foil multilaminate bags as part of the Penn State Coal Sample Bank (DECS-34 and 36, respectively). The much larger fines sample was processed using a Derrick Model K Vibrating Screen machine a combination vibrating/wet sieving apparatus (**Figure 5-1**). The frother effluent was processed through two nested 58" x 17.5" screens with opening of 150 μm and 45 μm that were adjusted to 15° from horizontal and vibrated at 3600 cycles per minute. A high-pressure spray of water was maintained across the entire width of the screens so that a <150 μm x >45 μm product could be collected. The higher ash yield <45 μm material and the higher inertinite >150 μm were discarded. Many days of wet sieving and decanting the liquid resulted in cake the consistency of mud that was spread in thin layers on pans to be stirred and dried at 50-104°C. For each coal this resulted in an intermediate product having about 3-4% ash yield.



Figure 5-1 – The Derrick Model K Vibrating Screen used to obtain a low ash yield, narrow size fraction product from the Pittsburgh and Marfork froth flotation streams.

A series of float/sink tests were conducted on representative aliquots of the raw 100 x 325 mesh product to determine what specific gravity liquid would provide the lowest ash yield and highest yield to meet our requirements, i.e., target was <1.0% ash and 20 kg of clean coal product. Using a starting specific gravity solution of tetrachloroethylene and toluene in the range of 1.265 – 1.285 g/mL the best quality and recovery were determined. It was found that the optimum specific gravity was different for the two coals, i.e., the Pittsburgh seam product required 1.280 g/mL, whereas the Marfork product needed 1.268 g/mL. Recovery was a little higher for the Marfork product (4.9%) compared to an estimated recovery for the Pittsburgh seam product of 3.1%. The final product was homogenized, split into 1.3 kg aliquots and stored under argon gas in foil multilaminate bags to protect them from deterioration until coked.

5.1.2 Results and Discussion

Subsamples were taken from one of the storage bags at random for evaluation. Owing to the amount of time that had passed between original sample collection and because of the many stages of processing and intermediate drying, there was concern that the properties of the clean coal effluent may have deteriorated. Analytical information provided in **Table 5-1** compares the run-of-mine (DECS-34 and 36) and clean coal products for the Pittsburgh (EI-186) and Marfork (EI-187) samples. Generally, the data shows that the ash yield target of <1.0% was met, thermoplastic properties were maintained or improved and that the process of cleaning concentrated the vitrinite portion of the coal. Although the magnitude of the mineral matter was greatly reduced by cleaning, a significant amount of the remaining mineral components were aluminosilicate clays and micron-sized particles of pyrite and calcite intimately dispersed in the vitrinite matrix.

In addition to the values shown in **Table 5-1**, particle size distribution and vitrinite reflectance analyses were determined for the two coal products. Particle size was measured using a Malvern 2600C Droplet and Particle Sizer using ethanol as a dispersant and carrier. The test showed that particles range in size from 295 to 15 μm where 80% of the particles were between 50 and 148 μm and 10% were above or below this range. A comparison of the vitrinite reflectance distributions of the run-of-mine and clean coal products (**Table 5-2**) showed that the cleaning process exhibited minor influence over the Pittsburgh seam coal, but a significant shift for the Marfork Product was observed. About 15% of the higher reflectance vitrinite particles were eliminated from the run-of-mine product (DECS-36) either in the cleaning plant or as a result of our processing scheme. Segregation of components from different seams may have occurred during processing in the Marfork product, but there is no way to accurately assess this type of separation.

5.1.3 Conclusions

During the course of this project two of the three identified coal prospects were prepared into clean coal products suitable for co-coking and for the production of anode-quality carbon for the aluminum industry. Run-of-mine and flotation samples of the Pittsburgh seam and a coking coal product from the Marfork Cleaning Plant (a blend of coals) were collected, a process of wet sieving and gravity-liquid flotation were used to prepare ultra-clean coal products, each

Table 5-1 – Comparison of Coal Properties of Run-of-Mine and Clean Coal Samples for the Pittsburgh Seam FCE (EI-186) and Marfork JCE (EI-187)

Analytical Procedure	Pittsburgh Seam DECS-34	Pittsburgh FCE 1.280 Float EI-186	Marfork Product DECS-36	Marfork JCE 1.268 Float EI-187
Proximate Analysis: (dry)				
Fixed Carbon, %	54.3	63.4	58.3	66.5
Volatile Matter, %	38.4	35.6	34.5	32.6
Ash, %	7.4	1.0	7.2	0.9
Ultimate Analysis: (dry)				
Carbon, %	78.2	84.6	80.8	89.2
Hydrogen, %	5.2	5.3	5.1	5.5
Nitrogen, %	1.6	1.6	1.5	1.7
Sulfur, %	1.6	1.1	1.0	0.8
Oxygen, % (diff.)	6.0	6.4	4.4	1.9
Gieseler Plastometer:				
Softening Temperature, °C	381	385	384	375
Fluid Temperature Range, °C	91	93	108	121
Maximum Fluidity (ddpm)	16,418	29,527	30,000	29,516
Temperature at Maximum, °C	435	436	448	439
Ash Mineral Composition:				
Silicon Dioxide, %	48.47	41.8	57.38	40.8
Aluminum Oxide, %	23.15	27.3	25.60	27.8
Ferric Oxide, %	14.84	13.6	11.36	13.6
Titanium Oxide, %	1.00	nd	1.44	4.24
Phosphorus Pentoxide, %	0.53	0.61	0.23	<0.05
Calcium Oxide, %	2.49	5.65	1.21	6.85
Magnesium Oxide, %	0.76	0.74	0.93	1.42
Sodium Oxide, %	0.69	0.72	0.72	0.84
Potassium Oxide, %	1.87	1.64	1.87	1.43
Sulfur Trioxide, %	1.95	nd	0.47	nd
Organic Petrography: (volume %)				
Total Vitrinite	82.8	96.2	73.8	91.4
Total Liptinite	4.0	1.5	5.3	3.9
Total Inertinite	13.2	2.3	20.9	4.7

Table 5-2 Comparison of Vitrinite Reflectance Distributions of the Pittsburgh and Marfork Run-of-Mine (DECS-34 and 36) with Clean Coal Products (EI-186 and 187)

	Pittsburgh Seam		Marfork Product	
	DECS-34	EI-186	DECS-36	EI-187
Mean Max. Vitrinite Reflectance, %	0.83	0.83	1.03	0.99
% Vtype 6*	2.0	1.0		
% Vtype 7	26.0	25.0		2.0
% Vtype 8	59.0	64.0	5.0	13.0
% Vtype 9	13.0	10.0	37.0	37.0
% Vtype 10			39.0	44.0
% Vtype 11			17.0	4.0
% Vtype 12			2.0	

*Vtypes represent the percentage of reflectance readings taken in one tenth intervals, i.e., Vtype 7 equals the percentage of all readings taken between 0.70 and 0.799

exceeding the capabilities of current cleaning plant technology. Sufficient sample was prepared to generate ~19 kg of delayed co-coke for laboratory testing and coke quality assessment.

Coals were selected for their availability, thermoplastic range, and maceral composition and whether the cleaning plant facilities associated with the coal product employed some sort of flotation circuit. Froth or Jameson flotation cell effluent and run-of-mine coal products were collected from the cleaning plants and compared. Generally, our processing scheme reduced the ash yield to <1.0% and increased the concentration of vitrinite >90% without a decrease in the thermoplastic properties. It was felt that these properties would optimize our ability to generate volatile matter rich in two ring aromatics and give the greatest chance of generating a homogeneous co-coke composed of coal and decant oil derived carbons.

5.2 Co-Coking of Coal and Heavy Petroleum Stream:

5.2.1 Co-coking Runs Using the Pittsburgh (EI-186) and Marfork (EI-187) Coal Products

Based on the design of a similar delayed coking unit operated by PARC Technical Services, Harmarville, PA, The EMS Energy Institute built in-house a 102.5 cm high 7.5 cm ID coke drum of around 4.5 liters. After some design changes regarding the preheater, steam stripping and tapering of the drum for more easy extraction of the coke artifact, our unit became capable of co-coking blends of coal and heavy petroleum resid. This section will describe the

operation of this delayed coker with respect to the two clean coal products (Pittsburgh and Marfork) as they are blended with decant oil. It was determined that 12 consecutive runs would be required to fulfill coke requirements of other researchers involved in the project as well as by the assistance provided by Alcoa Inc. who developed an interest in the qualities of co-coke and provided valuable guidance and analytical assistance to this project. Because of the number of repetitive runs, statistical information on controlling operations as well as product quality could be addressed.

5.2.1.1 Experimental

Materials.

A commercial petroleum-based decant oil (EI-107) obtained from United Refining Corporation of the type used for making premium needle coke was used in this study. Ash and sulfur yields of the original decant oil (EI-107) were found to be 0.22% and 2.99%, respectively. The high volatile A bituminous coals used in this study (EI-186 and 187) were deeply cleaned from the flotation circuit of a cleaning plant as discussed in **Section 5.1**. Proximate and ultimate analyses, fluidity and organic petrography results for these feedstocks are compared in **Table 5-3**.

Apparatus.

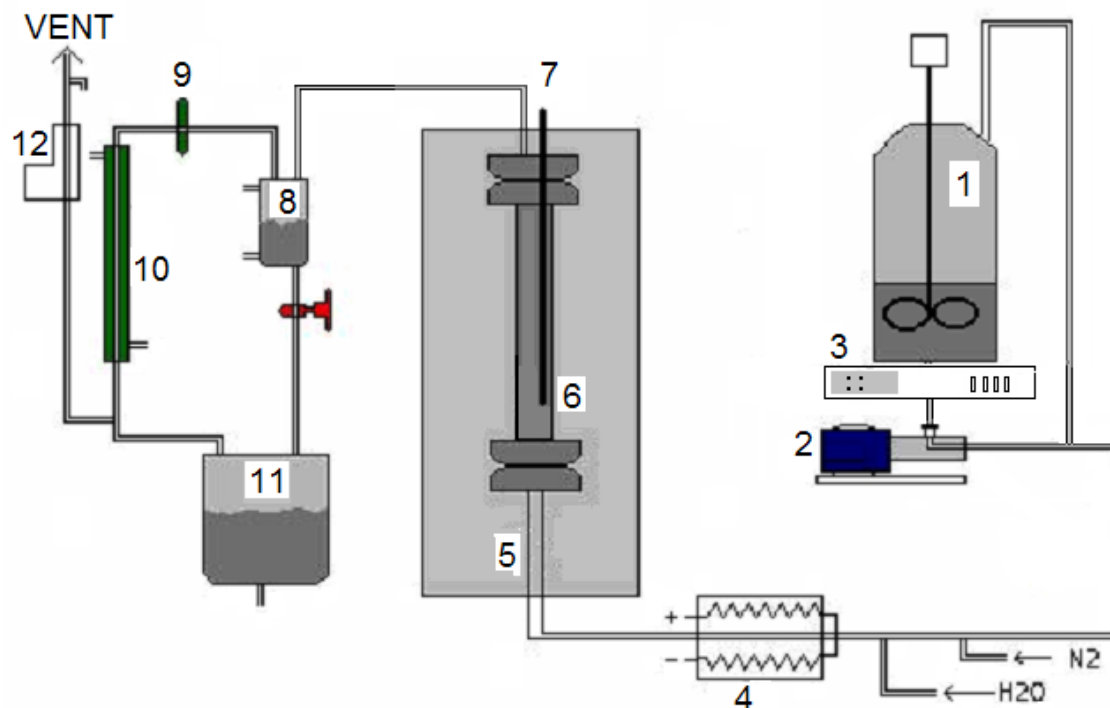
The EMS Energy Institute laboratory-scale delayed coker was used to provide continuous delayed coking for 6 hours to provide acceptable quantities of liquid and coke products for evaluation. The unit is capable of operating under most delayed coking process conditions. The system pressure, temperature and flow rates are monitored by a number of computer-controlled devices, and data from these devices are recorded throughout the run. The slurry feed rate (1.0 kg/hr) in these experiments was continuous and constant and was measured gravimetrically with time. Some of our earlier results have been published [5-7] and previous work has shown good reproducibility in terms of product distribution of delayed coker and vacuum fractionation distillates [5-8].

Table 5-3 Proximate and Ultimate Analysis of the Feeds Used in this Study

	EI-186 Pittsburgh	EI-187 Marfork	Decant Oil EI-107
Proximate analysis ^a			
Ash (%)	1.0	0.9	0.22
Volatile matter (%)	35.6	32.6	-
Fixed carbon (%)	63.4	66.5	-
Ultimate analysis ^a			
Carbon (%)	84.6	89.2	89.59
Hydrogen (%)	5.3	5.5	7.32
Nitrogen (%)	1.6	1.7	0.22
Sulfur (%)	1.1	0.8	2.99
Oxygen (by diff.) (%)	6.4	1.9	
Fluidity Data ^b			
Fluid Temperature Range (°C)	93	121	na
Maximum Fluidity (ddpm)	29,527	29,516	na
Softening Temperature (°C)	385	375	na
Organic Petrography, vol%			
Total Vitrinite (vol. %)	96.2	91.4	na
Total Liptinite (vol. %)	1.5	3.9	na
Total Inertinite (vol. %)	2.3	4.7	na

^a values reported on a dry basis^b Determined using a Gieseler plastometer

As shown in **Figure 5-2**, the apparatus consisted of a stirred and heated feed tank that was maintained at 120 °C during the current experimental program. This was connected to a 0.635 cm (1/4 in.) o.d. line that carried feedstocks from the feed pump. Feed materials were pumped directly to the preheater consisting of a 2.5 cm o.d. x 51 cm stainless steel tube fitted directly to the bottom of the reactor and heated to 120 °C using heating tape. The superpreheater and steam were not used in the co-coking experiments as the former was likely to plug and the latter complicated liquids collection (**Figure 5-2**). The temperature increase through this 51 cm preheater was on the order of 200 °C, with an outlet temperature of 420-460 °C. The laboratory coker consisted of a 7.5 cm i.d. x 102.5 cm cylindrical reactor unit (coker drum) having an internal volume of approximately 4.5 L. Nitrogen gas was used to maintain a back pressure in the system which was 25 psig for the co-coking runs. Vaporous materials (liquid and gaseous products) were vented at the top of the reactor drum and collected for evaluation and analysis.



- | | |
|--------------------------|----------------------------|
| 1. Heated Feedstock Tank | 7. Thermocouple Well |
| 2. Feedstock Pump | 8. DP Cell |
| 3. Balance | 9. Back Pressure Regulator |
| 4. Superpreheater | 10. Condenser |
| 5. Preheater | 11. Receiver Tank |
| 6. Coker Drum | 12. Mass Flow Meter |

Figure 5-2 A schematic of laboratory-scale delayed coker [5-7]

Reaction Procedures.

In the delayed coking process, feedstock is pumped into the coker drum where reactions between the coke and the liquid lead to the formation of light desirable liquids and carbonaceous solid. **Table 5-4** shows the average run conditions and ranges of operations for the consecutive runs of both the Pittsburgh and the Marfork co-coke experiments. During the experiments, a slurry of (20 wt.%) coal and (80 wt.%) decant oil was heated and stirred overnight. Operation of the coker began after the system was flushed with nitrogen and pressurized at 25 psig. Then the slurry was pumped at ~16.7 g/min into the preheater where the temperature was increased from 120° to ~439°C coker. Residence time to pass through the preheater at that feed rate was about 13 minutes before entering the coker drum that was preheated to about 500°C. As the slurry was

heated to maximum temperature volatile components of the coal and oil were vaporized and subsequently condensed. Light hydrocarbons vapor exited from the top of coker drum and passed through a series of condensers. Gases were passed through a mass flow meter and were vented. Feeding continued for about 6 hours and then the coke artifact was maintained at 500°C for 24 hours before cooling and extraction from the drum.

In the experiments reported here, the liquid products from the reaction were passed through a series of condensers and valves that facilitated their isolation as a function of reaction time. At the conclusion of the experiment the mass of the liquid condensate was weighed. Liquid products from multiple co-coking experiments were characterized and evaluated in terms of reproducibility are reported in **Section 5.3.2**.

Table 5-4 - Run Conditions used for Pittsburgh Seam FCE (EI-186) Compared with Marfork Clean Coal Product (EI-187)

Conditions	Coker Runs #50 - #61 Pittsburgh FCE EI-186		Coker Runs #84-92, 95-97 Marfork JCE EI-187	
	Average	Range	Average	Range
Feed Stock, hrs	5.86	5.6 – 6.0	6.0	6.0 – 6.2
Steam Stripping	0	0	0	0
Hold at 500°C, hrs	24	24	24	24
Feed Rate, g/min	16.76	16.7 – 16.8	16.7	16.7
Preheater inlet, °C	120.9	119 – 124	116.8	111 - 127
Preheater Outlet, °C	438.7	432 – 443	427.4	417 - 438
Coke Drum Inlet, °C	499.2	483 – 512	490	477 - 500
Coke Drum Low/Mid, °C	496.3	487 – 505	480.9	476 - 489
Coke Drum Top, °C	478.8	468 – 499	472.6	468 - 478
Material Fed, g	5750	5206 – 6054	5760.8	5248 - 5938
Products:				
% Coke	27.42	25.41 – 28.64	28.85	26.29 – 32.16
% Liquid Products	62.82	60.81 – 64.94	69.90	63.09 – 78.43
% Gas (diff.)	9.76	7.44 – 9.51	1.25	-9.87 – 3.45

Thermo-gravimetric Analysis.

In an effort to gather more understanding regarding pyrolysis of our clean coals, decant oil and co-coking blends, a number of tests were performed using the Perkin Elmer 7 Series Thermal Analyzer System. Thermo-gravimetric analyses were conducted under a nitrogen atmosphere, but under ambient pressure. The thermal program did not simulate the overnight mixing at pot temperature (120°C) or the extended soak period (24 hrs at 500°C) at the end of the heating program that would match the soak time employed in the coker. However, based on

the interior dimensions of the supply lines and the standard feed rate used (16.7 g/min), the heating rate and duration of heating match fairly well what occurs in the laboratory delayed coking unit (**Table 5-5**).

Table 5-5 – Thermo-gravimetric Analysis of Coals, Decant Oil and Blends

Sample Id.	% Weight Loss				% Coke Yield	% Total Weight Loss	Volatile Matter, 950°C , 7min Dry basis
	30°C, 60min	120°C, 30 min	120-500°C @ 25°C/min	Soak 500°C, 360 min			
Marfork JCE, 1.268, EI-187	0.73	0.82	25.38	5.80	67.27	32.73	32.6
Pittsburgh FCE, 1.280, EI-186	0.70	0.91	26.47	5.85	66.07	33.93	35.6
United Decant Oil, EI-107	0.24	8.42	89.92	0.18	1.25	98.75	nd
15.5/84.5Blend EI-187/EI-107	0.26	7.41	80.28	1.08	10.97	89.03	nd
18.5/81.5 Blend EI-186/EI-107	0.32	8.22	78.54	1.06	11.87	88.13	nd

Nd = not determined;

Run conditions, nitrogen atmosphere, ambient pressure; hold 60 min at 30°C; heat 30° to 120°C @ 20°C/min; hold 30 min at 120°C; heat 120 - 500°C @ 25°/min; hold 360 min @ 500°C

5.2.1.2 Results and Discussion

During the course of co-coking research and of receiving feedback data on the operability of the equipment or the quantity and quality of liquid and solid products, a number of test runs were made that contributed to or defined the run conditions selected for this investigation. Briefly, increasing the mix tank temperature from ~65° to ~120°C provided an improvement in the mixing of carbon regions attributable to coal and decant oil in the coke artifact and therefore resulted in a change of operations. Clearly, improvement could be made in blending and pumping the slurry into the preheater and then coke drum to enhance component interaction. Although no direct study was undertaken with co-coking slurries to test the influence of increasing system back pressure (>25 psig), some inadvertent pressure spikes during co-coking runs combined with some other proprietary work, suggested that increasing the pressure above 25 psig resulted in decreasing liquids and increased coke yields. The same response was obtained when the feed rate (from 16.7 g/min to 33.4 g/min) and amount of coal employed (from 80/20 to 70/30 decant oil:coal ratio) was increased, i.e., higher coke yield at the expense of

liquids yield. In addition, increasing feed rate and coal throughput separately or together resulted in the formation of shot coke, a lower value fuel coke.

The above information has contributed to the operating conditions employed in our co-coking work and shown in **Table 5-4**. However, it must be stated that our operating conditions and scale of operations departs significantly from the operation of a real delayed coker. There are no standard operating procedures for delayed coking, but in general we have learned that our back pressure (25 psig) was lower, our preheater operates within the same furnace (no possibility of cooling), there was no recycle of heavy resid components derived from the delayed coker and the coke drum was heated externally for 24 hours. Regardless of these many differences, if co-coking were to be implemented in a commercial unit, operating procedures that optimize efficient control and product quality and quantity would have to be established at the particular scale and with the selected raw materials.

To gain some better understanding of component (decant oil and coal) devolatilization under the operating conditions of our delayed coker, thermo-gravimetric analyses (TGA) of the individual feed materials and of their blends were undertaken. Results given in **Table 5-5** showed very clearly the influence of back pressure (or lack of) on the loss of volatile matter and coke yield. The coke yield determined from TGA for the EI-107 decant oil (1.25%) was significantly lower than that obtained from a 100% delayed coker run (19.8%) performed under similar conditions at 25 psig. Although the milligram-scale of testing made it difficult to obtain an exact 80/20 blend of decant oil and coal and there was no way of operating the unit under a back pressure, a number of pertinent observations can be made. After thermal stabilization of components and blends at 30°C, the act of increasing the temperature to 120°C and holding at that temperature caused a significant weight loss from the decant oil specimen employed in the experiment. This was found for the decant oil alone and the blends. The weight loss experienced by the coals could be attributed to the minor amount of associated moisture. By far the greatest loss of mass occurred in the 15.2 minute heat up from 120°C to 500°C amounting to 78 to 90% of the total weight loss depending upon the run. Clearly, the coals required more time at maximum temperature to devolatilize as can be seen by the weight lost during the 6 hour soak at 500°C and the maximum weight loss nearly equals that determined by the standard volatile matter test. The important observation that TGA provided was that devolatilization occurred early in the thermal process, which means that the volatile liquids and gases maintain contact

with the forming coke product at longer intervals as the drum is filled given ample opportunity for secondary reactions that may strip some of the two ring aromatics from the liquid products.

As shown in **Table 5-4**, operating conditions for the first two co-coking series (Pittsburgh and Marfork) were remarkably similar. Whereas the average coke yield was about 1.5% lower for the Pittsburgh product compared with the Marfork, there was a significant difference in the yield of liquids. A 7.0% increase in liquids was obtained when the Marfork product was employed in co-coking, largely as a result of much less gas being produced. The Marfork coal product was slightly higher in rank and lower in volatile matter than the Pittsburgh coal, and therefore one might expect a lower yield of liquids. Consequently, the chemical nature of these liquids will be of great interest, particularly those in the jet fuel range.

5.2.2 A Statistical Consideration of the Chemistry of Co-coking Liquids

During each run approximately 20-25 mL liquid samples were taken at pre-determined time intervals. In order to assess the liquid process repeatability, 4 of 12 Pittsburgh runs (#52, #54, #56 and #58, **Table 5-6**) were employed as representative samples. From each run, samples from the first, third, fifth hours of operation and composite oil were characterized to evaluate process repeatability in one specific experiment as well as repeatability between runs.

Analytical Procedures.

^1H and ^{13}C NMR analyses, using Bruker AMX 360 NMR spectrometer operating at 9.4 Tesla, were performed on liquid samples that had been taken previously at 1st, 3rd, and 5th hour during the run to study the compositional change during 6 hour feeding for 4 similar runs.

The overhead liquids collected from each co-coking experiment were fractional vacuum distilled into refinery cuts corresponding to gasoline, jet fuel, diesel, and fuel oil. The fractional vacuum distillations were performed on the bulk overhead liquid samples in order to obtain the actual yields of each refinery boiling range material. The use of vacuum minimized sample decomposition. The distillations were conducted in a 2 L flask mounted in a heating mantle. A 1200 grams liquid sample was weighed in to the 2 L flask and magnetic stirrer was used to

Table 5-6 - Conditions and product distributions for Pittsburgh FCE co-coking runs selected for statistical consideration

Run #	52	54	56	58	Mean & Std. Dev.
Conditions	DO/Coal (80/20)	DO/Coal (80/20)	DO/Coal (80/20)	DO/Coal (80/20)	
Feedstock, hours	6	6	6	6	
Steam strip at 500 °C, hrs	0	0	0	0	
Hold at 500 °C, hrs	24	24	24	24	
Feed rate, g/min	16.7	16.7	16.8	16.8	
preheater inlet, °C	120	123	122	120	
preheater outlet, °C	440	432	432	441	
coke drum inlet, °C	495	500	500	505	
coke drum lower/middle, °C	489	497	495	496	
coke drum top, °C	472	481	479	476	
Material Fed to Reactor	5898	5984	5746	6022	
Product					
coke +liquid product	5364	5405	5195	5474	
Liquid/coke	2.2	2.2	2.3	2.4	2.3 ± 0.1
%coke	28.2	28.6	27.6	26.8	27.8 ± 0.8
%liquid product	62.8	61.7	62.8	64.1	62.9 ± 1.0
%gas	9.05	9.68	9.59	9.10	9.4 ± 0.3

assure a uniform temperature in the liquid inside the flask. The flask, beaded-glass packed column, distillation head unit, condenser, vacuum application kit, and collection vessel were assembled. As the heating power was increased, the vapors came through the beaded-glass packed column and condensed in the condenser. Approximately 5-10 mm-Hg vacuum was used for distillation and a nomograph was used to correlate the temperature at a given pressure (vacuum pressure) and the temperature at atmospheric pressure. The pressure and temperature were constantly monitored during the distillation process.

The NMR analyses were also conducted for each refinery cut vacuum fractions that were obtained from each individual co-coking experiment. Samples were dissolved 1/1 volume ratio in CDCl₃ containing 1 vol % of tetramethylsilane (TMS) as standard. A pulse width was 5 µsec, pulse delay of 5 sec for ¹H with a 90° tip angle and 5 µsec pulse width of and a pulse delay of 45 seconds for ¹³C with a 70° tip angle were used to ensure quantitative results. In ¹³C analyses 20 mg Cr(AcAc)₃ was used for 2 mL of overhead liquid/CDCl₃ mixture. Regions of the spectra

were integrated and peaks were assigned based on literature chemical shift values for ^1H and ^{13}C [5-9].

GC/MS analysis, using a Shimadzu QP5000 spectrometer, was performed on vacuum fractionated liquid samples to study chemical composition. GC/MS temperature program for gasoline was 35°C (10 minutes), programmed from 35°C to 175°C at 4 degrees per minute, and then held at 175°C for an additional 5 minutes (total run time was 50 minutes). Temperature program for jet fuel was 40°C (4 minutes), programmed from 40°C to 220°C at 4 degrees per minute, and then held at 220°C for an additional 10 minutes (total run time was 59 minutes). Temperature program for diesel was set as: 40°C (0 minutes), programmed from 40°C to 120°C at 15 degrees per minute, from 120°C to 250°C at 4 degrees per minute, and then held at 250°C for an additional 8 minutes (total run time was 46 minutes). An XTI-5 ((Restek) 30 m x 0.25 mm x 0.25 μm) column was used for the GC/MS analyses.

Simulated distillation gas chromatography (SIMDIS GC) was performed on a small quantity of each bulk overhead liquid samples to determine the boiling point distribution and weight percent yield of each refinery cut fraction. The simulated distillation measurements were made according to ASTM D 2887 method by using an HP 5890 GC-FID fitted with an MXT-500 simulated distillation column (10 m, 0.53 mm ID and 2.65 μm) (Restek). Carrier gas flow rate was adjusted to 13 mL/min for Sim-Dist GC analysis, and SimDis Expert 6.3 software was used to calculate the percentage of fractions.

5.2.2.1 Results and Discussion

Product recovery.

The aim of this research was to study in terms of reproducibility the:

- pilot scale delayed coker product yield distributions (gas, liquid, and solid (coke)),
- compositions of overhead liquid and time-dependent samples obtained during 6 hours feeding period as well as reproducibility of overhead liquid's boiling point distributions between replicate experiments,
- vacuum distillation of bulk overhead liquids, i.e., gasoline, jet fuel, diesel, fuel oil, and chemical compositions of vacuum fractions.

In this investigation, coker runs from the deeply cleaned Pittsburgh seam bituminous coal (EI-186) and a decant oil (EI-107) were employed.

Table 5-3 shows the properties of the decant oil and coal used in the co-coking experiments. Four delayed coking runs have been performed to provide data for coker operating reproducibility. The conditions used in each of the co-coking experiments are described in **Table 5-6**, show that the applied temperatures and amount of material fed (between 5750 and 6000 g) were very close. Reproducibility of co-coking of coal with decant oil in four separate experiments was shown to be excellent (**Table 5-6**). Average values (including the average deviation) of percent coke, liquid and gas were $27.8\pm0.8\%$, $62.9\pm1.0\%$, and $9.4\pm0.3\%$, respectively. Liquid/coke ratios of these four replicate experiments were also found to be very close to each other ($2.3\pm0.1\%$). Liquids were obtained in suitable quantity for detailed chemical characterization, recombination and distillation into refinery cuts for further evaluations.

Composition of liquid product as a function of reaction time.

Small amounts of samples were taken at 1st, 3rd, and 5th hour during the six hours run time. These samples were studied in terms of monitoring the compositional change and boiling range material change. These three samples for four similar runs were analyzed using solution-state ^1H and ^{13}C NMR and SIMDIS GC. Regions of spectra were integrated and peaks were assigned based on literature chemical shift values for both ^1H and ^{13}C . **Tables 5-7** and **5-8** show distribution of ^1H and ^{13}C NMR integration results as a function of time of delayed co-coking, respectively.

Even though there was no significant difference between ^1H NMR integration bands of samples (pooled standard deviation for 12 samples was 1.7%) (**Table 5-7**), when each individual run was evaluated separately, the first sample (1st h sample) always had higher total aliphatic hydrogen than the second (3rd h sample) and third (5th h sample) samples. The reverse was true for the total aromatic hydrogen signal integrations. One can conclude that at first stage mostly long carbon-chain aliphatics or aliphatic side chain containing aromatics were thermally cleaved and distilled.

As determined by ^1H NMR, the average values were $57.2\pm1.7\%$ for total aliphatics and $42.8\pm1.7\%$ for total aromatics as calculated for 12 samples from four similar runs. These values were almost the same as the original decant oil feedstock values of 57.0% and 43.0%,

respectively. These data suggest that the light fraction of decant oil and coal-derived light hydrocarbons were co-distilled during the course of the delayed co-coking of decant oil and coal.

^{13}C NMR results confirm the total amount of aliphatic hydrogen decreased with time for each individual experiment (**Table 5-8**). The first samples always gave higher total aliphatic carbon signal integration in each individual experiment; a finding consistent with the ^1H NMR analyses results. Overhead liquid consisted mainly of aromatic carbons. From integration of the ^{13}C NMR signals, average total aliphatic carbons and total aromatic carbons were calculated as $23.1\pm 1.1\%$ and $76.9\pm 1.1\%$, respectively.

Total aliphatic carbon content of original decant oil was very slightly higher than overhead liquid (25.0% against 23%), but the reverse was true for the total aromatic carbons (75.0% against 77%) while these reported values are within the experimental error range.

Table 5-7. Distribution of ^1H NMR signals as a function of time of delayed co-coking of Pittsburgh FCE coal with decant oil (1:4 Ratio)

		#52			#54			#56			#58			Mean of 12 samples	s_{pool}
	Decant oil	1 st h	3 rd h	5 th h	1 st h	3 rd h	5 th h	1 st h	3 rd h	5 th h	1 st h	3 rd h	5 th h		
Aliphatic	57.0	59.6	56.8	57.1	59.2	55.5	55.7	58.4	56.6	56.6	58.1	55.3	58.1	57.2	1.7
Aromatic	43.0	40.4	43.2	42.9	40.8	44.5	44.3	41.6	43.4	43.5	41.9	44.7	41.9	42.8	1.7

Table 5-8. Distribution of ^{13}C NMR signals as a function of time of delayed co-coking of Pittsburgh Seam coal with decant oil (1:4 Ratio)

		#52			#54			#56			#58			Mean of 12 samples	s_{pool}
	Decant oil	1 st h	3 rd h	5 th h	1 st h	3 rd h	5 th h	1 st h	3 rd h	5 th h	1 st h	3 rd h	5 th h		
Aliphatic	25.0	24.4	22.3	23.9	23.0	22.1	20.9	24.3	23.3	22.9	24.5	22.3	23.3	23.1	1.1
Aromatic	75.0	75.6	77.7	76.1	77.0	77.9	79.1	75.7	76.7	77.1	75.5	77.8	76.7	76.9	1.1

Simulated distillation gas chromatograph (GC) was used to probe refinery boiling range materials change during six hours feeding. The refinery boiling ranges were gasoline, jet fuel, diesel fuel, and fuel oil. A summary of all cut point ranges on samples of 1st, 3rd, 5th hour for four replicate runs is given in **Table 5-9**. As seen, there was very good agreement between each fraction of each sample. Even though there were slight differences between simulated

distillation GC results of each fraction of each separate run, these differences were within experimental error. The reproducibility of cut point ranges between replicate experiments was also found to be excellent. Pooled standard deviation values for these four selected co-coking runs were calculated between 0.4% and 1.7%. The average and pooled standard deviation values of gasoline, jet fuel, diesel, and fuel oil ranges were calculated as $2.6\pm0.5\%$, $4.6\pm0.6\%$, $6.1\pm0.4\%$, and $86.1\pm1.7\%$, respectively.

Table 5-9. Boiling Point Distributions by Simulated Distillation Gas Chromatography of Time-Dependant Samples

	IBP-180°C IBP-356°F Gasoline	180-270 °C 356-518 °F jet fuel	270-332 °C 518-630 °F Diesel	332-FBP °C 630-FBP °F fuel oil
# 52 run				
1 st hr.	2.9	5.7	6.6	83.9
3 rd hr.	2.5	4.9	5.9	87.0
5 th hr.	2.6	4.8	5.9	87.0
Mean & Std dev.	2.7±0.2	5.1±0.5	6.1±0.4	86.0±1.8
# 54 run				
1 st hr.	3.5	5.3	6.9	83.4
3 rd hr.	2.1	3.7	5.9	87.4
5 th hr.	2.2	3.7	5.8	87.3
Mean & Std dev.	2.6±0.8	4.2±0.9	6.2±0.6	86.0±2.3
# 56 run				
1 st hr.	2.6	5.0	6.5	85.0
3 rd hr.	2.7	5.0	6.2	85.2
5 th hr.	2.1	3.9	5.6	87.5
Mean & Std dev.	2.5±0.3	4.6±0.6	6.1±0.5	85.9±1.4
# 58 run				
1 st hr.	2.8	4.7	6.0	85.5
3 rd hr.	2.3	4.0	5.5	87.3
5 th hr.	2.5	4.4	5.8	86.5
Mean & Std dev.	2.5±0.3	4.4±0.4	5.8±0.3	86.4±0.9
Mean & s_{pool} values for 12 samples				
Mean	2.6	4.6	6.1	86.1
s_{pool}	0.5	0.6	0.4	1.7

Comparison of fractionation yields and characterization of overhead liquid product.

Small quantities liquid samples were taken at determined time intervals during the 6 h run, as discussed in the previous section. The rest of the liquid product from the coker was collected in a separate container for further characterization and was called the *bulk overhead liquid*. Bulk overhead liquids were analyzed using SIMDIS GC (ASTM D 2887) as described above in terms of reproducibility. Product distributions by weight from SIMDIS GC of the bulk

overhead liquids are shown in **Table 5-10**. Reproducibility of SIMDIS GC analyses of replicate experiments was excellent and the values were all within experimental error. Average standard deviation values were found to be very low and these values were also within the experimental error range. According to simulated distillation GC analyses refinery boiling ranges were calculated as $2.1 \pm 0.1\%$ gasoline, $3.6 \pm 0.2\%$ jet fuel, $4.6 \pm 0.3\%$ diesel, and $88.8 \pm 0.5\%$ fuel oil.

The bulk overhead liquids were also vacuum-fractionated into refinery boiling ranges. Vacuum fractionation results by weight are given in **Table 5-11**. Reproducibility of vacuum distillation fractions for four replicate runs was in very good agreement. Average values for vacuum fractions as follows: gasoline $2.4 \pm 0.3\%$, jet fuel $4.0 \pm 0.7\%$, diesel $5.0 \pm 0.3\%$, and fuel oil $87.7 \pm 0.5\%$. There was excellent agreement between the results obtained by SIMDIS GC and the actual isolated yields of the fractions from the vacuum distillation (**Table 5-10** and **5-11**).

Table 5-10. Product Distributions of Overhead Liquid by Weight from Simulated Distillation Gas Chromatography

Run No	IBP-180°C	180-270 °C	270-332 °C	332-FBP °C
	IBP-356°F	356-518 °F	518-630 °F	630-FBP °F
	Gasoline	jet fuel	diesel	fuel oil
#52	2.1	3.4	4.4	89.1
#54	2.0	3.4	4.4	89.2
#56	2.2	3.7	4.4	88.7
#58	2.1	3.8	5.0	88.2
Mean & Average Deviation	2.1 ± 0.1	3.6 ± 0.2	4.6 ± 0.3	88.8 ± 0.5

Table 5-11. Product Distributions of Overhead Liquid by Weight from Vacuum Distillation

Run No	IBP-180°C	180-270 °C	270-332 °C	332-FBP °C
	IBP-356°F	356-518 °F	518-630 °F	630-FBP °F
	Gasoline	jet fuel	diesel	fuel oil
#52	2.6	5.0	5.0	87.3
#54	2.0	3.8	5.5	87.4
#56	2.4	3.6	4.8	87.9
#58	2.4	3.5	4.8	88.3
Mean & Average Deviation	2.4 ± 0.3	4.0 ± 0.7	5.0 ± 0.3	87.7 ± 0.5

Compositions of vacuum fractions.

Collected vacuum fractions (gasoline, jet fuel, diesel and fuel oil) were characterized using ^1H and ^{13}C NMR spectroscopy and GC/MS in terms of vacuum distillation repeatability,

chemical composition distribution, and compositional differences between fractions. **Figure 5-3** shows average values and standard deviations of aliphatic and aromatic hydrogen distributions in vacuum fractions and decant oil. Aliphatic protons showed a decrease from gasoline to fuel oil (89% to 53%), and the reverse was true for the aromatic protons (11% to 47%) (**Figure 5-3**).

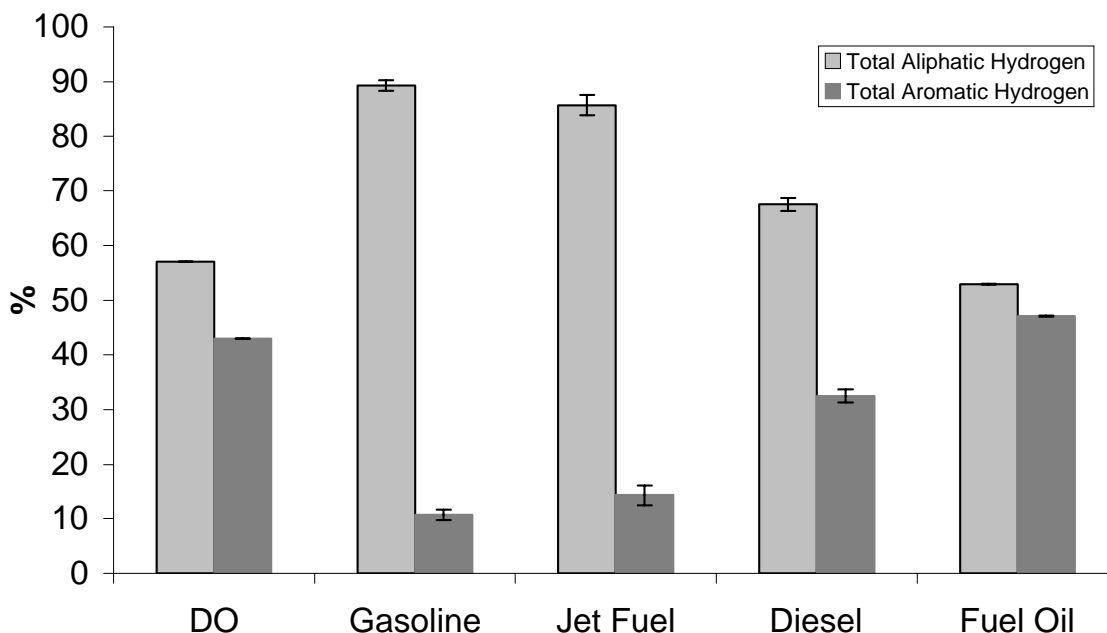


Figure 5-3. Aliphatic and aromatic hydrogen distributions of decant oil and vacuum fractions of Four replicate runs by ^1H NMR (including standard deviations).

^{13}C NMR integration results of vacuum fractions and decant oil are given in detail in **Figure 5-4**. **Figure 5-4** shows a similar trend to ^1H NMR – of a decrease in the aliphatic carbon percentage and an increase in the aromatic carbon percentage. Gasoline had the highest aliphatic carbon (66%) while the fuel oil fraction had the lowest aliphatic carbon (21%) (**Figure 5-4**).

Vacuum fractions from distillation were analyzed using GC/MS and the compositions of the fractions were grouped as: paraffins, cycloparaffins, benzenes, indanes, naphthalenes, and polycyclic aromatic compounds. No tetralins and decalins were observed with GC/MS, and they were not included to the related table. The results are given in **Table 5-12**. The percentage of each group was calculated by comparing the areas of each group to total area. **Table 5-12** reports that the gasoline fraction mostly consisted of paraffins, cycloparaffins and benzenes, including small amount of indanes and naphthalenes. Jet fuel had a higher percentage of paraffins and

naphthalenes, but lower benzenes and cycloparaffins than those of gasoline. Jet fuel also had very small quantity of polycyclic aromatics. The diesel fraction had the largest quantity of polycyclic aromatics (56%)

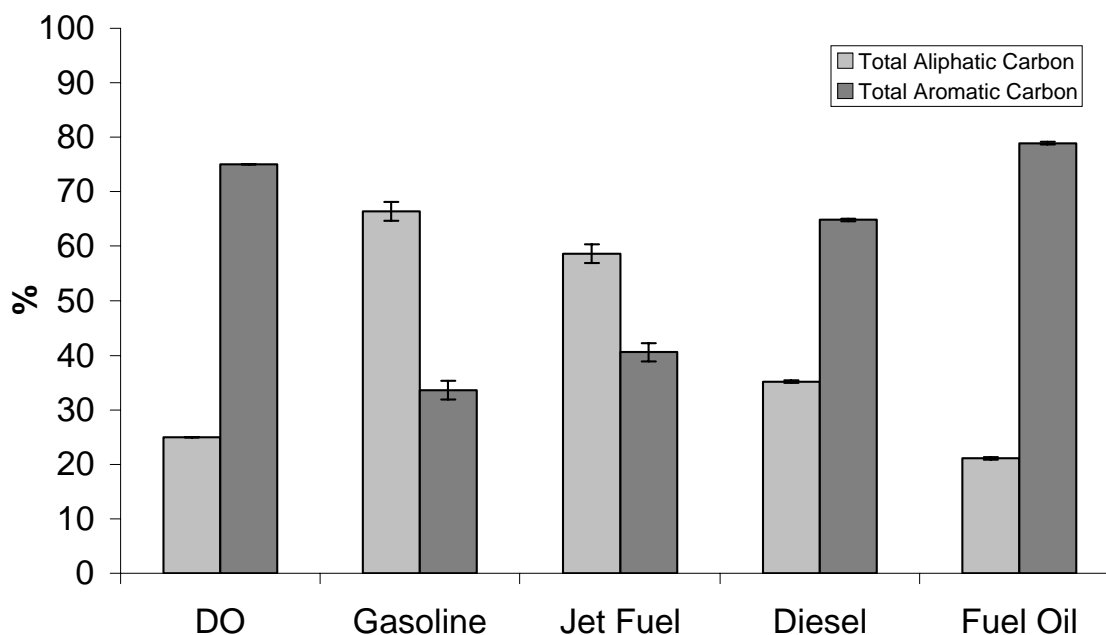


Figure 5-4. Aliphatic and aromatic carbon distributions of decant oil and vacuum fractions of 4 replicate runs by ^{13}C NMR (including standard deviations).

Table 5-12. - Composition of vacuum fractions based on quantitative GC/MS^a results (wt%)

Classification	Gasoline	Jet fuel	Diesel
paraffins	30.9	42.4	2.3
cyclo paraffins	18.4	4.2	1.9
benzenes	47.6	21.7	21.0
indanes	2.1	5.0	1.7
naphthalenes	1.0	26.6	17.6
PAH	0.0	0.1	55.5

^a Calculated using an external standard.

A primary goal of the present refinery integration project was to produce coal-based or coal-derived jet fuel. Hydroaromatics and cycloparaffins have been reported as having higher

thermal stability [5-10-5-15]. Coal-derived liquids that are rich in aromatic compounds can be converted into hydroaromatic and cycloparaffins by hydrotreatment and saturation processes [5-16]. Coal-derived liquids are thus ideal candidates to be upgraded into thermally stable jet fuel [5-10]. The diesel fraction had the least paraffins and cycloparaffins, but the most polycyclic aromatics (56%). These findings are consistent with proton NMR results.

5.2.2.2 Conclusions

Reproducibility of co-coking of coal with a decant oil in four separate experiments, in terms of yields of green coke, liquid and gas, was shown to be excellent. Standard deviations for yields of coke, liquid and gas were found 0.8, 1.0 and 0.3%, respectively. Time-dependent samples (as the reaction progressed), showed a slight decrease in aliphatic hydrogen/carbon but an increase in total aromatic hydrogen/carbon as determined ^1H and ^{13}C NMR analyses. SIMDIS GC analyses were also performed on time-dependent samples to provide gasoline, jet fuel, diesel, and fuel oil products. Time-dependent 1st hour samples always had higher amount of lower boiling range materials (gasoline, jet fuel, diesel) and had lower boiling point distributions than those of 3rd and 5th hour samples. Liquids taken in certain time intervals were shown to have reproducible characteristics. Use of the large laboratory scale coker provides sufficient quantities of distillate liquids so as to provide distillable product from coking or co-coking reactions. The boiling point distributions in co-coking experiments were found to be relatively independent of delayed coking runs. SIMDIS GC of the whole overhead liquid from co-coking experiments was performed to provide refinery boiling range materials. Excellent agreement was observed between runs and the calculated standard deviations were very low. Vacuum distillation of the whole overhead liquid product from co-coking experiments was performed to provide gasoline, jet fuel, diesel, and fuel oil products. Excellent agreement was observed between simulated distillation GC and vacuum distillation. The vacuum distillation fractions showed no significant difference between co-coking runs. Vacuum fractions and decant oil analyzed using ^1H and ^{13}C NMR and GC/MS were compared. When comparing the chemical character of the gasoline, jet fuel, and diesel fractions, the lighter liquids were more aliphatic and the heavier liquids were more aromatic. The NMR results of coking and co-coking liquids agreed with GC/MS. Gasoline mostly consisted of paraffins, cycloparaffins and alkyl benzenes. The jet fuel fraction included similar structures, but also contained a significant

quantity of two-ring aromatics, that upon hydrogenation, would produce an excellent thermally stable jet fuel. The diesel fraction comprised mostly polycyclic aromatic hydrocarbons, naphthalenes and alkyl benzenes. However, the main liquid product was material that boiled in the fuel oil range, therefore, this fraction may need to undergo catalytic cracking and hydrotreatment to produce additional jet fuel.

5.3 Analysis of Co-Coke

5.3.1 Petrographic Methods Applied to Delayed Coke

Delayed coking is a process designed to retrieve additional hydrocarbon distillate from residual materials generated from various processes during the refining of raw petroleum. This is accomplished by heating the residual materials in the range of 460°-500°C in one vessel and then pumping them into a second vessel where a solid coke forms as devolatilization occurs [5-17]. Of first importance to refining is the recovery of distillate and to effectively eliminate as much of these residual materials as quickly as possible so that production is not slowed for want of storage space. Of second importance to the refiner is to maximize liquid yield from the coker without adversely influencing production rate. Perhaps, of much less importance, is consideration of coke quality which can be influenced by the blend of crude oils being processed, the amount and quality of the various residuals being fed to the delayed coker at any given time, (fractionators or vacuum bottoms resid, catalytic cracking unit, hydrotreating, pyrolysis, etc.) and the operation of the coker (temperature, back pressure and amount recycled). Nevertheless, customers are available in a carbon industry that is growing at 3% per year to purchase the coke, provided that there can be some quality assurance [5-18].

In general, the delayed coker operator recognizes three types of petroleum coke, i.e., *shot*, *sponge* and *needle* coke listed here in order of increasing value and shown in **Figure 5-5**. **Shot coke** derives its name from the fact that it resembles BB shot mostly less than 2-6 mm in diameter, but some larger spheres have been observed [5-19]. It has been suggested that shot coke forms from the early and rapid devolatilization of the residuals that causes entrainment and accretion of the remaining asphaltenic fractions, but in general it forms when very heavy residuals are being processed. The internal textural properties of individual shot particles (**Figure 5-6**) exhibit a concentric arrangement of isochromatic elements signifying accretion

occurred as particles or packets and not at the molecular level. Although the coke is considered to be of low value, usually sold as a combustion fuel, the refiner may look on its production as a clear sign of efficient recovery of liquids.

Sponge coke derives its name from the variety of relatively large and rounded gas vacuoles that are visible in its rather bulky structure, similar to a sponge. The larger particle size and the trapping of many different sizes of gas vacuoles suggest that either devolatilization occurred more slowly or that the gas phase had more time to interact with the remaining viscous or plastic liquid within the coke drum. The slower solidification rate and the internal gas pressure exerted by adjacent gas vacuoles allows for better alignment of the polynuclear aromatic molecules into a turbostratic structure before solidification of the coke. The result is a carbon that contains larger, better aligned more elongated optical textures (see **Figure 5-6**); textures that promote better thermal and electrical conductivity. Thus, sponge coke is a much more attractive and valuable carbon product that, when calcined, is employed as a solid filler phase in the production of anodes for the aluminum industry or the preparation of TiO₂ pigments.

Needle coke derives its name from the acicular or needle-shaped particles that result when the carbon is crushed. As seen in **Figure 5-5**, needle coke has an elongated porosity which has apparently contributed to the alignment of basal planes within the carbon parallel to their long axis. Feed stocks used for making needle coke are largely highly aromatic residua (decant oil) that may or may not have been augmented by secondary processing. Clearly, the gas/plastic carbon phase interaction occurs within the coke drum in a manner that the viscoelastic system forms cylindrical shape gas vacuoles. As seen in **Figure 5-6**, the carbon exhibits very large and elongated carbon textures. This close association of texture and structure is useful in the production of extruded graphite electrodes used in electric arc steel making process and the production of synthetic graphite when properly calcined. The carbon therefore commands a very high price compared with the other petroleum cokes.

Figure 5-6 exhibits the most common textural elements of these petroleum coke types, micrographs taken with a Zeiss AxioCam 2 megapixel digital camera (purchased with funds from this project) employing on an optical microscope using reflected, polarized, white light and oil immersion at 625X magnification. The different colors are derived from the use of a retardation plate that increases the birefringence of the anisotropic carbon. The size and shape of

each isochromatic region bears some relationship with the imperfectly formed graphite lattice and can be quantified by optical microscopic techniques.



Figure 5-5 – Hand Specimens of Different Types of Petroleum Coke

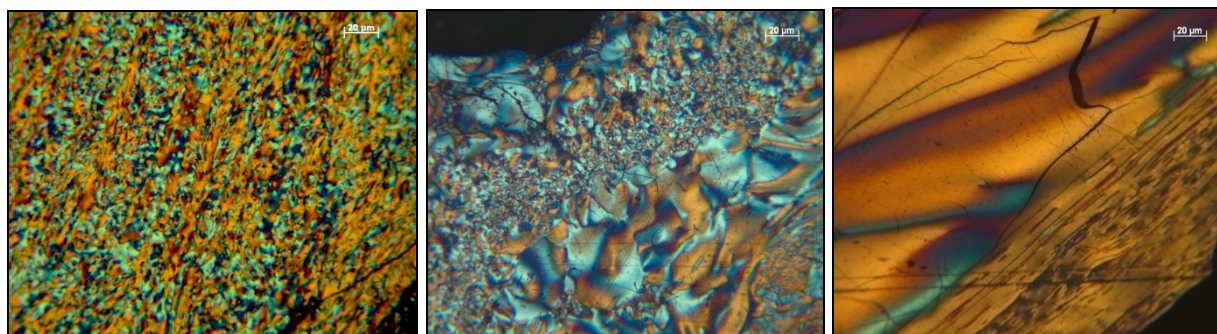


Figure 5-6 – Most Common Optical Textures Associated with Types of Petroleum Coke

Five different textural elements (some shown in **Figure 5-6**) belonging to carbon derived from most petroleum residua (including vacuum fractionation residua, decant oil, pyrolysis tar, etc.) and that were used in the point counting are described as follows;

Isotropic – a relatively low reflecting, dark gray (or violet) carbon material that displays little or no optical activity when the specimen is rotated under crossed-polarized light.

Mosaic – a higher reflecting carbon textural element that displays optical anisotropy and is characterized by isochromatic units of less than 10 µm.

Small Domain – is an anisotropic carbon texture, which exhibits isochromatic units of between 10 – 60 µm in diameter.

Domain – is an anisotropic carbon having much larger isochromatic units of greater than 60 µm diameter or long axis.

Flow Domain – is an anisotropic texture exhibiting elongated isochromatic areas of greater than 60 µm in length and ≤ 10 µm wide.

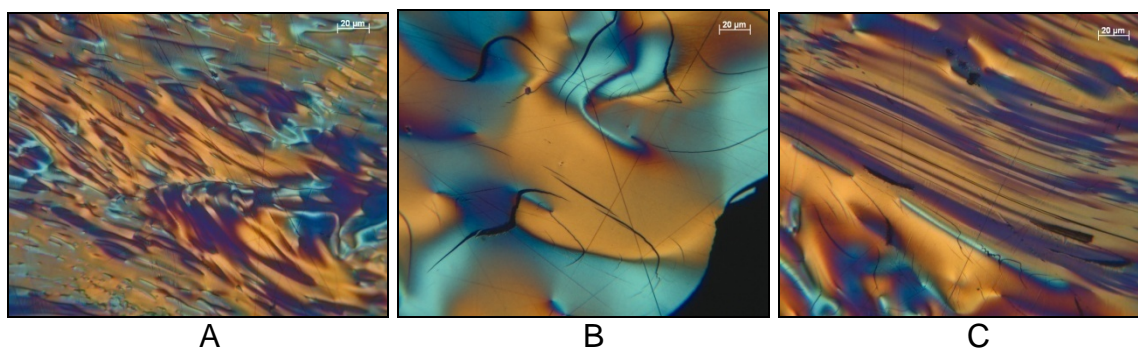


Figure 5-7 – Examples of Common Textural Elements In Laboratory Delayed Coke Made from United Refining Decant Oil EI-107 showing (A) Small Domain and Mosaic, (B) Domain, and Flow Domain, (C) Domain and Small Domain Textures

A point count analysis of the volume percentage distribution of carbon textures can be performed by traversing the polished surface of a representative sample based upon a 0.2 x 0.2 mm grid and identifying the textural element under a crosshair held in a microscope eyepiece. A total of 1000 counts are accumulated, 500 from each of two surfaces and the results are given as volume percentages in **Table 5-13**.

The first four petroleum cokes in **Table 5-13** were commercially-derived green delayed cokes and, as can be seen, as coke quality increased (shot < sponge < needle) there was an increase in the larger, more elongated optical textures (small domain, domain and flow domain) at the expense of the mosaic texture. In comparison, cokes made from our standard decant oil (EI-107) using our laboratory-scale coker gives coke with an even larger size distribution.

Table 5-13 - Comparison of Coke Types by Petrographic Analysis, vol. %

Sample Id.	Isotropic	Mosaic <10 µm	Small Domain 10 – 60 µm	Domain >60 µm	Flow Domain <10 µm Wide >60 µm Long
Shot Coke, Combustion Fuel	1.0	91.5	7.4	0.1	0.0
Resid-rich Sponge Coke	1.1	47.1	46.3	1.6	3.9
Decant Oil-rich Sponge Coke	2.5	25.0	58.7	7.4	6.4
Decant Oil Needle Coke,	0.4	22.4	51.7	9.7	15.8
EI-107, Standard DO	0.5	6.6	66.0	21.9	5.1

The addition of bituminous coal to the petroleum residua before delayed coking has a profound influence on the distribution, size and shape of the carbon textures. At least in the current study, coal suitable for producing metallurgical coke, possessing great thermoplastic properties, were

evaluated. Generally, when coal was added four additional textural components could be identified and are described as follows.

Vitrinite-Derived Mosaic – the characteristic 0.5-2.0 μm diameter isochromatic units typically generated during the carbonization of vitrinite of high volatile bituminous coals (see **Figure 5-8**). During co-carbonization with decant oil the isochromatic areas of bituminous rank vitrinite can become enhanced to between 2.0 - 6.0 μm . In this investigation a distinction was made between **enhanced** (approximately $>2.0 \mu\text{m}$) and **non-enhanced** (generally $<2.0 \mu\text{m}$) isochromatic areas derived from vitrinite. The enhanced textures of vitrinite can be distinguished from the rounded petroleum-derived mosaic by their irregular and sometimes angular shape.

Isotropic Vitrinite – It is possible that some vitrinite may become thermoplastic but not develop a mesophase during carbonization and therefore may remain isotropic.

Inertinite-Derived Texture – angular and irregular shaped particles trapped in the vitrinite or petroleum residua matrix, which may or may not display remnant cell structures and are mostly isotropic.

Mineral Matter – remnant particle of coal-derived mineral matter that usually includes clays, pyrite, quartz and carbonate minerals.

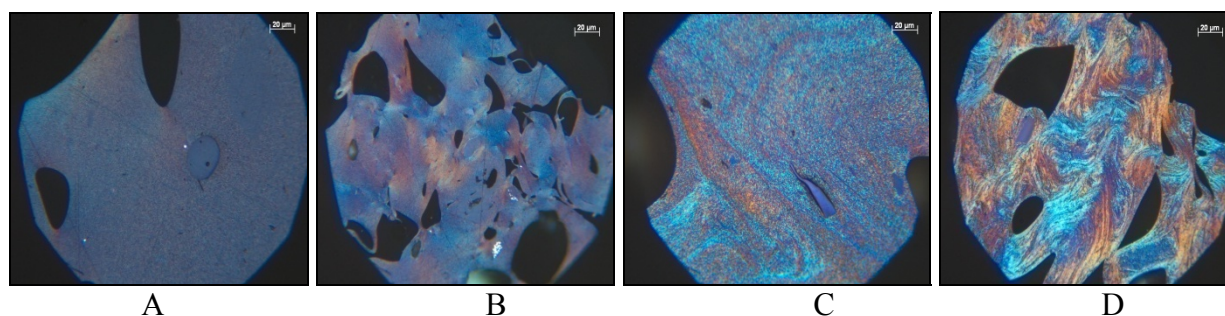


Figure 5- – Carbon Textures Observed the Plastometer Residues of the Pittsburgh Seam Clean Coal Product EI-186 (A & B) Compared with Those Derived from the Marfork Product EI-187 (C & D)

When bituminous coking coals are heated at $3^{\circ}\text{C}/\text{min}$ to 500°C , the vitrinite portion of the coal softens, swells, gives off volatile matter and attains thermoplasticity sufficient to bind inert (non-thermoplastic) mineral and organic matter within a consistent matrix. In the current investigation a great deal of effort was given to reducing the mineral and organic inert constituents and increasing the vitrinite concentration. Two coal products each $\leq 1.0\%$ ash yield were prepared from the flotation effluent from cleaning plants operating with Pittsburgh seam coal alone or from a blend of four coals (Powellton, Eagle, Lower Cedar Grove and #2 Gas)

called the *Marfork product*. When these coals were heated as suggested above in a Gieseler plastometer the carbon material generated had the optical appearance shown in **Figure 5-8**; very much smaller isochromatic textures compared with petroleum-derived materials shown in **Figures 5-6 and 5-7**. As shown, the optical textures obtained from the Pittsburgh seam vitrinite were typically less than 1.0 μm (**5-8B**) and a fair amount was less than 0.5 μm (**5-8A**). Textures obtained from the higher rank Marfork vitrinite exhibited mosaic units of around 2.0 μm (**5-8C**) which have been influenced by the stirring of the thermoplastic mass in the plastometer to form elongated lenticular textures (**5-8D**).

When these same bituminous coals were co-coked with decant oil at about 480° - 500°C in our 1.0 kg/hr laboratory delayed coker, an interaction occurred that influenced the carbon textures normally derived from the coal and those derived from the decant oil. As already shown (**Figure 5-7**), the decant oil in question generated very large isochromatic textures compared with the coals (**Figure 5-8**). **Figure 5-9** shows the different interactions of Marfork vitrinite and decant oil during co-coking that result in the enhancement of the vitrinite carbon texture. **Figure 5-9A** shows Marfork vitrinite has become thoroughly thermoplastic and developed a <2.0 μm optical texture. The angular inclusions (blue) scattered throughout the field of view are particles of inertinite (non-thermoplastic organic constituents of coal) that have an isotropic texture and are usually incorporated within the vitrinite-derived binder phase of coke. **Figures 5-9B and 5-9C** show stages in the process of co-mingling of carbon textures derived from the two raw materials such that they are inseparable as shown on the left side of **Figure 5-9C**.

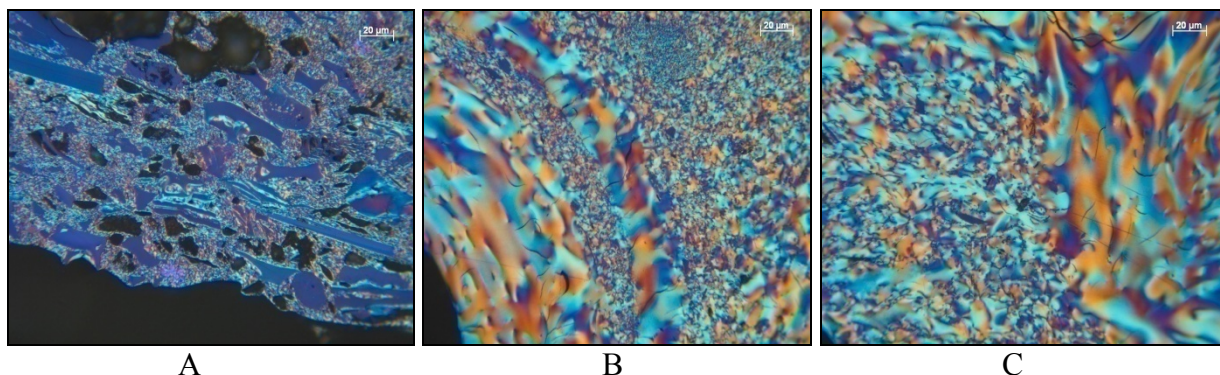


Figure 5-9 – The Different Degrees of Interaction of Vitrinite (Marfork EI-187) with Decant Oil during Laboratory Scale Co-coking; (A) no interaction, angular inclusions are inertinite; (B) partial interaction where mosaic textures have been enhanced >2.0 μm ; (C) completely dispersed

The apparent lack of interaction observed for some regions of vitrinite suggested a closer look at the distribution of coal- and decant oil- derived carbon throughout the carbon artifact. Following the coking, soaking time and cooling cycle, coke was generally removed from the coke drum as a tapered cylinder, although occasionally the artifact broke into several large pieces. One-centimeter thick sections were cut (diamond saw) from the full diameter (~80 mm) of the cylinders at ever increasing distance from the inlet (bottom) for one of the twelve artifacts generated from our two co-cokes, i.e., Run #55 for the Pittsburgh seam coke and Run #85 for the Marfork. Exterior (~0-20 mm) and interior (~20-40 mm) radial sections or composites of the entire section were prepared for optical microscopy and proximate analysis in an effort to define the homogeneity of the coke.

Tables 5-14-5-16 provide data for the Pittsburgh artifact from Run #55, whereas **Tables 5-17-5-19** give data for the Marfork Run #85. **Tables 5-14** and **5-17** show the volume percentage of each carbon textural category for each radial section and composite for six segments from 1.0 cm to 31.0 cm above the inlet for the two different co-cokes. **Tables 5-15** and **5-18** condense the data into the percentage of coal-derived and petroleum-derived textures and normalizes the concentration of decant-oil derived textures to 100% so that the influence of coal addition on the decant oil textures might be described. Close inspection of the petrographic data from both cokes agree that;

- 1). Coal-derived components tend to be concentrated at the bottom and the center of the coke drum.
- 2). Most of the non-enhanced vitrinite texture was found within the bottom 7 cm of the coke drum.
- 3). Size of isochromatic textures attributable to the decant oil have decreased significantly, whereas before coal addition small domain and domain textures dominated and after coal addition mosaic and small domain were predominant.
- 4). For both artifacts the percentage of coal-derived materials decreased to the 12-13 cm above inlet segment and then increased slightly in the next two segments (18-19 cm and 24-25 cm).

Table 5-14– Petrographic Analysis of Carbon Textures in Pittsburgh Coker Sample #55 by Size and Origin, Vol. %

Long. Interval, cm	Cross Section, mm	Vitrinite-derived		Inert- derived	Isotropic Vitrinite	Min. Matter	Isotropic Petroleum derived	Mosaic, <10µm	Small Domain, 10-60µm	Domain >60µm	Flow Domain, >60µm L, <10µm W
		Enhanced	Non- enhan.								
1.0 – 2.0	0.0 – 19.5	15.1	0.0	0.8	0.0	0.0	0.2	58.2	25.3	0.4	0.0
	19.5 – 43.0	32.3	17.3	3.7	0.0	0.3	0.2	45.2	1.0	0.0	0.0
	Composite*	24.5	9.4	2.4	0.0	0.2	0.2	51.1	12.0	0.2	0.0
6.0 – 7.0	0.0 – 19.0	19.2	0.0	1.2	0.0	0.0	0.1	54.9	24.2	0.1	0.3
	19.0 – 40.0	16.3	11.9	1.9	0.0	0.1	0.2	41.8	26.8	0.1	0.9
	Composite	17.7	6.2	1.6	0.0	0.0	0.2	48.0	25.6	0.1	0.6
12.0 – 13.0	0.0 – 21.0	1.9	0.0	0.0	0.0	0.0	0.8	12.2	71.0	8.3	5.8
	21.0 – 43.0	7.3	0.0	0.4	0.0	0.0	0.2	14.1	60.7	10.2	7.1
	Composite	4.7	0.0	0.2	0.0	0.0	0.5	13.2	65.7	9.3	6.4
18.0 – 19.0	0.0 – 21.0	6.9	0.0	0.3	0.0	0.1	0.2	19.3	66.8	4.4	2.0
	21.0 – 43.0	13.9	0.1	0.4	0.0	0.2	0.1	23.0	58.0	3.5	0.8
	Composite	10.5	0.0	0.4	0.0	0.2	0.2	21.2	62.2	3.9	1.4
24.0 – 25.0	0.0 – 24.0	15.6	0.0	1.0	0.0	0.0	0.2	43.8	37.6	0.4	1.4
	24.0 – 42.0	8.5	0.0	0.7	0.0	0.0	0.5	26.2	58.8	3.7	1.6
	Composite	12.6	0.0	0.9	0.0	0.0	0.3	36.2	46.7	1.8	1.5
30.0 – 31.0	0.0 – 18.0	2.8	0.0	0.4	0.0	0.0	0.5	36.6	56.7	1.7	1.3
	18.0 – 35.0	8.1	0.2	0.5	0.0	0.0	0.3	38.5	49.5	1.4	1.5
	Composite	5.4	0.1	0.4	0.0	0.0	0.4	37.5	53.2	1.6	1.4

*Calculated from the sum of the fractional contribution of inner and outer intervals.

Table 5-15– Proportion of Textures Derived from Pittsburgh Seam Coal and Decant Oil Compared with the Normalized Concentration of Decant Oil Textures in Coke from Run #55, Vol. %

Long. Interval, cm	Cross Section, mm	% Coal- derived	% Petroleum- derived	Isotropic Petroleum- derived	Mosaic, <10µm	Small Domain, 10-60µm	Domain >60µm	Flow Domain, >60µm L, <10µm W
1.0 – 2.0	0.0 – 19.5	15.9	84.1	0.2	69.2	30.1	0.5	0.0
	19.5 – 43.0	53.6	46.4	0.4	97.4	2.2	0.0	0.0
	Composite	36.5	63.5	0.3	80.5	18.9	0.3	0.0
6.0 – 7.0	0.0 – 19.0	20.4	79.6	0.1	69.0	30.4	0.1	0.4
	19.0 – 40.0	30.2	69.8	0.3	59.9	38.4	0.1	1.3
	Composite	25.5	74.5	0.3	64.4	34.4	0.1	0.8
12.0 – 13.0	0.0 – 21.0	1.9	98.1	0.8	12.4	72.4	8.5	5.9
	21.0 – 43.0	7.7	92.3	0.2	15.3	65.8	11.0	7.7
	Composite	4.9	95.1	0.5	13.9	69.1	9.8	6.7
18.0 – 19.0	0.0 – 21.0	7.3	92.7	0.2	20.8	72.1	4.7	2.2
	21.0 – 43.0	14.6	85.4	0.1	26.9	68.0	4.1	0.9
	Composite	11.1	88.9	0.2	23.8	70.0	4.4	1.6
24.0 – 25.0	0.0 – 24.0	16.6	83.4	0.2	52.5	45.1	0.5	1.7
	24.0 – 42.0	9.2	90.8	0.6	28.8	64.7	4.1	1.8
	Composite	13.5	86.5	0.3	41.9	54.0	2.1	1.7
30.0 – 31.0	0.0 – 18.0	3.2	96.8	0.5	37.8	58.6	1.8	1.3
	18.0 – 35.0	8.8	91.2	0.3	42.2	54.4	1.5	1.6
	Composite	5.9	94.1	0.4	39.9	56.5	1.7	1.5

Table 5-16 – Proximate Analysis of Pittsburgh Run #55 from Different Levels above Inlet Compared with the Green and Calcined Coke Composite Provided by A. J. Edmond

Sample Id.	% Moisture	% Ash, dry	% Volatile Matter, dry	% Fixed Carbon, dry	Sulfur
1-2 cm, A	1.26	1.38	7.44	91.18	nd
1-2 cm, B	1.42	3.25	7.55	89.20	nd
12-13 cm, A	1.27	0.39	6.97	92.64	nd
12-13 cm, B	1.17	0.53	8.89	90.58	nd
24-25 cm, A	1.15	0.69	7.03	92.28	nd
24-25 cm, B	1.25	1.06	6.64	92.30	nd
Green Composite	0.55	1.25	6.65	92.10	1.29
Calcined Composite	0.05	1.52	1.51	96.97	1.34

**Table 5-17 – Petrographic Analysis of Carbon Textures in Coker Sample #85 by Size and Origin, Vol. %:
80% EI-107 DO + 20% Marfork EI-187**

Long. Interval, cm	Cross Section, mm	Vitrinite-derived		Inert- derived	Isotropic Vitrinite	Min. Matter	Isotropic Petroleum derived	Mosaic, <10µm	Small Domain, 10-60µm	Domain >60µm	Flow Domain, >60µm L, <10µm W
		Enhanced	Non- enhan.								
1.0 – 2.0	0-15	47.4	5.9	1.2	0.0	0.0	0.0	33.1	12.2	0.2	0.0
	19-38	44.6	24.5	4.0	0.0	0.0	0.0	23.2	3.4	0.3	0.0
	Composite*	45.1	13.8	3.2	0.0	0.0	0.0	27.3	10.3	0.2	0.1
6.0 – 7.0	0-19	9.2	0.5	0.8	0.0	0.0	0.2	11.9	64.9	9.3	3.2
	23-42	1.6	0.0	0.8	0.0	0.0	0.2	8.2	76.7	9.4	3.1
	Composite	6.8	1.4	0.4	0.0	0.0	0.0	17.7	65.2	5.4	3.1
12.0 – 13.0	0-18	0.4	0.1	0.3	0.0	0.0	0.0	7.4	85.4	4.9	1.5
	22-43.5	6.3	0.1	0.3	0.0	0.0	0.1	10.1	76.1	4.9	2.1
	Composite	4.1	0.5	0.4	0.0	0.0	0.4	19.5	70.5	3.7	0.9
18.0 – 19.0	0-21.5	5.6	1.1	0.5	0.0	0.0	0.2	11.2	79.0	1.7	0.7
	25.5-43.5	15.4	4.6	2.9	0.0	0.0	0.1	30.9	44.7	0.6	0.8
	Composite	12.0	2.8	0.8	0.0	0.1	0.0	30.0	53.2	0.8	0.3
24.0 – 25.0	0-20	10.1	0.0	1.6	0.0	0.0	0.2	20.7	64.4	2.7	0.3
	24-45	6.7	0.1	1.2	0.0	0.1	0.4	16.4	72.3	2.2	0.6
	Composite	7.6	0.5	0.6	0.0	0.0	0.1	25.8	63.1	1.6	0.7
30.0 – 31.0	0-19	0.0	0.0	0.3	0.0	0.0	0.8	11.8	83.3	2.3	1.5
	23-43	0.0	0.0	0.4	0.0	0.1	0.5	7.1	85.1	4.8	2.0
	Composite	4.7	0.2	0.6	0.0	0.0	0.1	22.9	67.7	2.7	1.1

* Composite of remainder of section crushed to -20 mesh and analyzed for comparison.

Table 5-18 – Proportion of Textures Derived from Pittsburgh Seam Coal and Decant Oil Compared with the Normalized Concentration of Decant Oil Textures in Coke from Run #85, Vol. %

Long. Interval, cm	Cross Section, mm	% Coal- derived	% Petroleum- derived	Isotropic Petroleum- derived	Mosaic, <10µm	Small Domain, 10-60µm	Domain >60µm	Flow Domain, >60µm L, <10µm W
1.0 – 2.0	0-15	54.5	45.5	0.0	72.8	26.8	0.4	0.0
	19-38	73.1	26.9	0.0	86.3	12.6	1.1	0.0
	Composite	62.1	37.9	0.0	72.0	27.2	0.5	0.3
6.0 – 7.0	0-19	10.5	89.5	0.2	13.3	72.5	10.4	3.6
	23-42	2.4	97.6	0.2	8.4	78.6	9.6	3.3
	Composite	8.6	91.4	0.0	19.4	71.3	5.9	3.4
12.0 – 13.0	0-18	0.8	99.2	0.0	7.5	86.1	4.9	1.5
	22-43.5	6.7	93.3	0.1	10.8	81.6	5.3	2.2
	Composite	5.0	95.0	0.4	20.5	74.2	3.9	1.0
18.0 – 19.0	0-21.5	7.2	92.8	0.2	12.1	85.1	1.8	0.8
	25.5-43.5	22.9	77.1	0.1	40.1	58.0	0.8	1.0
	Composite	15.7	84.3	0.0	35.6	63.1	0.9	0.4
24.0 – 25.0	0-20	11.7	88.3	0.2	23.5	72.9	3.1	0.3
	24-45	8.1	91.9	0.4	17.8	78.7	2.4	0.7
	Composite	8.7	91.3	0.1	28.3	69.1	1.7	0.8
30.0 – 31.0	0-19	0.3	99.7	0.8	11.8	83.6	2.3	1.5
	23-43	0.5	99.5	0.5	7.2	85.5	4.8	0.0
	Composite	5.5	94.5	0.1	24.2	71.6	2.9	1.2

* Composite of remainder of section crushed to -20 mesh and analyzed for comparison.

Table 5-19 – Proximate Analysis of Marfork Run #85 from Different Levels above Inlet Compared with the Green and Calcined Coke Composite Provided by A. J. Edmond

Sample Id.	% Moisture	% Ash, dry	% Volatile Matter, dry	% Fixed Carbon, dry	Sulfur
1-2 cm, composite	1.52	2.00	7.60	90.40	nd
6-7 cm, composite	1.23	0.60	7.17	92.23	nd
12-13 cm, composite	1.11	0.52	6.91	92.58	nd
18-19 cm, composite	1.22	1.04	7.33	91.63	nd
24-25 cm, composite	1.18	0.69	7.05	92.26	nd
30-31 cm, composite	1.06	0.55	7.09	92.37	nd
AJE, Green Composite	1.02	0.65	5.68	93.67	nd
AJE, Calcined Composite	0.00	0.77	0.91	98.32	nd

Results from measurement of the moisture, volatile matter and ash yields and calculation of fixed carbon (proximate analysis) for both cokes are provided in **Tables 5-16** and **5-19**. Samples were prepared from the exterior and interior regions of three Pittsburgh segments, whereas composite samples of six segments were prepared from the Marfork co-coke. The ash yield was found to be greatest where coal-derived textures were more highly concentrated, i.e., mainly at the bottom and toward the interior of each segment. The volatile matter (fixed carbon) yield was considerably more variable, but tended to be of greater value in the interior of the coke mass.

The petrographic and proximate analysis data suggested that, although coal particles were becoming thermoplastic, the viscosity difference between coal and decant oil resulted in the partial agglomeration of coal particles and their collection and deposition near the coker drum inlet. Earlier work [5-20] in which the feed rate and blending pot temperature were increased, showed some improvement in forcing coal-derived carbon higher into the coker drum during co-coking. Increased blending temperature was more successful, but was also responsible for some loss of volatile matter from the decant oil which would undoubtedly change the chemistry of that raw material. Clearly, more effort is needed to determine feed conditions that would deliver coal near its thermoplastic maximum as it is blended with the hot decant oil as it was being fed to the coke drum. Nevertheless, a pot temperature of 120°C and a feed rate of 16.7 g/min were established as standard run conditions for this investigation, with the realization that a more homogeneous coke could probably be achieved with a better feed procedure.

Composite Coke Characterization

As described earlier, Alcoa, Inc. agreed to perform cursory laboratory tests using our two co-cokes in replacement of their “standard or plant petroleum coke” for laboratory evaluation of calcined coke, production of bench-scale anodes, and measurement of baked apparent density and electrical resistivity. Although the details of this investigation will be covered in a following section (5.4), certain aspects of coke characterization will be introduced here.

Preparation and testing of bench-scale anodes required a considerable amount of coke (~19 kg) after calcining in order to meet the strict particle size distribution. Consequently, twelve consecutive coker runs were made to prepare the proper amount of coke from each clean coal product (Pittsburgh and Marfork). The group of coke artifacts for each coal was shipped to

A.J. Edmond Company where they were crushed, homogenized and batch calcined at 1275°C for 10 minutes. Certain analyses specific to the aluminum industry were requested as well as the return of representative sample of both the green and calcined cokes. The remainder of the coke was built into several 5 kg aliquots of the proper particle size distribution and provided to Dr. Angelique Adams at Alcoa, Inc. for evaluation.

In addition to the petrographic analyses, both point count and reflectance were done, completed for the green and calcined coke composites (**Tables 5-20-5-22**) and detailed analytical information was provided by A.J. Edmond Company (**Table 5-23**). Briefly, from this information a number of observations can be made. First, on a volume percentage basis, coal amounted to between 11-17% of the coke (green or calcined, **Table 5-21**). Based on weight percentage and estimated coke yields from decant oil (~19%) and coal (~66%) under delayed coking conditions, the volume percentages measured are low and should have been more in the range of 54% derived from decant oil and 46% derived from coal. Second, although there was some variation noted with the Marfork coke textures, there was only minor differences between green and calcined coke, i.e., more flow domain and mosaic and less small domain and domain textures as a result of calcination.

A much greater influence was observed in determining the mean maximum reflectance values for green and calcined cokes (**Table 5-22**). In this work, fifty reflectance readings were collected from isochromatic domains greater than 30 μm in diameter and that exhibited birefringence by diverting light to a standardized photomultiplier and recording the maximum and minimum values during a 360° rotation of the stage. Reflectance values were taken on carbon textures derived from decant oil and not the coal using a Leitz MPV2 research microscope at 625 x magnification in white light and oil immersion. As can be seen in **Table 5-22**, co-coking coal and decant oil to ~500°C causes the carbon textures derived from decant oil to attain a fairly high reflectance (6.6-7.3%), in the range equivalent to anthracite or meta-anthracite coals. Heating to 1275°C more than doubled the maximum reflectance (16.1-17.0%) and saw a much reduced mean minimum reflectance. Bireflectance, a value calculated by subtracting the minimum reflectance value from the maximum, an apparent measure of anisotropy, also increased significantly due to calcinations. As will be discussed in other sections of this report, calcinations not only reduces the volatile matter content, but has a profound influence on d_{002} spacing, L_c , and L_a measured from x-ray diffraction. Basically,

heating resulted in a condensation of the forming carbon lattice, and as shown in **Table 5-23**, there was a decrease in the HGI and volatile matter, whereas there was an increase real density. In addition, although the ash yield of the composite coke was much lower than would have been predicted by the coal ash yields (0.9 and 1.0%), calcinations increases the concentration of ash as well as a certain number of elements important to anode quality.

5.3.2 Co-coking With 30% Coal Additions

Table 5-24 shows the basic properties of three coals that were tested at 30 wt% concentration in the Penn State delayed coker; all previous runs were done at 20 wt% coal. As seen, the Canterbury Lower Kittanning seam coal was relatively higher in rank and ash yield and had been an early candidate for deep cleaning and consecutive co-coking runs. However, during the course of evaluation it was found that the coal product was a blend of two coals of distinctly different rank, i.e., high volatile A and medium volatile bituminous. Even though the thermoplastic properties of the test sample were within our experimental range, potential variable contributions of medium volatile coal fed to the cleaning plant and the potential that medium volatile coal could be concentrated by our cleaning technique, it was decided that in this product should be rejected as a potential for co-coke. During the course of evaluating the Canterbury product, several co-coking runs were conducted that included using 30 wt% coal. Because the coal was rejected from our experimental plan for the reasons outlined above, no further work was performed on the delayed coke liquid or solid products. During this investigation, increasing the weight percentage of coal to 30 % was revisited using the Pittsburgh (EI-186) and Marfork (EI-187) clean coal products as a potential means of increasing the amount of coal-derived liquids that may be generated during co-coking as well as determining what influences a higher concentration of coal might have on the operability of our laboratory delayed coker and on coke quality.

Table 5-24 – Comparison of Properties of the Pittsburgh and Marfork Clean Coal Products with Canterbury Lower Kittanning Coals Used in Co-coking Runs Using 30 Wt. % Coal

Analytical Procedure	Pittsburgh FCE 1.280 Float EI-186	Marfork JCE 1.268 Float EI-187	Canterbury Lower Kittanning*
Proximate Analysis: (dry)			
Fixed Carbon, %	63.4	66.5	68.5
Volatile Matter, %	35.6	32.6	31.5
Ash, %	1.0	0.9	10.0
Ultimate Analysis: (dry)			
Carbon, %	84.6	89.2	87.2
Hydrogen, %	5.3	5.5	6.0
Nitrogen, %	1.6	1.7	1.5
Sulfur, %	1.1	0.8	1.9
Oxygen, % (diff.)	6.4	1.9	3.3
Gieseler Plastometer:			
Softening Temperature, °C	385	375	381
Fluid Temperature Range, °C	93	121	110
Maximum Fluidity (ddpm)	29,527	29,516	27,469
Temperature at Maximum, °C	436	439	449
Organic Petrography: (volume %)			
Total Vitrinite	96.2	91.4	81.7
Total Liptinite	1.5	3.9	2.4
Total Inertinite	2.3	4.7	15.9

* Vitrinite reflectance analysis revealed this coal sample to be composed of two distinct coals; 73% hvAb and 27% mvb.

5.3.2.1 Results and Discussion

Run conditions and product yield comparing the three coal products are given in **Table 5-25**. As shown, operating conditions for three of the runs were similar, but the feed rate used for run #83 was much higher, owing to gearing problems with the newly repaired feed pump. Also, the standard soak time for coke held in the reactor at 500°C had been increased from 6h to 24h. Nevertheless, for each coal the overall liquids yields were lower and coke yields higher when 30 wt.% coal was used during co-coking compared with 20 wt% concentration.

Table 5-25 – Run Conditions used for Pittsburgh Seam FCE (EI-186) and Canterbury Lower Kittanning Coals at 30 wt% Co-coking

Conditions	Canterbury Lower Kittanning		Pittsburgh FCE EI-186		Marfork JCE EI-187	
	37	36	50-61	83	84-92,95-97	98
Run #	20	30	20	30	20	30
Wt. % Coal	5.5	5.5	5.86	3.75	6.0	6.0
Feed Stock, hrs	0	0	0	0	0	0
Steam Stripping	6	6	24	24	24	24
Hold at 500°C, hrs	16.7	16.7	16.76	26.6	16.7	16.7
Feed Rate, g/min	108	109	120.9	116	116.8	128
Preheater inlet, °C	443	436	438.7	425	427.4	428
Preheater Outlet, °C	470	468	499.2	466	490	469
Coke Drum Inlet, °C	471	468	496.3	491	480.9	476
Coke Drum Low/Mid, °C	470	474	478.8	474	472.6	470
Coke Drum Top, °C	4931	4676	5750	5558	5760.8	5676
Material Fed, g						
Products:						
% Coke	30.2	37.5	27.42	33.6	28.85	38.99
% Liquid Products	60.4	51.8	62.82	58.4	69.90	59.87
% Gas (diff.)	9.4	10.7	9.76	8.0	1.25	-0.72

Briefly, liquid products obtained from the Marfork runs (compared to runs with Pittsburgh seam coal) showed a significant increase in the lighter distillates (gasoline IBP-180°C, jet fuel 180-270°C and diesel 270-332°C) and a decrease in the fuel oil fraction (332-FBP°C) when measured by SIMDIS GC and by vacuum distillation. In addition to the liquid products the coke yield also increased. The gasoline fraction was 2.92%, the jet fuel fraction 5.16%, the diesel fraction 23.8%, and the fuel oil fraction 66.8%. Some of the coke materials have been evaluated by optical microscopy and these results are provided in **Tables 5-26** and **5-27**. What prompted this evaluation was the observation that the 30% Pittsburgh (EI-186) run generated shot coke. As seen in the photograph below (**Figure 5-10**), the cross-sectional area of the coke artifact about 14 cm above the coker inlet shows the aggregate of rounded (1-3mm diameter) particles filling the interior and surrounded by a competent rim of coke that formed against the reactor wall. As was discussed earlier, a higher feed rate tended to generate a minor amount of rounded particles similar to shot coke, but this was the first observation of significant production. It appears that a combination of higher feed rate and coal concentration may be at fault. Coke artifacts from both the Canterbury (Run#36) and Marfork (Run#98) 30% runs also exhibited shot coke formation, although not to the extent observed for the Pittsburgh seam 30% run performed at a higher feed rate.

Comparison of the distribution of carbon textures in these cokes are given in **Tables 5-26** and **5-27** to show that at least for the Pittsburgh seam coal, the amount of mosaic carbon had increased significantly, apparently at the expense of the small domain texture. Furthermore, a marked increase was observed in the amount of carbon textures that were derived from coal. This was not as apparent for the Marfork coal product compared with the Pittsburgh coal. For all coals, textures derived from vitrinite were larger (or were enhanced) than would have been produced out of the presence of decant oil. In comparison, the amount of coal-derived material observed in the Canterbury coke far exceeds that found in the Pittsburgh and Marfork specimens, which might suggest a lower inter-reactivity of coal and decant oil as a result of the presence of medium volatile coal.



Figure 5-10: Cross-sectional View of Coke Artifact from Run #83 Using 30 wt.% Pittsburgh FCE Clean Coal Product Showing the Development of Shot Coke

Table 5-26 – Petrographic Analysis of Carbon Textures in Composite of Twelve Coker Runs of Pittsburgh and Marfork (Green and Calcined) at 20% Compared with 30% Runs Including Canterbury by Size and Origin, Vol. %

Sample Id. & Run #	Vitrinite-derived		Inert-derived	Isotropic Vitrinite	Min. Matter	Isotropic Pet.-derived	Mosaic, <10µm	Small Domain, 10-60µm	Domain >60µm	Flow Domain, >60µm L, <10µm W
	Enhanced	Non-enhanced								
*P,Green	10.7	1.4	0.8	0.0	0.3	0.3	29.4	52.4	3.5	1.2
P,Calcined	10.4	2.8	1.0	0.0	0.0	0.2	37.4	43.9	2.0	2.3
P,#83, 30%	37.0	2.9	1.2	0.0	0.2	0.2	42.2	16.1	0.0	0.2
M,Green	8.0	2.0	0.3	0.1	0.1	0.0	22.6	62.8	2.8	1.3
M,Calcined	13.2	2.6	0.8	0.0	0.0	0.0	30.3	48.1	2.5	2.5
M#98, 30%	20.2	2.3	0.6	0.0	0.0	0.3	28.8	45.3	1.2	1.3
C,#36, 20%	nd	nd	nd	nd	nd	nd	nd	nd	nd	nd
C,#36, 30%	53.1	8.2	12.3	0.0	0.7	0.0	21.2	4.5	0.0	0.0

P = Pittsburgh, M = Marfork and C = Canterbury

Table 5-27 – Proportion of Textures Derived from Coal and Decant Oil Compared with the Normalized Concentration of Decant Oil Textures in 20% Composite and 30%, Vol. %

Sample Id. & Run #	% Coal-derived	% Petroleum-derived	Isotropic Petroleum-derived	Mosaic, <10µm	Small Domain, 10-60µm	Domain >60µm	Flow Domain, >60µm L, <10µm W
P,Green	13.2	86.8	0.3	33.9	60.4	4.0	1.4
P,Calcined	14.2	85.8	0.2	43.6	51.2	2.3	2.7
P,#83, 30%	41.3	58.7	0.3	71.9	27.5	0.0	0.3
M,Green	10.5	89.5	0.0	25.2	70.2	3.1	1.5
M,Calcined	16.6	83.4	0.0	36.3	57.7	3.0	3.0
M#98,30%	23.2	76.8	0.4	37.5	58.9	1.5	1.7
#36, 20%	nd	nd	nd	nd	nd	nd	nd
#36, 30%	74.3	25.7	0.0	82.5	17.5	0.0	0.0

P = Pittsburgh, M = Marfork and C = Canterbury

5.3.2.2 Conclusions

From this investigation, it appeared that the main influence of increasing the coal concentration to 30 wt% during co-coking was a decrease of the overall liquids yield and thereby increasing the coke yield. Also, it was found that the yield of liquids (gasoline, jet fuel and diesel) was increased at the expense of the fuel oil fraction. It was suggested too that the quality of the coke produced was much diminished, as shot coke was generated from all three coals at the higher concentration. The 30% Pittsburgh seam co-coking run generated the most shot coke probably as a result of the higher feed rate.

5.4 Manufacture and Testing of Carbon Artifacts

It became evident early in the Refinery Integration project that to evaluate coke quality in a convincing manner, then industry procedures and standards must be adhered to as directly as possible within the means of the project. Because the petroleum coke market and quality requirements are rather diverse, it was decided to focus our efforts on the most likely premium carbon market and attempt to prepare a suitable co-coke, i.e., anode grade, calcined sponge coke for the production of pre-baked anodes for the smelting of aluminum. Although production of a suitable quality co-coke for anodes was our main objective, we have also investigated whether co-coke could be used in making graphite. This section describes our research efforts to make premium carbon products from co-coke.

Also, it was apparent that to fully evaluate petroleum coke fillers for the premium carbon industries, that the coke had to be calcined properly and that test anodes of various types, i.e., blends of calcined coke and coal tar or petroleum pitches or their blends, had to be prepared. With this in mind, a company was identified that could help with carbon preparation (A.J. Edmond, Co.), and it was decided to purchase equipment that would allow us to prepare test anodes; the R&D Carbon Bench Scale Unit for the preparation of 1:1000 scale anodes/electrodes shown in **Figure 5-11**. With the assistance of Alcoa, Inc., specifically for permission and technical guidance of Drs. Bernard Racunas, William Walsh and Angelique Adams as well as the preparation of anodes and training provided by Mr. Doug Bruce, we were able to evaluate our coke by the industry that might use the product and received valuable training and comparative information between our respective anode preparation units.

5.4.1 Evaluation of Co-coke as Carbon Filler for Anodes

In an effort to determine the value of our two co-coke samples (Pittsburgh and Marfork), Alcoa, Inc. agreed to perform cursory laboratory tests using our coke in place of their “standard petroleum coke” for laboratory evaluation of calcined coke, production of bench-scale anodes, and measurement of baked apparent density and electrical resistivity. All that was required for this service was to provide 19 kg of calcined coke. Alcoa, Inc. provided the name of a company that they employ, A.J. Edmond, for calcination and basic coke characterization. In October 2005 about 19 kg of co-coke derived from the Pittsburgh coal (EI-186) was shipped to A.J. Edmond for calcining, particle size preparation, and basic characterization, where upon it was shipped to Alcoa, Inc. for bench scale anode evaluation. A report of investigation was prepared by Dr. Adams in February 2006 and is included in this report as **Appendix 5-1**.



Figure 5-11 – R&D Carbon 1:1000 Bench Scale Test Anode Unit; Mixer on Right and Hydraulic Press on Left

In general, Dr. Adams' report said that even though there were some very good attributes regarding the Pittsburgh co-coke that, "the silicon and iron content of the calcined co-coke were well above current specifications, and would result in unacceptable metal purity for a commercial smelter". Consequently, one of our goals for processing the next coal, the Marfork product, was to do an even better job of reducing overall ash yield. Once this co-coke was generated (August 2007) it was processed and characterized by A.J. Edmond in the same manner as the Pittsburgh co-coke. The calcined and sized coke samples were used for training on the Bench Scale Anode Unit employed by Alcoa, Inc. in December 2007 and then anodes were prepared on our new unit (February 2008) for comparison. Selected anodes from the Pittsburgh and Marfork test series prepared by Alcoa, Inc., as well as those provided by Penn State were evaluated in further testing by A.J. Edmond.

5.4.1.1 Quality of Calcined Co-coke

Although the calcining and coke sizing procedure is described in more detail in **Appendix 5-1**, briefly, A.J. Edmonds received our co-cokes as competent cylinders of coke approximately 40 cm long and 8.0 cm in diameter. The twelve cylinders were rough crushed, homogenized, and approximately 3.5 kg of coke was loaded into stagnant calciners, heated to 1275°C for 10 minutes, and allowed to cool under an inert atmosphere. The dry aggregate coke was crushed and sized according to specification provided by Alcoa, Inc., and subsamples for analyses were taken and distributed.

Coke properties of greatest importance to smelting aluminum representing an impact on either the stability/longevity of the anode or the quality of the metal product, includes the real density, vibrated bulk density (VBD), sulfur and metals content (i.e., Si, Fe, Ni, V, Ca and Na). Perhaps of secondary importance is the Hardgrove grindability and pore size distribution, but these measures would be of more value in distinguishing between cokes. Of lowest priority would be the porosity, resistivity and isotropic coke values, although some of these values would be obtained from the test anodes to be discussed later. Most of these values were provided in **Table 5-23** for both the green and calcined coke, but only those for calcined coke have been

repeated below (**Table 5-28**) where they are compared with the target specification used by Alcoa, Inc. in 2006.

Both of the co-cokes generated a very hard, dense filler material having many positive attributes that included high VBD and real density values and lower concentrations of vanadium and nickel which catalyze carbon oxidation and reduce anode life. There was also the much

Table 5-28 – Comparison of Calcined Co-coke with Specification and Standard Coke Quality Employed by Alcoa, Inc. in 2006

Origin	Alcoa	Alcoa	PSU	PSU
Type	Calcined coke	Calcined Coke	Calcined Coke	Calcined Coke
Description	Ideal target specifications	Calcined coke used in production of “standard” anodes	80% EI-107 Oil/20% EI-186 Pittsburgh Coal	80% EI-107 Oil/20% EI-187 Marfork Coal
VBD -30 +50 (g/cc) (USM)	>0.85	0.86	0.925	0.921
Real Density (g/cc-He)	> 2.04	2.06	2.082	2.073
Sulfur (S)	<2.5	2.5	1.34	0.85
Ash%	< 0.5	0.3	0.89	0.77
Calcium (Ca)	< 200	200	262	284
Iron (Fe)	< 300	350	684	639
Nickel (Ni)	< 250	250	7	10
Silicon (Si)	< 250	200	1013	1029
Sodium (Na)	< 200	75	54	53
Vanadium (V)	< 200	350	18	11
Moisture %	< 0.5	ND	ND	ND
Volatile Content Matter %	<0.5	ND	0.71	0.91
Spec. Elec. Resistivity (ohm-in.)	<0.05	ND	0.035	0.037
HGI	~ 30	ND	23.7	26.7

lower total sulfur which would impact plants in meeting environmental specifications. However, the most detrimental problem with co-coke was the concentration of silicon and iron, both a direct transfer from coal mineral matter. As seen in **Table 5-28**, silicon was about four times and iron two times greater in concentration than allowed by the specification. This was noted earlier with the Pittsburgh seam co-coke and significant efforts were made to reduce mineral matter carry over from the coal. As seen, there was a significant decrease in ash yield of the Marfork co-coke, but it had little influence on improving carbon metal quality.

As observed under the optical- and electron- optical microscopes, nearly all of the coal minerals (predominantly silicates, aluminosilicate clay minerals, pyrite and calcite) were intimately distributed as <5µm size discrete particles trapped in the vitrinite matrix or associated with voids in inertinite macerals. Unfortunately, in order to liberate these minerals completely, the coals would need to be crushed below the mineral particle size, which would be impractical from a cost and materials handling point of view.

5.4.1.2 Quality of Test Anodes Using Co-coke

Test anodes are generated by combining dry aggregate with various concentrations of pitch to form a hot mix that is formed into a cylindrical shape in an hydraulic press. Although it depends on specific plant operations and available raw materials, the dry aggregate consists of the prospective petroleum coke (in our case co-coke) and some percentage of the crushed remains of spent anodes, referred to as *butts* or *butt coke*. Not only are the weight proportions of these components of importance, but the weight of the particle size distribution of aggregate components are significant. As shown in **Table 5-29**, our co-cokes were blended with about one quarter butt coke (provided by Alcoa, Inc.) that was considerably coarser than the test coke. For each test series, total aggregate weight was about 4500g.

Table 5-29 Sieve Analysis of Total Dry Aggregate Used in Preparation of Test Anodes Using Pittsburgh and Marfork Co-coke

Aggregate Type	Particle Size	26%	28%	7%	39%	Total %
		Butts	Coarse	Intermediates	Fines	
Butts	-3/4, +1/2	6.2%				1.6%
	-1/2, +1/4	38.9%	1.1%			10.4%
Coarse	-1/4, +4	10.1%	1.0%			2.9%
	-4, +8	16.8%	17.7%			9.3%
	-8, +12	9.8%	41.0%			14.0%
Intermed.	-12, +20	6.5%	27.0%	21.9%	0.1%	10.8%
	-20, +28	3.5%	10.0%	10.9%	0.5%	4.7%
	-28, +60	4.7%	2.3%	49.4%	3.4%	6.7%
Fine	-60, +100	1.5%		10.3%	8.4%	4.4%
	-100, +200	1.3%		6.0%	23.8%	10.1%
	-200, +325	0.4%		1.1%	16.1%	6.5%
	-325	0.4%		0.3%	47.7%	18.7%
		100.0%	100.0%	100.0%	100.0%	100.0%

In addition to obtaining information about coke quality, another important objective of preparing a series of test anodes was to determine the optimum amount of pitch required by the aggregate to make a good anode as well as to eliminate the over use of pitch. Consequently, a test program was developed beginning at some initial pitch concentration (14.5% or 15.5% used in our work) and then the amount of pitch needed to increase the pitch by 0.5% was calculated. Generally, ten test anodes were prepared by pre-heating the homogenized aggregate overnight to the mix temperature of 160°C, mixing the hot aggregate for about three minutes before adding the initial amount of pitch and allowing the green mix to blend for 30 minutes. After that period of blending, 390g of the green mix was removed and placed in a preheated (135°C) hydraulic press where it was molded into a cylinder at 8820 psig and held for 20 seconds before being removed to cool. While the press was working, a new aliquot of pitch was added to the green mix to increase the pitch percentage by 0.5% and was allowed to blend for 5 minutes. This procedure was repeated until the tenth green anode was prepared.

Following test anode preparation, some analytical information can be gathered (green bulk density, dimensions, mass), but usually the green anodes are placed into a baking furnace and heated slowly over a four day period to 1125°C in an inert atmosphere, then allowed to cool over two additional days. Most of the important analytical information was acquired from the baked anode.

5.4.1.2.1 Experimental

The general experimental procedure discussed above was followed for preparation of the Pittsburgh seam co-coke; more specific details are provided in **Appendix 5-1**. As much as possible the preparation of the Marfork co-coke into test anodes followed the general procedure above, however, there were differences in that the exact butt coke material used for the Pittsburgh aggregate preparation was no longer available and a different batch of pitch was used. In each case, the pitch was a high QI, Follansebee, 80% coal tar/20% petroleum pitch obtained from Koppers. A.J. Edmond used the exact calcining method and particles size preparation that had been used with the Pittsburgh co-coke and the same equipment and operator prepared and baked the test anodes for the Marfork co-coke. For both of the co-cokes, a “standard coke”

provided by Alcoa, Inc. was prepared at the same time for comparison, although the standard cokes were different.

In addition, the same blends of standard and Marfork coke with various concentrations of pitch were prepared for use in our new R&D Carbon Bench Scale Unit (**Figure 5-11**). Unfortunately, the operating instructions required a slightly different procedure to the unit used at Alcoa, Inc. The greatest difference was that the anode required only 300g of green mix compared to the 390g used earlier. Furthermore, mix temperature was higher (173°C vs 160°C) and temperature control was less stable in the new unit. The mold for the press could only reach 60°C vs 135°C in the Alcoa unit. Nevertheless, test anodes were prepared and shipped to A.J. Edmond for baking and analysis along with a few of the earlier baked test anodes from the Pittsburgh and Marfork series prepared and baked by Alcoa, Inc.

Two of the measurements made by Alcoa, Inc. (**Appendix 5-A**), baked apparent density (BAD) and electrical resistivity (ER), were performed on all test anodes either by Alcoa, Inc. or by A.J. Edmond. This information was used to select those anodes at or near the optimum pitch concentration for additional testing at A.J. Edmond, including air reactivity, thermal conductivity, air permeability and coefficient of thermal expansion (CTE). Further, A.J. Edmond determined the baked density and electrical resistivity of the test anodes made on the Penn State bench scale unit. Test anodes with 17.5% to 19.0% at 0.5% increment pitch addition were selected.

Test procedures employed by A.J. Edmond were in part dictated by the amount of material available for testing, the size and mass of the test anode segment required for the test, or whether a part of the sample needed to be crushed. The smaller amount of mass used in the Penn State Bench Anode Unit limited the number of tests. Consequently, measurement of baked bulk density, electrical resistivity and air permeability were non-destructive tests requiring uncrushed core segments. Although air reactivity and thermal conductivity measurements could share the same core segment, thermal conductivity like CTE (requiring different size samples of core segments) would result in mass loss and therefore the segment could not be used for other analyses.

Very briefly, the analytical tests that were purchased from A.J. Edmond and their importance are described as follows:

Air Reactivity requires a 50 mm diameter baked anode core 60 mm long, placed in a furnace for 10 hours and heated by a preset temperature program in the presence of air and that is cooled from 550°C to 400°C at 15°C/hour. After cooling, the weight lost to burning was determined and then the remaining sample was mechanically tumbled with steel balls to remove any loosely bound particles, thus providing the weight lost to dusting. This test provides information about the potential carbon loss from the upper surface of an anode (reaching temperatures between 550-650°C) resulting from gasification reactions and whether the permeation of gas into the anode body causing internal reactions that may preferentially attack the binder matrix rather than the filler and result in carbon losses due to dust formation.

Air Permeability requires a 50 mm diameter baked anode core 20 mm long and was determined by measuring the time that a gas needs to pass through a sample in order to refill a partly evacuated system. Although a green anode is gas impermeable, about 40% of the binder volatilizes during baking resulting in open porosity and to increased permeability. Relatively high permeability leads to increased burning and then to excess anode consumption.

Thermal Conductivity requires a 50 mm diameter baked anode core 20 mm long that was clamped between two surfaces, one at 60°C and the other at 20°C. As soon as thermal equilibrium was reached the thermal conductivity in watts per meter per Kelvin were determined. Relative higher thermal conductivity values relate to higher anode top temperature and the prospects of carbon loss due to air reactivity and relatively low number may suggest excessive mechanical strength which may lead to thermal shock and anode failure.

Coefficient of Thermal Expansion (CTE) requires a 50 mm diameter baked anode core 50 mm long. The cylinder of anode was heated within the range of 25°-300°C as a length gauge measured the expansion of the sample and the rate of expansion was recorded per degree of temperature. CTE measured in this manner provides some indication of the potential of the anode to be susceptible to thermal shock.

5.4.1.2.2 Results and Discussion

Basically all of the analytical information comparing anode quality and pitch concentration with co-cokes (Pittsburgh and Marfork) and standard petroleum cokes, prepared and baked at Alcoa, Inc. or prepared at PSU and baked by A.J. Edmond are summarized in **Figures 5-12** and **5-13** and in **Table 5-30**. As discussed by Dr. Adams in **Appendix 5-1**, the measurement of baked apparent density and electrical resistivity are most informative regarding the optimum pitch concentration as well as the value of the petroleum coke-butts-pitch system. Initially it was determined that test anodes made with Pittsburgh co-coke were more dense (**Figure 5-12A**) and had lower electrical resistivity (**Figure 5-13A**) in comparison to the standard petroleum coke employed. Test anodes made with the Marfork co-coke exhibited higher density and lower resistivity than the Pittsburgh co-coke or either of the standard petroleum cokes used for comparison. The significance of denser coke of lower resistivity, if it could be implemented in a plant, would be anodes of longer life and used with greater energy savings, respectively. These improvements were seen from the Pittsburgh co-coke at a 17% level of pitch addition, whereas maximum improvement was observed at about 18.5% pitch content for the Marfork co-coke. Of course the cost-benefit ratio of technological improvements versus materials cost would have to be made on plant-per-plant basis. However, with due consideration of a range of pitch levels showing significant improvement and that might cover all coke types and operator conditions, four baked anodes from 17.5% thru 19.0% at 0.5% increments were selected for additional testing.

Table 5-30 provides the results for the selected pitch range for the two co-coke and one of the standard cokes all prepared by Alcoa, Inc. Probably the most important observation regarding these additional analyses, was that baked anodes in the 17.5-19.0% pitch range made with co-coke were 1) significantly less reactive to air than the standard coke made under identical conditions and 2) the air permeability, thermal conductivity and CTE were about the same and well within the range of values reported in the literature for real baked anodes [5-20]

In consideration of those anodes prepared at PSU using the new R&D Carbon Bench Scale Anode Unit, results are also given in **Figures 5-12B** and **5-13B** and **Table 5-30**. In comparison to those anodes made at Alcoa, those made at PSU followed the same trends, i.e., Marfork co-coke exhibited higher baked apparent density, lower resistivity and nearly the same air reactivity values. However, the surprising result, if it can be believed, was the large increase in the air

permeability values. These values seem to be way out of line, when considering every other measure, including thermal conductivity and CTE were similar to values derived from the Alcoa-made samples. As seen in **Figures 12B and 13B**, after about 18% pitch addition, the baked anodes prepared in the PSU unit became less dense and had a higher electrical resistivity. This change perhaps could have been predicted from the general appearance of the green anodes. As shown in **Figure 5-14**, the size of the agglomerated coke and pitch particles in the green mix increased in diameter with increasing pitch concentration, i.e., compare PENN4-1 (15.5% pitch) with PENN4-10 (20.0% pitch) in **Figure 5-14**. All of the Alcoa-prepared green or baked anodes had the appearance of PENN4-1. The green mix was not homogenized in any way by the hot molding under pressure. On the other hand, it appeared that pitch concentration in excess of 17.5% are not necessary for the Pittsburgh co-coke or the two standard cokes.

5.4.1.2.3 Conclusions

The most important conclusion regarding the preparation of a premium petroleum coke product for co-coking deeply cleaned coal with a relatively low-sulfur decant oil, was that if not for the high silicon and iron content, co-coke appeared to be superior in every way to other straight-run petroleum cokes. The procedure employed to obtain the deeply cleaned coal (wet sieving to remove the +150 and <45 μm fraction and float/sink in low specific gravity solvents) cannot be duplicated cost effectively at a commercial scale at this time. The technique perhaps represents the best that can be done and, as we have demonstrated, that was insufficient to meet all of the current specification for premium anode grade calcined carbon.

Future work will include solvent extraction of coal using decant oil, a method to remove minerals and incorporate soluble coal into the liquid. The work will be done on a DOE project through the Consortium of Premium Carbon Products from Coal.

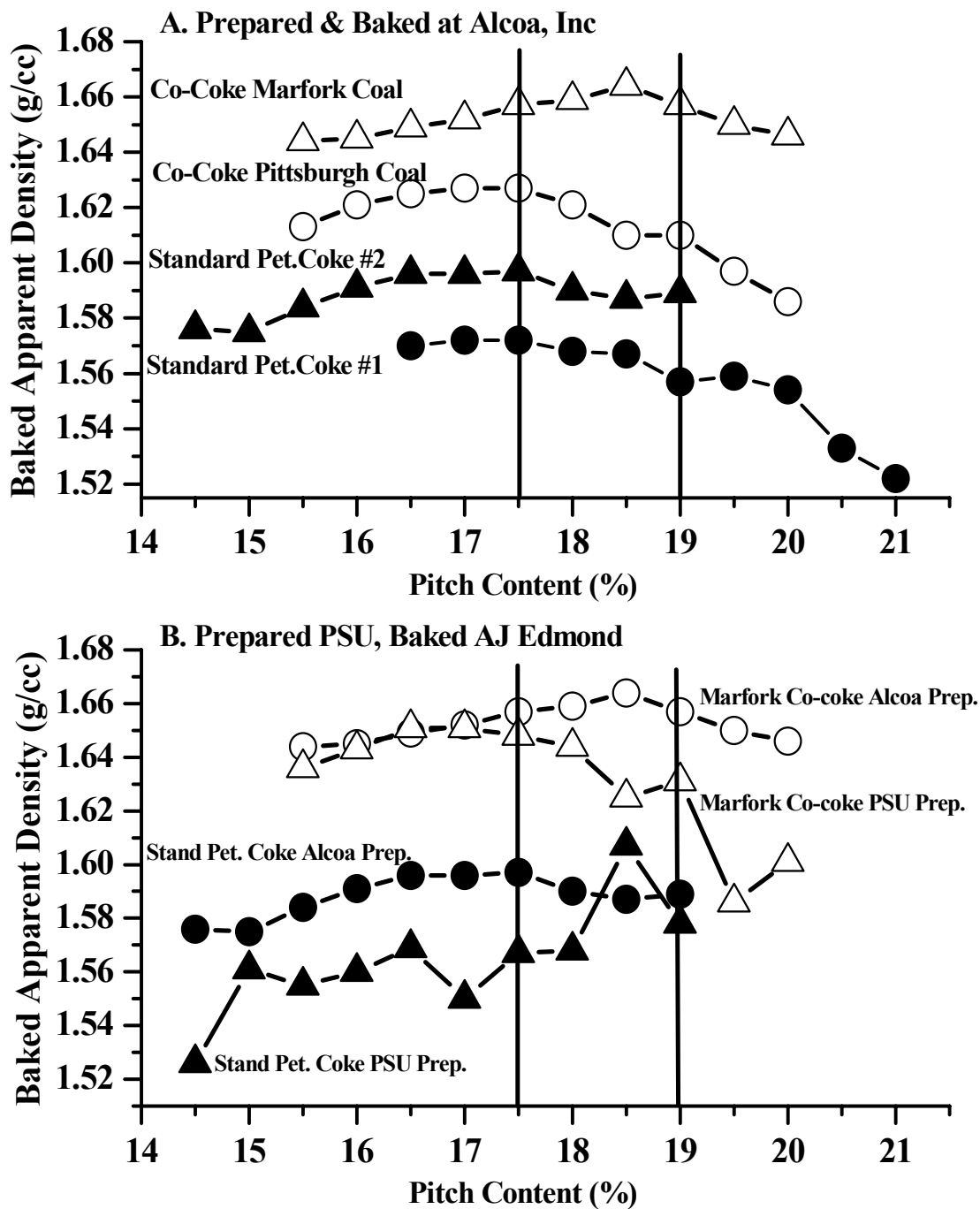


Figure 5-12 Comparison of Baked Apparent Density of Test Anodes and Pitch Content as a Function of Coke Type (A) and Operator (B)

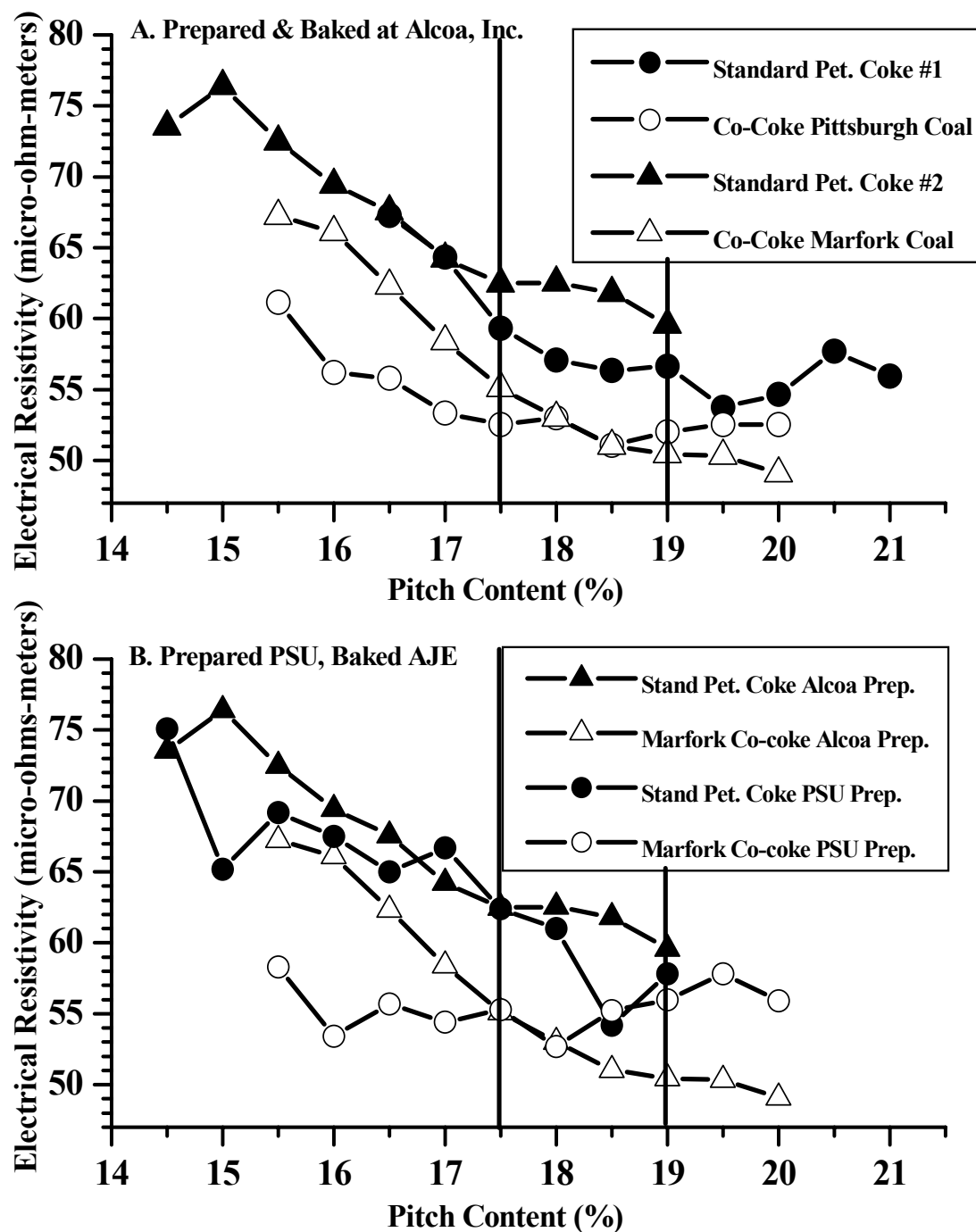


Figure 5-13 Comparison of Electrical Resistivity of Test Anodes and Pitch Content as a Function of Coke Type (A) and Operator (B).



Figure 5-14 Green Test Anodes Prepared at Penn State in the R&D Carbon Bench Scale Unit from Marfork Co-coke and 15.5% pitch (PENN4-1) Compared with 20.0% pitch (PENN4-10)

5.4.2 Evaluation of Co-coke as a Feedstock for Graphite

Over the past four years a significant amount of laboratory delayed coke was prepared using different raw materials and operating conditions. During this part of the Refinery Integration project, a broader range of petroleum coke and co-cokes were employed to the preparation of graphite.

5.4.2.1 Calcination

The coke artifact generated from Runs #13, #14, #35, #44 (**Table 5-31**) were cut into three or four (depending on the height of the coke artifact) different 4-5 cm thick sections from the bottom of the coke (or coker inlet). This was done to understand the distribution of coal derived materials in the whole coke artifact. Each coke section was calcined to 1300°C at a heating rate of 20°C/min and held at the maximum temperature for one hour (in a flow of argon). Several physical properties of green and calcined coke samples were determined. Although a detailed examination of each section was discussed in a previous semi-annual progress report [5-21], the important conclusion are provided below.

Table 5-31 Conditions and Product Distributions for Coking and Co-coking Experiments

Conditions	DO=Seadrift	DO=Seadrift/Coal Powellton/Eagle -150 μ m, 8.1% ash	DO107/Coal Pittsburgh Seam +45 μ m, 3.1% ash	DO107/Coal Pittsburgh Seam -250 μ m, 7.4% ash
Run #	13	14	35	44
Feedstock, hours	6	6	51/2	6
Hold at 500°C, hours	0	6	6	24 (550°C)
Feed rate, g/min	16.7	16.7	16.7	16.7
Preheater inlet, °C	82	87	108	120
Preheater outlet, °C	417	419	443	425
Coke drum inlet, °C	446	474	470	470
Coke drum middle, °C	493	481	471	471
Coke drum top, °C	458	466	470	475
Product Distributions:				
% Coke	14.27	31.67	30.24	26.81
% Liquid	79.63	65.84	60.35	58.74
%Gas (by difference)	6.10	2.44	9.41	14.45

Basically, the predominant results from evaluating different section of coke taken at increasing distance from the coke drum inlet were;

1. There was a variable distribution in coal-derived materials in the 3-4 different sections characterized largely by the ash yield concentrated in the lower section and decreasing in concentration with distance from the inlet.
2. Real densities were sufficiently high to meet the specifications for anode grade coke.
3. The concentrations of certain major elements (Si and Fe) of the calcined cokes were far outside of the range suitable for anode or electrode grade coke, but these co-cokes were made from intermediately cleaned coal products.
4. Although the calcining process reduced ash yield in the coke, the high ash content problem can only be solved by preparing better raw materials (i.e., a low ash yield coal).

The whole-coke artifacts from Runs #12, #16, #20, #24, #36, #38, #39 and #48 (**Table 5-32**) were homogenized and calcined. The cokes were selected for a variety of reasons, but the principal aim was to evaluate the influence of different coals and decant oils on final coke properties. Each of these coke samples were crushed and ground to pass a 0.85 mm, 20 mesh Tyler sieve, and were calcined under the same conditions (1300°C at 20°C/min. for 1 hour). Several physical properties of green and calcined coke samples were determined. Details of the investigation have been reported elsewhere [5-21], a brief discussion of the main results follows.

Results found for green and calcined cokes obtained by crushing and homogenizing the total coke artifact include;

- 1) Coking of Decant Oil Only: Two different decant oils were subjected to coking experiments and both behaved similarly during coking. Hold time and temperature have some influence on final carbon quality. Increasing holding temperature from 500°C to 600°C improved or increased carbon quality of the green coke, but showed little effect on calcined cokes.
- 2) Addition of Coal to Coking Experiments: Although there were differences in conditions among the coker runs being studied some general observations can be made.
 - a. Weight loss during calcinations was greater for runs containing coal compared with runs where decant oil alone was employed. It was suspected that because coals devolatilize more completely at higher temperatures, the coal remnants may retain more volatile matter to be released during calcinations at 1300 °C.

- b. Density values for green cokes made with coal were found to be higher than those from decant oil alone (except when held for 24 hours at 600 °C), but upon calcination the reverse observation was found, i.e., decant oil alone > co-coke.
- c. X-ray analysis of calcined cokes and the comparison of d-spacing and crystallite height (L_c) exhibited some minor differences which show that d-spacing and L_c decreased with the addition of coal to the system, although this was a variable result depending upon the coal used.
- d. Increasing the amount of coal in the blend with decant oil, in addition to causing operating problems, seemed to have a negative effect on the quality of the final carbon product.

Table 5-32 Conditions and Product Distributions for Coking and Co-coking Experiments

Run #	12	16	20	24	36	38	39	48
Conditions	DO-S	DO-S/PE	DO107/PE	DO107/C	DO107/C (70/30)	DO107	DO107	DO107
feedstock (h)	6	6	6	6	5.5	6	6	6
hold at 500 °C (h)	5	5	6	0	6	6	24	24 (at 600°C)
feed rate (g/min)	16.7	16.7	16.7	16.7	16.7	16.7	16.7	16.7
preheater inlet (°C)	87	85	114	109	109	62	64	120
preheater outlet (°C)	440	432	425	437	436	447	446	462
coke drum inlet (°C)	487	nd	480	480	468	476	471	516
coke drum lower/middle (°C)	490	482	499	490	468	474	474	506
coke drum top (°C)	430	466	478	476	474	476	476	478
Product Distributions (%)								
% coke	6.85	33.09	26.79	29.42	37.53	19.81	22.23	14.17
% liquid product	70.86	67.65	68.85	57.92	51.75	70.80	70.54	77.21
% gas (by difference)	22.29	-	4.36	12.66	10.72	9.39	7.23	8.62

DO-S = Seadrift Decant Oil; DO-S/P = Seadrift DO with Powellton/Eagle coal; DO107 = United Refining decant oil; DO107/PE United Refining decant oil and Powellton/Eagle; DO107/C = United Refining decant oil and Canterbury Coal; DO107/C (70/30) = United Refining decant oil and Canterbury Coal (70/30 ratio)

5.4.2.2 Graphitization

Selected coke samples were heat treated in a Centorr Vacuum Industry Series 45 furnace by weighing out 3-5 g of sample into a graphite crucible and covering with a graphite lid. Graphite lids and crucibles were provided by POCO Graphite. These crucibles were then placed in the hot zone of the furnace with dimensions of 6"(152.4 mm) inside diameter by 9"(228.6mm) high; usable size 3 ½"(88.9 mm) i.d. by 6.5"(165.1 mm) high. Graphitization was performed under argon atmosphere. The furnace was heated to either 2200°C or 2800°C with a heating rate of 20°C/min and held at the final temperature for one hour or 10 minutes, respectively. Two different types of sensors were used to check the temperature; 1). Type "C" w5%Re/w26%Re thermocouple with moly sheath and BeO insulation, 1/8" diameter by 12" (304.8 mm) long was used until 1800°C. 2). Two-color optical pyrometer obtained from Iacon Mirage. The pyrometer

was used to check the temperatures between 1500°C-3000°C, having an accuracy of 1% of full scale and repeatability 3% of full scale.

X-ray Diffraction

The diffractograms of the samples were recorded in a SCINTAG PAD-V X-ray diffractometer that used CuK α radiation. Diffraction data were collected by step scanning with a step size of 0.02° 2 θ and a scan step time of 1 s. Homogenized samples of 20 mesh were ground to a fine powder with the help of mortar and pestle and then placed on the surface of a zero background sample holder. To correct the instrument broadening an external standard (silicon) was used. **Figure 5-15** illustrates the X-ray diffraction (XRD) pattern for one of the samples graphitized at 2200°C showing the graphite peak positions as provided from the JADE library. The interlayer spacing, d_{002} , was calculated from the Bragg equation by using [002] peak [5-22]. The Bragg equation is (**Equation 5-1**):

$$n\lambda = 2d\sin\theta \quad \text{Equation 5-1}$$

where, n = diffraction order, which is taken as 1, λ = wavelength of CuK α radiation which is 1.54051Å, d = interlayer spacing, θ = diffraction angle of [002].

JADE 7.0 software uses the Scherrer equation to calculate the crystallite stacking height - L_c value, which can be represented as **Equation 5-2**:

$$L_c = \frac{K\lambda}{FW * \cos\theta} \quad \text{Equation 5-2}$$

where, $K=0.9$ (the value of K can be set by the user and the value here was taken from Gonzalez et al.), FW = Peak width at half maxima of the peak [002] in radians, θ = angle at which the [002] peak appears.

L_a was calculated from the JADE+ manually using the Scherrer equation (**Equation 5-3**):

$$L_a = \frac{K\lambda}{FW * \cos\theta} \quad \text{Equation 5-3}$$

where, L_a = crystallite size (length), $K = 1.84$, λ = wavelength of $\text{CuK}\alpha$ radiation which is 1.54051\AA , θ = angle at which the [10] peak appears, FW = Peak width at half maxima of the peak [10] in radians.

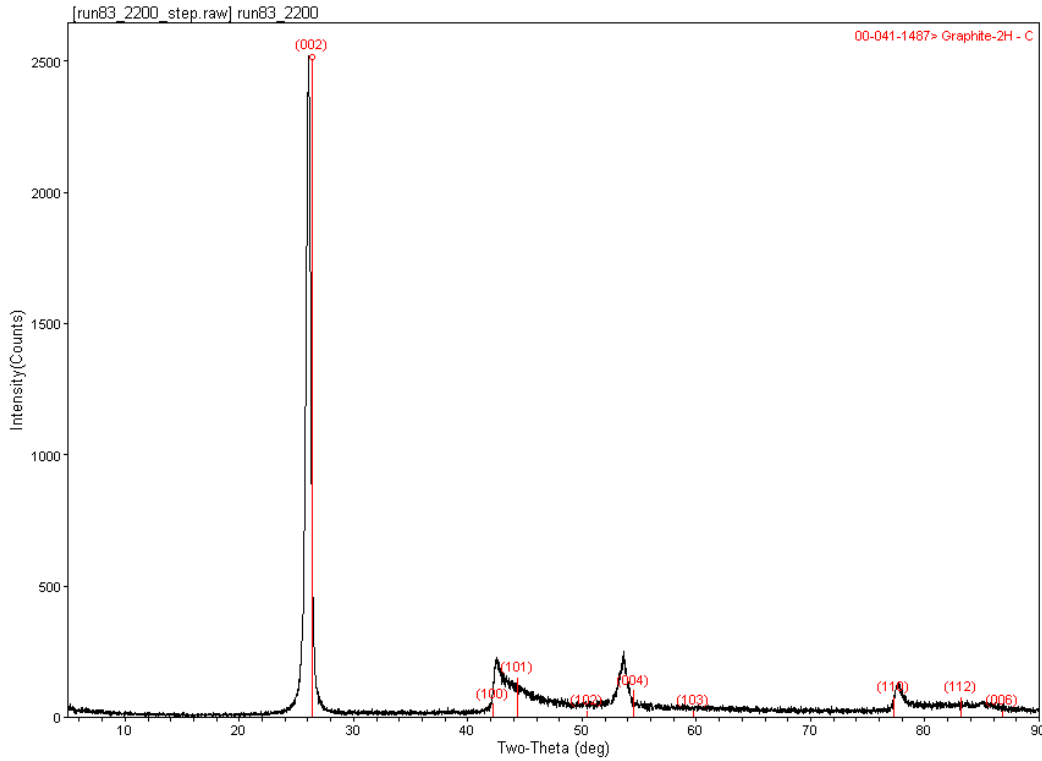


Figure 5-15 Diffraction peak profile of DO107/EI186 (70:30) carbon graphitized at 2200°C with graphite peak positions.

In addition, the degree of graphitization (DOG) for all carbons was calculated. For typical non-graphitic carbons the interlayer spacing represented by the (002) peak is constant at 3.440\AA (5.23 and 5.24), whereas the interlayer spacing in graphite is 3.354\AA . The degree of graphitization was calculated according to Equation 5-4:

$$\text{DOG} = g = \frac{3.440 - d_{002}}{3.440 - 3.354} = \frac{3.440 - d_{002}}{0.086} \quad \text{Equation 5-4}$$

where d_{002} is the average interlayer distance in \AA calculated by XRD. In some cases (for the coke samples graphitized at 2200°C) negative values were obtained for the degree of graphitization, but were not recorded.

5.4.2.2.1 Results and Discussion

Whole Coke Artifacts

The interlayer spacing (d_{002}), crystallite length (L_a), crystallite height (L_c) and the degree of graphitization (DOG) of graphitized carbons are summarized in **Tables 5-33** and **5-34**.

Effect of Coal:

The analysis of the XRD profiles of graphitized coke samples produced from co-coking of Seadrift decant oil and Powellton/Eagle coal showed that there was a decrease in the interlayer spacing (d_{002}) as the temperature increased, an expected result. For example, at 2200°C and 2800°C, the d_{002} for coke obtained from coking of Seadrift decant oil alone was 3.442Å and 3.384Å, respectively, whereas 3.436Å and 3.379Å were recorded for coke obtained from co-coking of Seadrift decant oil and Powellton/Eagle coal, respectively. The situation was the same for coke sample obtained from coking of DO-107 decant oil and Powellton/Eagle coal. For example at 2200°C and 2800°C, the d_{002} for coke obtained from coking of DO-107 decant oil alone was 3.445Å and 3.373Å, respectively, whereas 3.421Å and 3.369Å for coke obtained from co-coking of DO-107 decant oil and Powellton/Eagle coal, respectively. In all cases, when increasing the graphitization temperature, crystallite sizes increased, both L_c and L_a . Increasing temperature also reduced the interlayer spacing and so too increased the degree of graphitization. Some of the 2800°C graphitized samples approached the ideal interlayer spacing for graphite (3.354Å), but none attained this level of alignment.

After heat treatment to 2200°C, it appeared the carbons made from decant oil alone were significantly structurally disordered. In all cases, the interlayer spacing of carbons graphitized at 2200°C was equal to or higher than 3.440Å, which typically represents non-graphitic carbons. When adding coal into coking system, at 2200°C graphitization temperature, the carbon order was about the same or a little better. However, the situation was not the same for the coke samples graphitized at 2800°C. The data indicated that the largest change occurred for coke samples obtained from coking of decant oil above 2200°C. Adding coal into the coking system in some cases enhanced the interlayer spacing and crystallite sizes for coke samples graphitized at 2800°C. In terms of the values of four parameters, d_{002} , L_c , L_a and DOG, the graphitizability of the co-cokes made from the four coal samples was ranked in order Powellton/Eagle > Marfork > Canterbury > Pittsburgh (EI186). Co-coke made from the Powellton/Eagle coal graphitized

the best among these four coal samples. Furthermore, there appeared to be no relationship between coke ash and graphitizability, an indication that the minerals in the ash did not play a catalytic role in graphitization.

Increasing the coal ratio in the coking system increased the interlayer spacing and decreased the degree of graphitization and crystallinity. This effect was more obvious for 2800°C graphitization temperature. For example, for 2800°C graphitization temperature, the degree of graphitization was 0.756 and 0.570 for the DO107/Canterbury (80:20) and DO107/Canterbury (70:30), respectively. It would be interesting to increase the ratio of Powellton/Eagle coal in the coking system to see if better graphitization properties may be produced.

Effect of Coking Conditions:

Table 5-34 summarizes the crystallite parameters of the coke samples obtained from two different decant oil samples. Three parameters were different; decant oils, holding time of cokes at 500°C, and final holding temperature. The coking conditions for two different coke samples were not the same, for this reason it was not easy to compare the graphitizability parameters for these two coke samples, but in general it seemed that the graphitizability factors for both decant oils were very similar.

Table 5-33 XRD Crystallite Parameters of the coke samples obtained from the coking of decant oil only and co-coking of decant oil with four different coal samples.

Run	Feedstocks	Ash (%) (dry)	Temperature (°C)	d ₀₀₂ (Å)	L _c (nm)	L _a (nm)	DOG (or g)
12	Seadrift DO	0.43	2200	3.442	17.5	14.9	-
16	Seadrift DO/Powellton Eagle (80:20)	5.36	2200	3.436	17.3	22.7	0.046
12	Seadrift DO	0.43	2800	3.384	30.9	64.0	0.651
16	Seadrift DO/Powellton Eagle (80:20)	5.36	2800	3.379	26.7	54.6	0.709
19	DO107	0.74	2200	3.445	15.6	26.0	-
20	DO107/Powellton Eagle (80:20)	5.62	2200	3.421	19.4	29.0	0.209
24	DO107/Canterbury (80:20)	6.44	2200	3.434	16.2	14.7	0.070
36	DO107/Canterbury (70:30)	6.33	2200	3.434	14.1	15.4	0.070
55	DO107/EI186 (80:20)	1.29	2200	3.423	17.6	17.9	0.198
83	DO107/EI186 (70:30)	1.57	2200	3.425	17.7	18.9	0.174
86	DO107/Marfork	0.94	2200	3.420	19.8	19.9	0.232
19	DO107	0.74	2800	3.373	23.5	47.6	0.779
20	DO107/Powellton Eagle (80:20)	5.62	2800	3.369	23.8	41.8	0.825
24	DO107/Canterbury (80:20)	6.44	2800	3.375	21.8	35.3	0.756
36	DO107/Canterbury (70:30)	6.33	2800	3.391	20.4	23.4	0.570
55	DO107/EI186 (80:20)	1.29	2800	3.385	31.6	54.1	0.640
83	DO107/EI186 (70:30)	1.57	2800	3.386	25.0	48.3	0.628
86	DO107/Marfork (80:20)	0.94	2800	3.377	30.3	51.8	0.733

Table 5-34 XRD Crystallite Parameters of the coke samples obtained from the coking of decant oil only under different coking conditions.

Run	Feeds*	Hold (°C)	Hold (h)	Ash (%)	Graph Temp (°C)	d_{002} (Å)	L_c (nm)	L_a (nm)	DOG
12	Seadrift DO	500	0	0.43	2200	3.442	17.5	14.9	-
19	DO107	500	6	0.74	2200	3.445	15.6	26.0	-
39	DO107	500	24	0.19	2200	3.441	13.1	18.4	-
48	DO107	600	24	0.22	2200	3.455	14.0	17.6	-
12	Seadrift DO	500	0	0.43	2800	3.384	30.9	64.0	0.651
19	DO107	500	6	0.74	2800	3.373	23.5	47.6	0.779
39	DO107	500	24	0.19	2800	3.386	26.1	46.3	0.628
48	DO107	600	24	0.22	2800	3.387	27.5	62.8	0.616

* All feeds were fed into the coker for 6 h.

Increasing the final holding time did not improve structural ordering, and actually seemed to produce a more disordered carbon. Although there was not a significant change in crystallite size, the interlayer spacing changed. The degree of graphitization for coke sample graphitized at 2800°C was 0.779 for 6 hours holding time and 0.628 for 24 hours holding time. Increasing the final holding temperature from 500°C to 600°C had very little effect on interlayer spacing or degree of graphitization (2800°C graphitization temperature), but helped to increase both crystallite height and crystallite diameter. The L_a increased from 46.3 nm to 62.8 nm when the coke holding temperature was increased from 500°C to 600°C.

Sectioned Coke Samples

The interlayer spacing (d_{002}), crystallite length (L_a), crystallite height (L_c) and the degree of graphitization of carbons from different sections of different cokes are summarized in **Table 5-35** and **5-36**.

As discussed previously, for a better understanding of coking and co-coking mechanisms, some coke artifacts were sectioned. In this section, the XRD crystallite parameters for sectioned coke samples will be discussed. As expected, in all cases, by increasing the graphitization temperature, the crystallite size (both L_c and L_a) increased. As mentioned before, the ideal interlayer spacing for graphite is 3.354Å. With Powellton coal in the system, this spacing was nearly attained, for the section 1 sample of Seadrift DO:Powellton/Eagle (80:20) carbon graphitized at 2800°C, the interlayer spacing was 3.356Å (**Table 5-35**).

For the coke samples produced from coking of decant oil alone, crystallite parameters did not change much from section to section. The interlayer spacing and the degree of graphitization

varied little. The crystallite stacking length and height actually were higher in the first section for the coke sample graphitized at 2800°C, but for the most part the coke sample appeared to be homogeneous.

When Powellton/Eagle coal was added into coking system, a more structurally ordered carbon appeared to be produced. For co-coke samples graphitized at 2800°C, the degree of graphitization was very high for the bottom two sections. This may be explained by the fact that the bottom section saw relatively greater coking time and higher temperature, possibly allowing for improved structural growth. Although the L_c and L_a was not high for the bottom sections, the interlayer spacing (d_{002}) was very close to that of graphite for these two sections.

Table 5-36 summarizes the XRD crystallite parameters for the coke produced from the same coal and decant oil ratio, even though the coking conditions were different. These particular coke samples were selected in order to see the effect of coking conditions on the final graphitic properties. According to ash yields, remnants of the Pittsburgh Seam coal were not evenly distributed throughout the coke artifact. Coal-derived material mostly deposited in the bottom part of the artifact regardless of coking condition. By increasing coke holding time at 500°C from 6 hours to 24 hours, based on L_c and L_a , the coke lattice continued to grow. As can be seen, the degree of graphitization was zero or below zero for the final holding time 6 hours for sections 1 and 2, but for the 24 hours final holding time DOG was 0.128 and 0.221, respectively (graphitization at 2200°C). At both final holding times, the top section had the highest degree of graphitization (graphitization at 2800°C). Also the second section had the greatest crystallite height and length. Also, there appeared to be no relationship when comparing the ash content and crystallite parameters of the carbon samples.

Table 5-35 XRD Crystallite Parameters of the coke samples obtained from the coking of decant oil only and co-coking of decant oil with four different coal samples (sectioned samples).

Run	Feedstocks	Ash	Temp. (°C)	d ₀₀₂ (Å)	L _c (nm)	L _a (nm)	DOG (or g)
13section1	SeadriftDO	0.54	2200	3.445	19.9	16.7	-
13section2	SeadriftDO	0.18	2200	3.447	20.6	23.1	-
13section3	SeadriftDO	0.54	2200	3.448	19.9	17.2	-
13section1	SeadriftDO	0.54	2800	3.385	34.7	81.7	0.640
13section2	SeadriftDO	0.18	2800	3.381	33.2	66.2	0.686
13section3	SeadriftDO	0.54	2800	3.386	33.3	73.4	0.628
14section1	SeadriftDO:Powellton Eagle (80:20)	6.76	2200	3.403	23.0	32.1	0.430
14section2	SeadriftDO:Powellton Eagle (80:20)	8.25	2200	3.392	20.6	33.7	0.558
14section3	SeadriftDO:Powellton Eagle (80:20)	5.72	2200	3.398	21.5	24.6	0.488
14section4	SeadriftDO:Powellton Eagle (80:20)	6.23	2200	3.404	19.1	23.1	0.419
14section1	SeadriftDO:Powellton Eagle (80:20)	6.76	2800	3.356	29.7	44.7	0.977
14section2	SeadriftDO:Powellton Eagle (80:20)	8.25	2800	3.361	22.6	37.7	0.919
14section3	SeadriftDO:Powellton Eagle (80:20)	5.72	2800	3.379	31.7	52.1	0.709
14section4	SeadriftDO:Powellton Eagle (80:20)	6.23	2800	3.376	24.6	37.2	0.744

Table 5-36 XRD Crystallite Parameters of the coke samples obtained from the coking of decant oil only and co-coking of decant oil with four different coal samples (sectioned samples).

Run	Feedstocks	Ash	Temp. (°C)	d ₀₀₂ (Å)	L _c (nm)	L _a (nm)	DOG (or g)
Run 35: Feedstock hours: 6 Hold at 500°C: 6							
35section1	DO107/Pittsburgh Seam	4.53	2200	3.440	14.9	16.4	-
35section2	DO107/Pittsburgh Seam	0.73	2200	3.444	15.8	15.6	-
35section3	DO107/Pittsburgh Seam	0.12	2200	3.428	17.8	26.2	0.139
35section1	DO107/Pittsburgh Seam	4.53	2800	3.381	25.3	38.8	0.686
35section2	DO107/Pittsburgh Seam	0.73	2800	3.381	29.3	64.7	0.686
35section3	DO107/Pittsburgh Seam	0.12	2800	3.372	29.2	57.3	0.791
Run 44: Feedstock hours: 6 Hold at 500°C: 24							
44section1	DO107/Pittsburgh Seam	5.61	2200	3.429	18.9	23.5	0.128
44section2	DO107/Pittsburgh Seam	1.18	2200	3.421	20.5	25.3	0.221
44section3	DO107/Pittsburgh Seam	1.08	2200	3.433	22.1	27.5	0.081
44section1	DO107/Pittsburgh Seam	5.61	2800	3.384	25.2	44.2	0.651
44section2	DO107/Pittsburgh Seam	1.18	2800	3.386	32.0	80.9	0.628
44section3	DO107/Pittsburgh Seam	1.08	2800	3.370	26.1	57.8	0.814

5.4.2.2.2 Conclusions

The interlayer spacing (d₀₀₂), crystallite length (L_a), crystallite height (L_c) and the degree of graphitization were determined for different carbon samples graphitized at two different temperatures, i.e., 2200°C and 2800°C. The results are summarized briefly:

- 1) In terms of the values of four parameters, d₀₀₂, L_c, L_a and DOG, the graphitizability of the four coal samples in order are: Powellton/Eagle > Marfork > Canterbury > Pittsburgh (EI186). Powellton/Eagle co-coke graphitized the best among the four samples from co-coking with different coals.
- 2) No consistent relationship with the ash yield of coke samples and their graphitizability was observed.
- 3) In all cases, by increasing graphitization temperature, as expected, the crystallite size (both L_c and L_a) was increased. The effect of increasing temperature was to reduce the interlayer spacing and so to increase the degree of graphitization. The ideal interlayer

spacing for graphite is 3.354\AA , and for some of the sectioned samples, the interlayer spacing was close.

- 4) Increasing the coal ratio in the coking system, increased the interlayer spacing and decreased degree of graphitization and crystallinity.
- 5) In general, the graphitizability factors for coke samples obtained from the two decant oil-derived cokes were very similar.
- 6) Increasing the final holding time did not improve structural ordering when later graphitized. Increasing coke final holding temperature from 500°C to 600°C had very little effect on interlayer spacing and degree of graphitization (2800°C graphitization temperature), but appeared to increase crystallite height and diameter.

5.5 Analysis of Co-Coking Binder Pitch

In previous semi-annual reports, much of the discussion centered on characterization of pitches from various sources (coal tar – SCTP-2, petroleum pitch – PP-1, gasification pitch – GP-115, and coal tar pitch from West Virginia University – WVU-5), in order to determine the necessary properties for a pitch that would be produced from co-coking [5-21]. As discussed in detail previously [5-21], the liquid product from the co-coking Run #50 was further distilled to yield a pitch material, namely CCP-2. Conditions for Run #50 are shown in **Table 5-37**. It was reported that the mass distribution of CCP-2 was too light to be used as a binder for aluminum anode production. Two methods of heat treatment were used to produce more condensed aromatic-fused-ring compounds: heat soaking and oxidation. It was aimed to prepare new co-coking pitch samples to get a mass distribution closer to that of a standard coal tar pitch (SCTP) and petroleum pitch (PP).

Table 5-37: Conditions and Yields from the Experimental Delayed Coker

Conditions	Run #50
Date	
Components	4:1 Decant Oil/ +45 μ m Pittsburgh Froth
Feed, hrs	6
Held at 500°C, hrs	24
Feed Rate, g/min	16.7
Preheater Outlet, °C	443
Coke Drum Inlet, °C	491
Coke Drum Low/mid., °C	496
Coke Drum Top, °C	476
Total Feed, g	5730
Coke Product, g (%)	1541 (26.90%)
Liquid Product, g, (%)	3543 (61.83%)
Gas Product, g, (%)	646 (11.27%) by diff.

5.5.1 Experimental

Materials

The material for generating co-coking pitch was obtained by using a laboratory-scale vacuum distillation apparatus. The distillates from co-coking were placed in a round-bottom flask, which was connected to a riser and condenser assembly. The temperature of the boiling liquid was measured by a thermocouple. A cold trap immersed in liquid nitrogen was used to

collect any light product not condensed in the collection flask. After the pressure was reduced to 5 mmHg using a rotary-vane vacuum pump, the heating mantle was switched on. The temperature was increased and the distillates were collected until the desired cut point temperature reached. A 360°C cut point was chosen to obtain a final product of 360°C-FBP (Final Boling Point) remaining in the round-bottom flask. From GC/MS analysis (the spectra not shown in this report), this fraction did not contain any aliphatic compound and should be a good starting material to obtain good binder pitch samples.

There are two main methods of producing heavy compounds from petroleum fractions: heat soaking and oxidation (or polymerization with oxygen) [5-25]. These methods combined with distillation and solvent extraction have been widely used to produce petroleum pitch [5-25]. The 360°C-FBP fraction of co-coking liquid Run #50 was heat soaked and oxidized using the conditions described in **Table 5-38**. Thirty grams of the sample were placed in a 120 mL reactor. UHP N₂ and O₂ were used to purge and pressurize the sample in the heat soaking and oxidation experiments, respectively. A pressure gauge was attached to each reactor to monitor the pressure before, during, and after the reactions. The reactor was immersed in a fluidized, temperature controlled sand bath. After the reaction, the reactor was quenched in water. Noted that the term “heat-treated” has been used generally to describe both the heat-soaked and the oxidized experiments.

Table 5-38: Heat treatment conditions of co-coking liquid distillate Run#50.

Sample #	Type of Gas	Heat Soaking Conditions		
		Temp. (°C)	Time (min)	P _{ini} (psig)
HT111, HT112	UHP N ₂	460	75	0
HT113, HT114	UHP N ₂	460	45	0
OX107-OX110	O ₂	250	2	300

The heat-soaked (a mixture of HT111-HT114) and oxidized (a mixture of OX107-OX110) composites were mixed and distilled to remove light compounds using aforementioned vacuum distillation unit. The final cut point for pitch was ~350°C-FBP. Both heat-treated pitches were then mixed with SCTP-2 at 30% by weight. The mixing was done at 100°C for 15 hours under nitrogen atmosphere. Final blends of the heat-soaked and oxidized pitch are referred

to as “heat-soaked co-coking pitch” (HTCCP) and “oxidized co-coking pitch” (OXCCP), respectively.

Characterization of Pitch

Pitches are complex mixtures of polycyclic aromatic hydrocarbons and some heterocyclic compounds. Generally, compounds are in pitch range from about 150 to ~2500 amu [5-26]. Each characterization technique has its own limitations of measurement. Hence, combining different techniques will provide better and useful information on the pitch composition. The following sections summarize the techniques used in this study.

General Characterization of Pitch

In general, pitch samples were characterized by their softening point, solvent extractability, viscosity at different temperatures, proximate and ultimate analyses as summarized in **Table 5-39**.

Table 5-39: General characterization of pitch.

Properties	Method or Instrument
Softening Point	ASTM D3104
γ -resin (HI-TI)	Soxhlet extraction
β -resin (TI-PI)	Soxhlet extraction
QI	ASTM D2318
Mesophase	ASTM D4616
Ash	Proximate analysis
Viscosity	ASTM D5018
CHN content	Ultimate analysis
Sulfur	Sulfur analyzer

Note: HI = hexane insolubles; TI = toluene insolubles, PI = pyridine insolubles, QI = quinoline insolubles

Soxhlet Extraction

Soxhlet extraction was done using both cellulose and ceramic thimbles. Thimbles were dried in an oven for at least 1 hour and subsequently cooled in a desiccator. A 2-gram ground pitch sample of 60-100 mesh size was weighed, placed in a weighed dried thimble and then put into a Soxhlet unit. About 250 mL of solvent was used to extract the pitch. The series of solvents used in the extraction were hexane, toluene and pyridine, respectively. For each

solvent, the extraction was continued until the color of the solvent ran clear from the sample chamber. This process normally took about 1-3 days per solvent depending on the sample. After the first solvent was removed from the Soxhlet extraction apparatus, the second one was put in and the extraction continued while the insoluble material remained in the thimble.

The solvent was then separated from the extracted material using a vacuum rotary evaporator. The extracted material from each solvent was subsequently dried in a vacuum oven at ~60-80°C and weighed. This process was repeated for the next solvent, i.e. toluene and pyridine, respectively. These extractable materials were called HI-TI for the fraction of hexane insoluble and toluene soluble and TI-PI for the fraction of toluene insoluble and pyridine soluble. The final insoluble material, i.e. from the pyridine extraction, remained in the thimble was washed with acetone and air-dried for 1 hour and then placed into a vacuum oven at ~60-80°C overnight to remove all remaining solvent. The thimble with dried pyridine insoluble material was then placed in a desiccator before weighing.

Viscosity Measurement

Two viscometers were used in this study. The Rheology International Model RI:2:M/H1/H2 was used to measure the viscosity of SCTP-2, PP-1, GP-115, and WVU-5. Access to this instrument was generously provided by The School of Civil Engineering, University of Nottingham, UK and the analyses were performed at The School of Chemical, Environmental and Mining Engineering, University of Nottingham, UK. The viscosity measurement of HTCCP and OXCCP was performed on a Brookfield Viscometer Model DV-III V3.3 RV with the Rheocalc V2.4: Rheometer 1 software interface. The latter instrument was generously made available by The Pennsylvania Transportation Institute, The Pennsylvania State University. All the measurements were done based on ASTM D5018 and the temperature ranges were 100-200°C.

Chemistry, Structure and Molecular Masses Distribution of Pitches

The characterization techniques of the pitch samples include Laser Desorption Mass Spectrometry (LDMS), Gas-Chromatography/Mass Spectrometry (GC/MS), High Performance Liquid Chromatography (HPLC), and Nuclear Magnetic Resonance (NMR). A summary of

techniques used for characterization of different fractions of the pitch samples along with the molecular mass range limitations are shown in **Table 5-40**.

Table 5-40: Summary of techniques used for characterization of different fractions of the pitch samples and the molecular mass ranges of each technique.

Technique	Fraction	Molecular mass ranges
Solid-state ^{13}C NMR	Whole pitch	No limit
Solution-state ^{13}C NMR	Chloroform-soluble	No limit
Solution-state ^1H NMR	Chloroform-soluble	No limit
GC/MS	HS	< 300 Da
HPLC	HI-TI	< 600 Da
MALDI	Whole pitch	> 200 Da

Laser Desorption Mass Spectrometry (LDMS)

Since compounds in pitch are complex and distributed up to 2500 amu [5-27], the characterization of pitch by many techniques is limited. Laser desorption mass spectrometry provides a considerable extension of mass ranges to very high values. It was reported that compounds in pitch could be detected as high as 100,000-200,000 amu when the matrix assistance was used [5-27]. In this study, pitch samples were sent for analysis at the Huck Institute, Department of Chemistry, PSU.

A Waters Micromass Matrix Assisted Laser Desorption Ionization Time of Flight (MALDI-TOF) mass spectrometer was used to determine the average molecular weight of the pitch samples. The MALDI-LR is equipped with linear and reflectron detectors. More detail is described in previous semi-annual reports [5-28]. MALDI experiments were carried out by pulsing a Nitrogen UV laser (337nm wavelength) onto the sample.

The MALDI-LR was operated in a positive reflectron mode in a mass range of 10 m/z to 3,000 m/z. A 20 mg whole pitch was dissolved in 1 mL toluene and sonicated for 30 minutes. A 1.0 μL of each sample was spotted in a separate well on a 96 stainless steel well plate and air dried before insertion in the mass spectrometer ion source. No matrix was used in the experiments. The sample itself absorbed laser energy sufficiently for the ionization of molecules. Each spectrum represents a sum of 20 individual spectra. The background of the summed spectrum was subtracted and the spectrum itself was smoothed, which leaves monoisotopic ions.

Monoisotopic ions are composed only of the lightest isotopes of various elements (C, H, N, O and S).

Gas-Chromatography/Mass Spectrometry (GC/MS)

GC is the method for determining pitch constituents with molecular masses less than 350 amu [5-29]. The smallest molecules present in the HS fraction of pitch can be individually identified. Analyses were performed on a Shimadzu QP5000 with 70 eV electron ionization. More detail is described in previous semi-annual reports [5-28]. A 20 mg pitch sample was dissolved in 1 mL dichloromethane (DCM) and sonicated for 5 minutes in a vial with a septum. A 0.5 μ L solution was automatically injected into a GC using a splitless mode. The temperature of the GC/MS transfer line was set at 290°C. The temperature program applied to the GC oven was: isothermal at 40°C for 4 min; temperature programmed at 10°C/min to 180°C; at 4°C/min to 320°C; isothermal at 320°C for 15 min. The mass spectrometer was operated in full scan mode (m/z 40–450 and 1 scan/s).

High Performance Liquid Chromatography (HPLC)

HPLC is suited for the detection and quantitative determination of higher-molecular weight compounds up to 600 amu [5-29]. The HI-TI fractions were analyzed by HPLC using a Waters system incorporated with the Pinnacle II™ PAH column from Restek USA. The Pinnacle II™ PAH stationary phase is packed with a specialized polymer with pore size 110 Å and has an average particle size of 5 μ m. The mobile phase was Acetonitrile (ACN), water and Dichloromethane (DCM). A gradient flow was used and the solvent program is shown in **Table 5-41**. An HPLC equipment (Waters Model 600E) incorporating a Waters 996 Photodiode array detector, operating between 190 and 800 nm, was used to obtain UV spectra. To obtain most of the polycyclic aromatic compounds peaks in pitch, a UV detector operating at 254 nm was generally used.

Table 5-41: Gradient flow of solvents used in the HPLC analyses.

Time	Flow	%ACN	%DCM	%Water	Curve
0	0.5	60	0	40	6
180	0.5	100	0	0	5
200	1	100	0	0	1
300	1	0	100	0	6
330	1	0	100	0	1

Note: ACN = acetonitrile; DCM = dichloromethane;

*Curve “1” = linearly increase concentration; Curve “6” = same concentration from the beginning time and sharply ramp up at the final time.

The HI-TI fraction of pitch was dried by purging with UHP N₂ at room temperature. A 20 mg dried sample was dissolved in 1 mL dichloromethane (DCM) and sonicate for 5 minutes in a vial. A 5µL solution was injected into the HPLC for analysis.

Solid State ¹³C Nuclear Magnetic Resonance (Solid State ¹³C NMR)

It has been accepted that single-pulse excitation (SPE) or simple Bloch decay by the solid-state ¹³C NMR can be used to obtain reliable aromaticity values and the degree of condensation [5-30, 5-31]. In this study both cross-polarization magic-angle-spinning (CP/MAS) and SPE techniques were employed. Dipolar dephasing (DD) experiments were performed in both CP/MAS and SPE techniques to obtain the degree of condensation as explained by Love et al. [5-31].

Cross-polarization (CP) and simple Bloch decay or single-pulse excitation (SPE) measurements were carried out at 75.47 MHz on a Bruker 300 MHz spectrometer with magic-angle-spinning (MAS) at 12 kHz at the Energy Institute, PSU. A Bruker wide-bored variable temperature magic angle probe was used in this study. The magnetic field was adjusted weekly with adamantane to obtain a lower frequency resonance at 29.5 ppm.

CP/MAS

A 90° ¹³C pulse width of 4 µs with ~83 kHz ¹H decouple was used. A recycle delay of 5 seconds was generally used for all samples.

SPE

A high power decoupling (hpdec) was used in the SPE experiment. A 90° ^{13}C pulse width of 4 μs with ~ 40 kHz ^1H decoupling was used. Recycle delays of 400 to 960 seconds were used depending on the spin-lattice relaxation time of each sample.

Dipolar Dephasing

Dipolar dephasing (DD) experiments were performed in both CP/MAS and SPE using dephasing times of 1-600 μs to determine the fraction of non-protonated carbon and further calculation of bridgehead aromatic carbons (C_{BR}).

Solution-State ^1H NMR Spectroscopy

Samples were analyzed on a Bruker AMX 360 NMR operating at 9.4 Tesla and 360 MHz at 27°C . About 30 mg of whole pitch sample ground to pass the Tyler 200 mesh screen was dissolved in 1 ml of 99.8% atom deuterated chloroform which contains 1% (v/v) tetramethylsiloxane (TMS). The pitch solution was placed in a 5 mm o.d. NMR tube without filtering. A recycle time of 5 seconds was used with a 90° pulse length of 5 μs .

Solution-State ^{13}C NMR Spectroscopy

The solution-state ^{13}C NMR measurements were acquired at 90.56 MHz using a Bruker AMX 360 NMR operating at 9.4 Tesla. About 400 mg of >200 mesh size whole pitch sample was dissolved in 4 mL of deuterated chloroform (99.8% purity with 1% (v/v) TMS). The pitch solution was filtered and placed in a 5-mm o.d. NMR tube. The ^1H decoupling and spin-lock field was ca. 3 kHz and a 70° ^{13}C pulse width of 5.0 μs was employed. Chromium (III) acetylacetonate ($\text{Cr}(\text{AcAc})_3$) was added to ensure complete relaxation. A recycle delay of 2.5 seconds was used and at least 15,000 scans were acquired for each sample.

5.5.2 Results and Discussion

General characterization of pitch

Previous work on a coal tar pitch (SCTP-2), petroleum pitch (PP-1), gasification pitch (GP-115), and coal tar pitch from West Virginia University (WVU-5) has been described in detail in previous reports [5-21]. General properties of SCTP-2, PP-1, HTCCP and OXCCP are compared as listed in **Table 5-42**. The HS fractions of HTCCP and OXCCP were 16% and 20% by weight, respectively. This shows that too many light compounds have been removed from the samples during the vacuum distillation. Although these light compounds cause the pitch to have lower softening point, they are important and could help the pitch wet the surface of the coke particles during the carbon anode forming. The majority of the compounds in HTCCP and OXCCP were in the range of HI-TI fractions which were 70% and 66% by weight, respectively. These percentages were too high for pitch as compared to SCTP-2 and PP-1. The TI-PI fractions of HTCCP and OXCCP were 7% and 10% by weight, respectively, and are comparable to those of SCTP-2 (i.e. 8% by weight). The PI fractions of HYCCP and OXCCP were 8% and 7% by weight, respectively. Since these HTCCP and OXCCP contain 30% by weight of SCTP-2, the PI fractions may be derived mainly from the SCTP-2.

Another important property of the pitch was the percentage of fixed carbon which contributes to the property of the baked carbon anodes. The higher the fixed carbon, the lower the mass lost during the baking process of carbon anodes. From **Table 5-42**, the percentages of fixed carbon of HTCCP and OXCCP were 38% and 33% by weight, respectively. These values were considerably lower than those of SCTP-2 and PP-1 which are 59% and 47% by weight, respectively.

Viscosity Measurement

Figure 5-15 shows the plot of viscosity versus temperatures of SCTP-2, PP-1, GP-115, WVU-5, HTCCP and OXCCP. Upon heating a pitch from its glassy state, pitch becomes soft, and the viscosity decreases at its softening point. The viscosity then rapidly decreases with increasing temperature. The viscosity of SCTP-2, PP-1, GP-115 and WVU-5 fall in the same window over the temperatures of 120-210°C whereas those of HTCCP and OXCCP are significantly lower for the whole range of temperatures. These relationships can be explained by

the softening point of these pitches. The lower the softening point of the pitch, the lower the viscosity is observed. This observation is in agreement with previous studies by Fitzer et al. [5-34]. Although the softening point of PP-1 is comparable to that of SCTP-2 and GP-115, i.e. softening points of 112-115°C, the viscosity of PP-1 is lower than the other two samples. This may due to the higher HS fraction of PP-1 as compared to that of SCTP-2 and GP-115. As expected, the viscosity of WVU-5 is higher than the rest due to its higher softening point.

The viscosities of HTCCP and OXCCP are comparable for the whole ranges of temperature, due to their close softening points. On closer look, the viscosities of OXCCP are a little higher than those of HTCCP due to its slightly higher softening point. However, this relationship does not hold at the temperatures closer to 200°C where their viscosities are approaching to each other.

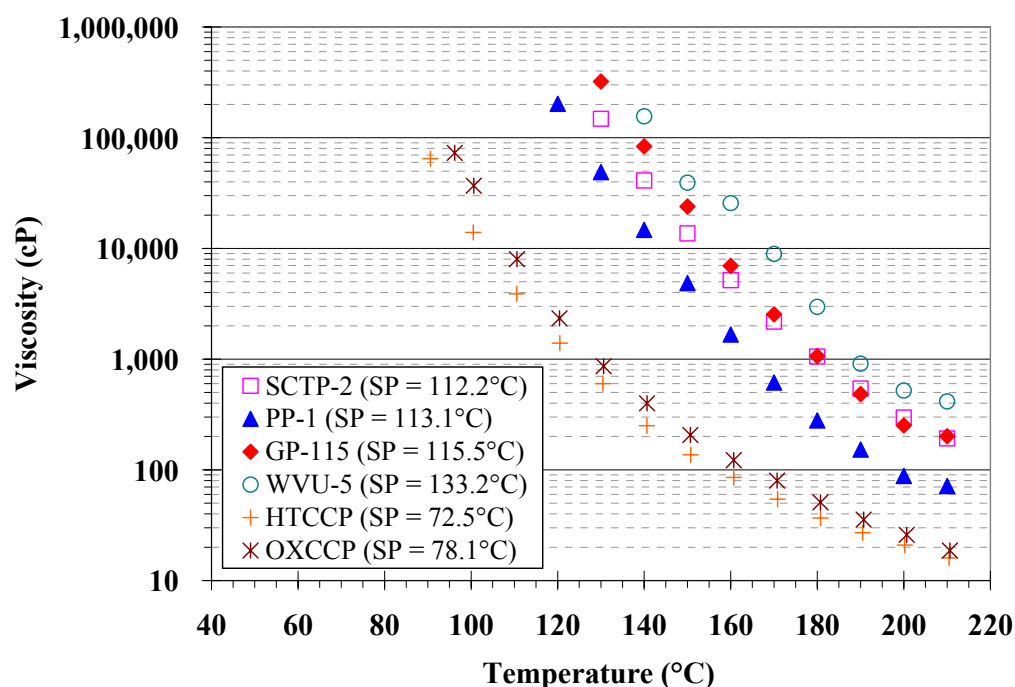


Figure 5-15: Viscosity measurement of SCTP-2, PP-1, GP-115, WVU-5, HTCCP and OXCCP by the ASTM D5018. Numbers in parentheses are the softening points of these pitches.

Table 5-42: General properties of SCTP-2, DO-107, PP-1, GP-115, WVU-5, Run #50, HTCCP, and OXCCP.

Property	SCTP-2	DO-107	Run#50 (360°C-FBP)	PP-1	GP-115	WVU-5	HTCCP	OXCCP
<u>Elemental Analysis</u> [†]								
C	93.83±0.20	90.33±0.14	89.00±0.00	93.48±0.21	87.30±0.23	88.42±0.14	90.4±0.10	90.6±0.20
H	3.87±0.16	6.55±0.08	6.49±0.11	5.55±0.44	6.43±0.51	6.17±0.42	4.3±0.09	3.91±0.06
N	1.03±0.05	0.48±0.06	0.03±0.00	0.20±0.07	1.66±0.01	2.01±0.04	0.04±0.00	0.04±0.00
S	0.56±0.01	3.22±0.03	3.36±0.00	1.21±0.08	0.36±0.00	0.42±0.00	2.66±0.15	2.59±0.02
O (by difference)	0.71	-0.58	1.12	-0.45	4.25	2.98	2.60	2.86
Atomic H/C	0.50	0.87	0.88	0.71	0.88	0.84	0.57	0.52
<u>Other Properties</u>								
Softening Point (°C) [†]	112.2±0.8	N.D.	N.D.	113.1±1.5	115.5±0.5	133.2±0.6	72.5±0.30	78.1±0.10
HS (wt%) [†]	24.67±0.35	N.D.	N.D.	47.77±0.63	43.42±4.96	19.66±0.70	15.52±3.49	19.41±0.23
HI/TS (wt%) [†]	43.08±2.61	N.D.	N.D.	42.77±3.27	32.60±0.75	49.04±0.53	70.34±1.25	65.77±0.76
TI/PS (wt%) [†]	8.31±0.20	N.D.	N.D.	3.72±1.63	21.54±2.13	26.48±3.90	6.67±1.47	10.32±1.53
PI (wt%) [†]	30.64±0.19	N.D.	N.D.	N.D.	0.25±0.08	7.21±1.18	7.59±1.27	6.90±0.31
QI (wt%) [†]	14.30	N.D.	N.D.	0.07	0.24	1.09	3.53	3.95
Moisture (wt%, dry) [†]	0.08±0.06	0.22±0.03	0.23±0.11	0.00±0.00	0.02±0.02	0.32±0.04	0.26±0.32	0.30±0.11
Volatile Matter (wt%, dry) [†]	40.56±0.22	96.51±0.01	98.17±0.31	53.46±0.12	62.61±1.97	49.72±0.02	60.78±1.16	65.31±0.35
Fixed Carbon (wt%) [†]	59.12±0.34	3.49±0.15	1.54±0.18	46.51±0.06	37.26±1.99	49.94±0.02	38.90±0.99	34.39±0.29
Ash Content (wt%) [†]	0.25±0.06	0.00±0.00	0.07±0.03	0.04±0.06	0.12±0.01	0.03±0.04	0.06±0.12	0.00±0.00

N.D. = Not Determined; N.A. = Not Available; [†] Data obtained from The Energy Institute; [‡] Data provided by Koppers Co., Ltd

Chemistry, Structure and Molecular Masses Distribution of Pitches

Mass Distribution by LDMS

Figure 5-16 shows the LDMS spectra of the HTCCP and OXCCP as compared to those of SCTP-2 and PP-1. Consider the materials ranging from 175-350 daltons as a monomer group (see **Figure 5-16(c)**). After heat soaked and oxidized the 360°C-FBP fraction, di-, tri-mers and so on were formed (see **Figure 5-16(d)** and **Figure 5-16(e)**). OXCCP contained more heavy mass material than HTCCP; however, they both were lighter than SCTP-2 and PP-1. Although both HTCCP and OXCCP were mixed with SCTP-2 at 30% by weight, there was still a gap of masses ranging from 350-450 daltons that needed to be filled. **Table 5-43** summarizes number and weight average molecular mass and the polydispersity obtained, and the information is used for determination of an average structure for each pitch material. Several heat soaking and oxidation conditions were tested and discussed in previous report [5-21]; however, under all conditions, the masses ranging from 350-450 daltons were still vacant.

Table 5-43: Number and weight average molecular weight and polydispersity of CTP-2, PP-1, GP-115, WVU-5, HTCCP and OXCCP obtained from MALDI technique.

SCTP-2	(MW) _n	(MW) _w	Polydispersity
PP-1	398.73	504.49	1.27
GP-115	434.18	517.06	1.19
WVU-5	349.59	431.48	1.23
HTCCP whole	501.52	623.86	1.24
OXCCP whole	309.38	365.47	1.18

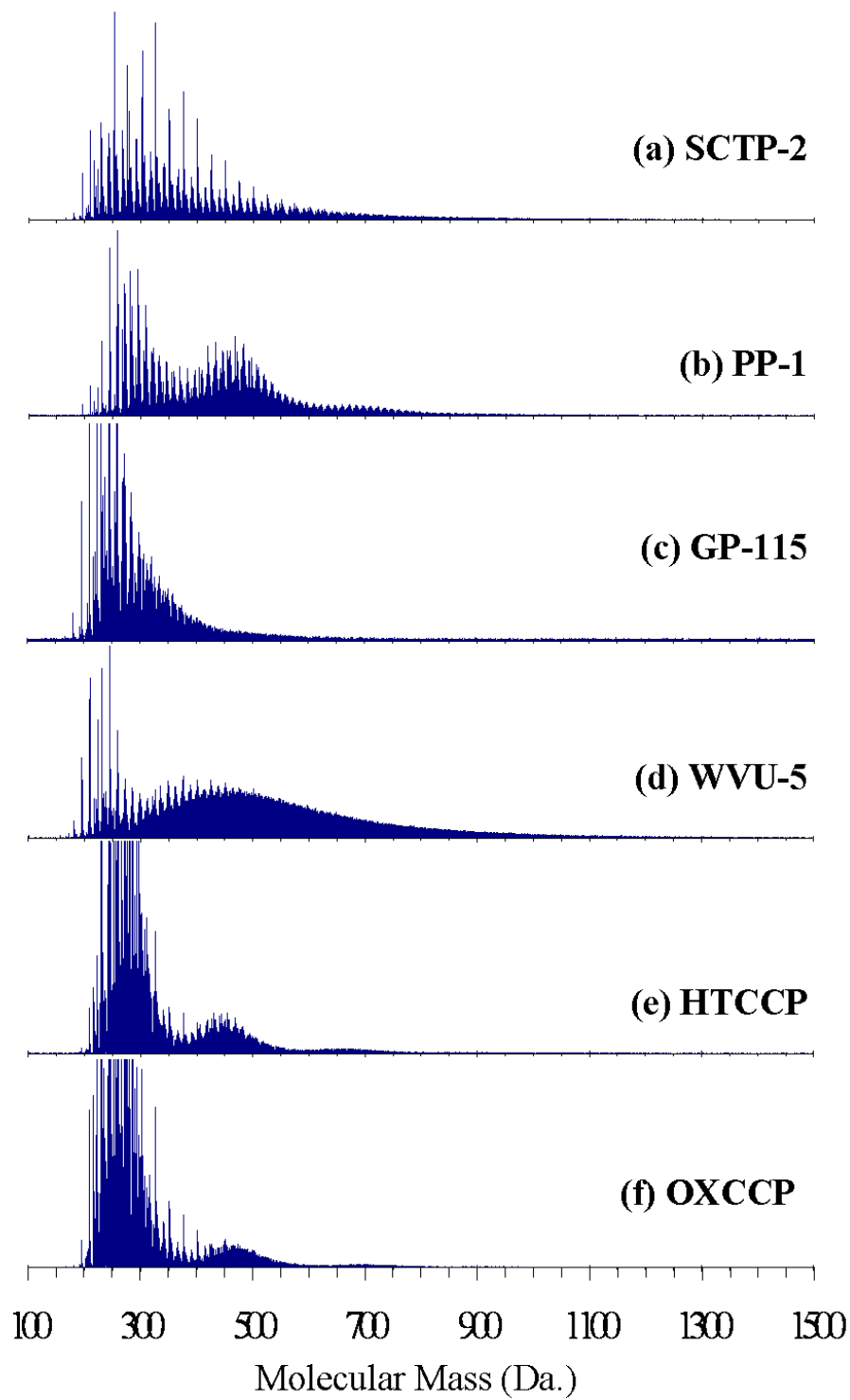
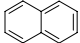
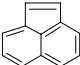
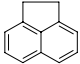
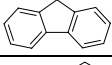
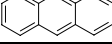
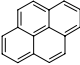
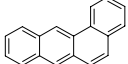
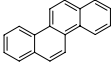
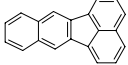
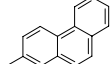
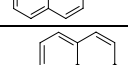
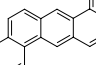


Figure 5-16 MALDI spectra of (a) Sctp-2, (b) PP-1, (c) GP-115, (d) WVU-5, (e) HTCCP and (f) OXCCP.

Table 5-44: Response factors of 16 PAC standards obtained from the GC/MS analyses.

ID #	Retention Time	Compound Name	Structure	Formula	MW	Response factor	R ² from calibration curve
1	13.567	Naphthalene		C ₁₀ H ₈	128	1.205	0.95
2	18.154	Acenaphthylene		C ₁₂ H ₈	152	1.3577	0.95
3	18.858	Acenaphthene		C ₁₂ H ₁₀	154	1.5821	0.95
4	20.920	Fluorene		C ₁₃ H ₁₀	166	1.6209	0.96
5	25.383	Phenanthrene		C ₁₄ H ₁₀	178	1.6324	0.96
6	25.613	Anthracene		C ₁₄ H ₁₀	178	1.5271	0.97
7	31.739	Fluoranthene		C ₁₆ H ₁₀	202	1.5156	0.96
8	32.778	Pyrene- <i>d</i> 10 (IS)		C ₁₆ D ₁₀	212	-	-
9	32.911	Pyrene		C ₁₆ H ₁₀	202	1.5849	0.96
10	39.824	Benz[a]anthracene		C ₁₈ H ₁₂	228	1.3545	0.95
11	40.058	Chrysene		C ₁₈ H ₁₂	228	1.3321	0.96
12	45.660	Benzo[b]fluoranthene		C ₂₀ H ₁₂	252	1.0902	0.95
13	45.803	Benzo[k]fluoranthene		C ₂₀ H ₁₂	252	1.104	0.95
14	47.200	Benzo[a]pyrene		C ₂₀ H ₁₂	252	0.9239	0.94
15	52.289	Indeno[1,2,3-cd]pyrene		C ₂₂ H ₁₂	276	0.5289	0.92
16	52.468	Dibenz[a,h]anthracene		C ₂₂ H ₁₄	278	0.5935	0.92
17	53.312	Benzo[ghi]perylene		C ₂₂ H ₁₂	276	0.5135	0.92

Chemical Analysis of HS Fraction by GC/MS

The total ion chromatograms (TICs) of the HS fractions for SCTP-2, PP-1, SS-115, WVU-5, HTCCP, and OXCCP are shown **Figure 5-17**. Most of the compounds are in the ranges of four- to five-ring PACs. The highest molecular masses observed in the HS fractions by GC/MS technique are in the range of 270-300 Da. Although the mass spectrometer of the instrument can analyze compounds up to 450 Da, it is limited by the volatility and size of the compounds that can pass through the GC column.

Retention times of different types of PACs are shown in **Table 5-44**. One-ring aromatic compounds in the pitch samples eluted at temperatures less than $\sim 150^{\circ}\text{C}$ (or retention time of less than 16 min.) These one-ring compounds were only found in WVU-5 pitch, and they are mainly alkylated phenols. Two-ring aromatic compounds elute from the GC column at the temperatures of ~ 135 - 175°C (or retention times of ~ 13.5 -23 min). They are mainly alkyl-substituted naphthalenes, and are observed in GP-115, WVU-5, and OXCCP. Three-ring PACs elute at the temperatures of ~ 160 - 225°C (or retention times of ~ 18.5 -35 min). Alkyl-substituted PACs are the majority in this group. A few hetero-atomic compounds were also observed in these three-ring PACs.

Four-ring PACs elute at the temperatures of 200 - 265°C (or retention times of 30-45.5 min), and are the majority of PACs in the HS fractions. Most of the hetero-atomic compounds observed in the HS fractions are in this category. Five- and six-ring PACs elute at the temperatures of ~ 265 - 320°C (or retention times of 45 min to >60 min). The temperature of 320°C is the limitation of this column. The holding time at this temperature is 15 min and any increase in the holding time could not detect any more compounds.

Apart from the aromatic compounds, some alkanes were detected in the pitch samples, especially in the GP-115 and WVU-5. The reason for the presence of these alkanes in the coal-derived pitch is not known; however, it is presumed that they may appear in coal in the form of aliphatic hydroxyl compounds, or R-OH, or alkylated phenols. During the pitch preparation, i.e. heat treatment, polymerization of these compounds may occur and long-chain alkanes were formed. Once the bonds between the alkyl and hydroxyl or phenol groups were cleaved by the heat treatment, these alkanes were then left in the pitch sample.

The identification of compounds in the pitch samples was done by matching the mass spectral patterns with those of the compounds in the library. The compounds that match with both retention times and mass spectral patterns with the external standards can be directly quantified by their response factors previously calculated using the external standard method. Details on the response factors can be found in previous publications [5-32]. **Table 5-45** summarizes the quantitative analyses of the HS fractions of all six pitch samples. The compounds are categorized based on the number of fused rings, their alkyl substitution and hetero-atomic substitution.

Figure 5-17 compares the spectra of the HS fractions of all six pitch samples. The spectrum of SCTP-2 is the simplest. The PP-1, HTCCP and OXCCP spectra are very complex, since they contain tremendous amounts of alkyl-substituted compounds that are characteristic of petroleum-derived materials. Peaks in PP-1, HTCCP and OXCCP show a similar retention time profile but differ in their intensities. It is observed that compounds found in the HS fractions are mainly composed of four-ring PACs. Only GP-115 and WVU-5 contain compounds in the ranges of two- or three-ring PACs.

Py-GC/MS was done on all six samples [5-32]. Data obtained from this technique were similar to data obtained from the GC/MS of the HS fraction, except the py-GC/MS had a higher concentration of heavier compounds. The data obtained by py-GC/MS supported the GC/MS conclusions, but because 1) the data obtained from py-GC/MS qualitative, 2) it was difficult to clean the heavy compounds from the column and were found to contaminate subsequent runs, and 3) the pyrolysis was at 300°C (a temperature only high enough to volatilize the lighter components which should be similar to the HS fraction), the py-GC/MS was not included within the report.

Table 5-45: Type of compounds and their concentration of SCTP-2, PP-1, GP-115, WVU-5, HTCCP and OXCCP observed by GC/MS analyses.

Type of Compounds		SCTP-2	PP-1	GP-115	WVU-5	HTCCP	OXCCP
Alkane	Alkane	0	0	39	185	2	0
	Total alkane (ug/mL)	0	0	39	185	2	0
	% of total alkane	0%	0%	2%	9%	0%	0%
1-ring	1-ring (ug/mL)	0	0	0	0	0	0
	hydrogenated or alkylated 1-ring (ug/mL)	0	0	0	1	0	0
	sulfur- and alkyl-substituted 1-ring (ug/mL)	0	0	0	0	0	0
	oxygen- and alkyl-substituted 1-ring (ug/mL)	0	0	0	9	0	0
	nitrogen- and alkyl-substituted 1-ring (ug/mL)	0	0	0	0	0	0
	Total 1-ring (ug/mL)	0	0	0	11	0	0
	% of total 1-ring	0%	0%	0%	1%	0%	0%
2-ring	2-ring (ug/mL)	0	0	1	30	0	0
	hydrogenated or alkylated 2-ring (ug/mL)	0	0	8	168	0	0
	sulfur- and alkyl-substituted 2-ring (ug/mL)	0	0	0	0	3	44
	oxygen- and alkyl-substituted 2-ring (ug/mL)	0	0	0	8	0	1
	nitrogen- and alkyl-substituted 2-ring (ug/mL)	0	0	0	2	0	0
	Total 2-ring (ug/mL)	0	0	9	209	3	46
	% of total 2-ring	0%	0%	1%	10%	0%	1%
3-ring	3-ring (ug/mL)	72	26	32	46	7	5
	hydrogenated or alkylated 3-ring (ug/mL)	128	147	141	226	425	900
	sulfur- and alkyl-substituted 3-ring (ug/mL)	2	0	0	0	32	53
	oxygen- and alkyl-substituted 3-ring (ug/mL)	0	0	12	9	0	26
	nitrogen- and alkyl-substituted 3-ring (ug/mL)	29	0	32	9	18	1
	Total 3-ring (ug/mL)	232	172	217	289	483	985
	% of total 3-ring	5%	8%	14%	14%	10%	23%
4-ring	4-ring (ug/mL)	1435	128	212	310	413	311
	hydrogenated or alkylated 4-ring (ug/mL)	586	1182	371	500	1571	1044
	sulfur- and alkyl-substituted 4-ring (ug/mL)	133	170	0	9	1134	857
	oxygen- and alkyl-substituted 4-ring (ug/mL)	40	108	54	26	229	262
	nitrogen- and alkyl-substituted 4-ring (ug/mL)	117	85	20	10	83	164
	Total 4-ring (ug/mL)	2312	1673	656	854	3429	2637
	% of total 4-ring	47%	75%	42%	41%	74%	61%
5-ring	5-ring (ug/mL)	1543	117	255	194	280	233
	hydrogenated or alkylated 5-ring (ug/mL)	151	183	58	249	214	168
	sulfur- and alkyl-substituted 5-ring (ug/mL)	49	4	0	0	0	10
	oxygen- and alkyl-substituted 5-ring (ug/mL)	52	47	236	29	126	198
	nitrogen- and alkyl-substituted 5-ring (ug/mL)	14	9	0	0	0	0
	Total 5-ring (ug/mL)	1809	361	549	471	620	609
	% of total 5-ring	37%	16%	35%	23%	13%	14%
6-ring	6-ring (ug/mL)	580	29	92	57	60	58
	hydrogenated or substituted 6-ring (ug/mL)	7	10	7	0	5	16
	Total 6-ring (ug/mL)	587	38	99	57	65	74
	% of total 6-ring	12%	2%	6%	3%	1%	2%
Total (ug/mL)		4940	2244	1570	2076	4601	4350

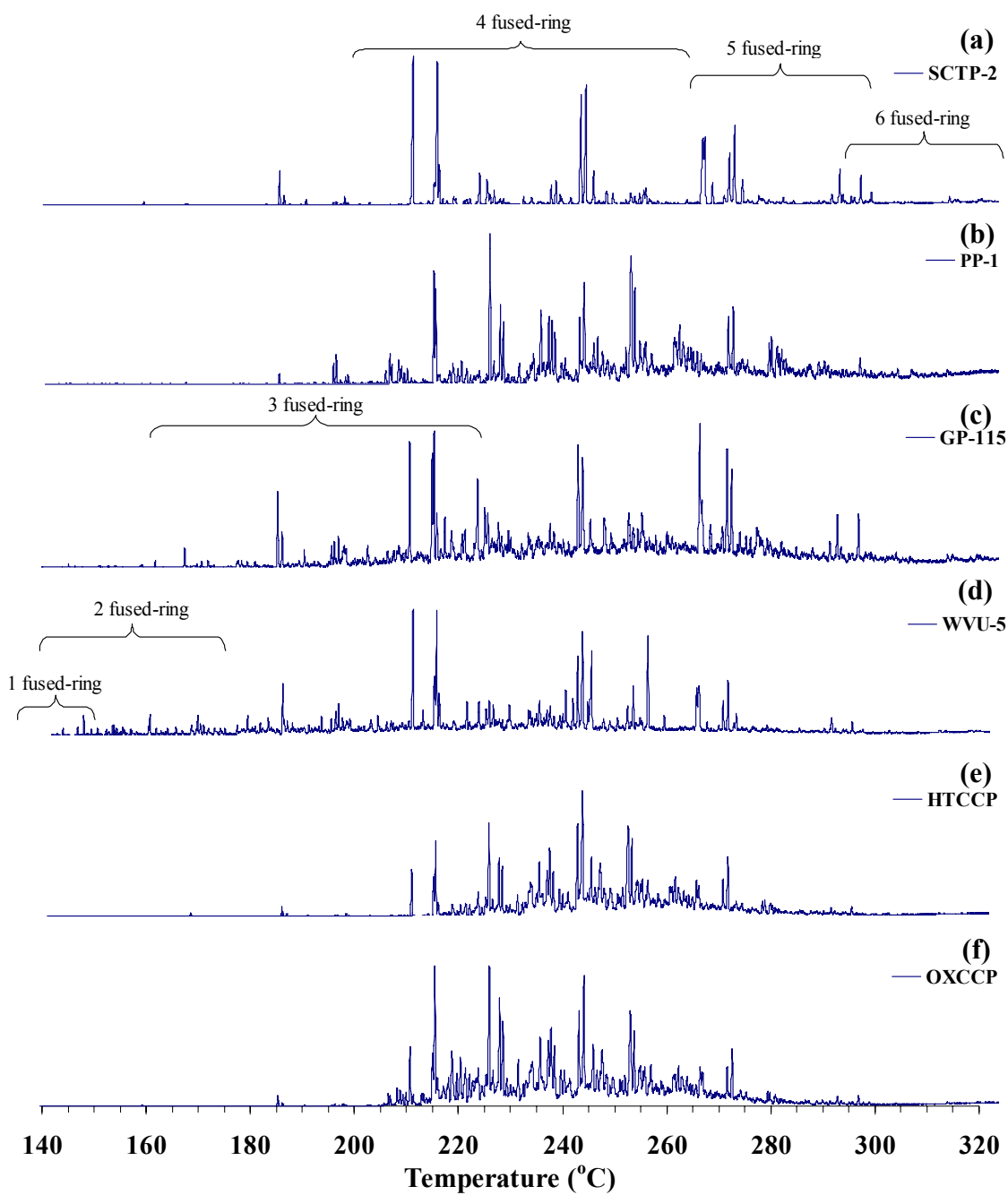


Figure 5-17: GC/MS Chromatogram of HS fractions of (a) Sctp-2, (b) PP-1, (c) GP-115, (d) WVU-5, (e) HTCCP and (f) OXCCP.

Chemical Analysis of HI-TI and TS Fraction by HPLC

HPLC was used to analyze the HI-TI fractions of the SCTP-2, HTCCP and OXCCP and the TS fractions of PP-1, GP-115 and WVU-5. The TS fractions were used in the PP-1, GP-115 and WVU-5 because of the poor resolution obtained in the HI-TI fractions from these samples. The Pinnacles II column from Restek used in this study was able to discriminate compounds in terms of their molecular size and the number of fused rings, as shown in **Figure 5-18** for the 16 standard PACs. The order of compounds eluted from the HPLC column is the same as observed from the GC/MS analysis, except the last three compounds where dibenzo[a,h]anthracene (peak 16), eluted first from the HPLC column following by benzo[ghi]perylene (peak 17) and indeno[1,2,3-cd]pyrene (peak 15), respectively (see **Figure 5-18**).

Figure 5-19 shows a comparison of HPLC chromatograms of HI-TI fractions of SCTP2, HTCCP and OXCCP and TS fraction of PP-1, GP-115 and WVU-5 extracted at a wavelength of 254 nm. This wavelength was used because it can cover a wide range of PACs. The resolution of the chromatograms is fairly good for all samples although the baseline is shifted after a retention time of 200 minutes. The introduction of dichloromethane (DCM) into the column was observed to cause the baseline to shift after 200 minutes and distort at ~230 minutes. However, it was necessary to introduce DCM since it was used to wash out all remaining sample from the column due to its high solvating power.

Figure 5-19 reveals the information on the compositions of heavy PACs found in pitch that could not be obtained from the GC/MS analysis. Since there is only a UV detector attached to the HPLC unit, the only way to quantify the compounds is to inject known standard compounds. Although only compounds in the 16 standard PACs (see **Figure 5-18**) could be identified, the HPLC chromatograms were still useful in terms of comparison between samples. A visualized comparison of peaks and their retention from the chromatogram was done as discussed below.

As observed earlier in the GC/MS analysis, the chromatograms of the petroleum-derived pitches, i.e. PP-1, HTCCP and OXCCP, are more complex than the coal-derived pitch since the petroleum-derived pitches contain more isomers of alkylated PACs. The baselines of the petroleum-derived pitches were shifted due to their complexity and this

caused a broad hump from the retention time of 20 to 200 minutes as shown in **Figure 5-19(b), (e) and (f)**. Since the last known compound eluted from the column is indeno[1,2,3-cd]pyrene, or peak 15 shown in **Figure 5-19**, which is a six-ring PAC, it is presumed that peaks eluting after this peak 15 are those corresponding to six-ring PACs or higher. Although the intensities of these heavy compound peaks are small, it does not mean that their concentrations are low since these heavy compounds tend to respond poorly.

Among all samples, only SCTP-2 (see **Figure 5-19(a)**) and PP-1 (see **Figure 5-19(b)**) have well-resolved peaks with high intensities eluting at long retention times, indicating that these two pitches contain a considerable amount of heavy compounds. SCTP-2 gives better-resolved heavy compound peaks as compared to those in PP-1, meaning that PACs in SCTP-2 are less complex in composition. **Figure 5-19(c) to Figure 5-19(f)** show that peaks eluted at the long retention times in GP-115, WVU-5, HTCCP and OXCCP give comparable resolution and intensities. This observation does not mean that these pitches have comparable quantities of heavy PACs. By comparing the chromatograms obtained from the MALDI and HPLC (see **Figure 5-16** vs. **Figure 5-19**), the results obtained from both techniques are in agreement for the mass ranges up to 600 Da, except for WVU-5. MALDI indicates that WVU-5 contains a high quantity of compounds ranging from 300-900 Da (see **Figure 5-16**). However, results from HPLC did not reveal these compounds, most probably due to their limited solubility in the solvents used in the HPLC technique.

Although this work could not fully utilize the capability of the HPLC technique due to the limitation of the photodiode array detector, a good mobile phase with suitable gradient flow for the pitch samples and the Pinnacle II™ PAH column from Restek was established. It should be of interest in the future to apply this column and the gradient flow to an HPLC/MS in order to identify heavy compounds in the pitch samples.

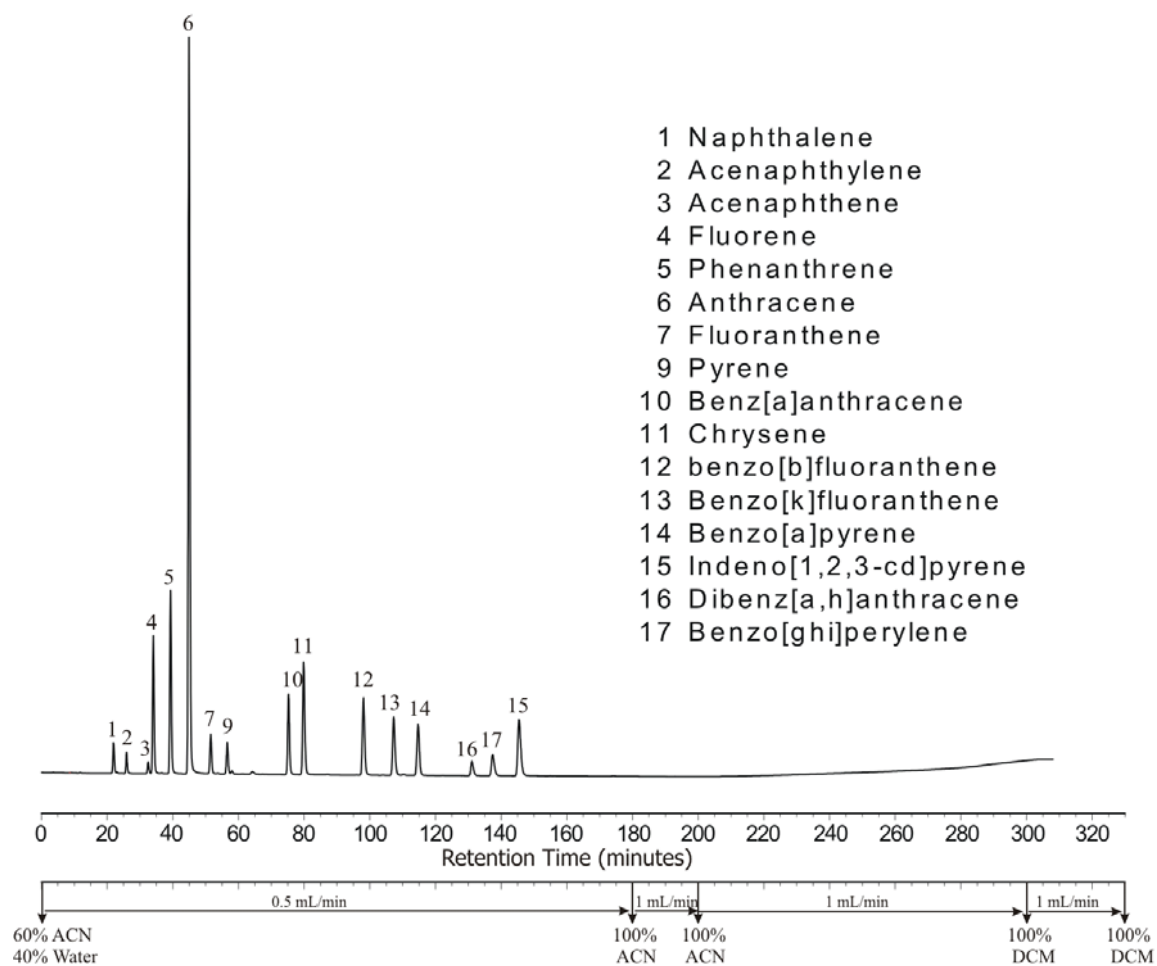


Figure 5-18: HPLC chromatogram of 16 PAC standards.

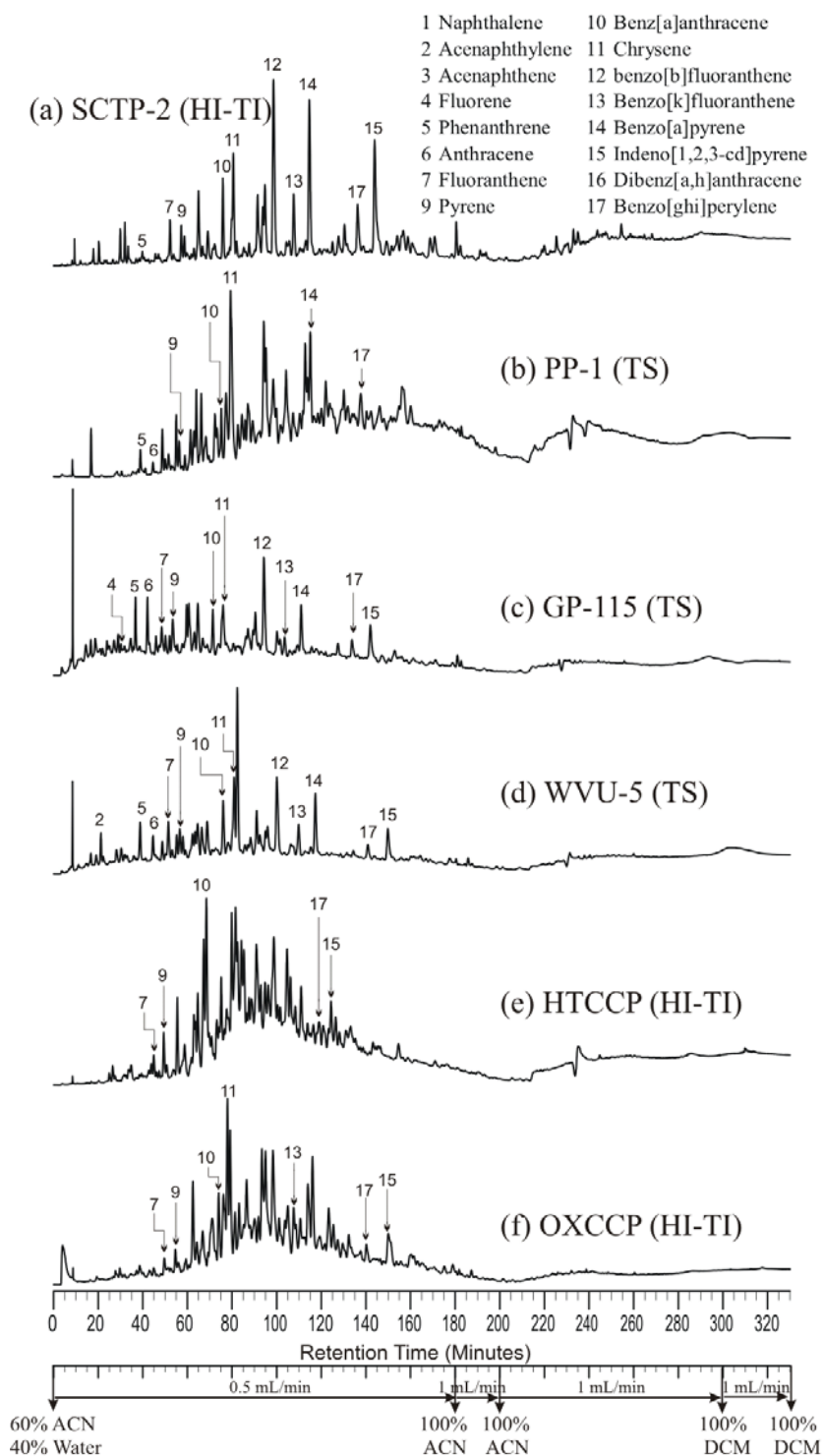


Figure 5-19: HPLC Chromatograms of (a) SCTP-2 (HI-TI), (b) PP-1 (TS), (c) GP-115 (TS), (d) WVU-5 (TS), (e) HTCCP (TS) and (f) OXCCP (TS).

Solution-State NMR

¹H Solution-State NMR

The ¹H solution-state spectra of SCTP-2, PP-1, GP-115, WVU-5, HTCCP and OXCCP are compared in **Figure 5-20(a)** to **Figure 5-20(f)**, respectively. The ¹H NMR spectra are mainly divided into aromatic (at chemical shift 6-9.3 ppm), and aliphatic (at chemical shift 0.5-4.5 ppm) domains. **Table 5-46** tabulated ¹H distributions of SCTP-2, PP-1, GP-115, WVU-5, HTCCP and OXCCP from the solution state NMR. Only SCTP-2 contains the highest aromatic ¹H, i.e. 84% of all ¹H observed. The percentages of aromatic ¹H of other petroleum-derived pitches, PP-1, HTCCP and OXCCP, are ranging from 56 to 64 of all ¹H observed. For other coal-derived pitches, GP-115 and WVU-5, the percentages of aromatic ¹H are 47% and 41%, respectively. ¹H NMR can discriminate ¹H in H_{Ar, 2} (aromatic ¹H in very pericondensed PAHs or next to heteroatoms and some ¹H joined to nitrogen) and H_{Ar, 1} (all other aromatic ¹H). These parameters can be used to identify how condensed the aromatics in the pitch are. SCTP-2 and PP-1 are among the most highly condensed pitches as compared to the others. The degree of condensation of pitch can be determined by using the solid-state NMR technique discussed in the following section.

From the aliphatic ¹H distributions, around 40% to 75% of ¹H is H_α, aliphatic ¹H on carbons α to the aromatic ring, for most pitches. This indicates the presence of alkyl substitution in these pitches. GP-115 contains higher H_β, aliphatic ¹H on carbons β to the aromatic ring, indicating that it contains higher portions of ethyl or longer chains than other pitches. PP-1 contains a high portion of H_α, 74%, meaning that it contains mostly methyl substituents and few longer chains.

¹³C Solution State NMR

The ¹³C solution-state spectra of SCTP-2, PP-1, GP-115, WVU-5, HTCCP and OXCCP are compared in **Figure 5-21(a)** to **Figure 5-21(f)**, respectively. The spectra can be divided into aromatic (chemical shift between 108 and 160 ppm) and aliphatic (chemical shift between 10 and 60 ppm) domains. The resolutions of all pitch spectra are rather good when taking into account their complexity. **Table 5-46** tabulates ¹³C distributions of SCTP-2, PP-1, GP-115, WVU-5, HTCCP and OXCCP from the solution-

state NMR. As expected, Sctp-2 contains 79% aromatic C-C based on the total aromatic carbon, which is the highest (chemical shift greater than 129.5 ppm) among all pitches. The percentages of aromatic C-C of the other pitches are 54-70% of total aromatic carbons. From **Figure 5-21**, PP-1, GP-115, WVU-5, HTCCP and OXCCP have a higher proportion of the shoulder of the aromatic peak, i.e. chemical shift greater than 138 ppm, than that of Sctp-2. This shoulder is mainly alkyl-, naphthenic-, and heteroatomic-substituted aromatic carbons. These substituents, as well as those protonated carbons, are typically deducted from the aromatic carbons to obtain the bridgehead aromatic carbons, which in turn give the degree of condensation of the pitch. More details of the degree of condensation are discussed in the solid-state NMR section. Hence, Sctp-2 clearly contains more densely condensed aromatic units than other pitch samples.

Table 5-46: ^1H and ^{13}C distributions of Sctp-2, PP-1, GP-115, WVU-5, HTCCP and OXCCP obtained by peak integration of ^1H and ^{13}C solution state NMR spectra.

Types of ^1H or ^{13}C	Sctp-2	PP-1	GP-115	WVU-5	HTCCP	OXCCP
Solution state ^1H NMR						
Total aromatic ^1H (%Total ^1H)	83.89%	56.61%	46.95%	41.41%	63.65%	58.84%
- $\text{H}_{\text{Ar},2}$ (8.3-9.0 ppm) (%Aro ^1H)	17.24%	16.75%	11.06%	13.31%	10.40%	10.09%
- $\text{H}_{\text{Ar},1}$ (6.0-8.3 ppm) (%Aro ^1H)	82.76%	83.25%	88.94%	86.69%	53.25%	48.75%
Total aliphatic ^1H (%Total ^1H)	16.11%	43.39%	53.05%	58.59%	36.35%	41.16%
- Ring joining methylene, methine H (3.5-5.0 ppm) (%Ali ^1H)	14.29%	7.26%	5.76%	5.74%	2.32%	1.36%
- H on α -carbon to aromatic carbons (1.9-3.5 ppm) (% Ali ^1H)	50.96%	74.20%	42.53%	60.21%	28.71%	31.98%
- H on β -carbon to aromatic carbons (< 1.9 ppm) (%Ali ^1H)	34.76%	18.54%	51.71%	34.05%	5.33%	7.82%
Solution state ^{13}C NMR						
Total aromatic ^{13}C (%Total ^{13}C)	96.30%	86.16%	74.41%	70.17%	91.32%	89.85%
- Aromatic C-H (108.0-129.5 ppm) (%Aro ^{13}C)	21.31%	33.49%	30.57%	32.11%	29.76%	35.98%
- Aromatic C-C (> 129.5 ppm) (%Aro ^{13}C)	78.69%	66.51%	69.43%	67.89%	61.56%	53.87%
Total aliphatic ^{13}C (%Total ^{13}C)	3.70%	13.84%	25.59%	29.83%	8.68%	10.15%
- CH, CH_2 (24.0-60.0 ppm) (%Aro ^{13}C)	85.60%	48.48%	70.41%	70.21%	18.18%	27.27%
- CH_3 (10.0-24.0 ppm) (%Aro ^{13}C)	14.40%	51.52%	29.59%	29.79%	81.82%	72.73%

Notes: $\text{H}_{\text{Ar},2}$ = aromatic ^1H in very pericondensed PAHs or next to heteroatoms and some ^1H joined to nitrogen.
 $\text{H}_{\text{Ar},1}$ = all other aromatic ^1H .

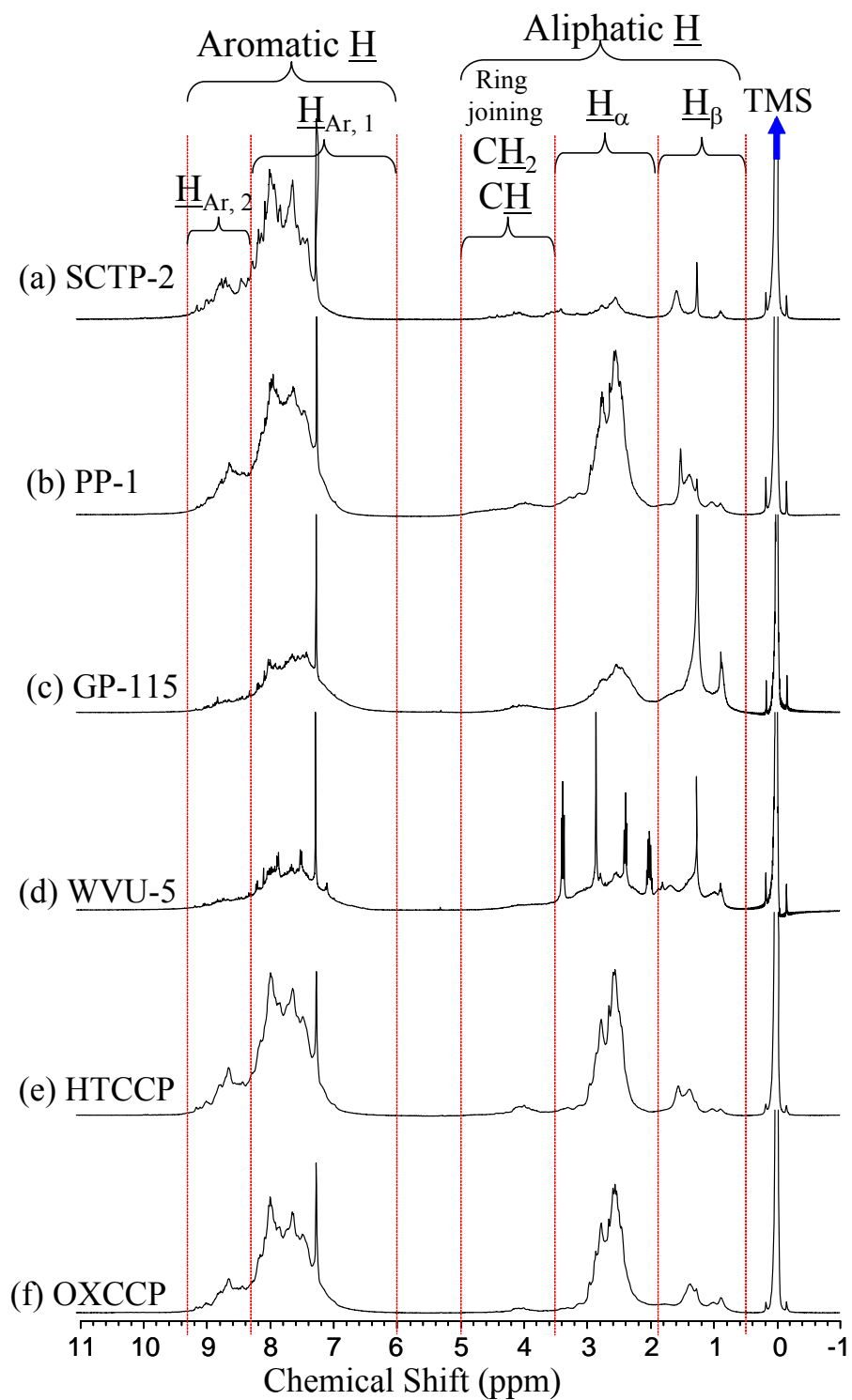


Figure 5-20: ^1H spectra of (a) SCTP-2, (b) PP-1, (c) GP-115, (d) WVU-5, (e) HTCCP and (f) OXCCP obtained from the ^1H solution state NMR.

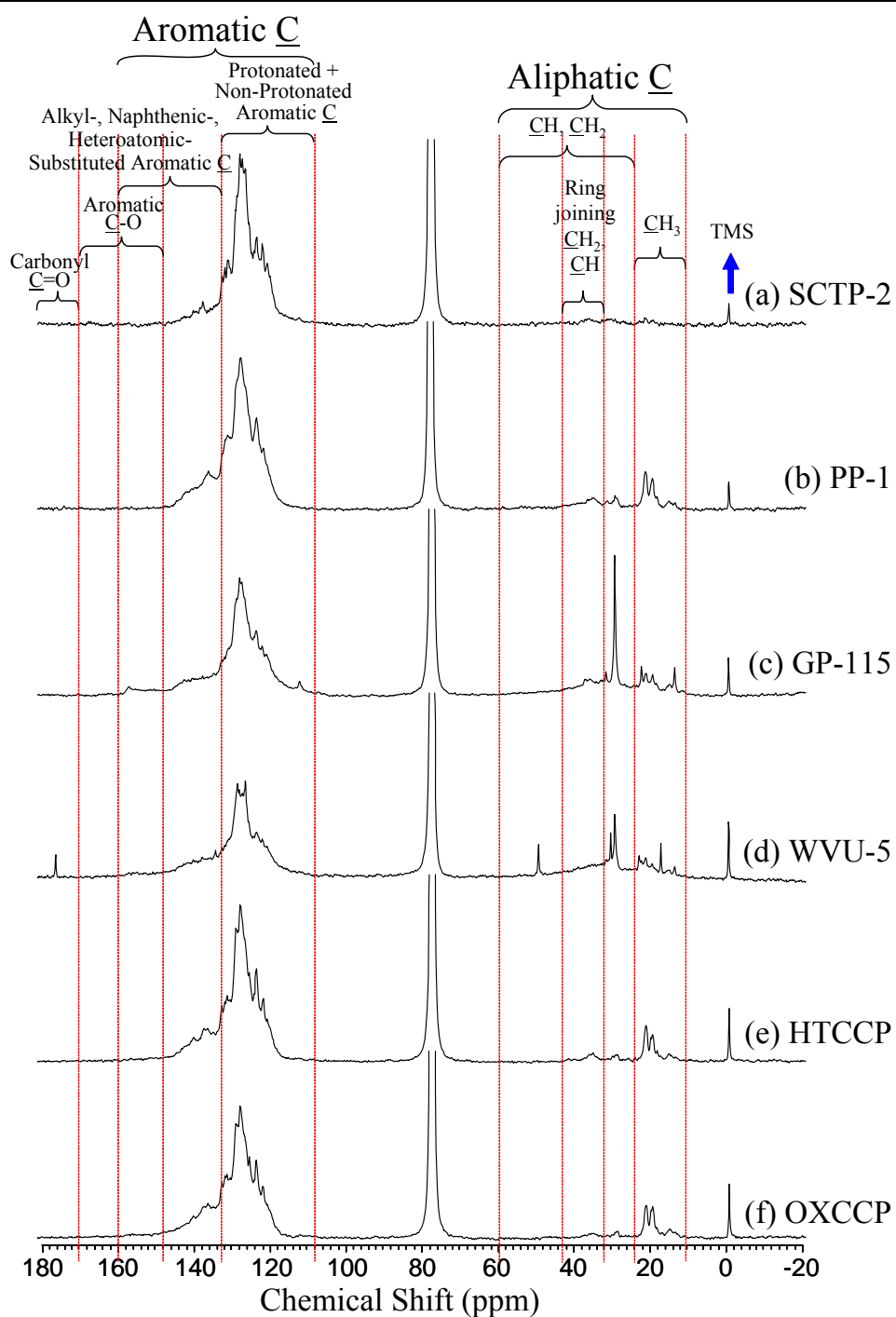


Figure 5-21: ^{13}C spectra of (a) SCTP-2, (b) PP-1, (c) GP-115, (d) WVU-5, (e) HTCCP and (f) OXCCP obtained from the ^{13}C solution state NMR.

Solid State ^{13}C NMR

The solid state ^{13}C NMR of SCTP-2, PP-1, GP-115, WVU-5, HTCCP, and OXCCP were obtained using both the CP- and SPE-MAS techniques. Essentially, the spectra contain mainly an aromatic peak, which is centered at ~ 126 ppm, and an aliphatic band distributed between 10 and 60 ppm (see **Figure 5-22**). The spinning sidebands, which are part of the aromatic peak, accounted for 4-9% of the total peak areas for these pitch samples. All the contact times in the CP experiment are between 2.5 and 5.0 ms for all pitch samples, depending on their maximum intensity in the variable contact time cross polarization experiments. The aromaticity determined by SPE is in general 3-7% greater than that obtained by the CP technique, except SCTP-2 whose aromaticity is only $\sim 0.6\%$ different (see **Table 5-47**). It is observed that the higher the aromaticity, the closer the gap between the aromaticity obtained by CP and SPE. This observation is in agreement with the results observed by Maroto-Valer et al. [5-33].

Table 5-47: Aromatic and aliphatic contents of SCTP-2, PP-1, GP-115, HTCCP, and OXCCP measured by CP-MAS and SPE experiments.

	CP-MAS		SPE-MAS	
	% Aromatic	% Aliphatic	% Aromatic	% Aliphatic
SCTP-571	97.17%	2.83%	97.83%	2.17%
PP-1	87.15%	12.85%	91.18%	8.82%
GP-115	80.10%	19.90%	85.46%	14.54%
WVU-5	79.53%	20.47%	86.33%	13.67%
HT-CCP	88.50%	11.50%	92.09%	7.91%
OX-CCP	86.15%	13.85%	90.41%	9.59%

Figure 5-22(a) compares the aromatic peaks of SCTP-2, PP-1, GP-115, WVU-5, HTCCP and OXCCP spectra obtained by the SPE technique. To relatively compare these peaks, the spectra of these samples were adjusted until the intensities of the aromatic peaks were equal. Pitches contain highly aromatic carbons whose chemical shifts range from 108 to 160 ppm. Shoulders of the aromatic peak starting from *ca.* 135 ppm and greater show the presence of naphthenic, alkyl and heteroatomic substituted aromatic carbons (see chemical shift assignment in **Table 5-48**). GP-115 and WVU-5 apparently

contain a peak covering the chemical shifts between 148 and 168, which are assigned to the aromatic C-O. This observation is not unexpected for GP-115 and WVU-5, since they contain 4% and 3% by weight of oxygen, respectively (see **Table 5-42**). OXCCP consists of relatively higher intensities of the aromatic C-O band as compared to the HTCCP. Although these two samples were derived from the same feedstock, OXCCP was heat treated under an oxygen environment. Hence, the SPE results reflect how the samples were prepared. The spectra of WVU-5 and OXCCP indicate the presence of carbonyl groups to some extent, as shown as broad and short humps around 170-190 ppm in **Figure 5-22(a)**. These humps are not well resolved due to the poor signal to noise ratio.

Figure 5-22(b) shows the aliphatic spectral regions of the six pitch samples. These spectra are from the same experiments as those shown in **Figure 5-22(a)**; however, the scale was expanded in order to show more spectral details. The signal to noise ratios of each spectrum are acceptable even though a long recycle delay was used, i.e. five times the T_1^C of aromatic carbons. The quantitative proportions of CH₃ (10-24 ppm), and CH and CH₂ (24-60 ppm) groups are tabulated in **Table 5-49**.

The proportion of CH₃ accounts for 45% to 67% of the aliphatic carbons for the coal-derived pitches, i.e. SCTP-2, GP-115, and WVU-5, and 79% to 89% of the aliphatic carbons for the petroleum-derived pitches, i.e. PP-1, HTCCP and OXCCP. A band ranging from 32 to 43 ppm likely shows the existence of ring-joining methylene bridges. This evidence supports the proposed superstructure by Zander [5-29] as discussed below. GP-115, WVU-5 and OXCCP also show some broad humps around 60-80 ppm. Since the oxygen contents of these samples are relatively higher than other samples, these humps likely resulted from ester or alcohol groups.

The degree of condensation of the aromatic structure is often obtained by the relative proportion of bridgehead and peripheral aromatic carbons [5-35, 5-36]. The ¹³C solid- state dipolar dephasing experiments were employed for this purpose. It is generally accepted that SPE or Bloch decay measurements are the best approach for obtaining quantitative ¹³C NMR results [5-31]. **Figure 5-23(a)** and **Figure 5-23(b)** show the dipolar dephasing spectra of WVU-5 at various dephasing times obtained from the CP and SPE experiments, respectively. When the dephasing times increase, the center of the

aromatic peak is shifted from *ca.* 126 ppm to *ca.* 128 ppm, indicating the absence of the protonated carbons and that only quaternary carbons remain. The heteroatomic-substituted aromatic bands ranging from 148-180 ppm, i.e. aromatic ethers and carbonyls, still remain even at 600 microseconds dephasing time. These are caused by a substantially long decay of quaternary and carbonyl carbons. The methyl carbons (chemical shifts between 10-24 ppm) also remain at long dephasing times, exhibiting a long decay probably strongly influenced by their molecular motion [5-37].

Table 5-48: NMR Chemical shift assignments of different types of carbons in coal and petroleum products.

Assignments	Chemical shift
	ppm
<u>Carbon</u>	
Total aromatic carbon	
Carbonyl	170-210
Aromatic C-O	148-168
Alkyl (other than methyl) substituted aromatic	138.0-160.0
Heteroatom (N, O, S) aromatic	
Naphthenic substituted aromatic	135.0-138.0
Methyl substituted aromatic	133.0-135.0
Most internal aromatic	129.5-133.0
Protonated aromatic	118.0-129.5
Some internal (quaternary) aromatic	
Aromatic CH ortho to ether or OH groups	108.0-118.0
Some olefinic (others spread through aromatic region)	
Total aliphatic carbon	
Fraction of CH, CH ₂ in aliphatic carbon	24.0-60.0
Ring joining methylene	32.0-43.0
Fraction of CH ₃ in aliphatic carbon	10.0-24.0
<u>Hydrogen</u>	
Total aromatic hydrogen	
H _{Ar, 2} (aromatic hydrogens in very peri-condensed PAHs or next to heteroatoms and some hydrogens joined to nitrogen)	8.3-9.3
H _{Ar, 1} (all the other aromatic hydrogen)	6.0-8.3
Total aliphatic hydrogen	
Ring joining methylene, methine H	3.5-5.0
H _α (H on α-carbon to aromatic carbons)	1.9-3.5
H _β (H on β-carbon to aromatic carbons)	<1.9

Note: Chemical shift assignments taken from Snape et al. [7], Rodriguez [8] and Guillen et al. [9].

Table 5-49: Proportions of different types in aliphatic carbons observed in SCTP-2, PP-1, GP-115, WVU-5, HTCCP and OXCCP obtained from SPE.

	Fraction of CH, CH ₂ in aliphatic carbon	Fraction of CH ₃ in aliphatic carbon
SCTP-2	33.18%	66.82%
PP1	18.24%	81.76%
GP-115	53.81%	46.19%
WVU-5	63.46%	36.54%
HTCCP	11.10%	88.90%
OXCCP	21.27%	78.73%

Note: Ester and alcohol bands are not taken into account.

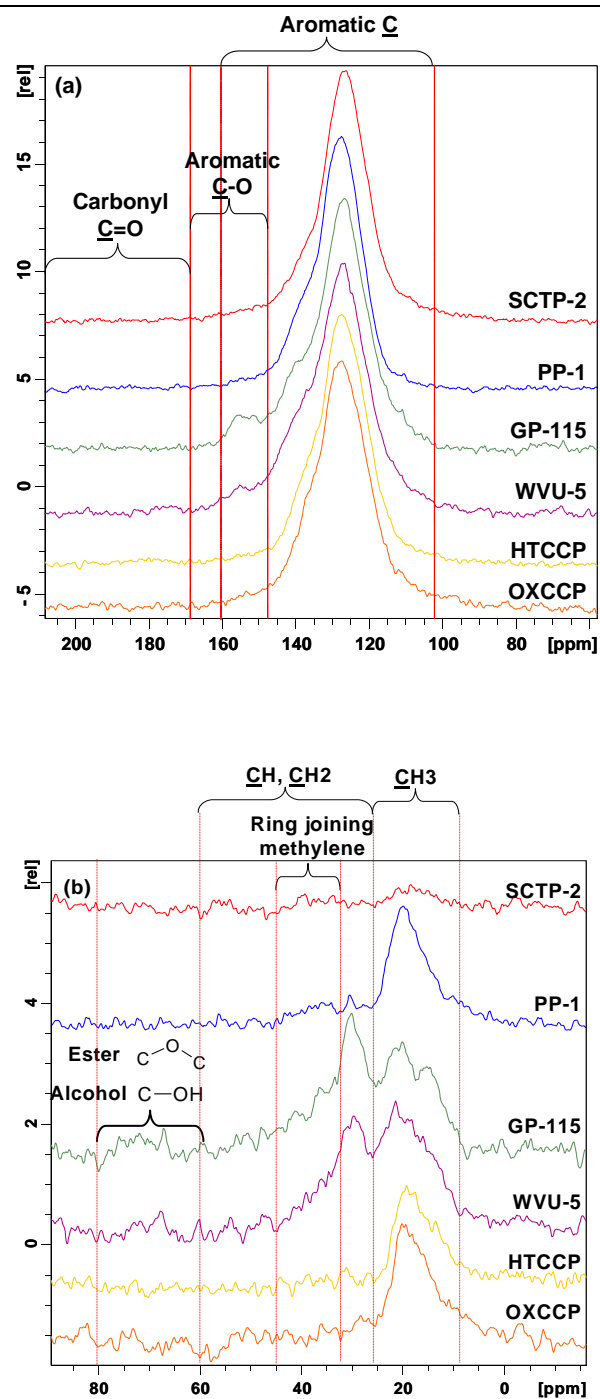


Figure 5-22: Comparison of (a) aromatic and (b) aliphatic domains of Sctp-2, PP-1, GP-115, WVU-5, HTCCP and OXCCP spectra obtained by the SPE-MAS technique.

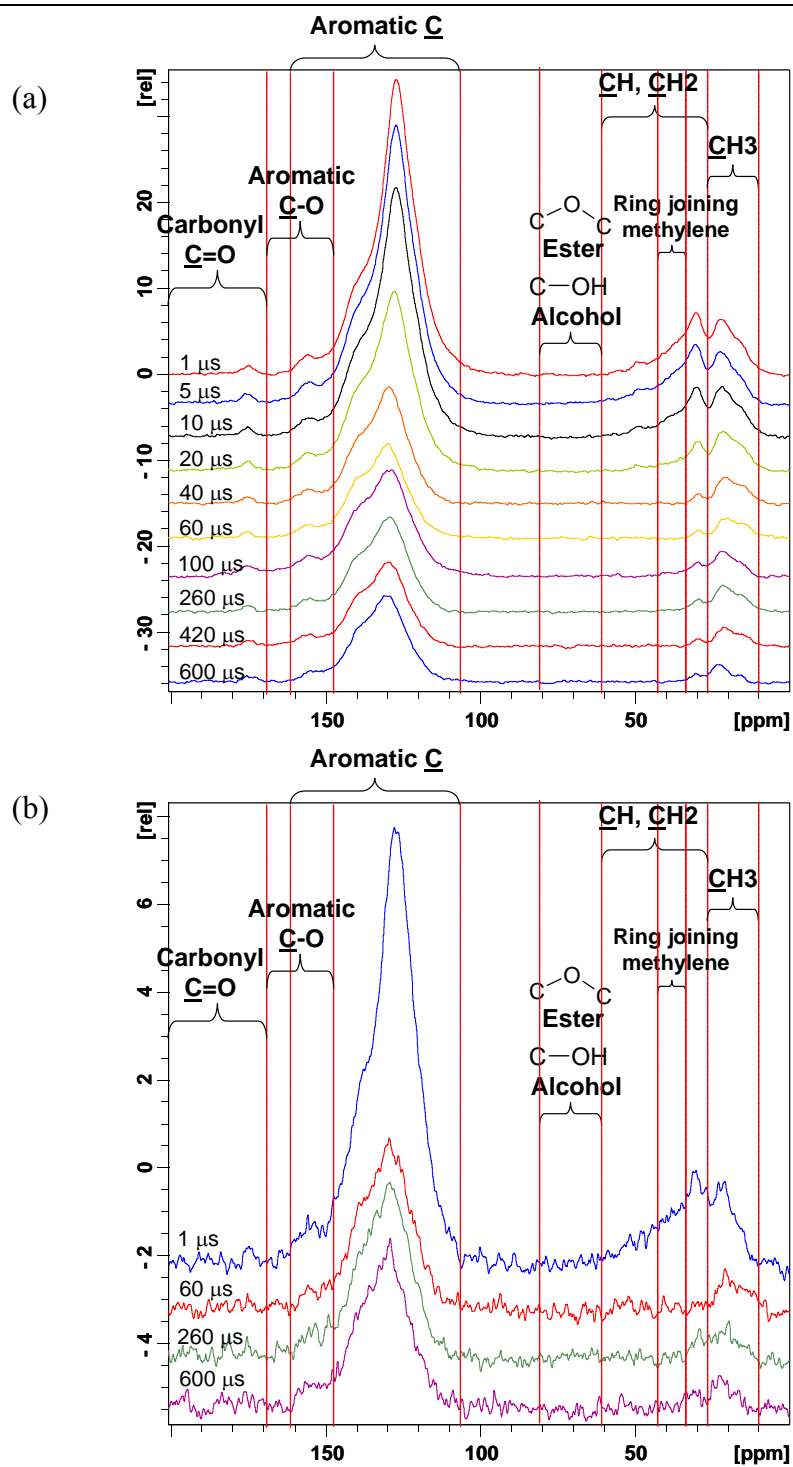


Figure 5-23: (a) CP-DD and (b) SPE-DD ^{13}C NMR spectra at various dephasing times of WVU-5.

Figure 5-24(a) and **Figure 5-24(b)** compare the SPE-DD spectra of WVU-5 obtained at 1 and 60 microseconds dephasing times, respectively. GRAMS/AI version 7.01 was used to deconvolute the spectra into various Gaussian components. It is clearly seen that only the long-decay components, i.e. heteroatomic-substituted and quaternary aromatic carbons, remain at 60 microseconds dephasing time.

The fraction of non-protonated aromatic carbons can be determined by plotting a relative peak integral of the aromatic peak against its dipolar dephasing times. **Figure 5-25** shows a logarithmic plot of relative aromatic peak integral versus dephasing times in the CP-DD and SPE-DD experiments. It is assumed that there is no decay of the signal at the dephasing time of one microsecond, i.e. the relative peak integral at 1 microsecond dephasing time is equal to 100. Because the recycle delay in the SPE experiment has to be at least five times the T_1^C value, i.e. 3 minutes for OXCCP up to 15 min for PP-1 per scan, the number of points for SPE-DD runs is minimal. In most samples, only three points for the 256-scan SPE-DD were done. This required about two to eight consecutive days to finish the SPE-DD runs for each sample in this study. In CP-DD, the recycle delay is only 5 seconds for all samples; hence, it took only 85 minutes to finish a 1024-scan CP-DD run. Since the CP-DD experiment takes only about one day to accomplish a series of 13-point dephasing times, it is used to create a trend line for the dipolar dephasing experiment.

Figure 5-25 shows a rapid decay of the protonated carbons from 0 to 60 microseconds dephasing times and a slow decay of the non-protonated carbons at the dephasing times greater than 60 microseconds. The oscillation of this decaying plot after the rapid decay of protonated carbons was a result of MAS-induced heteronuclear dipolar oscillations [5-31] as observed earlier [5-31, 5-33, 5-38]. This amplitude of this oscillation could be 10-15% of the non-protonated carbon intensities [5-31]. The plots of aromatic integral against dephasing times from the SPE-DD and CP-DD are similar for all six pitch samples in this study.

The procedure for calculating the fraction of non-protonated aromatic carbon, $f_{non-prot.}$, is the same as that used previously for coals [5-31]. The recycle delays of up to 600 μ s were used to take account of the pitch fractions having considerably long ^{13}C T_1 [5-

38]. In brief, a straight line is fitted to the slow decaying part of the plot shown in **Figure 5-25** $f_{non-prot}$ is equal to the relative

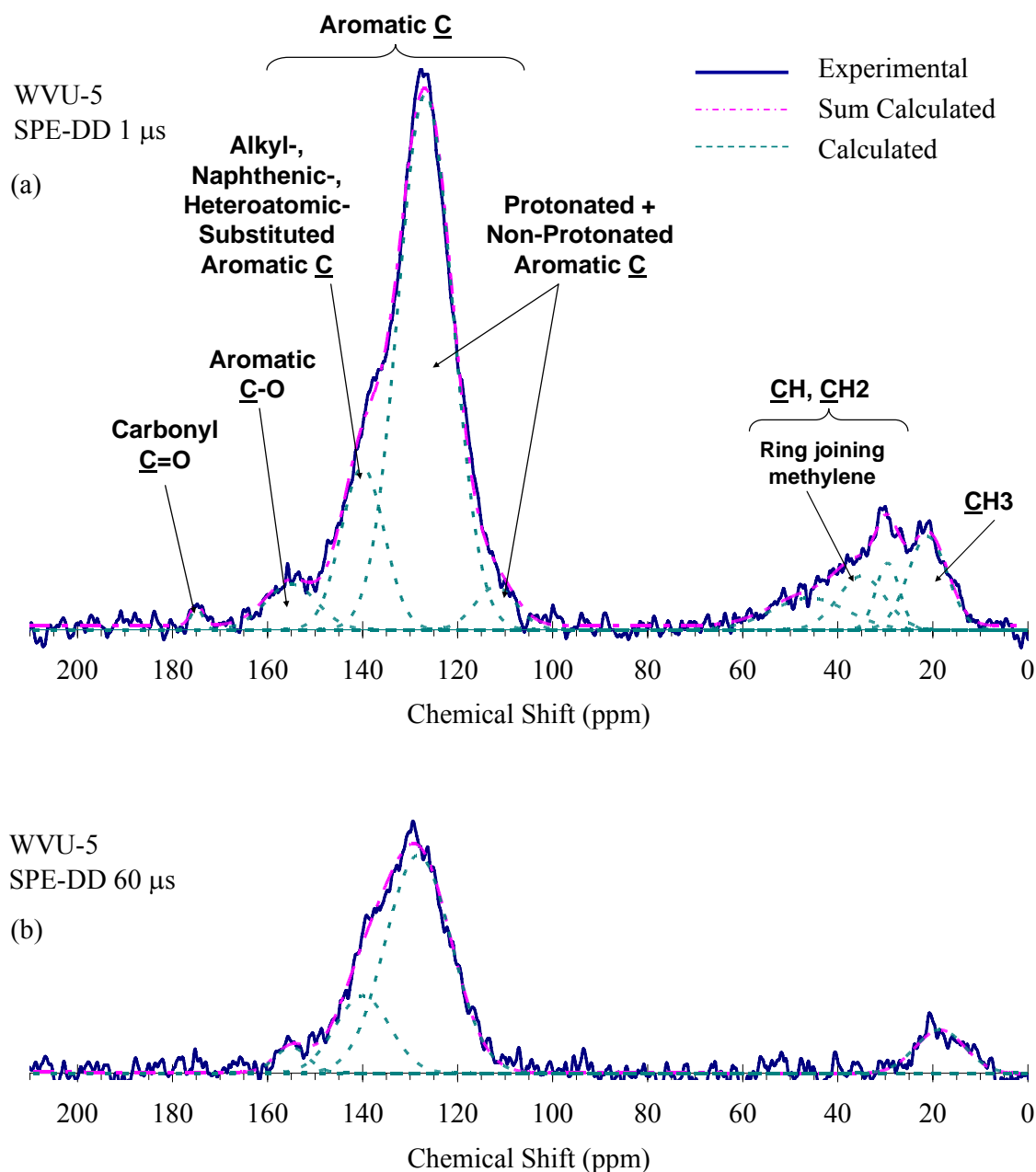


Figure 5-24: Comparison of WVU-5 spectra obtained from (a) SPE-DD at 1 microsecond and (b) SPE-DD at 60 microsecond dephasing times. The solid lines show the spectra from the experiment and the dotted lines show the spectra obtained from the deconvolution.

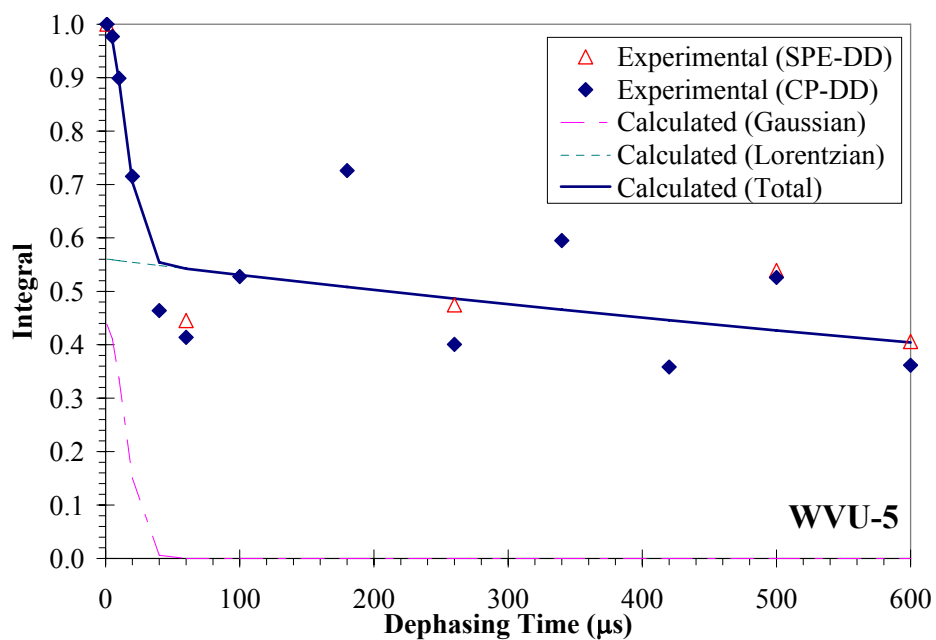


Figure 0-25: Decay of aromatic peak integral with dephasing times of WVU-5 from the CP-DD and SPE-DD experiments. The fitted lines show Gaussian (protonated carbons) and Lorentzian (non-protonated carbons) decaying components.

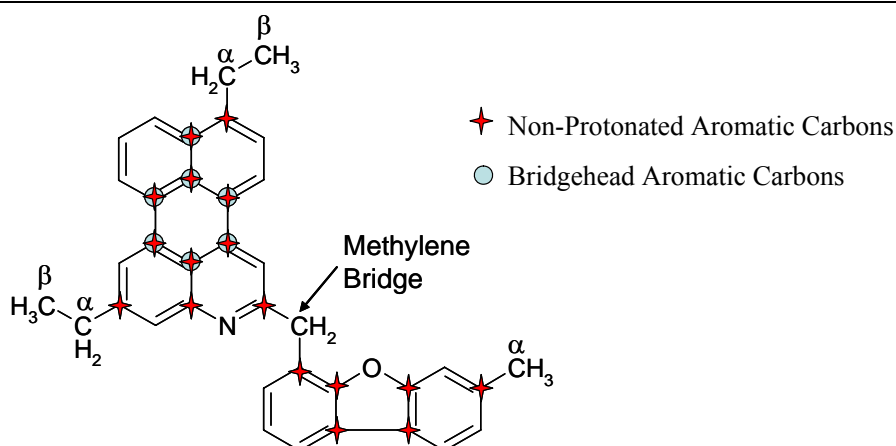


Figure 5-26: Types of different aromatic and aliphatic carbons.

peak integral calculated at 60 microseconds on this straight line. The value of $f_{non-prot}$ of each pitch sample is tabulated in **Table 5-50**. **Figure 5-26** shows different types of aromatic and aliphatic carbons expected for the pitches used in this study.

The fraction of bridgehead aromatic carbon (f_{BR}) can be derived by subtracting the fraction of aromatic carbons bound to aliphatic carbon and heteroatoms from the total fraction of non-protonated aromatic carbon [5-35, 5-38]. It is assumed that half of the oxygen is phenolic with the remainder being condensed furans [5-38]. Hence, on average each oxygen is bound to *ca.* 1.5 non-protonated aromatic carbons. For nitrogen, it is assumed that half are aromatic secondary amines (carbazoles) and the remainder is basic (aza) compounds [5-38]. An average attachment to non-protonated aromatic carbons for nitrogen is assumed to be 1. For sulfur, it is assumed that most of the sulfurs are in the form of thiophene, hence, on average each sulfur is bound to *ca.* 2 non-protonated aromatic carbons. Since about 40% to 90% of aliphatic carbons are methyl and the rest are methylene and methylene bridges between aromatic units, it is assumed that each aliphatic carbon is bound to 1.3 to 1.6 aromatic carbons, depending on the fraction of methyls in that sample. f_{BR} is then calculated by **Equation 5-5**.

$$f_{BR} = f_{non-prot} - \frac{1}{f_a} \left[1.5 \frac{O}{C} + \frac{N}{C} + 2 \frac{S}{C} + (1.3 \text{ to } 1.6) \frac{C_{AL}}{C} \right] \quad \text{Equation 5-5}$$

where f_{BR} is the fraction of bridgehead aromatic carbon over the total aromatic carbons, f_a is the aromaticity, $f_{non-prot}$ is the fraction of non-protonated carbon over the total aromatic carbons, $\frac{C_{AL}}{C}$ is the fraction of aliphatic carbon substitution over the total aromatic carbons, $\frac{O}{C}$, $\frac{N}{C}$, $\frac{S}{C}$ are the atomic oxygen, nitrogen, and sulfur to carbon ratio, respectively (determined by the ultimate analysis).

The average ring structure can be calculated from the f_{BR} value by assuming the structure to be fully peri-condensed as described by Solum [5-39] and Sethi [5-40]. A linear relationship was established from a plot of f_{BR} versus $1/\sqrt{\#carbons}$ in the peri-condensed aromatic cluster [5-40]. The number of carbons in the peri-condensed aromatic cluster is then calculated by **Equation 5-6** [5-40].

$$C_{aro-unit} = \frac{6}{(1 - f_{BR})^2} \quad \text{Equation 5-6}$$

The number of 6-fused ring aromatics can be calculated by **Equation 5-7**.

$$N_{peri} = 1 + \left(\frac{C_{aro-unit} - 6}{3} \right) \quad \text{Equation 5-7}$$

Table 5-50 tabulates the structural parameters obtained from the SPE-DD experiments. The fractions of non-protonated carbons are ranging from 0.52 to 0.56 for SCTP-2, PP-1, GP-115 and WVU-5, whereas those of HTCCP and OXCCP are 0.45 and 0.49, respectively. These values are not too different among all samples. However, the fractions of bridgehead aromatic carbons are significantly different among these pitch samples. f_{BR} of SCTP-2 and PP-1 are among the highest, i.e. 0.47 and 0.42, respectively. f_{BR} of GP-115, WVU-5, HTCCP and OXCCP are ranging from 0.18 to 0.29. The SPE-DD technique suggested that SCTP-2 contains highly condensed structures. This may derive from its high value of QI content [5-38], i.e. 15 wt.% as well as its less aliphatic and heteroatomic substitutions as compared to other pitches. It is suggested that on average the molecular mass of the condensed structure of SCTP-2 is

281 amu (*ca.* 6 peri-condensed aromatic rings), whereas that of PP-1 is 232 amu (*ca.* 5 peri-condensed aromatic rings). GP-115 and WVU-5 consist of only *ca.* 2 and 3 peri-condensed aromatic rings on average, respectively, due to their high aliphatic, naphthenic and heteroatomic substituents.

The assumption of pitch as a peri-condensed structure may not be consistent with the pitch chemistry. Although highly condensed PACs such as a dibenzocoronene (9-ring, 400 Da) or ovalene (ten- ring, 398 Da) were identified in a coal tar pitch [5-41], these compounds may only exist in high-softening-point pitch samples at very low concentrations. It was proposed that the structure of pitch is a three-dimensional oligomer and interconnected by C-C bonds or other bridging groups such as -CH₂-, -NH-, or ethers (-O-) [5-29]. It was further proposed that this three-dimensional structure of pitch can act as a superstructure host molecule and smaller molecules can be captured inside [5-29]. This type of pitch structure is highly supported by the high solubility of pitch in many organic solvents despite its high number average molecular weight. As observed in the MALDI spectra, a number of small molecules were observed in the toluene-insoluble fractions of the pitch samples. The observation in this study supports the superstructure previously proposed.

The atomic H/C ratio can be derived from the data obtained from the SPE experiment. This is also used as a self-consistency test for the SPE technique [5-33]. Atomic H/C ratios derived from the SPE parameters can be estimated by **Equation 5-8**.

$$Atomic\ H/C = f_a(1 - f_{non-prot}) + (1 - f_a)(H/C)_{ali} + (OH_{phenolic}/C) \quad \text{Equation 5-8}$$

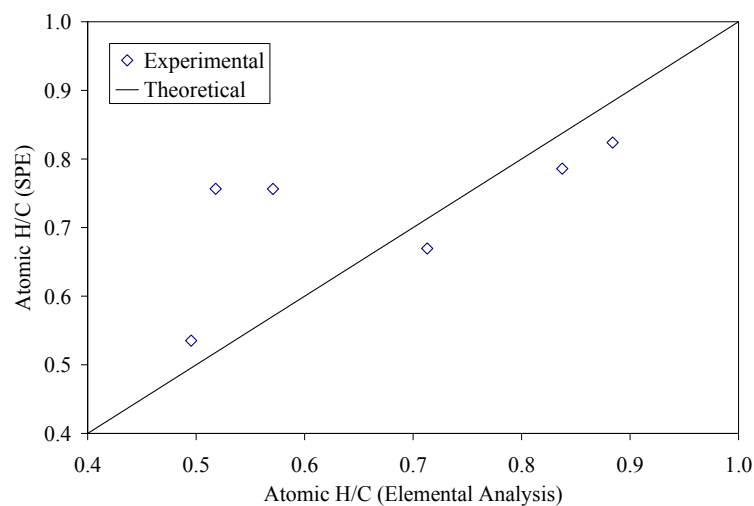


Figure5-27: Comparison of the atomic H/C ratio obtained from the SPE ^{13}C NMR and elemental analysis. A straight line shows an ideal situation where the two values match.

It is assumed that the values of aliphatic ratio, $(H/C)_{ali}$, are 2.7-3.0 for pitch [5-33], depending on the proportion of the CH_3 groups taken from the aliphatic regions of the SPE ^{13}C NMR spectra. It is assumed that the about half of the oxygen is phenolic. **Figure 5-27** shows a good agreement between the atomic H/C ratio from the SPE experiment and from the elemental analysis. Hence, the SPE ^{13}C NMR is a quantitative and reliable technique for pitch characterization.

Average Structure Determination of Pitch

Due to the complexity of the materials, solution-state and solid-state NMR were used to study the average structural parameters. This average structure may only be a minor component if it exists at all and may not adequately represent the variety of components in the samples [5-42]. However, the average structure could be very useful, especially when comparing complex materials such as pitch from different origins and processes. The details of carbon and hydrogen present in different forms in SCTP-2, PP-1, GP-115, WVU-5, HTCCP and OXCCP are shown in **Table 5-51** along with their average molecular weights. Based on data from the SPE ^{13}C solid-state NMR and ^1H solution-state NMR, combined with the average molecular weight data from MALDI and heteroatomic data from the elemental analysis, the structural parameters for SCTP-2, PP-1, GP-115, WVU-5, HTCCP and OXCCP were calculated in **Table 5-52** using the methods described by Kershaw and Black [5-43] and others [5-42, 5-44].

In Kershaw's work [5-42, 5-43, 5-45], proton and carbon parameters were obtained from the ^1H and ^{13}C solution-state NMR spectra, respectively. However, the solution-state ^{13}C NMR clearly can underestimate the number of carbons in pitch since not all compounds in pitch dissolve in the solvent. In this work, the spectra obtained from the solid-state SPE ^{13}C NMR and the ^1H solution-state NMR are used to derive the structural parameters for carbons and protons, respectively. To be more specific, the types of carbon atoms and aromaticity of pitch were derived from the SPE ^{13}C solid-state NMR, where as the SPE-DD ^{13}C solid-state NMR gave the degree of condensation. The structural parameters are listed as follows:

- (a) Aliphatic H/C ratio (Ali H/C)

$$(H/C)_{ali} = \frac{H}{C} \times \frac{\text{Aliphatic } H}{H} \times \frac{C}{\text{Aliphatic } C} \quad \text{Equation 5-9}$$

- (b) Average chain length of alkyl substituents

$$\text{Average Alkyl Length} = \frac{\text{Total Aliphatic H}}{H_{\alpha} + H_{R/M}} \quad \text{Equation 5-10}$$

- (c) Degree of substitution of aromatic rings (σ)

$$\sigma = 2RJM + AG + H_{AR}^* \quad \text{Equation 5-11}$$

where RJM = number of ring joining methylene group = $H_{RJM}/2$, AG = number of other alkyl groups = $H_{\alpha}/(H/C)_{ali}$, and H_{AR}^* = aromatic hydrogen.

- (d) Number of hydrogens for the hypothetical unsubstituted aromatic ring system

$$H_{ARU} = 2 \times RJM + H_{AR} + AG \quad \text{Equation 5-12}$$

- (e) H/C ratio for the hypothetical unsubstituted peri-condensed aromatic ring system, $\frac{H_{ARU}}{C_{ARU}}$, where C_{ARU} is the number of aromatic carbons.

- (f) H/C ratio for the hypothetical unsubstituted cata-condensed aromatic ring system, $\frac{H_{ARU} - 6}{C_{ARU} - 6}$

The average molecular masses calculated from MALDI from **Table 5-51** for Sctp-2 and PP-1 are *ca.* 400 and 430 daltons, respectively. These indicate that these two pitch samples contain approximately 31 and 34 carbon atoms on average per molecule. Although Sctp-2 and PP-1 contain comparable numbers of non-protonated aromatic carbons, i.e. *ca.* 51% of total carbons (see **Table 5-51**), PP-1 contains a higher degree of alkyl and heteroatomic substituents. As a result, PP-1 contains fewer bridgehead aromatic carbons and, hence, it is less condensed than Sctp-2. If a peri-condensed structure is assumed for the pitch, Sctp-2 and PP-1 contain six and five aromatic rings, respectively, on average as tabulated in **Table 5-50**.

The structural parameters from **Table 5-52** suggest that Sctp-2 contains on average one CH₃ for every two molecules. Nitrogen occurs on average one atom for every four molecules. Since Sctp-2 is unlikely to contain any alkyl substituents of more than one carbon, the aliphatic band between 24 and 60 ppm is presumed to be ring-joining methylenes. Hence, a ring-joining methylene group is present on average for every five molecules. **Figure 5-28** shows possible average structures of Sctp-2 as suggested by the aforementioned criteria. The results obtained from the GC/MS analyses were also used to formulate these possible average structures. The H_{ARU}/C_{ARU} and

$(H_{ARU} - 6)/(C_{ARU} - 6)$ values of SCTP-2 are the lowest among all pitches, indicating the higher degree of condensation of this pitch.

PP-1 contains on average two $-CH_3$ and one $-CH_2-$ per one molecule. The portion of H_α , H_β and different types of aliphatic carbons indicates that PP-1 contains on average one $-CH_2-CH_3$ for every two molecules. One in five molecules of PP-1 contains a ring-joining methylene group on average. As suggested from the GC/MS analysis, sulfur typically is present in PP-1 in the form of thiophene derivatives. Hence, it is suggested that one in 5-6 molecules of PP-1 contains a sulfur atom.

GP-115 and WVU-5 contain only two and three peri-condensed-aromatic-rings on average, respectively (see **Table 5-50**). High proportions of hydrogen from the elemental analysis confirm that the average structures of GP-115 and WVU-5 are less dense than SCTP-2 and PP-1. The structural parameters suggest that on average GP-115 contains two $-CH_2-CH_3$ for every molecule. Among all pitches studied, GP-115 consists of the longest alkyl chain length on average, as shown in **Table 5-52**. Naphthenic substituents are also likely present in GP-115, as suggested by GC/MS. A ring-joining methylene is present on average every three molecules. Oxygen and nitrogen are present on average in every molecule and every 2-3 molecules, respectively. WVU-5 contains a higher proportion of naphthenic substituent's than other pitch samples, as observed by the GC/MS technique in Chapter 4. The structural parameters suggest that WVU-5 contains two $-CH_3$ for every molecule, on average. Oxygen and nitrogen are present on average every molecule and every 1-2 molecules, respectively. A ring-joining methylene is present on average for every two molecules. Some representative average structures of these pitches are shown in **Figure 5-28**.

HTCCP and OXCCP have comparable structural parameters (see **Table 5-52**), suggesting similar average structures as schematically shown in **Figure 5-28**. The ^{13}C SPE solid-state NMR suggests that there are three peri-condensed-aromatic-fused-ring present in HTCCP and OXCCP on average (see **Table 5-50**). A sulfur atom is present on average for every four molecules of HTCCP and OXCCP. Oxygen contents of these co-coking pitches are rather high as compared to SCTP-2 and PP-1, possibly due to a high oxygen content of their raw material, i.e. the 360°C-FBP fraction of Run #50 (see **Table 5-42**) and the heat-treatment techniques. From the structural parameters, HTCCP and

OXCCP contain an oxygen atom on average for every two molecules. The average length of alkyl substituent's is approximately one (see **Table 5-52**), meaning that $-\text{CH}_3$ substituent's are mainly present. On average HTCCP and OXCCP contains two $-\text{CH}_3$ substituent's for every molecule.

Table 5-50: Structural parameters of the aromatic carbons as calculated from SPE-DD ^{13}C solid state NMR techniques.

	SCTP-2	PP-1	GP-115	WVU-5	HTCCP	OXCCP
f_a	0.98	0.91	0.85	0.86	0.92	0.90
$f_{non-prot}$	0.52	0.56	0.53	0.55	0.45	0.49
f_{BR}	0.47	0.42	0.18	0.26	0.27	0.29
$C_{aro-unit}$	22	18	9	11	12	13
N_{peri}	6	5	2	3	3	3
MW_{ave}	281	232	124	149	159	172

Table 5-51: SPE ^{13}C solid state NMR, ^1H solution state NMR and MALDI data for the structural parameters calculations of SCTP-2, PP-1, GP-115, WVU-5, HTCCP and OXCCP.

	SCTP-2	PP-1	GP-115	WVU-5	HTCCP	OXCCP
<u>Solution state ^1H NMR</u>						
Total aromatic hydrogen (%H)	83.89%	56.61%	46.95%	41.41%	63.65%	58.84%
Total aliphatic hydrogen (%H)	16.11%	43.39%	53.05%	58.59%	36.35%	41.16%
- Ring joining methylene, methine H (3.5-5.0 ppm) (%H)	2.30%	3.15%	3.06%	3.36%	2.32%	1.36%
- H on α -carbon to aromatic carbons (1.9-3.5 ppm) (%H)	8.21%	32.20%	22.56%	35.28%	28.71%	31.98%
- H on β -carbon to aromatic carbons (< 1.9 ppm) (%H)	5.60%	8.05%	27.43%	19.95%	5.33%	7.82%
<u>Solid state SPE ^{13}C NMR</u>						
Total aromatic carbon (%C)	97.83%	91.18%	85.46%	86.33%	92.09%	90.41
- Non-protonated aromatic carbon (from SPE-DD) (%C)	50.77%	50.68%	44.88%	47.29%	41.27%	44.70%
- Bridgehead aromatic carbon (from SPE-DD) (%C)	45.72%	38.06%	15.65%	22.05%	27.70%	29.31%
- Protonated aromatic carbon (from SPE-DD) (%C)	47.06%	40.50%	40.58%	39.04%	50.83%	45.71%
Total aliphatic carbon (%C)	2.17%	8.82%	14.54%	13.67%	7.91%	9.59%
- CH, CH ₂ (24.0-60.0 ppm) (%C)	0.77%	1.61%	7.97%	8.61%	0.66%	1.23%
- CH ₃ (10.0-24.0 ppm) (%C)	1.40%	7.21%	6.57%	5.06%	7.24%	8.36%
<u>Molecular weight calculated from MALDI</u>						
Average molecular weight (Da.)	398.73	434.18	349.59	501.52	309.38	304.67

Table 5-52: Number of various atoms in average molecule and structural parameters for Sctp-2, PP-1, GP-115, WVU-5, HTCCP and OXCCP derived by the SPE ^{13}C solid state NMR, ^1H solution state NMR, MALDI and elemental analyses.

	SCTP-2	PP-1	GP-115	WVU-5	HTCCP	OXCCP
C	31	34	25	37	23	23
H	15	24	22	31	13	12
N	0	0	0	1	0	0
S	0	0	0	0	0	0
O	0	0	1	1	1	1
Average MW calculated from elemental analysis	399	4340	350	502	309	305
<u>Hydrogen</u>						
Total aromatic hydrogen	13	14	11	131	8	7
Total aliphatic hydrogen	2	10	12	18	5	5
- Ring joining methylene, methine H (3.5-5.0 ppm)	0	1	1	1	0	0
- H on α -carbon to aromatic carbons (1.9-3.5 ppm)	1	8	5	11	4	4
- H on β -carbon to aromatic carbons (< 1.9 ppm)	1	2	6	6	1	1
<u>Carbon</u>						
Total aromatic carbon	31	31	22	32	21	21
- Non-protonated aromatic carbon (from SPE-DD)	16	17	11	18	10	10
- Bridgehead aromatic carbon (from SPE-DD)	14	13	4	8	5	5
- Protonated aromatic carbon (from SPE-DD)	15	14	10	14	12	11
Total aliphatic carbon	1	3	4	5	2	2
- CH, CH ₂ (24.0-60.0 ppm)	0	1	2	3	0	0
- CH ₃ (10.0-24.0 ppm)	0	2	2	2	2	2
Average alkyl chain length of alkyl substituents	2	1	2	2	1	1
Aliphatic H/C	4	4	3	4	3	2
RJM	0	0	0	1	0	0
AG (number of other alkyl groups)	0	2	2	3	2	2
sigma (degree of substitution of aromatic ring)	0	0	0	0	0	0
Haru/Caro	0	1	1	1	0	0
(Haru-6)/(Caro-6)	0	0	0	0	0	0

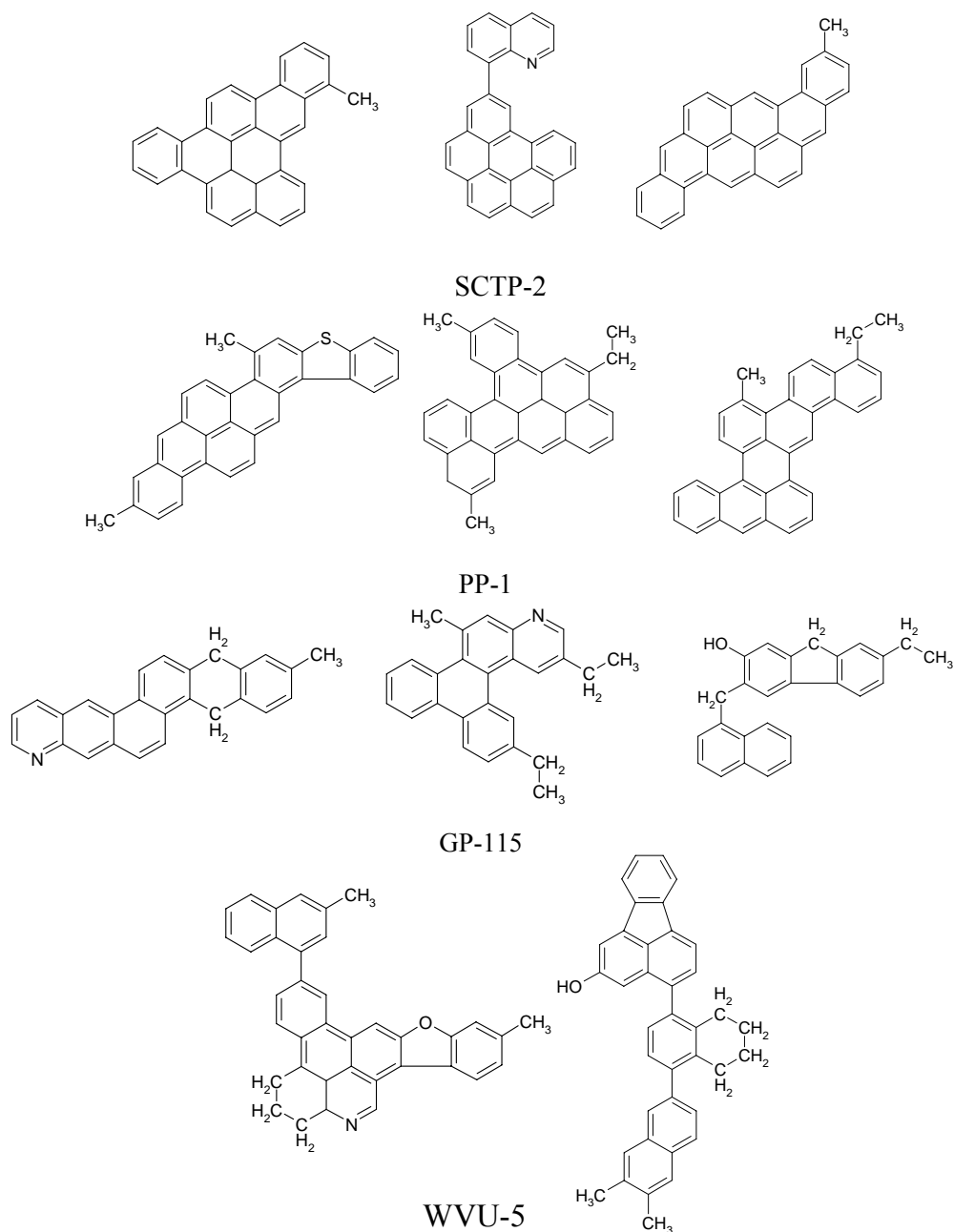
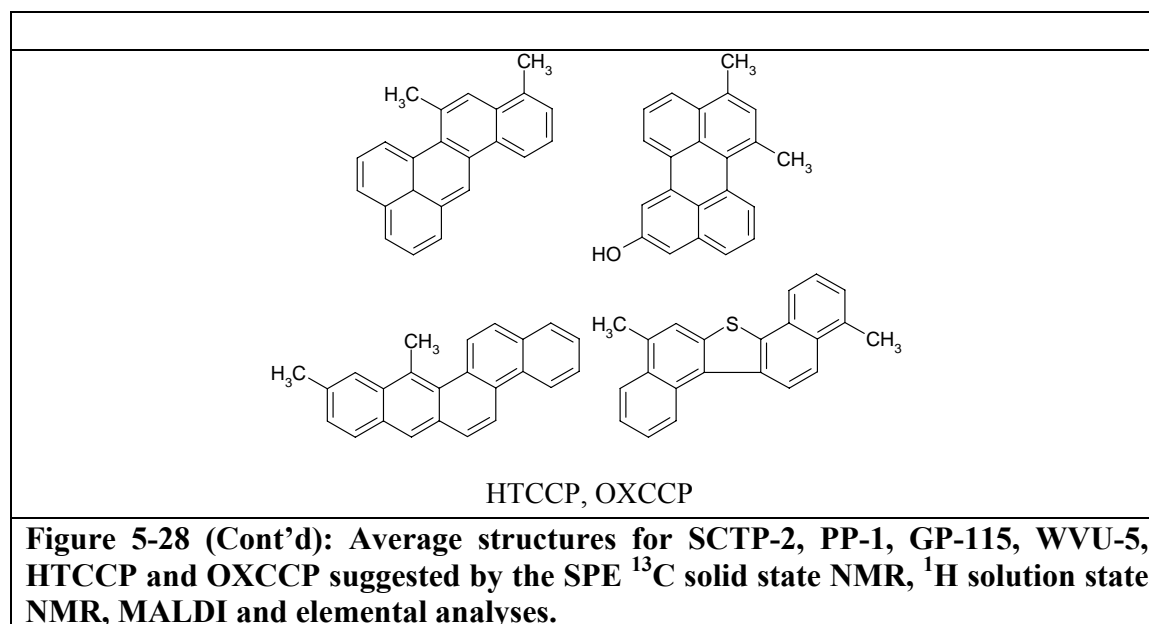


Figure 5-28: Average structures for Sctp-2, Pp-1, Gp-115, Wvu-5, HTCCP and OXCCP suggested by the SPE ^{13}C solid state NMR, ^1H solution state NMR, MALDI and elemental analyses.



High-Temperature ^1H Nuclear Magnetic Resonance Spectroscopy (NMR) on Solid State NMR

Carbon anodes are manufactured from calcined petroleum coke (i.e. sponge coke), and recycled anode butts as fillers, and coal tar pitch (SCTP) as the binder. Coal tar pitch is mixed with calcined petroleum coke. The remaining parts of spent anodes from the aluminum production, called recycled anode butts, are also crushed and used as filler for economic reasons [5-46]. The mix of binder, filler and some additives is heated to about 50°C above the softening point of the pitch to enable the pitch to wet the coke particles [5-47]. The mix is then either extruded, vibrated, or pressed to form a green anode. The wetting of coke by pitch is very important to the anode properties since pitch has to coat the coke particles, penetrate and fill the coke pores during mixing and forming green anodes, and form pitch-coke bridges between the coke particles during the baking process [5-47].

The wetting behavior, or in other words the interactions in the pitch-coke system, is the main interest in this Chapter. It has been shown that high-temperature ^1H nuclear magnetic resonance spectroscopy (NMR) is a promising technique to study the molecular interaction between different materials [5-48-5-61]. The fraction of the mobile protons in the sample and their mobility as measured by the spin-spin relaxation time (T_2^*), which is inversely proportional to the peak width at half maximum height ($\Delta H_{1/2}$),

$$T_2^* = \frac{1}{\pi\Delta H_{1/2}}.$$

Equation 5-13

seems to have potential to probe the extent of the interaction between pitch and coke. Since pitch is a complex material, a study of some model compounds commonly found in pitch was undertaken to understand the relationship between the NMR results and the extent of interaction between these compounds with petroleum coke. A range of compounds from two to five fused rings is listed in **Table 5-54**. These compounds are both cata- and peri-condensed aromatic compounds with and without heteroatoms. This understanding would help interpret the extent of interaction of pitch from different sources and processes, i.e. coal tar pitch, petroleum pitch, gasification pitch, coal extract pitch and co-coking pitch, with petroleum coke. Since co-coking pitches were newly developed in this work, it was expected that the understanding developed from model compounds and pitches could be extended to explain the behavior of these new and unique pitches.

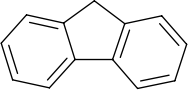
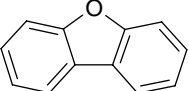
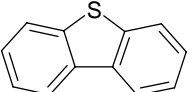
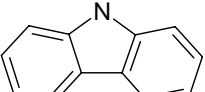
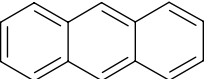
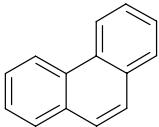
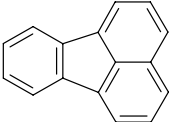
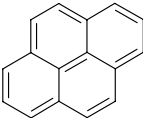
The high-temperature ^1H NMR is a powerful technique to study *in-situ* the change in molecular mobility of each model compound and its interaction with the petroleum coke at elevated temperatures. In general, the ^1H NMR spectra of a substance acquired during a melting stage consist of a rigid (Gaussian) and a mobile (Lorentzian) component. The line width or the spin-spin relaxation (T_2^*) of the mobile component can be used to observe the change in mobility. This technique has been used to observe the rigid and mobile components in coals [5-52, 5-55, 5-56, 5-59, 5-62-5-66], coals swollen by solvents [5-49, 5-50, 5-67-5-69], coal mixtures [5-37, 5-38, 5-48, 5-51, 5-53, 5-54, 5-61, 5-70], and mesophase development in pitch [5-71, 5-72].

While this area of research is very interesting, the interpretation of the data was difficult, as this area of research is not well understood; therefore, data for this part of the project can be found in detail in the appendix of the PhD thesis by Suriyapraphadilok [5-32].

In conclusion, ^1H *in-situ* high temperature NMR and the solid echo pulse program were used to study the change in mobility of model compounds, pitch and their mixtures with petroleum coke. Topology seemed to play an important role in enhancing the mobility of the model compound when mixed with petroleum coke. Peri-condensed and branched cata-condensed molecules tended to have higher mobility enhancement than the cata-condensed

PACs. In the pitch/coke mixtures, pitch that contains higher HS fraction seems to enhance the mobility between pitch and coke. Green density and the mobility enhancement were in agreement in comparing the ability of a pitch to wet the coke surface and form a good carbon anode.

Table 5-54: List of model compounds used in the study of high-temperature ^1H NMR.

Formula	MW (g/mol)	Structure	Name	Melting point ¹ (°C)	Boiling point ¹ (°C)	Specific gravity ²
$\text{C}_{13}\text{H}_{10}$	166.22		Fluorene	114.79	297.3	1.085
$\text{C}_{12}\text{H}_8\text{O}$	168.19		Dibenzofuran	82.16	285.2	1.105
$\text{C}_{12}\text{H}_8\text{S}$	184.26		Dibenzothiophene	98.67	331.5	1.125
$\text{C}_{12}\text{H}_9\text{N}$	167.21		Carbazole	244.8	354.7	1.178
$\text{C}_{14}\text{H}_{10}$	178.23		Anthracene	215.78	342.0	0.972
$\text{C}_{14}\text{H}_{10}$	178.23		Phenanthrene	99.23	336.9	1.067
$\text{C}_{16}\text{H}_{10}$	202.25		Fluoranthene	110.18	382.6	1.097
$\text{C}_{16}\text{H}_{10}$	202.25		Pyrene	156	394.8	1.094

Note ¹ Experimental values obtained from DIPPR Version 2.7.0.

² Density at the melting point estimated from obtained $\rho = \frac{A}{B \left(1 + (1 - T/C)^D \right)}$ from DIPPR Version 2.7.0.

5.5.3 Conclusions and Future Work

Six pitch samples, SCTP-2, PP-1, GP-115, WVU-5, HTCCP and OXCCP, were analyzed by various techniques including MALDI, GC/MS, Py-GC/MS, and HPLC. The majority of the compounds in these pitch samples are in the ranges of 200-700 Da. as analyzed by the MALDI technique. The results in this study show that toluene is a suitable solvent for pitch as an aid to spot the sample on the MALDI sample well. Both toluene-solubles and toluene-insolubles can be studied using this technique.

The HS fractions of all of the pitch samples in this study mainly consist of four- ring PACs as observed by the GC/MS and Py-GC/MS techniques. SCTP-2 and WVU-5 contains mainly cata- and peri-condensed PACs and a few alkylated- and heteroatomic-substituted PACs, which reflect the nature of the coal-derived materials. For those petroleum-derived pitches, i.e. PP-1, HTCCP and OXCCP, the GC/MS analyses show that they consist of a number of alkylated-substituted PACs with high sulfur substitution.

The GC/MS results of the coal gasification pitch, GP-115, surprisingly show that GP-115 contains both coal- and petroleum-derived compounds. Hence, it is possible that GP-115 was mixed with the petroleum-derived compounds to some extent during its preparation.

The chemical analysis by the HPLC technique in this study was limited by the ability to identify the compounds in the sample since there is no mass spectrometry integrated into the instrument. All of the HPLC spectra except WVU-5 confirm the results obtained by the MALDI in terms of mass distribution. The heavy compounds in WVU-5 were not well-resolved by the HPLC analysis, possibly due to its limited solubility in the mobile phase used in this study.

Bulk characterization of pitch by means of nuclear magnetic resonance (NMR) was performed on six pitch samples, SCTP-2, PP-1, GP-115, WVU-5, HTCCP and OXCCP. By combining results obtained from the NMR techniques, i.e. aromaticity, degree of condensation, and types of hydrogen and carbon atoms, with the elemental analysis and number average molecular mass from MALDI, average structural information of pitch can be determined.

SCTP-2 has the lowest degree of substituents as compared to other pitches. This is in agreement with the results obtained from the GC/MS analysis. SCTP-2 and PP-1 contain six and five fused rings on average, respectively, whereas GP-115 and WVU-5 contain two and three fused rings on average, respectively. The alkyl substituents of these pitches are mostly methyls and few are ethyls. WVU-5 contains a higher degree of naphthenic substituents as compared to

other pitches as confirmed by the GC/MS analysis. HTCCP and OXCCP are similar in their structures. They contain three peri-condensed fused rings on average for every molecule. The main substituents in these co-coking pitches are methyls. Some configurations of the average pitch structures were proposed.

^1H *in-situ* high temperature NMR and the solid echo pulse program were used to study the change in mobility of model compounds, pitch and their mixtures with petroleum coke. Topology seemed to play an important role in enhancing the mobility of the model compound when mixed with petroleum coke. Peri-condensed and branched cata-condensed molecules tended to have higher mobility enhancement than the cata-condensed PACs. In the pitch/coke mixtures, pitch that contains higher HS fraction seems to enhance the mobility between pitch and coke. Green density and the mobility enhancement were in agreement in comparing the ability of a pitch to wet the coke surface and form a good carbon anode.

5.6 Deeply Hydrotreated Decant Oil Reactions

Another aspect of the co-coking process was to determine the effect of hydrotreating decant oil (HT DO) to see the effect on the coke and liquid production and quality of products when blending with coal. The rationale behind the project was an expectation that the HT DO could enhance the coke quality when hydroaromatics and cycloalkanes were present in the coking process and that the liquids generated during coking would be of better quality, i.e., more 1-3 rings aromatics and hydroaromatics would be present in the liquids, precursors necessary for production of thermally stable jet fuel. Section 5.6.1 focuses on the characterization of the decant oil EI-107, the hydrotreated derivatives of decant oil, and coal. Section 5.6.2 focuses on quality of the co-cokes generated when using four of the HT DO's. Section 5.6.3 focuses on the quality of the liquids generated during co-coking in our large laboratory scale coker.

5.6.1 Feedstock Characterization

Characterization was carried out on EI-107 decant oil, the six hydrotreated derivatives, and the coal used for this process, a 50/50 blend of Powellton and Eagle seams, both very similar coals of high volatile A bituminous rank. The characteristic properties of the decant oils studied were compared to the properties of preferred feedstocks reported by Goval et al. [5-73]. All the feed oils studies met the requirements for boiling range (260°C+), asphaltene content (<8 wt. %), nitrogen (0.7%), and aromatics (50-80 wt. %). All the decant oils except the original decant oil, EI-107, met the requirement for API gravity (0-10), and four out of the seven decant oils met the requirement for sulfur content (0-0.7 wt. %) (i.e., EI-135, EI-136, EI-137, and EI-138). For Section 5.6.2, only four decant oils were selected for characterization of coke under different reaction conditions (type of reactor and reaction variation).

5.6.1.1 Experimental

The analyses performed to characterize the decant oils were elemental analysis, ^1H NMR, ^{13}C NMR, asphaltene content, boiling point distribution, API gravity, GC/MS, preparative liquid chromatography (PLC) followed by GC/MS, and viscosity. Two structural parameters which were derived from the ^1H NMR spectra and elemental analysis were calculated: aromaticity, f_a ; and the fraction of aromatic edge carbons carrying substituents, σ . Details of these various

characterization methods have been described previously in Sections 5.2, 5.5, and in previous reports [5-21, 5-28].

5.6.1.2 Results and Discussion

5.6.1.2.1 Characterization of Decant Oil and Hydrotreated Derivatives

Elemental analysis

Table 5-55 shows the elemental analysis and H/C ratios for the original decant oil and its hydrotreated versions. The oxygen was calculated by difference.

The decreasing sulfur content in the hydrotreated decant oils indicates the effectiveness of the hydrotreatment and the increasing hydrogen content is evidence of the hydrogenation of aromatic compounds.

Table 5-55: Elemental analysis and H/C ratios for the decant oil and its hydrotreated versions

Sample ID	Carbon* ± 0.27	Hydrogen* ± 0.13	Nitrogen* ± 0.08	Sulfur* ± 0.01	Oxygen**	Atomic H/C ratio
EI-107	89.59	7.32	0.22	2.99	-0.11	0.98
EI-133	90.09	8.40	0.18	1.39	-0.05	1.12
EI-134	89.93	8.98	0.24	0.94	-0.09	1.20
EI-135	90.80	8.71	0.17	0.44	-0.12	1.15
EI-136	90.23	8.98	0.50	0.33	-0.04	1.19
EI-137	90.02	10.00	0.10	0.03	-0.15	1.33
EI-138	90.59	9.24	0.12	0.02	0.03	1.22

*as determined

** by difference

± is the reproducibility of a measurement.

Liquid state ¹H NMR

The ¹H NMR spectra give a direct measurement of the distribution of protons in different chemical environments. **Table 5-56** shows the range of chemical shift and the assignment of proton signals [5-74].

Table 5-56: Range of chemical shifts (δ ppm) and assignment of proton signals [5-74].

Range of signal (δ ppm)	Group assignment and symbol
6.2 to 9.2	Aromatic, H_{AR}
1.7 to 4.4	Aliphatic, H_{α} α -CH ₂ , α -CH ₃ benzylic
1.0 to 1.7	Aliphatic, H_{β} β -CH ₂ tetralins, β -CH ₂ indans, β -CH ₃ , remote CH ₂ , β -CH ₂ alicyclics
0.7 to 1.0	Aliphatic, H_{γ} remote CH ₃

The characteristic ranges of chemical shifts are listed in **Table 5-57** for the original decant oil and its hydrotreated versions. The total integrated signal, H (chemical shift 0.7-9.2) is divided into several ranges according to the chemical shift of protons assigned to different groups, as shown in **Table 5-56**. The fraction of any given group assignment, or the percentage of protons in any different environment, H_{χ} , is calculated by dividing the integrated signal that correspond to H_X by the total integrated signal, H . Hence,

$$H_{\chi}^* = \frac{H_{\chi}}{H}$$

Equation 5-14 [5-75]

Similarly, the fraction of protons in other structural environments is defined as follows:

$$H_{\gamma}^* = \frac{H_{\gamma}}{H}, H_{\alpha}^* = \frac{H_{\alpha}}{H}, H_{AR}^* = \frac{H_{AR}}{H} \text{ and } H_{\beta}^* = \frac{H_{\beta}}{H}.$$

Then, the percentage of protons in any different environments (H_{χ}) is obtained:

$\%H_{\chi} = (H_{\chi}^*) \times 100$, where $\chi = AR, \alpha, \beta, \gamma$. The proton distributions are shown in **Table 5-57**, and it is observed that the various H_{χ} vary by little from one sample to another.

Table 5-57: Distribution of proton among the various types of functional groups based on ^1H NMR peak assignments.

Range of band δ (ppm)	Symbol ($\text{H}\chi^*$)	EI-107	EI-133	EI-134	EI-135	EI-136	EI-137	EI-138
		H, atomic % ± 0.01						
0.7-1.0	H γ^*	5.17	5.44	5.38	5.63	5.87	5.82	5.27
1.0-1.7	H β^*	12.43	12.34	12.70	12.73	12.64	12.60	12.64
1.7-4.4	H α^*	43.66	44.53	43.41	43.10	43.90	43.98	44.03
6.2-9.2	H AR^*	38.74	37.69	38.51	38.54	37.59	37.60	38.06

Liquid state ^1H NMR

The band assignments for integrating intensities were selected based on the breakdowns reported by Rodriguez et al [5-76]. **Table 5-58** shows the percent of each functional group.

Table 5-58: Distribution of carbon among the various types of functional groups based on ^{13}C NMR peak assignments.

Functional group	Symbol	Band, TMS (ppm)	EI-107	EI-133	EI-134	EI-135	EI-136	EI-137	EI-138
			C, atomic % ± 0.02						
Alkanes	$-\text{CH}_3$	11-22.5	14.59	11.90	14.17	14.61	13.12	14.07	12.54
	$-\text{CH}_2-$	22.5-37	9.10	14.13	23.23	20.74	23.28	25.93	28.14
	$>\text{CH}-$	37-60	3.94	1.13	6.35	5.53	5.72	7.53	9.59
N-aliphatic*	$\text{N}-\text{C}_{\text{al}}$	60-65	0.13	0.00	0.00	0.00	0.00	0.00	0.00
O-aliphatic*	$\text{O}-\text{C}_{\text{al}}$	65-75	0.08	0.00	0.00	0.00	0.00	0.00	0.00
olefinic	$-\text{HC}=\text{CH}-$	108-118	1.49	1.50	1.55	1.52	0.54	1.22	1.38
Internal aromatic	$>\text{C}=\text{ar}$	118-128	44.54	45.29	29.12	34.83	31.45	30.54	30.55
protonated aromatic	$\text{Har}-\text{C}=\text{C}$	128-135	17.36	18.50	17.44	15.70	18.03	14.13	12.69
naphthenic substituted aromatics	$>\text{CH}_2$	135-138	4.08	4.18	3.88	3.20	3.75	3.04	2.55
Heteroatom ($\text{N}, \text{O}, \text{S}$)**	$\text{N}, \text{O}, \text{S}-\text{C}_{\text{ar}}$	138-160	4.69	3.37	4.28	3.88	4.11	3.54	2.57

*aliphatic heteroatom; **aromatic heteroatom

TMS or tetramethylsilane is the standard used for NMR calibration of chemical shifts

Asphaltene Content

This is an important parameter since the preferred feedstock to obtain a premium coke should have less than 8% in asphaltenes [5-77]. All the decant oils have a very low percentages of asphaltenes, meeting the requirement as a preferred feedstock for delayed cokers. The

asphaltene content is shown in **Table 5-59**. Asphaltenes are thought be some researchers to consist of sheets of condensed polynuclear and heterocyclic aromatic systems with naphthenic rings and alkyl side chains [5-78], with molecular weights that may vary from 1,000 to 100,000 amu [5-79]. A mixture of asphaltenes and aromatic hydrocarbons may display a high phase separation, which takes place when the mutual solubility of the components is low [5-80]. This accelerates the condensation reaction of the heavy precipitates, yielding condensed product through rapid coking in an early stage of the carbonization, forming a mosaic texture [5-80], which is undesirable in the coke.

Table 4-5: Asphaltene content (in wt. %)

ID decant oil	EI-107	EI-133	EI-134	EI-135	EI-136	EI-137	EI-138
Asphaltene, wt. % (± 0.03)	0.21	0.07	0.08	0.15	0.16	0.23	0.26

API gravity

In order to determine the API gravity, the density of the decant oils was calculated [5-21, 5-28, 5-81]. **Table 5-60** shows the results of density and the API gravity of the decant oils. **Equation 5-15** is used to convert density into API gravity [5-82]:

$$^{\circ}API = \frac{141.5}{sg_{60^{\circ}F}} - 131.5 \quad \text{Equation 5-15 [5-82]}$$

where $sg_{60^{\circ}F}$ is the specific gravity at 60°F.

Table 5-60: API of decant oils.

	Temperature (°F)	ρ (g/mL)	sg	API°	API° (corrected at 60F) ¹⁰
EI-107	81.5	1.11	1.11	-4.4	-4.1
EI-133	79.9	1.07	1.07	1.1	0.3
EI-134	80.6	1.06	1.06	2.2	1.4
EI-135	80.6	1.06	1.06	2.6	1.8
EI-136	81.5	1.05	1.05	3.7	2.8
EI-137	82.4	1.02	1.02	7.0	6.1
EI-138	80.6	1.02	1.02	7.3	6.4

$sg = \rho \text{ (g/mL) DO} / \rho \text{ (g/mL) H}_2\text{O}$; $\rho \text{ (g/mL) H}_2\text{O} = 1 \text{ g/mL}$

The API was corrected from the observed temperature to 60°F using Table 5A [5-83]: Generalized crude oils correction of observed API gravity to API gravity at 60°F.

Boiling point

The boiling point distribution is calculated by using the simulated distillation; initial boiling point, final boiling point, average boiling point, and boiling range are reported for the seven decant oils.

To calculate the weight average boiling point, five temperatures were recorded; the different temperatures correspond to the temperature at which 10, 30, 50, 70 and 90 weight percent was distilled. Temperatures are summed and then divided by five. An example is shown in **Table 5-61**.

Table 5-61: Average boiling point calculation for the raw decant oil.

Wight % distilled	Run 1 T(°C)	Run 2 T(°C)	Mean T(°C)
10	349.0	351.8	350.4
30	393.4	393.8	393.6
50	413.3	412.9	413.1
70	438.3	437.0	437.7
90	481.2	475.1	478.2
SUM			2073.0
Average boiling point (SUM/5)			414.6

Table 5-62 shows the initial boiling point (IBP), final boiling point (FBP), the average boiling point distribution, and boiling range for all the decant oils. It is observed that the IBP decreases while boiling range increases as the degree of hydrotreatment increases. According to the characteristics for the preferred feedstocks suitable to make premium coke, the boiling range, Δ , should be greater than 260°C, so that all the feedstocks studied here follow the requirement of the boiling point range.

Table 5-62: Average boiling point distribution (simulated distillation).

Sample No.	IBP (°C)	FBP (°C)	Average boiling point °C ± 1.1	boiling range, Δ (FBP-IBP)°C
EI-107	234.1	518.8	414.6	284.7
EI-133	229.7	556.8	400.7	327.1
EI-134	202.7	510.2	392.9	307.7
EI-135	212.0	512.9	391.4	300.9
EI-136	154.0	562.6	388.0	408.6
EI-137	122.0	506.6	370.1	384.6
EI-138	110.8	512.8	371.0	402.0

IBP=initial boiling point; FBP=final boiling point

As a result of the hydrogenation, lighter components are formed. With the exception of EI-133 and EI-136, the final boiling point is roughly constant for the rest of the oils. This suggests that the hydrotreatment and hydrogenation are not affecting the heavy molecules in the oil.

Gas Chromatography/Mass Spectrometry

This analysis determines the general chemical composition of the decant oils. For the analysis, each peak in the chromatogram is identified with the built-in library and is classified as alkane or paraffin, cycloalkane, hydroaromatic, alkylbenzene, naphthalene, and polycyclic aromatic. The percentage of each individual compound is calculated and the percentages of each group are added to give the total percent that corresponds to each group.

Table 5-63 shows the composition of the decant oils using the GC/MS. This table shows that EI-107 is the one that has the highest values of polycyclic compounds ($3\geq$ rings) *plus* heteroatoms.

The alkanes component for all the decant oils is very low. Cycloalkanes are a greater proportion of most of the hydrotreated decant oils (in particular EI-137 and EI-138) when compared to the raw (EI-107) and mildly hydrotreated decant oils (EI-133, EI-134, EI-135, EI-136). There is no presence of hydroaromatics detected in the original decant oil, while the hydroaromatic content is comparable for the hydrotreated decant oils, except for the least hydrotreated decant oil, EI-133.

Table 5-63 : Composition of decant oils by GC/MS

Compound group	EI-107	EI-133	EI-134	EI-135	EI-136	EI-137	EI-138
	wt, % (± 1)						
Paraffins	0.43	0.00	1.07	0.42	0.00	3.68	2.05
• Cycloalkanes							
Saturated cyclics*	0.99	1.28	1.98	3.73	3.89	6.73	14.40
Decalins	0.00	0.00	0.00	0.00	0.00	6.27	6.69
<i>Total</i>	0.99	1.28	1.98	3.73	3.89	13.00	21.09
• Hydroaromatics							
Indenes	0.10	0.11	2.77	6.92	5.59	2.32	4.19
Tetralins	0.00	4.47	6.53	2.98	1.57	6.15	6.81
<i>Total</i>	0.10	4.58	9.30	9.90	7.16	8.47	11.00
alkyl benzenes	7.00	21.04	24.85	17.02	24.62	13.32	11.42
Naphthalenes	3.24	4.03	5.61	2.95	2.60	8.92	4.16
Polycyclic compounds (3\geq rings) plus heteroatoms	88.24	69.08	57.19	65.99	61.63	52.61	50.28

*other than decalins

Aromaticity

Aromaticity, f_a , is defined as that fraction of the total of carbon atoms which are aromatic carbons. The method has a wide application in petroleum and coal research, being used to characterize such various materials as coal extracts [5-84, 5-85] coal-tar pitches [5-84-5-86] coal carbonization products [5-84], oils and asphaltenes from coal hydrogenation [5-84, 5-87] and petroleum fractions [5-84, 5-85, 5-87-5-89]. Aromaticity can be calculated using the two most popular methods reported by the literature that are relevant to petroleum oils: a method developed by Brown and Ladner [5-90] and a method using solution state ^{13}C NMR [5-89]. The Brown and Ladner method is stated as follows:

$$fa = \left[\left(\frac{C}{H} \right) - \left(\frac{H_a^*}{x} \right) - \left(\frac{H_0^*}{y} \right) \right] / \left(\frac{C}{H} \right)$$

Equation 5-16 [5-90]

where H_0^* has been subdivided:

$$H_0^* = \frac{H_\beta^*}{x} - \frac{H_\gamma^*}{y}$$

Equation 5-17 [5-75]

Thus, **Equation 5-17** is substituted into **Equation 5-16** to finally obtain the equation used for calculating the aromaticity in this work:

$$fa = \left[\left(\frac{C}{H} \right) - \left(\frac{H_{\alpha}^*}{x} \right) - \left(\frac{H_{\beta}^*}{y_i} \right) - \left(\frac{H_{\gamma}^*}{y_{ii}} \right) \right] / \left(\frac{C}{H} \right) \quad \text{Equation 5-18 [5-75]}$$

where $x = 2$; $y_i = 2$; $y_{ii} = 3$; these values have been reported elsewhere [5-75].

In order to use **Equation 5-18**, elemental analysis and ^1H NMR are needed. The percentage of protons in the different environments is reported in **Table 5-56**, so that the fraction of protons (H_X^*) is obtained.

The degree of substitution of aromatic rings (σ) is defined as that fraction of the aromatic edge carbons which are substituted. Then,

$$\sigma = \frac{\left(\frac{H_{\alpha}^*}{x} \right) + \left(\frac{O}{H} \right)}{\left(\frac{H_{\alpha}^*}{x} \right) + \left(\frac{O}{H} \right) + H_{AR}^*} \quad \text{Equation 5-19 [5-75]}$$

Table 5-64 shows the results of the calculations to obtain the f_a , and σ . Looking at these two structural parameters, it is observed that σ is relatively constant, meaning that if any hydrocracking of side chains occurred, it was at carbons β - or further from the ring.

Table 5-64: Results of f_a , σ and H_{ar}/C_{ar} for the seven decant oils.

	C/H*	$H_{\alpha}^*/2$	$H_{\beta}^*/2$	$H_{\gamma}^*/3$	H_{AR}^*	f_a	σ
EI-107	1.02	0.22	0.06	0.02	0.39	0.71	0.36
EI-133	0.89	0.22	0.06	0.02	0.38	0.67	0.37
EI-134	0.83	0.22	0.06	0.02	0.39	0.64	0.36
EI-135	0.87	0.22	0.06	0.02	0.39	0.67	0.36
EI-136	0.84	0.22	0.06	0.02	0.38	0.64	0.37
EI-137	0.75	0.22	0.06	0.02	0.38	0.58	0.37
EI-138	0.82	0.22	0.06	0.02	0.38	0.59	0.37

*C/H corresponds to the reciprocals of the H/C values shown in **Table 5-55**. The ratio C/H is needed to determine f_a , in **Equations 5-18 and 5-19**.

The ^{13}C NMR method is stated as follows: f_a is the aromatic carbon fraction which corresponds to the integrated signal between 118-160 ppm [5-89]. Then, from **Table 5-58**, f_a can be calculated:

$$f_a = \Sigma(\text{internal aromatic plus protonated aromatic plus naphthenic substituted aromatics and heteroatom})/100.$$

Quian et al. [5-89] compared aromaticity values of 29 coal-derived products of varying f_a , from 0 to 0.95, using the ^{13}C NMR method and the Brown-Ladner method. Deviations for the two methods for different feedstocks reported by Quian et al. [5-89] are shown in **Table 5-65** as well as the deviations for seven decant oils used in this study. As noticed in **Table 5-65**, the greatest deviation between f_a using the ^{13}C NMR and the f_a using the Brown-Ladner equation, expressed as a percentage of the Brown-Ladner method, is 25%, meaning that there is a discrepancy in counting one of every four carbon atoms. The objective in this case is not to discuss about discrepancy of these two methods or establish which method is more accurate, but only to compare the current results with ones reported in the literature where authors have reported aromaticity using both methods. The Brown and Ladner method is the method most reported by those authors whose research deals with carbonization of petroleum streams [5-80, 5-91, 5-92], and coal tars [5-93, 5-94]. Some other authors, although they do not report f_a , provide the ^1H NMR and elemental analysis information, making it possible to calculate the f_a using the Brown-Ladner equation [5-95-5-98].

Hereafter, to differentiate the f_a obtained from the Brown-Ladner method and f_a obtained from ^{13}C NMR method, Brown-Ladner method is represented as f_a whereas ^{13}C NMR method is represented as f'_a . The samples used by Quian [5-89] show the highest deviation between the two methods, 0.06, while the highest deviation for the decant oils used here is 0.11 (EI-138), as shown in **Table 5-65**; this deviation value reported by Quian shows agreement with the highest deviation $|f'_a - f_a|$ reported by Retcofsky et al. [5-84], which is 0.07. A deviation of 0.11 units between the two methods of aromaticity determination seems to be a very serious error, since it means that 11 atoms out of 100 are being under- or over-counted.

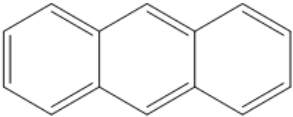
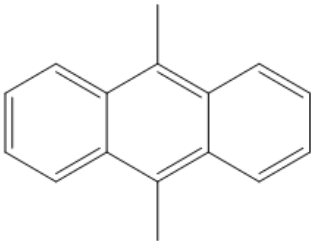
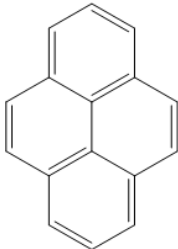
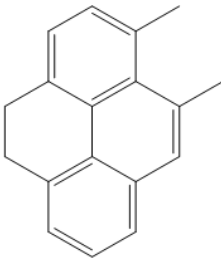
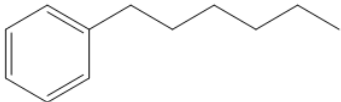

Table 5-65: Comparison of aromaticity f_a derived from ^{13}C NMR and Brown-Ladner.

Sample	f_a		Deviation
	Brown-Ladner (^1H NMR)	Method ^{13}C NMR	
Petroleum Pitch ^a	0.29	0.29	0.00
Thermally cracked residue ^a	0.77	0.69	0.08
Decant oil ^a	0.71	0.66	0.05
Heavy coker distillate ^a	0.76	0.70	0.06
EI-107	0.71	0.71	0.00
EI-133	0.68	0.67	0.01
EI-134	0.64	0.56	0.08
EI-135	0.67	0.58	0.09
EI-136	0.64	0.53	0.09
EI-137	0.58	0.48	0.10
EI-138	0.59	0.48	0.11

^a Based on reference [19]MT.

According to the results shown in **Table 5-65**, it is observed that the deviation increases as the hydrotreatment of the decant oil is increased, which suggests that the deviation between the two methods depends on the chemical composition of the feedstock. The materials that have been characterized in the literature are mostly high-aromatic compounds such as coal-tar pitches and petroleum fractions; this could be a factor as to why the deviation is high. Oils with none or very low aromaticity content have been reported by Retcofsky et al. [5-84] and they display a low deviation which suggests that aliphatic compounds do not present this problem. Likewise, asphaltenes, which tend to be aliphatic-rich compounds, display a low aromaticity deviation [5-84]. In order to evaluate that the deviation, $|f_a' - f_a|$, depends on the chemical composition of the feedstock, the f_a' and f_a was determined for six model compounds using the Software X Win NMR 2.5, and the results are shown in **Table 5-66**. The results were as expected: higher deviations are found for alkyl aromatics and alkyl hydroaromatic compounds (compounds No. 2 and 4), which tends to agree with the deviations found in the HT DO's.

Table 5-66: Aromaticity difference of some Model hydrocarbons obtained by the ^{13}C NMR and Brown and Ladner method

No.	Compound	f_a'	f_a	$ f_a' - f_a $
		^{13}C NMR	Brown and Ladner	
1		1.00	1.00	0.00
2		0.88	0.80	0.08
3		1.00	1.00	0.00
4		0.78	0.69	0.09
5		0.50	0.47	0.03
6		0.00	0.05	0.05

According to Weinberg [5-87], aromaticity of oils is a parameter that can be adjusted. Large planar molecules are needed for mesophase formation, since mesophase is formed from a precursor that is highly aromatic and polycondensed with short aliphatic side chains [5-87]. Less aromatic precursors, which have a small degree of polycondensation and longer aliphatic side chains, tend to suppress mesophase formation by dealkylation during pyrolysis, disrupting the

order of the mesophase and hindering condensations of large planar molecules [5-87]. According to Weinberg, aromaticity, f_a , must be between 0.7 and 0.9, so that mesophase can nucleate, grow and coalesce [5-87]. In the present work, the decant oil that has f_a within the desired range of aromaticity is the raw decant oil, designated as EI-107, for which $f_a=0.71$.

Four out of seven decant oils were selected to perform carbonization reactions. First, the raw decant oil, EI-107, was chosen because its physical and chemical properties are unique with respect to hydrotreated versions and because this is the parent decant oil from where the other decant oils were derived. Second, the decant oils EI-137 and EI-138 display similar physical and chemical properties, but EI-138 was chosen over EI-137 since it displays greater differences when compared with the properties of the raw decant oil regarding naphthenic content. The decant oils EI-133 and EI-135 display similar chemical composition and aromaticity, as EI-134 and EI-136 do; however, EI-134 and EI-135 were chosen because their sample quantity (in gallons) was higher when compared to the quantity of EI-133 and EI-136. The results of the further heat treatment of the four decant oils, EI-107, EI-134, EI-135 and, EI-138, to generate cokes and co-cokes, are discussed in Section 5.6.2.

For further discussions purposes along this document, it is important to recall the sequence of aromaticity of the four chosen decant, which is:

$$EI - 107 > EI - 135 > EI - 134 > EI - 138$$

Saybolt Viscosity of Decant Oils

The viscosity was measured following the methodology in discussed in previous reports, where the Saybolt seconds were determined experimentally [RI reports] and is shown in **Table 5-67**.

Table 5-67: Viscosity of decant oil and hydrotreated decants oils.

	t (s) Saybolt seconds	ρ at T_0	Temperature °C		δ_T	μ (centipoises)
			T_0	T		
EI-107	3721.0	1.1137	27.5	30	1.1104	904.8
EI-134	698.7	1.0579	27.0	30	1.0542	161.1
EI-135	659.8	1.0553	27.0	30	1.0516	151.7
EI-136	444.8	1.0469	27.5	30	1.0438	101.3
EI-137	191.8	1.0220	28.0	30	1.0196	42.0
EI-138	187.5	1.0197	27.0	30	1.0161	40.9

ρ = specific gravity; ρ at T_0 is the density determined experimentally at temperature T_0 ; δ_T is the density corrected at temperature T.

Proposed Structure models for original decant oil and hydrotreated derivatives

The proposed structures for each decant oil are based on the based structure proposed by Mochida et al. [5-80] and characterization data, including GC/MS, ¹H NMR, aromaticity, and elemental analyses. The details of how the proposed models are contained in an appendix of Escallon's PhD thesis [5-81].

Solubility Parameter

The good solubility and/or interaction between the coal and decant oil may be very important to obtain high quality co-coke, as good dissolution would be important to avoid mosaic texture formation. Solubility parameter will be discussed in greater detail in Section 5.8.

The solubility parameters of all the decant oils are shown in **Table 5-68**. The solubility parameter of the coal, which is calculated through comparative swelling, is ~10.8 hildebrands, and is shown in **Figure 5-29** (the interaction of the coal with several solvents of varying solubility). The highest Q corresponds to when coal was swollen in quinoline, and since quinoline's solubility parameter is ~10.8 hildebrands, we are reporting that the solubility parameter of Powellton/Eagle is 10.8 hildebrands. The coal and all the decant oils met the requirement of good solubility since the difference between the coal and decant oils are less than 2.4 hildebrands (1.4 or less). Since the difference in solubility parameter is greatest with the HT DO's compared to the decant oil, the original decant oil may have a slightly better interaction with the coal than the HT DO's.

Table 5-68: Solubility parameters of the decant oils.

ID	Decant oils (fa)	δ ^{13}C NMR (hildebrands)	δ actual (hildebrands)
EI-107	0.71	9.9	9.4
EI-135	0.67	9.5	9.1
EI-134	0.64	9.4	9.0
EI-138	0.62	9.4	9.0

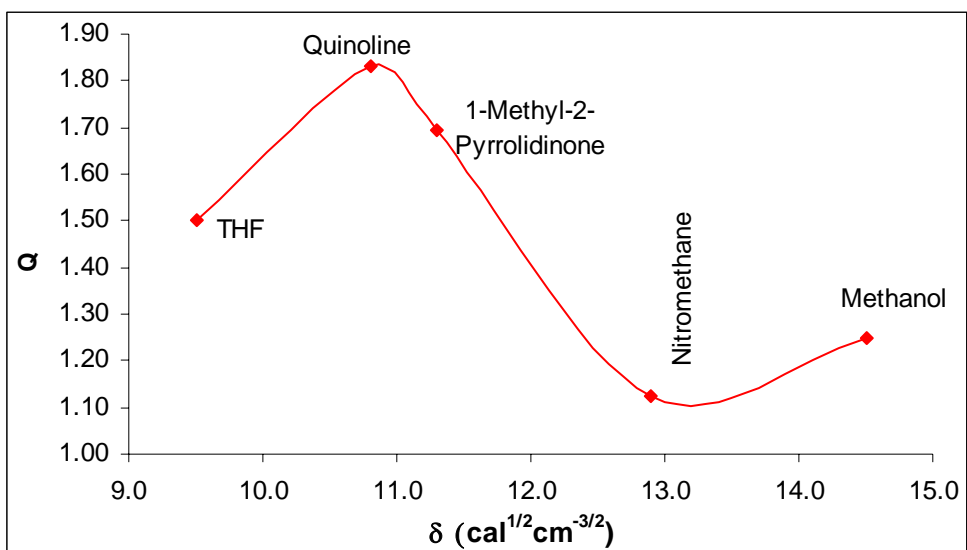
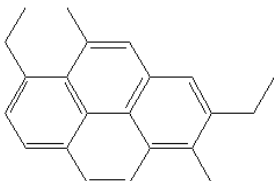
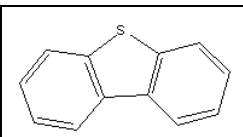
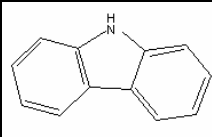
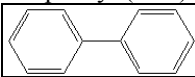
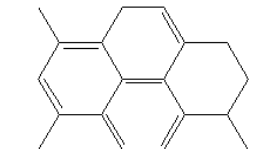
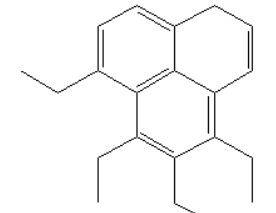
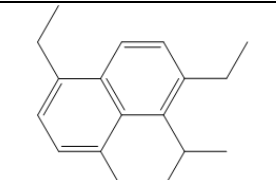


Figure 5-29: Swelling spectrum. Coal and hydrogen bonding solvents.

Table 5-69: Proposed structures for the raw decant oil and its three selected hydrotreated versions

Decant oil	Average structure (%)		Heteroatoms (%)		Bi-cyclic compounds	
EI-107	81.29		18.71	<div> <div>17.2%</div> <div></div> <div>Dibenzothiophene (DBT)</div> </div> <div> <div>1.51%</div> <div></div> <div>Carbazole (CZ)</div> </div> <div>+</div>	0.17	<div>Bi-phenyl (BPh)</div> <div></div>
EI-135	86.21		4.98	4.70% (DBT) + 0.28% (CZ)	8.81	BPh
EI-134	84.95		8.31	8.03% (DBT) + 0.28% (CZ)	6.74	BPh
EI-138	91.47		0.28	0.28% (CZ)	8.25	BPh

5.6.1.2.2 Characterization of Coal

The characteristics of the coal and original decant oil are shown in Table X-X. The coal used in this study was a Powellton (high volatile A bituminous) coal. Proximate and ultimate analyses for these feedstocks are shown in **Table 5-70**. The composition of the high-temperature ash is also given in **Table 5-70**. Over 70% of the ash in the coal is composed of silica and alumina principally derived from clay and quartz minerals. The iron is predominantly iron sulfides (pyrite and pyrrhotite).

Figure 5-30 shows the solid state ^{13}C NMR spectrum of the Powellton-Eagle. The aromaticity of the coal, f_a , was calculated by integrating the peak area of aromatic carbons divided by the integrated peak areas of both aromatic and aliphatic carbons. The aromaticity, f_a , is 0.87.

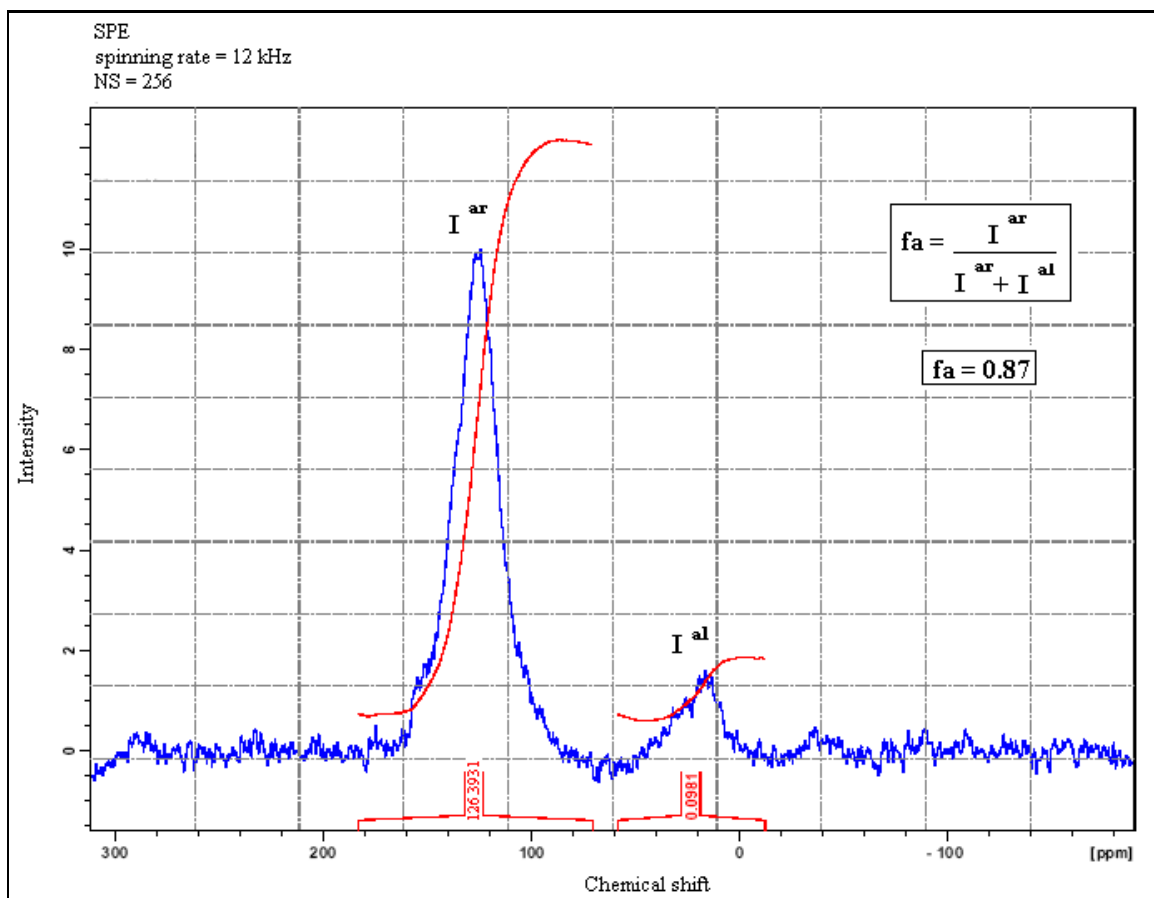


Figure 5-30: ^{13}C NMR spectra of the Powellton-Eagle coal.

Table 5-70: Proximate and Ultimate Analysis of the Feeds

	Coal	Decant Oil
Proximate analysis ^a	EI-106	EI-107
Ash (%)	8.12	0.22
Volatile matter (%)	27.27	-
Fixed carbon (%)	64.61	-
Ultimate analysis ^a		
Carbon (%)	80.92	89.59
Hydrogen (%)	4.55	7.32
Nitrogen (%)	1.28	0.22
Sulfur (%)	0.88	2.99
Oxygen (by diff.) (%)	4.25	
Fluidity Data ^b		
Fluid Temperature Range (°C)	88	na
Maximum Fluidity (ddpm)	7,002	na
Softening Temperature (°C)	397	na
Organic Petrography, vol%		
Total Vitrinite (vol. %)	86.5	na
Total Liptinite (vol. %)	1.4	na
Total Inertinite (vol. %)	12.1	na

^a values reported on a dry basis

^b Determined using a Gieseler plastometer

5.6.2 Evaluation of Co-cokes Generated from Hytrotreated Decant Oil and Coal

The carbonization process (coking) was carried out on raw decant oil and three out of the six hydrotreated derivatives of the raw decant oil. The selection of the three HT DO's was based on the HT DO's with the greatest differences of chemical composition between the HT DO's when compared to the raw decant oil.

The four selected decant oils, as discussed before, were carbonized using two different reactors, one operated under atmospheric pressure (LSC_{open}) and the other under near-atmospheric pressure (1.7 atm) in our large laboratory-scale coker (PSC). Different reactors were used since no single reactor was able to produce the samples needed to fulfill the objectives of the current work.

The summary of the operational similarities and differences between these two reactors are shown in **Figure 5-31**. Both reactors, LSC_{open} and PSC are operated under

comparable conditions of pressure, and temperature, being the working pressure and temperature of 1 atm and 465°C in the LSC_{open} and 1.7 atm and 470±5°C in the PSC.

There are two main differences between these two reactors. The first difference is the reactor size: LSC_{open} can produce between 1-3 g of coke depending on the feedstock while the PSC produces 1kg or more. The advantage of using the PSC is being able to obtain a large amount of coke, for which the material can then be used to determine the Coefficient of Thermal Expansion (CTE), an indicator of end-use of the coke. The cokes formed in the PSC were ground and shipped to GrafTech in Parma (OH). The methodology has been reported elsewhere [5-99]; for graphite electrodes, the cokes are heated up 3000°C.

The other difference is the “recycle” ratio. The PSC is not designed to operate under different recycle ratios, it worked under a zero recycle ratio. Likewise, the LSC_{open} did not operate under different recycling ratios; however, the recycling of the products of the pyrolysis is high since the products remain in the reactor, except for those whose boiling point is below 45°C. Consequently, the high recycling present in the LSC_{open} facilitates the formation of side reactions and increase the contact time between the components present in the decant oil and components present in the coal, when blends are used as feedstocks.

Yields and coke evaluation: comparison between LSC open and PSC

Pyrolysis of the raw decant oil

The coke yields obtained from the raw decant oil, EI-107, in the LSC_{open} and PSC are compared. The conditions and yields obtained when the raw decant oil was coked is shown in **Table 5-71**. The conditions used in the LSC_{open} were 465°C and 12h reaction time.

The coke yield percent obtained in the LSC_{open} at 12h is 54.71% while the coke obtained in the PSC is 19.81%. Therefore, additional 34.71% of coke was formed as the result of the secondary reactions that occur in the LSC_{open}. It is important to point out that the coke reported here in the LSC_{open} is reported on a gas and THF-S free basis, as shown in **Equation 20**, in order to make those two cokes or TI obtained from both

reactors comparable, since gas is not measured in the PSC and the coke is not Soxhlet extracted with THF in the PSC.

$$TI\% \text{ gas and THF} - S \text{ free} = \frac{TI\%}{100 - (gas\% + THF\%)} \quad \text{Equation 20}$$

The CTE corresponding to the coke derived from the raw decant oil in the PSC is $0.368 \times 10^{-6}/^{\circ}\text{C}$, and is classified as premium needle coke [5-100]; the CTE of the cokes obtained in the LSC_{open}, could not be determined because of the limited amount of sample. Since CTE cannot be used to compare the coke quality of the cokes generated from the same feedstock but different reactor, X-Ray diffraction (XRD) can be used to compare the cokes generated, as it is a technique widely used for coke comparison [5-101, 5-102].

The coke obtained in the LSC_{open} and the coke obtained in the PSC were analyzed by XRD. Their parameters were compared and are shown in **Table 5-72**.

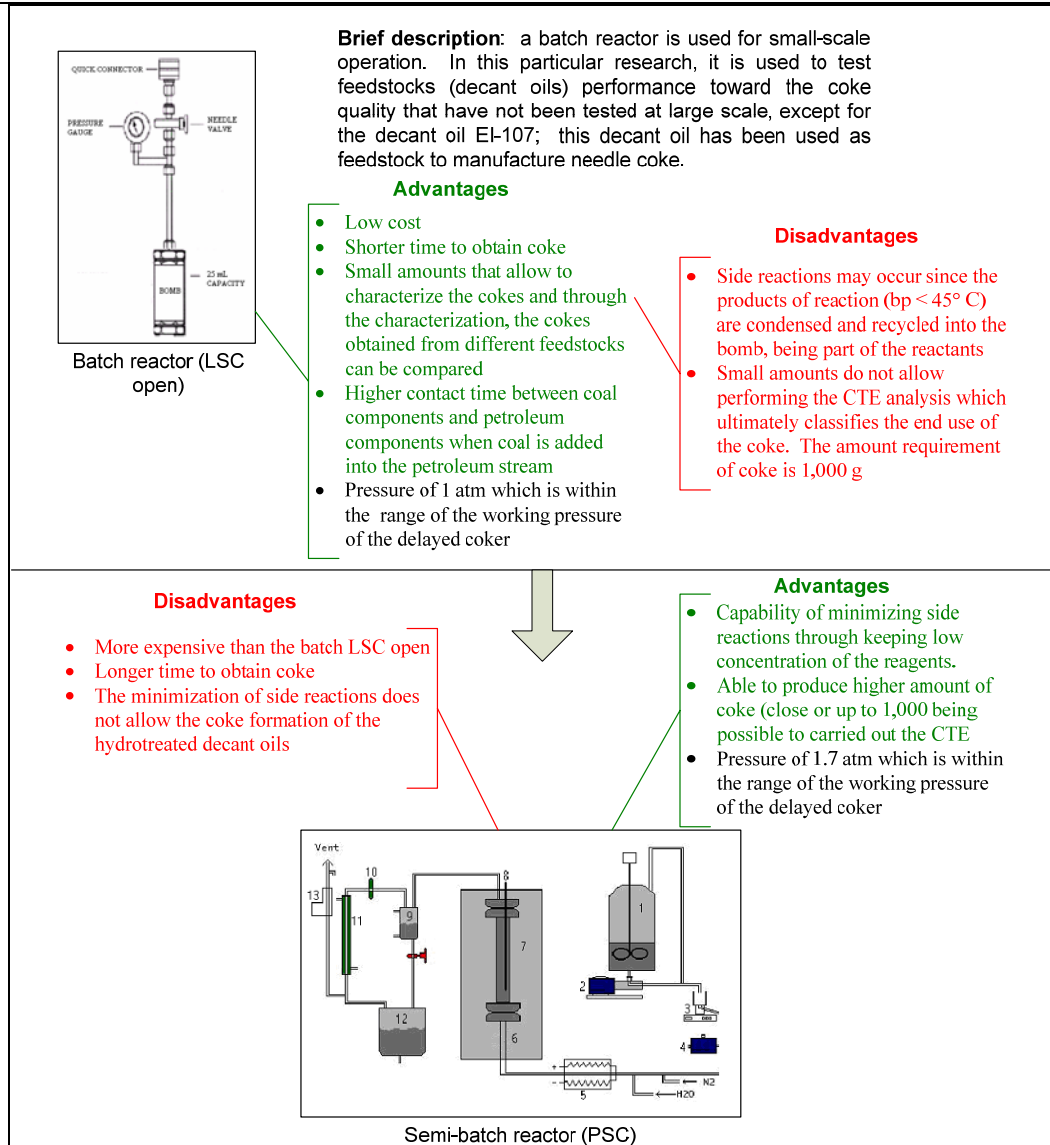


Figure 5-31: Summary of the operational similarities and differences between LSC_{open} and PSC.

Table 5-71: Conditions and yields obtained from raw decant oil alone.

Conditions	PSC	LSC _{open}
Feedstock (h)	6	NA
hold* at 500°C (h)	6	NA
Total reaction time (h)	12	12
feed rate, g/min	16.7	NA
preheater inlet, °C	144	NA
preheater outlet, °C	445	NA
coke drum inlet, °C	475	NA
coke drum lower/middle, °C	474	NA
coke drum top, °C	476	NA
Average temperature °C	467	465
Material Fed to Reactor (g)	5932	5
Coke (g)	1175	NA
Liquid (g)	4200	NA
coke+liquid product	5375	NA
liquid/coke	3.57	NA
% coke	19.81	54.71**
% liquid product	70.80	45.29**

*the drum was hold at 500°C to release volatiles. Pressure is 1.7 atm

** Gas and THF-S free basis

NA, not applicable

Table 5-72: XRD parameters.

SAMPLE ID	X-ray diffraction parameters			
	FWHM (°) ±0.011	diff Angle ±0.006	L _c (Å)	d ₀₀₂ (Å) ±0.007
EI-107-LSC _{open}	3.376	26.029	24	3.4205
EI-107-PSC	3.260	26.031	25	3.4203

Based on XRD, the cokes generated in both reactors were of similar quality. The values of diffraction angle and d₀₀₂ for both cokes are within the reproducibility of the measurement (±); however, looking to FWHM and L_c is observed that the coke obtained in the PSC has a higher quality when compared to the one obtained in the LSC_{open}. Despite of the lower FWHM and higher L_c displayed by EI-107 generated in the PSC compared to the one generated in the LSC_{open}, this small difference does not suggest that by downscaling the reactor and by increasing the “recycle”, the coke quality decreases

from premium to regular needle coke, although this cannot be proved since the CTE cannot be determined in the cokes obtained in the LSC_{open}.

Pyrolysis of Hydrotreated Decant Oils

The raw decant oil was hydrotreated at different levels in order to study the effect of the hydrotreatment of the decant oils in the coke quality, when they are pyrolyzed. Two different comparisons were made: comparison of yields and coke quality when using different reactors and comparison of yields and coke quality between the raw decant oil and the hydrotreated decant oils, when using the LSC_{open} reactor. No coke was obtained in the PSC reactor when using the HT DO's, as the boiling point of the HT DO's was low enough that almost all the material distilled before carbon was made, therefore the data presented in this case is only from the LSC_{open} reactor. Consequently, this section discusses the comparison in yields and coke quality of the cokes obtained in the LSC_{open} alone, which were obtained at 18h.

The cokes obtained at 18h were evaluated by optical microscopy analysis, from where the Optical Texture Index (OTI) is calculated using the **Equation 5-21** [5-103]. The correspondent OTI and XRD parameters are shown below in **Table 5-73**.

$$OTI = (0 * \%I) + (1 * \%m) + (5 * \%d) + (50 * \%D) + (100 * \%FD) \quad \text{Equation 0-21}$$

where I= isotropic carbon; m= mosaic; d= small domain; FD= flow domain and D= domain.

Table 5-73: The relationship between optical textures and X-ray diffraction parameters with near-constant anisotropic carbon content. Atmospheric pressure at 18h.

SAMPLE ID	X-ray diffraction parameters				Optical texture				
	FWHM (°) ±0.011	diff Angle ±0.006	Lc (Å)	d ₀₀₂ (Å) ±0.007	I	m	d	D	OTI
EI-107	3.376	26.029	24	3.4205	2.5	5.3	57.0	35.5	23.1
EI-135	3.361	25.998	24	3.4245	1.2	5.2	68.2	28.6	19.6
EI-134	2.950	26.083	26	3.4136	1.4	1.8	48.6	47.2	29.3
EI-138	3.236	26.038	26	3.4194	4.8	2.2	50.3	39.2	23.6

I=isotropic carbon; m=mosaic; d=small domain; D=flow domains + domain.

It has been reported that the highest domain content (isochromatic units > 60 μm), leads to the lowest the CTE and hence, the better the coke quality [5-104]. According to the domain values, and assuming that all the cokes have the same amount of fine particles (particle size is lower than 60 μm and OTI is comparable), the coke quality sequence is: EI-134> EI-138> EI-107> EI-135. All the cokes derived from the hydrotreated decant oils have a higher coke quality when compared to the raw decant oil, EI-107, except EI-135, which suggests that the presence of bi-phenyls and five-membered ring compounds, forms small isochromatic units as reported elsewhere [5-105].

Pyrolysis of Raw Decant Oil and Coal

This section compares the yields and coke quality when the two different reactors (LSC_{open} and PSC) are used and compares the yields and coke quality when the coke derived from the decant oil alone is compared to the coke derived from the decant oil and coal blend. **Table 5-74** shows the conditions and yield results for the blends derived from the raw decant oil and Powellton/Eagle coal in a 4:1 wt. ratio.

Table 5-74: Conditions and yield for the blends derived from EI-107 and Powellton/Eagle coal, EI-107/coal, using LSC_{open} and PSC reactors.

Conditions	PSC	LSC _{open}
Feedstock, hours	6	NA
Hold* at 500°C, h	6	NA
Total time, h	12	12
Feed rate, g/min	16.8	NA
Preheater inlet, °C	120	NA
Preheater outlet, °C	464	NA
Coke drum inlet, °C	503	NA
Coke drum lower/middle, °C	490	NA
Coke drum top, °C	477	NA
Average temperature, °C	483	465
Material fed to reactor, g	5506	5
Coke	1523	NA
Liquid	3460	NA
Coke+liquid product	5506	NA
Liquid/coke	2.27	NA
% coke	27.66	55.59
% liquid product	62.84	44.41

*the drum was hold at 500°C to release volatiles

The co-cokes derived from blending the raw decant oil were evaluated and the yields were compared when they were obtained using different reactors, LSC_{open} and PSC. **Table 5-75** shows the XRD parameters of the cokes derived from the blend. The XRD data show the cokes from both types of reactors are comparable. The CTE of the co-coke derived in the PSC was determined to be $1.800 \times 10^{-6}/^{\circ}\text{C}$, which exceeds the value of $0.8 \times 10^{-6}/^{\circ}\text{C}$, and hence, this co-coke cannot be classified as graphite grade or needle coke.

Table 5-75: XRD parameters of the cokes derived from the blend obtained at 18h using both reactors.

	PSC				LSC _{open}			
	Diffraction angle	d ₀₀₂	FWHM	Lc	Diffraction angle ± 0.02	d ₀₀₂ ± 0.0003	FWHM ± 0.008	Lc
EI-107/coal	26.187	3.4003	4.077	20	26.045	3.4185	4.087	20

The co-cokes were tested for anodes for the aluminum industry, or sponge coke; testing indicated that the co-cokes exceed all the specifications except for the amount of ash in the coke. Therefore, the co-cokes have a potential to be used in the aluminum industry, but only if the minerals in the coal can be removed by cleaning or by solvent extraction. [5-21, 5-28, 5-106] Section 5.X.X discusses the co-coke quality using Pittsburgh and Marfork coals, for use as anode and electrode filler and for use as graphite. The co-coke has also been tested for use as an activated carbon, and results indicate the material could make a good activated carbon [5-107]. Future work will determine if the co-coke could be used as filler for nuclear graphite, which a isotropic graphite is necessary. It is important to recall that the coke derived from the decant oil alone is classified as premium needle coke.

Pyrolysis of Hydrotreated Decant Oils and Coal

Table 5-76 shows the yields of the blends between coal and hydrotreated decant oils generated in the PSC and LSC_{open}. It is observed that the coke yield is always higher when coke is obtained in the LSC_{open} when compared to the coke yield obtained in the PSC. This shows agreement with what it has been observed in the previous sections,

where the low coke yield obtained in the PSC was explained based on its zero-recycling operation.

Table 5-76: Yields for the blends generated in the PSC and LSC_{open}.

Conditions	EI-134/coal		EI-135/coal		EI-138/coal	
	PSC	LSC _{open}	PSC	LSC _{open}	PSC	LSC _{open}
Total time (h)	12	12	12	12	12	12
Average temperature, °C	463	465	462	465	477	465
Material fed to reactor	5948	5	5752	5	5850	5
% coke**	24.43	48.36	18.76	43.19	17.25	38.96
% liquid product	70.95	51.64	72.27	56.81	73.98	61.14

*the drum was hold at 500°C to release volatiles

**Gas and THF-S free basis for the data obtained in the LSC_{open}

To determine the co-coke quality, some correlations were founds between the CTE and XRD in the co-cokes generated in the PSC only, since CTE could not be performed on the cokes generated from the LSC_{open} due to quantity limitation. It is important to recall that no petroleum-derived coke was formed in the PSC, except for that of the raw decant oil; hence, no correlation was possible to carry out between CTE and XRD in the petroleum cokes. The CTE, as well as the XRD parameters are shown in **Table 5-77**. According to what is shown in **Table 5-77**, the co-cokes cannot be classified as graphite grade since the CTE value of $0.8 \times 10^{-6}/^{\circ}\text{C}$ exceeds the graphite value.

Table 5-77: CTE of the graphites rods made of the co-cokes generated in the PSC and XRD parameters calculated in the green co-cokes.

	CTE x 10 ⁻⁶	Diffraction angle	d ₀₀₂	FWHM	Lc
EI-134/coal	1.800	26.288	3.3874	3.622	23
EI-135/coal	1.880	26.231	3.3946	3.717	22
EI-107/coal	2.090	26.187	3.4003	4.077	20
EI-138/coal	2.230	25.894	3.4380	5.600	15

A deviation from the general trend is observed from the co-coke EI-107/coal, which suggests that this coke suffers significant dilation (called puffing) during the graphitization process, which is attributed to its higher sulfur content compared to the co-cokes derived from coal and hydrotreated decant oil. The coke quality is decreasing as

the CTE increases due to the presence of higher sulfur content in EI-107 when compared to the hydrotreated decant oils (see **Figure 5-32**).

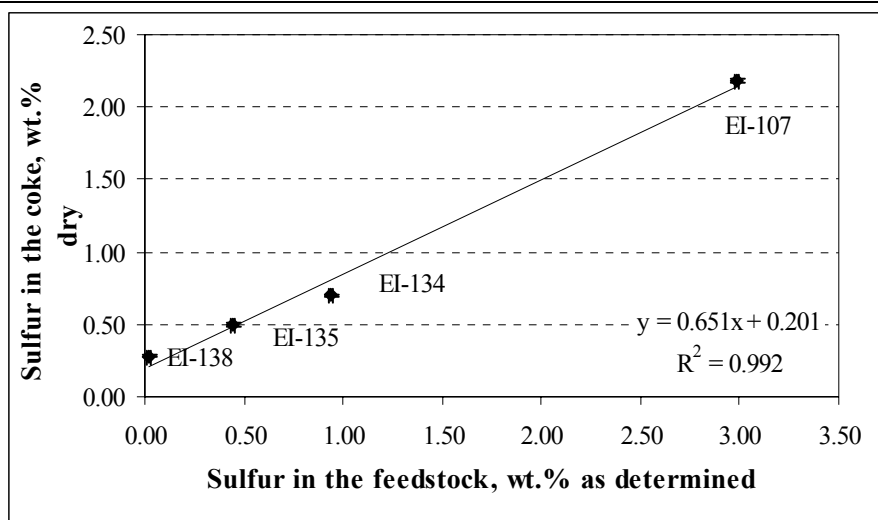


Figure 5-32: Correlation between the sulfur content present in the feedstocks and the sulfur content present in the cokes obtained in the LSC_{open} at 18h.

5.6.3 Liquids from Co-Coking of Hydrotreated Decant Oil and Coal Blends in PSC: Product Distribution of Distillates

This section discusses the distillates produced during co-coking of HT DO's and Powellton/Eagle coal when using the PSC reactor.

5.6.3.1 Experimental

Materials

A commercial petroleum-based decant oil (EI-107) obtained from United Refining Corporation of the type used for making premium needle coke was used in this study. This decant oil was hydrotreated to different levels of severity at PARC using a NiMo Syncat-37 catalyst to provide a series of samples of decant oils with different levels of hydrotreating severity (see details in Task 1 and previous reports, [5-21, 5-28]). Hydrotreatment conditions and related information can be found elsewhere [5-108]. Hydrotreated decant oils were labeled as EI-133, EI-134, EI-135, EI-136, EI-137 and EI-138. Six hydrotreated products were produced with a wide range of sulfur and nitrogen removal. **Figure 5-33** shows the sulfur and nitrogen removal levels of HT DO's.

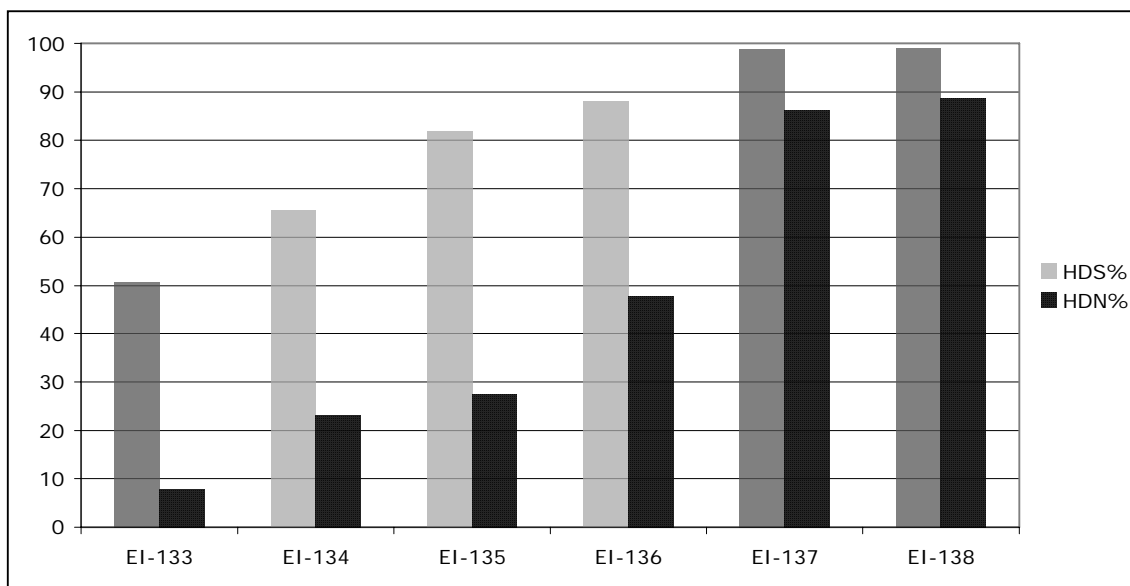


Figure 5-33. Hydrodesulfurization % (HDS %) and Hydrodenitrogenation % (HDN %) of HT DO's.

The coal used in this study (EI-106) was a 50/50 blend of the Powellton and Eagle seams, both very similar coals of high volatile A bituminous rank. Proximate and ultimate analyses, fluidity and organic petrography results for these feedstocks are shown in **Table 5-70**, in section 5.6.1. Ash and sulfur yields of the original decant oil (EI-107) were found to be 0.22% and 2.99%, respectively.

Reaction Procedures.

The following operating conditions were used: coke drum inlet temperature 465 °C, coke drum pressure 25 psig, slurry feed rate 16.7 g/min, and feed introduction to the coker for 360 min. At the conclusion of each experiment, the coke drum was maintained at temperature for an additional 360 min to ensure carbonization of nonvolatile components. Detailed description of delayed coking is given under **Section 5.2.1**.

Analytical Procedures.

Gas chromatography/mass spectroscopy (GC/MS) analysis, using a Shimadzu QP5000 spectrometer, was performed on liquid samples to determine their chemical composition. GC/MS temperature programs for gasoline, jet fuel, diesel fuel and fuel oil were described under **Section 5.2.2**. Simulated distillation gas chromatography (GC) analyses described under **Section 5.2.2** as well.

Finally, the distillate liquids from each co-coking experiment were vacuum distilled into refinery cuts corresponding to gasoline, jet fuel, diesel, and fuel oil. These fractions were characterized in detail using GC/MS.

5.6.3.2 Results and Discussion

Characterization of feedstock

The objective of this study was to compare the results of the co-coking of the different severity hydrotreated-decant oil and a coal. In co-coking experiments, the coal was used at 20 wt% and the slurry was continuously heated (66 °C) and stirred to ensure homogeneity of the slurry during introduction to the coking reactor. The rate of feed material was maintained at 16.7 g/mL.

The coal used in this study was a Powellton/Eagle blend of high volatile A bituminous coals. The petroleum-based decant oil (EI-107) used in this study represents a typical decant oil. Decant oil was hydrotreated at PARC Technical Services (Harmarville) to provide a series of samples of decant oils with different levels of hydrotreating severity. These materials were characterized using a variety of analytical techniques. This information was used to correlate decant oil structure and composition with the quality and yield of the liquid products produced by co-coking with coal.

Figure 5-33 shows the hydrodesulfurization (HDS) and hydrodenitrogenation (HDN) levels of hydrotreated decant oils. Increased hydrotreatment severity of decant oil increased both HDS and HDN percentages of decant oil from 50.6 to 99.0% and 7.7 to 88.7 %, respectively.

The original decant oil (EI-107) and hydrotreated versions of original decant oil (EI-133 to EI-138) were analyzed using GC/MS and the compositions of the oils were grouped as the following: paraffins, saturated cyclics, alkyl benzenes, indanes, naphthalenes, tetralins, decalins and polycyclic compounds (Tri-ring +). The GC/MS results in area percentages of these materials are shown in **Table 5-78**.

The original feedstock (EI-107) almost completely consisted of aromatic components (mostly tri-ring +), while the hydrotreated versions have a larger composition, tri-, di-, and mono- aromatics. As noted in **Table 5-78**, hydrotreatment resulted in increased amounts of paraffins, saturated cyclics, alkyl benzenes, indanes, naphthalenes, tetralins, decalins but decreased amounts of polycyclic compounds in the liquid. One can conclude that as the hydrotreating severity increased, tri-ring + molecules were hydrogenated and converted into smaller aromatic molecules, such as naphthalenes, indanes, and benzenes, and as a result of thermal hydrocracking, the amount of tri-ring + compounds decreased. Hydrogenated homologs of naphthalenes (tetralins and decalins) also were observed in increasing amounts in hydrotreated decant oils as a result of hydrotreatment. The lowest severity hydrotreated decant oil, EI-133, had no decalins, the lowest amount of saturated cyclics, and the highest amount of tri-ring + compounds, while the highest severity hydrotreated decant oil, EI-138, had the highest amounts of saturated cyclics, tetralins, decalins and the lowest amount of tri-ring +

compounds. GC/MS observations were consistent with the hydrotreatment levels of decant oils.

Table 5-78. Percent distribution of the product fractions of original hydrotreated-decant oils*.

Group Classification	Decant Oils						
	EI-107 (Original Decant Oil)	EI-133	EI-134	EI-135	EI-136	EI-137	EI-138
Paraffins	0.4	0.0	1.1	0.4	0.0	3.7	2.1
Saturated cyclics	1.0	1.3	2.0	3.7	3.9	6.7	14.4
Benzenes	7.0	21.0	24.9	17.0	24.6	13.3	11.4
Indanes	0.1	0.1	2.8	6.9	5.6	2.3	4.2
Naphthalenes	3.2	4.0	5.6	3.0	2.6	8.9	4.2
Tetralins	0.0	4.5	6.5	3.0	1.6	6.2	6.8
Decalins	0.0	0.0	0.0	0.0	0.0	6.3	6.7
Tri-ring +	88.2	69.1	57.2	66.0	61.7	52.6	50.3

*: Percent distributions belong to the ratio of GC-MS peak areas

Product recovery

The six co-coking experiments (Runs #27-32) used feedstocks in an 80:20 ratio of hydrotreated decant oil to coal, and the severity of hydrotreatment increased with increasing run number. The decant oils used were EI-133 to EI-138, as stated above, with EI-133 having the least degree of hydrotreating and EI-138 (run 32) having the greatest degree of hydrotreating. Conditions and product yields from each of the co-coking runs are summarized in **Table 5-79** as well as in reference [5-21, 5-28, 5-109].

Table 5-79. Conditions and product distributions for co-coking experiments

Run #	27		28		29		30		31		32	
Conditions	DO 100 EI-107	DO/Coal 80/20 DO=EI-107 C= EI-106	DO/Coal 80/20 DO=EI-133 C= EI-106	DO/Coal 80/20 DO=EI-134 C= EI-106	DO/Coal 80/20 DO=EI-135 C= EI-106	DO/Coal 80/20 DO=EI-136 C= EI-106	DO/Coal 80/20 DO=EI-137 C= EI-106	DO/Coal 80/20 DO=EI-137 C= EI-106	DO/Coal 80/20 DO=EI-138 C= EI-106	DO/Coal 80/20 DO=EI-138 C= EI-106	DO/Coal 80/20 DO=EI-138 C= EI-106	DO/Coal 80/20 DO=EI-138 C= EI-106
Feedstock, hours	6	6	6	6	6	6	6	6	6	6	6	6
Hold at 500 °C, hrs	6	6	6	6	6	6	6	6	6	6	6	6
Feed rate, g/min	16.7	16.7	16.7	16.7	16.7	16.7	16.7	16.7	16.7	16.7	16.7	16.7
Preheater inlet, °C	181	188	230	236	227	223	225	225	225	224	224	224
Preheater outlet, °C	417	419	456	440	443	445	439	439	439	425	425	425
Coke drum inlet, °C	446	474	470	470	460	462	468	468	468	472	472	472
Coke drum lower/middle, °C	493	481	472	471	470	470	473	473	473	468	468	468
Coke drum top, °C	458	466	474	472	474	473	478	478	478	472	472	472
Material Fed to Reactor (g)	6028	6054	6093	5948	5752	6229	6076	6076	6076	5926	5926	5926
Product												
Coke (g)	860	1917	1099	1453	1079	990	1130	1130	1130	1068	1068	1068
Liquid (g)	4800	3989	4366	4220	4157	4727	4532	4532	4532	4513	4513	4513
Gas (by difference) (g)	368	148	486	128	383	369	283	283	283	232	232	232
Preheater content (g)			142	147	133	143	131	131	131	113	113	113
Coke + Liquid product (g)	5660	5906	5465	5673	5236	5717	5662	5662	5662	5581	5581	5581
Liquid / Coke	5.58	2.08	3.97	2.90	3.85	4.77	4.01	4.01	4.01	4.23	4.23	4.23
Coke (wt%)	14.27	31.67	18.0	24.4	18.8	15.9	18.6	18.6	18.6	18.0	18.0	18.0
Liquid product (wt%)	79.63	65.89	71.7	71.0	72.3	75.9	74.6	74.6	74.6	76.2	76.2	76.2
Gas (wt%)	6.10	2.44	8.0	2.2	6.7	5.9	4.7	4.7	4.7	3.9	3.9	3.9

The conditions applied for co-coking were nearly the same for all of co-coking experiments, e.g., amount of fed material, feed rate and temperatures used along the coker. Using similar conditions for each of the experiments, the yields of coke, liquid, and gas were 15 - 32 %, 66 - 80 %, and 2 - 8 %, respectively. When comparing the addition of coal to the original decant oil to the run with decant oil, the coke yield increased and the liquid product decreased. However, when using the HT DO's, the coke yield was higher than decant oil without coal, but significantly lower than co-coking with the original decant oil. The co-coking with the decant oils with the greatest hydrotreatment severity tended to increase the liquid product percentage. The process was found to be reproducible in terms of the yields of green coke and liquids isolated from experiments, with the error between runs 1% or less [5-110].

Product distributions of distillates

The concept of co-coking stemmed from the need to produce coal-based liquids that would ultimately be converted into thermally stable jet fuel. With the introduction of coal to the process stream, it was assumed that the volatile constituents of coal may be produced along with the volatiles from the petroleum feed and subsequently fractionated. Previous studies have determined that the compounds present in jet fuel that are derived from coal account for improved thermal stability [5-111-5-118].

The liquid products from six co-coking studies were analyzed to determine the proportion of materials in each of the refinery cut boiling ranges. The collected overhead liquids from each co-coking experiment were distilled into conventional refinery boiling ranges by vacuum distillation; boiling point distribution of the liquid products was determined. Vacuum distillation was carried out using approximately 1200 g of the liquid products from the co-coking runs. Each fraction was cut and collected according to the given cut-point temperatures given below at a measured system pressure.

The following boiling point ranges for the liquid products from the fractionation of co-coking overhead liquid were used in this study: gasoline (Initial Boiling Point to 180 °C), jet fuel (180 - 270 °C), diesel (270 - 332 °C) and fuel oil (332°C - Final Boiling Point). It has been hypothesized that the yields of products in the given boiling range depends on the degree of hydrotreating of the decant oil feedstock.

Vacuum distillation product distribution of the collected distillate liquids from co-coking experiments with decant oil/coal are shown in **Table 5-80**. The accuracy of the vacuum distillation fractionation of the overhead liquids was confirmed using simulated Distillation GC according to ASTM 2887. The product yields from vacuum distillation show that the percentage of the liquid products corresponding to jet fuel increases with increasing hydrotreatment (6.0%-15.3%), the higher end corresponding to a more hydrotreated decant oil, but the yields lower than the runs when using the original decant oil until severe hydrotreatment. Similarly, it is also worth noting that the yield of the diesel fraction increases with the increasing degree of hydrotreatment of the decant oil; on the other hand the fuel oil fraction decreases with increasing hydrotreatment. The total percentages that correspond to gasoline and diesel are approximately 1.7-2.8 wt% and 7.3-19.8 wt%, respectively. The percent fuel oil decreased from approximately 84.0 to 64.2 wt%. This information provides a good basis for determining the relationship between severity of hydrotreating and product yield.

GC/MS analyses have been performed to assess compositional changes of gasoline, jet fuel and diesel fractions obtained from vacuum distillation of overhead liquids of the co-coking experiments. Evaluations of GC/MS analyses results were performed according to the same evaluation technique for the original hydrotreated decant oils as described above. The compositions of the gasoline, jet fuel and diesel were grouped as the following: paraffins, saturated cyclics, indanes, alkyl benzenes, naphthalenes, tetralins, and polycyclic compounds. GC/MS analyses results of gasoline, jet fuel and diesel fractions are given in **Tables 5-81-5-83**, respectively.

Gasoline fractions consisted mainly of paraffins, saturated cyclics and benzenes and small quantities of indanes, tetralins and decalins. No polycyclic aromatic hydrocarbon (tri-ring +) was observed in gasoline fractions (**Table 5-81**). These analyses showed that the amounts of saturated species, e.g., saturated cyclics (from ~25% to ~40%) and decalins (from 0% to 4%) increased as hydrotreatment severity increased; in contrast, the amounts of paraffins (from ~40% to ~20%) decreased. Alkylated benzenes were observed in lower quantities in Runs # 29 and 30 (~28%).

Table 5-80. Liquid product boiling point distributions by weight percentage, determined by vacuum distillation.

FEEDS	IBP-180°C	180-270 °C	270-332 °C	332-FBP °C
	IPB-356 °F	356-518 °F	518-630 °F	630-FBP °F
	Gasoline	Jet fuel	Diesel	Fuel oil
EI-107	6.07	11.55	9.34	73.05
EI-107/Coal	6.39	10.41	9.35	73.84
EI-133/Coal	2.8	6.0	7.3	84.0
EI-134/Coal	1.8	7.0	10.3	81.0
EI-135/Coal	2.0	7.7	13.0	77.3
EI-136/Coal	1.7	11.0	16.9	70.4
EI-137/Coal	2.3	15.3	17.5	65.0
EI-138/Coal	2.3	13.7	19.8	64.2

Table 5-81. Percent distribution of the product fractions of gasoline obtained from vacuum distillation of co-coking overhead liquid.

Group Classification	Run 27 (EI-133)	Run 28 (EI-134)	Run 29 (EI-135)	Run 30 (EI-136)	Run 31 (EI-137)	Run 32 (EI-138)
Paraffins	38.9	37.8	40.1	35.1	23.4	21.6
Saturated cyclics	25.6	23.5	29.7	38.0	42.3	38.1
Benzenes	35.5	37.7	28.7	26.7	32.6	35.4
Indanes	0.0	0.1	0.1	0.0	0.0	0.5
Naphthalenes	0.0	0.4	0.3	0.0	0.0	0.0
Tetralins	0.0	0.5	0.5	0.1	0.1	0.3
Decalins	0.0	0.0	0.5	0.1	1.7	4.1
Tri-ring +	0.0	0.0	0.0	0.0	0.0	0.0

Table 5-82. Percent distribution of the product fractions of jet fuels obtained from vacuum distillation of co-coking overhead liquid.

Group Classification	Run 27 (EI-133)	Run 28 (EI-134)	Run 29 (EI-135)	Run 30 (EI-136)	Run 31 (EI-137)	Run 32 (EI-138)
Paraffins	33.8	27.6	26.8	29.4	21.6	20.0
Saturated cyclics	12.5	18.3	17.3	21.7	31.0	35.8
Benzenes	32.2	26.7	29.5	27.9	18.5	20.9
Indanes	0.8	3.7	2.0	1.3	0.6	1.5
Naphthalenes	11.5	13.7	14.0	11.5	9.6	6.5
Tetralins	8.8	9.5	8.8	6.0	10.0	9.9
Decalins	0.5	0.6	1.6	2.2	8.7	5.6
Tri-ring +	0.0	0.0	0.0	0.0	0.0	0.0

Table 5-83. Percent distribution of the product fractions of diesel fuels obtained from vacuum distillation of co-coking overhead liquid.

Group Classification	Run 27 (EI-133)	Run 28 (EI-134)	Run 29 (EI-135)	Run 30 (EI-136)	Run 31 (EI-137)	Run 32 (EI-138)
Paraffins	5.2	4.3	2.3	2.3	2.7	9.1
Saturated cyclics	4.9	4.5	4.4	7.9	10.4	23.4
Benzenes	39.9	47.4	56.2	60.0	43.1	40.1
Indanes	5.5	4.5	0.5	3.5	0.9	0.8
Naphthalenes	23.2	12.2	15.8	11.0	11.8	8.4
Tetralins	2.5	1.2	0.3	0.6	0.3	0.6
Decalins	0.0	0.0	0.0	0.0	1.0	0.5
Tri-ring +	19.0	25.9	20.6	14.7	29.8	17.2

GC/MS analyses showed that the jet fuel fractions were composed of paraffins, saturated cyclics, benzenes, and lower quantities of naphthalenes, tetralins, decalins and very little (~2%) indanes (**Table 5-82**). No tri-ring + compounds were identified in jet fuel fraction. As observed in gasoline fractions, saturated cyclic species were observed in higher quantities as the hydrotreatment level of decant oil increased. These results are consistent with the hydrotreatment levels of decant oil and increased quantity of saturated cyclic species provide an advantage to jet fuel against to thermal cracking at elevated temperatures.

Diesel fraction GC/MS analyses showed that these fractions consisted mainly of highly-alkylated benzenes, naphthalenes and tri-ring + structures (**Table 5-83**). An obvious increasing trend was observed for the saturated cyclics (~5% to ~23%), but decreasing trends were observed for indanes (~6% to ~1%) and naphthalenes (~23% to ~8%) as the hydrotreatment level increased (from run # 27 to #32). In gasoline and jet fuel fractions saturated cyclic compounds were generally alkyl substituted cyclohexanes, but in the diesel fraction, these saturated cyclic structures also contained saturated higher-ring species. In the diesel fractions, either no decalins were observed (for the first four co-coking experiments (Run # 27-30)), or very small amounts of decalins (~1%) were observed (in the other two co-coking runs (Run # 31 and 32)).

Our earlier decant oil/coal co-coking studies showed that both decant oil light fraction and coal-derived light hydrocarbons were co-distilled [**5-110**]. In these six co-coking experiments, the only changing parameter was the hydrotreatment severity of decant oil used. The effect of hydrotreatment level of decant oil can be seen in each of the vacuum fractions, such as an increase of hydrogenated species (saturated cyclics, decalins, etc.) and a decrease of aromatics (naphthalenes, benzenes, etc.).

5.6.3.3 Conclusions

Increased hydrotreating severity resulted in decreased tri-ring + molecules and increased smaller molecules (e.g., naphthalenes, indanes, benzenes) and hydrogenated species of these smaller molecules (e.g., tetralins, decalins, saturated cyclics). Use of the PSC provides sufficient quantities of distillate liquids so as to provide distillable product from co-coking reactions. Vacuum distillation of the collected distillate liquids from co-coking experiments was performed to provide gasoline, jet fuel, diesel, and fuel oil products. The boiling point distributions and

chemical compositions in the co-coking experiments were found to be relatively dependent on hydrotreatment levels of decant oil. An increase in saturated cyclics, tetralins and decalins, but a decrease in paraffins, benzenes, and naphthalenes in the co-coking experiments, was measured by GC/MS as the hydrotreatment severity increased. No tri-ring + compounds were identified in gasoline and jet fuel fractions. The data support hydrotreatment of the decant oil as a means of providing a potentially thermal stable jet fuel [5-119] via increasing the saturated cyclics and decalins contents of jet fuel fraction. Our earlier results also showed [5-108] that coal introduction to the delayed coker increased the aromatic content of delayed coker distillate liquid. Further hydrotreatment/hydrogenation of the overhead liquid could increase the quantities of thermally stable jet fuel.

5.7 Production of Coal Tar from Coal Extraction

Refined Chemical Oil (RCO) is a distillate produced from the refining of coal tar (a by-product of metallurgical coke industry) and it represents around 10% of the coal tar yield. RCO consists mainly of a mixture of naphthalene (70%), indene and their derivatives. It is of special interest to current research at Penn State as it is blended with Light Cycle Oil (LCO) derived from the catalytic cracking of petroleum, for further processing. Upon hydroprocessing, the blend can be converted to process streams containing a high concentration of two-ring aromatic compounds (tetralin and decalin) that can then be used to formulate a thermally stable jet fuel. Unfortunately, under current environmental regulations it is unlikely that new by-product coke ovens will be built in the United States and the older remaining facilities are in danger of being closed. Therefore, a stable supply of RCO for the future is questionable.

With this in mind, it is important to consider alternative ways of producing RCO from coal in a very inexpensive process. Direct coal liquefaction would not be considered as an option, because there is no indication that this process would be economically competitive with petroleum processes. In order for a new process to be economic, it should be able to be integrated into a refinery. Therefore, it should use operating units, chemical reagents and/or solvents that are used or produced in a refinery. In this sense, the processes expected to be used are those that do not require expensive chemical reagents (in particular catalysts and consumption of hydrogen) and do not consume high quantities of energy. The processes that could possibly produce useful two-ring compounds from coal and meet these criteria are some form of solvent extraction of coal.

Because our objective is to use coal-derived materials in blends with LCO, it was decided to try LCO as the solvent for the extraction. This would save the steps of stripping the solvent off the extract, blending the extract with LCO, and recycling the solvent. Our initial aim was to produce an extract using a 1:1 LCO/Coal blend that could be sent to a hydrotreating and hydrogenation process up-stream in the refinery to end with the production of the highly thermal stable jet fuel. In the research performed during the project and discussed below, a variety of coal-extraction processing schemes were evaluated to meet these goals.

5.7.1 Experimental

Samples

A variety of coals were obtained from Argonne National Laboratory Premium Coal Sample Bank as well as the Penn State Coal Sample Bank to cover a broad distribution of rank and thermoplastic properties. The coals used in this work were ground to –60 mesh (250 μm) and their ultimate and proximate analyses are given in **Table 5-84**. The LCO used as a solvent to extract organic components from these coals was obtained from United Refining Company, Warren PA. The properties of this solvent are listed in **Table 5-85**.

Table 5-84 Coal properties.

	Pittsburgh	Powellton	Blind Canyon	Illinois # 6	Upper Freeport	Splash Dam
ASTM Rank	hvAb	hvAb	hvAb	hvCb	mvp	mvp
Proximate Analysis (dry)						
Ash, %	10.25	5.00	5.84	13.39	13.18	3.89
Volatile Matter, %	36.02	29.90	44.50	40.83	27.45	30.13
Fixed Carbon, %	53.73	65.10	49.66	45.78	59.37	65.98
Ultimate Analysis (dry)						
Carbon, %	83.32	87.60	81.28	76.26	85.5	87.83
Hydrogen, %	5.69	5.80	6.24	5.30	4.7	5.36
Nitrogen, %	1.37	1.60	1.55	1.32	1.55	1.57
Sulfur, %	1.25	0.90	0.42	6.38	2.32	0.82
Oxygen, %	8.37	4.10	10.50	10.74	7.5	4.42
Thermoplastic Properties (Gieseler Plastometer & Free Swelling Index)						
Initial Softening Temperature, °C	387	385	400	366	373	383
Maximum Fluidity Temperature, °C	440	448	419	410	450	458
Solidification Temperature, °C	477	488	438	444	497	500
Fluid Temperature Range, °C	90	103	38	78	124	117
Maximum Fluidity (ddpm)	20002	30000	3	49	30000	28188
Free-swelling index	7.5	7.5	2	3	8.5	8

Thermal Extraction

Single-stage extraction at room temperature filtration

Figure 5-34 shows a schematic of the 165-mL stirred batch reactor initially used to carry out the extraction experiments. The reactor has a fitted impeller, which gives good mixing of the LCO/coal dispersion during the reaction. The reaction conditions were 350 °C, 100 psi and 1

hour reaction time. Coals were dried in a vacuum oven at 100 °C at 30 mmHg overnight and cooled for one hour in a desiccator. The appropriate amount of LCO and coal were loaded in the reactor. The reactor was sealed and then placed in the heater. The sealed reactor was purged three times with 1000 psi (7 MPa) of ultra-high-purity N₂ (UHP, 99.999%) and finally pressurized to a 100 psi of N₂. When the temperature reached 70-80 °C below the reaction temperature, the stirrer was started and set at 1500 rpm. After the reaction, the reactor was brought to room temperature by immersing it in a cold water bath for 1 hour.

Table 5-85 LCO properties.

Properties		
API Gravity @ 60 °F, ASTM D-287	10.3	
Specific Gravity (gr/mL), ASTM D-1298	0.9979	
Sulfur (wt %), ASTM D-5453	1.92	
Nitrogen (ppm), ASTM D-5762	535	
Distillation (° C)	ASTM D-86	ASTM D-2887
IBP	220	146
10	266	249
20	277	271
30	286	279
50	296	301
70	313	324
80	324	341
90	336	359
FBP	354	396

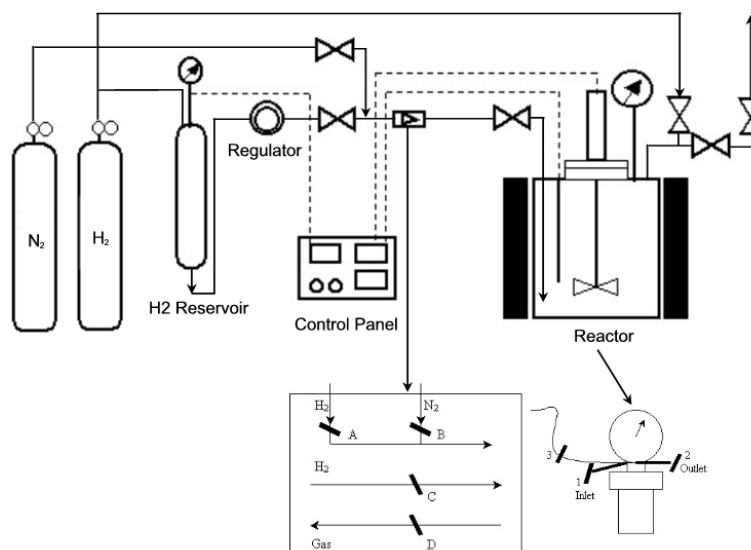


Figure 5-34 Schematic single-stage extraction at room temperature filtration reactor.

The LCO/coal dispersion was filtered using a Millipore filter (fine porosity) with a previously weighed PTFE filter. The reactor and the solid were washed with dichloromethane (DCM) until the supernatant became almost colorless. The resulting solid material, which is called the “residue” hereafter, was quantitatively transferred to a previously weighed Petri dish and then dried in a vacuum oven at 110 °C and 30 mmHg for at least 4 hours, cooled to room temperature in a desiccator for an hour and then weighed. This was repeated until a constant weight was obtained. The resulting solution, which is called the “extract” hereafter, was rotary evaporated in a water bath at 60 °C until all the dichloromethane was removed. In order to eliminate any remaining dichloromethane, the solution was held overnight in a vacuum oven without heating and then weighed. This was repeated until the loss of weight was less than 200 mg.

The extraction yields were calculated from the weight of initial amount of coal and residue on a dry ash-free basis according to **Equation 22**.

$$\text{Extraction Yield} = \frac{1 - \frac{\text{residue weight (gr)}}{\text{coal weight (gr)}}}{1 - \frac{\text{ash (wt \%, db)}}{100}} \times 100 \quad (1) \quad \text{Equation 22}$$

The extract yields were calculated with respect to the initial amount of coal according to **Equation 23** and with respect to the initial amount of LCO according to **Equation 24**.

$$\text{Extract Yield}_{\text{coal}} = \frac{\text{extract weight (gr)} - \text{LCO weight (gr)}}{\text{coal weight (gr)} \times \left(1 - \frac{\text{ash (wt \% , db)}}{100}\right)} \times 100 \quad \text{Equation 23}$$

$$\text{Extract Yield}_{\text{LCO}} = \frac{\text{extract weight (gr)} - \text{LCO weight (gr)}}{\text{LCO weight (gr)}} \times 100 \quad \text{Equation 24}$$

Single-stage extraction at high temperature filtration

Figure 5-35 shows a schematic of the high temperature extraction/filtration device. Initially coal extractions were carried out using a 1 L stirred autoclave (single-stage extraction) under typical reaction conditions of 350 °C, 100 psi and 1 hour reaction time. The coal/solvent slurries were prepared using different coal/solvent ratios. After the reaction, the reactants flowed down to a filter system for hot liquid/solid separation. The filtration system in the extraction device consists of a 47 mm stainless steel autoclave funnel holding a 0.45 µm PTFE filter.

The filtration system containing the remaining solid material can be separated from the extraction device. The funnel and solids were washed with dichloromethane (DCM) until the supernatant became almost colorless. The solid residue was dried in a vacuum oven at 110 °C and 30 mmHg for at least 4 hours, cooled to room temperature in a desiccator for an hour and then weighed. This was repeated until a constant weight was obtained.

Coal conversion was calculated using ash as a tracer according to Equation 4.

$$\text{Coal Conversion \%} = 100 \left[1 - \frac{A_0(100 - A')}{A'(100 - A_0)} \right] \quad \text{Equation 25}$$

Where A' = ASTM ash of the dry residue and A₀ = ASTM ash of the dry coal.

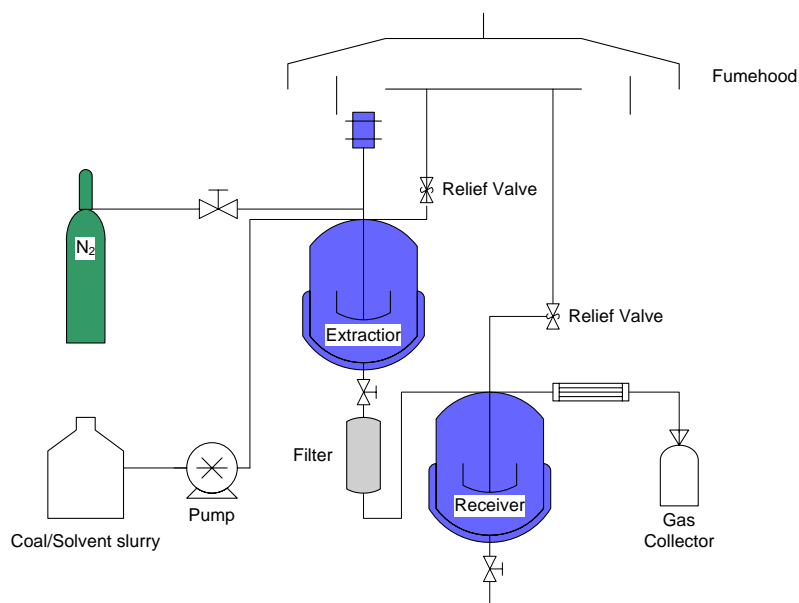


Figure 5-35. Schematic of the single-stage extraction at high temperature filtration device.

Multi-stage extraction in a flow reactor

Figure 5-36 shows a schematic of a flow reactor designed to carry out multi-stage extraction of coal. Coals were dried in a vacuum oven at 100 °C and 30 mmHg overnight and cooled for one hour in a desiccator. The three extraction cells were loaded with 3 gr of coal each. The system was purged three times with 1000 psi (7 MPa) of ultra-high-purity N₂ (UHP, 99.999%) and finally pressurized to 100 psi of N₂. The LCO was continuously flowed to the system by means of the HPLC pump using a rate of 1 mL/min and was preheated at 300 °C before entering in the extraction cells that were heated to 350 °C. After 1 hour of reaction time the HPLC pump and the furnace were turned off and allowed to cool down.

The remaining solid materials from each extraction cell were separately filtered using a previously weighed Millipore apparatus and a 0.45 µm PTFE filter. The cells and the solid were washed with dichloromethane (DCM) until the supernatant became almost colorless. The resulting residues were quantitatively transferred to a previously weighed Petri dish and then dried in a vacuum oven at 110 °C and 30 mmHg for at least 4 hours, cooled to room temperature in a desiccator for an hour and then weighed. This was repeated until a constant weight was obtained.

Coal conversion was calculated on a dry ash-free basis according to **Equation 26**.

$$\text{Coal Conversion (wt \% daf)} = \frac{\text{feed coal (daf)} - \text{residue (daf)}}{\text{feed coal (daf)}} \times 100 \quad (5) \quad \text{Equation 26}$$

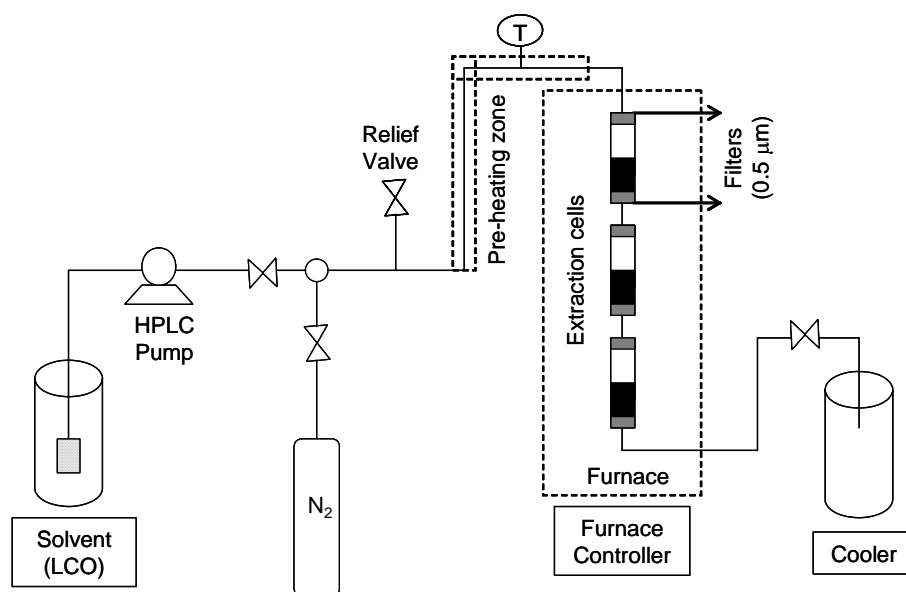


Figure 5-36. Schematic of the multi-stage extraction in a flow reactor.

Analyses

Fractionation of LCO and LCO/Pittsburgh extract

To characterize the material extracted from coal, the original LCO and the extract obtained from the Pittsburgh coal at 350 °C and LCO/coal 10:1 ratio were fractionated using preparative liquid chromatography. This method, known as PLC-8, was used to separate samples into eight discrete fractions with chemical identity very well defined [5-120] and has been used before to characterize the hydrocarbon products from coal processing [5-121].

In this procedure 300 mg of sample were dissolved in a minimal amount of THF, stirred with 2 g of Silica gel (Merck, grade 10181, 35-70 mesh) pre-activated for 4 hours at 180 °C and then the solvent was evaporated. The separation was carried out in triplicate using three 50 cm (L) x 11 mm (I.D.) glass columns fitted with a Teflon stopcock that were slurry packed. A plug of glass wool on the end was used to support the solid adsorbent. The slurry was packed by first adding the pre-activated Silica gel (18 g) a little at a time to hexane (60 mL) in a beaker, swirling the beaker and placing the slurry into a draining column previously filled about 1/3 full with hexane that was mechanically agitated. The sample-coated silica gel was placed on the top of the column. The elution was performed with the mobile phases and the volume listed in **Table 5-86**. The flow rate at the column outlet was maintained at 1.2 mL/min. The separation was

followed by collecting fractions of 10 mL in 20 mL vials previously weighted. The solvents were evaporated to constant weight in a vacuum oven and then weighed; the material mass in the vial was determined by difference.

GC-MS Analyses

The GC-MS analyses were conducted on a Shimadzu GC174 coupled with a Shimadzu QP-5000 MS detector. The column used was a Restek XT15 (5% diphenyl/95% dimethylsiloxane) and the starting temperature is 40 °C, hold for 4 min, then heated up in stages to 150°C with a heating rate of 6 °C/min and then from 150 to 290 °C with a rate of 4 °C/min and held for 10 min. The initial and final pressures in the column were 48.9 and 144 kPa, respectively.

Table 5-86. Fractionation of samples by PLC.

Fraction	Fraction eluted	Eluent	Volume (mL)	Vials
F1	Saturated Hydrocarbon	Hexane	40	1-4
F2	Monoaromatic Hydrocarbon	Hexane	27	5-7
F3	Diaromatic Hydrocarbon	11.5% v/v benzene in hexane	36	8-11
F4	Triaromatic Hydrocarbon	32% v/v benzene in hexane	24	12-14
F5	Polynuclear Aromatic Hydrocarbon	32% v/v benzene in hexane	25	15-17
F6	Resins	3:4:3 v/v benzene/acetone/CH ₂ Cl ₂	65	18-23
F7	Asphaltenes	2:8 v/v acetone/THF	60	24-29
F8	Asphaltols	Methanol	65	30-35

Proximate Analyses

The proximate analyses were carried out using a LECO MAC-400 analyzer. This instrument measures moisture, volatile matter and ash yields by determining the weight lost after having been heated under different atmospheric and thermal conditions. The fixed carbon is a calculated value determined as the difference from 100 of the measured values (moisture, volatile matter and ash).

5.7.2 Results and Discussion

Single-stage extraction at room temperature filtration

The extraction and extract yields at 350 °C and different LCO/coal ratio are shown in **Figure 5-37**. The extraction yields are in the range of 30 to 50 wt %. These results are comparable to the results reported by Takanohashi et al. [5-122] using LCO and crude methylnaphthalene oil at 360 °C to extract bituminous and sub-bituminous coals to produce an ashless coal (hypercoal). In this work extraction yields between 34-42 wt % were obtained. In the current investigation, the highest extraction yields were found using a LCO/coal ratio of 10:1, which suggests that the greater the amount of LCO available in the process, the better extraction and extract yields. Under these conditions and as shown in **Figure 5-37** the extraction yields were 39 wt % for Pittsburgh, 29 wt % for Powellton, 51 wt % for Illinois#6, 36 wt % for Upper Freeport and 46 wt % for Blind Canyon.

Takanohashi et al. [5-122 – 5-125] have reported that the high extraction yields obtained with industrial, non-polar and non-hydrogen donor solvents like LCO may be the result of heat-induced structural relaxation followed by solubilization of coal component in the solvent. This means that there is not a strong interaction between LCO and coal that would make it possible to break the bonds that keep the coal network structure intact. Instead, it appears that the LCO acts to disperse the components derived from the coal bulk during the onset of the softening process. **Figure 5-38** shows that under the thermal conditions employed, there is a very strong relationship between coal rank (volatile matter) and extraction yields. This result seems to confirm that LCO can act as an effective vehicle to move material out of the coal network during the extraction process.

Another way to evaluate extract yields would be to calculate them with respect to the initial amount of coal and LCO. The extract yield with respect to the initial amount of LCO provides a measure of the amount of material dispersed from coal into the LCO. If we call the material extracted RCO, then a RCO/LCO ratio can be determined. **Figure 5-37** shows that these extract yields ranged between 3 to 7 wt % and that the LCO/Blind Canyon extraction gave the best extraction yields since the resultant blend raised almost 1/9 RCO/LCO.

The results presented here suggest that even when extraction yields were high enough, the high LCO/coal ratios (10:1) used produced a RCO/LCO blend that was still too concentrated

with respect to LCO and too diluted with respect to RCO. It was not possible to employ a RCO/LCO 50/50 blend in a coal extraction process conducted in one single-stage. Presumably, greater extraction yields would be obtained from a multi-stage extraction process. However, the greatest level of extraction and extract yields were obtained in this study at 350 °C, 10:1 LCO/coal ratio, 1 hour reaction time and 100 psi N₂. Conditions such as these, at relatively low severity, may be the basis for an economic extraction process.

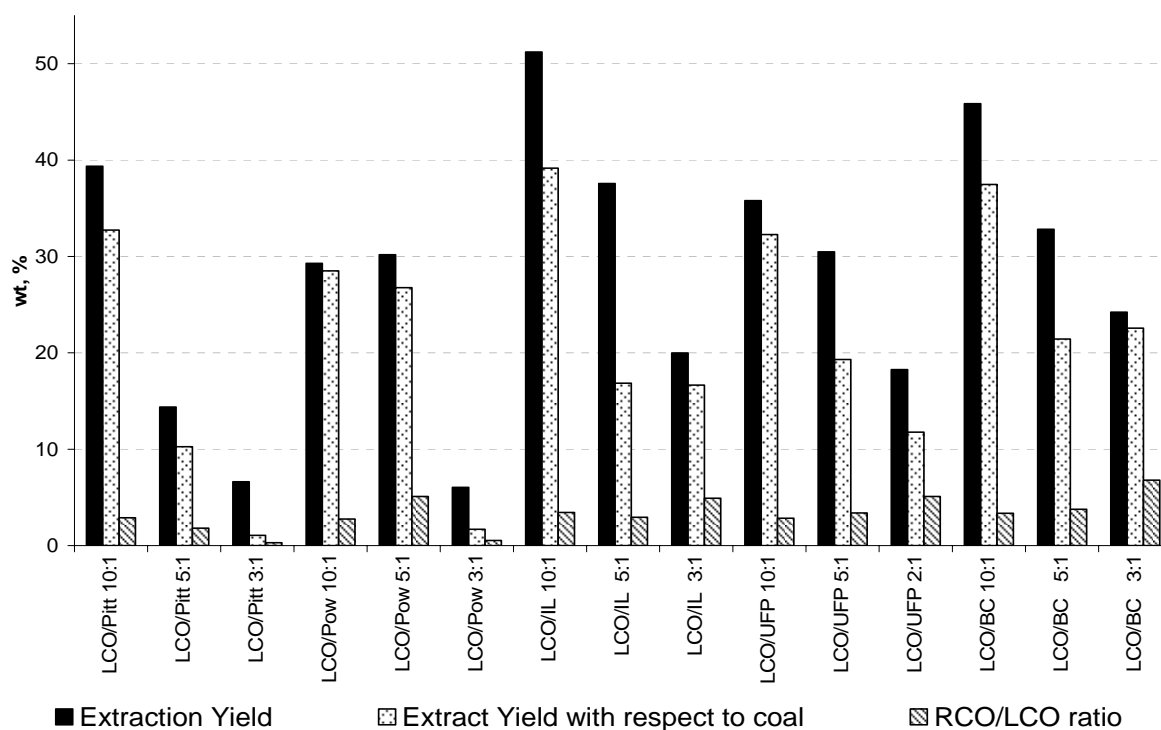


Figure 5-37 Extractions yields for LCO/coal extraction of bituminous coals at 350 °C.

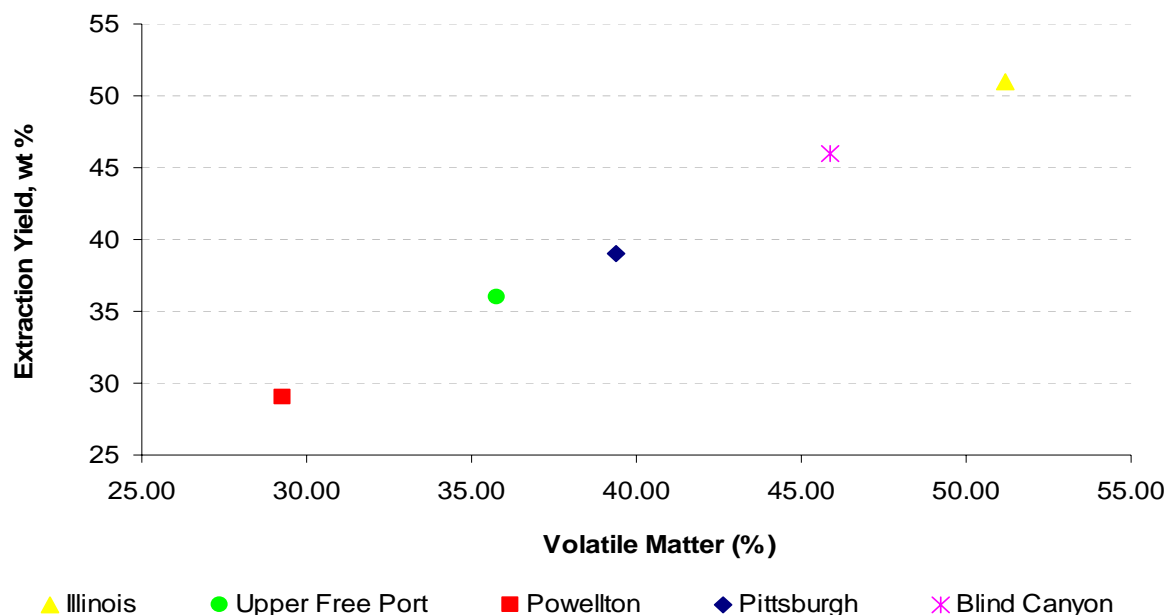


Figure 5-38 Correlation between the extraction yields and the coal volatile matter.

A combination of preparative liquid chromatography and GC/MS were used to determine the chemical nature of materials that may have been extracted from the Pittsburgh seam coal. **Figure 5-39** shows the results obtained from preparative liquid chromatography. In the fraction 5 (F-5) of the LCO/Pittsburgh extract, a material was detected that was not present in the original LCO used to make the extraction. GC-MS analyses of at least one vial for each fraction obtained from this separation were studied.

The GC-MS analyses are shown in **Figure 5-40**. Fraction 1 (F-1) of the LCO and the LCO/Pittsburgh extract were very similar in that they contained mainly saturated hydrocarbons in the range of C_{13} - C_{23} . Fraction 2 (F-2) of the LCO and the LCO/Pittsburgh extract were also very similar and these contain only monoaromatic hydrocarbons with long side chains (C_9 - C_{15}). Fraction 3 (F-3) of LCO and LCO/Pittsburgh extract were still very similar, but they were more complex than the two previous fractions. The major constituents of these fractions were basically naphthalene and alkyl-naphthalenes, although indans and tetralins were also found in very low concentrations. To this point fractionation was very selective in the kind of compound concentrated in each one of these fractions.

In Fraction 4 (F-4), the GC-MS analyses begin to show some differences between the sample coming from LCO and the sample coming from LCO/Pittsburgh extract. These fractions

contained a mixture of diaromatic and triaromatic compounds. The chromatogram corresponding to the fraction of LCO showed that the concentration of diaromatic compounds appeared to decrease as the concentration of triaromatic compounds increased. In the case of the chromatogram corresponding to the fraction of LCO/Pittsburgh extract the concentration of diaromatic compounds was still very high.

Fraction 5 (F-5) of the LCO/Pittsburgh extract appeared to contain material extracted from coal. Comparison of the chromatograms of LCO and LCO/Pittsburgh extract showed that the concentration of organic material was higher in the LCO/Pittsburgh extract. The presence of naphthalene, biphenyl, fluorene, benzothiophene, dibenzothiophene, phenanthrene and anthracene in extracts from coal also have been reported by other researchers [5-126 – 5-130].

Fraction 6 (F-6) from LCO/Pittsburgh contained mainly oxygen and nitrogen containing compounds that were not present in the original LCO. Fractions 7 and 8 (F-7 and F-8) from LCO/Pittsburgh were similar to Fraction 6 (chromatogram are not shown here). More details about the characterization of these fraction can be found elsewhere [5-131].

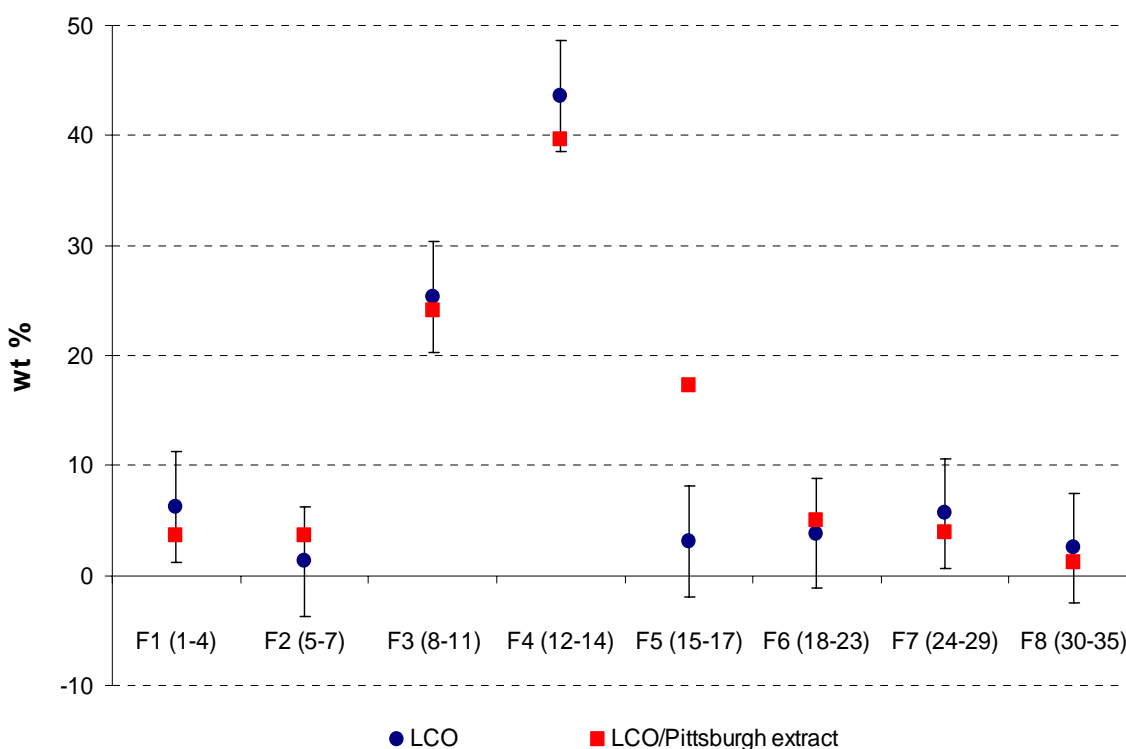


Figure 5-39 Results of the fractionation of LCO and Pittsburgh coal extract obtained from preparative liquid chromatography.

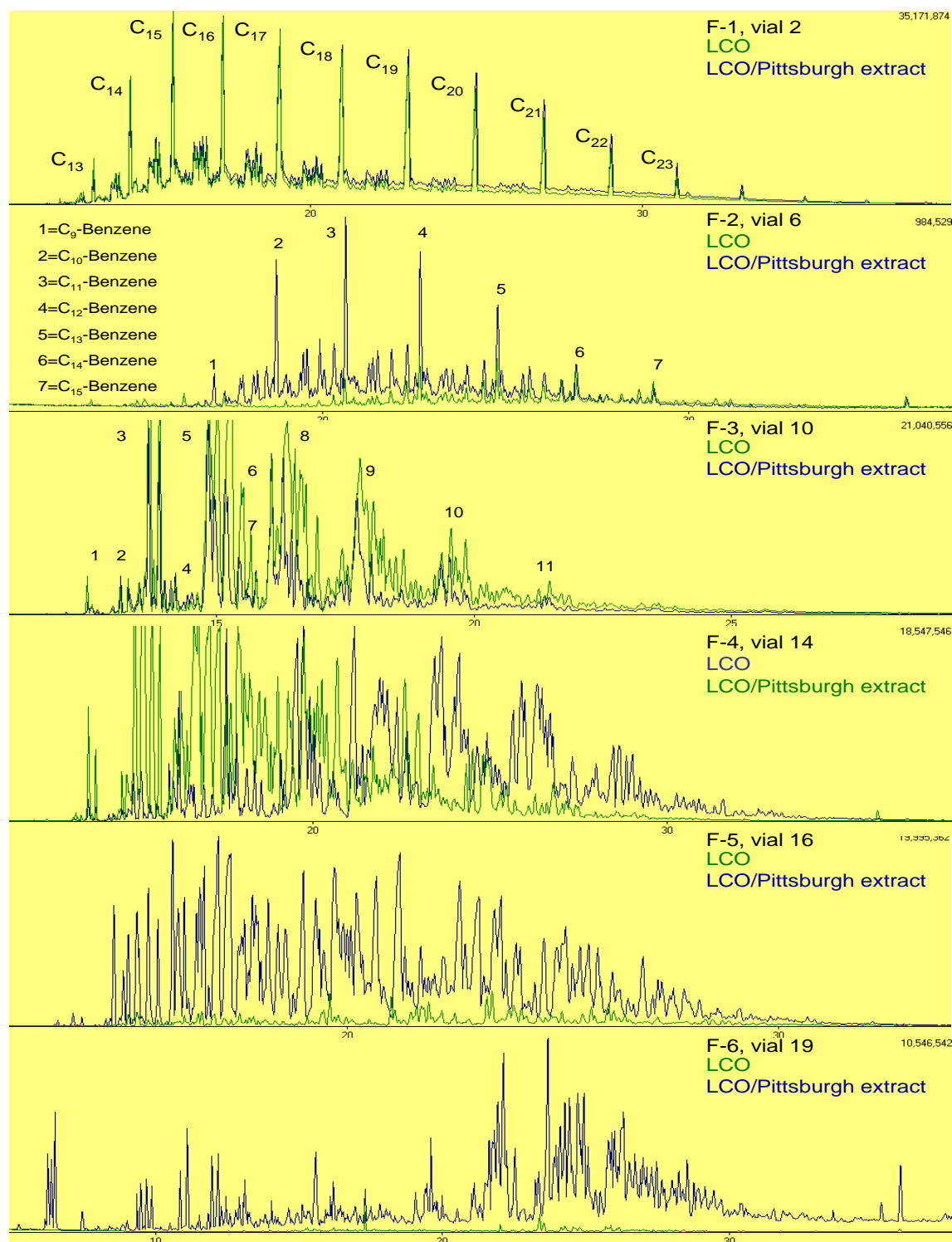


Figure 5-40 GC-MS results from the fractionation of LCO and Pittsburgh coal extract obtained from preparative liquid chromatography.

Single-stage extraction at high temperature filtration

Results of coal conversion using single-stage extraction at high temperature filtration are shown in **Table 5-87**. Coal conversion was found to be in the range of 36-59 % wt. and, as expected, was higher for the hvAb coals than for the mvb coal. Also, it was observed that conversion yields were higher for this series of experiments than those obtained in previous results that did not employ hot filtration. Using high temperature filtration allowed the extraction of the heavy material that was soluble at high temperature which in consequence increased the coal conversion [5-132 – 5-134].

Table 5-87. Coal conversion for single-stage extraction at high temperature filtration.

Coal Seam	Coal Conversion, % wt
Pittsburgh	52
Powellton	54
Blind Canyon	59
Illinois # 6	55
Splash Dam	36

Figure 5-41 shows the result of the proximate analysis for the original coals and their residues. From the comparison of the volatile matter of the original coal and the residue from the extraction, it can be observed that the volatile matter decreased in the residue as a consequence of the loss of organic matter that have been extracted with LCO and resulted in an increase in the ash yield and fixed carbon.

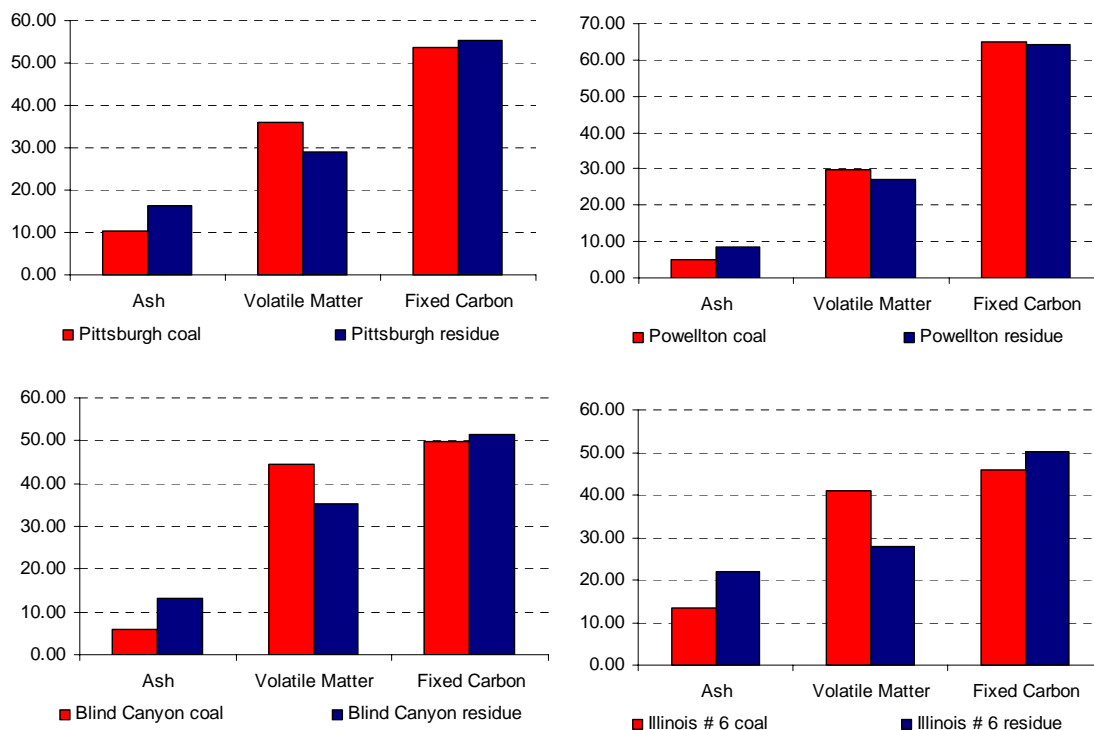


Figure 5-41 Proximate analysis of original coal and residue.

Figure 5-42 shows the result of the MALDI analysis of the extract. It can be observed that in all the extracts, except for the LCO/Blind Canyon extract, there was a higher concentration of the material with molecular weight ranging 200-400 mass/charge. It is suspect that this material was mainly composed of aromatic units with 4-6 fused rings, but further characterization needs to be done.

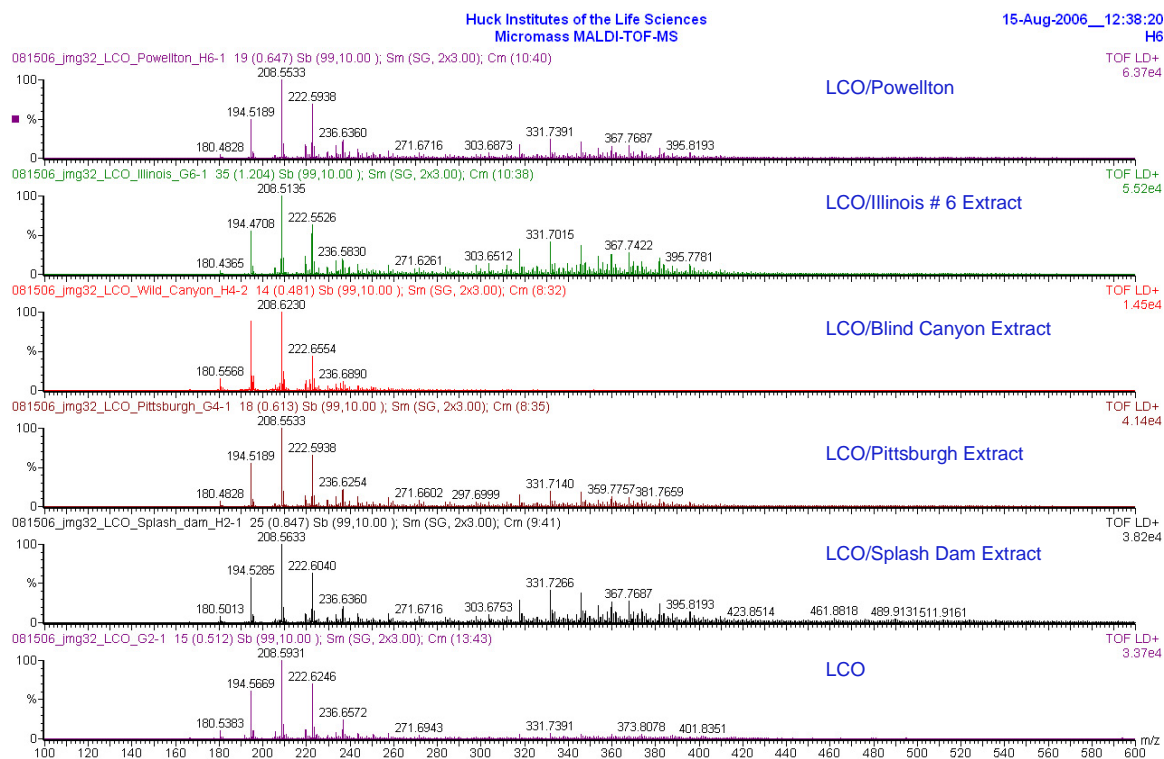


Figure 5-42 Result of the MALDI analysis of the extract.

Multi-stage extraction in a flow reactor

The results of coal conversion from the extraction of Pittsburgh seam coal in the flow reactor system are shown in **Table 5-88**. Conversion of Pittsburgh coal from the three cells was found to be between 64-74 wt%, which represents a significant increase with respect to conversion reached using the single-stage systems. It has been reported by others [5-132 – 5-134], that hot filtration increases coal conversion because it permits extraction of the coal fraction soluble at high temperature. In the multi-stage system investigated here a steady increase in conversion was observed from cell 1 to 3. One possible explanation for increased conversion is that the RCO enrichment of the LCO has a positive influence in extraction process.

Unfortunately, we were unable to run more experiments in the flow reactor system because the porous metal filter used in this reactor became plugged. During our second trial system pressure reached a very high level and was consider unsafe to continue. As these porous metal filters are very expensive, we will continue to explore another type of filter. Future research will include the mass balance and coal conversion for the extraction process for bituminous coals using LCO and DO (decant oil) as solvents.

Table 5-88. Results of Pittsburgh extraction using a flow reactor system.

Cell	Feed coal (gr)	Residue (gr)	Coal Conversion wt, %
1	3.085	1.316	63.891
2	3.120	1.125	71.245
3	3.093	1.046	73.740

5.8 Solubility Prediction of Coals in Some Petroleum Streams

Previous work at The Energy Institute at Penn State University has shown that hydrogenated two-ring compounds are desirable components of a jet fuel, as these compounds have good resistance to pyrolytic decomposition in aircraft fuel systems [5-135]. These desirable bicyclic compounds can be made by hydrogenation of two-ring aromatic compounds liberated from coals. In principle, any coal conversion process that gives high yields of two-ring compounds could be suitable as a “front end” for the production of highly thermally stable coal-based jet fuel. The research project discussed in this paper specifically focuses on understanding the solubility of bituminous coal with various petroleum derived solvents for coal extraction and co-coking in a delayed coking process.

This work was an attempt to predict the coal and solvent interaction by calculating the solubility parameter of the solvent and the coal. Hence, according to the solubility parameter, a given coal will be miscible in a solvent with a similar solubility parameter value [5-136]. The solubility parameters have been reported for pure solvents; however, these values have not been reported for complex mixtures (i.e. petroleum streams and coal liquids). In this work, the solubility parameters of complex mixtures were calculated using Hoy’s method using the solubility parameter of group contribution [5-137]. The solubility parameter of the coal is determined by comparative swelling with pure solvents. In addition, some swelling experiments were carried out with pure solvents to know more about the interaction between coal and components that are potentially present in petroleum streams.

Two thermal processes have been identified as possible processing methods of coal-based feedstock for the production of jet fuel with high concentrations of cycloalkanes and hydroaromatics: 1) co-coking and 2) coal solvent extraction. The advantages of these two processes relative to coal liquefaction are no need of an external source of hydrogen, no catalyst requirement, and low pressure operation. Solvent extraction of coal under thermal conditions has been examined as a potential route to produce 2-ring compounds from coal. As discussed in Section 5.7, light cycle oil (LCO) was used as the solvent with coal at 350°C to produce a blend suitable for JP-900 formulation [5-138, 5-139]. The co-coking process involved the thermal treatment of a bituminous coal with decant oil (DO) at 456°C to produce a high value carbon product [5-140, 5-141] and liquids (see Sections 5.2.2, 5.6.2) that could be upgraded to produce JP-900.

Both processes involve the solubilization of bituminous coals in a petroleum stream, i.e., LCO or DO, as well as the reactivity of coal and solvent at the temperatures of each type of reaction. If either of these processes is going to be scaled-up, it is important to understand how the solubility of the coal in either of these solvents may affect each reaction. The following reports the calculated solubility parameter of pyrolysis tar (PyTar) from ethylene processing, refined chemical oil (RCO) from metallurgical coking, LCO, and DO from petroleum processing. These parameters will be compared with the solubility parameters of the coals used in co-coking and coal extraction to predict the solvent–coal interaction.

5.8.1 Experimental

Calculation of solubility parameter of complex mixtures

Hoy developed a method to calculate the solubility parameter using the molar volume and the molar attraction constants determined by van Krevelen [5-137]. **Table 5-89** shows the constants for various functional groups [5-137]. Rodriguez et al. [5-142] adapted this method from ¹³C-NMR data, integrating the area of the spectrum related to functional groups. These data are used to calculate the solubility parameter, δ , according to **Equations 5-26-5-31**.

The percentages of each functional group (N_i) were calculated by integrating the ¹³C-NMR spectra according to the chemical shift reported in **Table 5-90**. The calculation is shown in **Equation 26**.

$$N_i = \frac{\text{peak integration range functional group}_i \text{ } ^{13}\text{CNMR}}{\text{total integration } ^{13}\text{CNMR}} \times 100 \quad \text{Equation 5-26}$$

F_i^* and V_i^* are reported in the literature for each functional group [5-137]. ΔF was then calculated by multiplying each percentage (N_i) by the F^* reported for each individual functional group; ΔV was calculated by multiplying each percentage (N_i) by the V^* reported for each individual group. These calculations are shown in **Equations 27 and 28**.

$$\Delta F = F_i^* \times N_i \quad \text{Equation 5-27}$$

$$\Delta V = V_i^* \times N_i \quad \text{Equation 5-28}$$

F_T and V_T are calculated summing the F and V of each functional group

$$F_T = \sum ^F \quad \text{Equation 5-29}$$

$$V_T = \sum ^V \quad \text{Equation 5-30}$$

Then, solubility parameter δ , is calculated by:

$$\delta = \frac{F_T}{V_T} \quad \text{Equation 5-31}$$

¹³C-NMR analysis of complex mixtures for solubility parameter

The samples were analyzed on a Bruker AMX 360 NMR operating at 9.4 Tesla and a 70° tip angle. PyTar, RCO, LCO and DO were dissolved in CDCl₃ for analyses. **Table 5-90** shows the regions of integration for various functional groups. The integration from the area for each functional group was used to determine the percentage contribution of functionality (N_i) for the solubility parameter calculation.

Swelling experiments to determine coal solubility parameter

Six different bituminous coals were studied and their properties are listed in **Table 5-91**. The coals were previously extracted under N₂ atmosphere with pyridine at its boiling point (115 °C) for 48 hours. Eight pure solvents were used to determine the maximum swelling of the coals and their properties are listed in **Table 5-92**. Under this procedure, the swelling was carried out in NMR tubes 5 mm id and 7" long. About 0.1 g of coal was weighed into each NMR tube and then centrifuged at 7500 rev/min for 3 min; the initial height of the coal (h_1) was measured. About 1 g of solvent was added to the NMR tube, allowed to interact with the coal for 24 h, and then again centrifuged at 7500 rv/min for 3 min. The final height of the swollen coal (h_2) was recorded at regular time intervals. The swelling ratios $Q=h_2/h_1$ were reported.

Table 5-89: Molar volume, attraction constant, based on Hoy's calculation [5-137].

Functional group	Molar Volume Constant V^* (cm ³ /mol)	Molar Attraction Constant F^* ((J.cm ³) ^{0.5} /mol)
-CH ₃	21.55	303.5
-CH ₂ -	15.55	269.0
>CH-	9.56	176.0
>C<	3.56	65.5
=CH ₂	19.17	259
=CH-	13.18	249
=C<	7.18	173
CH ar	13.42	241
C ar	7.42	201
-C≡N	23.1	725
-O- ether	6.45	235
acetal	6.45	236
epoxy	6.45	361
-OH phenolic	12.45	350

F^* is reported in (J.cm³)^{0.5}/mol;
hildebrands (cal.cm³)^{0.5}/mol = ((J.cm³)^{0.5}/mol) / 2.0455

Table 5-90: Match between functional groups reported by Rodriguez et al. [5-142] (¹³C NMR) and by Hoy [5-137] method (molar attraction constant).

Functional group		Band, TMS (ppm)	Molar Volume Constant V^* (cm ³ /mol)	Molar Attraction Constant F^* ((J.cm ³) ^{0.5} /mol)
	-CH ₃	11-22.5	21.6	303.5
	-CH ₂ -	22.5-37	15.55	269
	>CH-	37-60	9.56	176
N-C _{aliphatic} [^]		60-65	23.1	725
O-C _{aliphatic} [*]		65-75	6.45	236
Olefinic		108-118	13.18	249
Internal quaternary aromatic	>C Ar	118-128	7.42	201
protonated aromatic	>C=HAr	128-135	13.42	241
Naphthenic substituted Ar		135-138	7.18	173
Heteroatom (N,O,S) aromatic ^{&}		138-160	12.45	350

[&] phenol was selected as the example for heteroatom (N,O,S) aromatic;

^{*} acetal was selected as the example for O-C aliphatic;

[^] -C≡N was selected as the example for N-C aliphatic

5.8.2 Results and Discussion

An example of the solubility parameter calculation is shown in **Table 5-93** for heptane. Molar attraction functions F and V are reported elsewhere [5-137]. As discussed in the experimental section, the integration values obtained from the experimental ^{13}C -NMR are used to calculate the percentage of each functional group (N_i). The solubility parameters of ten solvents (heptane, pentadecane, decalin, tetralin, toluene, THF, 1-methylnaphthalene, quinoline, nitromethane and methanol) were calculated using the method described above. The solubility parameter values reported in the literature, δ , are compared to the values calculated using the solubility parameter component group contributions by using ^{13}C -NMR, and these are shown in **Figure 5-43**. The correlation from the solvents was used as a way to correct the solubility parameter values for our complex liquids; the equation developed from the slope in **Figure 5-43** is shown in **Equation 5-32**.

Table 5-91: Coal Properties.

Seam	Pittsburgh	Upper Kittanning	Blind Canyon	Illinois # 6	Marfork Plant	Powelton-Eagle
Locality	Greene Co., PA	Barbour Co., WV	Emery Co., UT	Macoupin Co., IL	Raleigh Co., WV	Raleigh Co., WV
Rank	hVAb	hVAb	hVAb	hVCb	hVAb	hVAb
Proximate Analysis (dry)						
Ash, %	10.25	10.25	6.57	13.39	7.2	5.00
Volatile Matter, %	36.02	32.59	46.75	40.83	34.5	29.90
Fixed Carbon, %	53.73	56.89	46.68	45.78	58.3	65.10
Ultimate Analysis (daf)						
Carbon, %	83.32	85.20	81.61	76.26	87.1	87.60
Hydrogen, %	5.69	5.46	6.21	5.30	5.5	5.80
Nitrogen, %	1.37	1.45	1.38	1.32	1.6	1.60
Sulfur, %	1.25	2.01	0.47	6.38	1.1	0.90
Oxygen, %	8.37	5.87	10.33	10.74	4.7	4.10
Gieseler Coal Plastometer and FSI						
Initial Softening Temperature, °C	387	376	387	366	384	385
Maximum Fluidity Temperature, °C	440	446	420	410	448	448
Solidification Temperature, °C	477	485	442	444	492	488
Fluid Temperature Range, °C	90	109	55	78	108	103
Maximum Fluidity (ddpm)	20002	29930	5	49	30000	30000
Free-swelling index	7.5	8	2	3		7.5

Table 5-92: Solvent Properties.

Solvent	MF	MW (g/mol)	BP (°C)	MP (°C)	D (gr/mL)	δ cal ^{1/2} cm ^{-3/2}	δ d1	δ p1	δ h1
Pentadecane	C ₁₅ H ₃₂	212.42	270	9.9	0.769	8.21	8.2	0.0	0.0
Toluene	C ₇ H ₈	92.1	110.6	-93	0.865	8.9	8.8	0.7	1.0
THF	C ₄ H ₈ O	72.1	65-67	-108	0.889	9.1	8.2	2.8	3.9
Carbon Disulfide	CS ₂	76.1	46	-112 to -111	1.263	9.97	10.0	0.0	0.3
Quinoline	C ₉ H ₇ N	129.16	237.1	-15	1.093	10.81	9.5	3.4	3.7
1-Methyl-2-Pyrrolidinone	C ₅ H ₉ NO	202	202.0	-24	1.033	11.30	8.8	6.0	3.5
Nitromethane	CH ₃ NO ₂	61.0	101.2	-29	1.127	12.9	7.7	9.2	2.5
Methanol	CH ₃ OH	32	64.6	-98	0.791	14.47	7.4	6.0	10.9

Table 5-93: Example of solubility parameter calculation for the heptane.

Band, TMS	Molar Volume Constant	Molar Attraction Constant	Integration from NMR	N _i	ΔF ((J.cm ³) ^{0.5} /mol)	ΔV (cm ³ /mol)
(ppm)	V* (cm ³ /mol)	F* ((J.cm ³) ^{0.5} /mol)				
11-22.5	21.6	303.5	20.572	28.77	8731.31	619.9662
22.5-37	15.55	269	31.695	44.32	11923.05	689.2319
37-60	7.18	173	18.004	25.18	4431.246	240.6972
75-80	6.45	236				
108-118	13.18	249	0	0.00	0	0
118-128	7.42	201	0.11685	0.16	32.84498	1.212486
128-135	13.42	241	0.05149	0.07	17.35338	0.966317
135-138	7.18	173	0.06885	0.10	16.6569	0.69131
138-160	12.45	350	1.00000	1.40	489.4544	17.41059
			$\Sigma J = 71.50819$	100	F _T =25641.91	V _T =1570.176
					F _T /V _T = δ	16.2 J ^{1/2} cm ^{-3/2}
			Experimental		$\delta =$	7.9 cal ^{1/2} cm ^{-3/2}
			Reported ²		$\delta =$	7.4 cal ^{1/2} cm ^{-3/2}

cal^{1/2}cm^{-3/2} or hildebrands = (J^{1/2} cm^{-3/2}) / 2.0455

F, V, and the solubility parameter δ before and after correction of the various complex liquids are shown in **Table 5-94**.

$$\delta_{corrected} = \frac{\delta_{^{13}\text{C NMR}} + 3.961}{1.484} \quad \text{Equation 5-32}$$

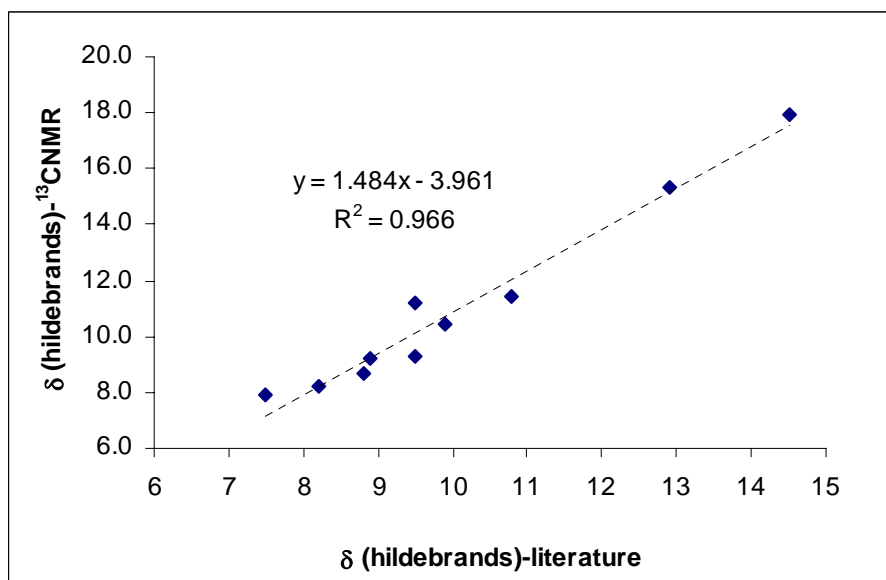


Figure 5-43: Correlation between the solubility parameters (experimental values obtained by ¹³C NMR vs. reported by the literature (van Krevelen, 1990))

Table 5-94: Solubility parameters of the petroleum streams

Petroleum streams	F _T (¹³ C NMR) (J.cm ³) ^{0.5} /mol)	V _T (¹³ C NMR) (cm ³ /mol)	F _T / V _T (¹³ C NMR) J ^{1/2} cm ^{-3/2}	F _T / V _T (¹³ C NMR) cal ^{1/2} cm ^{-3/2} or hildebrands	δ corrected from Eq.7 (hildebrands)
LCO	23,902.41	1,215.35	19.7	9.6	9.1
DO	23,525.67	1,158.52	20.3	9.9	9.4
Pytar	23,014.09	1,053.05	21.9	10.7	9.9
RCO	22,171.16	965.45	22.9	11.2	10.2

cal^{1/2}cm^{-3/2} or hildebrands = (J^{1/2} cm^{-3/2}) / 2.0455

The swelling spectra obtained for the six coals are shown in the **Figure 5-44**, representing the swelling of each coal in pentadecane, toluene, THF, carbon disulfide, quinoline, NMP, nitromethane and methanol. The maximum Q represents the maximum interaction between the solvent and coal, with the solvent solubility parameter δ listed above each solvent. The observation of these spectra allows us to say four of the five coals studied have two different maximum with different solvents. Marfork, Illinois and Blind Canyon coals present a maximum interaction with solvents with solubility parameters around 9 hildebrands, while Illinois and

Blind Canyon have a second maximum around 11.3 hildebrands; the second maximum of Marfork and Powellton-Eagle seemed to be centered between 10.8 and 11.3 hildebrands. On the other hand, Pittsburgh and Kittanning seem to have better interaction with solvents having solubility parameters around 10.8 hildebrands.

According to solubility parameter theory, the closer the solubility parameter values between coal and solvent, the better the interaction between the coal and solvent. Consequently we expect to achieve better coal/solvent interaction from Marfork, Blind Canyon, Illinois # 6 and possibly with Pittsburgh coal when they will be processed with LCO and DO (9.1 and 9.4 hildebrand, respectively) in our coal extraction plant. Kittaning and Powellton-Eagle coals should interact better with solvent of high solubility parameter. However, when thermal interactions are occurring simultaneously with the solubility, the interactions may change, especially for the co-coking process where the temperature is high enough cause significant carbon formation. For future work, after getting actual coal conversions from both processes, we will compare results and determine if the solubility parameter solubility parameter theory can provide insight into the reaction chemistry.

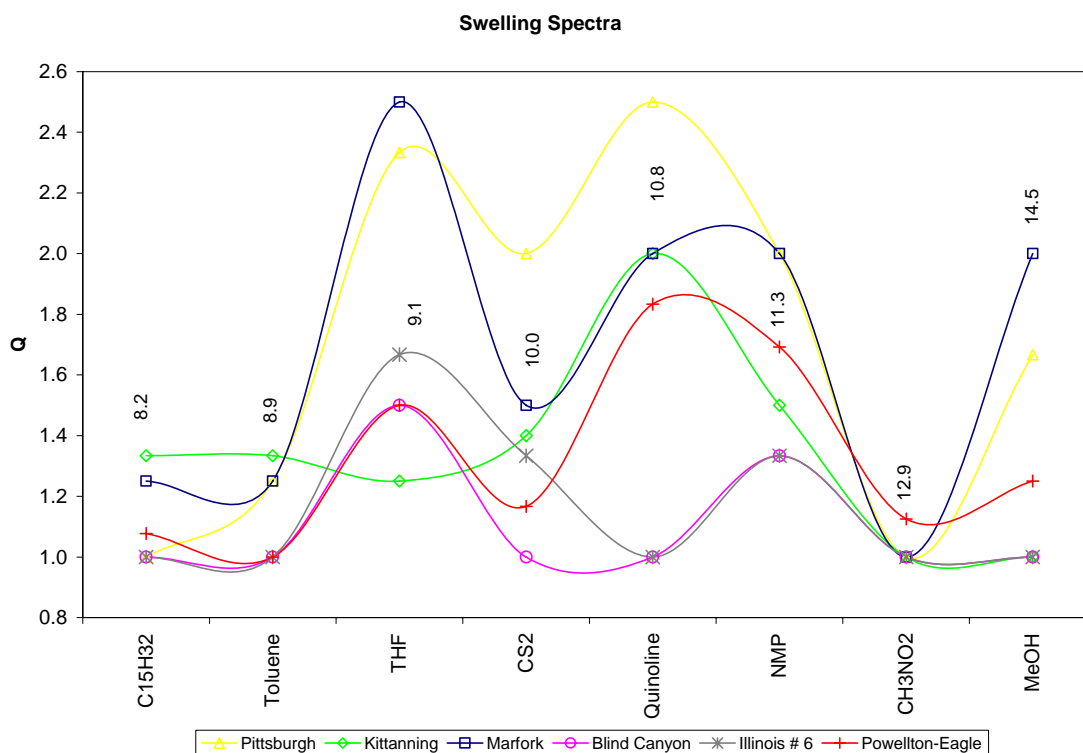


Figure 5-44: Swelling spectra of coals.

5.8.3 Conclusions

The solubility parameter of PyTar, RCO, LCO, and DO were calculated and compared to coals that were swelled using a range of solvents. According to our results, we expect to achieve better coal conversions from Marfork, Blind Canyon, Illinois # 6 and possibly with Pittsburgh coal when processed with LCO and DO (9.1 and 9.4 hildebrand, respectively) in our coal extraction plant. Kittaning coal should interact better with solvent of a higher solubility parameter. For future work, after getting actual coal conversions from both processes, we will compare results and determine if the solubility parameter solubility parameter theory can provide insight into the reaction chemistry. The information gleaned from these results may be useful in determining solvents that may interact well with particular coals.

References

- 1-1 Schobert, H. H., Advanced Thermally Stable Coal-Based Jet Fuels, *Annual Progress Report*, AFOSR Grant F49620-99-1-0290, 2001-2002
- 1-2 Schobert, H. H., Advanced Thermally Stable Coal-Based Jet Fuels, *Annual Progress Report*, AFOSR Grant F49620-99-1-0290, 2000-2001
- 1-3 Schobert, H. H., Advanced Thermally Stable Coal-Based Jet Fuels, *Annual Progress Report*, AFOSR Grant F49620-99-1-0290, 1999-2000
- 1-4 Coleman, M. M., Fearnley, S. P., Kumar, S. and Sobkowiak, M., Fuel Stabilization, AFRL-PR-WP-TR-2000-2007, Final Report for 07/01/1995 – 12/31/1998, September 1999.
- 1-5 Song, C., Lai, W.-C., Schobert, H.H. Hydrogen-Transferring Pyrolysis of Long-Chain Alkanes and Thermal Stability Improvement of Jet Fuels by Hydrogen Donors. *Ind. Eng. Chem. Res.*, **1994**, 33 (3), 548-557
- 1-6 Lai, W.-C and Song, C., *Prepr. Pap.- Amer. Chem. Soc. Div. Fuel Chem.* **1996a** 41:524
- 1-7 Lai, W.-C and Song, C., *Fuel Processing Technology*, **1996b** 48:1
- 1-8 Selvaraj, L., Sobkowiak, M., Song, C., Stallman, J., Coleman, M. M. A Model System for the Study of Additives Designed to Enhance the Stability of Jet Fuels at Temperatures Above 400°C. *Energy & Fuels*, **1994**, 8 (4), 839-845.
- 1-9 Yoon, E.M., Selvaraj, L., Song, C., Stallman, J., Coleman, M. M., High Temperature Stabilizers for Jet Fuels and Similar Hydrocarbon Mixtures. 1. Comparative Studies of Hydrogen Donors. *Energy & Fuels*, **1996a**, 10 (3), 806-811.
- 1-10 Yoon, E.M., Selvaraj, L., Eser, S. and Coleman, M. M., High Temperature Stabilizers for Jet Fuels and Similar Hydrocarbon Mixtures. 2. Kinetic studies, *Energy & Fuels*, **1996a**, 10 (3), 812-815.
- 1-11 Andrésen, J.M., Strohm, J.J., Boyer, M.L., Song, C, Schobert, H.H. and Butnark, S., *Am. Chem. Soc. Div. Petrol. Chem. Prepr.*, **2001a**, 46(1), 208-209.
- 1-12 Andrésen, J.M., Strohm, J.J., Sun, L., Song, C. *Energy & Fuels*, **2001b**, 15(3), 714-723.
- 1-13 Badger, M. W., Fickinger, A. E., Martin, S. C., Mitchell, G. D. and Schobert, H. H., *Proc. 8th Austrian Coal Science Conference*, **1998**, 245.

- 1-14 Badger, M. W., Fickinger, A. E., Mitchell, G. D., Adams, A. N. and Schobert, H. H., *Proc. 205th International Technical Conference on Coal Utilization and Fuel Systems (in press)*.
- 1-15 Butnark, S., Badger, M.W. and Schobert, H.H., *Amer. Chem. Soc., Div. Fuel Chem. Prepr.*, **1999**, 44 (3), 662-665.
- 1-16 Butnark, S., Badger, M. W. and Schobert, H. H., *Prepr. Pap.- Amer. Chem. Soc. Div. Petrol. Chem.*, **2000** 45:493.
- 1-17 Fickinger, A. E., **2000**, M. S. Thesis, The Pennsylvania State University, University Park, PA.
- 1-18 Fickinger, A. E., Badger, M. W., Mitchell, G. D. and Schobert, H. H., , *Prepr. Pap.- Amer. Chem. Soc. Div. Fuel Chem*, **1999**, 44:106.
- 1-19 Fickinger, A. E., Badger, M. W., Mitchell, G. D. and Schobert, H. H., , *Prepr. Pap.- Amer. Chem. Soc. Div. Fuel Chem*, **2000**, 45:299.
- 1-20 Song, C., and Schobert, H. H., , *Prepr. Pap.- Amer. Chem. Soc. Div. Fuel Chem.*, **2000**, 45:819.
- 1-21 Butnark, S., Badger, M. W. and Schobert, H. H., Determining the Desired Chemical Composition for Thermally Stable Jet Fuel, *Amer. Chem. Soc., Div. Fuel Chem. Prepr.*, **2001**, 46 (2), 492-494.
- 1-22 Butnark, S., Badger, M. W. and Schobert, H. H. and Wilson, G. R., Selection of Prototype Thermally Stable Jet Fuels 3. Jet Fuel Boiling Range and its Affect on Pyrolytic Stability, *Prepr. Pap.- Amer. Chem. Soc. Div. Petrol. Chem.*, **2002**, 47(3), 201.
- 1-23 Schobert, H. H., Badger, M. W. and Santoro, R. J., Progress Toward Coal-Based JP-900, *Prepr. Pap.- Amer. Chem. Soc. Div. Petrol. Chem.*, **2002**, 47:192.
- 1-24 Wilson, G. R., Project Report on AFOSR-Subcontract for Advanced Thermally Stable Coal-Based Jet Fuels for the Pennsylvania State University, PARC Technical Services Inc., Pittsburgh, PA. August **2002**.
- 1-25 Burgess-Clifford, C.E., Boehman, A., Song, C., Miller, B., Mitchell, G., “Refinery Integration of By-Products from Coal-derived Jet Fuels,” Semi-Annual Progress Report for Grant DE-FC26-03NT41828, May, 14, **2007**.
- 1-26 Rudnick, L. R., Boehman, A., Song, C., Miller, B., Mitchell, G. “Refinery Integration of By-Products from Coal-Derived Jet Fuels”, Semi-Annual Progress Report, Grant No. DE-FC26-03NT41828, November 17, **2005**.

- 2-1 Heywood, J. B. *Internal Combustion Engine Fundamentals*, McGraw-Hill: New York, 1988.
- 2-2 Yang, Y., J. P. Szybist, and A. L. Boehman, "Low Temperature Oxidation of Methylcyclohexane in an SI Engine," *Prepr. Pap.-Am. Chem. Soc., Div. Fuel Chem.* **2006**, 51(1), 329-330.
- 2-3 Lovell, W.G., "Knocking characteristics of hydrocarbons", *Industrial and Engineering Chemistry*, 1948, 40 (12), 2388-2438.
- 2-4 Tanaka, S.; Ayala, F.; Keck, J. C.; Heywood, J. B., *Combustion and Flame* **2003**, 132, (1-2), 219-239.
- 2-5 Lemaire, O.;Ribaucour, M.;Carlier, M.; and Minetti, R., "The production of benzene in the low-temperature oxidation of cyclohexane, cyclohexene, and cyclohexa-1,3-diene", *Combustion and Flame*, **2001**, 127(1-2), 1971-1980.
- 2-6 Gulati, S.K.; and Walker, R.W., "Additon of cyclohexane to slowly reacting H₂-O₂ mixtures at 480°C", *J. Chem. Soc.-Faraday Trans. II*, **1989**, 85, 1799-1812.
- 2-7 Szybist, J.P.;Boehman, A.L.;Haworth, D.C.; and Koga, H., "Premixed ignition behavior of alternative diesel fuel-relevant compounds in a motored engine experiment", *Combustion and Flame*, **2007**, 149(1-2), 112-128.
- 2-8 Boehman, A.L., J. Song, and M. Alam, "Impact of biodiesel blending on diesel soot and the regeneration of particulate filters." *Energy & Fuels*, **2005**. 19(5), 1857-1864.
- 2-9 Song, J., M. Alam, A.L. Boehman and U. Kim, "Examination of the oxidation behavior of biodiesel soot," *Combustion & Flame*, **2006**, 146:589-604.
- 2-10 Al-Qurashi, K. and A.L. Boehman, "The impacts of simulated exhaust gas recirculation on the oxidative reactivity of diesel soot," *Prepr. Pap.-Am. Chem. Soc., Div. Fuel Chem.* **2006**, 51(2), 805-807.
- 2-11 Kirby, S.R., A. L. Boehman, and D. J. Clifford, "Evaluation of coal-based diesel products affect on fuel quality," *Prepr. Pap.-Am. Chem. Soc., Div. Fuel Chem.* **2005**, 50 (2), 732-733.
- 2-12 **The Institute of Petroleum**, *Modern Petroleum Technology*, 3rd ed.; London **1962**; p 609.
- 2-13 Westbrook K. C., Pitz J. W., and Curran J. H, "Chemical Kinetic Modeling Study of the Effects of Oxygenated Hydrocarbons on Soot Emissions from Diesel Engines," *Phys.Chem. A* **2006**, 110, 6912-6922.
- 2-14 Vala, M., Eyler, R.J., Rearson, W., "Theoretical Study of Photo dissociation and Hydrogenation of Fluorene Cation," *J. Physics. Chem. A* **2001**, 105, 9388-9395.
- 2-15 Kittelson, D.B., "Engines and Nanoparticles: A Review.", *J. Aerosol Sci.*, **1998** , 29 (5-6), 575-588.

- 2-16 Rudnick, L. R., Boehman, A., Song, C., Miller, B., Mitchell, G. "Refinery Integration of By-Products from Coal-Derived Jet Fuels", Semi-Annual Progress Report, Grant No. DE-FC26-03NT41828, November 17, **2005**.
- 2-17 Tuinstra, F. and J.L. Koenig, "Raman Spectrum of Graphite." *Journal of Chemical Physics*, **1970**. 53(3), 1126-1130.
- 2-18 Chen, H.X. and R.A. Dobbins, "Crystallogenes of particles formed in hydrocarbon combustion," *Combustion Science and Technology*, **2000**. 159, 109-128.
- 2-19 VanderWal, R., "Soot Nanostructure: Dependence upon Synthesis Condition," *Combustion and Flame*, **2004**, 136, 129-140.
- 2-20 Escribano, R., et al., "Raman spectroscopy of carbon-containing particles," *Vibrational Spectroscopy*, **2001**. 26(2), 179-186.
- 2-21 Liu, F.S., et al., "The chemical effects of carbon dioxide as an additive in an ethylene diffusion flame: Implications for soot and NO_x formation," *Combustion and Flame*, **2001**, 125(1-2), 778-787.
- 2-22 Du, D. X., Axelbaum R. L., and Law, C. K., "The Influence of Carbon Dioxide and Oxygen as Additives on Soot Formation in Diffusion Flames," *23rd Symposium (International) on Combustion/ The Combustion Institute*, **1990**, 1501-1507.
- 2-23 Kim, C.H., et al., "Soot surface growth and oxidation in laminar diffusion flames at pressures of 0.1-1.0 at,". *Combustion and Flame*, **2004**. 136(1-2), 191-207.
- 3-1 Song, C. and Ma, X. *Appl. Catal. B:Env.*, 2003, 41, 207; Whitehurst, D. D.; Isoda, T. and Mochida, I. *Adv. Catal.* 1998, 42, 345.
- 3-2 Lee, S.-W.; Ryu, J. W. and Min, W. *Catal. Surv. Asia* 2003, 7, 271.
- 3-3 Sano, Y.; Choi, K.-H.; Korai, Y. and Mochida, I. *Appl. Catal. B* 2004, 49, 219.
- 3-4 Oyama, S. T.; Wang, X.; Lee, Y.-K.; Bando, K. and Requejo, F. G., *J. Catal.* 2002, 210, 207.
- 3-5 Stinner, C.; Prins, R. and Weber, Th., *J. Catal.* 2001, 202, 187.
- 3-6 Oyama, S. T., *J. Catal.* 2003, 216, 343.
- 3-7 Sie, S. T., *Fuel Proc. Tech.* 1999, 61, 149.
- 3-8 Sano, Y.; Choi, K.-H.; Korai, Y. and Mochida, I. *Energy & Fuels* 2004, 18, 644.
- 3-9 J.H. Kim, X. Ma, C. Song, Y. Lee and S. T. Oyama, *Energy & Fuel*, 2005, 19, 353-364
- 3-10 Topsoe, H., Clausen, B. S., Topsoe, N. Y., Pedersen, E., Niemann, W., Müller, A., Bögge, H., and Lengeler, B., *J. Chem. Soc. Faraday Trans*, 1987, 83, 2157.

- 3-11 B. Delmon, *Surf. Rev. Lett*, 1995, 2, 1, 25-41.
- 3-12 Song, C. *Am. Chem. Soc. Div. Petrol. Chem. Prepr.*, 1998, 43, 573.
- 3-13 Song, C. *CHEMTECH*, 1999, 29, 26-30.
- 3-14 Johnson, C.D and Worrall, F. *Microporous and Mesoporous Materials* 2004, 73, 191.
- 3-15 S.T. Wilson, B.M. Lok, C.A. Messina, E.R. Cannan and E.M. Flanigen, *J. Am. Chem. Soc.* 104 (1982) 1146.
- 3-16 M.E. Davis, *Nature* 417 (2002) 813.
- 3-17 S.T. Wilson, B.M. Lok, E.M. Flanigen, US Pat. 4 310 440, (1982).
- 3-18 J.M. Bennett, Jr. Richardson, J.W. Pluth, J.V. Smith, *Zeolite*, 7, (1987) 160.
- 3-19 D.B. Akolekar, *J. Mol. Catl. A: Chem.*, 104 (1995) 95.
- 3-20 S.H. Jhung, J-S. Chang, D.S. Kim, S-E. Park, *Micropor. Mesopor. Mater.* 71 (2004) 135.
- 3-21 M.H. Kim, H.X. Li, M.E. Davis, *Micropor. Mater.* 1 (1993) 191.
- 3-22 M. Matsukata, M. Ogura, T. Osaki, P.R.H.P. Rao, M. Nomura, E. Kikuchi., *Topics in Catal.* 9 (1999) 77.
- 3-23 Bandyopadhyay, R.K. Ahedi, Y. Kubota, M. Ogawa, Y. Goto, Y. Fukushima, and Y. Sugi, *J. Mater. Chem.* 11 (2001) 1869.
- 3-24 R. Bandyopadhyay, Y. Kubota, N. Sugimoto, Y. Fukushima, and Y. Sugi, *Micropor. Mesopor. Mater.* 32 (1999) 81.
- 3-25 T. Tatsumi and N. Jappar, *J. Phys. Chem. B*, 102 (1998) 7126.
- 3-26 A. Bhaumik and T. Tatsumi, *Micropor. Mesopor. Mater.* 34 (2000) 1.
- 3-27 R. Bandyopadhyay, M. Bandyopadhyay, Y. Kubota, Y. Sugi, *J. Porous Mater.* 9 (2002) 83.
- 3-28 S.K. Saha, Y.Kubota, Y. Sugi, *Chem. Lett.* 32(11) (2003) 1026.
- 3-29 S.K. Saha, S.B. Waghmode, Y.Kubota, Y. Sugi, *Mater. Lett.* 58 (2004) 2918.
- 3-30 S.B. Waghmode, S.K. Saha, Y.Kubota, Y. Sugi, *J. Catl.* 228 (2004) 192.

- 3-31 S.K. Saha, S.B. Waghmode, H. Maekawa, K. Kumora, Y.Kubota, Y. Sugi, Y.Oumi and T. Sano, Micropor. Mesopor. Mater. 81 (2005) 289.
- 3-32 T. Tatsumi, Q. Xia, N. Jappar, Chem. Lett. (1997) 677.
- 3-33 P.R.H.P. Rao, M. Matsukata, Chem. Commun. (1996) 1441.
- 4-1 Singer, J.G. (editor), Combustion: Fossil Power Systems, Combustion Engineering, Inc., pp. 2-28 – 2-31, **1981**.
- 4-2 Federal Register, Title 40 CFR Part 63, National Emission Standards for Hazardous Air Pollutants for Industrial, Commercial, and Institutional Boilers and Process Heaters; Final Rule, 55218-55286, **2004**.
- 4-3 Wilhelm, S.M. and Bloom, N., Mercury in petroleum, Fuel Processing Technology, March, **2000**.
- 4-4 U.S. EPA, Mercury study report to Congress, Volume II: an inventory of anthropogenic mercury emissions in the United States, US Office of Air Quality, Planning and Standards; Research Triangle, NC, EPA-452/R-97-004, **1997**.
- 4-5 U.S. EPA, Locating and estimating air emission from sources of mercury and mercury compounds, US Office of Air Quality, Planning and Standards; Research Triangle, NC, EPA-454/R-97-012, December, **1997**.
- 4-6 Bloom, N.S., Analysis and stability of mercury speciation in petroleum hydrocarbons, Fresenius J. Anal. Chem., vol 366(5), **2000**.
- 4-7 Liang, L., Horvat, M. and Danilchik, P., A novel analytical method for determination of pictogram levels of total mercury in gasoline and other petroleum-based products, Sci. Tot. Environ., 187, 57, **1996**.
- 4-8 Rising, B., Sorurbakhsh, P., Wu., J., Survey of ultra-trace metals in gas turbine fuels, 11th Annual International Petroleum Environmental Conference, Proceedings, Albuquerque, NM, October, **2004**.
- 4-9 Wilhelm, S.M., Mercury in fuel oil, www.hstech.com/Data/Oil?Fuel%20Oil.htm, March 25, **2005**.
- 4-10 Wilhelm, S.M. and Kirchgessner, D.A., Mercury in US crude oil: a study by US EPA, API and NPRA, SPE/EPA/DOE Exploration and Production Environmental Conference, San Antonio, TX, Society of Petroleum Engineers Paper 80573, **2003**.

- 4-11 Standards of Performance for New and Existing Stationary Sources: Electric Utility Steam Generating Units, amended. Code of Federal Regulations, Part 60, 63, 72, and 75, Title 40, **2005**.
- 4-12 Rule to Reduce Interstate Transport of Fine Particulate Matter and Ozone (Clean Air Interstate Rule); Revisions to Acid Rain Program; Provisions to the NO_x SIP Call. Code of Federal Regulations, Parts 51, 72, 73, 77, 78, and 96, Title 40, **2005**, p. 23.
- 4-13 ASTM D5184-01, Standard Test Methods for Determination of Aluminum and Silicon in Fuel Oils by Ashing, Fusion, Inductively Coupled Plasma Atomic Emission Spectrometry, and Atomic Absorption Spectrometry. American Society Testing Materials.
- 4-14 LECO Corporation, AMA254 Instruction Manual, October **2003**.
- 4-15 Lawn, C.J. (editor), Principles of Combustion Engineering for Boilers, Chapter on The Combustion of Heavy Fuel Oils authored by C.J. Lawn, A.T.S. Cunningham, P.J. Street, K.J. Matthews, M. Sarjeant, and A.M. Godridge, Academic Press, pp.61-196, **1987**.
- 4-16 Miller, B.G., A.W. Scaroni, S.A. Britton, D.A. Clark, J.L. Morrison, S.V. Pisupati, R.L. Poe, P.M. Walsh, R.T. Wincek, J. Xie, R.L. Patel, D.E. Thornock, and R.W. Borio, "Coal-Water Slurry Fuel Combustion Testing in an Oil-Fired Industrial Boiler Final Report," Prepared for the U.S. Department of Energy Pittsburgh Energy Technology Center, Pittsburgh, Pennsylvania, March 10, **1997b**, DE-FC22-89PC88697, 800 pages.
- 4-17 Chung, I-P., C. Strupp, and J. Karan, New Fuel Oil Atomizer for Improved Combustion Performance and Reduced Emissions, Proceedings of the 6th European Conference on Industrial Furnace and Boilers, **2000**.
- 4-18 Steam Generating Units Power Test Codes, ASME PTC 4.1, The American Society of Mechanical Engineers, **1965** (with **1968** and **1969** addenda, reaffirmed **1973**).
- 4-19 Habelt, W. W., "The Influence of Coal Oxygen to Coal Nitrogen Ratio on NO_x Formation," Presented at the 70th Annual AIChE Meeting, New York, November 13-17, **1977**.
- 4-20 Clarke, Lee B. and Sloss, Lesley L., Trace elements – emissions from coal combustion and gasification, IEACR/49, IEA Coal Research, London, 111 pp., **1992**.
- 4-21 U.S. EPA, Office of Air Quality planning and Standards, Compilation of Air Pollution Emission Factors” (AP-42), <http://www.epa.gov/ttn/chief/ap42/ch01/>, **1993**.

- 4-22 Federal Register, Title 40 CFR Parts 60 and 61, Standards of Performance for New Stationary Sources National Emission Standards for Hazardous Air Pollutants Addition of Method 29 to Appendix A of Part 60 and Amendments to Method 101A of Appendix B of Part 61, 18260-18279, **1996**.
- 4-23 U.S. Environmental Protection Agency, Standard Test Method for Elemental, Oxidized, Particle-bound and Total Mercury in Flue Gas Generated from Coal-Fire Stationary Sources (Ontario-Hydro Method), http://www.epa:80/ttnemc01/prelim/pre_003.pdf, May 12, **1999**.
- 4-24 Falcone Miller, S., R. T. Wincek, B. G. Miller and A. W. Scaroni, Evaluation of a Hybrid Sampling Train for Measuring Trace Elements and Identifying Mercury Species in Combustion Flue Gas, presented at 24th International Technical Conference on Coal Utilization and Fuel Systems, Clearwater, FL, March 8-11, **1999**.
- 4-25 Falcone Miller, S., R. T. Wincek, B. G. Miller and A. W. Scaroni, Development of a PSU Methodology for Measuring Trace Elements and Identifying Mercury Species in Combustion Flue Gas, presented at EPRI-DOE-EPA Combined Utility Air Pollution Control Symposium: The MEGA Symposium, Atlanta, GA, August 16-20, **1999**.
- 4-26 U.S. Environmental Protection Agency, Methods 3050, 3051, 6010, 7470 and 7471, Test Methods for Evaluating Solid Waste: Physical/Chemical Methods. SW-846, 3rd Ed., NTIS, September **1988**.
- 4-27 U.S. EPA, Report on Revisions to 5th Edition AP-12, Section 1.3, Fuel Oil Combustion, Office of Air Quality planning and Standards, Compilation of Air Pollution Emission Factors” (AP-42), <http://www.epa.gov/ttn/chief/ap42/ch01/final/c01s03.pdf>, **1996**.
- 4-28 Mercury in Air Emissions, Mercury Emissions from Combustion Sources (U.S. EPA Report, **1997**), <http://www.hgtech.com/Information/Air%20Emissions.htm>.
- 5-1 Polat, M., Polat, H. Chander, S., Physical and chemical interactions in coal flotation, International Journal of Mineral Processing, 2003, 72 (1-4), 199-213.
- 5-2 Hower, J. C., Kuehn, K. W., Parekh, B. K., and Peters, W. J., Maceral and microlythotype beneficiation in column flotation at the Powell Mountain Coal Mayflower Preparation Plant, Lee County, Virginia. Fuel Processing Technology, 2000, 67 (1), 23-33.
- 5-3 Cloke, M., Barraza, J., Miles, N. J., Pilot-scale studies using hydrocyclone and froth flotation for the production of beneficiated coal fractions for improved coal liquifaction, Fuel 1997, 76(13) 1217-1223.

- 5-4 Sun, Q., Li, W., Chen, H., Li, B. The variation of structural characteristics of macerals during pyrolysis, *Fuel* 82 (2003) 669-676.
- 5-5 Kidena, K., Katsuyma, M., Murata, S., and Nomura, M., Study on plasticity of maceral concentrates in terms of their structural features, *Energy & Fuels*, 2002, 16 (5) 1231-1238.
- 5-6 Maroto-Valer, M. M., Taulbee, D. N., Andresen, J. M., Hower, J. C., Snape, C. E., The role of semifusinite in plasticity development for a coking coal, *Energy & Fuels*, 1998, 12 (5), 1040-1046.
- 5-7 Gül, Ö.; Rudnick, L.R.; Schobert, H.H. "Delayed Coking of Decant Oil and Coal in a Laboratory-Scale Coking Unit" *Energy & Fuels*, 2006, 4, 1647-1655.
- 5-8 Gül, Ö., Clifford, C.E.B., Rudnick, L.R. and Schobert, H.H. "Process repeatability of co-coking of coal and decant oil in a pilot-scale delayed coker" [2nd International Symposium on Hydrotreating/Hydrocracking Technologies, Division of Petroleum Chemistry, The 232nd ACS National Meeting, San Francisco, CA, September 10-14, 2006](#)
- 5-9 Rodriguez, J., Tierney, J.W. and Wender, I., Evaluation of a delayed coking process by ^1H and ^{13}C n.m.r. spectroscopy: 2. Detailed interpretation of liquid n.m.r. spectra, *Fuel*, 73, (1994), 1870-1875.
- 5-10 Gül, Ö., Rudnick, L.R., and Schobert, H.H., The Effect of Chemical Composition of Coal-Based Jet Fuels on the Deposit Tendency and Morphology, *Energy & Fuels* 2006, 20, 2478-2485
- 5-11 Rudnick, L. R.; Whitehurst, D. D. The effect of Solvent Composition of the Liquefaction Behavior of Western Sub-Bituminous Coal. Presented at the EPRI Contractor's Meeting, Palo Alto, CA, May 7-8, 1980.
- 5-12 Derbyshire, F. J.; Odoerfer, G. A.; Rudnick, L. R.; Varghese, P.; Whitehurst, D. D. Fundamental studies in the conversion of coals to fuels of increased hydrogen content. Volume 1: The chemistry and mechanics of coal conversion to clean fuel. Volume 2: Appendixes. EPRI Report AP- 2117 under Research Project 1655-1, EPRI: Pleasant Hill, CA, November 1981; Vols 1 and 2.
- 5-13 Whitehurst, D. D.; Buttrill, S. E., Jr.; Derbyshire, F. J.; Farcasiu, M.; Odoerfer, G. A.; Rudnick, L. R. *Fuel* 1982, 61, 994-1005.
- 5-14 Rudnick, L. R.; Whitehurst, D. D. *New Approaches in Coal Chemistry*; Blaustein, B. D., Bockrath, B. C., Friedman, S., Eds.; ACS symposium series 169; American Chemical Society: Washington, D.C., 1981; pp 153-171.

- 5-15 Rudnick, L. R.; Whitehurst D. D.; Derbyshire, F. J. Solvent Compositional Changes During SCT Coal Conversion. Presented at the AIChE Meeting, Orlando, FL, February 28-March 3, 1982.
- 5-16 Gül, Ö., Rudnick, L.R., and Schobert, H.H., Delayed coking of decant oil and coal in a laboratory-scale coking unit, *Energy & Fuels* 2006, 20, 1647-1655.
- 5-17 Petroleum Refining Technology and Economics, Chapter 5 Coking and Thermal Processes, 3rd edition, 1994, (James H. Gary and Glen E. Handwerk, eds.), Marcel Dekker, Inc., p. 71-99.
- 5-18 Driscoll, K., GLCC. 6th Carbon Confernece, September 26-28, 2000, Houston, USA, Ch. 14.
- 5-19 Ellis, P.J. and Bacha, J.D., 1996, Shot Coke, Light Metals, TMS Light Metals Annual Meeting, Anaheim, CA, February 4-8, 1996, p. 477-484.
- 5-20 McClung, M., Chovanec, G.F. and Ross, J.A., 1999, Plant Experience in Qualifying Raw Materials for the Carbon Plant, Light Metals, 128 TMS Annual Meeting, San Diego, CA, February 28 – March 4, 1999.
- 5-21 Burgess-Clifford, C.E., Boehman, A., Song, C., Miller, B., Mitchell, G., “Refinery Integration of By-Products from Coal-derived Jet Fuels,” Semi-Annual Progress Report for Grant DE-FC26-03NT41828, November 30, **2006**.
- 5-22 Gonzalez, D., Montes-Moran, M. and Garcia, A.B. *Energy and Fuels*, 2005, 19, 263-269.
- 5-23 Feret, F. R. *Analyst*, 1998, 123, 595-600.
- 5-24 Atria, J.V., Rusinko, F., Schobert, H.H. *Energy and Fuels*, 2002, 16, 1343-1347.
- 5-25 Newman, J.W., and Newman, K.L. (1997). A History of Pitch Technologies. In *Introduction to Carbon Technologies*, H. Marsh, Heintz, E. A., and Rodriguez-Reinoso, F., ed. (Secretariado de Publicaciones), pp. 269-328.
- 5-26 Boenigk, W., Haenel, M.W., and Zander, M. (1990). Structural features and mesophase formation of coal-tar pitch fractions obtained by preparative size exclusion chromatography. *Fuel* 69, 1226-1232.
- 5-27 Lazaro, M.J., Herod, A.A., Cocksedge, M., Domin, M., and Kandiyoti, R. (1997). Molecular mass determinations in coal-derived liquids by MALDI mass spectrometry and size-exclusion chromatography. *Fuel* 76, 1225-1233.

- 5-28 Burgess-Clifford, C.E., Boehman, A., Song, C., Miller, B., Mitchell, G., "Refinery Integration of By-Products from Coal-derived Jet Fuels," Semi-Annual Progress Report for Grant DE-FC26-03NT41828, April, 2007.
- 5-29 Zander, M. (1997). Pitch Characterization for Industrial Applications. In Introduction to Carbon Technologies, H. Marsh, Heintz, E. A., and Rodriguez-Reinoso, F., ed. (Secretariado de Publicaciones), pp. 425-459.
- 5-30 Franz, J.A., Garcia, R., Linehan, J.C., Love, G.D., and Snape, C.E. (1992). Single-pulse excitation carbon-13 NMR measurements on the Argonne premium coal samples. *Energy & Fuels* 6, 598-602.
- 5-31 Love, G.D., Law, R.V., and Snape, C.E. (1993). Determination of nonprotonated aromatic carbon concentrations in coals by single pulse excitation carbon-13 NMR. *Energy & Fuels* 7, 639-644.
- 5-32 Suriyaphadilok, U., (2008), PhD Thesis, The Pennsylvania State University.
- 5-33 Maroto-Valer, M.M., Andresen, J.M., Rocha, J.D., and Snape, C.E. (1996). Quantitative solid-state C-13 nmr measurements on cokes, chars and coal tar pitch fractions. *Fuel* 75, 1721-1726.
- 5-34 Fitzer, E., Kompalik, D., and Yudate, K. (1987). Rheological Characteristics Of Coal-Tar Pitches. *Fuel* 66, 1504-1511.
- 5-35 Snape, C.E., Kenwright, A.M., Bermejo, J., Fernandez, J., and Moinelo, S.R. (1989). Evaluation Of The Aromatic Structure Of Coal-Tar Pitch By Solid And Solution State NMR. *Fuel* 68, 1605-1608.
- 5-36 Solum, M.S., Pugmire, R.J., Grant, D.M., Fletcher, T.H., and Solomon, P.R. (1989). Solid-State C-13 Nmr-Studies Of Coal Char Structure Evolution. *Abstr. Pap. Am. Chem. Soc.* 198, 88-FUEL.
- 5-37 Axelson, D.E. (1985). Solid State Nuclear Magnetic Resonance of Fossil Fuels: An Experimental Approach (Canada: Multiscience Publications Limited).
- 5-38 Andrésen, J.M., Luengo, C.A., Moinelo, S.R., Garcia, R., and Snape, C.E. (1998). Structural uniformity of toluene-insolubles from heat-treated coal tar pitch as determined by solid state C-13 NMR spectroscopy. *Energy & Fuels* 12, 524-530.
- 5-39 Solum, M.S., Pugmire, R.J., and Grant, D.M. (1989). *Energy & Fuels* 3, 187-193.

- 5-40 Sethi, N.K., Pugmire, R.J., Facelli, J.C., and Grant, D.M. (1988). Quantitative Determination of Different Carbon Types in Fusinite and Anthracite Coals from Carbon-13 Nuclear Magnetic Resonance Chemical Shielding Line-Shape Analysis. *Analytical Chemistry* 60, 1574-1579.
- 5-41 Fetzner, J.C., and Kershaw, J.R. (1995). Identification of Large Polycyclic Aromatic-Hydrocarbons in a Coal-Tar Pitch. *Fuel* 74, 1533-1536.
- 5-42 Kershaw, J.R. (1989). Average Structure Determinations. In *Spectroscopic Analysis of Coal Liquid*, J.R. Kershaw, ed. (NY: Elsevier), pp. 247-265.
- 5-43 Kershaw, J.R., and Black, K.J.T. (1993). Structural Characterization of Coal-Tar and Petroleum Pitches. *Energy & Fuels* 7, 420-425.
- 5-44 Attalla, M.I., Vassallo, A.M., and Wilson, M.A. (1989). Nuclear Magnetic Resonance Studies of Coal Liquefaction. In *Spectroscopic Analysis of Coal Liquids*, J.R. Kershaw, ed. (NY: Elsevier), pp. 195-245.
- 5-45 Kershaw, J.R. (1993). The Chemical Composition of a Coal-Tar Pitch. *Polycyclic Aromatic Compounds* 3, 185-197.
- 5-46 Schmidt-Hatting, W., Kooijman A. A., and R., P. (1991). Investigation of the Quality of Recycled Anode Butts. *Light Metals*, 705-720.
- 5-47 Gray, R.J., and Krupinski, K. C. (1997). Pitch Production: Supply, Coking, Optical Microscopy and Applications. In *Introduction to Carbon Technologies*, H. Marsh, Heintz, E. A., and Rodriguez-Reinoso, F., ed. (Secretariado de Publicaciones), pp. 329-424.
- 5-48 Diaz, M.C., Steel, K.M., Drage, T.C., Patrick, J.W., and Snape, C.E. (2005). Determination of the effect of different additives in coking blends using a combination of in situ high-temperature H-1 NMR and rheometry. *Energy & Fuels* 19, 2423-2431.
- 5-49 Jurkiewicz, A., Marzec, A., and Idziak, S. (1981). Immobile and Mobile Phases of Bituminous Coal Detectable by Pulse Nuclear Magnetic Resonance and Their Chemical Nature. *Fuel* 60, 1167-1168.
- 5-50 Jurkiewicz, A., Marzec, A., and Pislewski, N. (1982). Molecular Structure of Bituminous Coal Studied With Pulse Nuclear Magnetic Resonance. *Fuel* 61, 647-650.
- 5-51 Maroto-Valer, M.M., Andersen, J.M., and Snape, C.E. (1998). *In-situ* ¹H NMR study of the fluidity enhancement for a bituminous coal by coal tar pitch and a hydrogen-donor liquefaction residue. *Fuel* 77, 921-926.

- 5-52 Maroto-Valer, M.M., Andresen, J.M., and Snape, C.E. (1997). In-situ H-1 NMR investigation of particle size, mild oxidation, and heating regime effects on plasticity development during coal carbonization. *Energy & Fuels* 11, 236-244.
- 5-53 Maroto-Valer, M.M., Andresen, J.M., and Snape, C.E. (1997). In-situ H-1 NMR study of hydrogen-donor and non-donor solvent extraction of bituminous coals. *Abstr. Pap. Am. Chem. Soc.* 213, 120-FUEL
- 5-54 Maroto-Valer, M.M., Andresen, J.M., and Snape, C.E. (1997). Quantification by in situ H-1 nmr of the contributions from pyridine-extractables and metaplast to the generation of coal plasticity. *Fuel* 76, 1301-1308.
- 5-55 Maroto-Valer, M.M., Taulbee, D.N., Andresen, J.M., Hower, J.C., and Snape, C.E. (1998). The role of semifusinite in plasticity development for a coking coal. *Energy & Fuels* 12, 1040-1046.
- 5-56 Sakurovs, R. (1997). Direct evidence that the thermoplastic properties of blends are modified by interactions between the component coals. *Fuel* 76, 615-621.
- 5-57 Sakurovs, R. (1998). Interactions between a bituminous coal and aromatic hydrocarbons at elevated temperatures. *Energy & Fuels* 12, 631-636.
- 5-58 Sakurovs, R. (2003). Interactions between coking coals and plastics during co-pyrolysis. *Fuel* 82, 1911-1916.
- 5-59 Sakurovs, R. (2003). Interactions between coking coals in blends. *Fuel* 82, 439-450.
- 5-60 Sakurovs, R. (1997). A method for identifying interactions between coals in blends. *Fuel* 76, 623-624.
- 5-61 Sakurovs, R., and Lynch, L.J. (1993). Direct Observations On The Interaction Of Coals With Pitches And Organic-Compounds During Co-Pyrolysis. *Fuel* 72, 743-749.
- 5-62 Barton, W.A., Lynch, L.J., and Webster, D.S. (1984). Aspects Of The Molecular-Structure Of A Bituminous Vitrinite - Nuclear Magnetic-Resonance Study Of The Effects Of Imbibed Pyridine. *Fuel* 63, 1262-1268.
- 5-63 Lynch, L.J., Webster, D.S., Sakurovs, R., Barton, W.A., and Maher, T.P. (1988). The Molecular-Basis Of Coal Thermoplasticity. *Fuel* 67, 579-583.
- 5-64 Sakurovs, R. (2000). Some factors controlling the thermoplastic behaviour of coals. *Fuel* 79, 379-389.

- 5-65 Sakurovs, R., Lynch, L.J., and Barton, W.A. (1993). Proton Magnetic-Resonance Thermal-Analysis Of Argonne Premium Coals. In *Magnetic Resonance of Carbonaceous Solids*, R.E. Botto and Y. Sanada, eds. (Washington DC: American Chemical Society), pp. 229-251.
- 5-66 Sakurovs, R., Lynch, L.J., Maher, T.P., and Banerjee, R.N. (1987). Molecular Mobility During Pyrolysis Of Australian Bituminous Coals. *Energy & Fuels* 1, 167-172.
- 5-67 Steel, K.M., Diaz, M.C., Patrick, J.W., and Snape, C.E. (2004). Use of rheometry and H-1 NMR spectroscopy for understanding the mechanisms behind the generation of coking pressure. *Energy & Fuels* 18, 1250-1256.
- 5-68 Andréseñ, J.M., Martin, Y., Moinelo, S.R., Maroto-Valer, M.M., and Snape, C.E. (1998). Solid state C-13 NMR and high temperature H-1 NMR determination of bulk structural properties for mesophase-containing semi-cokes prepared from coal tar pitch. *Carbon* 36, 1043-1050.
- 5-69 Azami, K., Yokono, T., Sanada, Y., and Uemura, S. (1989). Studies on the Early Stage of Carbonization of Petroleum Pitch by Means of High-Temperature H-1-Nmr and Esr. *Carbon* 27, 177-183.
- 5-70 Steel, K.M., Diaz, M.C., Patrick, J.W., and Snape, C.E. (2004). Use of rheometry and H-1 NMR spectroscopy for understanding the mechanisms behind the generation of coking pressure. *Energy & Fuels* 18, 1250-1256.
- 5-71 Andréseñ, J.M., Martin, Y., Moinelo, S.R., Maroto-Valer, M.M., and Snape, C.E. (1998). Solid state C-13 NMR and high temperature H-1 NMR determination of bulk structural properties for mesophase-containing semi-cokes prepared from coal tar pitch. *Carbon* 36, 1043-1050.
- 5-72 Azami, K., Yokono, T., Sanada, Y., and Uemura, S. (1989). Studies on the Early Stage of Carbonization of Petroleum Pitch by Means of High-Temperature H-1-Nmr and Esr. *Carbon* 27, 177-183.
- 5-73 Goval, S. K.; Kolstad, J. J.; Hauschildt, F.; Venardos, D. G.; Joval, C. L., Process for producing needle coke, United States Patent, 5,286,371. February 15, 1994.
- 5-74 Zander, M. In *Sciences of Carbon Materials*; Marsh, H., Rodriguez-Reinoso, F., Eds.; Publicaciones Universidad de Alicante: Alicante, 2000.
- 5-75 Collin, P. J.; Tyler, R. J.; Wilson, M. A. 1H n.m.r. study of tars from flash pyrolysis of three Australian coals, *Fuel* 1980, 59. 479.

- 5-76 Rodriguez, J.; Tierney, J. W.; Wender, I. Evaluation of a delayed coking process by ^1H and ^{13}C NMR spectroscopy: 2. Detailed interpretation of liquid NMR spectra, *Fuel* **1994**, 73. 1870-1875.
- 5-77 Goval, S. K.; Kolstad, J. J.; Hauschildt, F.; Venardos, D. G.; Joval, C. L., Process for producing needle coke, US Patent, 5,286,371. 1994.
- 5-78 Speight, J. G. In *Petroleum Chemistry and Refining*; Speight, J. G., Ed.; Marcel Dekker: New York, 1998, pp 103-120.
- 5-79 Heinrich, G. In *Crude Oil, Petroleum Products, Process Flowsheets*; Wauquier, J. P., Ed.; Technip: Paris, 1995; Vol. 1, pp 366-413.
- 5-80 Mochida, I.; Oyama, T.; Korai, Y.; Qing, F. Y. Study of carbonization using a tubing bomb: evaluation of lump needle coke, carbonization mechanism and optimization, *Fuel* **1988**, 67. 1171-1181.
- 5-81 Escallon, M.M., PhD Thesis, The Pennsylvania State University, 2008.
- 5-82 Berkowitz, N. *Fossil Hydrocarbons, Chemistry and Technology*; Academic Press, 1997. Chapter 6.
- 5-83 API/ASTM *Petroleum measurement tables: volume correction factors*, 1st ed.; American Petroleum Institute: Washington DC, 1980.
- 5-84 Retcofsky, H. L.; Schweighardt, F. K.; Hough, M. Determination of aromaticities of coal derivatives by nuclear magnetic resonance spectrometry and the Brown-Ladner equation, *Anal. Chem.* **1977**, 49. 585-588.
- 5-85 Arai, T.; Nakagawa, T.; Mogi, F.; Oshiguri, N., Process of producing carbonaceous pitch, Foreign Application, 4,663,021. 1987.
- 5-86 Murakami, T.; Nakaniwa, M.; Nakayama, Y.; Masuo, M., Hydrogenation catalyst for coal tar, a method of hydrogenation of coal tar with use of such catalyst and a method of producing super needle coke from the hydrogenation product of coal tar, Foreign Application, 4,855,037. 1989.
- 5-87 Weinberg, V. L.; Sadeghi, M.-A.; Yen, T. F., Method of optimizing mesophase formation in graphite and coke precursors, US Patent, 4,773,985. 1988.
- 5-88 Clutter, D. R.; Petrakis, L.; Stenger, R. L.; Jensen, R. K. Nuclear magnetic resonance spectrometry of petroleum fractions. Carbon-13 and proton nuclear magnetic resonance characterizations in terms of average molecule parameters, *Anal. Chem.* **1972**, 44. 1395-1405.

- 5-89 Quian, S.-A.; Li, C.-F.; Zhang, P.-Z. Study of structural parameters on some petroleum aromatic fractions by ^1H n.m.r./i.r. and ^{13}C , ^1H n.m.r. spectroscopy, *Fuel* **1984**, *63*. 268.
- 5-90 Brown, J. K.; Ladner, W. R. A Study Of The Hydrogen Distribution In Coal-Like Materials By High-Resolution Nuclear Magnetic Resonance Spectroscopy.2. A Comparison With Infra-Red Measurement And The Conversion To Carbon Structure, *Fuel* **1960**, *39*. 87-96.
- 5-91 Nesumi, Y.; Oyama, T.; Todo, Y.; Azuma, A. Properties of fluid catalytic cracking decant oils of different origins in their single carbonization and cocarbonization with a petroleum vacuum residue, *Ind. Eng. Chem. Res.* **1990**, *29*. 1793-1801.
- 5-92 Nesumi, Y.; Todo, Y.; Oyama, T. Carbonization in the tube bomb leading to needle coke: II. Mechanism of cocarbonization of a petroleum vacuum residue and a FCC-decant oil, *Carbon* **1989**, *27*. 367-373.
- 5-93 Mochida, I.; Toshima, H.; Korai, Y.; Varga, T. Comparative-Evaluation Of Mesophase Pitches Derived From Coal-Tar And FCC-DO, *Journal of Material Science* **1990**, *25*. 3484-3492.
- 5-94 Mochida, I.; Fei, Y. Q.; Korai, Y. Carbonization in the tube bomb leading to needle coke: III. Carbonization properties of several coal-tar pitches, *Carbon* **1989**, *27*. 375-380.
- 5-95 Martinez-Escandell, M.; Marsh, H.; Rodriguez-Reinoso, F.; Santamaria-Ramirez, R.; Gomez-De-Salazar, C.; Romero-Palazon, E. Pyrolysis of petroleum residues: I. Yields and product analyses, *Carbon* **1999**, *37*. 1567-1582.
- 5-96 Rodriguez-Reinoso, F.; Santana, P.; Romero-Palazon, E.; Diez, M. A.; Marsh, H. Delayed coking: industrial and laboratory aspects, *Carbon* **1998**, *36*. 105-116.
- 5-97 Torregrosa-Rodriguez, P.; Martinez-Escandell, M.; Rodriguez-Reinoso, F.; Marsh, H.; de Salazar, C. G.; Palazon, E. R. Pyrolysis of petroleum residues II. Chemistry of pyrolysis, *Carbon* **2000**, *38*. 535-546.
- 5-98 Santamaria-Ramirez, R.; Romero-Palazon, E.; Gomez-de-Salazar, C.; Rodriguez-Reinoso, F.; Martinez-Saez, S.; Martinez-Escandell, M.; Marsh, H. Influence of pressure variations on the formation and development of mesophase in a petroleum residue, *Carbon* **1999**, *37*. 445-455.
- 5-99 Miller, D. J.; Chang, J. C.; Lewis, I. C.; Lewis, R. T.; Schobert, H. H.; Escallon, M. M.; Rudnick, L. R.; CPCPC, Ed.; Department of Energy Report DE-FC26-03NT41874, June 2006.

- 5-100 Casiello, G. L.; Chang, J. *Needle coke application and quality*, Carbon quality conference, Houston TX Sept 26-28, 1995; 21.
- 5-101 Oya, A.; Qian, Z.; Marsh, H. Structural study of cokes using optical microscopy and X-ray diffraction, *Fuel* **1983**, 62. 274-278.
- 5-102 Alvarez, A. G.; Martinez-Escandell, M.; Molina-Sabio, M.; Rodriguez-Reinoso, F. Pyrolysis of petroleum residues: analysis of semicokes by X-ray diffraction, *Carbon* **1999**, 37. 1627.
- 5-103 Eser, S.; Andresen, J. M. In *Fuels and Lubricants Handbook: Technology, Properties, Performance, and Testing*; Totten, G. E., Ed.; American Society for Testing and Materials, 2003, pp 757-786.
- 5-104 Mochida, I.; Korai, Y.; Fujitsu, H.; Oyama, T.; Nesumi, Y. Evaluation Of Several Petroleum Residues As The Needle Coke Feedstock Using A Tube Bomb, *Carbon* **1987**, 25. 259-264.
- 5-105 Smith, W. E.; Harper, H. L.; Union Carbide Corporation: Oak Ridge, Tennessee, 1971, pp 38-43.
- 5-106 Badger, M. W.; Mitchell, G. D.; Karacan, O.; Herman, N.; Senger, B.; Adams, A.; Schobert, H. H.; CPCPC, Ed.; Department of Energy Report DE-FC26-98FT40350, April 2002.
- 5-107 Gafarova-Aksoy, P., Mitchell, G.D., **Burgess-Clifford, C.**, Rudnick, L.R., and Schobert, H.H., "The evaluation of cokes from co-coking of decant oil and coal with various methods," *ACS Division of Petroleum Chemistry Preprints*, **51** (2), 318-321, 2006.
- 5-108 Rudnick, L.R., Boehman, A., Song, C., Miller, B., Mithchell, G. Refinery Integration of By-Products from Caol-Derived Jet Fuels, Grant DE-FC26-03NT41828, Semi-Annual Progress Report, November 17, 2005.
- 5-109 Gül, Ö.; Rudnick, L.R.; Schobert, H.H. "Delayed Coking of Decant Oil and Coal in a Laboratory-Scale Coking Unit" *Energy & Fuels*, 2006, 4, 1647-1655.
- 5-110 Gül, Ö., Clifford, C.E.B., Rudnick, L.R. and Schobert, H.H. "Process repeatability of co-coking of coal and decant oil in a pilot-scale delayed coker" [2nd International Symposium on Hydrotreating/Hydrocracking Technologies](#), , *Prepr. Pap.-Am. Chem. Soc., Div. Petroleum Chem.* 2006, 51(2), 342-347.
- 5-111 Gül, Ö., L. Rudnick, Schobert, H.H. "The Effect Of Reaction Temperature And Fuel Treatment On Deposit Formation Of Jet Fuels." *Prepr. Pap.-Am. Chem. Soc., Div. Fuel Chem.* 2005, 50 (1&2), 744-746.

- 5-112 Rudnick, L., Gül, Ö., Schobert, H.H. "The effect of chemical composition of coal derived jet fuels on carbon deposits." *Prepr. Pap.-Am. Chem. Soc., Div. Fuel Chem.* 2004, 49(2), 770-772.
- 5-113 Strohm, J., S. Butnark, Keyser, T.L., Andresen, J.M., Badger, M., Schobert, H.H., Song, C. "Use Of Coal Pyrolysis Products For The Development Of Thermally Stable Jet Fuels." *Prepr. Pap.-Am. Chem. Soc., Div. Fuel Chem.* 2002, 47(1), 177-178.
- 5-114 Andrésen, J., J. Strohm, Boyer, M.L., Song, C.S., Schobert, H.H., Butnark, S. "Thermal Stability Of Hydrotreated Refined Chemical Oil Derived Jet Fuels In The Pyrolytic Regime." *Prepr. Pap.-Am. Chem. Soc., Div. Fuel Chem.* 2001, 46(1), 208-210.
- 5-115 Fickinger, A., M. Badger, Mitchell, G.D., Schobert, H.H. "Co-Coking: An Alternative Process For Coal Derived Jet Fuel Production." *Prepr. Pap.-Am. Chem. Soc., Div. Fuel Chem.* 1999, 44(1), 106-109.
- 5-116 Song, C., W. Lai, Schobert, H.H. "Hydrogen-Transferring Pyrolysis Of Long-Chain Alkanes And Thermal-Stability Improvement Of Jet Fuels By Hydrogen Donors." *Industrial & Engineering Chemistry Research* 1994, 33(3): 548-557.
- 5-117 **Burgess, C.E.** and Schobert, H.H. "Direct Liquefaction for Production of High Yields of Feedstocks for Specialty Chemicals or Thermally Stable Jet Fuels," *Fuel Processing Technology*, **64**, 57-74, 2000.
- 5-118 Song, C., Eser, S., Schobert, H.H., Hatcher, P.G., "Pyrolytic Degradation Studies of A Coal-Derived And A Petroleum-Derived Aviation Jet Fuel." *Energy & Fuels* 1993, 7(2): 234-243.
- 5-119 Gül, Ö.; Rudnick, L. R.; Schobert H. H. "The Effect of Chemical Composition of Coal-Based Jet Fuels on the Deposit Tendency and Morphology" *Energy & Fuels*, 2006, 20(6), 2478-2485.
- 5-120 F. M. Lanças, H. S. Karam and H. M. McNair, *LC-GC, magazine of liquid and gas chromatography* **1987**, 5, 41-48.
- 5-121 C. Dariva, J. V. de Oliveira, M. G. R. Vale and E. B. Caramão, *Fuel* **1997**, 76, 585-591.
- 5-122 T. Yoshida, C. Li, T. Takanohashi, A. Matsumura, S. Sato and I. Saito, *Fuel Processing Technology* **2004**, 86, 61-72.
- 5-123 T. Yoshida, T. Takanohashi and K. Katoh, *Fuel* **2000**, 79, 399-404.

- 5-124 T. Yoshida, T. Takanohashi, K. Sakanishi and I. Saito, *Energy&Fuels* **2002**, *16*, 1006-1007.
- 5-125 T. Yoshida, T. Takanohashi, K. Sakanishi, I. Saito, M. Fujita and K. Mashimo, *Fuel* **2002**, *81*, 1463-1469.
- 5-126 C. Song and W.-C. Lai, *Fuel* **1995**, *10*, 1436-1451.
- 5-127 E. B. Caramão, L. M. F. Gomes, A. Bristoti and F. M. LanVas, *Fuel Science and Technology International* **1990**, *8*, 173-190.
- 5-128 F. M. Lanças and M. C. R. Peralba, *Fuel Science and Technology International* **1993**, *11*, 541-560.
- 5-129 F. M. Lanças and E. B. Caramão, *Fuel Science and Technology International* **1992**, *10*, 1197-1205.
- 5-130 F. M. Lanças and E. B. Caramão, *Fuel Science and Technology International* **1996**, *14*, 427-450.
- 5-131 J. M. Griffith, L. R. Rudnick and H. H. Schobert, *Preprints of ACS Division Petroleum Chemistry* **2006**, *51*, 231-237.
- 5-132 K. Miura, *Fuel Processing Technology* **2000**, *62*, 119-135.
- 5-133 K. Miura, K. Mae, H. Yoo Sock, R. Ashida and M. Morimoto, *Preprints of ACS Division Fuel Chemistry* **1999**, *45*, 652-656.
- 5-134 K. Miura, M. Shimada, K. Mae and H. Yoo Sock, *Fuel* **2001**, *80*, 1573-1582.
- 5-135 Song, C., Lai, W.-C., Schobert, H.H. (1994). Hydrogen-transferring pyrolysis of long-chain alkanes and thermal stability improvement of jet fuels by hydrogen donors. *Ind. Eng. Chem. Res.*, 33 (3), 548-557.
- 5-136 Painter, P. C.; Coleman, M. M. In *Fundamentals of Polymer Science: An introductory text*; Technomic Pub Co., Inc.: Lancaster, PA, 1997, pp 307-337.
- 5-137 van Krevelen, D. W. In *Properties of Polymers. Their correlation with chemical structure: their numerical estimation and prediction from additive group contributions*, Third ed.; Elsevier Science Publishers: Amsterdam - Oxford - New York - Tokyo, 1990, pp 189-225.
- 5-138 Griffith, J. M., Burgess Clifford, C. E., Rudnick, L. R. and Schobert, H. H. (2004). Coal extraction using light cycle oil: A factorial design. *Preprints of ACS Division Fuel Chemistry*, 49, 627-629.

- 5-139 Griffith, J. M., Rudnick, L. R. and Schobert, H. H. (2006). Assembling and operation of a solvent coal extraction device. *Preprints of ACS Division Petroleum Chemistry*, 51, 231-237.
- 5-140 Fickinger, A. E. (2000). Laboratory-scale coking of coal/petroleum mixtures. *M. S. Thesis*, The Pennsylvania State University, University Park, PA.
- 5-141 Escallón, M. M.; Gafarova, P.; Mitchell, G. D.; Gul, O.; Schobert, H. (2005). *Prepr. Pap.-Am. Chem. Soc., Division Petroleum Chemistry*, 50, 401-404.

Appendices

Appendix 4-A. Total Mercury Determination in Crude Oil by Microwave Digestion and Cold Vapor Atomic Absorption Spectrometry

Instrumentation

- *Microwave:*

A Model MDS-2100 microwave oven (CEM Corporation) with the temperature control probe was used. The power range, (maximum 950W), of the oven was adjusted to ramp in 1% increments. Since sample decomposition consists of several separate stages of control, the microwave is also equipped with a removable 6-position carousel. 100 ml Teflon Heavy Duty Vessels (HDV), rated to a maximum 600 psi pressure, were used.

- *Mercury Analyzer:*

A CETAC Inc. M6000A automated mercury analyzer was used to measure mercury in the digested solutions.

Reagents and Standards

Ultra trace metal grade concentrated nitric and concentrated hydrochloric acids were used. Analytical grade SnCl_2 , $\text{Mg}(\text{ClO}_4)_2$ as drying reagent, and mercury standards were used.

Procedure

- *Microwave Digestion*

Place approximately 0.5 gram of crude oil, accurately weighed to 0.001gram, in a HDV with 5 ml of concentrated nitric acid added. Cap and place the digestion vessels in the microwave and run heating stage one. Put the digestion vessels through additional heating steps, (heating stage 2 and 3), until the solution is clear, (light yellow in color). Add 2.5 ml of concentrated hydrochloric acid and dilute the solution to 25.0 ml with DI water in volumetric flask. Filter the solution and run on the CVAA mercury analyzer using matrix matched standards.

- *Cold vapor Atomic Absorption Mercury Analyzer*

In general, gas flow affects sensitivity. Higher gas flows always shorten the washout time, improve the signal profile shape and give less sensitivity. Low gas flow (below 80ml/minute) only be used for determination of samples contain less than 0.1ppb of mercury.

The CETAC mercury analyzer used for mercury analysis in crude oil was setup for low level mercury analysis. The sample uptake time was 60 second, the rinsing time was 140 second and the gas flow was 40 ml/minute.

- *Quality Control and Quality Assurance*

Allow the mercury lamp to equilibrate about two hours, and perform a four point calibration. Analyze a quality control standard (made from a different source of calibration standard) immediately after instrument standardization to verify the calibration accuracy.

Analyze a calibration check standard every tenth sample. If a check standard does not read within 10% of the expected value, recalibrate the instrument. Analyze a sample spike every tenth sample as well as for each different matrix to verify analyte recovery. Run

a digestion blank and one standard reference material along with the samples for quality assurance.

Table 1. Instrumental Precision

	Chevron Crude Oil, ng/L	Mandan Crude Oil, ng/L
reading # 1	21.4	80.1
reading # 2	21.9	79.8
reading # 3	21.6	80.2
reading # 4	21.4	79.9
reading # 5	21.8	80.2
reading # 6	21.3	80.0
reading # 7	21.6	80.1
% RSD	1.03	0.19

% RSD was calculated from 7 readings of same solution

Crude Oil Digestion Step 1

Stage	(1)	(2)	(3)	(4)
Power	25	35	40	40
PSI	50	80	120	120
Time(min)	10	10	30	60
TAP(min)	1	1	20	60
Temperature ° C	100	130	150	160
Fan	100	100	100	100

Crude Oil Digestion Step 2

Stage	(1)	(2)	(3)	(4)
Power	40	45	50	50
PSI	160	160	160	160
Time(min)	10	10	30	30
TAP(min)	1	1	30	60
Temperature ° C	130	150	170	190
Fan	100	100	100	100

Crude Oil Digestion Step 3

Stage	(1)	(2)	(3)	(4)
Power	40	45	50	50
PSI	160	160	160	160
Time(min)	10	10	30	30
TAP(min)	1	1	20	60
Temperature ° C	130	150	170	190
Fan	100	100	100	100

Crude Oil Digestion Step 4

Stage	(1)	(2)	(3)	(4)
Power	60	60	60	60
PSI	160	160	160	160
Time(min)	10	10	30	30
TAP(min)	1	1	20	60
Temperature ° C	130	150	170	190
Fan	100	100	100	100

Appendix 4-B. Boiler Efficiency Calculations

Research Boiler Efficiency Calculations

Date of Operation **8/2/06**
 Test Fuel Burned **X610**
 Test Program **Refinery Int.**

Operating Conditions

System Temperatures (°F)

Primary Air	340
Condensate Return	60
Low Pressure Steam	267
Flue Gas Boiler Exit - West	477
Flue Gas Economizer Inlet	483
Flue Gas Boiler Exit - East	486
High Pressure Steam	336
Stack	269
Bag Filter Entrance	362
Quarl Top	1246
Secondary Air	692
Condensor Water Exit	113
Quarl Bottom	1079
Boiler Feed Water	203
Calorimeter	276
Liquid Fuel	111
Ambient (°C)	24 (75 F)

System Pressures

High Pressure Steam (psig)	96.6
Low Pressure Steam (psig)	5.4
Liquid Fuel (psig)	37.2
Atomizing Media (psig)	56.7
Secondary Air (psig)	63.4
Primary Air (inch w.c.)	3.5

System Flow Rates

Natural Gas (lb/hr)	0.0
Primary Air (lb/hr)	1176
High Pressure Steam (lb/hr)	1152
Liquid Fuel (lb/hr)	83.7
Atomizing Media (lb/hr)	70.4
Secondary Air (lb/hr)	163
Solid Fuel (lb/min)	0.0
Cooling Air (lb/hr)	25.0

Flue Gas Analysis (dry basis)

Oxygen (%)	4.1
Carbon Monoxide (ppm)	165
Carbon Dioxide (%)	13.6
Sulfur Dioxide (ppm)	13
Nitrogen Oxides (ppm)	186
Hydrocarbons (ppm)	0

Additional System Data

Steam Quality (%)	99.0
Primary Air Humidity (%RH)	42.7
Feeder Weight (lbs)	0
Combustion Efficiency (%)	98.0
Firing Rate (Btu/hr)	1,497,393

Primary Air Percent Humidity Calculation

Water vapor press. @ ambient temp (atm)	0.0287
Partial press of water @ air temp (atm)	0.0123
Primary Air Percent Humidity (%H)	42.0

Liquid Fuel Analyses

	<u>Weight %</u>
Carbon	89.10
Hydrogen	7.65
Nitrogen	0.12
Sulfur	0.06
Oxygen	3.05
Moisture	0.00
Ash	0.02
Total =	100.00

HHV (determined at constant volume)	17,890	Btu/lb
HHV (determined at constant pressure)	17,910	Btu/lb

Steam Data

Enthalpy of Sat. Liq. (Btu/lb)	307.1 (saturated liquid @ absolute drum pressure)
Enthalpy of Sat. Vapor (Btu/lb)	1,189.0 (saturated vapor @ absolute drum pressure)
Enthalpy of Sat. Vapor (Btu/lb)	1,180.6 (saturated vapor @ absolute atomization pressure)
Enthalpy of Feed Water (Btu/lb)	171.07 (saturated liquid @ feedwater temperature)
Enthalpy of water vap. At Boiler Exit Temp (Btu/lb)	1,278.85 (Superheated steam @ 1psia & exit temperature)
Enthalpy of water at reference temp. (Btu/lb)	48.04 (Sat. liquid @ fuel temperature - 80F)

Boiler Efficiency Calculations (Based on ASME PTC 4.1)

Input - Output Method

$$\text{Efficiency} = (\text{Output}/\text{Input}) * 100$$

$$\begin{aligned}\text{Output} &= (\text{steam flow rate})(\text{steam quality}/100)(\text{enthalpy of steam @ drum pressure} - \text{enthalpy of} \\ &\quad \text{feedwater}) + (\text{steam flow rate})((100 - \text{steam quality})/100)(\text{enthalpy of water @ drum} \\ &\quad \text{pressure} - \text{enthalpy of feed water})\end{aligned}$$

$$= \quad \mathbf{1,162,762 \text{ Btu/hr}}$$

$$\text{Input} = (\text{fuel flow rate})(\text{high-heat value of fuel}) + \text{heat credits}$$

$$\begin{aligned}\text{Heat Credits} &= \text{heat supplied in dry primary air} + \text{heat supplied in preheated fuel} + \text{heat supplied in} \\ &\quad \text{atomizing steam} + \text{heat supplied from moisture in primary air} \\ &= \text{Bae} + \text{Bfe} + \text{Bze} + \text{Bmae}\end{aligned}$$

$$\begin{aligned}\text{Bae} &= (\text{flow rate of primary air})(\text{wt\% dry air})(\text{specific heat of air})(\text{primary air temp} - \text{reference air} \\ &\quad \text{temp}) \\ &= \quad \mathbf{73,486 \text{ Btu/hr}} \quad (\text{assumes primary air temperature of } \sim 350\text{F for } C_p)\end{aligned}$$

$$\begin{aligned}\text{Bfe} &= (\text{flow rate of fuel})(\text{specific heat of fuel})(\text{fuel inlet temp} - \text{reference air temp}) \\ &= \quad \mathbf{1,073 \text{ Btu/hr}}\end{aligned}$$

$$\begin{aligned}\text{Bze} &= (\text{flow rate of atomizing steam})(\text{enthalpy of atomizing steam} - \text{enthalpy of sat. vapor @} \\ &\quad \text{reference temp}) \\ &= \quad \mathbf{79,733 \text{ Btu/hr}}\end{aligned}$$

$$\begin{aligned}\text{Bmae} &= (\text{flow rate of primary air})(\text{wt\% water vapor in dry air})(\text{specific heat of water vapor}) \\ &\quad (\text{primary air temp} - \text{reference air temp}) \\ &= \quad \mathbf{1,106 \text{ Btu/hr}} \quad (\text{assumes primary air temperature of } \sim 350\text{F for } C_p)\end{aligned}$$

$$\text{Input} = \quad \mathbf{1,652,791 \text{ Btu/hr}}$$

$$\text{Boiler Efficiency} = \quad \mathbf{70.4 \%}$$

Heat Loss Method

$$\text{Efficiency} = (\text{Losses}/\text{Input}) * 100$$

$$\begin{aligned}\text{Input} &= \text{determined from Input-Output method} \\ &= \mathbf{1,652,791 \text{ Btu/hr}}\end{aligned}$$

$$\begin{aligned}\text{Losses} &= \text{heat loss due to dry gas} + \text{heat loss due to unburnt carbon} + \text{heat loss due to moisture in the fuel} + \\ &\quad \text{heat loss due to moisture produced from burning hydrogen in the fuel} + \text{heat loss due to moisture} \\ &\quad \text{in the combustion air} + \text{heat loss due to formation of carbon monoxide} + \text{heat loss due to heat in} \\ &\quad \text{atomizing steam} + \text{heat loss due to surface radiation and convection} \\ &= L_g + L_{uc} + L_{mf} + L_{mfh} + L_{ma} + L_{co} + L_z + L_b\end{aligned}$$

Dry Gas

$$\begin{aligned}&\text{Pounds of dry gas per pound of "as fired" fuel (Lg)} \\ W_g' &= ((c\%)(C.\text{Efficiency})(44.01 \text{ (CO}_2\text{)} + 32.00 \text{ (O}_2\text{)} + 28.02 \text{ (N}_2\text{)} + (28.01 \text{ (CO)}/12.01 \text{ (CO}_2\text{+CO))} + \\ &\quad 12.01 \text{ (S)}/32.07\end{aligned}$$

$$W_g' = \mathbf{16.25 \text{ lb dry gas/lb of as fired fuel}}$$

$$\begin{aligned}L_g' &= (W_g')(C_{pg})(\text{boiler exit temp} - \text{reference air temperature})(\text{fuel flow rate}) \\ &= \mathbf{131,153 \text{ Btu/hr}}\end{aligned}$$

Unburnt Carbon

$$\begin{aligned}L_{uc} &= (\% \text{ Carbon in the "as fired Fuel"})(1 - \text{Comb.Efficiency})(\text{fuel flow rate})(14500) \\ &= \mathbf{21,627 \text{ Btu/hr}}\end{aligned}$$

Moisture in Fuel

$$\begin{aligned}L_{mf} &= (\text{lb moisture per lb of fuel})(\text{enthalpy of water vapor at boiler exit temp} - \\ &\quad \text{enthalpy of water at reference temperature})(\text{fuel flow rate}) \\ &= \mathbf{0 \text{ Btu/hr}}\end{aligned}$$

Moisture from Burning Hydrogen

$$\begin{aligned}L_{mfh} &= (8.936)(\% \text{ hydrogen in "as fired" fuel})(\text{enthalpy of water vapor @ boiler exit temp} - \\ &\quad \text{enthalpy of water @ reference temperature})(\text{fuel flow rate}) \\ &= \mathbf{70,424 \text{ Btu/hr}}\end{aligned}$$

Heat Loss Method - Continued

Moisture in Combustion Air (Primary air only)

Primary Air Flow Rate =	1176 lbs/hr	
lbs Air per lb of Fuel =	14.05 lbs air/lb fuel	
Primary Air % Humidity =	42.0	
Moisture in Primary Air =	0.008 lb water vapor/lb of dry air	(Figure 24-2, p. 748 McCabe and Smith, Unit Operations of Chemical Engineering - 3rd Edition)

$$\begin{aligned} L_{ma} &= (\text{lbs air per lb of fuel})(\text{lb of water vapor per lb of air})(\text{enthalpy of water vapor @ boiler exit temp} - \\ &\quad \text{enthalpy of water vapor @ reference temperature})(\text{fuel flow rate}) \\ &= \mathbf{11,579 \text{ Btu/hr}} \end{aligned}$$

Formation of Carbon Monoxide

$$\begin{aligned} L_{co} &= (\text{CO}/(\text{CO}_2 + \text{CO})) (10160) (\text{Combustion Efficiency}) (\% \text{ carbon in 'as fired fuel}) (\text{fuel flow rate}) \\ &= \mathbf{902 \text{ Btu/hr}} \end{aligned}$$

Atomizing Steam

$$\begin{aligned} L_z &= (\text{lbs of atomizing steam per hour})(\text{enthalpy of water vapor @ boiler exit temp} - \text{enthalpy of} \\ &\quad \text{water vapor @ reference temp}) \\ &= \mathbf{86,649 \text{ Btu/hr}} \end{aligned}$$

Radiation

Maximum Continuous Boiler Output =	2,000,000 Btu/hr
Actual Output =	1,497,393 Btu/hr

$$L_b = \mathbf{8.5 \%} \quad (\text{Figure 8, p. 67, ASME PTC 4.1})$$

$$\text{Total Heat Losses} = \mathbf{462,822 \text{ Btu/hr}}$$

$$\text{Boiler Efficiency} = \mathbf{72.0 \%}$$

Calculation of Pollutant Emission Factors

EPA CFR Title 40 Emissions Factor

$$\# \text{ Pollutant/MMBtu} = (1.194 \times 10^{-7} \times (\text{vol. concentration of pollutant} - \text{ppm})) \times ((3.64(\%H) + 1.53(\%C) + 0.57(\%S) + 0.14(\%N) - 0.46(\%O_2))/GCV) \times 10^6 \times (20.9/(20.9 - \%O_2))$$

(EPA, Code of Federal Register, Title 40, Part 75, Chapter 1, Section 3, pp. 321 -323.)

<u>Pollutant</u>	<u>Emissions Factor (lbs./MM Btu)</u>
CO	0.223
CO ₂	183.0
SO ₂	0.017
NO _x	0.251
Hydrocarbons (C ₁ -C ₃)	0.000

Mass Balance Around the Boiler

Total Mass Input = lbs. of fuel (dry basis) + lbs. of primary air (dry basis) + lbs. of secondary air +
lbs. of cooling air

= 1381 lbs/hr

Conversion of Gas Composition from Volume% to Wt%

	<u>Mole %</u>	<u>lbs in each mole of gas</u>	<u>Weight %</u>	<u>Emission Factors (lbs/MM Btu)</u>	
Oxygen	4.069921262	1.3024	4.29		
Carbon Monoxide	0.016489139	0.0046	0.02	0.140	<-- CO
Carbon Dioxide	13.6	5.9692	19.67	181.4	<-- CO ₂
Sulfur Dioxide	0.00127356	0.0008	0.00	0.025	<-- SO ₂
Nitrogen Oxides	0.01859097	0.0056	0.02	0.260	<-- NO _x
Nitrogen	82.3	23.0608	76.00		<-- Hydrocarbons
Total =	100.0	30.3433	100.00		

Research Boiler Efficiency Calculations

Date of Operation **8/7/06**
 Test Fuel Burned **#6 Fuel Oil**
 Test Program **Refinery Int.**

Operating Conditions

System Temperatures (°F)

Primary Air	340
Condensate Return	60
Low Pressure Steam	267
Flue Gas Boiler Exit - West	477
Flue Gas Economizer Inlet	483
Flue Gas Boiler Exit - East	486
High Pressure Steam	336
Stack	269
Bag Filter Entrance	362
Quarl Top	1246
Secondary Air	692
Condensor Water Exit	113
Quarl Bottom	1079
Boiler Feed Water	203
Calorimeter	276
Liquid Fuel	111
Ambient (°C)	24 (75 F)

System Pressures

High Pressure Steam (psig)	96.8
Low Pressure Steam (psig)	5.7
Liquid Fuel (psig)	40.9
Atomizing Media (psig)	59.6
Secondary Air (psig)	62.3
Primary Air (inch w.c.)	4.1

System Flow Rates

Natural Gas (lb/hr)	0.0
Primary Air (lb/hr)	1128
High Pressure Steam (lb/hr)	1153
Liquid Fuel (lb/hr)	81.4
Atomizing Media (lb/hr)	71.6
Secondary Air (lb/hr)	161
Solid Fuel (lb/min)	0.0
Cooling Air (lb/hr)	25.0

Flue Gas Analysis (dry basis)

Oxygen (%)	4.0
Carbon Monoxide (ppm)	43
Carbon Dioxide (%)	13.0
Sulfur Dioxide (ppm)	879
Nitrogen Oxides (ppm)	337
Hydrocarbons (ppm)	0

Additional System Data

Steam Quality (%)	99.0
Primary Air Humidity (%RH)	58.9
Feeder Weight (lbs)	0
Combustion Efficiency (%)	98.0
Firing Rate (Btu/hr)	1,500,772

Primary Air Percent Humidity Calculation

Water vapor press. @ ambient temp (atm)	0.0287
Partial press of water @ air temp (atm)	0.0169
Primary Air Percent Humidity (%H)	58.2

Liquid Fuel Analyses

	<u>Weight %</u>
Carbon	86.40
Hydrogen	11.30
Nitrogen	0.30
Sulfur	1.80
Oxygen	0.00
Moisture	0.00
Ash	0.20
Total =	100.00

HHV (determined at constant volume)	18,437	Btu/lb
HHV (determined at constant pressure)	18,467	Btu/lb

Steam Data

Enthalpy of Sat. Liq. (Btu/lb)	307.3 (saturated liquid @ absolute drum pressure)
Enthalpy of Sat. Vapor (Btu/lb)	1,189.1 (saturated vapor @ absolute drum pressure)
Enthalpy of Sat. Vapor (Btu/lb)	1,181.4 (saturated vapor @ absolute atomization pressure)
Enthalpy of Feed Water (Btu/lb)	171.07 (saturated liquid @ feedwater temperature)
Enthalpy of water vap. At Boiler Exit Temp (Btu/lb)	1,278.85 (Superheated steam @ 1psia & exit temperature)
Enthalpy of water at reference temp. (Btu/lb)	48.04 (Sat. liquid @ fuel temperature - 80F)

Boiler Efficiency Calculations (Based on ASME PTC 4.1)

Input - Output Method

$$\text{Efficiency} = (\text{Output}/\text{Input}) * 100$$

$$\begin{aligned}\text{Output} &= (\text{steam flow rate})(\text{steam quality}/100)(\text{enthalpy of steam @ drum pressure} - \text{enthalpy of} \\ &\quad \text{feedwater}) + (\text{steam flow rate})((100 - \text{steam quality})/100)(\text{enthalpy of water @ drum} \\ &\quad \text{pressure} - \text{enthalpy of feed water})\end{aligned}$$

$$= \quad \mathbf{1,163,818 \text{ Btu/hr}}$$

$$\text{Input} = (\text{fuel flow rate})(\text{high-heat value of fuel}) + \text{heat credits}$$

$$\begin{aligned}\text{Heat Credits} &= \text{heat supplied in dry primary air} + \text{heat supplied in preheated fuel} + \text{heat supplied in} \\ &\quad \text{atomizing steam} + \text{heat supplied from moisture in primary air} \\ &= \text{Bae} + \text{Bfe} + \text{Bze} + \text{Bmae}\end{aligned}$$

$$\begin{aligned}\text{Bae} &= (\text{flow rate of primary air})(\text{wt\% dry air})(\text{specific heat of air})(\text{primary air temp} - \text{reference air} \\ &\quad \text{temp}) \\ &= \quad \mathbf{70,277 \text{ Btu/hr}} \quad (\text{assumes primary air temperature of } \sim 350\text{F for } C_p)\end{aligned}$$

$$\begin{aligned}\text{Bfe} &= (\text{flow rate of fuel})(\text{specific heat of fuel})(\text{fuel inlet temp} - \text{reference air temp}) \\ &= \quad \mathbf{1,044 \text{ Btu/hr}}\end{aligned}$$

$$\begin{aligned}\text{Bze} &= (\text{flow rate of atomizing steam})(\text{enthalpy of atomizing steam} - \text{enthalpy of sat. vapor @} \\ &\quad \text{reference temp}) \\ &= \quad \mathbf{81,146 \text{ Btu/hr}}\end{aligned}$$

$$\begin{aligned}\text{Bmae} &= (\text{flow rate of primary air})(\text{wt\% water vapor in dry air})(\text{specific heat of water vapor}) \\ &\quad (\text{primary air temp} - \text{reference air temp}) \\ &= \quad \mathbf{1,454 \text{ Btu/hr}} \quad (\text{assumes primary air temperature of } \sim 350\text{F for } C_p)\end{aligned}$$

$$\text{Input} = \quad \mathbf{1,654,693 \text{ Btu/hr}}$$

$$\text{Boiler Efficiency} = \quad \mathbf{70.3 \%}$$

Heat Loss Method

$$\text{Efficiency} = (\text{Losses}/\text{Input}) * 100$$

$$\begin{aligned}\text{Input} &= \text{determined from Input-Output method} \\ &= \mathbf{1,654,693} \text{ Btu/hr}\end{aligned}$$

$$\begin{aligned}\text{Losses} &= \text{heat loss due to dry gas} + \text{heat loss due to unburnt carbon} + \text{heat loss due to moisture in the fuel} + \\ &\quad \text{heat loss due to moisture produced from burning hydrogen in the fuel} + \text{heat loss due to moisture} \\ &\quad \text{in the combustion air} + \text{heat loss due to formation of carbon monoxide} + \text{heat loss due to heat in} \\ &\quad \text{atomizing steam} + \text{heat loss due to surface radiation and convection} \\ &= L_g + L_{uc} + L_{mf} + L_{mfh} + L_{ma} + L_{co} + L_z + L_b\end{aligned}$$

Dry Gas

$$\begin{aligned}&\text{Pounds of dry gas per pound of "as fired" fuel (Lg)} \\ W_g' &= ((c\%)(C.\text{Efficiency})(44.01 \text{ (CO}_2) + 32.00 \text{ (O}_2) + 28.02 \text{ (N}_2) + (28.01 \text{ (CO)}/12.01 \text{ (CO}_2 + \text{CO})) + \\ &\quad 12.01 \text{ (S)}/32.07\end{aligned}$$

$$W_g' = \mathbf{16.40} \text{ lb dry gas/lb of as fired fuel}$$

$$\begin{aligned}L_g' &= (W_g')(C_{pg})(\text{boiler exit temp} - \text{reference air temperature})(\text{fuel flow rate}) \\ &= \mathbf{128,734} \text{ Btu/hr}\end{aligned}$$

Unburnt Carbon

$$\begin{aligned}L_{uc} &= (\% \text{ Carbon in the "as fired Fuel"})(1 - \text{Comb.Efficiency})(\text{fuel flow rate})(14500) \\ &= \mathbf{20,396} \text{ Btu/hr}\end{aligned}$$

Moisture in Fuel

$$\begin{aligned}L_{mf} &= (\text{lb moisture per lb of fuel})(\text{enthalpy of water vapor at boiler exit temp} - \\ &\quad \text{enthalpy of water at reference temperature})(\text{fuel flow rate}) \\ &= \mathbf{0} \text{ Btu/hr}\end{aligned}$$

Moisture from Burning Hydrogen

$$\begin{aligned}L_{mfh} &= (8.936)(\% \text{ hydrogen in "as fired" fuel})(\text{enthalpy of water vapor @ boiler exit temp} - \\ &\quad \text{enthalpy of water @ reference temperature})(\text{fuel flow rate}) \\ &= \mathbf{101,167} \text{ Btu/hr}\end{aligned}$$

Heat Loss Method - Continued

Moisture in Combustion Air (Primary air only)

Primary Air Flow Rate =	1128 lbs/hr	
lbs Air per lb of Fuel =	13.86 lbs air/lb fuel	
Primary Air % Humidity =	58.2	
Moisture in Primary Air =	0.011 lb water vapor/lb of dry air	(Figure 24-2, p. 748 McCabe and Smith, Unit Operations of Chemical Engineering - 3rd Edition)

$$\begin{aligned} L_{ma} &= (\text{lbs air per lb of fuel})(\text{lb of water vapor per lb of air})(\text{enthalpy of water vapor @ boiler exit temp} - \\ &\quad \text{enthalpy of water vapor @ reference temperature})(\text{fuel flow rate}) \\ &= \mathbf{15,272 \text{ Btu/hr}} \end{aligned}$$

Formation of Carbon Monoxide

$$\begin{aligned} L_{co} &= (\text{CO}/(\text{CO}_2 + \text{CO})) (10160) (\text{Combustion Efficiency}) (\% \text{ carbon in 'as fired fuel}) (\text{fuel flow rate}) \\ &= \mathbf{230 \text{ Btu/hr}} \end{aligned}$$

Atomizing Steam

$$\begin{aligned} L_z &= (\text{lbs of atomizing steam per hour})(\text{enthalpy of water vapor @ boiler exit temp} - \text{enthalpy of} \\ &\quad \text{water vapor @ reference temp}) \\ &= \mathbf{88,126 \text{ Btu/hr}} \end{aligned}$$

Radiation

Maximum Continuous Boiler Output =	2,000,000 Btu/hr
Actual Output =	1,500,772 Btu/hr

$$L_b = \mathbf{8.5 \%} \quad (\text{Figure 8, p. 67, ASME PTC 4.1})$$

$$\text{Total Heat Losses} = \mathbf{494,574 \text{ Btu/hr}}$$

$$\text{Boiler Efficiency} = \mathbf{70.1 \%}$$

Calculation of Pollutant Emission Factors

EPA CFR Title 40 Emissions Factor

$$\# \text{ Pollutant/MMBtu} = (1.194 \times 10^{-7} \times (\text{vol. concentration of pollutant} - \text{ppm})) \times ((3.64(\%H) + 1.53(\%C) + 0.57(\%S) + 0.14(\%N) - 0.46(\%O_2))/GCV) \times 10^6 \times (20.9/(20.9 - \%O_2))$$

(EPA, Code of Federal Register, Title 40, Part 75, Chapter 1, Section 3, pp. 321 -323.)

<u>Pollutant</u>	<u>Emissions Factor (lbs./MM Btu)</u>
CO	0.060
CO ₂	181.2
SO ₂	1.225
NO _x	0.470
Hydrocarbons (C ₁ -C ₃)	0.000

Mass Balance Around the Boiler

Total Mass Input = lbs. of fuel (dry basis) + lbs. of primary air (dry basis) + lbs. of secondary air +
lbs. of cooling air

= 1300 lbs/hr

Conversion of Gas Composition from Volume% to Wt%

	<u>Mole %</u>	<u>lbs in each mole of gas</u>	<u>Weight %</u>	<u>Emission Factors (lbs/MM Btu)</u>	
Oxygen	3.951798069	1.2646	4.18		
Carbon Monoxide	0.004279794	0.0012	0.00	0.034	<-- CO
Carbon Dioxide	13.0	5.7247	18.91	163.8	<-- CO ₂
Sulfur Dioxide	0.087923022	0.0563	0.19	1.611	<-- SO ₂
Nitrogen Oxides	0.033727238	0.0101	0.03	0.444	<-- NO _x
Nitrogen	<u>82.9</u>	<u>23.2244</u>	<u>76.70</u>		<-- Hydrocarbons
Total =	100.0	30.2813	100.00		

Research Boiler Efficiency Calculations

Date of Operation **8/7/06**
 Test Fuel Burned **#6 Fuel Oil**
 Test Program **Refinery Int.**

Operating Conditions

System Temperatures (°F)

Primary Air	344
Condensate Return	60
Low Pressure Steam	266
Flue Gas Boiler Exit - West	486
Flue Gas Economizer Inlet	487
Flue Gas Boiler Exit - East	487
High Pressure Steam	335
Stack	273
Bag Filter Entrance	368
Quarl Top	1254
Secondary Air	691
Condensor Water Exit	115
Quarl Bottom	1151
Boiler Feed Water	203
Calorimeter	276
Liquid Fuel	159
Ambient (°C)	24 (75 F)

System Pressures

High Pressure Steam (psig)	96.6
Low Pressure Steam (psig)	5.9
Liquid Fuel (psig)	41.3
Atomizing Media (psig)	60.1
Secondary Air (psig)	64.0
Primary Air (inch w.c.)	4.0

System Flow Rates

Natural Gas (lb/hr)	0.0
Primary Air (lb/hr)	1118
High Pressure Steam (lb/hr)	1164
Liquid Fuel (lb/hr)	81.0
Atomizing Media (lb/hr)	71.5
Secondary Air (lb/hr)	165
Solid Fuel (lb/min)	0.0
Cooling Air (lb/hr)	25.0

Flue Gas Analysis (dry basis)

Oxygen (%)	4.0
Carbon Monoxide (ppm)	48
Carbon Dioxide (%)	13.0
Sulfur Dioxide (ppm)	881
Nitrogen Oxides (ppm)	344
Hydrocarbons (ppm)	0

Additional System Data

Steam Quality (%)	99.0
Primary Air Humidity (%RH)	44.9
Feeder Weight (lbs)	0
Combustion Efficiency (%)	98.0
Firing Rate (Btu/hr)	1,493,397

Primary Air Percent Humidity Calculation

Water vapor press. @ ambient temp (atm)	0.0287
Partial press of water @ air temp (atm)	0.0129
Primary Air Percent Humidity (%H)	44.2

Liquid Fuel Analyses

	<u>Weight %</u>
Carbon	86.40
Hydrogen	11.30
Nitrogen	0.30
Sulfur	1.80
Oxygen	0.00
Moisture	0.00
Ash	0.20
Total =	100.00

HHV (determined at constant volume)	18,437	Btu/lb
HHV (determined at constant pressure)	18,467	Btu/lb

Steam Data

Enthalpy of Sat. Liq. (Btu/lb)	307.2 (saturated liquid @ absolute drum pressure)
Enthalpy of Sat. Vapor (Btu/lb)	1,189.0 (saturated vapor @ absolute drum pressure)
Enthalpy of Sat. Vapor (Btu/lb)	1,181.5 (saturated vapor @ absolute atomization pressure)
Enthalpy of Feed Water (Btu/lb)	171.42 (saturated liquid @ feedwater temperature)
Enthalpy of water vap. At Boiler Exit Temp (Btu/lb)	1,281.12 (Superheated steam @ 1psia & exit temperature)
Enthalpy of water at reference temp. (Btu/lb)	48.04 (Sat. liquid @ fuel temperature - 80F)

Boiler Efficiency Calculations (Based on ASME PTC 4.1)

Input - Output Method

$$\text{Efficiency} = (\text{Output}/\text{Input}) * 100$$

$$\begin{aligned}\text{Output} &= (\text{steam flow rate})(\text{steam quality}/100)(\text{enthalpy of steam @ drum pressure} - \text{enthalpy of} \\ &\quad \text{feedwater}) + (\text{steam flow rate})((100 - \text{steam quality})/100)(\text{enthalpy of water @ drum} \\ &\quad \text{pressure} - \text{enthalpy of feed water})\end{aligned}$$

$$= \quad \mathbf{1,174,450 \text{ Btu/hr}}$$

$$\text{Input} = (\text{fuel flow rate})(\text{high-heat value of fuel}) + \text{heat credits}$$

$$\begin{aligned}\text{Heat Credits} &= \text{heat supplied in dry primary air} + \text{heat supplied in preheated fuel} + \text{heat supplied in} \\ &\quad \text{atomizing steam} + \text{heat supplied from moisture in primary air} \\ &= \text{Bae} + \text{Bfe} + \text{Bze} + \text{Bmae}\end{aligned}$$

$$\begin{aligned}\text{Bae} &= (\text{flow rate of primary air})(\text{wt\% dry air})(\text{specific heat of air})(\text{primary air temp} - \text{reference air} \\ &\quad \text{temp}) \\ &= \quad \mathbf{66,164 \text{ Btu/hr}} \quad (\text{assumes primary air temperature of } \sim 350\text{F for } C_p)\end{aligned}$$

$$\begin{aligned}\text{Bfe} &= (\text{flow rate of fuel})(\text{specific heat of fuel})(\text{fuel inlet temp} - \text{reference air temp}) \\ &= \quad \mathbf{2,599 \text{ Btu/hr}}\end{aligned}$$

$$\begin{aligned}\text{Bze} &= (\text{flow rate of atomizing steam})(\text{enthalpy of atomizing steam} - \text{enthalpy of sat. vapor @} \\ &\quad \text{reference temp}) \\ &= \quad \mathbf{81,043 \text{ Btu/hr}}\end{aligned}$$

$$\begin{aligned}\text{Bmae} &= (\text{flow rate of primary air})(\text{wt\% water vapor in dry air})(\text{specific heat of water vapor}) \\ &\quad (\text{primary air temp} - \text{reference air temp}) \\ &= \quad \mathbf{9,956 \text{ Btu/hr}} \quad (\text{assumes primary air temperature of } \sim 350\text{F for } C_p)\end{aligned}$$

$$\text{Input} = \quad \mathbf{1,653,159 \text{ Btu/hr}}$$

$$\text{Boiler Efficiency} = \quad \mathbf{71.0 \%}$$

Heat Loss Method

$$\text{Efficiency} = (\text{Losses}/\text{Input}) * 100$$

$$\begin{aligned}\text{Input} &= \text{determined from Input-Output method} \\ &= \mathbf{1,653,159} \text{ Btu/hr}\end{aligned}$$

$$\begin{aligned}\text{Losses} &= \text{heat loss due to dry gas} + \text{heat loss due to unburnt carbon} + \text{heat loss due to moisture in the fuel} + \\ &\quad \text{heat loss due to moisture produced from burning hydrogen in the fuel} + \text{heat loss due to moisture} \\ &\quad \text{in the combustion air} + \text{heat loss due to formation of carbon monoxide} + \text{heat loss due to heat in} \\ &\quad \text{atomizing steam} + \text{heat loss due to surface radiation and convection} \\ &= L_g + L_{uc} + L_{mf} + L_{mfh} + L_{ma} + L_{co} + L_z + L_b\end{aligned}$$

Dry Gas

$$\begin{aligned}&\text{Pounds of dry gas per pound of "as fired" fuel (Lg)} \\ W_g' &= ((c\%)(C.\text{Efficiency})(44.01 \text{ (CO}_2) + 32.00 \text{ (O}_2) + 28.02 \text{ (N}_2) + (28.01 \text{ (CO)}/12.01 \text{ (CO}_2+\text{CO})) + \\ &\quad 12.01 \text{ (S)}/32.07\end{aligned}$$

$$W_g' = \mathbf{16.40} \text{ lb dry gas/lb of as fired fuel}$$

$$\begin{aligned}L_g' &= (W_g')(C_{pg})(\text{boiler exit temp} - \text{reference air temperature})(\text{fuel flow rate}) \\ &= \mathbf{129,593} \text{ Btu/hr}\end{aligned}$$

Unburnt Carbon

$$\begin{aligned}L_{uc} &= (\% \text{ Carbon in the "as fired Fuel"})(1 - \text{Comb.Efficiency})(\text{fuel flow rate})(14500) \\ &= \mathbf{20,295} \text{ Btu/hr}\end{aligned}$$

Moisture in Fuel

$$\begin{aligned}L_{mf} &= (\text{lb moisture per lb of fuel})(\text{enthalpy of water vapor at boiler exit temp} - \\ &\quad \text{enthalpy of water at reference temperature})(\text{fuel flow rate}) \\ &= \mathbf{0} \text{ Btu/hr}\end{aligned}$$

Moisture from Burning Hydrogen

$$\begin{aligned}L_{mfh} &= (8.936)(\% \text{ hydrogen in "as fired" fuel})(\text{enthalpy of water vapor @ boiler exit temp} - \\ &\quad \text{enthalpy of water @ reference temperature})(\text{fuel flow rate}) \\ &= \mathbf{100,856} \text{ Btu/hr}\end{aligned}$$

Heat Loss Method - Continued

Moisture in Combustion Air (Primary air only)

Primary Air Flow Rate =	1118 lbs/hr	
lbs Air per lb of Fuel =	13.80 lbs air/lb fuel	
Primary Air % Humidity =	44.2	
Moisture in Primary Air =	0.08 lb water vapor/lb of dry air	(Figure 24-2, p. 748 McCabe and Smith, Unit Operations of Chemical Engineering - 3rd Edition)

$$\begin{aligned} L_{ma} &= (\text{lbs air per lb of fuel})(\text{lb of water vapor per lb of air})(\text{enthalpy of water vapor @ boiler exit temp} - \\ &\quad \text{enthalpy of water vapor @ reference temperature})(\text{fuel flow rate}) \\ &= \mathbf{110,287 \text{ Btu/hr}} \end{aligned}$$

Formation of Carbon Monoxide

$$\begin{aligned} L_{co} &= (\text{CO}/(\text{CO}_2 + \text{CO})) (10160) (\text{Combustion Efficiency}) (\% \text{ carbon in 'as fired fuel}) (\text{fuel flow rate}) \\ &= \mathbf{258 \text{ Btu/hr}} \end{aligned}$$

Atomizing Steam

$$\begin{aligned} L_z &= (\text{lbs of atomizing steam per hour})(\text{enthalpy of water vapor @ boiler exit temp} - \text{enthalpy of} \\ &\quad \text{water vapor @ reference temp}) \\ &= \mathbf{88,166 \text{ Btu/hr}} \end{aligned}$$

Radiation

Maximum Continuous Boiler Output =	2,000,000 Btu/hr
Actual Output =	1,493,397 Btu/hr

$$L_b = \mathbf{8.5 \%} \quad (\text{Figure 8, p. 67, ASME PTC 4.1})$$

$$\text{Total Heat Losses} = \mathbf{589,973 \text{ Btu/hr}}$$

$$\text{Boiler Efficiency} = \mathbf{64.3 \%}$$

Calculation of Pollutant Emission Factors

EPA CFR Title 40 Emissions Factor

$$\# \text{ Pollutant/MMBtu} = (1.194 \times 10^{-7} \times (\text{vol. concentration of pollutant} - \text{ppm})) \times ((3.64(\%H) + 1.53(\%C) + 0.57(\%S) + 0.14(\%N) - 0.46(\%O_2))/GCV) \times 10^6 \times (20.9/(20.9 - \%O_2))$$

(EPA, Code of Federal Register, Title 40, Part 75, Chapter 1, Section 3, pp. 321 -323.)

<u>Pollutant</u>	<u>Emissions Factor (lbs./MM Btu)</u>
CO	0.067
CO ₂	181.6
SO ₂	1.230
NO _x	0.480
Hydrocarbons (C ₁ -C ₃)	0.000

Mass Balance Around the Boiler

Total Mass Input = lbs. of fuel (dry basis) + lbs. of primary air (dry basis) + lbs. of secondary air +
lbs. of cooling air

= 1217 lbs/hr

Conversion of Gas Composition from Volume% to Wt%

	<u>Mole %</u>	<u>lbs in each mole of gas</u>	<u>Weight %</u>	<u>Emission Factors (lbs/MM Btu)</u>	
Oxygen	3.987976444	1.2762	4.21		
Carbon Monoxide	0.004811612	0.0013	0.00	0.036	<-- CO
Carbon Dioxide	13.0	5.7264	18.91	154.1	<-- CO ₂
Sulfur Dioxide	0.088142452	0.0565	0.19	1.519	<-- SO ₂
Nitrogen Oxides	0.03441867	0.0103	0.03	0.426	<-- NO _x
Nitrogen	82.9	23.2127	76.65		<-- Hydrocarbons
Total =	100.0	30.2834	100.00		

Research Boiler Efficiency Calculations

Date of Operation **8/14/06**
 Test Fuel Burned **X1333**
 Test Program **Refinery Int.**

Operating Conditions

System Temperatures (°F)

Primary Air	347
Condensate Return	52
Low Pressure Steam	259
Flue Gas Boiler Exit - West	419
Flue Gas Economizer Inlet	418
Flue Gas Boiler Exit - East	422
High Pressure Steam	333
Stack	230
Bag Filter Entrance	304
Quarl Top	1169
Secondary Air	551
Condensor Water Exit	88
Quarl Bottom	1054
Boiler Feed Water	212
Calorimeter	273
Liquid Fuel	198
Ambient (°C)	24 (75 F)

System Pressures

High Pressure Steam (psig)	92.9
Low Pressure Steam (psig)	2.5
Liquid Fuel (psig)	36.1
Atomizing Media (psig)	58.0
Secondary Air (psig)	63.9
Primary Air (inch w.c.)	7.7

System Flow Rates

Natural Gas (lb/hr)	0
Primary Air (lb/hr)	742
High Pressure Steam (lb/hr)	794
Liquid Fuel (lb/hr)	67.2
Atomizing Media (lb/hr)	79.8
Secondary Air (lb/hr)	165
Solid Fuel (lb/min)	0.0
Cooling Air (lb/hr)	25.0

Flue Gas Analysis (dry basis)

Oxygen (%)	5.1
Carbon Monoxide (ppm)	74
Carbon Dioxide (%)	13.5
Sulfur Dioxide (ppm)	299
Nitrogen Oxides (ppm)	505
Hydrocarbons (ppm)	0

Additional System Data

Steam Quality (%)	98.9
Primary Air Humidity (%RH)	36.6
Feeder Weight (lbs)	0
Combustion Efficiency (%)	98.0
Firing Rate (Btu/hr)	1,130,506

Primary Air Percent Humidity Calculation

Water vapor press. @ ambient temp (atm)	0.0287
Partial press of water @ air temp (atm)	0.0105
Primary Air Percent Humidity (%H)	35.9

Liquid Fuel Analyses

	<u>Weight %</u>
Carbon	90.30
Hydrogen	5.10
Nitrogen	0.35
Sulfur	0.54
Oxygen	3.68
Moisture	0.00
Ash	0.03
Total =	100.00

HHV (determined at constant volume)	16,823	Btu/lb
HHV (determined at constant pressure)	16,836	Btu/lb

Steam Data

Enthalpy of Sat. Liq. (Btu/lb)	304.4 (saturated liquid @ absolute drum pressure)
Enthalpy of Sat. Vapor (Btu/lb)	1,188.4 (saturated vapor @ absolute drum pressure)
Enthalpy of Sat. Vapor (Btu/lb)	1,181.0 (saturated vapor @ absolute atomization pressure)
Enthalpy of Feed Water (Btu/lb)	180.47 (saturated liquid @ feedwater temperature)
Enthalpy of water vap. At Boiler Exit Temp (Btu/lb)	1,249.79 (Superheated steam @ 1psia & exit temperature)
Enthalpy of water at reference temp. (Btu/lb)	48.04 (Sat. liquid @ fuel temperature - 80F)

Boiler Efficiency Calculations (Based on ASME PTC 4.1)

Input - Output Method

$$\text{Efficiency} = (\text{Output}/\text{Input}) * 100$$

$$\text{Output} = (\text{steam flow rate})(\text{steam quality}/100)(\text{enthalpy of steam @ drum pressure} - \text{enthalpy of feedwater}) + (\text{steam flow rate})((100 - \text{steam quality})/100)(\text{enthalpy of water @ drum pressure} - \text{enthalpy of feed water})$$

$$= \quad \mathbf{792,393 \text{ Btu/hr}}$$

$$\text{Input} = (\text{fuel flow rate})(\text{high-heat value of fuel}) + \text{heat credits}$$

$$\begin{aligned} \text{Heat Credits} &= \text{heat supplied in dry primary air} + \text{heat supplied in preheated fuel} + \text{heat supplied in} \\ &\quad \text{atomizing steam} + \text{heat supplied from moisture in primary air} \\ &= \text{Bae} + \text{Bfe} + \text{Bze} + \text{Bmae} \end{aligned}$$

$$\begin{aligned} \text{Bae} &= (\text{flow rate of primary air})(\text{wt\% dry air})(\text{specific heat of air})(\text{primary air temp} - \text{reference air temp}) \\ &= \quad \mathbf{44,772 \text{ Btu/hr}} \quad (\text{assumes primary air temperature of } \sim 350\text{F for } C_p) \end{aligned}$$

$$\begin{aligned} \text{Bfe} &= (\text{flow rate of fuel})(\text{specific heat of fuel})(\text{fuel inlet temp} - \text{reference air temp}) \\ &= \quad \mathbf{3,237 \text{ Btu/hr}} \end{aligned}$$

$$\begin{aligned} \text{Bze} &= (\text{flow rate of atomizing steam})(\text{enthalpy of atomizing steam} - \text{enthalpy of sat. vapor @ reference temp}) \\ &= \quad \mathbf{90,408 \text{ Btu/hr}} \end{aligned}$$

$$\begin{aligned} \text{Bmae} &= (\text{flow rate of primary air})(\text{wt\% water vapor in dry air})(\text{specific heat of water vapor})(\text{primary air temp} - \text{reference air temp}) \\ &= \quad \mathbf{5,895 \text{ Btu/hr}} \quad (\text{assumes primary air temperature of } \sim 350\text{F for } C_p) \end{aligned}$$

$$\text{Input} = \quad \mathbf{1,274,818 \text{ Btu/hr}}$$

$$\text{Boiler Efficiency} = \quad \mathbf{62.2 \%}$$

Heat Loss Method

$$\text{Efficiency} = (\text{Losses}/\text{Input}) * 100$$

$$\begin{aligned}\text{Input} &= \text{determined from Input-Output method} \\ &= \mathbf{1,274,818} \text{ Btu/hr}\end{aligned}$$

$$\begin{aligned}\text{Losses} &= \text{heat loss due to dry gas} + \text{heat loss due to unburnt carbon} + \text{heat loss due to moisture in the fuel} + \\ &\quad \text{heat loss due to moisture produced from burning hydrogen in the fuel} + \text{heat loss due to moisture} \\ &\quad \text{in the combustion air} + \text{heat loss due to formation of carbon monoxide} + \text{heat loss due to heat in} \\ &\quad \text{atomizing steam} + \text{heat loss due to surface radiation and convection} \\ &= L_g + L_{uc} + L_{mf} + L_{mfh} + L_{ma} + L_{co} + L_z + L_b\end{aligned}$$

Dry Gas

$$\begin{aligned}&\text{Pounds of dry gas per pound of "as fired" fuel (Lg)} \\ W_g' &= ((c\%)(C.\text{Efficiency})(44.01 \text{ (CO}_2\text{)} + 32.00 \text{ (O}_2\text{)} + 28.02 \text{ (N}_2\text{)} + (28.01 \text{ (CO)}/12.01 \text{ (CO}_2\text{+CO))} + \\ &\quad 12.01 \text{ (S)}/32.07\end{aligned}$$

$$W_g' = \mathbf{16.58} \text{ lb dry gas/lb of as fired fuel}$$

$$\begin{aligned}L_g' &= (W_g')(C_{pg})(\text{boiler exit temp} - \text{reference air temperature})(\text{fuel flow rate}) \\ &= \mathbf{91,053} \text{ Btu/hr}\end{aligned}$$

Unburnt Carbon

$$\begin{aligned}L_{uc} &= (\% \text{ Carbon in the "as fired Fuel"})(1 - \text{Comb.Efficiency})(\text{fuel flow rate})(14500) \\ &= \mathbf{17,598} \text{ Btu/hr}\end{aligned}$$

Moisture in Fuel

$$\begin{aligned}L_{mf} &= (\text{lb moisture per lb of fuel})(\text{enthalpy of water vapor at boiler exit temp} - \\ &\quad \text{enthalpy of water at reference temperature})(\text{fuel flow rate}) \\ &= \mathbf{0} \text{ Btu/hr}\end{aligned}$$

Moisture from Burning Hydrogen

$$\begin{aligned}L_{mfh} &= (8.936)(\% \text{ hydrogen in "as fired" fuel})(\text{enthalpy of water vapor @ boiler exit temp} - \\ &\quad \text{enthalpy of water @ reference temperature})(\text{fuel flow rate}) \\ &= \mathbf{36,804} \text{ Btu/hr}\end{aligned}$$

Heat Loss Method - Continued

Moisture in Combustion Air (Primary air only)

Primary Air Flow Rate =	742 lbs/hr	
lbs Air per lb of Fuel =	11.04 lbs air/lb fuel	
Primary Air % Humidity =	35.9	
Moisture in Primary Air =	0.07 lb water vapor/lb of dry air	(Figure 24-2, p. 748 McCabe and Smith, Unit Operations of Chemical Engineering - 3rd Edition)

$$\begin{aligned} L_{ma} &= (\text{lbs air per lb of fuel})(\text{lb of water vapor per lb of air})(\text{enthalpy of water vapor @ boiler exit temp} - \\ &\quad \text{enthalpy of water vapor @ reference temperature})(\text{fuel flow rate}) \\ &= \mathbf{62,419 \text{ Btu/hr}} \end{aligned}$$

Formation of Carbon Monoxide

$$\begin{aligned} L_{co} &= (\text{CO}/(\text{CO}_2 + \text{CO})) (10160) (\text{Combustion Efficiency}) (\% \text{ carbon in 'as fired fuel}) (\text{fuel flow rate}) \\ &= \mathbf{331 \text{ Btu/hr}} \end{aligned}$$

Atomizing Steam

$$\begin{aligned} L_z &= (\text{lbs of atomizing steam per hour})(\text{enthalpy of water vapor @ boiler exit temp} - \text{enthalpy of} \\ &\quad \text{water vapor @ reference temp}) \\ &= \mathbf{95,900 \text{ Btu/hr}} \end{aligned}$$

Radiation

Maximum Continuous Boiler Output =	2,000,000 Btu/hr
Actual Output =	1,130,506 Btu/hr

$$L_b = \mathbf{8.5 \%} \quad (\text{Figure 8, p. 67, ASME PTC 4.1})$$

$$\text{Total Heat Losses} = \mathbf{412,464 \text{ Btu/hr}}$$

$$\text{Boiler Efficiency} = \mathbf{67.6 \%}$$

Calculation of Pollutant Emission Factors

EPA CFR Title 40 Emissions Factor

$$\# \text{ Pollutant/MMBtu} = (1.194 \times 10^{-7} \times (\text{vol. concentration of pollutant} - \text{ppm})) \times ((3.64(\%H) + 1.53(\%C) + 0.57(\%S) + 0.14(\%N) - 0.46(\%O_2))/GCV) \times 10^6 \times (20.9/(20.9 - \%O_2))$$

(EPA, Code of Federal Register, Title 40, Part 75, Chapter 1, Section 3, pp. 321 -323.)

<u>Pollutant</u>	<u>Emissions Factor (lbs./MM Btu)</u>
CO	0.108
CO ₂	196.9
SO ₂	0.436
NO _x	0.737
Hydrocarbons (C ₁ -C ₃)	0.000

Mass Balance Around the Boiler

Total Mass Input = lbs. of fuel (dry basis) + lbs. of primary air (dry basis) + lbs. of secondary air +
lbs. of cooling air

= 916 lbs/hr

Conversion of Gas Composition from Volume% to Wt%

	<u>Mole %</u>	<u>lbs in each mole of gas</u>	<u>Weight %</u>	<u>Emission Factors (lbs/MM Btu)</u>	
Oxygen	5.1	1.6320	5.37		
Carbon Monoxide	0.0074	0.0021	0.01	0.055	<-- CO
Carbon Dioxide	13.5	5.9414	19.55	158.5	<-- CO ₂
Sulfur Dioxide	0.0299	0.0192	0.06	0.511	<-- SO ₂
Nitrogen Oxides	0.0505	0.0152	0.05	0.620	<-- NO _x
Nitrogen	<u>81.3</u>	<u>22.7755</u>	<u>74.96</u>		<-- Hydrocarbons
Total =	100.0	30.3853	100.00		

Appendix 4-C. Emissions Data Sheets

Test No:	RI-PSU-3A					Sampling Parameters			Isokineticity Calc.			
Test Date:	05/24/05					Total H2O (g):	344.3		Vw(std): SCF	16.320		
Fuel Type:	Coal-derived Oil					Total Dust (g):	0.0267		VmC: ACF	62.088		
Cal. Value						Pb (in Hg):	29.9		Vm(std): SCF	61.001		
(Btu/lb)	18,376					Delta H (in H2O):	3.8		Vt(std): SCF	77.321		
						Tm (R):	544		% H2O:	21.11		
Firing Rate:						Ts (R):	850		Vs: FM	1760.752		
lbs/hr	82.2					Ps (in Hg):	29.2		Qn: ACFM	2.400		
Btu/hr	1,510,507					Delta P (in H2O):	0.12		Qn(std): SCFM	1.460		
						Cp:	0.99		% Isokinetic:	56.95		
PSU Method	Total Volume or					Dn (in):	0.5000					
Sample Train	Weight Collected					Total Vm (ACF):	61.687		Dust Loading Calc.			
Splits	(mL or g)					Sample Time (min):	93		DCL: (grains/scf)	0.0053		
Rinse & KCl	1000					Duct Dia: (ft)	0.652		Stack Flow: ACFM	587.575		
H2O2	500								Stack Flow: SCFM	357.475		
KMnO4	500											
Filter	2.4949											
Test 3A Lab Analysis Data - Uncorrected for Split Size (volume or mass)						Test 3A Lab Analysis Data - Corrected Totals						
Analyte	Rinse & KCl (mg/L)	H2O2 (mg/L)	KMnO4 (mg/L)	Filter (mg/kg - Hg) (mg/L - other analytes)		Rinse & KCl (µg)	H2O2 (µg)	KMnO4 (µg)	Filter (µg)	Total (µg)	Total Emissions (lb/10^12 Btu)	
Al	1.94	< 0.01		180		388	< 2.04		89566	89954	36419.10	
As	0.06	0.02		1.08		12.0	4.08		537	553	224.08	
Ba	< 0.01	< 0.01		0.93		< 2.00	< 2.04		463	463	187.35	
Be	< 0.001	< 0.001		0.06		< 0.20	< 0.20		30	30	12.09	
Cd	0.001	0.001		0.006		0.20	0.20		2.99	2.99	1.21	
Co	< 0.01	< 0.01		0.24		< 2.00	< 2.04		119	119	48.35	
Cr	< 0.01	0.01		0.34		< 2.00	2.04		169	171	69.32	
Cu	0.08	< 0.01		0.28		16.0	< 2.04		139	155	62.89	
Hg	0.001	0.001	0.001	1.27		1.00	0.50	0.50	3.17	5.17	2.09	
Mn	105	< 0.01		0.63		21000	< 2.04		313	21313	8629.09	
Mo	< 0.01	< 0.01		0.61		< 2.00	< 2.04		304	304	122.89	
Ni	0.03	< 0.01		0.57		6.00	< 2.04		284	290	117.26	
Pb	0.55	0.010		7.62		110	2.04		3792	3904	1580.45	
Sb	0.04	< 0.01		0.12		8.00	< 2.04		60	68	27.41	
Se	0.01	< 0.01		0.03		2.00	< 2.04		15	17	6.85	
Sr	< 0.01	< 0.01		0.61		< 2.00	< 2.04		304	304	122.89	
V	< 0.01	< 0.01		1.13		< 2.00	< 2.04		562	562	227.64	
Zn	2.42	1.6		1.45		484	320.4		722	1526	617.79	
Baseline No. 6 Oil					Coal-Derived Heavy Oil							
Analyte	(mg/L)	(lb/10^12 Btu)	(mg/L)	(lb/10^12 Btu)								
Al	0.028	635.3	< 0.001	< 18.8								
As	< 0.001	< 22.7	< 0.001	< 18.8								
Ba	0.085	1,928.7	0.058	1,093.3								
Be	< 0.001	< 22.7	< 0.001	< 18.8								
Cd	< 0.001	< 22.7	< 0.001	< 18.8								
Co	0.005	113.5	0.004	75.4								
Cr	0.001	22.7	< 0.001	< 18.8								
Cu	< 0.001	< 22.7	< 0.001	< 18.8								
Hg												
Mn	0.015	340.4	0.005	94.2								
Mo	0.008	181.5	0.007	131.9								
Ni	0.003	68.1	< 0.001	< 18.8								
Pb	0.001	22.7	0.001	18.8								
Sb	0.005	113.5	0.001	18.8								
Se	0.003	68.1	0.002	37.7								
Sr	0.003	68.1	0.002	37.7								
V	0.024	544.6	0.007	131.9								
Zn	0.005	113.5	< 0.001	< 18.8								

Appendix 5-A

FROM	A. ADAMS	TO	G. MITCHELL
	HALL PROCESS IMPROVEMENT		THE PENNSYLVANIA STATE
	TENNESSEE OPERATIONS		UNIVERSITY

2006-02-14

RE: EVALUATION OF COKE DERIVED FROM THE CO-COKING OF COAL AND
PETROLEUM FRACTIONS FOR USE IN HALL CELL ANODES

Letter Report No. 06-038

Summary

At the request of Gareth Mitchell and Les Rudnick of the Pennsylvania State University, a preliminary evaluation of carbonaceous material produced from the delayed coking of a blend of 20% coal and 80% decant oil was conducted. This assessment was made as part of the Refinery Integration Project. The evaluation included a quantitative comparison of the properties of the calcined coke, production of bench-scale anodes, and measurement of the baked apparent density and electrical resistivity of the anode specimens.

The calcined coke product produced from the co-coking process had an ash content too high to be suitable for use in anodes. Specifically, the silicon and iron content of the calcined co-coke were well above current specifications, and would result in unacceptable metal purity for a commercial smelter. This finding would eliminate the material from being a candidate coke source for anodes. Other results were more encouraging. Concentrations of other undesirable oxidation catalysts were lower than standard petroleum coke. Additionally, the properties of the baked anodes (baked apparent density and electrical resistivity) were improved with utilization of the co-coked carbon. If the silicon and iron levels can be sufficiently decreased to < 300 ppm each, it is recommended that the co-coked material be reevaluated as a potential coke source for anodes.

Experimental

Coke Analysis

The green coke was analyzed by A.J. Edmond Company using standard industrial practices. Tests included in the evaluation are listed below:

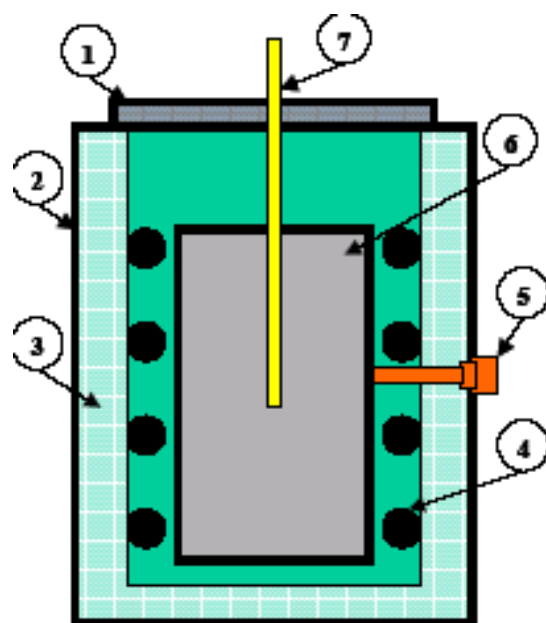
1. Vibrated bulk density (g/cc)
2. Moisture (%)
3. Mercury porosity (mm³/g)

4. Isotropic coke (%)*
5. Specific electrical resistance (Ω -in)
6. Hardgrove grindability index
7. Volatile matter (%)
8. Ash (%)
9. Elemental analysis
 - a. Calcium
 - b. Iron
 - c. Sodium
 - d. Nickel
 - e. Silicon
 - f. Vanadium
 - g. Sulfur

*It should be noted that in this case the term isotropic coke refers to the presence of shot coke. This material is identified by its spherical BB-type appearance. It does not refer to the microtexture of the coke as observed by ASTM optical light microscopy procedures.

Coke Calcining and Sizing

The green coke was also calcined at A.J. Edmond Company using a stagnant calciner. A schematic of the coke calciner used is given in Figure 1. 3.5 kg of coke was loaded into the calciner, heated to the desired calcination temperature, and allowed to soak for 10 minutes. The standard practice for A.J. Edmond is to calcine the material to a temperature of 1325°C. For typical petroleum cokes, this results in a real density of 2.06 g/cc. For the co-coke material, 1325°C resulted in a real density of 2.11 g/cc. A.J. Edmond decided to back off on temperature to 1275°C, which resulted in a real density of 2.08 g/cc. They decided not to reduce the temperature any further. The reported density is an average of the different runs needed to calcine the 19 kg of coke shipped from Penn State.



Calcining Furnace

- 1) Insulating Lid
- 2) Steel Shell
- 3) Insulating Brick
- 4) Heating Elements
- 5) Control Thermocouple
- 6) Sample Crucible
- 7) Sample Thermocouple

Figure 1: Schematic of A.J. Edmond Stagnant Coke Calciner Operation

A.J. Edmond crushed and sized the calcined co-coke to a sieve analysis that ATC specified. The sieve analysis was based on work currently going on at the lab. For laboratory anode production, recycled butts from an Alcoa smelter were added to the aggregate. The sieve analysis for the total dry aggregate is given in Table 1.

Table 1: Sieve Analysis of Total Dry Aggregate

	26%	28%	7%	39%
	Butts	Coarse	Intermediates	Fines
-3/4, +1/2	6.2%			
-1/2, +1/4	38.9%	1.1%		
-1/4, +4	10.1%	1.0%		
-4, +8	16.8%	17.7%		
-8, +12	9.8%	41.0%		
-12, +20	6.5%	27.0%	21.9%	0.1%
-20, +28	3.5%	10.0%	10.9%	0.5%
-28, +60	4.7%	2.3%	49.4%	3.4%
-60, +100	1.5%		10.3%	8.4%

-100, +200	1.3%		6.0%	23.8%
-200, +325	0.4%		1.1%	16.1%
-325	0.4%		0.3%	47.7%
	100.0%	100.0%	100.0%	100.0%

Production of Laboratory-Scale Anodes

Bench-scale anodes were produced using the facilities at the Alcoa Technical Center. The aggregate was preheated overnight at the mixing temperature of 160°C. A batch of 4,500 grams of the aggregate was charged to a 10-liter sigma blade mixer and mixed dry for three minutes. The desired amount of pitch was then added to the aggregate. The green paste was mixed for 30 minutes. Four hundred grams of mix were removed from the mixer for pressing into green anodes. The material was pressed into an anode specimen in a 50 mm diameter mold preheated to 135°C. The mix was pressed to 600 bar (8,820 psig) and held at that pressure for 20 seconds.

The amount of pitch needed to increase the pitch level by 0.5% was added then to the mixer and mixed for 3 minutes. Another anode was made. The process was repeated until 10 anodes of varying pitch concentration were produced. The anodes were then baked to a finishing temperature of 1125°C using the temperature profile shown in Figure 2. Once cooled, several measurements were taken to determine the baked apparent density and electrical resistivity of the anode specimens.

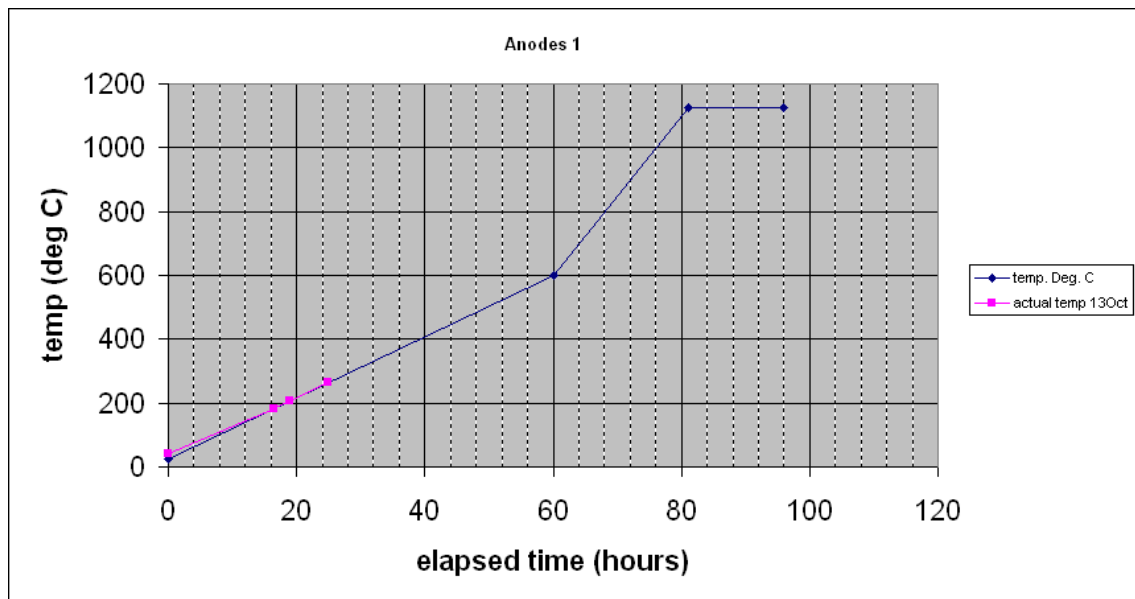


Figure 2: Heat Curve for Anode Baking

Testing of Laboratory-Scale Anodes

Baked Apparent Density

The baked apparent density of the anodes was calculated based on weight and volume measurements. Digital calipers were used to measure the volume of the anode. Four diameter measurements were made 90° apart from each other at the top, center, and bottom of the anode. Four length measurements were taken 90° apart from each other and averaged. Equation 1 was used to calculate the baked apparent density of the anode specimens.

Equation 1: Bake Apparent Density

$$BAD = \frac{W_b}{V_b}$$

Where:

BAD, Baked apparent density (g/cm³)

W_b, weight of baked specimen (g)

V_b, volume of baked specimen (cm³)

Electrical Resistivity

The room-temperature electrical resistivity of the carbon anode specimens was determined using an eight-point method. The ends of the cylindrical specimens were first flattened using a belt sander. The specimen was then placed between two copper plates and nine amps of DC current were applied. A 7.15 cm millivoltmeter probe was placed in eight different spots, 45° apart, around the anode. The voltage drop across the probe was measured, and the electrical resistivity was calculated using Equation 2.

Equation 2: Electrical Resistivity

$$Resistivity = \frac{A \times B}{C \times D}$$

Where:

A, millivolts reading

B, average cross sectional area (cm²)

C, probe length (cm)

D, current supplied to sample (amps)

Results

Coke

The calcined coke analysis from A.J. Edmond is summarized below. To put the results into context, an analysis from the calcined coke used to make the standard anodes in this study are included along with a list of ideal specifications. It should be noted that coke specifications are plant-dependent and are a function of the type of metal produced and the environmental regulations in effect at each location. A coke that could meet the desired specification limits listed below would have wide-spread applicability across the Alcoa smelting system.

Table 2: Calcined Coke Analysis

Origin	Alcoa	Alcoa	PSU
Type	Calcined coke	Calcined Coke	Calcined Coke
Description	Ideal target specifications	Calcined coke used in production of “standard” anodes	80% EI-107 Oil/20% EI-186 Pitts Seam Coal
VBD -30 +50 (g/cc) (USM)	>0.85	0.86	0.925
Real Density (g/cc-He)	> 2.04	2.06	2.082
Sulfur (S)	<2.5	2.5	1.34
Ash%	< 0.5	0.3	0.89
Calcium (Ca)	< 200	200	262
Iron (Fe)	< 300	350	684
Nickel (Ni)	< 250	250	7
Silicon (Si)	< 250	200	1013
Sodium (Na)	< 200	75	54
Vanadium (V)	< 200	350	18
Moisture %	< 0.5	ND	ND
Volatile Content Matter %	<0.5	ND	0.71
Spec. Elec. Resistivity (ohm-in.)	<0.05	ND	0.035
HGI	~ 30	ND	23.7

The results show that co-coke is a very hard, dense material. Concentrations of the aluminum mental contaminants silicon and iron are significantly higher than currently-used anode grade coke, and would negatively impact metal purity. On the other hand, concentrations of nickel and vanadium, oxidation catalysts, are well under the desired limit of 200 ppm, and would likely contribute to increase anode life. Additionally, the sulfur level of 1.34% is less than the typical 2.0-2.5% of most anode grade material, and would assist plants in meeting environmental specifications.

Anodes

As a first-cut evaluation, the baked apparent density and electrical resistivity of the anodes were considered. The baked apparent densities of anodes made from standard and co-coke coke are shown below in Figure 3. It is estimated that the maximum baked apparent density is achieved at 17.0% pitch for both sets of test anodes. The maximum density achieved for the standard and co-coke anodes is 1.57 and 1.63 g/cc, respectively. The density of the co-coke anodes is considered significantly higher and, if realized in commercial production, would extend the life of the anode.

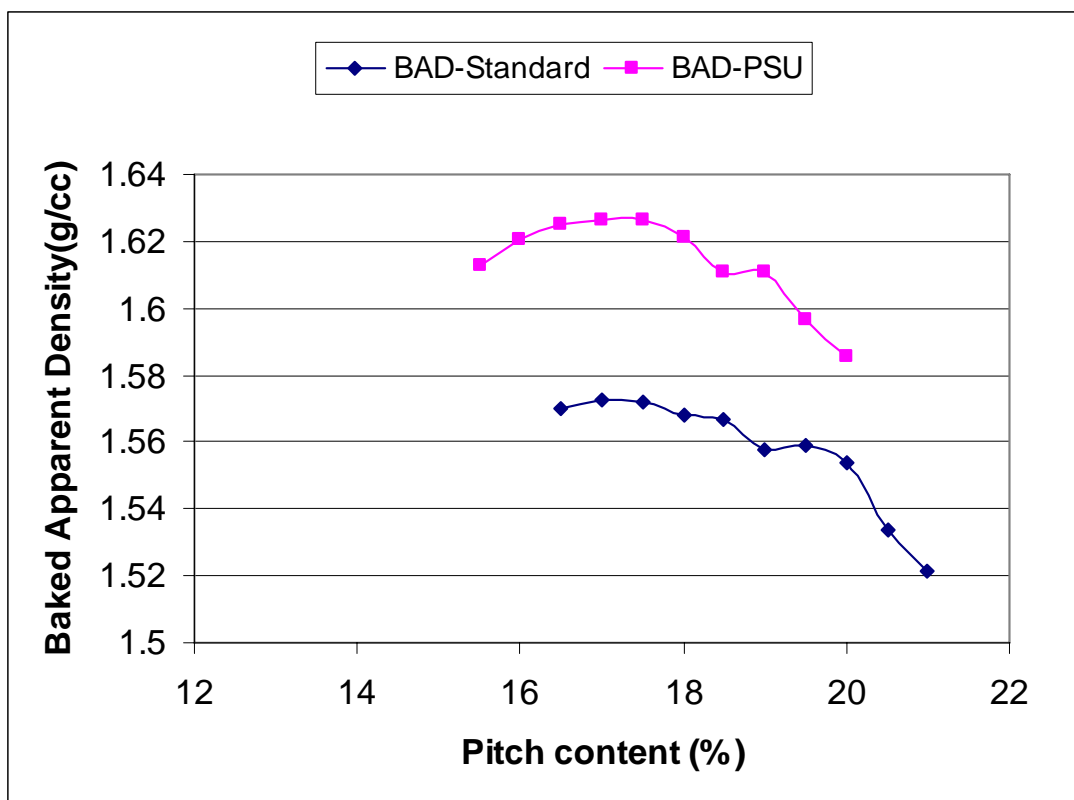


Figure 3: Baked Apparent Density of Penn State and Standard Anode Specimens

At 17% pitch the electrical resistivities of the Penn State and standard anodes are 53 and 64 $\mu\Omega$ -m respectively. This is also a significant difference between the two types of anodes. If realized in commercial production, energy savings in the form of reduced voltage drop across the anodes could be realized with the co-coke material.

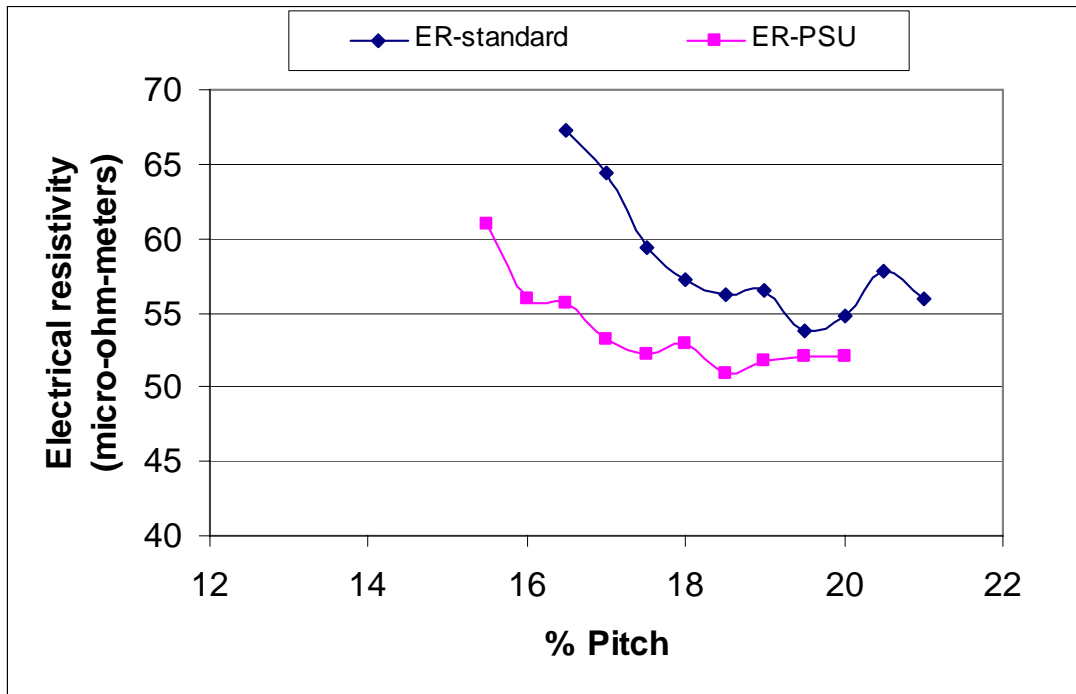


Figure 4: Electrical Resistivity of Penn State and Standard Anodes

Conclusions

The iron and silicon content of the calcined co-coke material evaluated would immediately rule it out as a candidate coke source for use in anodes. The concentration of silicon and iron were 1013 and 684 ppm, respectively, where the target specification limit is < 300 ppm for both elements. However, if these two impurities could be reduced to below 300 ppm each, a more comprehensive evaluation of the material would be warranted because of other favorable characteristics. The high density and low concentration of oxidation catalysts in the coke could contribute to increased anode life. The low sulfur content could assist plants in meeting their environmental requirements for SO₂ emissions.

A full evaluation of the coke would include production of several batches of anodes and testing of the cores for air and CO₂ reactivity, compressive and flexural strength, air permeability, and thermal conductivity.

Acknowledgements

Doug Bruce is gratefully acknowledged for conduction of the bench anode production and testing. Mark Wyborney from A.J. Edmond Company is acknowledged for calcining the coke and providing the coke analysis.

A. N. ADAMS

cg0456

cc: ID-D